International Association of Geodesy Symposia
141

Urs Marti *Editor*

Gravity, Geoid and Height Systems

Proceedings of the IAG Symposium GGHS2012, October 9–12, 2012, Venice, Italy

Springer

International Association of Geodesy Symposia

Chris Rizos, Series Editor
Pascal Willis, Assistant Series Editor

More information about this series at
http://www.springer.com/series/1345

International Association of Geodesy Symposia

Chris Rizos, Series Editor
Pascal Willis, Assistant Series Editor

Symposium 101: Global and Regional Geodynamics
Symposium 102: Global Positioning System: An Overview
Symposium 103: Gravity, Gradiometry, and Gravimetry
Symposium 104: Sea SurfaceTopography and the Geoid
Symposium 105: Earth Rotation and Coordinate Reference Frames
Symposium 106: Determination of the Geoid: Present and Future
Symposium 107: Kinematic Systems in Geodesy, Surveying, and Remote Sensing
Symposium 108: Application of Geodesy to Engineering
Symposium 109: Permanent Satellite Tracking Networks for Geodesy and Geodynamics
Symposium 110: From Mars to Greenland: Charting Gravity with Space and Airborne Instruments
Symposium 111: Recent Geodetic and Gravimetric Research in Latin America
Symposium 112: Geodesy and Physics of the Earth: Geodetic Contributions to Geodynamics
Symposium 113: Gravity and Geoid
Symposium 114: Geodetic Theory Today
Symposium 115: GPS Trends in Precise Terrestrial, Airborne, and Spaceborne Applications
Symposium 116: Global Gravity Field and Its Temporal Variations
Symposium 117: Gravity, Geoid and Marine Geodesy
Symposium 118: Advances in Positioning and Reference Frames
Symposium 119: Geodesy on the Move
Symposium 120: Towards an Integrated Global Geodetic Observation System (IGGOS)
Symposium 121: Geodesy Beyond 2000: The Challenges of the First Decade
Symposium 122: IV Hotine-Marussi Symposium on Mathematical Geodesy
Symposium 123: Gravity, Geoid and Geodynamics 2000
Symposium 124: Vertical Reference Systems
Symposium 125: Vistas for Geodesy in the New Millennium
Symposium 126: Satellite Altimetry for Geodesy, Geophysics and Oceanography
Symposium 127: V Hotine Marussi Symposium on Mathematical Geodesy
Symposium 128: A Window on the Future of Geodesy
Symposium 129: Gravity, Geoid and Space Missions
Symposium 130: Dynamic Planet - Monitoring and Understanding . . .
Symposium 131: Geodetic Deformation Monitoring: From Geophysical to Engineering Roles
Symposium 132: VI Hotine-Marussi Symposium on Theoretical and Computational Geodesy
Symposium 133: Observing our Changing Earth
Symposium 134: Geodetic Reference Frames
Symposium 135: Gravity, Geoid and Earth Observation
Symposium 136: Geodesy for Planet Earth
Symposium 137: VII Hotine-Marussi Symposium on Mathematical Geodesy
Symposium 138: Reference Frames for Applications in Geosciences
Symposium 139: Earth on the Edge: Science for a Sustainable Planet
Symposium 140: The 1st International Workshop on the Quality of Geodetic Observation and Monitoring Systems (QuGOMS'11)

Gravity, Geoid and Height Systems

Proceedings of the IAG Symposium GGHS2012,
October 9-12, 2012, Venice, Italy

Edited by

Urs Marti

Springer

ISSN 0939-9585
ISBN 978-3-319-10836-0 ISBN 978-3-319-10837-7 (ebook)
DOI 10.1007/978-3-319-10837-7
Springer Cham Heidelberg New York Dordrecht London

Library of Congress Control Number: 2014958313

Associate Editors

Preface

These proceedings include a selection of 42 papers presented at the IAG international symposium "Gravity, Geoid and Height Systems 2012" (GGHS2012), which was organized by IAG Commission 2 "Gravity Field" with the assistance of the International Gravity Field Service (IGFS) and GGOS Theme 1 "Unified Global Height System." It was arranged by the OGS (Istituto Nazionale di Oceanografia e di Geofisica Sperimentale, Trieste) which has presently the role of the Central Bureau of the IGFS. The symposium was successfully held on the island of San Servolo in the Venetian Lagoon from October 9 to 12, 2012, with 140 participants from 31 countries. 30 of them were registered as students who had free access to the symposium. The list of participants and other information can be downloaded from the website of the IGFS Central Bureau www.gravityfield.org.

GGHS2012 was the fifth event of the traditional conferences organized by IAG Commission 2 every 4 years after "Gravity, Geoid and Marine Geodesy" (Tokyo, Japan, 1996), "Gravity, Geoid and Geodynamics" (Banff, Canada, 2000), "Gravity, Geoid and Space Missions" (Porto, Portugal, 2004), and "Gravity, Geoid and Earth Observation" (Chania, Greece, 2008). GGHS2012 covered all activities of IAG Commission 2 except from satellite altimetry, which was covered in a special symposium "20 years of progress in radar altimetry" just 2 weeks before the GGHS2012—as well held in Venice.

An important part of the conference was the presentation of the results of the very successful space missions GRACE and GOCE and their application in oceanography, mass transport and solid earth modeling, hydrology, and atmospheric sciences. Special attention was given to the loss of ice masses over Greenland and Antarctica and the resulting global sea level rise. Another important topic of the conference was the continuation of gravity space missions. It seems now that a GRACE follow-on mission is advancing well and probably can be launched in 2017 as a result of a collaboration of American and European agencies.

The various groups working on the realization of a global height system met during the conference and presented their results. The realization of a global height system which can be presented to other interested institutions and be adopted by the scientific communities seems to be possible in the near future.

Another open issue of the gravity community is the replacement of the outdated International Gravity Standardization Network IGSN71 by considering modern absolute measurements and the time series of superconducting gravimeters. These activities in the corresponding working groups are on a good way and the future of the international comparison campaigns of absolute gravimeters could be assured for the next years.

A total of 89 oral presentations and 64 posters were presented during the conference. A part of them can be downloaded at the IAG Commission 2 website at www.iag-commission2.ch. The presentations were organized in the following eight sessions:

Session 1 Gravimetry and Gravity Networks
Conveners: Leonid Vitushkin, **Herbert Wilmes**, Vojtech Pálinkáš
Session 2 Global Gravity Field Modeling, Assessments and Applications
Conveners: **Jianliang Huang**, Thomas Gruber, Roger Haagmans
Session 3 Future Gravity Field Missions
Conveners: Roland Pail, **Isabelle Panet**
Session 4 Advances in Precise Local and Regional High-Resolution Geoid Modeling
Conveners: Hussein Abd-Elmotaal, **Riccardo Barzaghi**, Yan Ming Wang
Session 5 Establishment and Unification of Vertical Reference Systems
Conveners: Michael Sideris, **Laura Sánchez**, Daniel Roman
Session 6 Gravity Field and Mass Transport Modeling
Conveners: **Shuanggen Jin**, Jürgen Kusche
Session 7 Modeling and Inversion of Gravity-Solid Earth Coupling
Conveners: **Carla Braitenberg**, Jörg Ebbing
Session 8 Gravity Field of Planetary Bodies
Conveners: **Oliver Baur**, Shin-Chan Han, Pieter Visser

Many thanks go to all the conveners who devoted a lot of time in the compilation of the program of the symposium and helped to make it successful. The conveners outlined in bold in the above list acted as well as associate editors of these proceedings for their sessions. They organized the reviews and supervised their papers until the final acceptance for publication. Sincere thanks go as well to Pascal Willis, the editor-in-chief of the IAG Symposia series who advanced and kept on track the publication of these proceedings and to the co-organizers of the conference Rene Forsberg and Michael Sideris.

The Local Organizing Committee was led by Iginio Marson and consisted of Bruno Cataletto, Dario Colonello, Franco Coren, Margherita Persi, and Michele Zennaro. It was invaluable in helping arrange a very memorable conference and provided essential support before, during, and after the conference. And lastly, sincere thanks go out to all the participating scientists and graduate students who made the GGHS2012 symposium and these proceedings a success.

Wabern, Switzerland Urs Marti
14 June 2013

Contents

Part I

Gravimetry and Gravity Networks

Towards the Establishment of New Gravity Control in Poland

J. Krynski, M. Barlik, T. Olszak, and P. Dykowski

Abstract

The existing Polish gravity control (POGK) was established in the last few years of twentieth century (Sas-Uhrynowski et al. (A new national gravity control network—POGK97 (in Polish). Proceedings of the Institute of Geodesy and Cartography, 1999); Sas-Uhrynowski et al. (A new gravimetric control network for Poland. Reports on Geodesy, 2000)) according to the international standards (Boedecker (BGI Bull d'Inf 63:51–56, 1988)). It is based on 12 absolute gravity stations surveyed with four different types of absolute gravimeters. Relative measurements performed by various groups on nearly 350 points with the use of LaCoste & Romberg (LCR) gravimeters were linked to those 12 stations.

The development of absolute gravity survey technologies, in particular instruments for precise field absolute gravity measurements, provides an opportunity to establish a new type of gravity control consisting of stations surveyed with absolute gravimeters. The projects of the densification of the gravity control with absolute gravity measurements using the A10 gravimeter were performed in France (Duquenne et al. (Gravity measurements on the French geodetic network. Symposium of the IAG subcommission for Europe (EUREF), Vienna, 2005)) and in Germany (Falk et al. 2009). The establishment and maintenance of this kind of gravity control is much easier than the one performed with the use of relative gravity measurement technique. It also better fulfills the recent requirements of geodesy and geodynamics in terms of accuracy and efficiency of its re-survey. The two absolute gravimeters: the FG5-230 of the Warsaw University of Technology and the A10-020 of the Institute of Geodesy and Cartography, Warsaw, along with a set of LCR gravimeters are available to be used for the establishment of new gravity control in Poland planned for the years 2012–2014.

New gravity control will consist of 28 fundamental points (surveyed with the FG5 gravimeter), and 169 base points (surveyed with the A10 gravimeter). Base points include chosen existing POGK points, POLREF and EUVN stations, as well as eccentric stations of the Active Geodetic Network (ASG-EUPOS). The fundamental stations are located in the

J. Krynski • P. Dykowski (✉)
Institute of Geodesy and Cartography, 27 Modzelewskiego St, 02-679 Warsaw, Poland
e-mail: jan.krynski@igik.edu.pl; przemyslaw.dykowski@igik.edu.pl

M. Barlik • T. Olszak
Warsaw University of Technology, Pl. Politechniki 1, 00-661 Warsaw, Poland

U. Marti (ed.), *Gravity, Geoid and Height Systems*, International Association of Geodesy Symposia 141,
DOI 10.1007/978-3-319-10837-7_1,

basements of buildings, 14 of them coincide with those of the existing gravity control, while base stations are well monumented field stations. Methodology and measurement schemes for both gravimeters, as well as the technology for vertical gravity gradient determinations in the new gravity control were developed and tested. Also the way to assure proper gravity reference level with relation to ICAG (International Comparison of Absolute Gravimeters) and ECAG (European Comparison of Absolute Gravimeters) campaigns as well as local absolute gravimeter comparisons are described. As the new gravity control will be based on absolute gravity determinations, metrology plays an especially important part of the whole project. Integral part of the project are proposals of re-computation of old gravity data and their transformation to a new system (as second order network) as well as a definition of gravity system as "zero-tide" system.

Keywords
Gravity control • Absolute gravimeter • Gravity system • Metrology

1 The Existing Polish Gravity Control (POGK)

The existing Polish gravity control (POGK) has been established between 1994 and 1997 (Sas-Uhrynowski et al. 1999, 2000) according to the international standards (Boedecker 1988). It is based on 12 absolute gravity stations (1 in 26,000 km^2) surveyed with four different types of absolute gravimeters (teams from Finland, Germany, Italy, Poland, and United States). Relative measurements on 363 points (1 in 870 km^2) performed by various groups with the use of LaCoste & Romberg (LCR) gravimeters were linked to those 12 absolute gravity stations (Fig. 1). A network of 24 long spans connecting absolute gravity stations, surveyed with LCR gravimeters with the use of the strategy developed by the Institute of Geodesy and Cartography (IGiK), Warsaw, was established to verify the consistency of absolute gravity measurements (Krynski et al. 2003).

The POGK was the basis of the extensive analysis and unification of gravity data from the area of Poland that resulted in developing local quasigeoid models of a centimetre accuracy (e.g. Krynski and Lyszkowicz 2006, 2007; Krynski 2007).

From 1999 the Polish gravity control, including gravimetric calibration baselines, was being systematically modernized (Barlik et al. 2010). Twenty new absolute gravity stations were surveyed with the FG5-230 gravimeter of the Warsaw University of Technology (WUT): five for network densification (1 in 18,500 km^2); seven for Central Gravimetric Calibration Baseline; four for Western Gravimetric Calibration Baseline; two for newly established Vertical Gravimetric Calibration Baseline in the Tatra Mountains; and two for newly established Vertical Gravimetric Calibration Baseline in the Sudety Mountains. Also two new network points were set up. New stations were linked with the gravity network by means of 14 spans measured with the LCR gravimeters. In addition, 13 new long spans connecting absolute gravity stations were measured with the LCR gravimeters to verify the consistency of absolute gravity measurements in the network (Fig. 2).

2 The Need for the New Gravity Control in Poland

The extension of Polish gravity control by the new absolute gravity stations as well as gravity network stations within its modernization process created the need for re-adjustment of the modernized gravity network. Activities towards modernization of Polish gravity control indicated substantial discrepancy between the values of absolute gravity measured at some stations. Moreover, field reconnaissance conducted in 2009, supplemented by visiting gravity stations while running different projects in the area, showed that almost 100 stations of existing gravity control were destroyed or not found. Recognizing the role of geodynamics in modern vertical and gravity reference systems (Krynski and Barlik 2012) and that existing gravity control in Poland has significant weaknesses, the need of new gravity control in Poland had been strongly suggested to the Head Office of Geodesy and Cartography, Warsaw, responsible for geodetic control in the country. Simultaneously the development of technologies of absolute gravity measurements has opened new possibilities of replacing traditional methods of establishing gravity control with the use of absolute gravity surveys on field stations. Availability of the FG5 as well as the A10 absolute gravimeters and the experience gained in the gravity control re-surveying with the FG5-230 (e.g. Walo 2010) and the A10-020 (e.g. Mäkinen et al. 2010) were also important factors supporting that suggestion. It should be noted that this type of gravity control is so far one of a few planned and performed in the world.

Fig. 1 Polish gravity control (POGK) 1994–1997

3 Objectives of the Establishment of the New Gravity Control in Poland

Development of absolute gravity survey technologies, in particular instruments for precise field gravity measurements, provides an opportunity to establish a new type of gravity control consisting of stations surveyed with absolute gravimeters. The establishment and maintenance of this kind of gravity control is much easier than the traditional one performed with the use of relative gravity measurement technique. Modern gravity control (using absolute measurements) will also better fulfill the needs of contemporary geodesy and geodynamics considering the temporal variations of the gravity field (Krynski 2012).

The concept of the new gravity control should take into account and incorporate:

- recent technological development,
- accuracy and reliability requirements,
- assurance of its efficient maintenance.

The new gravity control in Poland should assure proper gravity reference level with relation to ICAG and ECAG campaigns. As many as possible existing POGK stations should be included in the new gravity control to link it with the historical networks and to enable an estimate of gravity changes across the country. On the other hand, as many eccentric stations of the ASG-EUPOS system as possible should be included in the new gravity control to build up the integrated geodetic network.

Gravity stations of the modern gravity control should be classified into two groups. The first group consists of the fundamental stations located in buildings, and surveyed possibly in one epoch with the use of the FG5-type gravimeters. The second group consists of the base stations, surveyed in a few campaigns within 2 years with the use of portable A10-type gravimeters. The suggested uncertainty level of gravity determined should not exceed 4 μGal, and 10 μGal at the fundamental stations, and at the base stations, respectively.

The average distribution of stations has been suggested as follows: one fundamental station in 15,000 km^2 and one base station in 2,000 km^2. Special requirements have also been specified for the location of the stations of the gravity control. All gravity control stations need a solid monumentation ensuring durability and stability required for absolute gravity measurements and their repeatability.

At all fundamental stations the same strategies of measuring gravity and the vertical gravity gradient should be applied, if possible. Also at all base stations the measurements

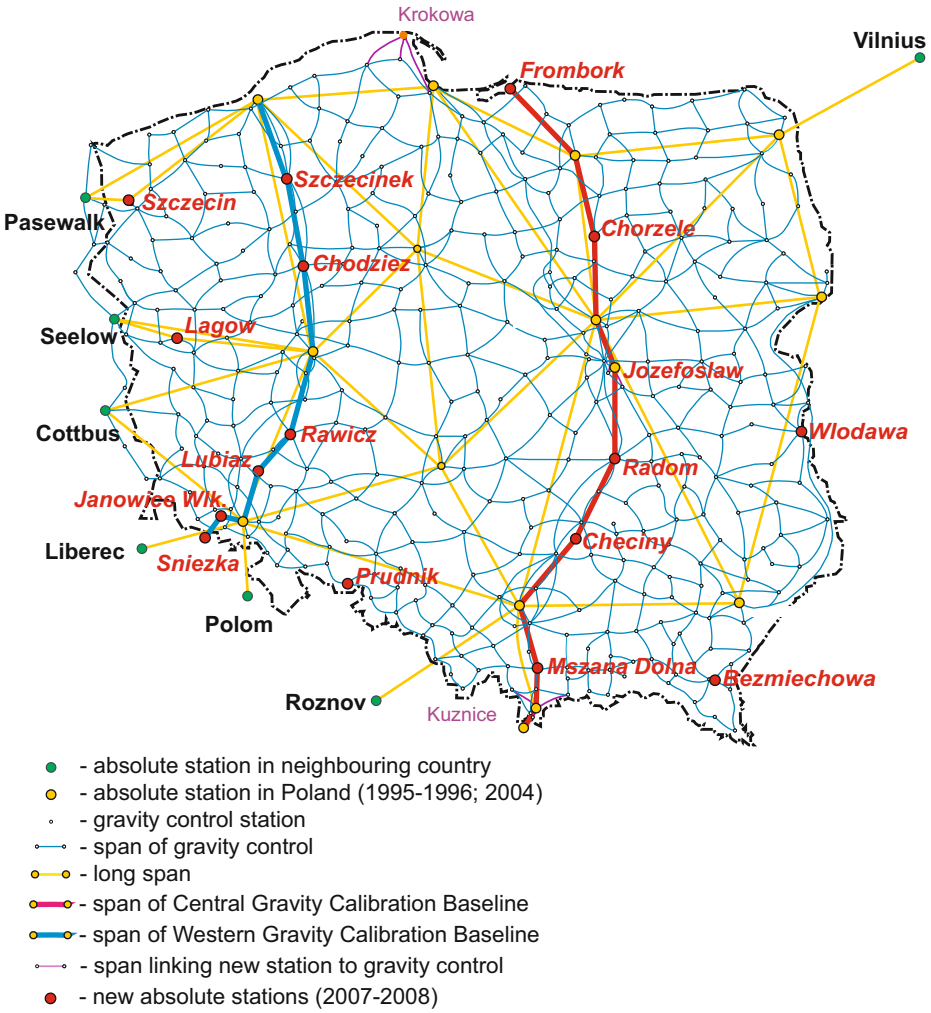

Fig. 2 Modernization of Polish gravity control (POGK) 1999–2010

of gravity and the determinations of vertical gravity gradient should be performed with the use of the same measuring strategies.

Temporal variations of gravity in the gravity control should be monitored by regular periodic re-survey of gravity control stations. Additional monitoring of those variations should be supported by the network of gravity stations equipped with superconducting (SG) gravimeters that are regularly calibrated with the use of free-fall gravimeters.

The gravity reference level of the gravity control should be determined by metrological procedures and parameters in relation to ICAG and ECAG campaigns. More frequent verification of gravity reference level should be performed by simultaneous FG5 and A10 gravity measurements, within the so called local absolute gravimeter comparisons.

Two absolute gravimeters: the FG5-230 of WUT and the A10-020 of IGiK, along with a set of LCR gravimeters are available to be used for the establishment of new gravity control in Poland. The results of last few ICAG and ECAG campaigns indicate that the uncertainty of gravity determined with the FG5-type gravimeters is better than 4 μGal. It concerns in particular the FG5-230 gravimeter what has been shown in numerous comparisons with other FG5 gravimeters, including ICAG2009. The accuracy and the repeatability of the A10-020 gravimeter was widely investigated by the authors. The results obtained together with those from ICAG2009 (offset of 3.2 μGal) and ECAG2011 (offset of 5.8 μGal) show that the A10-020 is able to fulfill the desired uncertainty level of 10 μGal (Dykowski et al. 2012).

4 Design and Realization of the New Gravity Control in Poland

The project of the new gravity control in Poland developed in 2011 by the team of IGiK and WUT has been accepted in 2012 by the Head Office of Geodesy and Cartography (Barlik et al. 2011). New gravity control is to be established within the years 2012–2014. It will consist of 28 fundamental points (surveyed with the FG5 gravimeter) (1 in 15,000 km^2 and 7 of the gravimetric calibration baselines) and 169 base points

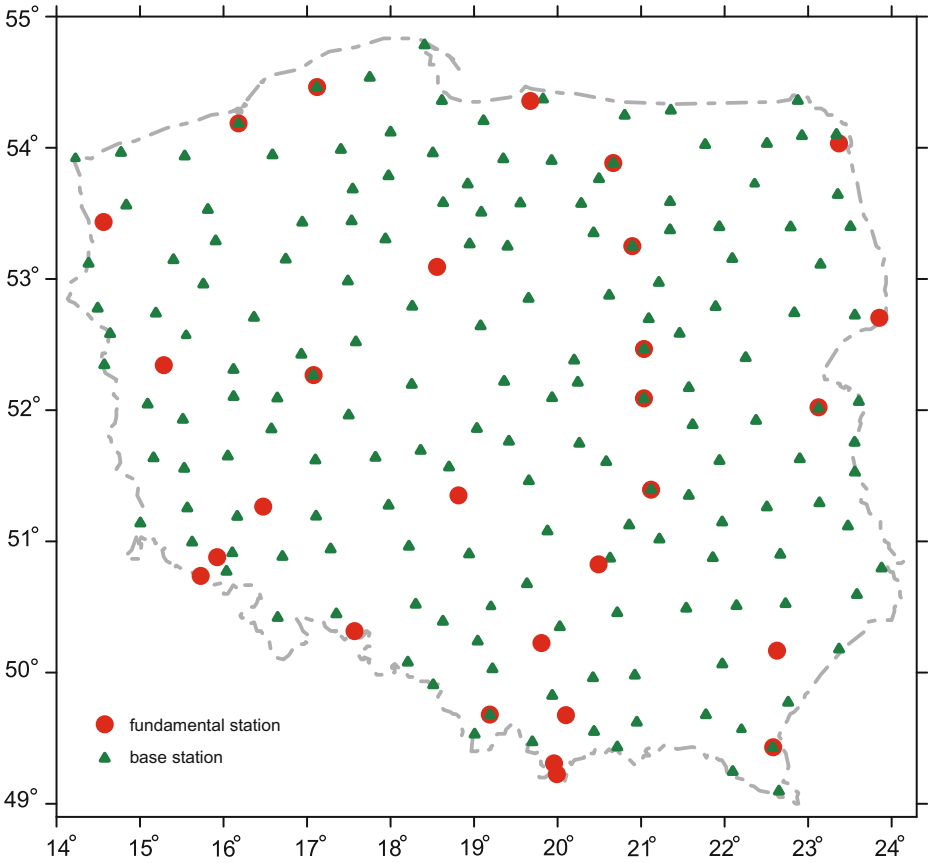

Fig. 3 New gravity control in Poland to be established within the years 2012–2014

(surveyed with the A10 gravimeter) (1 in 2,000 km^2) (Fig. 3). Base points include chosen existing POGK points (87), POLREF (9) and EUVN (5) stations, as well as eccentric stations of the Active Geodetic Network (ASG-EUPOS) network (63). Fundamental stations are located in the basements of buildings, 14 of those coincide with the existing gravity control while base stations are well-monumented field stations. The uncertainty level of gravity determined at fundamental stations and at base stations would not exceed 4 μGal, and 10 μGal, respectively.

To each fundamental station two eccentric stations are assigned: one of them possible in the vicinity of the fundamental station and the second—the closest base station. The spans of the triangle formed by the fundamental station and eccentric stations will be surveyed using spring gravimeters.

All stations of new gravity control in Poland will have position and height determined in the national datum. The base stations with coordinates precisely determined using appropriate static GNSS survey (class B standard according to EUREF) will be included into the national combined geodetic network.

Methodology and measurement schemes for both gravimeters as well as the technology for vertical gravity gradient determinations in the new gravity control were developed and tested (Walo 2010; Dykowski et al. 2012).

Absolute gravity determination at the fundamental station is based on the measurements of 24 series of minimum 100 drops, every 10 s each in 1 h time intervals. Vertical gravity gradient at the fundamental station will be derived from the two independent gravity measurements using a spring gravimeter at four levels (cm): 0–60–100–140–140–100–60–0 (Barlik et al. 2011).

Absolute gravity measurement at the base station will consist of at least two independent setups, each of 8 series of 120 drops, every 1 s each in 3 min time intervals. Vertical gravity gradient at the base station will be derived from the two independent gravity measurements using a spring gravimeter at six levels (cm): 20–40–60–80–100–120–100–60–20. Special stand manufactured at IGiK will be used for the determination of vertical gravity gradient at base stations (Fig. 4) (Dykowski 2012). Internal compliance (measurement error) of a single relative survey should be smaller than 10 μGal. Difference between reductions obtained from two vertical gradient determinations should not exceed 5 μGal for fundamental stations and 10 μGal for base stations.

Also the way to assure the proper gravity reference level with relation to ICAG and ECAG campaigns as well as local absolute gravimeter comparisons are described. As the new gravity control will be based on absolute gravity determinations, metrology plays an especially important part of the

Fig. 4 Gravity measurements at a field station for vertical gradient determination with the use of the stand constructed in the Institute of Geodesy and Cartography, Warsaw

whole project. The technical project of the gravity control (Barlik et al. 2011) states that calibrations for the frequency and length standard should be performed at least twice a year for the A10 gravimeter and for the FG5 gravimeter at least once a year. The results of calibrations will be included in reprocessing of all performed absolute measurements.

5 Gravity Level of the Gravity Control in Poland

The new gravity control in Poland is not any longer a network. The spans between its stations are not expected to be surveyed with the static gravimeters. No traditional network adjustment will be performed since no functional link of the gravity control stations by measurements exists. The role of the adjustment is replaced by employing adequate tools of metrology to all absolute gravity surveys performed.

The gravity level of the gravity control will be determined by using free-fall FG5-type and A10-type gravimeters that participated in the international absolute gravimeter comparison campaigns (ICAG) organized every second year. The FG5-type gravimeters should every year take part in local absolute gravimeter comparison campaign with at least one absolute gravimeter that participated in EURAMET (European Association of National Metrology Institutes) project.

Both FG5-type and A10-type gravimeters used to survey the gravity control should participate at least twice a year in local comparison campaigns. The results obtained will determine a reference for relating gravity observed on base stations with gravity determined on fundamental stations.

Participation in the absolute gravimeter comparison campaigns will provide an estimate of the bias of gravity determined with subsequent gravimeters and their repeatability.

Variability of metrological parameters of FG5-type and A10-type gravimeters makes it necessary to perform their calibration (verification of stability) to ensure reliable determination of gravity. Neglecting variations of metrological parameters may result in observation errors that exceed total uncertainties of the gravimeters. Both, laser and frequency standard of absolute gravimeters used to survey the gravity control should be regularly calibrated. In case of FG5 gravimeter calibration should be performed in the annual cycle while in case of A10—at least twice a year. Calibration data of laser and frequency standard will be applied in reprocessing of gravity measurements to provide final results of survey.

Regular, periodic gravity measurements with FG5-type and A10-type gravimeters used to survey the gravity control should be repeated on monthly basis at the gravimetric laboratories.

To keep the standard of gravity control it must be regularly re-surveyed every few years. It would be beneficial to run a number of stations continuously recording gravity, equipped preferably with SGs, in the area covered with the gravity control.

The determination of the gravity reference level with the use of high-precision absolute gravimeters is affected by hydrology (local, global). The global hydrological effect will be computed with the use of WorldGAP Hydrology Model (WGHM) output (Döll et al. 2003). Its range for the stations across Poland does not exceed 4 μGal (peek to peek). Estimation of the local hydrological effect is, however, difficult and could be performed only for a few gravity stations.

The integral part of the project is a proposal of recomputation of old gravity data and their transformation to a new system (as second order network) as well as a definition of gravity system as "zero-tide" system.

Acknowledgements The research was carried out within the framework of the statutory project "Problems of geodesy and geodynamics" of the Institute of Geodesy and Cartography, Warsaw, and in the framework of the statutory project "Investigation of the geoid shape by geodetic, gravimetric and astronomical methods" at the Department of Geodesy and Geodetic Astronomy of the Warsaw University of Technology.

References

Barlik M, Krynski J, Olszak T, Sas A, Pachuta A, Cisak M, Prochniewicz D, Walo J, Szpunar R (2010) Modernization of absolute gravity zero order network in Poland. In: IAG symposium on terrestrial gravimetry: static and mobile measurements (TG-SMM2010), Saint Petersburg, Russia, 22–25 June 2010, pp 112–115

Barlik M, Krynski J, Olszak T, Cisak J, Pachuta A, Dykowski P, Walo J, Zak L, Szpunar R, Jedrzejewska A, Marganski S, Prochniewicz D, Drozdz M (2011) Design and control survey of gravity control in Poland—first stage (in Polish). Technical report for the Head Office of Geodesy and Cartography

Boedecker G (1988) International absolute gravity basestation network (IAGBN)—absolute gravity observations data processing standards and station documentation. BGI Bull d'Inf 63:51–56

Döll P, Kaspar F, Lehner B (2003) A global hydrological model for deriving water availability indicators: model tuning and validation. J Hydrol 270:105–134

Duquenne F, Duquenne H, Gattacceca T (2005) Gravity measurements on the French geodetic network. In: Symposium of the IAG subcommission for Europe (EUREF), Vienna, Austria, 1–4 June 2005. http://www.euref-iag.net/symposia/2005Vienna/7-02.pdf

Dykowski P (2012) Vertical gravity gradient determination for the needs of contemporary absolute gravity measurements—first results. Reports on Geodesy, No 1(92), Warsaw University of Technology, pp 23–35

Dykowski P, Sekowski M, Krynski J (2012) Stability of metrological parameters and performance of the A10 absolute gravimeter. Geophysical Research Abstracts, vol 14, EGU2012-4449, EGU GA 2012, Vienna, Austria, 22–27 April 2012

Falk R, Müller J, Lux N, Wilmes H, Wzionek H (2009) Precise gravimetric surveys with the field absolute gravimeter A-10. IAG Symp 136:273–279. doi:10.1007/978-3-642-20338-1_33

Krynski J (2007) Precise quasigeoid modelling in Poland—results and accuracy estimate (in Polish). Monographic series of the Institute of Geodesy and Cartography, Nr 13, Warsaw 2007, 266 pp

Krynski J (2012) On the new international gravity reference system. Workshop at the Joint Meeting of JWG 2.1 Techniques and Metrology in Absolute Gravimetry and JWG 2.2 Absolute Gravimetry and Absolute Gravity Reference System, Vienna, Austria, 14–15 February 2012

Krynski J, Barlik M (2012) On a lasting role of geodynamics in modern vertical and gravity reference systems. Reports on Geodesy, No 1(92), Warsaw University of Technology, pp 61–68

Krynski J, Lyszkowicz A (2006) The overview of precise quasigeoid modelling in Poland. In: 2nd workshop on international gravity field research 2006, Smolenice, Slovakia, 8–9 May 2006. Contributions to Geophysics and Geodesy, Special issue, WIGFR 2006, Geophysical Institute of Slovak Academy of Sciences, pp 113–149

Krynski J, Lyszkowicz A (2007) Centimetre quasigeoid modelling in Poland using heterogeneous data. In: IAG proceedings of the 1st international symposium of the international gravity field service (IGFS) "Gravity Field of the Earth", Istanbul, Turkey, 28 August–1 September 2006, pp 37–42

Krynski J, Sas-Uhrynowski A, Siporski L (2003) Verification of the absolute gravity measurements in Poland. In: Proceedings of the workshop on instrumentation and metrology in gravimetry, vol 22. "Institut de Europe", Castle of Münsbach, Luxembourg, Cahiers du Centre Européen de Géodynamique et de Séismologie, 28–30 October 2002, pp 129–136

Mäkinen J, Sekowski M, Krynski J (2010) The use of the A10-020 gravimeter for the modernization of the Finnish First Order Gravity Network. Geoinformation Issues 2(1):5–17

Sas-Uhrynowski A, Cisak M, Sas A, Siporski L (1999) A new national gravity control network—POGK97 (in Polish). In: Proceedings of the institute of geodesy and cartography, vol XLVI, No 98, pp 41–49

Sas-Uhrynowski A, Cisak M, Mroczek S, Sas A, Siporski L (2000) A new gravimetric control network for Poland. Reports on Geodesy, Warsaw University of Technology, No 8, pp. 55–60

Walo J (ed) (2010) The unified gravimetric reference system for Polish GNSS stations and geodynamic fields (in Polish). Warsaw University of Technology, Warsaw, 184 pp

Testing the Suitability of the A10-020 Absolute Gravimeter for the Establishment of New Gravity Control in Poland

P. Dykowski, J. Krynski, and M. Sekowski

Abstract

The A10 absolute gravimeter is the first fully operational equipment to perform absolute gravity determinations in field conditions. A long time series of gravity determinations with the A10-020 performed since 2008 on a monthly basis on three stations in Borowa Gora Observatory provides an invaluable data source for quality estimation of the meter and its performance. Data from regular metrological calibrations of both, linear-polarized and stabilized laser and rubidium oscillator of the A10-020 are a complementary material for the analysis of the gravimeter performance. In May 2012 a measurement campaign at nearly 15 points was conducted to test and verify the developed methodology of absolute gravity survey with the A10 for establishing a new gravity control in Poland. Measurements were performed at absolute gravity stations of current Polish gravity control and their eccentric points. The obtained results were analyzed considering different types of station monumentation. At five laboratory stations the A10-020 results were compared with the recent FG5-230 determinations. The comparison included unification of vertical gravity gradient determinations as well as metrological parameters. At all occupied stations the vertical gravity gradient had been determined with two LaCoste & Romberg gravimeters with the use of a special stand made in the Institute of Geodesy and Cartography. The importance of vertical gravity gradient determination for the establishment of the new gravity control is discussed. The experience with the A10-020, including its suitability for modernization and re-measurement of gravity control in Finland, Sweden, Norway, and Denmark proves its high efficiency and accuracy. Furthermore it allows to develop a complete methodology for the establishment of a new type of gravity control.

Keywords

A10 absolute gravimeter • Gravity control • Relative gravimetry • Metrology

1 Introduction

The currently existing gravity control in Poland (POGK) is based on nearly 350 points. Since the end of the twentieth century nearly 100 of them were destroyed, making it impossible to re-measure completely the entire network. Following the suggestions of scientific community in Poland (Krynski 2009) the Head Office of Geodesy and Cartography initiated in 2011 the activity towards the modernization of the existing gravity network. As the technology of gravity determinations has significantly improved during the last 20 years it is possible to set a new type of gravity control (Krynski et al. 2012). The major tool to be used to determine gravity at the sites of gravity control could be the A10 gravimeter manufactured for over 10 years by the Micro-g LaCoste (Micro-g Lacoste Inc. 2008a) that ensures sufficient accuracy and efficiency

P. Dykowski (✉) • J. Krynski • M. Sekowski
Institute of Geodesy and Cartography, 27 Modzelewskiego St, 02-679 Warsaw, Poland
e-mail: przemyslaw.dykowski@igik.edu.pl

U. Marti (ed.), *Gravity, Geoid and Height Systems*, International Association of Geodesy Symposia 141,
DOI 10.1007/978-3-319-10837-7_2, © Springer International Publishing Switzerland 2014

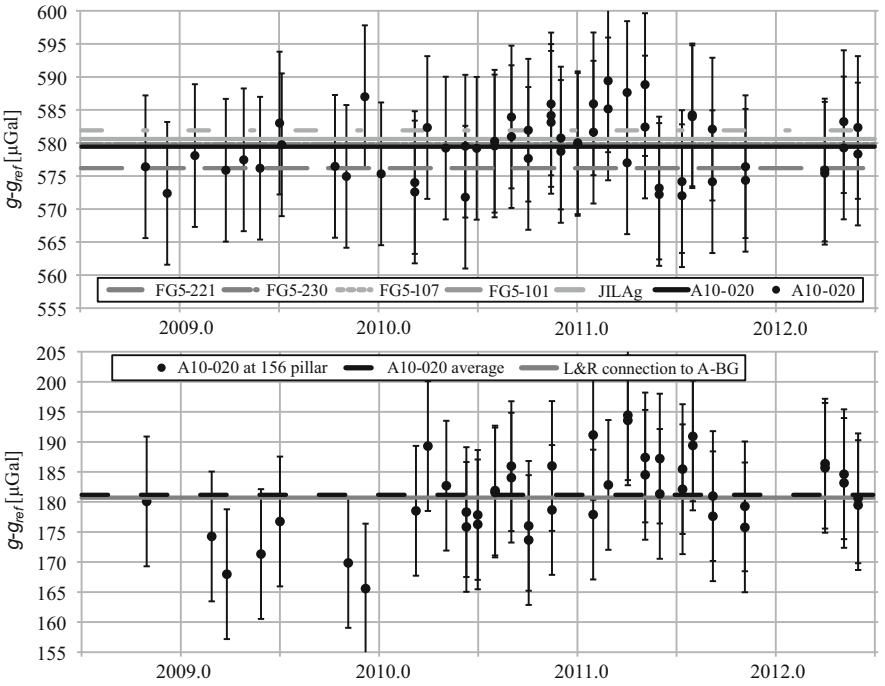

Fig. 1 Results of repeated gravity measurements at A-BG (*top*) and 156 (*bottom*) stations at Borowa Gora Observatory ($g_{ref} = 981{,}250{,}000$ μGal)

of gravity determination. Its performance investigated by a number of research teams (Pujol 2005; Schmerge and Francis 2006; Sousa and Santos 2010; Falk et al. 2012) indicates the potential usefulness of the A10 in the establishment of the gravity control. As each A10 gravimeter is handmade, it needs, to be tested in various measurement conditions, especially those characteristic for the country, in order to verify its suitability for the establishment of the new gravity control. The A10 gravimeters had already been used for the modernization of existing gravity control, e.g. in France (Duquenne et al. 2005), Spain (Pujol 2005), and Germany (Falk et al. 2012). Throughout the last couple of years the A10-020 operated by the team of the Institute of Geodesy and Cartography, Warsaw (IGiK) had been used in the field work on the gravity control in Scandinavia: Finland (Mäkinen et al. 2010), Norway (Pettersen et al. 2012), Sweden and Denmark.

The paper presents the results obtained in the process of extensive investigations and test survey with the A10-020 on some absolute stations and their eccentric sites of the POGK. The discussion concerns stability and reliability of the A10-020 with special attention to the monumentation of sites, metrology and vertical gravity gradient determination.

2 Stability and Reliability of the A10-020

Since 2008 quasi regular monthly gravity measurements were performed with the A10-020 at three pillars (two laboratory and one field station) of the Borowa Gora Geodetic-Geophysical Observatory (BG) of IGiK. Figure 1 (top) presents the results at A-BG absolute gravity station (laboratory station) in the Observatory at which numerous absolute gravity determinations were performed since 1978 by a number of teams, while Fig. 1 (bottom)—the results at the field station 156. The reference gravity at the 156 pillar was obtained by transferring to it the average gravity value at the A-BG pillar with a group of LaCoste & Romberg (LCR) gravimeters. Results at A-BG and 156 pillars reduced to the benchmark level show a very good agreement with previous precise gravity determinations.

All shown gravity determinations performed at the BG Observatory sites since 2008 were re-calculated with the use of new vertical gravity gradient ($\Delta g/\Delta h$) determinations performed in 2011 (Dykowski 2012) as well as with the use of calibration data of the ML-1 HeNe laser of

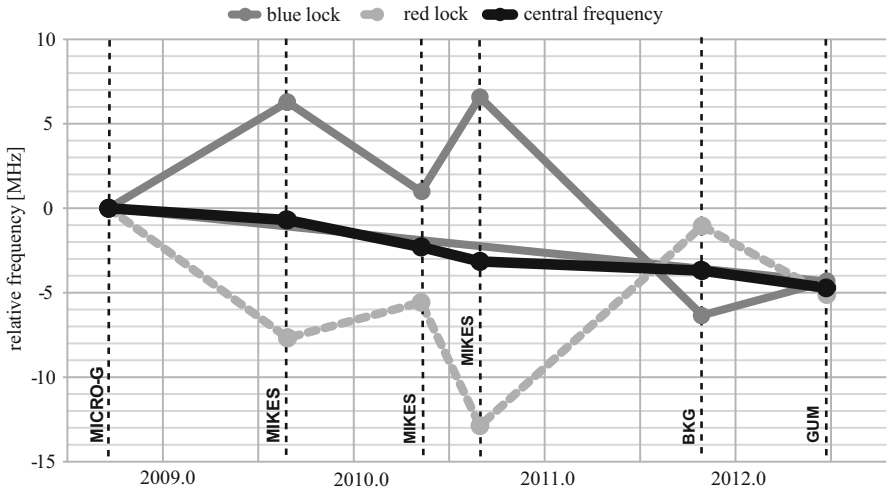

Fig. 2 Calibration data of the ML-1 laser of the A10-020

Table 1 Comparison of relative gravity determinations and A10-020 results between stations in the Borowa Gora Observatory [μGal]

Span	LCR_{2012}	A10 new $\Delta g/\Delta h$	A10 old $\Delta g/\Delta h$
A-BG—BG-G2	135.0 ± 2.2	136.8 ± 4.6	140.6 ± 4.6
A-BG—156	398.7 ± 1.9	399.0 ± 4.6	418.6 ± 4.6
BG-G2—156	263.6 ± 2.6	262.2 ± 5.5	278.0 ± 5.5

Table 2 Statistics at BG stations

Pillar	No of determinations	Std [μGal]	Max-Min [μGal]
A-BG	56	4.6	17.6
BG-G2	84	4.6	22.4
156	44	6.2	28.9

the A10-020 (Fig. 2). Both, metrological data and new $\Delta g/\Delta h$ data substantially contributed to the improvement of the results shown in Fig. 1. Particular attention has been paid to the quality of $\Delta g/\Delta h$ data. The effect of replacing "old" $\Delta g/\Delta h$ determined at two heights (1 m apart) (Sas-Uhrynowski 2002) with "new" $\Delta g/\Delta h$ determined in 2011 with the use of precise multiple-height strategy and special stand (Dykowski 2012) is shown in Table 1. Long term averages of gravity determined with the A10-020 at the BG Observatory sites were compared with the precise relative survey performed in April 2012. The results obtained show much better agreement of the A10 results with the use of currently determined $\Delta g/\Delta h$ than with those determined in the past (Krynski and Sękowski 2010).

Table 2 presents the basic statistics of the results at all three BG pillars. The observed standard deviations are much smaller than 10 μGal uncertainty suggested by the manufacturer (Micro-g Lacoste Inc. 2008a) while the differences between the maximum and the minimum value at each station exceed double of that uncertainty. These discrepancies are most probably due to environmental or geophysical phenomena. The trend observed in the results of gravity determinations (Fig. 1) is consistent with water table level recordings in the Observatory, which varies within 2 m. Unfortunately those recordings, due to short and not continuous time series, are still insufficient to apply a hydrological correction. More thorough analysis of time series of gravity determinations in the BG Observatory include metrological and environmental effects (Dykowski et al. 2012; Sekowski et al. 2012a).

Laser calibrations clearly prove the importance of the measurement traceability, assured by a correct application of metrological specifications, to the reprocessing of absolute gravity measurements with the A10-020. The observed change in the central frequency reaches 5 MHz (Fig. 2) which corresponds to a nearly 10 μGal shift in determined gravity (Niebauer et al. 1995). The trend observed in the laser calibration parameters shows a steady decrease in the central frequency with the red and blue mode experiencing much more significant variations.

The rubidium oscillator being the frequency standard of the A10-020 gravimeter is for the last 4 years stable within 5×10^{-3} Hz specified by the manufacturer. A contribution of such stability to the uncertainty of gravity determined is below 1 μGal, it corresponds well to the uncertainty specification suggested by the manufacturer. Since it is much lower than the total uncertainty of gravity measurement with the A10, there is no need to the correction to the gravity determinations for this effect. Metrological issues concerning the A10-020 have been more widely described in previous works of the authors (Dykowski et al. 2012; Sekowski et al. 2012a, b).

The ability of the A10-020 to provide reliable, high quality gravity has been proved in multiple gravity survey projects (nearly 180 stations in Scandinavia). In 2012 first 50 stations of the new gravity control in Poland were surveyed with the A10-020 within the 2 years project. The gravimeter took part in the ICAG2009 and ECAG2011 campaigns and

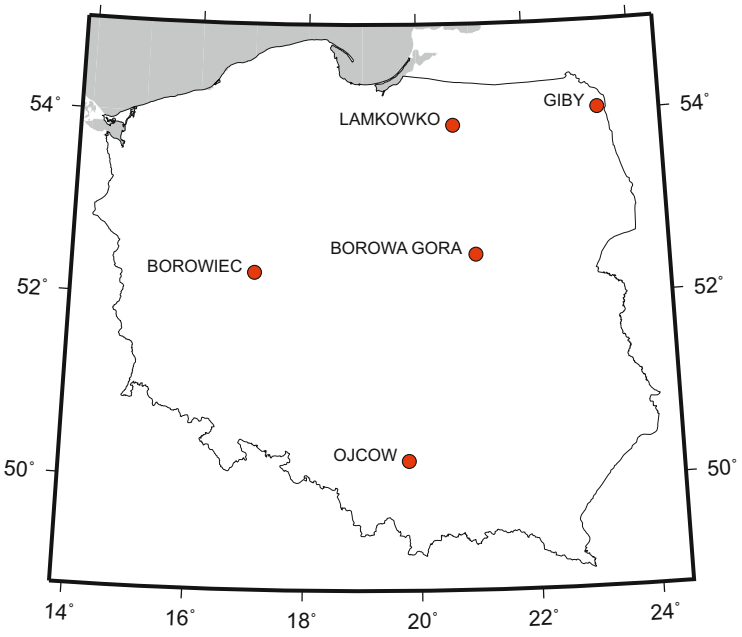

Fig. 3 Fundamental gravity sites selected for the test survey

has proven itself to provide reliable gravity values (Jiang et al. 2012; Francis et al. 2012).

3 Test Measurements with the A10-020 on the Sites of the Polish Gravity Network

Before the works on the modernization of the current gravity control in Poland could begin, a decision to perform a test survey at selected stations of the existing POGK network was made. Five fundamental gravity stations of the current Polish gravity network: Borowa Gora, Borowiec, Giby, Lamkowko, and Ojcow (Fig. 3) were selected for test measurements. Back in the 1990s absolute gravity measurements on the gravity network were performed with a few types of gravimeters by different teams (Sas-Uhrynowski 2002). At most of the mentioned sites the measurements with the A10-020 gravimeter were performed also at the eccentric points for the fundamental stations. At all points surveyed a new vertical gravity gradient was determined with two LCR gravimeters using a special stand (Dykowski 2012) and following a measurement schedule developed at IGiK.

The idea of test measurements was to generate and verify a strict and consequent methodology to obtain a good quality gravity value at any surveyed station. Measurements with the A10-020 were performed using a procedure tested multiple times by the IGiK team (Krynski and Sękowski 2010; Mäkinen et al. 2010). It includes two separate gravimeter setups consisting of eight sets each. In each set 120 drops are performed with 1 s drop interval. The agreement between two setups was verified at the spot. The difference between both setups below 10 μGal is considered acceptable. In case of larger difference third or consecutive setup was performed. Further discrepancies not explained by any geophysical phenomena (earthquakes, manmade seismic noise) or setup errors, indicate instability of the site what disqualifies it from the measurements as there is no possibility to determine gravity value with proper accuracy.

Various types of sites monumentation were selected for test measurements. All fundamental stations are stabilized with a 1×1 m and at least 1 m high concrete block. It is safe to say that this kind of stabilization is good enough for any type of gravimetric surveys, especially for the A10 gravimeter. A few of the eccentric points also have the same kind of monumentation. Other types of stabilizations are shown in Fig. 4. A mushroom-type block (at the first Lamkowko eccentric point—Fig. 4—right) gave a reliable result. At the EUREF site of the Borowiec second eccentric point (Fig. 4—middle) only one reliable result and several not conclusive results were obtained. The stabilization itself is massive enough but a thin layer of concrete that had been layed on the top of the block created an unstable surface. The last shown monumentation is a tile floor (Fig. 4—left). It showed very high and regular single drop residuals (Fig. 5—top) on which System Response Compensation (SRC) option of the g8 software was used (Micro-g Lacoste Inc. 2008b). Even though high residuals were observed, the single set scatter and set distribution were very good (Fig. 5—bottom).

Fig. 4 The A10-020 absolute gravimeter at sites of various types of monumentation

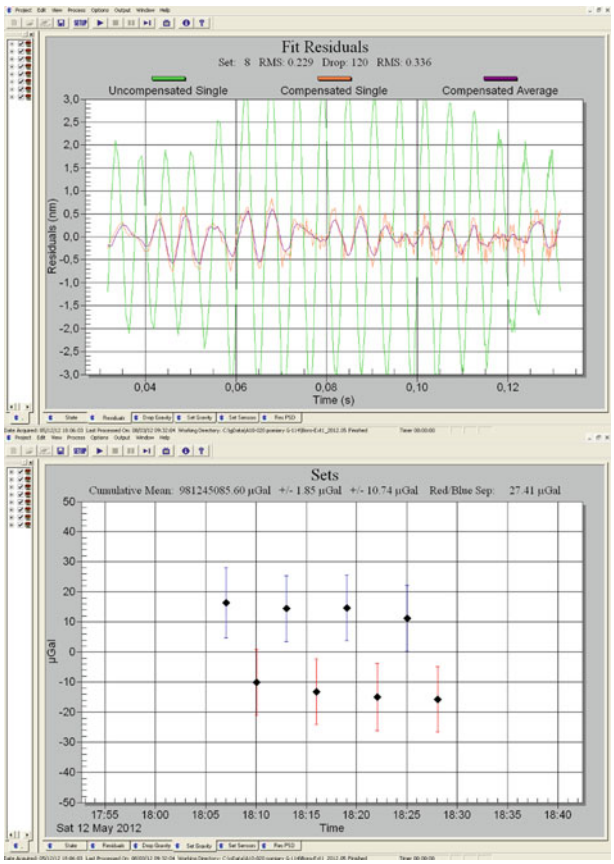

Fig. 5 SRC compensation on Borowiec second eccentric station (Fig. 4—*left*)

4 Analysis of Survey Results

At all sites selected for the test measurements absolute gravity determinations were performed in the past. The most recent were obtained with the FG5-230 of the Warsaw University of Technology (WUT) in 2006, 2007 and 2008 (Barlik 2010; Walo 2010). The other were performed with several different types of absolute gravimeters (FG5, IMGC, JILAg, ZZG) in 1994–1998 within the project of establishing

Table 3 Differences between survey results with the A10-020 on fundamental stations and previous absolute gravity determinations with the FG5-230 [µGal]

Site	$FG5_{2006}$	$FG5_{2007}$	$FG5_{2008}$	$FG5_{2006–2008}$
Borowa Gora	–	+0.9	+1.1	+1.0
Giby	+1.0	+0.4	+0.4	+0.7
Lamkowko	+4.5	−2.6	+4.4	+2.1
Borowiec	−0.4	+0.9	+6.3	+2.3
Ojcow	+1.5	−1.7	−3.4	−1.2

Table 4 Differences between survey results with the A10-020 on fundamental stations and absolute gravity determinations from 1994 to 1998 [µGal]

Site	FG5-101	FG5-107	IMGC	JILAg-5	ZZG
Borowa Gora	+2.1	+1.1	–	+1.7	−18.6
Giby	–	–	–	–	−11.7
Lamkowko	–	–	−8.2	–	−28.1
Borowiec	−3.6	–	+0.8	–	−24.2
Ojcow	–	−13.0	–	–	–

POGK (Sas-Uhrynowski 2002). To allow a proper comparison of absolute gravity determination results they all had been unified with the use of the vertical gravity gradient determined in 2012. Unified offsets of gravity determinations with the A10-020 and with respect to the FG5-230 are presented in Table 3. Differences between gravity determined with the A10-020 and the FG5-230 results over 3 years (2006, 2007, 2008) at all surveyed sites are optimistic as the biggest discrepancy does not exceed 6.3 µGal.

Table 4 presents the differences between the A10-020 results and absolute gravity determinations performed in 1994–1998 by different types of absolute gravimeters. Gravity values determined with the A10-020 seem consistent with most FG5 and IMGC determinations but significant discrepancies occur when compared to the results of the ZZG gravimeter.

As the test survey with the A10-020 was also performed at a few eccentric sites of the mentioned fundamental stations, a comparison could be made with the relative measurements performed with LCR gravimeters in 1994–1998 (Sas-Uhrynowski 2002). Differences between those determinations are presented in Table 5. Unfortunately not all eccentric stations survived until 2012, hence the lack of results for some stations.

The first eccentric point of the Borowiec station is a special case (Fig. 4—left). High single drop residuals contaminated the proper gravity determination at that site even though the measurement looks very good in terms of low single set noise, and stable set distribution. In this case SRC option of the g8 software had been used during the reprocessing of the measurements (Micro-g LaCoste Inc. 2008b). For the spans with this site two values are shown in

Table 5 Comparison of A10 survey results on eccentric points with relative determinations [μGal]

Site	$A10_{2012}$	$LCR_{1994–1998}$	Difference
Borowa Gora			
ABS-EX1	136.0	135.0	1.0
ABS-EX2	397.4	398.7	−1.3
EX1-EX2	261.3	263.6	−2.3
Lamkowko			
ABS-EX1	326.6	325.0	1.6
Borowiec			
ABS-EX1	1,056.4	1,061.0	−4.6/*17.8*
ABS-EX2	873.2	873.0	0.2
EX1-EX2	183.2	188.0	−4.8/*18.0*
Ojcow			
ABS-EX1	568.4	566.0	2.4

the "difference" column in Table 5. The left one corresponds to the difference obtained with the use of the SRC option while the right one is a non modified value from the original measurement. This example shows significant improvement in the obtained gravity value coming from the use of SRC option.

Conclusions and Recommendations

No significant problems occurred during the performed test gravity survey. At almost all open field stations a tent was used for protection from wind and other environmental effects. It is recommended to use it for this purpose. As for the suitability of the A10-020 for the establishment of the new Polish gravity control it can be stated that:

- A10-020 gravimeter provides stable results at the reliability level required in the modern gravity control (10 μGal or better);
- described and tested schedule of two independent setups with 8 sets of 120 drops every second is reliable for the detection of gross errors and for assuring a good quality of the determined gravity value at any stable site.

To assure proper gravity determinations several factors need to be taken account:

- point localization—no high and dense settled trees, no heavy traffic, etc. to minimize the noise during the survey;
- proper monumentation—stations planned to be surveyed during the modernization/establishment of the gravity control should be properly stabilized;
- precise and reliable determination of vertical gravity gradients, both the measurement and its reduction including the possible non-linearity of the determined gradient;
- control of metrological standards, especially for the HeNe laser as it seems to be the more "drifting" factor, control of the rubidium frequency standard to verify its long term stability. Such control is recommended every 6 months.

Test absolute gravity determinations with the A10-020 on the Polish gravity control along with the previous gravity network experiences of the IGiK team confirm the suitability of the A10-type gravimeters for the establishment of the gravity control in Poland.

Acknowledgements The research was supported by the Polish Ministry of Science and Higher Education. This work was carried out within the grant No N N526 160340 research. Some parts of the project had been carried out within the statutory project of the Institute of Geodesy and Cartography, Warsaw "Problems of geodesy and geodynamics".

References

Barlik M (ed) (2010) Study on long-term absolute gravity changes on main tectonic units on Polish territory between 2006-2009 (in Polish). Warsaw University of Technology, Warsaw, 92 pp

Duquenne F, Duquenne H, Gattacceca T (2005) Gravity measurements on the French geodetic network. In: Symposium of the IAG subcommission for Europe (EUREF), Vienna, Austria, 1–4 June 2005. http://www.euref-iag.net/symposia/2005Vienna/7-02.pdf

Dykowski P (2012) Vertical gravity gradient determination for the needs of contemporary absolute gravity measurements—first results. Reports on Geodesy, No 1(92), Warsaw University of Technology, Warsaw, pp 23–35

Dykowski P, Sekowski M, Krynski J (2012) Stability of metrological parameters and performance of the A10 absolute gravimeter. Geophysical Research Abstracts vol 14, EGU2012-4449, EGU GA, Vienna, Austria, 22–27 April 2012

Falk R, Müller J, Lux N, Wilmes H, Wzionek H (2012) Precise gravimetric surveys with the field absolute gravimeter A-10. IAG Symp 136:273–279. doi:10.1007/978-3-642-20338-1_33

Francis O et al (2012) Final report of the regional key comparison EURAMET.M.G-K1: European comparison of absolute gravimeters ECAG-2011. Metrologia 49(1A):07–014. doi:10.1088/0026-1394/49/1A/07014

Jiang Z et al (2012) The 8th international comparison of absolute gravimeters 2009: the first key comparison (CCM.G-K1) in the field of absolute gravimetry. Metrologia 49(6):666–684. doi:10.1088/0026-1394/49/6/666

Krynski J (2009) The concept of gravity control considering technological development in gravity survey (in Polish). In: Seminar of the committee on Geodesy, Warsaw, Poland (CD), 3–4 December

Krynski J, Sękowski M (2010) Surveying with the A10-20 absolute gravimeter for geodesy and geodynamics—first results. Geophysical Research Abstracts 12, EGU2010-8167. Reports on Geodesy 1(88):27–35

Krynski J, Barlik M, Olszak T, Dykowski P (2012) Towards the establishment of new gravity control in Poland. In: International symposium on gravity, geoid and height systems 2012, Venice, Italy, 9–12 October 2012

Mäkinen J, Sękowski M, Kryński J (2010) The use of the A10-020 gravimeter for the modernization of the Finnish first order gravity network. Geoinf Issues 2(1):5–17

Micro-g LaCoste Inc. (2008a) A10 portable gravimeter user's manual, July 2008, 59 pp

Micro-g LaCoste Inc. (2008b) g8 user's manual, March 2008, 48 pp.

Niebauer TM, Sasagawa GS, Faller JE, Hilt R, Klopping F (1995) A new generation of absolute gravimeters. Metrologia 32:159–180

Pettersen BR, Sprlak M, Lysaker DI, Omang OCD, Sekowski M, Dykowski P (2012) Validation of GOCE by absolute and relative gravimetry, EGU GA 2012, Vienna, Austria, 22–27 April

Pujol E (2005) Absolute gravity network in Spain. Fisica de la Tierra 17:147–163

Sas-Uhrynowski A (2002) Absolute gravity measurements in Poland. Monograph series No 3, IGiK, Warsaw

Schmerge D, Francis O (2006) Set standard deviation. Repeatability and offset of absolute gravimeter A10-008. Metrologia 43:414–418

Sekowski M, Krynski J, Dykowski P, Mäkinen J (2012a) Effect of laser and clock stability and meteorological conditions on gravity surveyed with the A10 free-fall gravimeter—first results. Reports on Geodesy, No 1(92), Warsaw University of Technology, Warsaw, pp 47–59

Sekowski M, Krynski J, Mäkinen J, Dykowski P (2012b) On the estimate of accuracy and reliability of the A10 free fall gravimeter. In: IAG Symposium, vol 139. Springer, Heidelberg

Sousa M, Santos A (2010) Absolute gravimetry on the Agulhas Negras calibration line. Revista Brasileira de Geofisica 28(2):165–174

Walo J (ed) (2010) The unified gravimetric reference system for polish GNSS stations and geodynamic fields (in Polish). Warsaw University of Technology, Warsaw, 184 pp

Part II

Global Gravity Field Modeling, Assessments and Applications

GOCE Long-Wavelength Gravity Field Recovery from 1s-Sampled Kinematic Orbits Using the Acceleration Approach

T. Reubelt, O. Baur, M. Weigelt, M. Roth, and N. Sneeuw

Abstract

The acceleration approach is an efficient and accurate tool for the estimation of the low-frequency part of GOCE (Gravity field and steady-state Ocean Circulation Explorer) gravity fields from GPS-based satellite-to-satellite tracking (SST). This approach is characterized by second-order numerical differentiation of the kinematic orbit. However, the application to GOCE-SST data, given with a 1s-sampling, showed that serious problems arise due to strong amplification of high frequency noise. In order to mitigate this problem, we developed a tailored processing strategy in a recent paper which makes use of an extended differentiation scheme acting as low-pass filter, and empirical covariance functions to account for the different precision of the components and the inter-epoch correlations caused by orbit computation and numerical differentiation. However, also a more "brute-force" strategy can be applied using the standard unextended differentiation scheme and data-weighting by error propagation of the provided orbit variance-covariance matrices (VCMs). It is shown that the direct differentiator shows a better approximation and the exploited method benefits from the stochastic information contained in the VCMs compared to the former strategy. A strong dependence on the maximum resolution, the arc-length and the method for data-weighting is observed, which requires careful selection of these parameters. By comparison with alternative GOCE hl-SST solutions we conclude that the acceleration approach is a competitive method for gravity field recovery from kinematic orbit information.

Keywords

GOCE • Satellite-to-satellite tracking • Kinematic orbits • Gravity field • Orbit variances • Data weighting

1 Introduction

The Gravity field and steady-state Ocean Circulation Explorer (GOCE) satellite collects science data for the recovery of the static terrestrial gravity field since autumn 2009. Its core instrument is a three-dimensional gravity gradiometer which provides high quality measurements within a bandwidth of 5 mHz to 0.1 Hz (ESA 1999), roughly corresponding to spherical harmonic degrees 30–250. As a consequence, gradiometry has to be complemented with data containing long-wavelength signals in the framework of GOCE-only

T. Reubelt • M. Roth • N. Sneeuw
Geodetic Institute, Stuttgart University, Geschwister-Scholl-Straße 24D, 70174 Stuttgart, Germany
e-mail: reubelt@gis.uni-stuttgart.de

O. Baur (✉)
Space Research Institute, Austrian Academy of Sciences, Schmiedlstraße 6, 8042 Graz, Austria
e-mail: Oliver.Baur@oeaw.ac.at

M. Weigelt
Faculty of Science, Technology and Communication, University of Luxembourg, 1359 Luxembourg, Luxembourg

U. Marti (ed.), *Gravity, Geoid and Height Systems*, International Association of Geodesy Symposia 141,
DOI 10.1007/978-3-319-10837-7_3,

gravity field recovery. This additional data is provided by kinematic orbit information in terms of high-low satellite-to-satellite tracking (hl-SST) with GPS.

Besides the classical method for dynamic orbit analysis based on variational equations (Reigber 1989), efficient alternative methods have been developed that exploit kinematic orbit information. The most prominent of these alternative methods are the energy-balance approach (EBA, e.g. Han et al. 2002), short-arc analysis expressed as a boundary value problem (BVP, Mayer-Gürr et al. 2005) and acceleration approaches (ACA) exploiting either point-wise accelerations (Reubelt et al. 2003, 2006) or averaged accelerations (Ditmar and van Eck van der Sluijs 2004). It can be shown that all approaches perform similar except the EBA which is worse by a factor of 1.5–2 (e.g. Löcher 2010; Reubelt 2009; Reubelt et al. 2012). Also the variational equations concept can be applied to kinematic orbits, known as the celestial mechanics approach (CMA), as used by Jäggi et al. (2011).

In a recent publication (Baur et al. 2012) concerning GOCE-SST analysis we showed that the point-wise acceleration approach (i) performs comparable to the CMA, (ii) is superior to the EBA solution used for the GOCE-TIM (Pail et al. 2011) estimates, and (iii) is able to improve the GOCE-TIM solutions up to spherical harmonic degree and order 20–30.

In Baur et al. (2012) we applied an extended differentiation filter (EDF(30s)) to the 1s-sampled kinematic GOCE orbit. The EDF(30s) acts as a low-pass filter; it damps noise and gravity signal on high frequencies but keeps gravity signal for spherical harmonic degrees $l \leq 90$ untouched. As far as stochastic modeling is concerned, in Baur et al. (2012) we used robust estimation in combination with data-weighting by means of empirical covariance functions estimated from residuals in the local frame. The quality of the solutions turned out to be largely independent of the arc-length (720 s, 1,440 s, 2,880 s) and maximum resolution $L_{\max}$ (90, 110, 120).

Apart from this tailored strategy, the application of the point-wise acceleration approach is also possible in a more direct way. Such a "brute-force" method is characterized by (i) the direct application of the differentiation operator to the 1s-sampled kinematic orbit (consistent with EDF(1s)) and (ii) the exploitation of the provided orbit VCMs in data-weighting by means of error-propagation to acceleration VCMs. The benefit of such a procedure might be

(i) a better approximation of the accelerations by the EDF(1s)
(ii) the use of stochastic information provided by the orbit VCMs. This is motivated by the higher accuracy of both the orbits and their VCMs (Bock et al. 2011) compared to former CHAMP orbits.

Applying this strategy, a careful error propagation for data weighting is necessary in order to treat the high-frequency noise generated by the direct differentiation of the 1s-sampled orbits correctly. As reported in Baur et al. (2012), unsatisfying results have been obtained by this procedure. The aim of this paper is to investigate this "brute-force" strategy in more detail.

2 Method

The acceleration approach makes use of the direct application of the equation of motion in the space-fixed reference system. To achieve this, the satellite's acceleration vector has to be determined from the kinematic orbit by means of numerical double differentiation. In general this is established by means of a 9-point differentiation scheme based on Gregory-Newton-interpolation (Reubelt et al. 2003). The gravitational vector is obtained after corrections for disturbing accelerations as caused by tidal effects and time-variable gravity signals (e.g. atmosphere and ocean signals), compare Baur et al. (2012). The spherical harmonic coefficients representing the Earth's gravity field are estimated by means of least-squares adjustment. As mentioned earlier, data weighting is important to account for the noise amplification caused by the direct application of the 9-point scheme to the 1s-sampled orbit (EDF(1s)) since there is no (or only slight) low-pass-filtering inherent compared to the EDF(30s). One possibility is data weighting with empirical covariance functions derived from residuals in the local frame together with robust estimation, i.e., a similar procedure as applied for EDF(30s) by Baur et al. (2012). Another possibility is brute-force error propagation of the provided orbit VCMs. Three versions of the latter have been tested: (i) epoch-wise full 3×3 VCMs, (ii) epoch-wise orbit variances with neglect of correlations (i.e., only diagonals of the VCMs), and (iii) four epoch-wise full VCMs, providing the epoch-wise 3×3 VCMs including full correlations with four points before and after the actual orbit point.

It is expected that the EDF(1s) provides a better approximation of accelerations than the EDF(30s) since a denser sampling is used for the differentiation. In Fig. 1 a simulated noise-free 1s-sampled GOCE-orbit over a period of 1 month is analyzed by means of both EDFs. As it can be seen, the gravity field approximation error using EDF(1s) is much smaller. However, also the approximation error when applying EDF(30s) is sufficiently small since its error curve is still below the errors of gravity retrievals from real GOCE orbits (compare with the black curve in Fig. 2). Concerning further improvements in kinematic orbit determination, however, the EDF(1s) or an EDF(Δt) with a shorter Δt than 30s is suggested in order to guarantee the approximation to be sufficiently small.

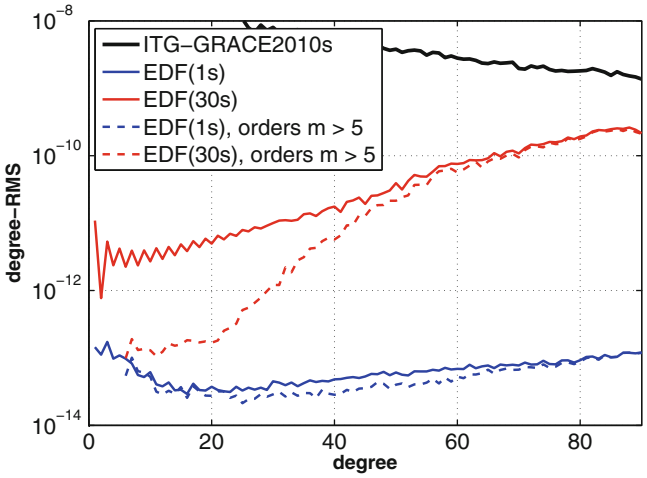

Fig. 1 Model errors: degree RMS obtained by application of EDF(1s) and EDF(30s) to a simulated noise-free GOCE-orbit; the *dashed lines* are obtained from exclusion of orders $m \leq 5$ in order to account for the polar gap

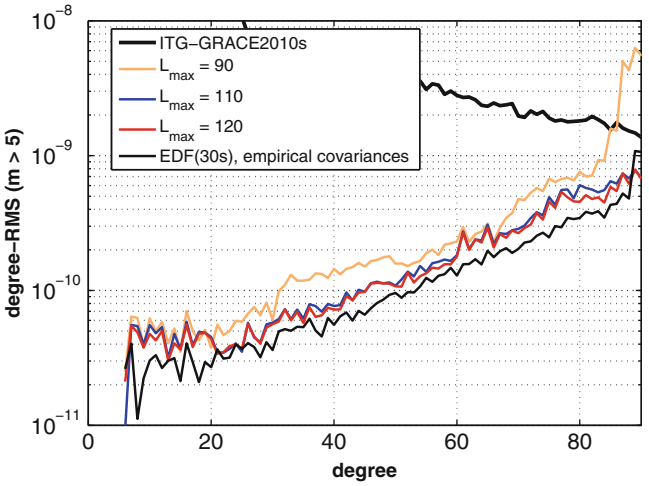

Fig. 3 Results from EDF(1s) for different maximum resolutions L_{max} and fixed arc-length = 1,440; data-weighting is performed by means of propagated epoch-wise VCMs

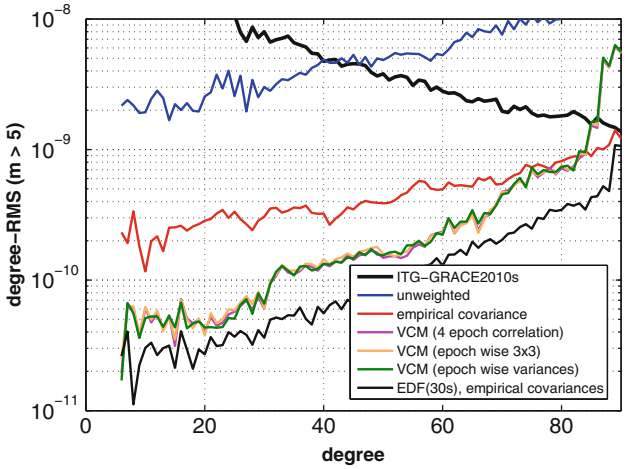

Fig. 2 GOCE-SST results from EDF(1s) using different weighting strategies; maximum resolution $L_{max} = 90$, arc-length = 1,440; for comparison the solution from EDF(30s) with application of empirical covariance-functions (Baur et al. 2012) is provided

3 Results

Kinematic orbit analysis was performed by the procedures described in the previous section. The results were compared to ITG-GRACE2010s (Mayer-Gürr et al. 2010), which is of superior quality due to the exploitation of GRACE K-band observations. The GOCE-hl-SST results in this contribution were obtained from a 61-days kinematic orbit (Bock et al. 2011) as provided via the GOCE SST_PSO_2 product (EGG-C 2010), covering the period November 1, 2009 to December 31, 2009. For comparison, the solution obtained from the EDF(30s) (Baur et al. 2012) is displayed (black curve). Dashed graphs show formal errors. If not mentioned explicitly, degree-RMS values are computed for orders $m > 5$ to account for the polar gap effect.

According to Fig. 2, the unweighted solution for EDF(1s) is almost two orders of magnitude worse compared to the EDF(30s) solution. This shows that in contrast to EDF(30s) (cf. Baur et al. 2012) the consideration of the inter-epoch correlations generated by numerical differentiation is important in order to filter the high-frequency noise. Applying empirical covariance functions leads to an improvement of about one order of magnitude, but the remaining errors show that empirical covariance functions are not able to represent the noise amplification of the double-differentiator for the EDF(1s) case sufficiently. The best results were obtained by application of error propagation of the provided orbit VCMs, where all three implementations (see previous section) perform similar. However, still a factor of 3 is missing compared to the EDF(30s) result. The strong increase of the errors for degrees $l > 80$ (spectral aliasing) hints to strong signal to be present in degrees $l > 90$. Thus, we also tested higher maximum resolutions L_{max} (see Fig. 3) for constant arc-lengths of 1,440s and found out that a higher L_{max} is able to improve the results over the whole spectrum. A large gain is obtained for $L_{max} = 110$ and a further smaller gain for $L_{max} = 120$, while $L_{max} = 130$ did not show any further improvements (not displayed).

Another parameter which was found to be important is the arc-length (arc-length means here that a complete propagated acceleration VCM was used for each arc with neglect of correlations between the arcs). Results for different arc-lengths (and constant $L_{max} = 90$) are displayed in Fig. 4. The best results are obtained for arc-lengths around one tenth of the orbital period. An arc-length of 480 s seems optimal

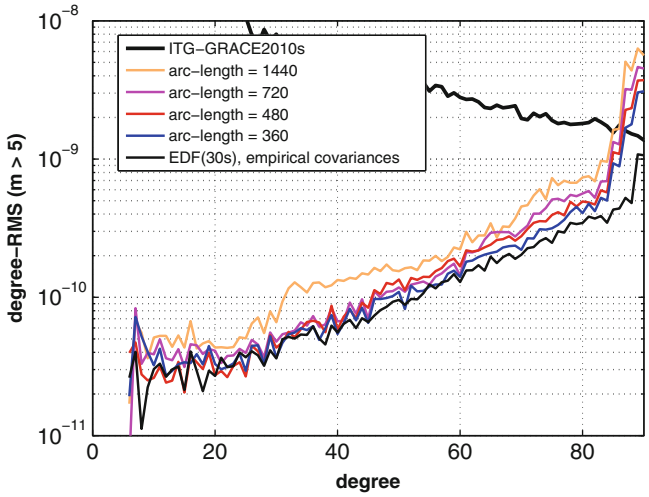

Fig. 4 Results from EDF(1s) for different arc-lengths and fixed maximum resolution $L_{max} = 90$; data-weighting is performed by means of propagated epoch-wise VCMs

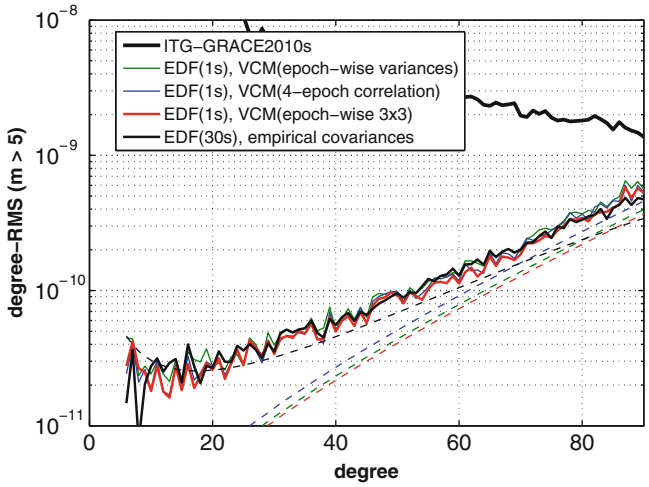

Fig. 5 Results from EDF(1s) using the arc-length = 480 (corresponding to 8 min) and maximum resolution $L_{max} = 120$; different versions of VCMs are applied for data-weighting; *dashed lines* represent formal errors

from Fig. 4, while very short arc-lengths (e.g. 360s) are a drawback for lower degrees. Finally, gravity field estimation from EDF(1s) applying maximum resolution $L_{max} = 120$ and arc-lengths of 480 s was performed using the three versions of orbit VCMs (see previous section) in Fig. 5. Again, a similar performance for all three versions is achieved, where the solution applying the epoch-wise 3×3 orbit VCMs shows a slightly lower error curve (red curve). The comparison with the EDF(30s) shows now a similar performance with slight improvements for certain degrees ($10 < l < 30$, $50 < l < 70$ and $l \cong 35$).

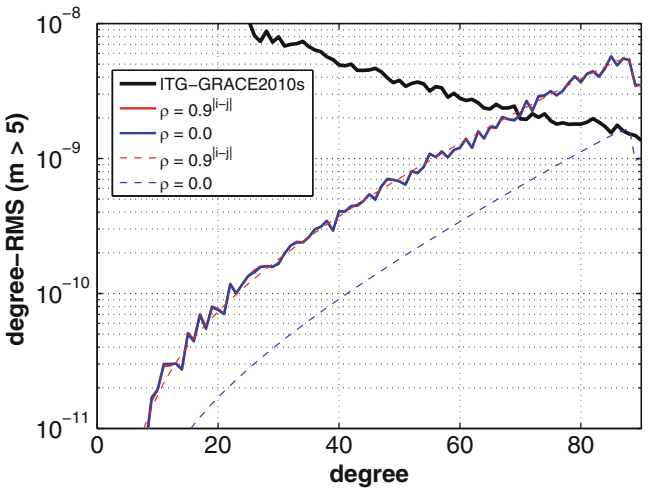

Fig. 6 Influence of under-estimating orbit error correlations in data-weighting; a 1s-sampled simulated 1-month GOCE orbit with correlated orbit noise ($\sigma_x = 1$ cm, $\rho_{i,j} = 0.9^{|i-j|}$) was analyzed; data-weighting was applied assuming orbit error correlations $\rho = 0.9^{|i-j|}$ and $\rho = 0.0$ respectively

An interesting aspect is the formal errors. While the formal errors of EDF(30s) are in good agreement with the quality of the solution the formal errors for the EDF(1s) are over-optimistic. A similar behavior when applying orbit VCMs for data-weighting is obtained from the CMA (Jäggi et al. 2011), displayed in Fig. 7. We attribute this to the fact that the orbit VCMs contain certain deficiencies. For explanation, we simulated a GOCE orbit with correlated orbit noise (standard deviation $\sigma_x = 1$ cm, inter-epoch correlations $\rho_{i,j} = 0.9^{|i-j|}$) and applied different orbit error correlations ($\rho_{i,j} = 0.9^{|i-j|}$, $\rho_{i,j} = 0.0$) for error propagation and data-weighting. As can be seen from Fig. 6, under-estimated orbit error correlations lead to over-optimistic formal errors while the effect on the true errors is negligible. Thus our assumption is that the inter-epoch correlations provided in the VCMs (4-epoch correlation), which amount up to 15 %, are too small.

Finally we compared our results (GIWF, Geodetic Institute/Space Research Institute) with two other solutions obtained from the same data time span: (i) a solution estimated with the EBA by INAS (Institute of Navigation and Satellite Geodesy, Graz University of Technology) applied in current official GOCE-TIM solutions (Pail et al. 2011) and (ii) a recovery from the CMA by AIUB (Astronomical Institute of the University of Bern) (Jäggi et al. 2011). According to Fig. 7, an improvement with respect to the INAS solution by a factor of about 1.5–2 is achieved and a similar performance as the AIUB solution is obtained. Compared to the AIUB solution, the GIWF estimate shows slightly lower errors for

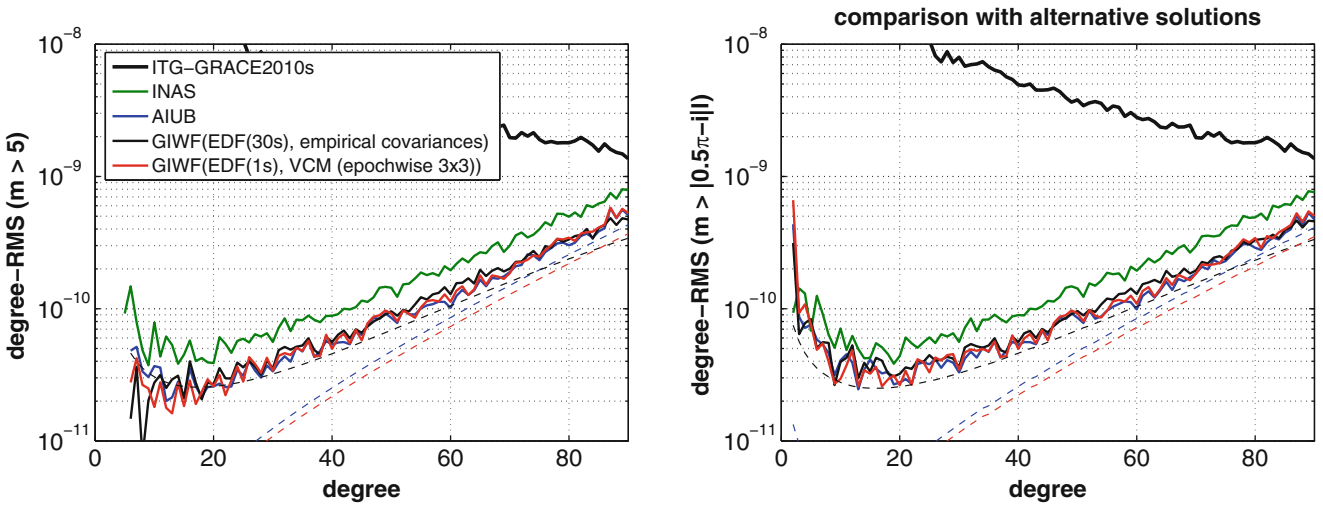

Fig. 7 Comparison of the GIWF models ($L_{max} = 120$) obtained from EDF(1s) and EDF(30s) with the solutions of INAS ($L_{max} = 100$) and AIUB ($L_{max} = 120$); left: orders $m < 5$ omitted; right: orders $m_l \leq |0.5\pi\text{-}i|l$ omitted (consideration of polar gaps according to van Gelderen and Koop (1997))

degrees $l < 20$; AIUB shows slightly better results for some of the higher degrees.

Conclusions and Outlook

Supplementary to the results by Baur et al. (2012), we successfully applied the (point-wise) acceleration approach to the 1s-sampled kinematic GOCE orbit without extended differentiation (i.e. without implicit low-pass filtering) and by data-weighting based on "brute-force" error-propagation of the provided orbit VCMs. An advantage of this implementation is the better approximation of the EDF(1s) differentiation filter, especially in case of a significant gain in kinematic orbit determination in future. Furthermore the investigations show that valuable stochastic information is contained in the provided orbit VCMs, especially concerning the relative accuracy of the three orbit components and their correlation. We assume that the slight improvements of the new implementation are rather related to the orbit VCMs than to the better approximation of the direct differentiator (EDF(1s)), since the approximation of the extended differentiation filter EDF(30s) seems sufficient for GOCE. Our results indicate that the inter-epoch correlations of the orbit errors are probably under-estimated in the VCMs, leading to over-optimistic formal error estimates, while the impact on the overall quality of the solution is minor.

In contrast to Baur et al. (2012) a high sensitivity of the quality of the solutions dependent on the arc-length, the maximum resolution and data-weighting can be observed. The maximum resolution has to be selected high enough (here: $L_{max} = 120$) in order to reduce spatial aliasing, an effect implicitly considered by low-pass filtering in Baur et al. (2012). The consideration of the inter-epoch correlations introduced by numerical differentiation is very important and only possible by means of error-propagation while empirical covariance functions fail for the direct differentiation of the 1s-samped orbit. The distinct dependence on the arc-length is not clarified but we assign it to the "mountain shape" of the weight-matrix, which values are growing with the arc-length (such an effect is not observed with empirical covariance functions). The identified arc-length is about one tenth of the revolution period and thus quite short. In general this might be critical due to the sensitivity of the low-degree harmonics to short arc-lengths.

We suggest to apply the orbit covariance matrices for data-weighting if they are of high quality and to use the method described in Baur et al. (2012) in case of missing or unreliable orbit covariance matrices and the presence of severe orbit outliers.

Improvements of hl-SST analysis methods are important not only for GOCE-only gravity modeling but also in view of the upcoming Swarm (Friis-Christensen et al. 2006) mission, being important as a filler of a possible gap between GRACE and a GRACE-Follow-On mission.

References

Baur O, Reubelt T, Weigelt M, Roth M, Sneeuw N (2012) GOCE orbit analysis: long wavelength gravity field determination using the acceleration approach. Adv Space Res 50(3):385–396. doi:10.1016/j.asr.2012.04.022

Bock H, Jäggi A, Meyer U et al (2011) GPS-derived orbits for the GOCE satellite. J Geod 85(11):807–818. doi:10.1007/s00190-011-0484-9

Ditmar P, Van Eck van der Sluijs A (2004) A technique for modeling the Earth's gravity field on the basis of satellite accelerations. J Geod 78(1):12–33. doi:10.1007/s00190-003-0362-1

EGG-C (2010) GOCE level 2 product data handbook. GO-MA-HPF-GS-0110 (4.3)

ESA (1999) The four candidate earth explorer core missions – gravity field and steady-state ocean circulation mission. ESA SP-1233, 1999

Friis-Christensen E, Lühr H, Hulot G (2006) Swarm: a constellation to study the earth's magnetic field. Earth Planets Space 58(4):351–358

Han SC, Jekeli C, Shum CK (2002) Efficient gravity field recovery using in situ disturbing potential observables from CHAMP. Geophys Res Lett 29:1789. doi:10.1029/2002GL015180

Jäggi A, Bock H, Prange L et al (2011) GPS-only gravity field recovery with GOCE, CHAMP, and GRACE. Adv Space Res 47(6):1020–1028. doi:10.1016/j.asr.2010.11.008

Löcher A (2010) Möglichkeiten der Nutzung kinematischer Satellitenbahnen zur Bestimmung des Gravitationsfeldes der Erde. Ph.D. Thesis, Rheinische Friedrich-Wilhelms-Universität zu Bonn (in German)

Mayer-Gürr T, Ilk KH, Eicker A, Feuchtinger M (2005) ITG-CHAMP01: a CHAMP gravity field model from short kinematic arcs over a one-year observation period. J Geod 78(7–8):462–480

Mayer-Gürr T, Kurtenbach E, Eicker A (2010) The satellite-only gravity field model ITG-Grace2010s. http://www.igg.uni-bonn.de/apmg/index.php?id=itg-grace2010

Pail R, Bruinsma S, Migliaccio F et al (2011) First GOCE gravity field models derived by three different approaches. J Geod 85(11):819–843. doi:10.1007/s00190-011-0467-x

Reigber C (1989) Gravity field recovery from satellite tracking data. In: Sansò F, Rummel R (eds) Theory of satellite geodesy and gravity field determination, lecture notes in earth sciences, vol 25. Springer, Berlin, pp 197–234

Reubelt T (2009) Harmonische Gravitationsfeldanalyse aus GPS-vermessenen kinematischen Bahnen niedrig fliegender Satelliten vom Typ CHAMP, GRACE und GOCE mit einem hoch aufösenden Beschleunigungsansatz, Deutsche Geodätische Kommission, C 632. Verlag der Bayerischen Akademie der Wissenschaften, Munich (in German)

Reubelt T, Austen G, Grafarend EW (2003) Harmonic analysis of the Earth's gravitational field by means of semi-continuous ephemerides of a low Earth orbiting GPS-tracked satellite. Case study: CHAMP. J Geod 77(5–6):257–278. doi:10.1007/s00190-003-0322-9

Reubelt T, Götzelmann M, Grafarend EW (2006) Harmonic analysis of the earth's gravitational field from kinematic CHAMP orbits based on numerically derived satellite accelerations. In: Flury J, Rummel R, Reigber C, Rothacher M, Boedecker G, Schreiber U (eds) Observation of the earth system from space. Springer, Berlin, pp 27–42

Reubelt T, Sneeuw N, Grafarend EW (2012) Comparison of kinematic orbit analysis methods for gravity field recovery. In: Sneeuw N, Novák P, Crespi M et al (eds) VII Hotine-Marussi symposium on mathematical geodesy, IAG Symp 137:259–265. Springer, Berlin

Van Gelderen M, Koop R (1997) The use of degree variances in satellite gradiometry. J Geod 71(6):337–343. doi:10.1007/s001900050101

Use of High Performance Computing for the Rigorous Estimation of Very High Degree Spherical Harmonic Gravity Field Models

Jan Martin Brockmann, Lutz Roese-Koerner, and Wolf-Dieter Schuh

Abstract

The estimation of the global Earth's gravity field parameterized as a finite spherical harmonic series is computationally demanding. The computational effort depends on the one hand on the maximal resolution of the spherical harmonic expansion and on the other hand on the number of observations which might be several millions. All global high-resolution Earth's gravity field models currently available above degree and order 360 were computed introducing approximations, significantly reducing the numerical complexity. For example, the prerequisites for the orthogonality of the spherical harmonic base functions, leading to a block diagonal system of normal equations, are often introduced artificially by working with equally distributed data along parallels assuming constant accuracy. These methods do not allow for a complex modeling of the observation errors, or the inclusion of redundant observations.

Within this contribution, we demonstrate how high-performance computers can be used for very high degree gravity field determination without introducing approximations. In addition, complex modeling of the observation errors is made possible within the algorithm to derive consistent error estimates for the spherical harmonic coefficients. Based on the high performance computing library ScaLAPACK, a gravity field solver was implemented which allows for the estimation of high degree gravity fields (e.g. degree and order 720, resulting in more than 500,000 unknown parameters) from various data sources with the direct solution method using assembly and solution of full normal equations.

Keywords

Assembling of normal equations • Data combination • Global gravity field • Massive parallel computations • ScaLAPACK • Spherical harmonics

1 Introduction

Recently published Global Earth Gravity field Models (GEGMs) can be divided into three main classes. The first class is that of satellite-only gravity field models, derived from the observations of individual, dedicated satellite missions such as CHAMP (CHAllenging Mini-Satellite Payload, Reigber et al. 2002), GRACE (GRAvity recovery and Climate Experiment, Tapley et al. 2004) and GOCE (Gravity field and steady-state Ocean Circulation Explorer, ESA 1999). Each of these models reflects the particular strengths of the satellite missions in terms of their spectral domain of sensitivity to the gravity signal. The resolutions of GEGMs derived from satellite data are quite limited e.g. maximum spherical harmonic degree 250 for the current GOCE mission. Due to this limitation of the spherical harmonic expansion to relatively low

J.M. Brockmann (✉) • L. Roese-Koerner • W.-D. Schuh
Department of Theoretical Geodesy, Institute of Geodesy and Geoinformation, University of Bonn, Nussallee 17, 53115 Bonn, Germany
e-mail: brockmann@geod.uni-bonn.de; roese-koerner@geod.uni-bonn.de; schuh@geod.uni-bonn.de

U. Marti (ed.), *Gravity, Geoid and Height Systems*, International Association of Geodesy Symposia 141,
DOI 10.1007/978-3-319-10837-7_4,

degrees/orders, however, the normal equations (NEQs) with respect to the unknown gravity field coefficients (see e.g. Pail and Plank 2002; van Geemert et al. 2000; Neumayer 2010; Baur and Keller 2010) are relatively easy to manage, requiring at most 30 Gigabytes (GB) of memory.

The second class of GEGMs consists of combined satellite-only models, which are computed by merging individual satellite-only models. Such combinations can be computed rigorously under the assumptions that the covariance matrices of the estimated spherical harmonic coefficients for each of the individual models reflect their true error characteristics and that the relative weighting can be determined correctly. Therefore, the processing centers make huge efforts, on the one hand, to derive the error characteristics of the individual models as realistically as possible (see e.g. van Loon and Kusche 2005; Mayer-Gürr et al. 2010 concerning GRACE, and Schuh 2003; Schuh et al. 2010 for GOCE). On the other hand, the relative weighting is usually determined via variance component estimation (VCE, cf. Koch and Kusche 2002). If the combination is carried out properly, a combined satellite-only model comprises the strengths of the individual models. The computation of a combined model is rather simple if the individual full normal equations are available. This strategy was performed, for instance, for a GRACE-GOCE combination (Pail et al. 2010; Förste et al. 2008, 2011).

This paper is concerned with the third class of GEGMs, which may be characterized as follows. The key idea behind these models is to assemble as much information into a GEGM as available. In addition to the satellite-only models, such information consists mainly in altimetry and terrestrial data measured via aero-gravimetry or as point-wise gravity anomalies on the Earth's surface. With the inclusion of these additional types of observation i.e., densely distributed point observations relatively close to the Earth's surface, the feasible resolution of the GEGM may be increased considerably (at least up to degree and order (d/o) 360 and realistically up to 2,159 such as for the Earth Gravitational Model 2008 (EGM2008), Pavlis et al. 2012), as the point-wise measurements contain all wavelengths of the gravity signal. For such high-degree GEGM determination, the computational and memory requirements increase considerably. To counteract this increase, some simplifications concerning altimetry and terrestrial observations were introduced into the determination of recently published GEGMs above d/o 360. These simplifications, which exploit the orthogonality properties of the Legendre base functions (see e.g. Förste et al. 2008; Pavlis et al. 2012), may be summarized as follows. If the data (1) are given at equidistant points along the parallels, (2) are uncorrelated, and (3) have the same accuracy, then the resulting normal equation matrices are order-wise block-diagonal (Colombo 1981). As these block-diagonal matrices are relatively small, the computational and memory requirements for their assembly, storage and solution of the equation system are also comparably small. It is well known, however, that these simplifying assumptions are not true for real altimetry and terrestrial gravity measurements. Terrestrial and altimetry data are either not available with global coverage, or their availability is restricted (Pavlis et al. 2012). Therefore, interpolation techniques (Andersen and Knudsen 2009), collocation-based prediction (Tscherning 1981) or computation of fill-in values from satellite-only models (e.g. Gruber 2001) are applied.

Within this contribution, it should be demonstrated, that a rigorous computation of a high degree spherical harmonic GEGM is possible. Using high performance computing (HPC), the assembly and solution of full normal equations (NEQs) is implemented for the least squares solution of at least spherical harmonic d/o 720. Thus, more than half a million of parameters are estimated from millions of observations. The resulting NEQs of about 2 Terabyte (TB) are assembled in parallel using a block-cyclic distribution and solved using Cholesky decomposition from the ScaLAPACK (Scalable Linear Algebra PACKage, Blackford et al. 1997) library. The inversion is performed to derive the corresponding covariance matrix. The software is implemented using HPC (quasi-)standards like the Message Passing Interface (MPI), PBLAS (Parallel Basic Linear Algebra Subprograms, Choi et al. 1995) and ScaLAPACK. Section 2 summarizes the general mathematical problem and the numerical challenges and defines fundamentals for the algorithmic design. Within Sect. 3, an overview about the implemented solver is given. The basic HPC challenges are summarized and an approach towards the solution is briefly presented. Section 4 describes the setup of a closed-loop simulation scenario, which is used as a proof of concept for the implemented solver. A summary and some conclusions are given in section "Summary and Conclusions".

2 Mathematical Model

The overall goal is to assemble and solve the combined least squares normal equation system

$$\left(\sum_{n=1}^{N}\frac{1}{\sigma_n^2}\mathbf{N}_n+\sum_{o=1}^{O}\frac{1}{\sigma_o^2}\mathbf{A}_o^T\mathbf{Q}_{\mathbf{l}_o\mathbf{l}_o}^{-1}\mathbf{A}_o\right)\mathbf{x}= \sum_{n=1}^{N}\frac{1}{\sigma_n^2}\mathbf{n}_n+\sum_{o=1}^{O}\frac{1}{\sigma_o^2}\mathbf{A}_o^T\mathbf{Q}_{\mathbf{l}_o\mathbf{l}_o}^{-1}\mathbf{l}_o, \tag{1}$$

$$\mathbf{N}\mathbf{x}=\mathbf{n} \tag{2}$$

where

– $\mathbf{N}_n$ and $\mathbf{n}_n$ are the N normal matrices and normal vectors of the band-limited normal equations of preprocessed data

(e.g. derived from the satellite missions CHAMP, GRACE and GOCE),
- for the use of VCE the number of observations n_n used in the assembly of the NEQs and the product $\mathbf{l}_n^T \mathbf{Q}_{\mathbf{l}_n\mathbf{l}_n}^{-1} \mathbf{l}_n$ have to be known,
- $\mathbf{A}_o$, $\mathbf{l}_o$ and $\mathbf{Q}_{\mathbf{l}_o\mathbf{l}_o}$ are the O design matrices, observation vectors and their covariance matrices of the observation equations of high resolution gravity data (e.g. point observations),
- $\frac{1}{\sigma_n^2}$ and $\frac{1}{\sigma_o^2}$ are unknown weights, which should be iteratively estimated using VCE,
- $\mathbf{N}$ and $\mathbf{n}$ are the normal matrices and normal vector of the weighted and combined final normal equations which should be solved to determine the unknown spherical harmonic parameters in $\mathbf{x}$.

The general assembly and solution of (1) is rather simple and straightforward. The scientific challenges arise from the aspired spherical harmonic resolution, and thus from the number of parameters to be estimated (at least half a million). To handle this, the assembly and solution of (1) is mapped to an implementation, which is capable to run on a distributed massive parallel supercomputer making use of thousands of processors. The C++ software is designed to meet the following fundamentals:

1. The software should process matrices in-core, i.e. the whole normal equation should be assembled without swapping parts of the matrix to disk. Thus expensive data in- and output is minimized. In addition disk-space is avoided to be a limiting criterion.
2. The number of already preprocessed normal equations N and the number of observation groups O should be arbitrary. Thus an arbitrary number of variance components (VCs) should be estimable.
3. HPC standard concepts and libraries should be used to derive a portable software and to guarantee a wide range of functionality (e.g. extension of the software, operations on matrices).

To make use of matrix related operations provided in the PBLAS library and linear algebra related operations provided in the ScaLAPACK library, all matrices involved in the computations are stored in the so called two-dimensional block-cyclic distribution (cf. Blackford et al. 1997, pp. 58–69). A matrix $\mathbf{A}$ (cf. Fig. 1b) is divided into sub blocks of dimension $b_r \times b_c$ and cyclically distributed along the rectangular processor grid of dimension $R \times C$ (cf. Fig. 1a) along the grids rows and columns. This block-cyclic distribution of a matrix results in block-cyclic distributed local matrices on individual processors as shown by Fig. 1c. Whereas the basic algorithms to operate on block-cyclic distributed matrices are available within PBLAS and ScaLAPACK (e.g. matrix multiplications, factorizations, etc), we implemented the setup, administration and distribution of the block-cyclic scheme, which served as a basis for the implemented solver.

3 Overview of the Implemented Solver

Within this section an overview of the implemented solver should be given. The computational demanding tasks and challenges are briefly summarized without going into the technical details. Instead fundamental concepts are explained.

3.1 Assimilation of Preprocessed Normal Equations

We assume, that the observation groups $n \in \{1 \dots N\}$ are already available as NEQs. Thus, one of the main tasks is to efficiently read the normal equations from disk and map them to the two-dimensional block-cyclic distribution, as characterized in Fig. 1. As this NEQs might be large (e.g. 30 GB for GOCE NEQs, or even larger), it can not be assumed that a single processor is able to read them and distribute parts to

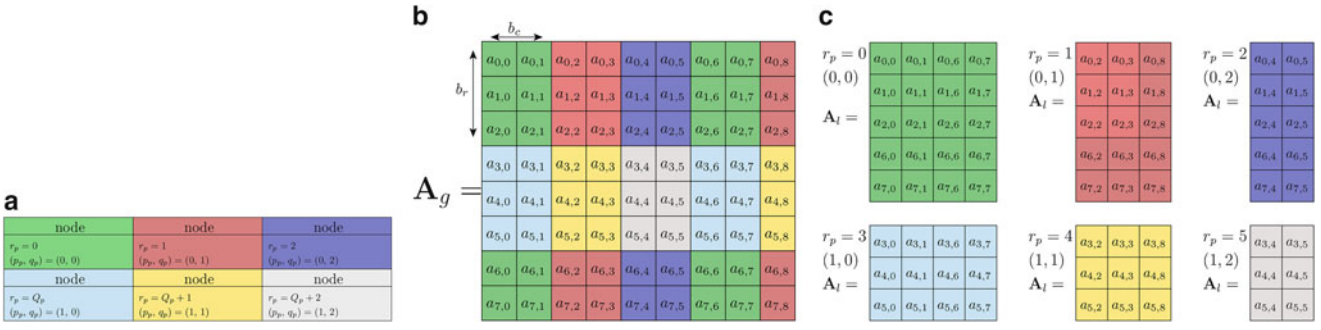

Fig. 1 Example of a two-dimensional matrix distribution. An 8×9 matrix is distributed to a 2×3 processor grid. The block size for distribution was chosen as $b_r = 3$ and $b_c = 2$. $\mathbf{A}_l$ are the locally stored sub matrices on the individual processors. (**a**) Example processor grid, (**b**) example matrix to distribute, (**c**) local matrices on individual processors

the other processors afterwards with MPI send and receive operations. Instead, based on the MPI2 (MPI-Forum 2009) standard, a parallel file reading was implemented, to directly read the normal equations into the block-cyclic distribution. The basic concept is to define processor specific views on the (linear) file, which hide elements of the matrix, which do not belong to the processors local matrix. If the file views are correctly set, the linear file can be directly read in parallel to the processors individual linear main memory reserved for the local part of the distributed matrix. For the general concept see e.g. Gropp et al. (1999, Chap. 3). This concept can be efficiently implemented as well for file/matrix readings as for the write operations. Using this technique, reading of large matrices is fast, with disk/network bandwidth as limiting factor. For example the time for the distributed reading of a 30 GB GOCE normal equation was measured to be 37 s on a 8×8 processor grid (64 processors), 33 s on a 48×48 processor grid (2,304 processors) and 39 s on a 80×80 processor grid (6,400 processors). It is important to realize, that after the reading operation, the matrices are already in the chosen block-cyclic distribution. The time for reading does neither significantly depend on the distribution chosen nor significantly on the number of processors used (for comparison, it takes 90 s to read the same matrix with Matlab on a single processor). Note that the file view is computed at runtime, thus a generally saved matrix (e. g. column-wise) can be directly read into every block-cyclic distribution possible.

After the individual normal equations $\mathbf{N}_n$ have been read, they need to be combined to the joint normal equations $\mathbf{N}$ and $\mathbf{n}$, respectively, by a weighted addition. The normal equations $\mathbf{N}_n$ are general available in different numbering schemes, as they are assembled for different spherical harmonic resolutions and are thus different in size. In addition, they are only assembled for a subset of the parameters $\mathbf{N}$ should be assembled for. Thus, it is necessary to implement reordering algorithms (i.e. a sequence of row and column interchanges) based on the distributed matrices. Either parts of $\mathbf{N}$ have to be reordered to the numbering scheme of $\mathbf{N}_n$ or the size of $\mathbf{N}_n$ has to be adjusted to the size of $\mathbf{N}$ (via inclusion of zero rows and columns) and reordered to the numbering scheme chosen for $\mathbf{N}$. To be as flexible as possible, for each normal equations involved in the processing, a symbolic numbering scheme is associated to the NEQs. Based on the symbolic numbering scheme, an index vector as well as the sequential permutation vector is computed at runtime. Using the sequential permutation vector, the ScaLAPACK function `pdlapiv` is used to perform firstly the column interchanges and secondly the row interchanges on the distributed matrix. Afterwards, the addition of the matrix subsets can be performed. For example, using the implemented methods, it takes less than 50 s to reorder 30 GB NEQs (measured on an 6×6 processor grid).

3.2 Assimilation of Observation Equations

The computational most demanding challenge within the processing of the groups $o \in \{1 \dots O\}$ is the assembly of the normal equations $\mathbf{N}_o = \mathbf{A}_o^T \mathbf{Q}_{\mathbf{l}_o\mathbf{l}_o}^{-1} \mathbf{A}_o$ from the original observations. As these observations are assumed to contain the maximal signal content as defined by the maximal degree of the spherical harmonic expansion chosen for the processing, the normal equations have to be assembled from millions of observations, for at least half a million of parameters resulting in a size of at least 2 TB.

A tailored highly scalable implementation of the computation of $\mathbf{N}_o$ was implemented for uncorrelated observations (diagonal matrices $\mathbf{Q}_{\mathbf{l}_o\mathbf{l}_o}$). In that case, the setup of $\mathbf{A}_o$ is relatively fast, compared to the computation time of $\mathbf{A}_o^T \mathbf{Q}_{\mathbf{l}_o\mathbf{l}_o}^{-1} \mathbf{A}_o$. Assume $\mathbf{N}_{o(r,c)}$ to be the local part of $\mathbf{N}_o$ stored on the processor with coordinates r, c in the processor grid. Let $\mathcal{P}_{r(r,c)}$ and $\mathcal{P}_{c(r,c)}$ be the set of parameters, contained in the rows and columns of the local matrix $\mathbf{N}_{o(r,c)}$, respectively. A rough estimation for the dimension of $\mathbf{N}_{o(r,c)}$ is number of parameters$/R$ or number of parameters$/C$, respectively, where $R \times C$ is the dimension of the processor grid. In reality, it is more complex, as the dimensions are of course integer numbers and depend on the block sizes b_r and b_c introduced in Fig. 1. Every processor can individually assemble $\mathbf{N}_{o(r,c)}$, via the computation of $\mathbf{A}_{o(\mathcal{P}_{r(r,c)})}^T \mathbf{Q}_{\mathbf{l}_o\mathbf{l}_o}^{-1} \mathbf{A}_{o(\mathcal{P}_{c(r,c)})}$, where $\mathbf{A}_{o(\mathcal{P}_{r/c(r,c)})}$ is the design matrix of all observations, but assembled only for the corresponding subset of the parameters. As the observations are assumed to be independent, $\mathbf{A}_{o(\mathcal{P}_{r(r,c)})}$ and $\mathbf{A}_{o(\mathcal{P}_{c(r,c)})}$ are not set up for all observations of group o at once, instead $\mathbf{N}_{o(r,c)}$ is updated in a loop of smaller observation blocks. The setup of the design matrices $\mathbf{A}$ has to be repeated for every single observation. This yields the advantage that the computation of $\mathbf{N}$ works without intra-processor communications. In addition, the runtime could be decreased by making use of symmetry of the resulting matrix $\mathbf{N}$ and via the selection of a proper numbering scheme for $\mathbf{N}$ (parameters in $\mathcal{P}_{r(r,c)}$ and $\mathcal{P}_{c(r,c)}$ should be of same orders, efficient recursive computation of base functions).

3.3 Estimation of Data Weights

As mentioned within Sect. 2, the implemented method should be in-core, thus the individual computed NEQs $\mathbf{N}_o$ are not stored on disk, instead they are directly added to $\mathbf{N}$. Thereby it is avoided that the number of observation groups is a limiting factor. Otherwise a number of e.g. $O = 50$ observation groups would result in at least 50 TB disk space for the test scenario of spherical harmonic d/o 720, just to store $\mathbf{N}_o$, for $o \in \{1 \dots 50\}$. Nevertheless, if weights should be derived using VCE (cf. Koch and Kusche 2002), the

partial normal equations are needed to derive the variance components (VCs) of the observation groups

$$1/\sigma_{0,o}^2 = \frac{n_o - u_o}{\mathbf{v}_o^T \mathbf{Q}_{\mathbf{l}_o\mathbf{l}_o}^{-1} \mathbf{v}_o}, \tag{3}$$

where $\mathbf{v}_o^T \mathbf{Q}_{\mathbf{l}_o\mathbf{l}_o}^{-1} \mathbf{v}_o$ is the weighted sum of squared residuals, n_o the number of observations in group o and u_o the partial redundancy $u_o = \frac{1}{\sigma_{0,o}^2} \text{trace}\left(\mathbf{N}_o \mathbf{N}^{-1}\right)$. Note that the same equations hold for the NEQ groups n, where in addition n_n and $\mathbf{l}_n^T \mathbf{Q}_{\mathbf{l}_n\mathbf{l}_n}^{-1} \mathbf{l}_n$ have to be known. As suggested by Koch and Kusche (2002), the estimation of the trace term within the computation of the partial redundancy can be replaced by a stochastic trace estimator. If this Monte-Carlo based technique is used, $\mathbf{N}_o$ is not required anymore, instead (1) has just to be assembled and solved for additional right hand sides (e.g. Koch and Kusche 2002; Brockmann and Schuh 2010). Thus, the number of observation groups involved is kept arbitrary and does not depend on the available storage.

4 Simulation Scenario

To test the implementation and to demonstrate that rigorous high resolution gravity field determination is possible within a reasonable amount of computing time, a simulated set of test data was generated. Based on the EGM2008 model, $(N + O) = 14$ individual (sub-)data sets were generated. The individual data sets should simulate (i) terrestrial high resolution data sets of different quality ($O = 11$) and (ii) different satellite gravity field data available as normal equations ($N = 3$).

4.1 Simulated Datasets

A global $0.2° \times 0.2°$ grid was partitioned to 11 patches using continent borders, simulating 11 different data sets of different quality. All in all 1.6 million gravity anomalies were simulated up to spherical harmonic d/o 720 using EGM2008. A data point and data group specific white noise was added to every observation i, with covariance

$$\boldsymbol{\Sigma}_{\mathbf{l}_o\mathbf{l}_o} = \sigma_{0,o}^2 \cdot \boldsymbol{Q}_{\mathbf{l}_o\mathbf{l}_o}, \quad \sqrt{\boldsymbol{Q}_{\mathbf{l}_o\mathbf{l}_o}(i,i)} \sim \mathcal{U}(0.9, 1.1), \tag{4}$$

where $\sigma_{0,o}$ is the group specific standard deviation to be estimated via VCE and $\sqrt{\boldsymbol{Q}_{\mathbf{l}_o\mathbf{l}_o}(i,i)}$ is the accuracy assumed to be a-priori known. All 11 datasets are summarized in the upper Table 1.

Within the simulation, realistic error characteristics of the satellite-only gravity fields should be assumed for $n \in \{1 \ldots 3\}$ groups which should be combined as NEQs (i.e. GRACE, GOCE satellite gravity gradients (SGG) and GOCE satellite-to-satellite tracking (SST)). Thus, right hand sides were simulated using the EGM2008 coefficients and a correlated error was added (generated with the full covariance matrix of a real model, cf. lower Table 1). In addition, a variance factor $\sigma_{0,n}^2$ was introduced to be recovered by VCE.

Table 1 Summary of all 14 simulated data sets

o	Dataset	# obs.	o	Dataset	# obs.
1	Africa	63,750	2	Antarctica	155,576
3	Australia	17,276	4	Eurasia	163,691
5	Greenland	17,061	6	Indonesia	5,095
7	Island	497	8	N. Zealand	724
9	N. America	75,048	10	S. America	38,504
11	Ocean	1,082,778			

n	Dataset	Resolution	Covariance	$\sigma_{0,n}$
1	GRACE	2–180	$\boldsymbol{\Sigma}_{\text{ITG-Grace2010s}}$	1.0541
2	GOCE SST	2–100	$\boldsymbol{\Sigma}_{\text{TIMRL03SST}}$	0.9129
3	GOCE SGG	2–250	$\boldsymbol{\Sigma}_{\text{TIMRL03SGG}}$	0.9535

4.2 Results

The software presented was used to recover the spherical harmonic coefficients of the degrees and orders of 2–720 from the simulated data described in Sect. 4.1. In addition, VCs were estimated to recover $\sigma_{0,n}$ and $\sigma_{0,i}$. The covariance matrix of the spherical harmonic coefficients is derived via the inversion of the full combined NEQs. Figure 2 shows the results from the three iteration steps compared to the reference model EGM2008. The EGM2008 coefficients were recovered within the estimated accuracy. The estimated formal errors are consistent to the coefficient errors. The derived VCs of all three iterations are shown in Table 2. The true values used in the simulation were recovered up to the first digit.

Summary and Conclusions

A gravity field solver for the estimation of very high degree spherical harmonic gravity field models was implemented within an high performance computing environment. With this solver it is possible to use thousands of processors in parallel to assemble, solve and invert the full NEQs. Approximations to reduce the computational complexity are avoided, the rigorous least squares solution is derived. An arbitrary number of data sets (normal and observation equations) can be combined and group specific weights are estimated from the data. Within a closed loop simulation NEQs of 2 TB (d/o 720, 520,000 parameters) were assembled from 1.6 mio observations and three groups available as normal equations. The combined NEQs were solved for the unknown parameters and inverted to derive the covariance matrix. The model

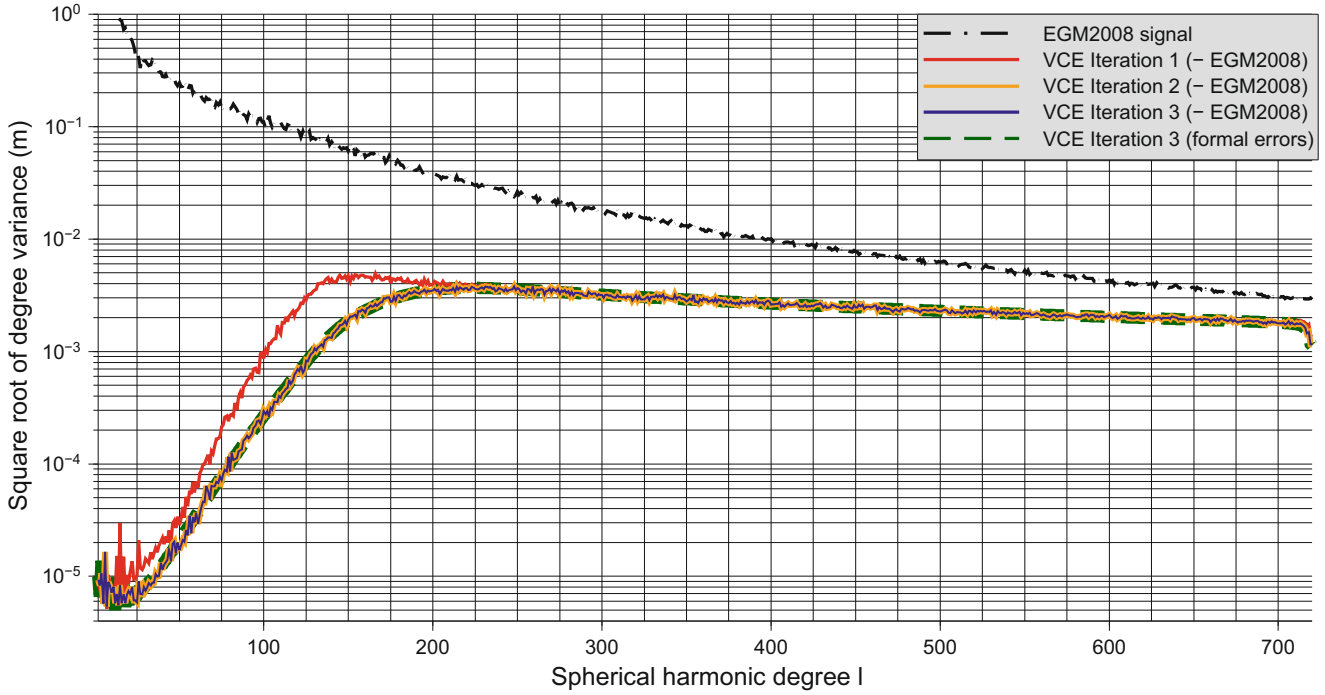

Fig. 2 Degree variances derived from absolute coefficient differences of the three iteration steps compared to EGM2008. Finally estimated formal errors are shown in green (in agreement with the *orange* and *blue line*) (Color figure online)

Table 2 Square root of derived VCs of the three iterations

Dataset	$\sigma_{0,o}$	$\hat{\sigma}_{0,o}^{(0)}$	$\hat{\sigma}_{0,o}^{(1)}$	$\hat{\sigma}_{0,o}^{(2)}$
Africa	15.0	1.00	14.81	14.92
Antarctica	25.0	1.00	24.85	24.88
Australia	6.0	1.00	6.01	6.02
Eurasia	8.0	1.00	7.95	7.97
Greenland	9.0	1.00	8.91	8.92
Indonesia	13.0	1.00	12.53	12.97
Island	7.0	1.00	6.92	7.02
N. Zealand	13.5	1.00	13.05	13.43
N. America	5.0	1.00	4.97	4.96
S. America	18.0	1.00	17.84	18.00
Ocean	6.0	1.00	6.04	6.00
Dataset	$\sigma_{0,n}$	$\hat{\sigma}_{0,n}^{(0)}$	$\hat{\sigma}_{0,n}^{(1)}$	$\hat{\sigma}_{0,n}^{(2)}$
GRACE	1.0541	1.00	1.0659	1.0534
GOCE SST	0.9129	1.00	0.9129	0.9129
GOCE SGG	0.9535	1.00	0.9599	0.9533

and unknown weights could be recovered within the accuracy of the estimated parameters.

The simulation was performed on a different number of processors on the supercomputer JUROPA/Jülich, 2,304 (minimal number required to store 2 TB NEQs), 2,704, 4,096, 6,400 and 7,744. For the computational most complex part, the assembling of $\mathbf{N}_o$, a nearly linear scaling behavior was achieved (2,704 procs–17,791.6 s $\Rightarrow$ 7,744 procs–6,080.4 s). Thus, the 520,000 $\times$ 520,000 NEQs can be assembled in about one and a half hour from 1.6 mio of observations and solved in less than 45 min.

Acknowledgements The study was founded within the DFG project G/O2000+ (SCHU2305/3-1). The computations were performed on the JUROPA supercomputer at FZ Jülich. The computing time was granted by the John von Neumann Institute for Computing (project HBN15). The comments of and the discussion with the three anonymous reviewers and the editor are gratefully acknowledged as they improved the quality of the manuscript.

References

Andersen O, Knudsen P (2009) DNSC08 mean sea surface and mean dynamic topography models. J Geophys Res 114:C11001. doi:10.1029/2008JC005179

Baur O, Keller W (2010) Computational considerations for satellite-based geopotential recovery. In: Nagel WE et al (eds) High performance computing in science and engineering 09. Springer, Berlin, pp 511–521. doi:10.1007/978-3-642-04665-0_35

Blackford LS, Choi J, Cleary A et al (1997) ScaLAPACK users guide. SIAM, Philadelphia

Brockmann JM, Schuh WD (2010) Fast variance component estimation in GOCE data processing. In: IAG symposia 135, Springer, Berlin Heidelberg, p 185–193. doi:10.1007/978-3-642-10634-7_25

Choi J, Dongarra JJ, Ostrouchov LS et al (1995) A proposal for a set of parallel basic linear algebra subprograms. Technical report 100, LAPACK Working Note, University of Tennessee, Knoxville

Colombo O (1981) Numerical methods for harmonic analysis on the sphere. No. 310. In: Reports of the department of geodetic science. The Ohio State University (OSU), Columbus

ESA (1999) The four candidate earth explorer core missions - gravity field and steady-state ocean circulation mission. ESA Report SP-1233(1), Granada

Förste C, Schmidt R, Stubenvoll R et al (2008) The GeoForschungsZentrum Potsdam/Groupe de Recherche de Gèodésie Spatiale satellite-only and combined gravity field models: EIGEN-GL04S1 and EIGEN-GL04C. J Geod 82:331–346. doi:10.1007/s00190-007-0183-8

Förste C, Bruinsma S, Shako R et al (2011) EIGEN-6 A new combined global gravity field model including GOCE data from the collaboration of GFZ-Potsdam and GRGS-Toulouse. In: Geophysical research abstract 13, EGU2011-3242-2, Vienna. http://icgem.gfz-potsdam.de/ICGEM/documents/Foerste-et-al-EGU_2011-01.pdf

Gropp W, Lusk E, Skjellum A (1999) Using MPI - portable parallel programming with the message-passing interface. In: Scientific and engineering computation. MIT, Massachusetts

Gruber T (2001) High resolution gravity field modeling with full variance-covariance matrices. J Geod 75:505–514. doi:10.1007/s001900100202

Koch K, Kusche J (2002) Regularization of geopotential determination from satellite data by variance components. J Geod 76:259–268. doi:10.1007/s00190-002-0245-x

Mayer-Gürr T, Eicker A, Kurtenbach E, Ilk KH (2010) ITG-Grace: Global static and temporal gravity field models from grace data. In: Stroink L et al (eds) System earth via geodetic-geophysical space techniques. Springer, Berlin, pp 159–168. doi:10.1007/978-3-642-10228-8_13

MPI-Forum (2009) MPI: A message-passing interface standard Version 2.2. University of Tennessee, Knoxville. http://www.mpi-forum.org/docs/mpi-2.2/

Neumayer K (2010) Parallelization and high performance computation for accelerated CHAMP and GRACE data analysis. In: Stroink L et al (eds) System earth via geodetic-geophysical space techniques. Springer, Berlin, pp 79–92. doi:10.1007/978-3-642-10228-8 7

Pail R, Plank G (2002) Assessment of three numerical solution strategies for gravity field recovery from GOCE satellite gravity gradiometry implemented on a parallel platform. J Geod 76:462–474. doi:10.1007/s00190-002-0277-2

Pail R, Goiginger H, Schuh WD et al (2010) Combined satellite gravity field model GOCO01s derived from GOCE and GRACE. Geophys Res Lett 37:L20314. doi:10.1029/2010GL044906

Pavlis NK, Holmes SA, Kenyon S, Factor JK (2012) The development and evaluation of the earth gravitational model 2008 (EGM2008). J Geophys Res 117:B04406. doi:10.1029/2011JB008916

Reigber C, Lühr H, Schwintzer P (2002) CHAMP mission status. Adv Space Res 30:129–134. doi:10.1016/S0273-1177(02)00276-4

Schuh WD (2003) The processing of band-limited measurements; filtering techniques in the least squares context and in the presence of data gaps. Space Sci Rev 108:67–78. doi:10.1023/A:1026121814042

Schuh WD, Brockmann JM, Kargoll B, Krasbutter I, Pail R (2010) Refinement of the stochastic model of GOCE scientific data and its effect on the in-situ gravity field solution. In: Lacoste-Francis H (ed) Proceedings ESA living planet symposium, ESA SP-686, Bergen

Tapley B, Bettadpur S, Ries J, Thompson P, Watkins M (2004) GRACE measurements of mass variability in the Earth system. Science 305:503–505. doi:10.1126/science.1099192

Tscherning C (1981) A FORTRAN IV program for the determination of the anomalous potential using stepwise least squares collocation. No. 220. Reports of the department of geodetic science, The Ohio State University (OSU), Ohio

van Geemert R, Koop R, Klees R, Visser P (2000) Application of parallel computing to gravity field recovery from satellite gravity gradiometric data. In: Ingber M, Brebbia HPCA (eds) High-performance computing in engineering VI. WIT Press, Southampton. doi:10.2495/HPC000101

van Loon J, Kusche J (2005) Stochastic model validation of satellite gravity data: a test with CHAMP pseudo-observations. In: IAG symposia 129. Springer, Berlin, pp 24–29. doi:10.1007/3-540-26932-0_5

Time Variable Gravity: Contributions of GOCE Satellite Data to Monthly and Bi-monthly GRACE Gravity Field Estimates

Moritz Rexer, Roland Pail, Thomas Fecher, and Ulrich Meyer

Abstract

A feasibility study by Pail et al. (Can GOCE help to improve temporal gravity field estimates? In: Ouwehand L (ed) Proceedings of the 4th International GOCE User Workshop, ESA Publication SP-696, 2011b) shows that GOCE ('Gravity field and steady-state Ocean Circulation Explorer') satellite gravity gradiometer (SGG) data in combination with GPS derived orbit data (satellite-to-satellite tracking: SST-hl) can be used to stabilize and reduce the striping pattern of a bi-monthly GRACE ('Gravity Recovery and Climate Experiment') gravity field estimate.

In this study several monthly (and bi-monthly) combinations of GRACE with GOCE SGG and GOCE SST-hl data on the basis of normal equations are investigated. Our aim is to assess the role of the gradients (solely) in the combination and whether already one month of GOCE observations provides sufficient data for having an impact in the combination. The estimation of clean and stable monthly GOCE SGG normal equations at high resolution (> d/o 150) is found to be difficult, and the SGG component, solely, does not show significant added value to monthly and bi-monthly GRACE gravity fields. Comparisons of GRACE-only and combined monthly and bi-monthly solutions show that the striping pattern can only be reduced when using both GOCE observation types (SGG, SST-hl), and mainly between d/o 45 and 60.

Keywords

Combination • GOCE • GRACE • Time variable gravity

1 Introduction

GRACE is the satellite mission which, today, is able to unprecedentedly observe temporal gravity variations globally at spatial scales of about 400 km (Tapley et al. 2007). An improvement of the performance of GRACE regarding the detection of time variable signals and their spatial resolution would be a real benefit not only from a geodetic perspective, but also for all applications relying on GRACE data, such as continental hydrology, cryospheric, ocean and solid Earth applications (see, e.g., Wahr and Molenaar 1998; Horwath et al. 2010, 2012; Güntner et al. 2007).

In contrast, GOCE is dedicated to observe the static part of the Earth's gravity field, and has not been designed to resolve time variable gravity signals (see ESA 1999). This is in accordance, e.g., with the study by Jarecki and Müller (2005) on gravity variations in GOCE gradiometer data. The authors find that de-aliasing of GOCE gradients regarding mass and gravity fluctuations in the system Earth is actually not necessary because the impact is found to be negligible. Their analyses show that modeled hydrological and ice mass

M. Rexer (✉) • R. Pail • T. Fecher
Institute for Astronomical and Physical Geodesy, Technische Universität München, Arcisstrasse 21, 80333 München, Germany
e-mail: m.rexer@tum.de; pail@bv.tum.de; fecher@tum.de

U. Meyer
Astronomical Institute, Universität Bern, Sidlerstrasse 5, 3012 Bern, Switzerland
e-mail: ulrich.meyer@aiub.unibe.ch

U. Marti (ed.), *Gravity, Geoid and Height Systems*, International Association of Geodesy Symposia 141,
DOI 10.1007/978-3-319-10837-7_5, © Springer International Publishing Switzerland 2014

changes are neither critical for GOCE gradients in terms of amplitude (< 1 mE) nor do the timescales of the changes fit into the gradiometer's measurement bandwidth ($5{\cdot}10^{-3}$ Hz to $1 \cdot 10^{-1}$ Hz, see ESA 1999). In the same way, the amplitudes of modeled gradients from oceanic and atmospheric mass changes as well as changes due to ocean and solid Earth tides are below the gradiometer's performance. It is pointed out, however, that de-aliasing can improve the stochastic modeling of the SGG errors.

According to Pail et al. (2011b) the improvement of GRACE temporal gravity field estimates by inclusion of GOCE data seems to be possible, because the error of GOCE is highly isotropic whilst GRACE suffers from anisotropic errors. These GRACE error-characteristics do not only evolve from short periodical gravity signals, affecting the observations and aliasing into monthly GRACE solutions, but also from the observation configuration (along-track ranging) being reflected in the normal equation matrix. Covariance propagation of the GRACE variance-covariance matrix to geoid heights gives evidence that the striping pattern already becomes visible in the geoid height errors at a spherical harmonic d/o of 30–40. It was shown when combining GRACE with GOCE (SGG + SST-hl) normal equations that the striping pattern is reduced significantly in the bi-monthly period November-December 2009, where GRACE flew a 7-day sub-cycle,mainly between d/o 30 and 40 (cf. Pail et al. 2011b)

In this contribution, monthly and bi-monthly gravity fields for the years 2009 and 2010 are estimated by a combination of full GRACE SST-ll, GOCE SGG and GOCE SST-hl normal equations, and the contribution of each of the two GOCE measurement types compared to pure GRACE fields is investigated. The aims are to find out (a) whether stable monthly GOCE SGG normal equations can be retrieved, (b) whether the gradiometer observations, solely or only in combination with GOCE SST observations, can reduce GRACE striping artefacts and (c) if the detected improvements (in Pail et al. 2011b) can be achieved also for monthly temporal gravity field estimates.

2 Background and Methodology

2.1 Processing Steps and Combination

The scheme in Fig. 1 illustrates the processing steps from the initial data sets to combined GRACE SST-hl and GOCE (SGG + SST-hl) gravity field estimates. The processing strategy was partly adopted from Rexer (2012), where combinations between GOCE gradients and GRACE have been performed.

Starting from GOCE's calibrated and corrected gravity gradient (GG) observations, previously corrected non-tidal

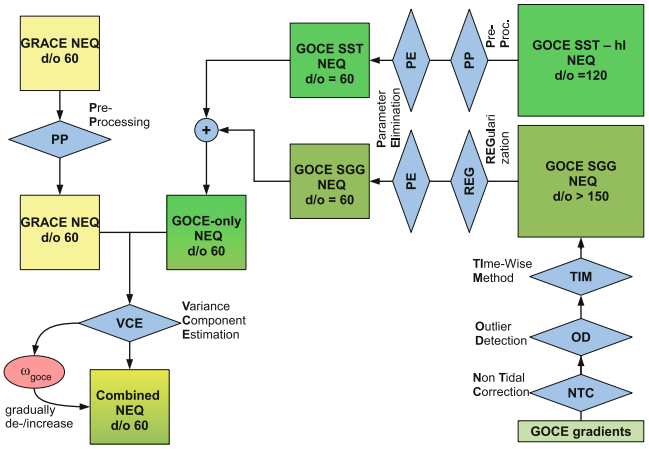

Fig. 1 Processing scheme for the combination of GOCE and GRACE observation types

time variable corrections are re-introduced (in order to be consistent to GRACE) and an outlier detection based on gravity gradient anomalies is performed. Here, gravity gradient anomalies are differences of the filtered GG observations and reference GGs computed from the ICGEM[1] listed gravity model *TIM_R3*, the third release of the purely GOCE derived (see e.g. Pail et al. 2010) gravity field model. Since it is based on more than 1 year of data, it has significantly higher accuracy than our monthly solutions, and thus can be used as a reference model. Each of the used GG components ($\frac{\partial^2}{\partial^2} T_{xx}$, $\frac{\partial^2}{\partial^2} T_{yy}$, $\frac{\partial^2}{\partial^2} T_{zz}$, $\frac{\partial^2}{\partial^2} T_{xz}$; T : potential; x,y,z : axes of gradiometer references frame) is searched for outliers, separately. An outlier is identified when the GG anomalies exceed a certain threshold, which is dependent on each component's inherit noise level. Here, following thresholds were used (expressed as multiples of the component's standard deviation σ) : $7 \cdot \sigma_{xx}$ for $\frac{\partial^2}{\partial^2} T_{xx}$, $6.5 \cdot \sigma_{yy}$ for $\frac{\partial^2}{\partial^2} T_{yy}$, $6.5 \cdot \sigma_{zz}$ for $\frac{\partial^2}{\partial^2} T_{zz}$, $7.5 \cdot \sigma_{xz}$ for $\frac{\partial^2}{\partial^2} T_{xz}$. Generally, 30 datapoints before and 300 datapoints after a detected outlier were flagged (accounting for 330 s data loss per detected outlier) and not used for the gravity field estimation.

In a next step full normal equations are assembled applying an implementation of the time-wise strategy (Pail et al. 2010). This strategy implies the complete decorrelation of the signal over its entire spectrum (Pail et al. 2011a). This is done by modeling the stochastic behavior of the gradiometer with an auto-regressive moving-average (ARMA) filter (for further information we refer to the list of publications on p. 822 in Pail et al. 2011a). Computations were done using the gravity modeling software at the *Institute for Astronomical and Physical Geodesy* (IAPG) on the local Linux cluster environment of the *Leibniz Rechenzentrum* (LRZ). The ill-conditioned SGG normal equations are regularized applying

[1] http://icgem.gfz-potsdam.de/ICGEM/ICGEM.html.

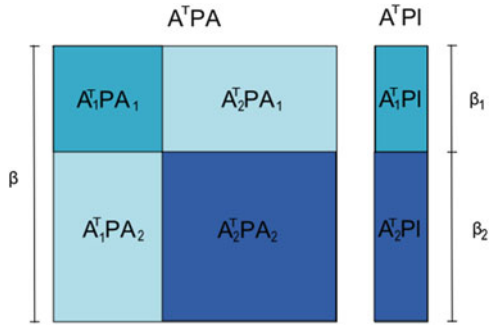

Fig. 2 Scheme of the full normal equation matrix $A^T PA$ and corresponding right-hand side $A^T Pl$ showing the division into parts which are relevant for the parameter elimination procedure

an order-dependent Kaula regularization (Metzler and Pail 2005), and afterwards the systems are reduced to d/o 60 by means of a least-squares parameter elimination. The least square parameter elimination is a useful and practical tool for reducing computational effort, simultaneously ensuring that there is no spectral loss or underparameterization as it would, e.g., result from a simple truncation at a lower spherical-harmonic degree. In other words, the coefficients of interest (here: up to d/o 60) are estimated from the complete information contained in the full normal equation system of the initial (larger) degree. Mathematically it is shown, e.g. by Niemeier (2008), that the reduced normal equation matrix $\bar{A}_1^T P \bar{A}_1$ of β_1 remaining and β_2 parameters to be eliminated is given by

$$\bar{A}_1^T P \bar{A}_1 = A_1^T PA_1 - A_1^T PA_2 \, (A_2^T PA_2)^{-1} \, A_2^T PA_1, \qquad (1)$$

where the quantities in the right side of the equation are parts of the full normal equation matrix $A^T PA$ with β parameters. Those parts are shown schematically in Fig. 2.

The reduced β_1 x 1 right-hand side $\bar{A}_1^T P \bar{l}$, likewise, can be computed from those parts using the expression

$$\bar{A}_1^T P \bar{l} = A_1 P l - A_1^T PA_2 (A_2^T PA_2)^{-1} A_2^T Pl \qquad (2)$$

with the reduced vector of observations $\bar{l}$, which follows:

$$\bar{l} = l - A_2 (A_2^T PA_2)^{-1} A_2^T Pl. \qquad (3)$$

Following Eqs. (1) and (2) the remaining parameters β_1 can be retrieved by solving the reduced normal equations as

$$\beta_1 = (\bar{A}_1^T P \bar{A}_1)^{-1} \, \bar{A}_1^T P \bar{l}. \qquad (4)$$

GRACE SST-ll (d/o 60) and GOCE SST-hl (d/o 120) full normal equations have been generated and provided by the *Astronomical Institute* at the *University Bern* (AIUB). In a pre-processing step their parameters are re-ordered with respect to their original sequence and the previously reduced static field AIUB-6YR is re-introduced to the right hand side. Therefore the residual field is solved first, following

$$\beta_{res} = (A^T PA)^{-1} \cdot A^T Pl, \qquad (5)$$

where β_{res} represents the coefficients of the residual field and then the *full* right hand side is retrieved by adding the AIUB-6YR coefficients according to

$$A^T Pl_{full} = (A^T PA) \cdot (\beta_{res} + \beta_{AIUB}). \qquad (6)$$

Similar to the GOCE SGG systems, the GOCE SST-hl normal equations are reduced to d/o 60 by means the parameter elimination.

For the optimum combination of the various normal equations, variance components (VCE) are estimated by an approach adapted from Koch and Kusche (2002). Due to the fact, that the VCE works correctly only for a pure stochastic error behavior, while GRACE's inherent stripes are highly systematic, weights varying up to plus/minus two orders of magnitude for GOCE (ω_{goce}) are tested. Doing so and analyzing the combinations in spectral domain, the optimum (maximum) weight for GOCE SGG (which would not degrade the total solution) can be easily found.

It is noted that the regularization in our approach affects the near-zonal coefficients only, and is needed to invert the ill-conditioned GOCE-SGG normal equations. In combined solutions, we find its impact to be insignificant and below noise level.

2.2 Evaluation of the Striping Error

In order to investigate the extent of the striping pattern in temporal gravity field estimates, a global *root mean square error* (RMSE) method is introduced. The basis for the RMSE is an hypothesized pure striping error which can be obtained by the subtraction of a smoothed GRACE solution (Gaussian smoothing (cf. Wahr and Molenaar 1998) with $R = 500$ km) of the same period. With this operation all stationary and time-variable gravity signals are eliminated in the respective month and only the (striping) error remains. Expressed in meters of equivalent water height, the RMSE is calculated from the gridded, point-wise striping error $\omega_{r,c}$ of a global grid with the size $R \times C$ (rows $\times$ columns) following

$$RMSE = \sqrt{\left(\frac{\sum_{r=1}^{R} \sum_{c=1}^{C} cos(\phi_r) \, \omega_{r,c}^2}{\sum_{r=1}^{R} \sum_{c=1}^{C} cos(\phi_r)} \right)}. \qquad (7)$$

A latitude Φ dependent weighting is applied in the RMSE calculation to take meridional convergence into account.

3 Results

3.1 Monthly GOCE SGG Solutions and Combinations with GRACE SST-II

In the attempt to create monthly normal equations solely from GOCE gradients, seven out of the nine operational months in the year 2010 delivered solvable solutions with resolutions ranging from d/o 150 to d/o 180 (with regularization applied, see Sect. 2.1). However, three of the solvable solutions show remaining error-structures in their spatial representations, which could not be removed, as flagging more outliers immediately led to an ill-conditioned system. Retrieving fields with reasonable resolution ($\geq$ d/o 150) is found to be necessary to avoid spectral leakage effects and to include potentially sensed temporal gravity (which would admittedly be of very small amplitude), well knowing that more stable systems could have been achieved at lower maximum degrees.

In the monthly combinations (using only months where no error structures in the spatial domain of SGG solutions were detected), no significant improvement w.r.t. the GRACE solution could be observed due to the inclusion of GOCE SGG data. In terms of the global RMSE, the improvements account for less than 1 % for all cases, at different degrees (see Table 1 for monthly and Table 2 for bi-monthly periods). Positive values in the table indicate a reduction of the striping error when compared to the GRACE-only solution, negative values denote an increase.

Table 1 RMSE improvement due to a combination with **GOCE SGG** data [in %] with respect to **monthly** GRACE-only solutions

Year	2009	2009	2010	2010	2010	2010
Period	November	December	January	May	June	December
d/o30	0.04	−0.05	0.21	0.64	−0.02	0.08
d/o35	−0.01	−0.07	0.36	0.08	0.30	0.40
d/o40	−0.04	0.00	0.41	−0.26	0.51	0.25
d/o45	−0.04	0.63	0.51	−0.47	1.90	0.11
d/o50	−0.11	0.11	0.16	0.62	0.27	1.02
d/o55	0.23	−0.13	−0.01	0.75	0.43	1.33
d/o60	0.56	−0.22	0.26	0.72	1.18	0.58
Average	0.09	0.01	0.28	0.30	0.65	0.54

Table 2 RMSE improvement due to a combination with **GOCE SGG** data [in %] with respect to **bi-monthly** GRACE-only solutions

Year	2009	2010
Period	November + December	May + June
d/o30	0.55	0.18
d/o35	0.13	0.00
d/o40	0.07	0.02
d/o45	0.55	0.04
d/o50	0.90	0.40
d/o55	0.01	0.57
d/o60	1.12	0.63
Average	0.01	0.26

3.2 Combined GRACE SST-hl, GOCE SGG and GOCE SST-hl Solutions

Analyzing the impact of both GOCE observation types in combination with the GRACE bi-monthly estimate of November+December 2009 shows, that the solution mainly gains (less error) in the degrees d/o 45–60. This becomes visible, e.g., looking at the standard deviations w.r.t. to the static satellite-only model GOCO02s (see Fig. 3). Note that the comparison to a static reference is not correct in a rigorous sense, as the investigated solutions contain temporal gravity signal. However, it is an indicator which in connection with the other results (see e.g., Figs. 4 and 5) shows that the error is being reduced in the combination.

Similar results are achieved for December 2009, but not to the same extent for the November 2009 monthly solution. A reason may be that the GRACE November solution is better and shows a lower formal error between d/o 45–60 than the December solution. Figure 4 shows the striping error (difference to corresponding smoothed field) and its reduction in

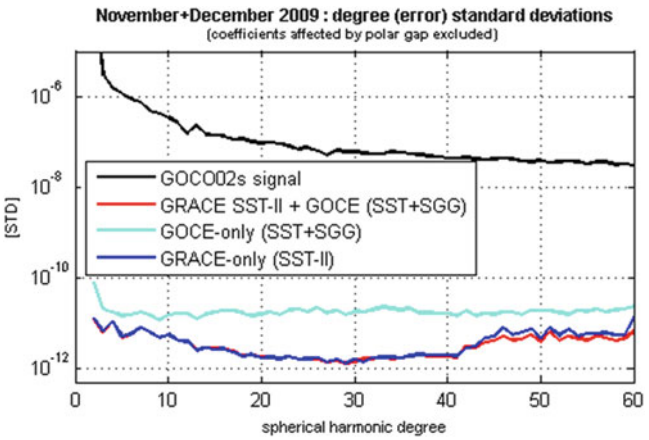

Fig. 3 (Error) degree standard deviations w.r.t. GOCO02s of the bi-monthly solution of 2009 (coefficients affected by the polar observation gap of GOCE satellite were excluded)

EWH for the bi-monthly period at d/o 50. Figure 5 shows the same matter for the monthly December 2009 solution. In terms of the global RMSE the striping could be reduced by nearly 22 % (from 21.11 to 16.56 cm) and 16 % (from 28.87 to 24.01 cm), respectively, due to the combination. Table 3 lists all the values for RMSE improvements of the combinations of the year 2009. Here, unfortunately, investigations must stay limited to the year 2009, as GOCE SST data could not be acquired for the year 2010.

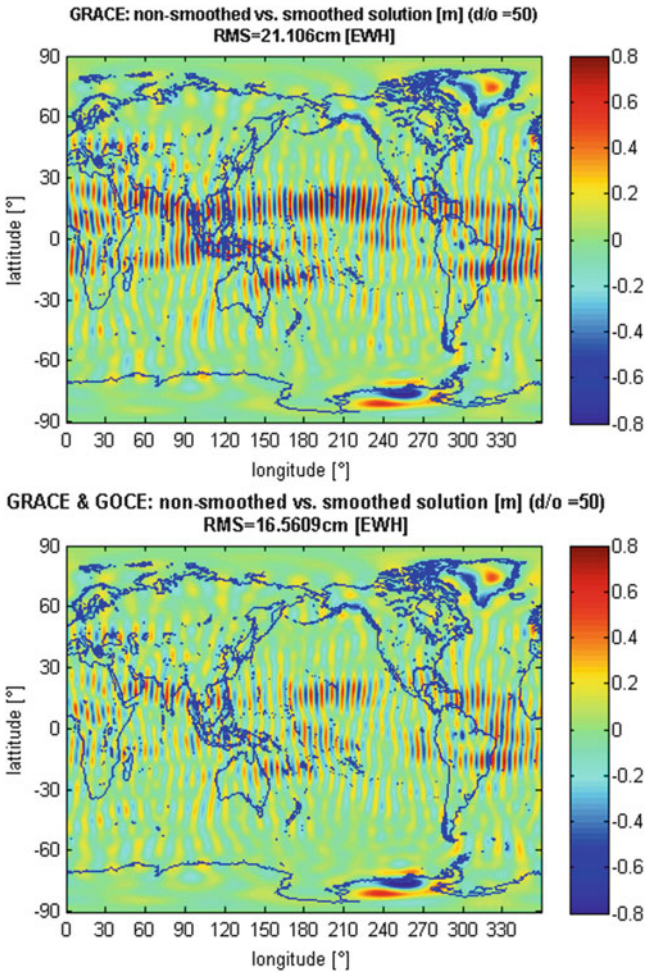

Fig. 4 Striping error of GRACE-only (*upper plot*) and combined solution (*lower plot*) for the bi-monthly November + December solution in [m] EWH

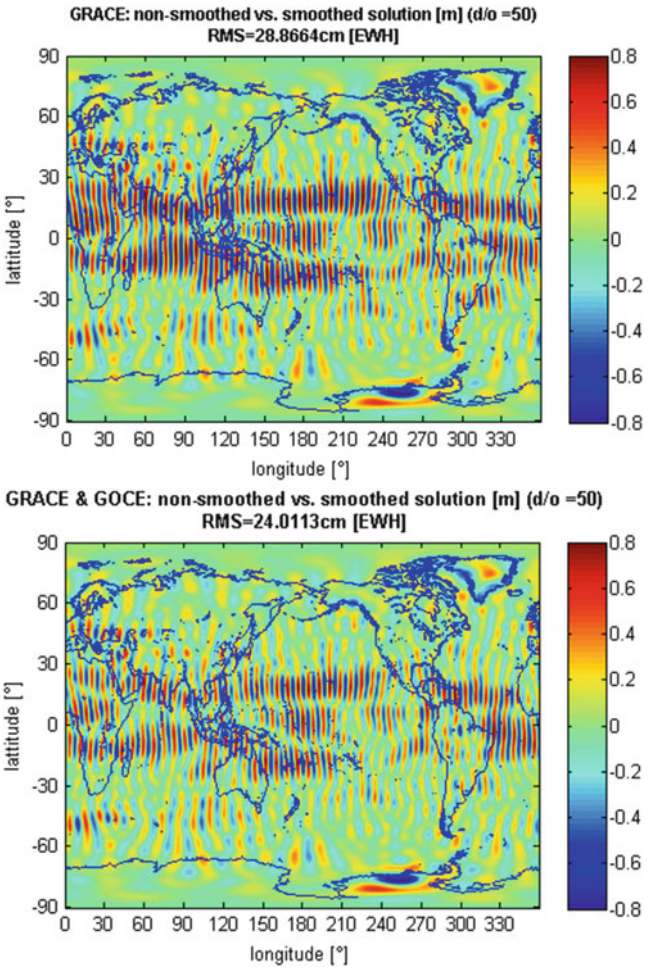

Fig. 5 Striping error of GRACE-only (*upper plot*) and combined solution (*lower plot*) for the monthly December solution in [m] EWH

3.3 GRACE Monthly Solutions

As a next step, we investigated whether this behavior might be restricted only to these two specific months, due to the 7-days sub-cycle of GRACE. Analyzing the 12 monthly GRACE fields in terms of formal errors indicates that the 7-day sub-cycle of November and December 2009 only degrades the gravity field estimate below d/o 20 and above d/o 45. The latter spectral range is similar to where we detected improvements (in the global RMSE and by visualizations in spatial domain) due to the combination. Thus, it seems likely that the impact of GOCE is only possible due to a weak GRACE performance in those months. However, between d/o 30 and d/o 40, where Pail et al. (2011b) found improvements due to a combination with GOCE data (also in November and December 2009), the GRACE solutions are similar to those of the other months regarding their quality and the severeness of their stripes. From this perspective, a reduction of the stripes due to a combination with both GOCE observation types might be possible in other periods. At this point further investigations are needed.

Table 3 RMSE improvement due to a combination with **GOCE SGG and SST** data [in %] with respect to the corresponding GRACE-only solutions

Year	2009	2009	2009
Period	November	December	November + December
d/o30	1.40	0.90	0.03
d/o35	1.46	1.52	0.25
d/o40	1.16	3.41	0.41
d/o45	2.37	3.97	10.35
d/o50	5.27	16.81	21.53
d/o55	6.24	14.77	22.63
d/o60	8.86	20.10	27.79
Average	3.83	8.78	11.02

Conclusion

Based on monthly combined GOCE and GRACE gravity field estimates for a period of more than one year, we can conclude that GOCE gravity gradients alone can

not substantially improve the performance of GRACE monthly temporal gravity fields. Only by including GOCE orbit information simultaneously, reductions of the striping error could be observed. This has been shown exemplarily for a combined monthly solution of December 2009, with an improvement of 16 % w.r.t. a pure GRACE solution and for the bi-monthly November + December 2009 solution with an improvement of 22 %—both for spatial scales of about 400 km (equivalent to d/o 50). It should be emphasized that such well-performing combined solutions could only be produced for selected months, where the amount and quality of GOCE data was sufficient to solve systems resolved at least up to d/o 150. However, due to the mentioned problems it turned out to be extremely difficult to produce systematically and continuously monthly combined temporal gravity model series. Finally, although in this research we have shown that it is mainly due to the SST component of GOCE causing the attenuation of the striping error, also the new version of reprocessed GOCE data (see, e.g., Pail et al. 2012) might have the potential to further improve the results of such combinations, because the reprocessing has an impact mainly on the low to medium spherical harmonic degrees. Further, it has to be mentioned that it is not totally clear, whether the reduction of the striping error does affect the actual temporal gravity signal of interest (it might, e.g., be damped). This, however, must remain topic for future research.

Acknowledgements We highly acknowledge the efforts of the reviewers who helped to improve this manuscript. Further, we want to honor the work of ESA and the HPF who make the GOCE products available and accessible in such a convenient way to the users. In the same way we want to thank the colleagues at AIUB involved in the processing of the used GRACE fields.

References

ESA (1999) Gravity field and steady-state ocean circulation mission. Report for the mission selection of the four candiate earth explorer missions (ESA SP-1233(1)). European Space Agency

Güntner A, Schmidt R, Döll R (2007) Supporting large-scale hydrogeological monitoring and modelling by time-variable gravity data. Hydrogeol J 15:167–170

Horwath M, Rülke A, Fritsche M, Dietrich R (2010) Mass variation signals in GRACE and in crustal deformations from GPS: a comparison. In: Flechtner F, Gruber T, Güntner A, Mandea M, Rothacher M, Schöne T, Wickert J (eds) System earth via geodetic-geophysical space techniques. Springer, Berlin, pp 399–406. doi:10.1007/978-3-642-10228-8_34

Horwath M, Legrésy B, Rémy F, Blarel F, Lemoine JM (2012) Consistent patterns of antarctic ice sheet interannual variations from ENVISAT radar altimetry and GRACE satellite gravimetry. Geophys J Int 189(2):863–876. doi:10.1111/j.1365-246X.2012.05401.x

Jarecki F, Müller J (2005) Temporal gravity variations in GOCE gradiometric data. In: Gravity, geoid and space missions, IAG symposia 129. Springer, Berlin, pp 333–338

Koch KR, Kusche J (2002) Regularization of geopotential determination from satellite data by variance components. J Geod 76:259–268. doi:10.1007/s00190-002-0245-x

Metzler B, Pail R (2005) GOCE data processing: the spherical cap regularization approach. Stud Geophys Geod 49(4):441–462. doi:10.1007/s11200-005-0021-5

Niemeier W (2008) In: de Gruyter (ed) Ausgleichsrechung - statistische auswertemethoden, 2nd edn. Berlin, New York

Pail R, Goiginger H, Mayrhofer R, Schuh WD, Brockmann JM, et al (2010) GOCE gravity field model derived from orbit and gradiometry data applying the time-wise method. In: Proceedings of ESA living planet symposium, 28 June-2 July (ESA SP-686)

Pail R, Bruinsma S, Migliaccio F, Förste C, Goiginger H, Schuh WD, Höck E, Reguzzoni M, Brockmann JM, Abrikosov O, Veicherts M, Fecher T, Mayrhofer R, Krasbutter I, Sanso F, Tscherning CC (2011a) First GOCE gravity field models derived by three different approaches. J Geod 85(11):819–843. doi:10.1007/s00190-011-0467-x. Special issue: "GOCE - The gravity and steady-state ocean circulation explorer"

Pail R, Fecher T, Jäggi A, Goiginger H (2011b) Can GOCE help to improve temporal gravity field estimates? In: Ouwehand L (ed) Proceedings of the 4th international GOCE user workshop. ESA Publication SP-696

Pail R, Fecher T, Murböck M, Rexer M, Stetter M, Gruber T, Stummer C (2012) Impact of GOCE L1b data reprocessing on GOCE-only and combined gravity field models. In: Studia geophysica et geodaetica. Springer, Netherlands. doi:10.1007/s11200-012-1149-8

Rexer M (2012) Time variable gravity : Contributions of GOCE gradiometer data to monthly and bi-monthly GRACE gravity field estimates. Master's thesis, Technische Universität München. www.iapg.bv.tum.de/mediadb/4731446/4731447/201211_rexer.pdf

Tapley B, Ries J, Bettadpur S, Chambers D, Cheng M, Condi F, Poole S (2007) The GGM03 mean earth gravity model from GRACE. In: AGU Fall Meeting Abstracts, p A3

Wahr J, Molenaar M (1998) Time variability of the earth's gravity field: Hydrological and oceanic effects and their possible detection using GRACE. J Geophys Res 103(B12):30,205–30,229

Application of Wavelets for Along-Track Multi-resolution Analysis of GOCE SGG Data

Rossen Grebenitcharsky and Philip Moore

Abstract

Due to limitations of the gradiometer the GOCE satellite gravity gradients (SGG) require filtering outside the measurement bandwidth. Several methodologies have been proposed and in use within the GOCE processing centre to filter the along-track data in the frequency domain. In this study we investigate the utilization of the localization properties of wavelets in both the frequency and space domains to decompose, analyze and reconstruct the gravity field signal in the SGG data at the different levels of a Wavelet Multi-resolution Analysis (WMRA). This approach can also be used to identify and eliminate temporally and spatially correlated errors in GOCE SGG data. The WMRA is applied in both the rotation of SGGs from the gradiometer reference frame to a local north orientated frame and in the downward (upward) continuation of the SGG tensor to a mean orbital height. Results presented here show that, at the GOCE mean orbital height, the MWRA has the potential to enhance the short-wavelength gravitational signal content of the along-track GOCE data.

Keywords

GOCE • SGG • Gravity gradients • Tensor rotations • Wavelets

1 Introduction

Global geopotential models (GPMs) are a level 2 product of the high level processing facility (HPF) for the European Space Agency's Gravity field and steady-state Ocean Circulation Explorer mission (GOCE). The GPM harmonics are derived from gravity field modeling of the GOCE satellite gravity gradients (SGGs) to about degree and order 240 in a process that requires regularization (smoothing) of the solution. By using global spherical harmonic functions there is a reduction in high frequency gravity field data (from ~8 km data resolution along track to 80–100 km resolution in GPMs—see Table 1) in addition to high-frequency omission errors due to upper measurement bandwidth (MB) limit of the SGG observations. However, the effective MB may differ from specifications (Fuchs and Bouman 2011) or from preliminary simulated studies. Filtering the signal along track using specified lower and upper limits of the MB could lead to loss of useful information especially near the MB limits. Further, if GPM SGGs are provided directly for regional modeling, or if the SGGs in the local north oriented frame (LNOF) are forced to follow a GPM, it is possible that additional, but unspecified, high frequency gravity information is lost. For regional gravity field modeling it is important to capitalize on the high resolution gravity field signals contained in the GOCE along track data and to reflect the resolution of the raw data in gravity field modeling. In practice, SGGs need to be presented in a LNOF linked to an Earth fixed coordinate system for synergy with other data sources for regional geoid modeling.

The level 2 SGGs in the terrestrial reference frame (TRF) and the gradiometer reference frame (GRF) at the satellite altitude form the basis of regional geoid modeling after a number of issues are resolved. According to Pail et al. (2011) gradiometer data in the GRF have large spatially

R. Grebenitcharsky (✉) • P. Moore
School of Civil Engineering and Geosciences, Newcastle University, Newcastle upon Tyne NE1 7RU, UK
e-mail: rgrebenitcharsky@gmail.com

U. Marti (ed.), *Gravity, Geoid and Height Systems*, International Association of Geodesy Symposia 141,
DOI 10.1007/978-3-319-10837-7_6, © Springer International Publishing Switzerland 2014

Table 1 Frequencies and resolution limits for WL levels of decomposition with approximate spherical harmonic (SH) degree equivalence

# WL level	Freq [Hz] upper bound	SH degree	Res. [km]	Freq [Hz] lower bound	SH degree	Res. [km]
1	0.4999	2565	8	0.2499	1282	16
2	0.2499	1282	16	0.1249	641	32
3	0.1249	641	32	0.0624	320	64
4	0.0624	320	64	0.0312	160	125
5	0.0312	160	125	0.0156	80	250
6	0.0156	80	250	0.0078	40	500
7	0.0078	40	500	0.0039	20	1,000
8	0.0039	20	1,000	0.0019	10	1,999
9	0.0019	10	1,999	0.0010	5	3,999
10	0.0010	5	3,999	0.0004	2	7,997
11	0.0004	2	7,997	0.0002	1	15,995
12	0.0002	1	15,995	0.0001	0	31,990

WL convention is from high to low frequencies

correlated long-wavelength errors and digital filters need to be applied to frequencies outside the MB. Versions of autoregressive moving average (ARMA) or Wiener filters (Pail et al. 2011) can be used for GPM modeling assuming that the differences between measured SGGs and GPM generated gradients are noise. Further leakage and error amplification are introduced by rotation of the gradiometer tensor to LNOF due the lower accuracy of two of the tensor components (Fuchs and Bouman 2011). As a result, TRF level 2 products are expected to be very close to an *a priori* GPM due to its strong influence through the applied filtering and rotation procedures (Fuchs and Bouman 2011; Bouman et al. 2011; Bouman 2007; Gruber et al. 2010). In addition, validation of along-track GOCE gradients and gridding procedures necessary for regional geoid modeling encounter difficulties due to the fact that the satellite orbital altitude varies by ∼20 km. Upward/downward continuation of data to a mean orbital height needs to be considered.

To overcome these issues wavelet (WL) base functions in the form of a multi-resolution analysis (MRA) (Mallat 1998; Keller 2004) can be applied along the GOCE satellite track. MRA can also be successfully combined with input output systems (IOS) (Sideris 1996, Andritsanos and Tziavos 2009) for upward/downward continuation of SGGs to a mean orbit. Wavelets allow the SGG signal to be split into different bandwidths which can be individually treated for every WL level. Thus, for GOCE data, the WL main advantage is the capability to analyze the decomposed SGG signal simultaneously in terms of the spectrum (different bandwidths) and spatial/time distribution on different levels (scales). As a signal processing tool WLs can be used for selective filtering and as high and low-pass filters in both the space/time and scale/frequency domain. Equally important, the orthogonality between scale and wavelet functions insures perfect signal decomposition and reconstruction if there are no changes in the wavelet coefficients.

The authors acknowledge that alternative methods exist for MRA (e.g. Freeden et al. 1998) which could be similarly useful for analyzing SGGs. However, wavelet MRA have become a well-established tool with proven efficiency in various signal processing applications within geosciences as explained in Sect. 2.

2 Motivation and General Background

2.1 Wavelet Multi-resolution Analysis (WMRA) for Filtering

To apply wavelets as *selective* filters, frame theory (a generalization of base functions) (Christensen 2001; Mallat 1998) needs to be utilized. As frame bounds are not unique the wavelet coefficients are similarly non-unique. From a mathematical point of view, the lack of uniqueness is not desirable but the frames provide flexibility. In particular, changes in the wavelet coefficients at the different levels of the decomposition frames facilitate both selective filtering (de-noising) and elimination of spatially correlated errors (noise) in the SGG signal. Furthermore, after filtering frames allow signal reconstruction. Wavelet frames are constructed by sampling the time and scale of a continuous 'mother' wavelet transform. These so-called 'child' wavelets are simply shifted and dilated versions of the 'mother wavelet'. To construct a wavelet frame the time-frequency plane needs to be covered with 'boxes' with sides given by units of scale and time (Keller 2004). The size of the box along the frequency axis depends on the scale while the width stays uniform along the time axis but is changed by the scale as the box is translated along the frequency axis.

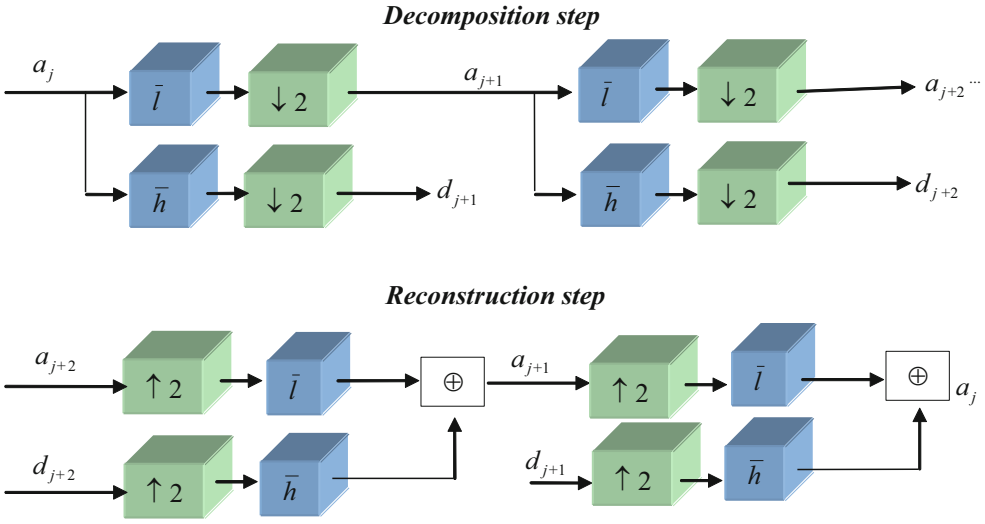

Fig. 1 Wavelet MRA—decomposition and reconstruction steps: a_i is the approximated (scale) component at ith level; d_i is the detailed (wavelet) component at ith level ($i = j, j+1, j+2, \ldots,$); $\bar{l}$ and $\bar{h}$ are low-pass (scale function) and high-pass filter (wavelet function) respectively; $\downarrow 2$, $\uparrow 2$ denote down-sampling and up-sampling operator by a factor 2; $\oplus$ the summation operator between approximated and detailed components at the wavelet level

The box representation of wavelets demonstrates their scale (frequency)/time localization properties and their capability to control selective filtering in both the scale (frequency) and time domains by decomposing the signal at different levels (scales).

Continuous wavelet transforms provide translation invariant representation in that, after translation, a signal pattern will be translated but not modified. Sampling the translation parameter (i.e. discretization along the time axis) will destroy this invariance. The loss of translation invariance occurs when the translation factor is not equal to the grid interval. It is necessary to preserve translation invariance to detect and filter spatially correlated errors (noise). Dyadic wavelets maintain translation invariance. MRA provides the basis for constructing filter banks to design dyadic wavelets (Mallat 1998) and is the key to the construction of orthogonal wavelet bases and fast decomposition and reconstruction of a signal into different frequency bands (see Fig. 1). Within regional gravity field modeling MRA facilitates investigation at the different wavelet levels by concentrating on geopotential information which is most relevant in terms of spatial resolution and accuracy.

Table 1 summarises the 12 levels of wavelet decomposition of the daily along track GOCE SGG data with approximate wavelengths and equivalent spherical harmonic decomposition. The lower limit (8 km) of level 1 coincides with the GOCE measurement rate with the upper limit being 16 km as required for a dyadic WL. Subsequent levels follow in the dyadic pattern. Level 12 corresponds to bandwidth with resolution between 15,995 km and 31,990 km encompassing the maximum resolution of 20,000 km on the Earth's surface assuming a circumference of 40,000 km. Level 12 contains very long-wavelength information (resolution between 15,995 km and 20,000 km). The long-medium wavelengths unobserved by GOCE are in levels 7–12. The wavelengths of levels 4–6 are included within the MB of GOCE data with the nominal limits in levels 3 and 7. Level 7 thus has its lower frequency limit greater than the lower effective MB determined by Fuchs and Bouman (2011).

2.2 Motivation for Along-Track Pre-processing Using WMRA

The aim of this study is to investigate the use of wavelets to optimise recovery of gravity signatures extracted from along track GOCE SGGs as required for regional geoid modeling. This is achieved by testing a global procedure along daily GOCE satellite tracks, taking advantage of the relatively equally distributed gradiometer data. WMRA is used for filtering the spatially correlated long-medium wavelength errors and for upward/downward continuation to a mean orbital height of 260 km. Frequencies with large energy in the SGG differences with respect to an *a priori* reference GPM are replaced with those from the GPM to incorporate the required long-wavelength gravity signal This procedure is conducted at every level of the WL decomposition and reconstruction.

2.3 Input-Output Systems (IOS) for Up/Downward Continuation and Filtering

The along-track WMRA for GOCE SGG needs to simultaneously incorporate upward/downward continuation, filtering of spatially correlated errors and the incorporation of the long wavelength part not sensed by the GOCE gradiometer. IOS (Andritsanos and Tziavos 2009) integrated with WMRA is suitable for this task.

Up/Downward Continuation The decomposition of the signal using wavelets allows along track upward/downward continuation to a mean orbital height to be undertaken at every WL level in a time-wise approach. In order to speed up the procedure, collocation in the frequency domain in the form of a Single Input Single Output System (SISOS) (Sideris 1996) is applied. IOSs can be utilized for along-track SGG processing as the large quantity of almost equally distributed 1D observations can be efficiently processed in daily batches in the frequency domain.

Selective Filtering For most filtering procedures differences between observed and modelled gradients are considered as noise, the influence of which should be eliminated or minimized. However, this may result in the filtered signal being very close to the *a priori* GPM. If those differences are considered as 'semi-signal', i.e. containing not only measurement noise but also long-wavelength correlated errors together with useful signal, an additional 'selective' type of filtering can be applied. As a result the signal can be reconstructed close to the model or to the observed data depending on the number of frequencies suppressed and replaced per WL level. In this study, the effect of pure measurement noise (internal accuracy) will be excluded in order to analyse the influence of filtering to keep the data as close as possible to the original SGGs.

Combination of IOS and Wavelets In this way, IOS can filter out specific frequencies responsible for large geographically correlated long-wavelength errors as well as being used for upward/downward continuation to a mean height per every wavelet level. Thus, in practice, frequencies sensed by the gradiometer with large probability spectral density (PSD) or with small amplitude/scale (due to low sensitivity of SGG in the long-wavelength part of the spectrum) can be replaced by a GPM.

2.4 Mathematical Formulation of IOSs for Upward/Downward Continuation and 'Selective' Filtering

Upward/downward continuation, considered as a convolution of the data and the Poisson kernel at a reference surface, leads to the idea of formulating the continuation operator as an IOS. The mathematical model of IOSs can be expressed by modification of expressions for SISOS (Sideris 1996). In detail,

$$\boldsymbol{FFT}\left(T_{zz}^{MO}\right) = \frac{\boldsymbol{PSD}^{MO,SA}\left(T_{zz,\ model}\right)}{\left[\boldsymbol{PSD}^{SA,SA}\left(T_{zz,\ model}\right)+\boldsymbol{PSD}^{SA,SA}\left(T_{zz,\ n}\right)\right]} \times \boldsymbol{FFT}\left(T_{zz}^{SA}\right) \tag{1}$$

where T_{zz} denotes the zz (radial) component of the disturbing potential gradient tensor; MO evaluation at the mean orbital height; SA evaluation at the altitude of the SGG measurement; **PSD** the power spectral density, **FFT** the Fast Fourier Transform; with the 'semi signal' expressed as $n = T_{zz,obs} - T_{zz,model}$. Also, in Eq. (1)

$$\boldsymbol{PSD}^{SA,SA}\left(T_{zz,\ n}\right) = \boldsymbol{FFT}\left\{T_{zz,obs}^{SA} - T_{zz,model}^{SA}\right\} \times \boldsymbol{FFT}\left\{T_{zz,obs}^{SA} - T_{zz,model}^{SA}\right\}^{conj} \tag{2}$$

where $\times$ denotes element by element multiplication and $\{.\}^{\text{conj}}$ the complex conjugate of the **FFT**. Furthermore, $\boldsymbol{PSD}^{MO,SA}(T_{zz,\,model})$ is the **PSD** of $T_{zz,\,model}$ for the change from the actual satellite height to the mean orbital height. Equation (1) accounts for the upward/downward continuation from the satellite altitude to the mean altitude. Simultaneously, to suppress the k^{th} frequency and replace by the corresponding signal from the model the following can be applied:

$$\boldsymbol{FFT}_k\left\{T_{zz,obs}^{SA}\right\} = \boldsymbol{FFT}_k\left\{T_{zz,model}^{SA}\right\} \text{ and } \boldsymbol{PSD}_k^{\boldsymbol{SA,SA}}\left(T_{zz,\ n}\right) = 0. \tag{3}$$

Similar expressions can be applied to all other components T_{xx}, T_{yy}, T_{xy}, T_{xz} and T_{yz} of the disturbing potential gravity gradient tensor by replacing zz in Eqs. (1)–(3) with the corresponding component.

2.5 Incorporation of IOS in WMRA

Implementation of the procedure can be summarised as: (1) Pre-processing GOCE LEVEL 2 SGGs for metadata; (2) Generation of SGGs of the disturbing Earth potential in GRF; (3) Decomposition of dyadic WMRA (see Fig. 1) up to level 12 for every SGG component; (4) Upward/downward continuation to the mean orbital height (260 km) together with selective filtering conducted in the decomposition step of Fig. 1, (between down-sampling and the next filtering step) and applied to the d_j signal component at the *j-level*; (5) Reconstruction of the dyadic WMRA using upward/downward continued and filtered d_j components for every tensor component; (6) Rotation of SGGs from GRF to LNOF as required for regional geoid modelling.

The pre-processing of GOCE LEVEL 2 SGG data involves daily GRF and dynamic orbital files. The GOCE EGG_NOM_2 and EGG_TRF_2 files were utilized according to GOCE HPF documents (De Sander 2011; Gruber et al. 2010). In total 45 daily files from 1 May 2010

to 30 June 2010 were used. The reference GPM was GOCE DIR 2I (GO-CONS-EGM-DIR-2I-HPF), a satellite-only model to degree 240 derived from a combination of GOCE, GRACE and LAGEOS. Model SGG data was generated with GOCE DIR21 at the satellite altitude and 260 km from code provided by Eshagh and Abdollahzadeh (2012). For all SGG components DB 10, 1D Daubechies wavelets (Mallat 1998) were applied. To reduce the effect of rotation errors, complete normal gradient tensors are rotated to GRF. This is necessary for computing gradients of the GRF disturbing potential as difference between the observed GOCE SGGs and the rotated normal gradient tensors. After that, all SGG components of disturbing potential can be pointwise rotated to the LNOF.

It is important to emphasize that the FFT in IOS, applied at every wavelet level, is simply a tool for upward/downward continuation in the frequency domain and to compute the spectrum of the signal inside the bandwidth for every wavelet level. This spectrum is required to suppress frequencies linked to spatially correlated errors which are present only at that wavelet level. Formally speaking, FFT application on the original signal will give the same result due to linearity of FFT and wavelet transforms if the same frequencies are identified and suppressed. However, the advantage of the WMRA procedure is in its capability to detect frequencies of spatially correlated errors at every bandwidth (scale domain) by simultaneous scale/time analysis of the reconstructed signal (time domain) at the given wavelet level.

3 Experiment Description and First Results

3.1 Experimental Scenarios

In order to demonstrate the capability of WMRA and the proposed procedure for upward/downward continuation for extracting signatures from SGG NOM Level 2 data the following scenarios and corresponding rationales are considered. Each scenario suppresses an increasing number of frequencies at WL levels 7–12 with replacement by modelled SGG frequencies. In *scenario 1,* no frequencies are suppressed. The original data is upward/downward continued to 260 km mean altitude without filtering; this scenario demonstrates the raw SGG data converted to a fixed height. *Scenario 2–6* suppress an increasing number of frequencies as powers of 10, from 10^0 to 10^4, between WL level 7 and level 12 (the long-wavelength bands outside the MB). Thus in *scenario 2* a single frequency of maximum PSD is replaced to remove the dominant long-wavelength correlated errors. *Scenarios 3–5* show the effect of *the replacement of* an increasing number of long-wavelength errors and progressively reveals the large scale global gravity field. *Scenario 6* (10^4 frequencies suppressed) accounts for almost complete recovery of the global gravity field features including the long-medium wavelengths which are, at best, marginally sensed by GOCE. This supplies an upper bound to the number of suppressed frequencies beyond which the recovered signal will not be significantly affected.

3.2 First Results and Data Analysis

In this study results for only the T_{zz} component are presented. In Fig. 2 the spectra of T_{zz} from the GOCE DIR 2I model and from the wavelets approach show that 30 % of the frequencies for the WL almost replicate the model spectrum in the MB, but the other 70 % (higher frequency part) have greater energy with a distinctive spectral shape. For frequencies below the MB the wavelet spectra is the same as that from the model model but for frequencies higher than the MB wavelets provides significantly greater spectrum energy than the model; more high frequency information is available.

In order to demonstrate the MWRA performance one revolution of T_{zz} data at the eighth WL level are presented in Fig. 3 (spectrum) and Fig. 4 (spatial distribution). It is seen that, by suppressing a single frequency (0.002037 Hz) in scenario 2, there is a significant improvement through removal of spatially correlated errors in the original T_{zz} data (blue dash line) in Fig. 4. The filtered signal (cyan) is now close to the corresponding component of the GPM (red). Figures 3 and 4 show the capability of WMRA to simultaneously analyse the along-track signal in both the spectral and spatial domains.

The results from the different scenarios are presented in Figs. 5, 6, 7, 8, 9, and 10. Figure 5 shows the unfiltered T_{zz} at 260 km with the striations caused by the long wavelength errors in the data. The modelled T_{zz} data is given in Fig. 6, showing the effect of orbital height variation. Figures 7, 8, 9, and 10 correspond to scenarios 2–5. These plots illustrate the efficiency of upward/downward continuation as the orbital heights variations of Fig. 6 are not evident. A comparison of Fig. 7 with Fig. 5 shows the that the WL approach eliminates large long wavelength geographically correlated errors after discarding *only* 1 frequency with maximum PSD in levels 7–12. The insensitivity of SGG to low-frequency gravity signals is evident in Fig. 7 as few of the dominant global gravity structures are visible although high frequency coherent signals are apparent in areas with sharp changes in the gravity field. Figures 7, 8, 9, and 10 progressively reveal the large scale global gravity field features from scenario 2

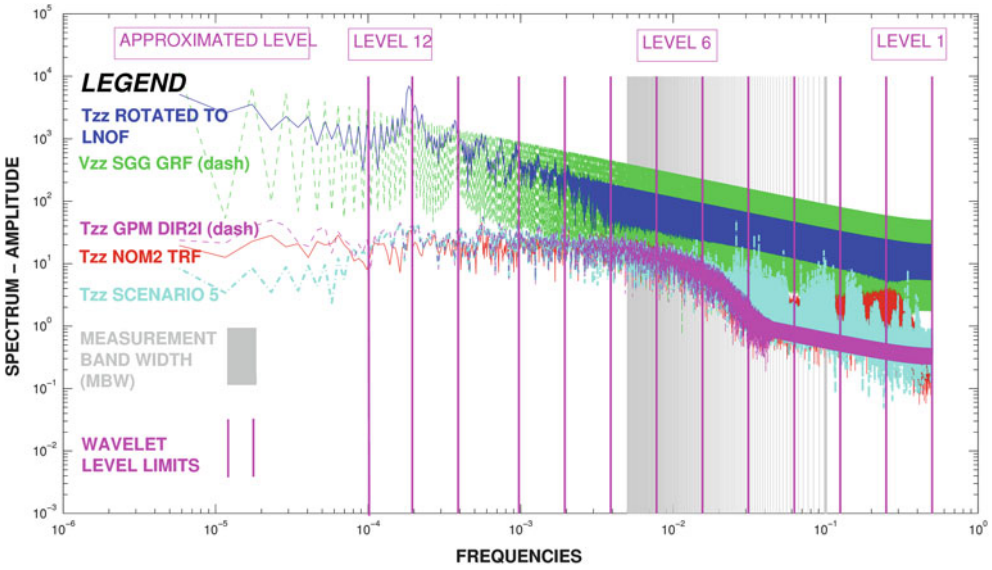

Fig. 2 Daily spectrum of SGG (T_{zz})

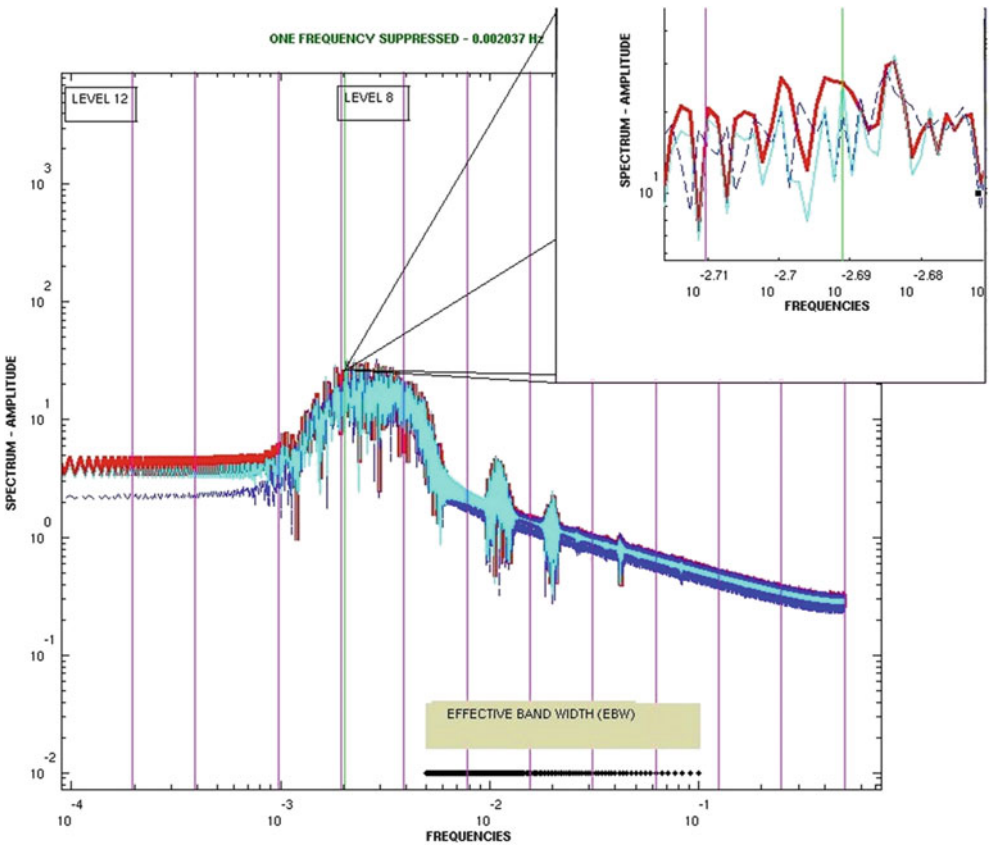

Fig. 3 Spectra of T_{zz} at eighth wavelet level: GPM at 260 km (*dark grey*); SGG at satellite altitude (*dash*); SGG single frequency filtered (0.002037 Hz) at 260 km (*light grey*), Inset: suppressed frequency (*light grey vertical line*); limits of wavelet level (*dark grey vertical line*); the Effective Band Width (EBW) of GOCE SGGs (*black*)

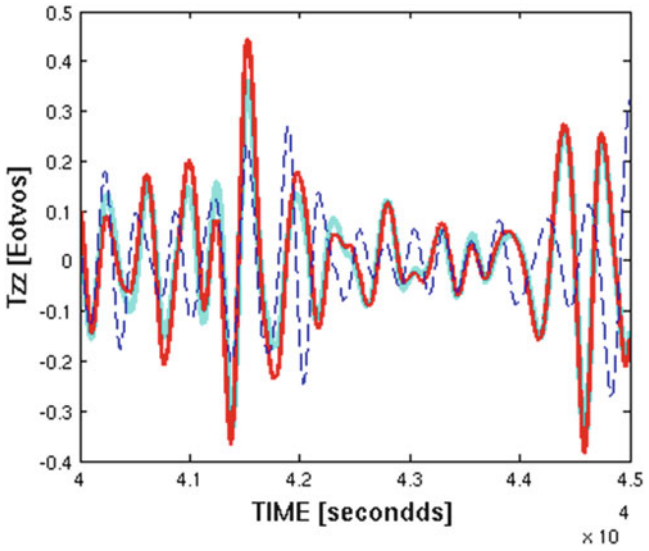

Fig. 4 Single revolution profile of T_{zz} for June 1, 2010: GPM km (*dark grey*); SGG at satellite altitude (*dash*); SGG single frequency filtered (0.002037 Hz) at 260 km (*light grey*)

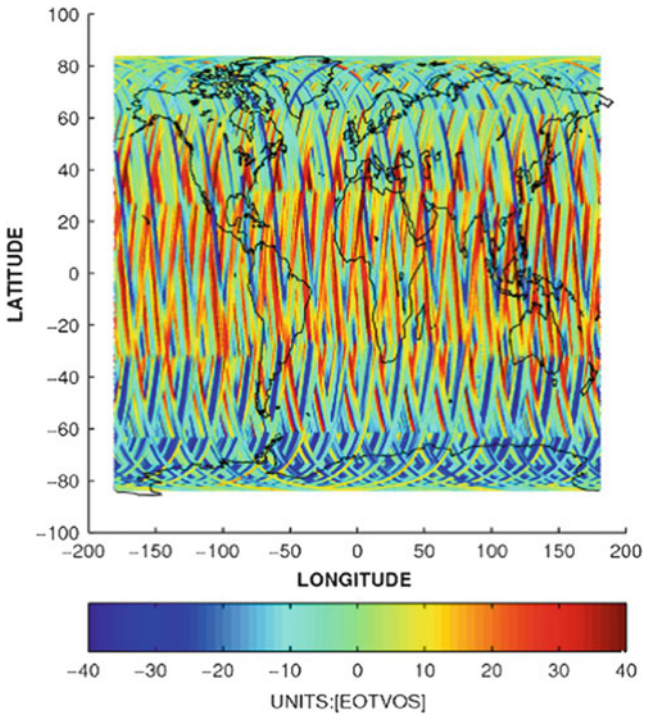

Fig. 5 T_{zz} component (original signal without filtering) in GRF at 260 km altitude (scenario 1)

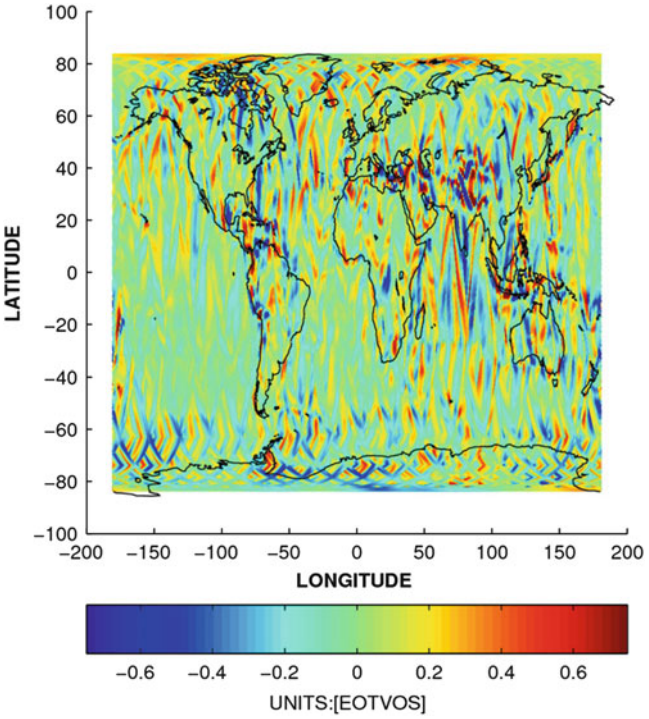

Fig. 6 T_{zz} GPM component in GRF at satellite altitude

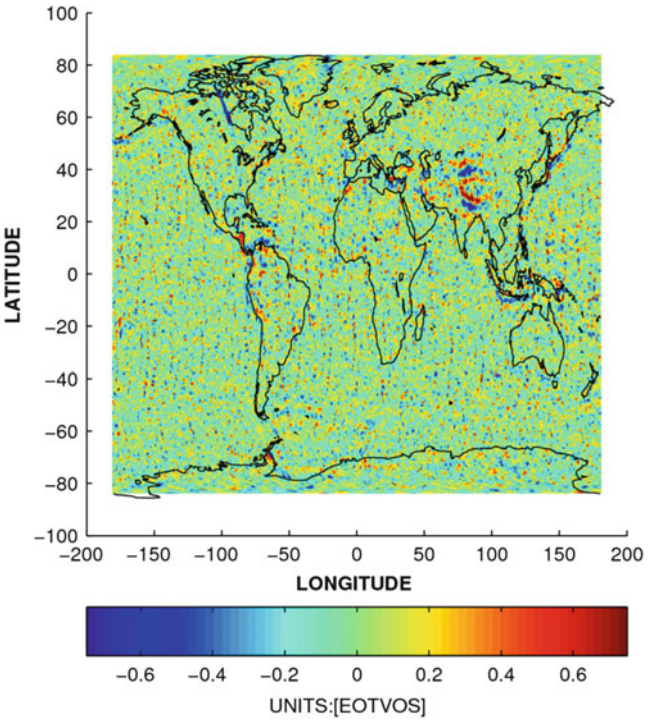

Fig. 7 T_{zz} in GRF at 260 km altitude after filtering: scenario 2

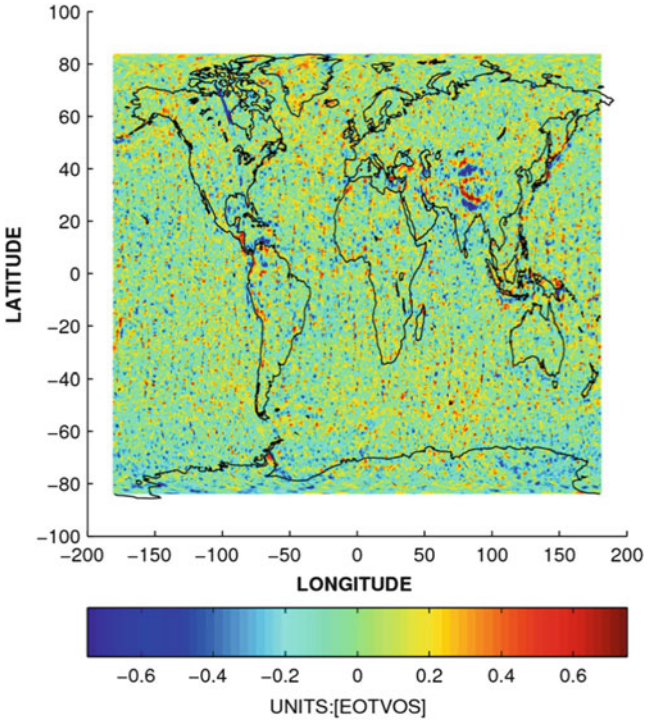

Fig. 8 T_{zz} in GRF at 260 km altitude after filtering: scenario 3

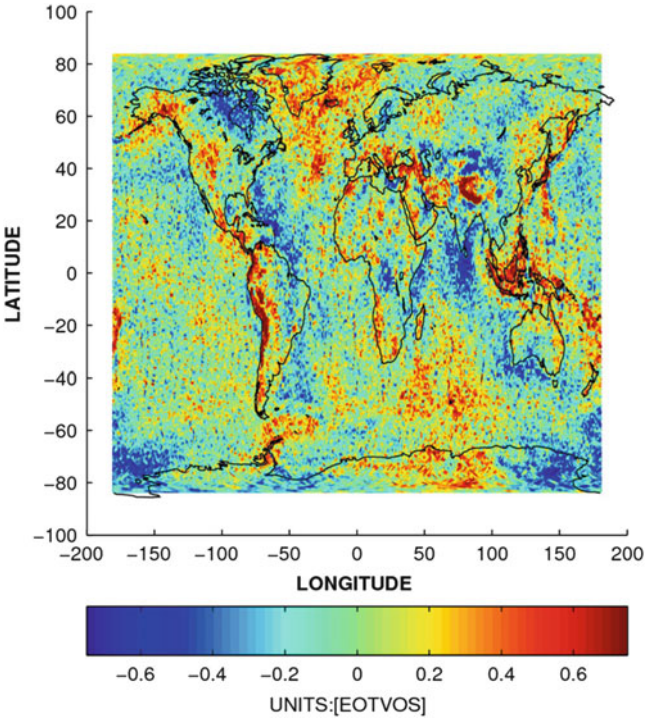

Fig. 10 T_{zz} in GRF at 260 km altitude after filtering: scenario 5

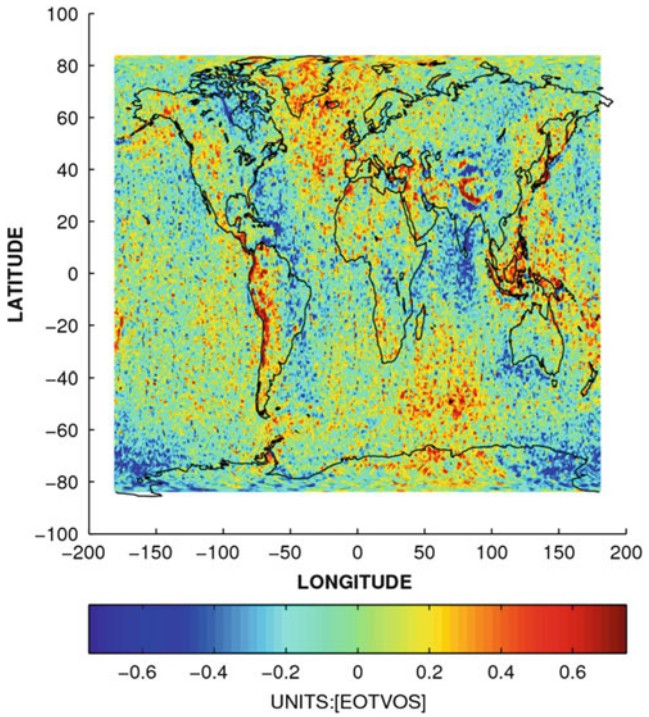

Fig. 9 T_{zz} in GRF at 260 km altitude after filtering: scenario 4

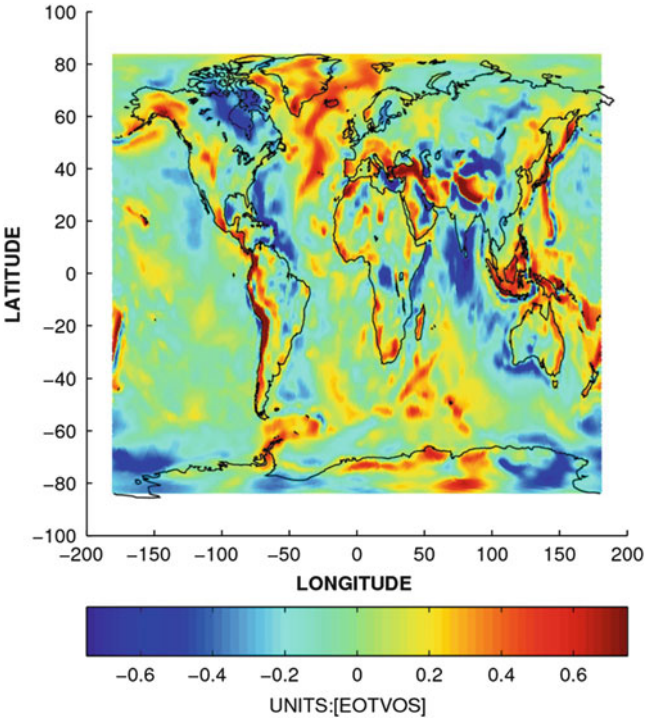

Fig. 11 T_{zz} GPM component in GRF at 260 km altitude

Table 2 Statistics of crossover differences (Eotvos) with respect to the filters for different experimental scenarios

Scenario	Min	Max	Mean	Std	Scenario description
1	−109.224	106.461	−2.153	18.013	Original SGG Tzz
2	−0.687	0.754	−0.002	0.146	10^0 max PSD freq discarded
3	−0.677	0.706	−0.004	0.154	10^1 max PSD freq discarded
4	−0.961	0.747	−0.012	0.171	10^2 max PSD freq discarded
5	−0.856	0.747	−0.017	0.163	10^3 max PSD freq discarded

through to scenario 4 (positive gradients in north Atlantic, south Indian ocean; north Indian ocean, east Antarctic and west Atlantic depressions). Finally, scenario 5 (Fig. 10) almost completely recovers the global gravity field of Fig. 11 in the long and medium wavelengths. The speckled pattern of Fig. 10 is due to just 45 days of data being utilised and to high frequency noise in the data. These numerical results show that the methodology can be used to remove the long wavelength errors as well as upward/downward continuation to a mean height while at the same time preserving high frequency gravity field data.

3.3 Crossover Validation

The max/min and mean SGG crossover differences (Table 2) at the mean altitude show that some errors or uncompensated effects of up/downward continuation exist in the data. This is expected as the procedure for upward/downward continuation is applied only in the along-track direction with no contribution from the gravity gradients across track for example. However, the crossover differences reveal mean values and standard deviations (std) that are relatively close between scenarios 2–5. It would appear that the residual error is linked to high frequencies that have been retained at this stage to preserve as much gravity signal as possible. The mean values can be considered as being close to zero taking into account that the std of ∼0.171 Eotvos (scenario 4) is still about 10 % of the magnitude of the gravity gradients for ∼3,000,000 global observation points.

3.4 Comparison with NOM EGG TRF 2

A half revolution along-track profile for 1 June 2010 for scenario 5 is plotted in Fig. 12. A comparison between T_{zz} from wavelets, the model generated T_{zz} and the T_{zz} from NOM EGG TRF 2 shows some interesting findings regarding the performance of the proposed method. As expected wavelets preserve more high frequency gravity field information compared to NOM EGG TRF 2 data. The latter replicates the shape of the GPM plus measurement noise but no additional high frequency information exists data compared to the WL solution. SGGs from wavelets follow the long wavelength behaviour of the GPM confirming that gradients from MWRA have successfully recovered the low frequencies of the gravity field. High frequency information can be seen in the WL results compared to the *a priori* GPM. Evidence of high frequency signatures from the WL approach is visible in regions of coherent signatures in Fig. 8; for example, the mountainous areas of the Alpo-Himalaya range, Alaska and the Andes and areas with large gravity variations such as Indonesia, Japan and the Caribbean islands. As stated previously, these high frequency signatures need to be validated as real gravity signals by using external data. Such a validation is beyond the scope of this paper and will be presented in a follow-on paper.

Conclusions and Recommendations

The first results from a WL approach show that the methodology can successfully preserve high frequency information from the T_{zz} component with respect to the Global Model (DIR2 I) and EGG_TRF_2 data together with a capability to include long wavelength gravity information missing in observed SGGs. Designation of upper and lower threshold values have a key role in selective filtering in specifying the spectrum of observed gradients which will either be replaced by modelled gradients or suppressed. The thresholds should be linked to objective criteria to distinguish between spatially correlated errors and noise and real gravity signals. In particular, the spectral upper limit is necessary in the separation of noise from high frequency gravity signatures, as required for the proper interpretation of SGG short wavelength components in Fig. 12, for example. One possible option is to determine threshold values through analysis of SGG tensor component crossover differences.

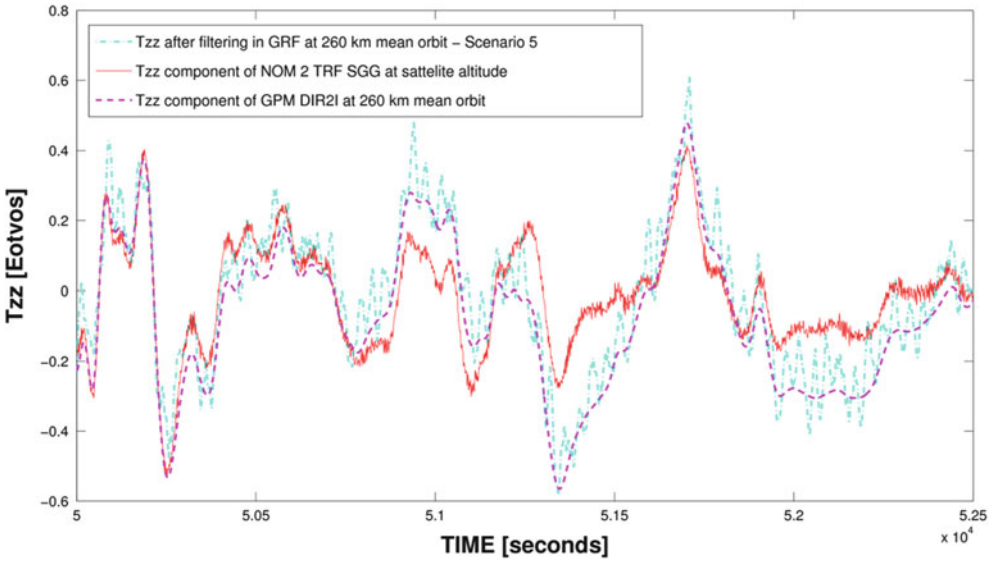

Fig. 12 Comparison between T_{zz} at 260 km after filtering (scenario 5), T_{zz} from NOM 2 TRF SGGs at satellite altitude and T_{zz} generated from GPM DIR2I at 260 km mean altitude

Future studies will utilize the other SGG components of the GOCE SGG data set, investigate the impact of the WL approach on gravity gradients rotated to LNOF and validate the results against independent regional data sets.

Acknowledgements This study was funded by a UK NERC NCEO award. The authors thank Prof. Roland Pail (Technical University Munich) and Dr. Johanes Bouman and Dr. Martin Fuchs (DGFI) for supplying SGG data to validate the rotation procedure from GRF to LNOF.

References

Andritsanos VD, Tziavos IN (2009) A sensitivity analysis in spectral gravity field modelling using systems theory. In: Kenyon S, Pacino M, Marti U (eds) Geodesy for planet Earth: proceedings of the 2009 IAG symposium, Buenos Aires, Argentina, 31 August–4 September 2009

Bouman J (2007) Alternative method for rotation to TRF, GO-TN-HPF-GS-0193, GOCE high level processing facility, Issue 1, Rev 0, Date 16/05/2007. The European GOCE gravity consortium EGG-C

Bouman J, Fiorot S, Fuchs M, Gruber T, Schrama E, Tscherning C, Veicherts M, Visser P (2011) GOCE gravitational gradients along the orbit. J Geod 85:791–805. doi:10.1007/s00190-0011-0464-0

Christensen O (2001) Frames, Riesz bases and discrete Gabor/Wavelet expansions. Bull Am Math Soc 38(3):273–291

De Sander W (2011) GOCE XML Parser, GO-TN-HPF-GS-0192, GOCE high level processing facility, Issue 2, Rev 7.2, Date 07/09/2011. The European GOCE gravity consortium EGG-C

Eshagh M, Abdollahzadeh M (2012) Software for generating gravity gradients using a geopotential model on an irregular semivectorization algorithm. Comput Geosci 39:152–160

Freeden W, Gervens T, Schreiner M (1998) Constructive approximation on the sphere, with applications to geomathematics. Oxford Science, New York

Fuchs MJ, Bouman J (2011) Rotation of GOCE gravity gradients to local frames. Geophys J Int 187:743–753. doi:10.1111/j.1365-246X.2011.0562.x

GO-CONS-EGM-DIR-2I-HPF, Third generation GOCE direct gravity field solution available, GOCE high level processing facility. https://earth.esa.int/web/guest/missions/esa-operational-eo-missions/goce/

Gruber Th, Rummel R, Abrikosov O, Van Hees R (2010) GOCE level 2 product data handbook, GO-MA-HPF-GS-0110, GOCE high level processing facility, Issue 4, Rev 3, Date 09/12/2010. The European GOCE gravity consortium EGG-C

Keller W (2004) Wavelets in geodesy and geodynamics. de Gruyter, Berlin, 2009

Mallat S (1998) A wavelet tour of signal processing. Academic Press, New York, NY

Pail R, Bruinsma S, Migliaccio F, Foerste C, Goiginger H, Shuh WD, Hoek E, Reguzzioni M, Brockman JM, Abrikosov O, Veicherts M, Fecher T, Mayrhofer R, Krasbutter I, Sanso F, Tscherning CC (2011) First GOCE gravity field models derived by three different approaches. J Geod 85:819–843. doi:10.1007/s00190-011-0467-x

Sideris MG (1996) On the use of heterogeneous noisy data in spectral gravity field modelling methods. J Geod 70:470–479

Assessment of High-Resolution Global Gravity Field Models and Their Application in Quasi-geoid Modelling in Finland

Mirjam Bilker-Koivula

Abstract

The two high-resolution global gravity field models, EGM2008 and EIGEN-6C, are compared with ground truth in Finland and surrounding areas. Thereafter, the models are used as background models in the calculation of a quasi-geoid model for Finland. The differences between height anomalies calculated from the global models and from two GPS-levelling datasets for Finland show standard deviations between 5 and 7 cm. Comparisons with free-air anomalies show small and homogeneously distributed differences over most of the area. In both comparisons the largest discrepancies are found close to the Russian border east of the 29° longitude line. This is most probably due to lower resolution Russian data used in the global models. When the global models are used as background models in the calculation of a quasi-geoid model for Finland, the problems around the 29° longitude line disappear. Comparison between the final quasi-geoid models and GPS-levelling data show an improvement over earlier models for Finland.

Keywords

Quasi-geoid modelling • EGM2008 • EIGEN-6C • GPS-levelling

1 Introduction

The current height conversion surface for Finland, used for the transformation between levelled heights and ellipsoidal heights, is FIN2005N00 (Bilker-Koivula 2010). This surface was derived by fitting the Nordic NKG2004 quasi-geoid model (Forsberg et al. 2004) to Finnish GPS-levelling data using least squares collocation. When compared to GPS-levelling data, the NKG2004 model has an accuracy of 4 cm in Finland. The accuracy of the FIN2005N00 surface is better than 2 cm in most of the country (Bilker-Koivula 2010).

With GPS-levelling, through the use of a geoid model, being commonly practised nowadays, the demands for more accurate geoid models increase all the time. Therefore, it was decided to calculate a new gravimetric quasi-geoid model for Finland. The study described here assesses two high-resolution global gravity field models, EGM2008 (Pavlis et al. 2008, 2012) and EIGEN-6C (Förste et al. 2011), with the goal to use them as background models calculating the quasi-geoid model for Finland.

First the global models and the available ground data are described. Then the models are compared with GPS-levelling data and with gravity observations available in the area. In the end the models are used to calculate a quasi-geoid model for Finland.

M. Bilker-Koivula (✉)
Finnish Geospatial Research Institute, National Land Survey of Finland, Kirkkonummi, Finland

Department of Real Estate, Planning and Geoinformatics, School of Engineering, Aalto University, Espoo, Finland
e-mail: Mirjam.Bilker-Koivula@nls.fi

2 Description of Data

2.1 High-Resolution Global Models

Two high-resolution global gravity models were analysed in this study: EGM2008 and EIGEN-6C.

U. Marti (ed.), *Gravity, Geoid and Height Systems*, International Association of Geodesy Symposia 141,
DOI 10.1007/978-3-319-10837-7_7,

The EGM2008 model was compiled using GRACE-data for the long wavelengths and $5' \times 5'$ terrestrial data and altimetry data for the short wavelengths (Pavlis et al. 2008, 2012). The model goes up to spherical harmonics degree 2190, with full degree and order coefficients up to degree 2159.

The EIGEN-6C model goes up to spherical harmonics degree 1420 (Förste et al. 2011). The model uses 6.5 years of LAGEOS and GRACE data and 6.7 months of GOCE data for the longer wavelengths of the gravity field. For the shorter wavelengths the DTU2010 global gravity anomaly dataset was used, which is identical to the EGM2008 gravity anomalies over land. The EIGEN-6C model provides time-variable coefficients up to degree and order 50. For this study, only the linear part of the time-dependency was used and the model values were evaluated at epoch 2006.25, the centre of the time span of the GRACE measurements used for the model. The cosine and sine terms were disregarded as seasonal variations were not taken into account in the ground measurements used in this study.

The evaluation of the global models was performed using the HARMONIC_SYNTH program by Holmes and Pavlis (NGA 2008), which is provided with the EGM2008 model.

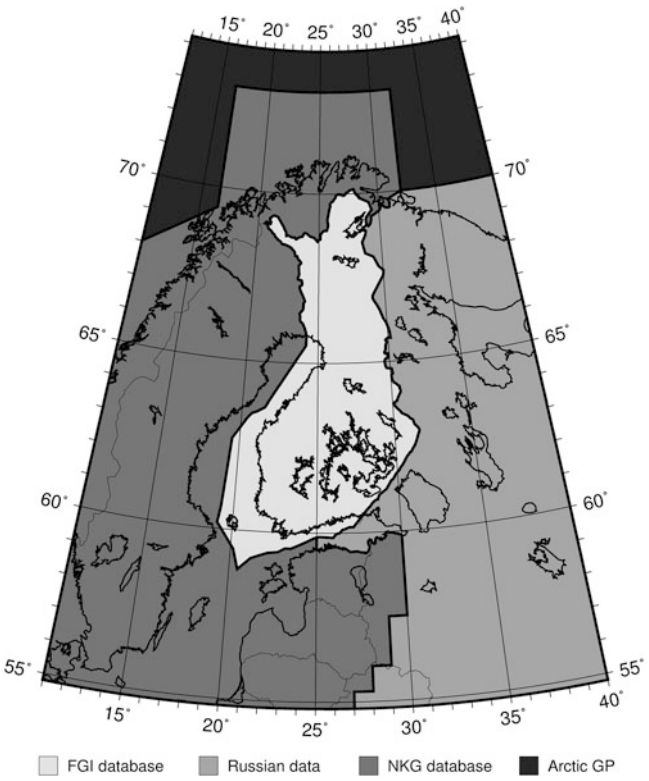

Fig. 1 Gravity datasets used in the study

2.2 GPS-Levelling Data

Two GPS-levelling datasets were used, the Finnish EUVN-DA dataset (Ollikainen 2006) and a dataset from the Finnish National Land Survey (NLS data).

The Finnish EUVN-DA dataset consists of 50 GPS/levelling points, of which 20 were part of the EUREF-FIN network measured in Finland in 1996–1997. The remaining 30 points were new and measured in the EUVN-DA GPS-campaign in 2005. All points are either first order levelling points or new points that were directly connected to the first order levelling network (Ollikainen 2006). The data used here had EUREF-FIN GPS coordinates as well as N2000 heights from the precise leveling (Bilker-Koivula 2010).

The NLS data consists of 526 points taken from the NLS point register. The points are in classes 1–3 and have levelled N2000 heights and measured EUREF-FIN coordinates (Puupponen 2011 personal communication). The accuracy and distribution of the points is not homogeneous and the dataset partly overlaps with the EUVN-DA dataset. However, tests showed no significant accuracy differences between the classes and it is the best available large dataset for Finland.

Both datasets were corrected for the land uplift taking place between the epoch of the N2000 levelling data (2000.0) and the epoch of the EUREF-FIN GPS data (1997.0). The corrections were depending on location between 8.5 mm and 28.1 mm over 3 years. Vertical velocities were taken from the NKG2005LU land uplift model (Vestøl 2007; Ågren and Svensson 2007).

2.3 Gravity Data

The gravity dataset was compiled from different sources (see Fig. 1). Within the territory of Finland the gravity database of the Finnish Geodetic Institute was used. For most of Russia a Russian dataset with gridded anomalies was used having a resolution of $5' \times 7.5'$. For the Arctic area the Arctic GP dataset (Kenyon et al. 2008) was used. It has a resolution of $5' \times 5'$. For all other areas free-air anomalies of the NKG database (Forsberg et al. 2004) were used. This is a database maintained by the Working group on geoid and heights systems of the Nordic Geodetic commission.

3 Comparisons with GPS-Levelling

To get a first impression of the performance of the global models in Finland, height anomalies were calculated from the global models using their full spectrum of coefficients; up to degree 2190 and order 2159 for EGM2008 and up

Table 1 Statistics of the differences between the height anomalies from GPS-levelling and the global models, EGM2008 (developed to degree 2190 and order 2159) and EIGEN-6C (developed to degree and order 1420), before and after trend removal: mean, standard deviation (std. dev.), minimum (min.) and maximum (max.)

		Differences (m)				Trend removed (m)			
		Mean	Std. dev.	Min.	Max.	Mean	Std. dev.	Min.	Max.
EGM2008	EUVN-DA	−0.58	0.06	−0.69	−0.30	0.00	0.06	−0.12	0.27
	NLS	−0.57	0.05	−0.88	−0.32	0.00	0.05	−0.31	0.23
EIGEN-6C	EUVN-DA	−0.62	0.07	−0.78	−0.41	0.00	0.07	−0.16	0.18
	NLS	−0.63	0.07	−0.95	−0.41	0.00	0.07	−0.32	0.21

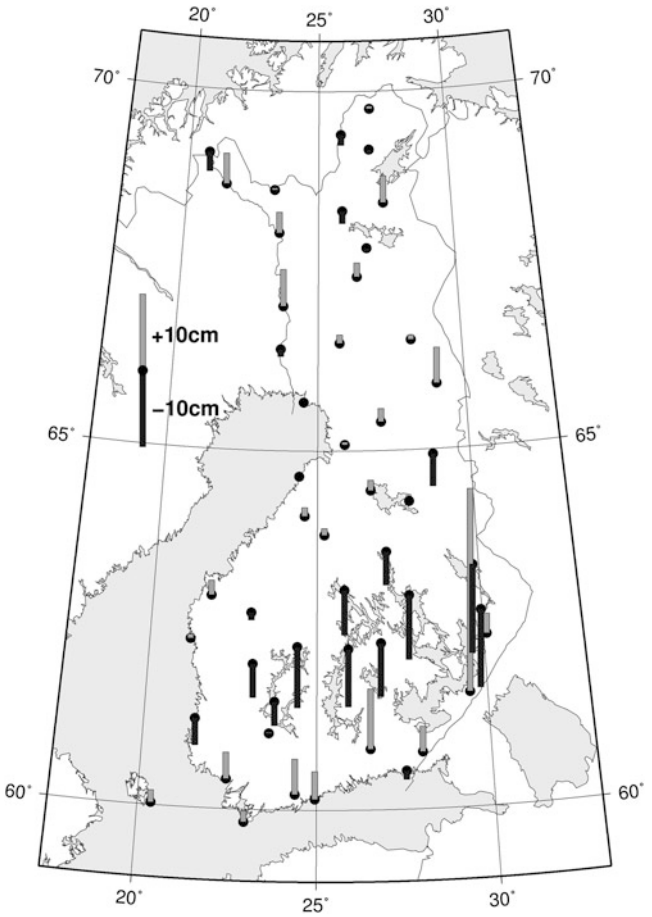

Fig. 2 Differences between height anomalies from the EGM2008 model and the EUVN-DA GPS-levelling data after trend removal

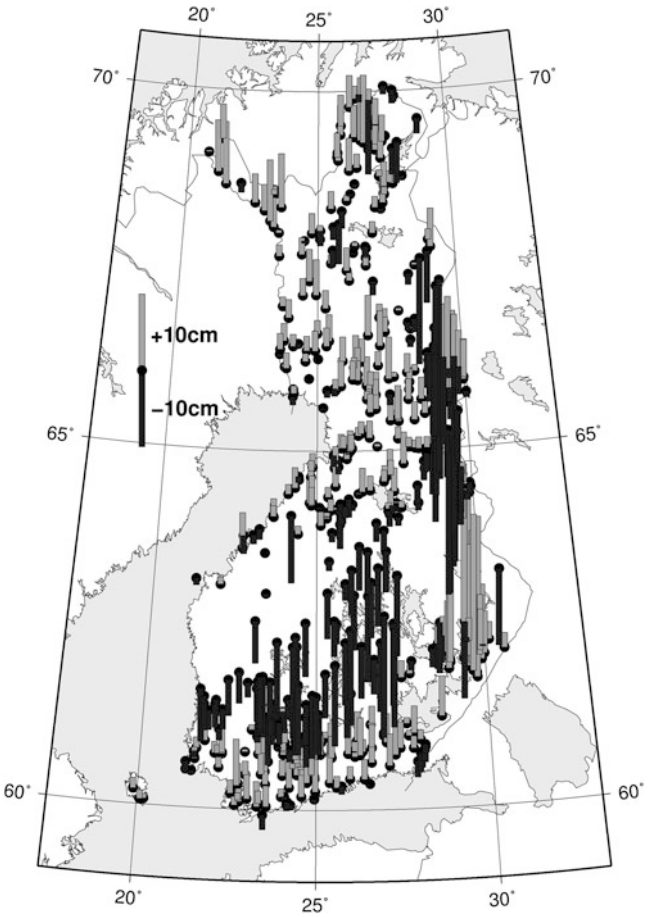

Fig. 3 Differences between height anomalies from the EGM2008 model and the NLS GPS-levelling data after trend removal

to degree and order 1420 for EIGEN-6C. These were then compared with height anomalies obtained from the GPS-levelling datasets.

The statistics of the differences are given in Table 1, as well as the statistics after removal of a trend (offset and tilt). Standard deviations between 5 and 7 cm are obtained. As expected the EGM2008 gives better results than the EIGEN-6C model, due to the higher maximum degree and order of the EGM2008 model. Removing a trend, reduces the mean value to zero, but does not make the standard deviations smaller, which implies that there is only an offset between the global models and the GPS-levelling, but no tilt.

The distribution of the differences over the country can be seen in Figs. 2, 3, 4, and 5. It can be seen that the distribution is not homogeneous over the country, however it is different for the EGM2008 and the EIGEN-6C model. This

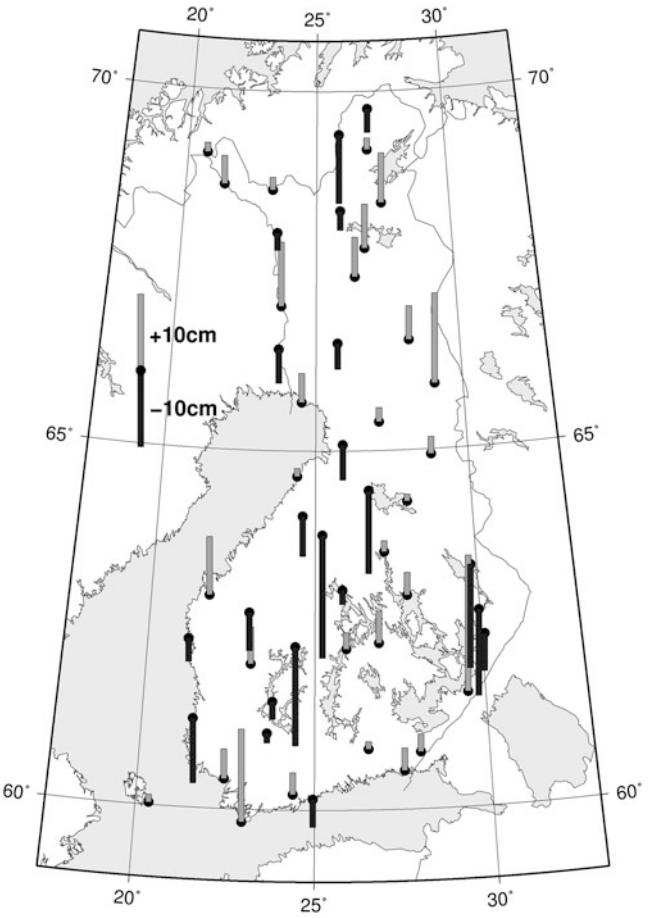

Fig. 4 Differences between height anomalies from the EIGEN-6C model and the EUVN-DA GPS-levelling data after trend removal

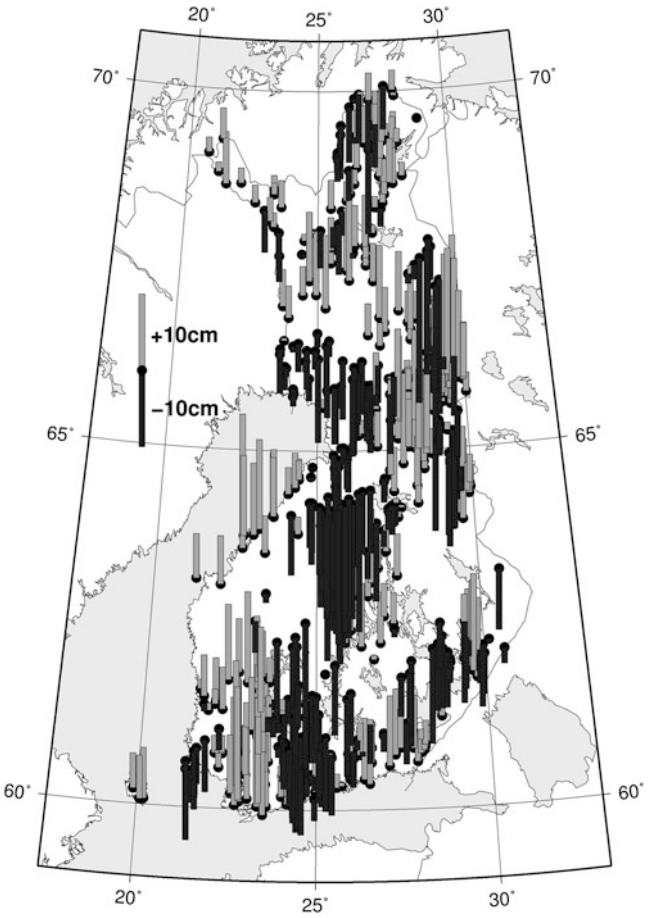

Fig. 5 Differences between height anomalies from the EIGEN-6C model and the NLS GPS-levelling data after trend removal

indicates that the areal differences are caused by differences in the mid- to short-wavelength parts of the global models. Furthermore, a division can be seen at the 29° east line. The differences are clearly larger east of the 29° line and smaller west of the line. This is most clearly seen in Fig. 3, where the standard deviation of the differences west of the 29° line is 4 cm and east of the 29° line 10 cm.

4 Comparisons with Gravity Data

For the comparison with the gravity data, free-air anomalies were calculated from the global models. These were then compared with the free-air anomalies available for the whole area. Differences with the EGM2008 model show a mean of −1.01 mGal and a standard deviation of 8.19 mGal. For the differences with the EIGEN-6C model the mean is −1.06 mGal and the standard deviation 10.09 mGal. Within the Finnish territory the differences have a mean and standard deviation of −0.56 mGal and 3.68 mGal for the EGM2008 model and −0.34 mGal and 5.84 mGal for the EIGEN-6C model.

The differences are homogeneously distributed over most of the Scandinavian countries, with the largest differences over the Norwegian mountains. However, over the Russian part of the data larger patterns can be seen (see Fig. 6). This is most probably due to lower resolution data used over Northern Russia in the EGMs. From Fig. 6 can be seen that this lower resolution data is used from 29° eastward. Most of the degree 29 line is within the Finnish borders, resulting in lower accuracies within Finland close to the borders with Russia. This explains also the larger standard deviations in this area seen in the comparison with GPS-levelling (see Sect. 4).

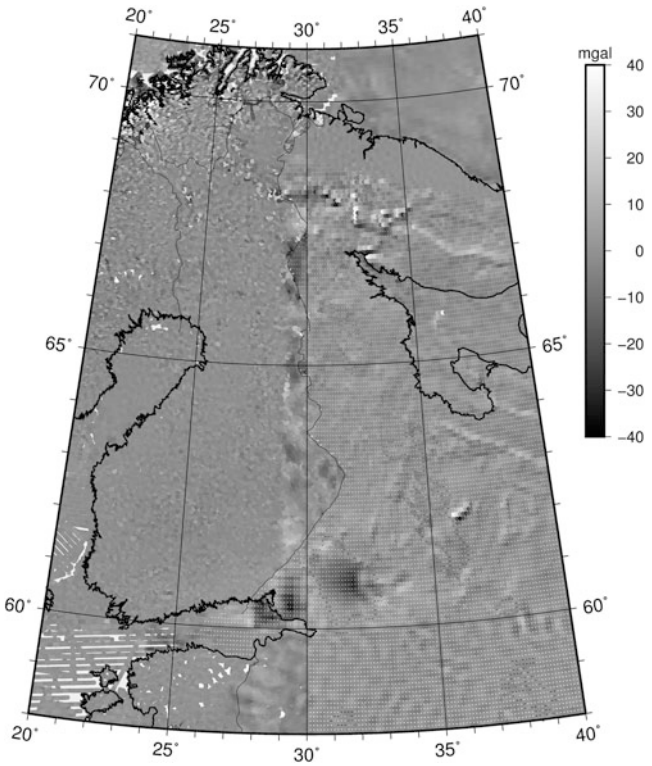

Fig. 6 Differences of the free-air anomalies from the EGM2008 model and the gravity dataset in the East of the study area

5 Regional Quasi-geoid Modelling

In the last part of the study the global models were combined with terrestrial data in the calculation of a quasi-geoid model for Finland.

5.1 Description of Calculations

The remove-compute-restore technique was applied, using the GRAVSOFT-software package (Forsberg 2003; Tscherning et al. 1992) for the calculations. Here, first the known signal from the global model, Δg_{EGM}, was removed from the free-air anomaly data, Δg_{FA}. Then residual terrain corrections, Δg_{RTM}, were removed, resulting in residual gravity anomalies, $\Delta g_{\mathrm{residual}}$:

$$\Delta g_{\mathrm{residual}} = \Delta g_{\mathrm{FA}} - \Delta g_{\mathrm{EGM}} - \Delta g_{\mathrm{RTM}}. \tag{1}$$

After gridding the residual gravity anomalies, residual height anomalies were calculated by evaluating Molodensky's integral using multi-banded spherical FFT (Forsberg and Sideris 1993). In the end the height anomaly effect of the residual terrain corrections, ζ_{RTM}, and the global model, ζ_{EGM}, were added to the residual height anomalies, $\zeta_{\mathrm{residual}}$, resulting in quasi-geoid heights, ζ, for Finland:

$$\zeta = \zeta_{\mathrm{residual}} + \zeta_{\mathrm{RTM}} + \zeta_{\mathrm{EGM}}. \tag{2}$$

For calculating the terrain corrections the digital terrain model Scandem was used, this model was compiled for calculation of the NKG2004 quasi-geoid model and has a resolution of 0.02° by 0.04°. Because it contained GTOPO30 heights (USGS 2013) for Finland, the heights for Finland were in this study replaced by heights derived from the 25 m resolution height model for Finland, korkeusmalli25 (NLS 2013). The mean elevation surface for the residual terrain corrections was taken from the EGM2008-height model, developed to the same degree and order as the used global gravity field model.

For the NKG-dataset accurate terrain corrections up to 50 km were available and these were converted to residual terrain corrections the same way as it was done in the NKG2004 calculations. First, the terrain corrections to 50 km were converted to residual terrain corrections through a Bouguer reduction to the reference level. Then, terrain corrections calculated from the reference surface were subtracted from terrain corrections calculated from the digital terrain model for distances beyond 50 km. These residual terrain corrections from beyond 50 km were then subtracted from the residual terrain corrections to 50 km.

In the GRAVSOFT package, the SPFOUR-routine for spherical multi-band FFT geoid determination allows for the Wong-Gore modification of the Stokes' integral kernel (Wong and Gore 1969). It was applied in this study to eliminate the effect of local data (for example remaining terrain effects of the Norwegian mountains) on the longer wavelengths. Here a tapered version of the Wong-Gore modification was applied, where the lowest harmonics are set to zero up to degree N_1, and then gradually go to full power at degree, N_2 (Forsberg 2003):

$$S_{\mathrm{mod}}(\psi) = S(\psi) - \sum_{n=2}^{N_2} \alpha(n) \frac{2n+1}{n-1} P_n \cos\psi \tag{3}$$

$$\alpha(n) = \begin{cases} 1 & \text{for } 2 \le n \le N_1 \\ \frac{N_2 - n}{N_2 - N_1} & \text{for } N_1 \le n \le N_2 \\ 0 & \text{for } N_2 \le n \le N \end{cases} \quad n = 2, \ldots, N,$$

where S_{mod} and S are the modified and original Stokes' kernel functions. Different values for N_1 and N_2 were tested with N_2 being always 10 higher than N_1. The final quasi-geoid heights were then compared with the GPS-levelling data to find the optimal values.

Table 2 Statistics of the residual height anomalies (m) at the beginning of the restore step for both global models, EGM2008 (developed to degree 2190 and order 2159) and EIGEN-6C (developed to degree and order 1420), first without modification of the Stokes' kernel and second with Wong-Gore modification of the kernel at 50° and 60°

	N_1, N_2	Mean	Std. dev.	Min.	Max.
EGM2008	0, 0	0.25	0.20	−0.33	0.98
	50, 60	0.00	0.07	−0.80	0.51
EIGEN-6C	0, 0	0.22	0.20	−0.29	0.92
	50, 60	0.00	0.08	−0.70	0.48

Table 3 Statistics of the differences between the final height anomalies and the gps-levelling data for the EGM2008 global model (developed to degree 2190 and order 2159), without and with Wong-Gore modification of the Stokes' kernel at 50° and 60°

	Differences (m)				Trend removed (m)			
EGM2008	Mean	Std. dev.	Min.	Max.	Mean	Std. dev.	Min.	Max.
$N_1 = 0, N_2 = 0$								
EUVN-DA	−0.858	0.094	−1.016	−0.681	0.000	0.055	−0.126	0.116
NLS	−0.865	0.084	−1.148	−0.654	0.000	0.055	−0.209	0.137
$N_1 = 50, N_2 = 60$								
EUVN-DA	−0.561	0.028	−0.635	−0.499	0.000	0.023	−0.084	0.048
NLS	−0.556	0.035	−0.695	−0.443	0.000	0.028	−0.164	0.075

Table 4 Statistics of the differences between the final height anomalies and the gps-levelling data for the EIGEN-6C global model (developed to degree and order 1420), without and with Wong-Gore modification of the Stokes' kernel at 50° and 60°

	Differences (m)				Trend removed (m)			
EIGEN-6C	Mean	Std. dev.	Min.	Max.	Mean	Std. dev.	Min.	Max.
$N_1 = 0, N_2 = 0$								
EUVN-DA	−0.871	0.094	−1.026	−0.694	0.000	0.056	−0.110	0.122
NLS	−0.878	0.084	−1.156	−0.665	0.000	0.056	−0.207	0.136
$N_1 = 50, N_2 = 60$								
EUVN-DA	−0.608	0.024	−0.678	−0.552	0.000	0.024	−0.076	0.053
NLS	−0.601	0.031	−0.572	−0.516	0.000	0.029	−0.164	0.069

5.2 Results

After removing the effects of the global model and the residual terrain effects, the residual anomalies had a mean of 0.18 mGal and standard deviation of 4.08 mGal when the EGM2008 model was used. In case of the EIGEN-6C model the mean of the residual anomalies was 0.17 mGal and the standard deviation 6.02 mGal.

The statistics of the residual height anomalies after integration over the Stokes' kernel function with and without Wong-Gore kernel modification are given in Table 2. Tables 3 and 4 show the corresponding statistics of the comparisons between the final quasi-geoid models and the GPS-levelling data.

In Table 2 can be seen that the residual height anomalies have an offset and standard deviation of about 20 cm when no modification of the Stokes' kernel is applied. When plotted, these anomalies show very long-wavelength patterns, that were not visible in the residual gravity anomalies. When modifying the Stokes' kernel the offset disappears and the standard deviations get smaller. The best results were obtained with a Wong-Gore modification of the Stokes' kernel at degrees $N_1 = 50$ and $N_2 = 60$.

The GPS-levelling comparisons in Tables 3 and 4 confirm these results. When no kernel modification is applied, there is a trend in the differences and even removal of the trend does not make the results much better than the global-model-only differences (Table 1). When kernel modification is applied, the GPS-levelling results show a significant improvement of the national quasi-geoid with respect to the global models. Now standard deviations between 2.5 and 3 cm are obtained, which is also an improvement over the NKG2004 quasi-geoid model. Before trend removal, the EIGEN-6C gives marginally better results than the EGM2008. But after trend removal the differences are gone.

The distribution of the differences with GPS-levelling over the country is shown in Figs. 7 and 8. Compared to Figs. 2, 3, 4, and 5, the differences are now smaller and distributed more homogeneously over the country. No division can be detected anymore at the 29° longitude line.

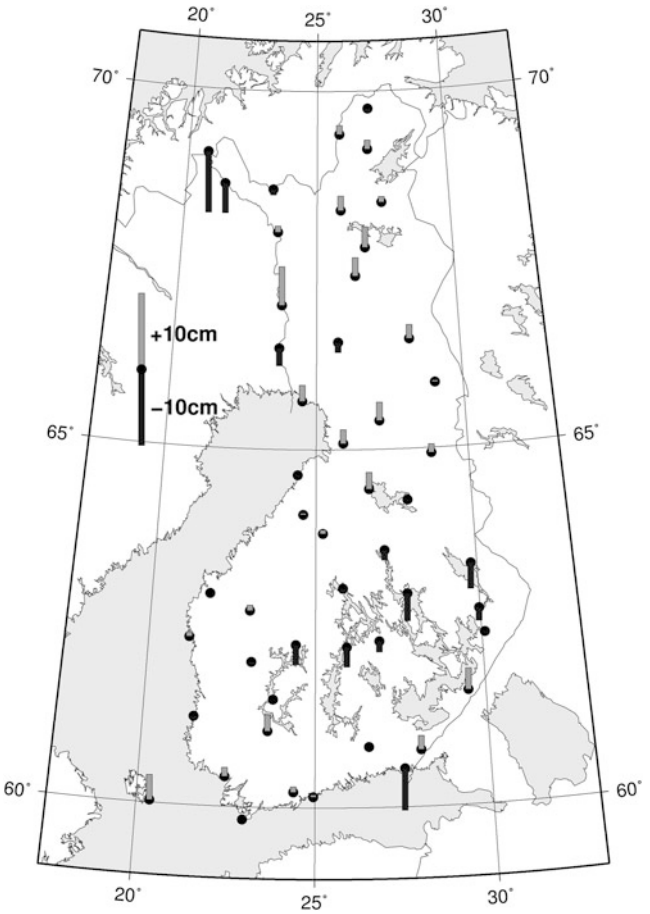

Fig. 7 Differences between height anomalies of the EUVN-DA GPS-levelling dataset and the best quasi-geoid solution (EGM2008, $N_1 = 50$, $N_2 = 60$) after trend removal

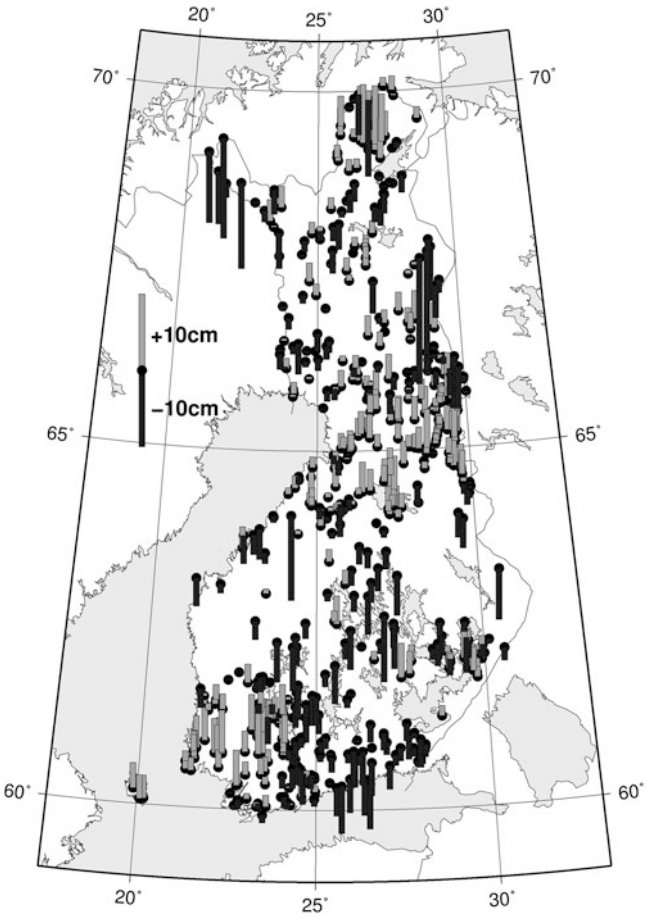

Fig. 8 Differences between height anomalies of the NLS GPS-levelling dataset and the best quasi-geoid solution (EGM2008, $N_1 = 50$, $N_2 = 60$) after trend removal

Conclusions

Comparison of the height anomalies from the global models, EGM2008 and EIGEN-6C, and the GPS-levelling data showed standard deviations of the differences between 5 and 7 cm. Large patterns could be detected, but no tilt. A division could be seen at the 29° longitude line.

The same division was detected when comparing gravity anomalies from both global models with measured anomalies. Gravity anomalies are small and rather homogeneously distributed over the area west of the 29° line, but east of the line large patterns can be seen. This is most probably due to lower resolution data used in the EGMs over northern Russia.

When the global models are used as background model in the calculation of the quasi-geoid model for Finland, the problems near the 29° longitude line disappear. The resulting quasi-geoid models show standard deviations between 2.5 and 3 cm when compared with GPS-levelling data. This is an improvement over earlier geoid models for Finland.

The study described here gave promising results and it is expected that next quasi-geoid models for Finland will perform even better, when GOCE-only models will be taken into account in the calculations. Also, more improvement is expected in the near future when the Finnish Geodetic Institute will publish the new First Order Gravity Network of Finland. After all gravity observations are connected to this network, a new improved quasi-geoid will be calculated for the country.

Acknowledgements This work was partially funded by the Academy of Finland (grant number 117132).

References

Ågren J, Svensson R (2007) Postglacial land uplift model and system definition for the new Swedish height system RH 2000. Reports in Geodesy and Geographical Information Systems, LMV-Rapport 2007:4, Gävle, 124 pp

Bilker-Koivula M (2010) Development of the Finnish height conversion surface FIN2005N00. Nordic J Surv Real Estate Res 7(1):76–88

Forsberg R (2003) An overview manual for the GRAVSOFT, Geodetic Gravity Field Modelling Programs. Draft–1, September 2003. National Survey and Cadastre of Denmark

Forsberg R, Sideris MG (1993) Geoid computations by the multi-band spherical FFT approach. Manuscripta Geodaetica 18:82–90

Forsberg R, Strykowski G, Solheim D (2004) NKG-2004 geoid of the Nordic and Baltic area. In: Proceedings on CDROM: IAG international symposium—gravity, geoid and space missions—GGSM2004—Abstracts, Presentations, Papers, Porto, Portugal, 30 August–3 September 2004

Förste C, Bruinsma S, Shako R, Marty J-C, Flechtner F, Abrikosov O, Dahle C, Lemoine J-M, Neumayer KH, Biancale R, Barthelmes F, König R, Balmino G (2011) EIGEN-6—a new combined global gravity field model including GOCE data from the collaboration of GFZ-Potsdam and GRGS-Toulouse. Geophysical Research Abstracts, vol 13, EGU2011-3242-2, EGU General Assembly 2011

Kenyon S, Forsberg R, Coakley B (2008) New gravity field for the arctic. Eos Trans AGU 89(32):289. doi:10.1029/2008EO320002

NGA (2008) EGM2008 model coefficients—original release. National Geospatial-Intelligence Agency. http://earth-info.nga.mil/GandG/wgs84/gravitymod/egm2008/first_release.html. Accessed 5 Feb 2013

NLS (2013) Elevation model 25 m. National Land Survey of Finland. http://www.maanmittauslaitos.fi/en/digituotteet/elevation-model-25-m. Accessed 28 Jan 2013

Ollikainen M (2006) The EUVN_DA campaign in Finland. Publications of the Finnish Geodetic Institute, 135, 39 p

Pavlis NK, Holmes SA, Kenyon SC, Factor JK (2008) An Earth gravitational model to degree 2160: EGM2008. Geophysical Research Abstracts, vol 10, EGU2008-A-01891, EGU General Assembly 2008

Pavlis NK, Holmes SA, Kenyon SC, Factor JK (2012) The development and evaluation of the Earth Gravitational Model 2008 (EGM2008). J Geophys Res 117, B04406. doi:10.1029/2011JB008916

Tscherning CC, Forsberg R, Knudsen P (1992) The GRAVSOFT package for geoid determination. In: Holota P, Vermeer M (eds) Proceedings of the 1st continental workshop on the geoid in Europe, Prague, May 1992, pp 327–334

USGS (2013) GTOPO30—Global 30 arc second elevation data set. U.S. Geological Survey. http://www1.gsi.go.jp/geowww/globalmap-gsi/gtopo30/gtopo30.html. Accessed 28 Jan 2013

Vestøl O (2007) Determination of postglacial land uplift in Fennoscandia from levelling, tide-gauges and continuous GPS stations using least squares collocation. J Geod 80:248–258

Wong L, Gore R (1969) Accuracy of geoid heights from modified stokes kernels. Geophys J R Astr Soc 18:81–91

Comparison of GOCE Global Gravity Field Models to Test Fields in Southern Norway

M. Šprlák, B.R. Pettersen, O.C.D. Omang, D.I. Lysaker, M. Sekowski, and P. Dykowski

Abstract

Numerous global gravity field models (GGFMs) have resulted from the satellite gradiometry mission GOCE. Validation is indispensable to test the performance of the new-generation models. For this purpose independent datasets of terrestrial data are very often used.

In this study, homogenous datasets of free-air gravity anomalies and GNSS/leveling points have been collected in southern Norway. These datasets have been exploited for validation of four GOCE-derived GGFMs (DIR_r3, GOCO03s, TIM_r3, and DGM-1S) by the spectral enhancement method.

Numerical experiments have proven that the effect of the residual terrain model is important to free-air gravity anomalies but not to height anomalies. Validation of GOCE GGFMs has revealed that performance of these models is very similar. However, in comparison to EGM2008, we have observed 10 % increase of the standard deviation for the GOCE-derived models at d/o 210, 20 % increase at d/o 230, and up to 65 % increase at d/o 250. In addition, validation by GNSS/leveling data suggests significant improvements delivered by the GOCE GGFMs with respect to EGM2008 between d/o 100–200 in our test field.

Keywords

Gravimetry • Gradiometry • Validation • Spectral enhancement method

M. Šprlák (✉)
Department of Mathematical Sciences and Technology, University of Environmental and Life Sciences, P.O. Box 5003, 1432 Ås, Norway

New Technologies for the Information Society, Faculty of Applied Sciences, University of West Bohemia, Univerzitní 22, 306 14 Plzeň, Czech Republic
e-mail: michal.sprlak@gmail.com

B.R. Pettersen
Department of Mathematical Sciences and Technology, University of Environmental and Life Sciences, P.O. Box 5003, 1432 Ås, Norway

O.C.D. Omang • D.I. Lysaker
Norwegian Mapping Authority, Geodetic Institute, 3507 Hønefoss, Norway

M. Sekowski • P. Dykowski
Institute of Geodesy and Cartography, Modzelewskiego St. 27, 02-679 Warsaw, Poland

1 Introduction

The satellite gradiometry mission GOCE (ESA 1999) was mapping the Earth's gravity field in a homogenous and nearly global way. The mission goals were very challenging. It was expected that GOCE will provide free-air gravity anomalies with an accuracy of 1 mGal and a geoid model with an accuracy of 1–2 cm, both at the spatial resolution of 100 km.

Global gravity field models (GGFMs) are the main products of the GOCE mission. They allow evaluation of an arbitrary functional of the disturbing potential. The performance of the models and the GOCE mission goals may thus be directly validated with respect to homogenous sets of terrestrial data. That is of high importance for gravity field modeling as well as for users of the models.

U. Marti (ed.), *Gravity, Geoid and Height Systems*, International Association of Geodesy Symposia 141,
DOI 10.1007/978-3-319-10837-7_8,

In this study, validation of GOCE-based GGFMs has been performed in southern Norway. Two independent test fields of free-air gravity anomalies and GNSS/leveling points have been exploited. Both datasets are described in Sect. 2. A total of four GOCE GGFMs have been tested in the numerical experiment using the spectral enhancement method (SEM). In the numerical experiments presented in Sect. 3 we first investigate the accuracy of the SEM and then report the results of the validation. The conclusions summarize the contributions of this study.

Within this paper we make use of the following nomenclature: the low frequencies of the gravity field quantities correspond to spherical harmonic degree and order (d/o) 2–100, the middle frequencies are those between d/o 101–250, high frequencies between d/o 251–2190, and very-high frequencies above d/o 2190.

2 Description of the Terrestrial Datasets

2.1 Terrestrial Free-Air Gravity Anomalies

Terrestrial gravity data provide essential information about the Earth's gravity field. Observed by relative and absolute instruments, they form the base for geoid/quasigeoid determination. They also contribute to studies of natural phenomena and physical processes, e.g. the inner structure of the Earth, sea level rise, ice melting and other mass movements. For these reasons, gravity networks have been established in many countries of the world.

The gravity reference frame in Norway (Harsson 1978) consists of 286 primary stations, connected by relative gravimeters in early 1970s. Four stations (Hammerfest, Bodø, Trondheim, and Oslo) were observed with FG5-226 between 2005 and 2011. Absolute gravity values were derived from these time series and referred to September 2011. At this time an observing campaign at 21 primary stations were also made with A10-020 absolute gravimeter.

Attached to the primary stations are loops of 7,791 secondary gravity stations, measured in the 1970s and early 1980s. The entire dataset was readjusted with respect to the absolute gravity values obtained with the FG5 and A10 instruments. This transformation compensates for the effects of postglacial uplift. The gravity values and also the observed free-air gravity anomalies are available in the zero tide system.

We have selected the data south of latitude 65°N as a test field, comprising 4,556 stations that are located more or less homogenously (see Fig. 1) with an average density of 1 station per 50 km^2. Here, the free-air gravity anomalies range from −103.0 mGal to 193.1 mGal, with a standard deviation of 45.7 mGal and a mean value of 14.6 mGal. The test field is characterized by very rough topographical features ranging in elevation from 0 (along the coast) to 2,500 m (in the central part). The accuracy of the observed free-air gravity anomalies is 0.1 mGal.

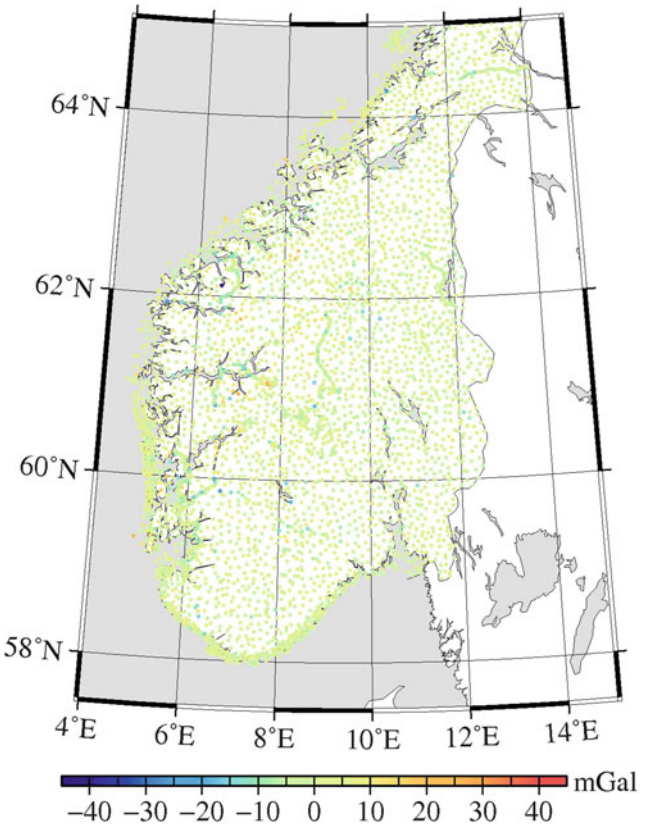

Fig. 1 Mean value reduced differences between the observed and the modeled (using EGM2008 and RTM) free-air gravity anomalies (RTM included)

2.2 GNSS/Leveling Points

Leveling is the traditional geodetic technique to determine the vertical distance of objects with relation to a reference surface such as a geoid or quasigeoid. It is important for many geodetic and surveying tasks where physical heights are required.

Due to time efficiency and costs, use of global navigation satellite systems (GNSS) is preferred. The GNSS techniques allow determination of the geometrical position very precisely. However, the height component measured by GNSS is purely geometrical related to a reference ellipsoid.

The differences between the GNSS and leveling observations provide a geometrical way to obtain geoid/quasigeoid heights. These are very often used for testing GGFMs.

For our validation purposes GNSS/leveling data compiled by the Norwegian Mapping Authority have been used. The dataset has been compiled from the latest measurement

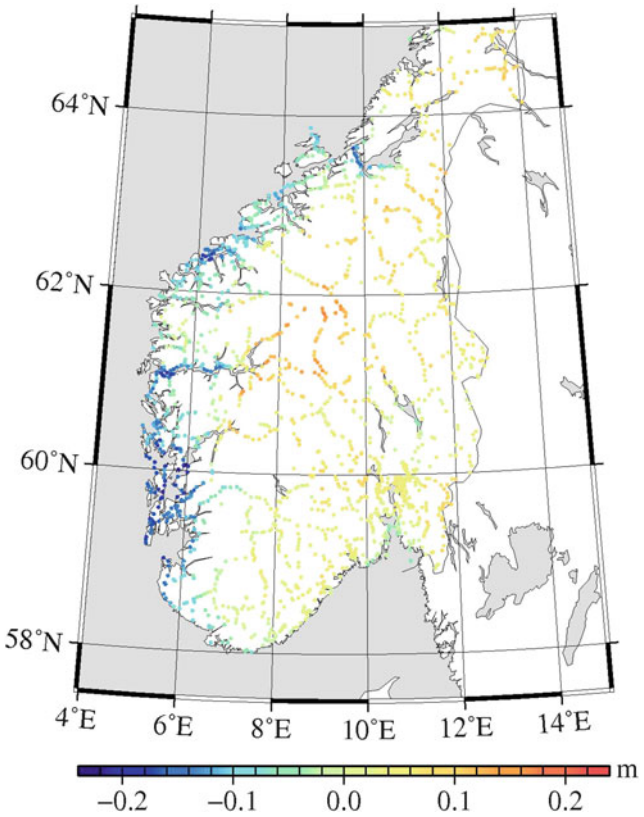

Fig. 2 Mean value reduced differences between the observed and the modeled (using EGM2008 and RTM) height anomalies (RTM included)

campaigns. Moreover, the dataset is based on the newest realizations of the vertical system and of the terrestrial reference frame in Norway.

The leveled heights are listed in the vertical system NN2000 (Lysaker and Vestøl 2012). It is a zero-tidal vertical reference system tied to Normal Amsterdam Peil at epoch 2000.0. In the NN2000 vertical system, normal heights have been adopted. Thus the GNSS/leveling dataset provides observed height anomalies which we will refer to in the following.

The GNSS observations are referred to the IGS05 reference frame at the epoch 2009.58. Conventionally, the ellipsoidal heights are provided in the tide-free system. Due to the different reference time epochs and tide systems adopted, the postglacial uplift as well as the tidal correction have to be applied, see Sect. 3.1 for details.

In the same test area as for the free-air gravity anomalies (south of latitude 65°N) 1,792 GNSS/leveling stations are located. The stations are distributed along the leveling lines (Fig. 2). Within the test field, the observed height anomaly varies from 32.34 m in the eastern part up to 47.64 m in the western part, with a standard deviation of 3.32 m and a mean value of 41.97 m. The accuracy of the observed height anomalies is 2–3 cm.

3 Numerical Experiment

3.1 Modeling of the Free-Air Gravity and Height Anomalies Using SEM

The SEM (Hirt et al. 2010) is a gravity field modeling approach combining a high-resolution GGFM and a digital elevation model (DEM). An important advantage of the SEM is that very high frequency features of the gravity field quantities may be recovered. It thus allows the consistent comparison between terrestrial (composing of all spectral constituents) and satellite (composing of low and middle frequency constituents) observations in validation activities.

The performance of our computational algorithms has been investigated by considering the accuracy of the SEM. This has been done by direct comparison between the observed and modeled free-air gravity and height anomalies.

The low, middle, and high frequencies of the modeled quantities have been calculated from EGM2008 (Pavlis et al. 2012) up to d/o 2190. The harmonic synthesis has been performed by the GRAFIM software (Janák and Šprlák 2006). Numerical problems of spherical harmonics have been avoided by implementing Horner's scheme (Holmes and Featherstone 2002). In the case of free-air gravity anomalies we have applied harmonic expansion based on the ellipsoidal approximation (Wenzel 2005).

The very-high frequencies have been computed from a residual terrain model (RTM, Forsberg 1984). The RTM has been obtained as the difference between high resolution DEMs ACE2 (Berry et al. 2010) or ASTER (Tachikawa et al. 2011) with respect to a smooth topographical surface, computed from the elevation model DTM2006.0 (Pavlis et al. 2007) in the form of the topographical spherical harmonic coefficients. The DTM2006.0 heights have been synthesized by the GRAFIM software up to d/o 2160.

At each station of the free-air gravity and height anomalies, numerical integration of the RTM has been performed using a newly developed program. We have assumed planar approximation of the corresponding kernels. To reduce the computational time, the numerical integration has been divided into two zones. The inner zone makes use of $1'' \times 1''$ discretization of the mass elements as provided by the ASTER DEM. Such discretization has been applied within the integration radius $\psi = 0.1°$. Beyond that, the outer integration zone makes use of $30'' \times 30''$ discretization of the mass elements as provided by the ACE2 DEM.

The size of the integration radius in the outer integration zone has been selected independently for each quantity. For free-air gravity anomalies the integration radius was $\psi_0 = 0.5°$ and for height anomalies the integration radius was $\psi_0 = 3.0°$. Numerical experiments using variable maximum radii showed that the contributions beyond the selected

Table 1 Statistics of the differences between the observed and the modeled (using EGM2008 and RTM) quantities with and without the RTM (in mGal for gravity anomalies and in meters for height anomalies)

Quantity	RTM	Min.	Max.	Mean	Std. Dev.
Δg	No	−158.4	100.1	−3.5	29.1
	Yes	−38.9	34.4	1.6	4.6
ζ	No	0.084	0.475	0.322	0.060
	Yes	0.187	0.599	0.424	0.076

integration radii are negligible. Throughout the numerical experiment, a standard rock density value 2,670 kg m^{-3} of the masses within the RTM was considered.

One of the critical points in evaluation of the RTM effect is the application of the harmonic correction for points located inside the constructed RTM. We have applied the approach proposed in (Kadlec 2011) which solves this issue implicitly.

To avoid inconsistencies between the observed and the modeled quantities we have applied the atmospheric correction (Wenzel 1985) and a tidal correction (from zero-tide to tide-free system; Mäkinen and Ihde 2008) to the observed free-air gravity anomalies. The observed height anomalies have been corrected by a 10-year correction due to the postglacial rebound based on the model NKG2005LU (Ågren and Svensson 2007) and a tidal correction (from zero-tide to tide-free system).

The statistics of the differences between the observed and the modeled quantities is given in Table 1. In the case of free-air gravity anomalies, the standard deviation of the differences decreases from 29.1 mGal (without RTM) to 4.6 mGal (with RTM). The effect of the RTM improves the modeling by 85 % showing the sensitivity of free-air gravity anomalies to very-high frequencies of the Earth's gravity field. The spatial behavior of mean value reduced differences between the observed and the modeled gravity anomalies is depicted in Fig. 1. Their random distribution may be a good indication of the correctness of our numerical algorithms.

For height anomalies, much less pronounced improvement due to the RTM should theoretically be expected since these are less sensitive to very-high frequency constituents. However, as indicated in Table 1, the effect of the RTM leads to the standard deviation increasing from 0.060 m (without RTM) to 0.076 m (with RTM). This result is in contradiction with Hirt et al. (2010) reporting significant improvements in height anomaly modeling due to the RTM contribution. On the other hand, Kadlec (2011) documented that the effect of the RTM does not necessarily lead to better performance of the SEM in modeling height anomalies.

Our result is one example where considering RTM leads to worse performance. In other words, our results suggest that the unmodified EGM2008 fits better to the observed height anomalies. This result may be tested in the future by e.g. spectral analysis of the observed and the modeled height anomalies within the test field. For methodological reasons, we will consider the case when RTM has been included in calculations. This does not affect any of the conclusions.

The spatial behavior of mean value reduced differences between the observed and the modeled height anomalies is plotted in Fig. 2. It is noted that the differences present systematic behavior with long-wavelength features overwhelming the effect of the RTM. We suspect that this is due to errors of the EGM2008 model or leveling errors within the test field. This will be investigated in the next subsection in more detail. Note that the similar behavior of the mean value reduced differences is also present when RTM is not included.

3.2 Validation of GOCE-Derived GGFMs

Numerous GGFMs have already been derived from GOCE observations. In general, these models make use of different theoretical strategies assuming various types of a-priori information, stochastic modeling of the gravitational tensor components, spatial resolution, and numerical technique for evaluation of the spherical harmonic coefficients in the low and high frequencies of the Earth's gravity field (Pail et al. 2011). Therefore, we may expect differences between the individual models.

Validation studies have shown quite consistent representations of the Earth's gravity field by the different analysis strategies (Gruber et al. 2011; Hirt et al. 2011; Janák and Pitoňák 2011; Šprlák et al. 2012). Successive improvements of the GOCE models with releases of more data have been reported for higher d/o spherical harmonic coefficients. Better performance of GOCE models with respect to EGM2008 in the spectral range 180–200 has been documented mainly in areas lacking gravity field observations (Pail et al. 2011).

We extend the study of Šprlák et al. (2012) where ten GOCE-based GGFMs were validated by using free-air gravity anomalies over the entire Norway. Here only the four most recent GOCE-derived GGFMs (available by September 2012) have been tested, see Table 2. The models DIR_r3 (Bruinsma et al. 2010) and TIM_r3 (Pail et al. 2011) are based on 12 months of GOCE observations (distributed over 18 months period). The first model has been determined by the direct approach. The second model is based on the time-wise approach. The time-wise approach has also been applied in GOCO03s (Mayer-Gürr et al. 2012), which includes observations of GOCE, GRACE, CHAMP, and satellite laser ranging. The DGM-1S (Hashemi Farahani et al. 2013) model has been determined by an optimal combination of GRACE and GOCE observations. In particular, K-band ranging and

Table 2 Characteristics of the validated GGFMs

GGFM	N_{max}	Reference
DIR_r3	240	Bruinsma et al. (2010)
TIM_r3	250	Pail et al. (2011)
GOCO03s	250	Mayer-Gürr et al. (2012)
DGM-1S	250	Hashemi Farahani et al. (2013)

kinematic orbital data of GRACE as well as kinematic orbital and gravity gradient data of GOCE are combined in this model.

The validation of these four GOCE-derived models has been performed in the following way. Firstly, the modeled quantities have been determined by the SEM. The lowest spectrum has been synthesized up to variable d/o of the spherical harmonic coefficients for each of the GOCE models (ranging from d/o 2 up to the maximum available d/o). Above this contribution, harmonic synthesis by using EGM2008 has been considered up to d/o 2190. Effect of the RTM has been evaluated above the d/o 2190. Secondly, the observed and the modeled quantities have been compared.

The standard deviations of differences between the observed and the modeled free-air gravity anomalies are depicted in Fig. 3. There are only negligible differences between all curves up to d/o 80. Therefore only the behavior above d/o 80 is presented. The standard deviation of the GOCE models increases exponentially with increasing d/o and is always greater than that corresponding to EGM2008. We note a 10 % increase of the standard deviation for GOCE models with respect to EGM2008 at d/o 210, 20 % increase at d/o 230, and up to 65 % increase at d/o 250. The four GOCE models perform very similar up to d/o 180. Above d/o 180, the DGM-1S model reaches the highest standard deviation. This is likely caused by DGM-1S exploiting only 10 months of gravity gradient observations, while 12 months of data have been used in the other models. We also note very good agreement between the TIM_r3 and GOCO03s models, based on the same theoretical strategy. The DIR_r3 model performs very similar to the time-wise based models except at the d/o 210–220 and 230–240 where differences on the level of several tenths of mGal are visible. These results are in very good agreement with Šprlák et al. (2012).

Validation by the height anomalies offers a possibility to confirm the above results. The standard deviations of differences between the observed and the modeled height anomalies are depicted in Fig. 4. Again, only the behavior above d/o 80 is shown. As for free-air gravity anomalies, we note similar performance of TIM_r3 and GOCO03s, and only small deviations of the DIR_r3 model. All models provide almost identical results up to d/o 180. Above this d/o the exponential increase is evident. Again DGM-1S reaches the highest standard deviation (except between d/o 240–250).

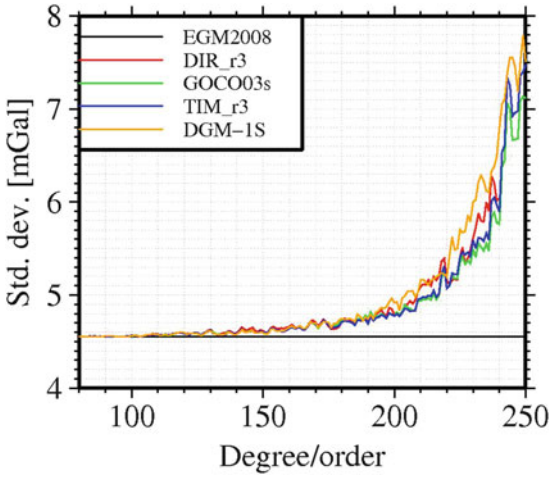

Fig. 3 Standard deviation of differences between the observed and the modeled (using validated GOCE-derived GGFMs, EGM2008 and RTM) free-air gravity anomalies as a function of d/o of the GOCE GGFMs (RTM included)

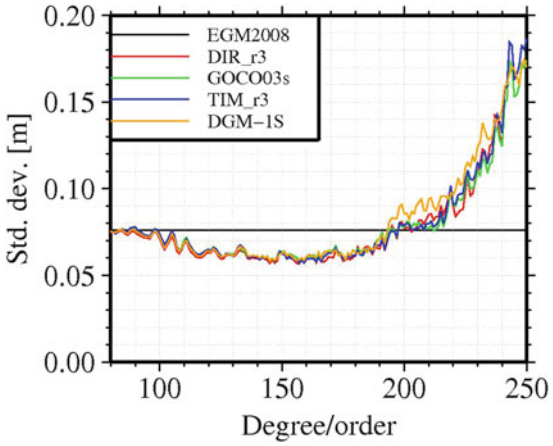

Fig. 4 Standard deviation of differences between the observed and the modeled (using the validated GOCE-derived GGFMs, EGM2008 and RTM) height anomalies as a function of d/o of the GOCE-derived GGFMs (RTM included)

Improvement relative to EGM2008 between d/o 100–200 is revealed in Fig. 4, reaching up to 1.5 cm.

We note that this improvement is not visible in the free-air gravity anomalies because of their sensitivity to higher frequencies. Also the accuracy of the SEM in the case of free-air gravity anomalies (on the level of 4.5 mGal, Table 1) overwhelms the magnitudes of the differences between EGM2008 and GOCE models (reaching only a few mGal).

The improvement in height anomalies as delivered by GOCE models have been investigated in more detail. This is of particular interest with reference to Fig. 2 where we have observed the systematic behavior of differences with low frequency features. In Fig. 4 the floor of the standard

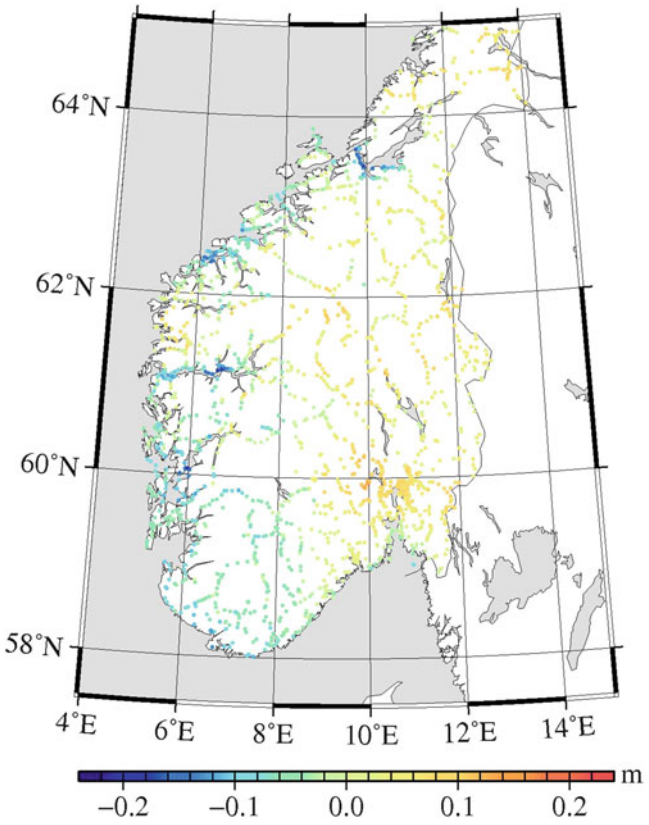

Fig. 5 Mean value reduced differences between the observed and the modeled (using TIM_r3 GGFM up to d/o 160, EGM2008 and RTM) height anomalies (RTM included)

deviation has been reached approximately at d/o 160. We have plotted the mean value reduced differences between the observed and the modeled height anomalies in Fig. 5 using the TIM_r3 model up to d/o 160. By comparing Figs. 2 and 5 we note that the differences are significantly reduced when the low and middle frequencies of GOCE are considered. This is visible on the west coast and in the central part of the test field. On the other hand, the differences are more pronounced in the south-east part of the test field.

Figure 5 still shows a low frequency pattern on the level of several centimeters across the test field. However, the low frequencies of EGM2008 and GOCE models differ by only a few millimeters. We may therefore suspect that the origin of the low frequency features is due to distortions in the leveling network.

The more pronounced differences in the south-eastern part may reveal some discrepancies present also in higher frequencies. The behavior of the differences in the test field above d/o 160 has therefore been investigated. The comparison has shown very similar performance as for EGM2008 between d/o 180–200 in the region above the latitude of 60.5°. Below this latitude, EGM2008 and TIM_r3 differ significantly which could indicate possible improvements of the GOCE models between d/o 180–200. However, since the performance is very close to the accuracy of the SEM, this indication cannot be stated explicitly.

Conclusions

Homogeneous sets of free-air gravity and height anomalies have been produced from new terrestrial measurements in southern Norway. They were used to validate four recent GOCE-derived models (available by September 2012). Numerical experiments have revealed that the gravitational attraction of local masses, computed from digital elevation models, is important to free-air gravity anomalies but not to height anomalies. The latter fits better to the pure EGM2008 model. We found the performance of the validated GOCE global gravity field models to be very similar. In comparison to EGM2008, we observed 10 % increase of the standard deviation for the GOCE models at d/o 210, 20 % increase at d/o 230, and up to 65 % increase at d/o 250. Validation by free-air gravity anomalies does not reveal any improvements over EGM2008. On the other hand, validation by height anomalies in Norway suggests improvements by the GOCE models in the middle frequencies.

Future experiments will be performed to investigate the better fit of pure EGM2008 model to the observed height anomalies. New releases of GOCE-based models will be validated. These tasks are important for improvements of the gravity field over Norway.

Acknowledgements The study is part of UMB's Nova-GOCE project supported by the Norwegian Research Council under project number 197635 and is carried out in the framework of UMB's ESA-category-1 project 4294 Application and Validation of GOCE and remote sensing data with focus on Northern latitudes.

References

Ågren J, Svensson R (2007) Postglacial land uplift model and system definition for the new Swedish height system RH 2000. Reports in geodesy and geographical information systems, LMV-Rapport 2007:4, National Land Survey of Sweden, Gävle, Sweden, 124 p

Berry PAM, Smith RG, Benveniste J (2010) ACE2: the new global digital elevation model. In: Mertikas SP (ed) Gravity, geoid and Earth observation, IAG symposia, vol 135, Chania, Greece, 23–27 June 2008, pp 231–238

Bruinsma SL, Marty JC, Balmino G, Biancale R, Förste C, Abrikosov O, Neumayer H (2010) GOCE gravity field recovery by means of the direct numerical method. In: Proceedings of the ESA living planet symposium, Bergen, Norway, 28 June–2 July 2010

ESA (1999) Gravity field and steady-state ocean circulation mission. Reports for Mission Selection, the Four Candidate Earth Explorer Core Missions, ESA SP-1233(1). ESA, Noordwijk

Forsberg R (1984) A study of terrain reductions, density anomalies and geophysical inversion methods in gravity field modeling. Report No. 355. Department of Geodetic Science and Surveying, Ohio State University, Columbus, USA

Gruber T, Visser PNAM, Ackermann C, Hosse M (2011) Validation of GOCE gravity field models by means of orbit residuals and geoid comparison. J Geod 85:845–860

Harsson BG (1978) Beregning av det norske gravimeterbasisnettet. In: Proceedings, NKG General Assembly, Oslo

Hashemi Farahani H, Ditmar P, Klees R, Liu X, Zhao Q, Guo J (2013) The static gravity field model DGM-1S from GRACE and GOCE data: computation, validation and an analysis of GOCE mission's added value. J Geod 87:843–867

Hirt C, Featherstone WE, Marti U (2010) Combining EGM2008 and SRTM/DTM2006.0 residual terrain model data to improve quasigeoid computations in mountainous areas devoid of gravity data. J Geod 84:557–567

Hirt C, Gruber T, Featherstone WE (2011) Evaluation of the first GOCE static gravity field models using terrestrial gravity, vertical deflections and EGM2008 quasigeoid heights. J Geod 85:723–740

Holmes SA, Featherstone WE (2002) A unified approach to the Clenshaw summation and the recursive computation of very high degree and order normalized associated Legendre functions. J Geod 76:279–299

Janák J, Pitoňák M (2011) Comparison and testing of GOCE global gravity models in central Europe. J Geodetic Sci 1:333–347

Janák J, Šprlák M (2006) A new software for gravity field modelling (in Slovak). Geodetic and Cartographic Horizon, 52: 1–8

Kadlec M (2011) Refining gravity field parameters by residual terrain modeling. Doctoral Thesis, Department of Mathematics, Faculty of Applied Sciences, University of West Bohemia, Pilsen, Czech Republic, 150 p

Lysaker DI, Vestøl O (2012) Norwegian vertical reference system NN2000. Norwegian Mapping Authority, Hønefoss, Norway (in preparation)

Mäkinen J, Ihde J (2008) The permanent tides in height systems. In: Sideris MG (ed) Observing our changing Earth, IAG symposia, vol 133, Perugia, Italy, 2–13 July 2007, pp 81–87

Mayer-Gürr T, Rieser D, Höck E, Brockmann JM, Schuh WD, Krasbutter I, Kusche J, Maier A, Krauss S, Hausleitner W, Baur O, Jäggi A, Meyer U, Prange L, Pail R, Fecher T, Gruber T (2012) The new combined satellite only model GOCO03s. Abstract submitted to GGHS2012, Venice (Poster)

Pail R, Bruinsma S, Migliaccio F, Förste C, Goiginger H, Schuh WD, Höck E, Reguzzoni M, Brockmann JM, Abrikosov O, Veicherts M, Fecher T, Mayrhofer R, Krasbutter I, Sansó F, Tscherning CC (2011) First GOCE gravity field models derived by three different approaches. J Geod 85:819–843

Pavlis NK, Factor JK, Holmes SA (2007) Terrain-related gravimetric quantities computed for the next EGM. In: Gravity field of the Earth, proceedings of the 1st international symposium of the international gravity field service, Harita Dergisi, Special Issue 18, Istanbul, Turkey, pp 318–323

Pavlis NK, Holmes SA, Kenyon SC, Factor JK (2012) The development and evaluation of the Earth Gravitational Model 2008 (EGM2008). J Geophys Res 117: B04406, 38 pp. doi:10.1029/2011JB008916

Šprlák M, Gerlach C, Pettersen BR (2012) Validation of GOCE global gravity field models using terrestrial gravity data in Norway. J Geod Sci 2:134–143

Tachikawa T, Hato M, Kaku M, Iwasaki A (2011) The characteristic of ASTER GDEM version 2. In: IEEE international geoscience and remote sensing symposium (IGARSS), Vancouver, Canada, 24–29 July, pp 3657–3660

Wenzel HG (1985) Hochauflösende Kugelfunktionsmodelle für das Gravitationspotential der Erde. Wissenschaftliche Arbeiten der Fachrichtung Vermessungswesen der Universität Hannover, Nr. 137, Geodätisches Institut der Universität Hannover

Wenzel HG (2005) Global models of the gravity field of high and ultra-high resolution. In: International school for the determination and use of the geoid, International Geoid Service, Budapest, Hungary, 31 January–5 February 2005, 36 p

Evaluation of Recent GRACE and GOCE Satellite Gravity Models and Combined Models Using GPS/Leveling and Gravity Data in China

Jiancheng Li, Weiping Jiang, Xiancai Zou, Xinyu Xu, and Wenbin Shen

Abstract

A total of 649 GPS/Leveling points and 799897 $2' \times 2'$ gridded mean gravity anomalies in mainland China are used for the evaluation of the recently released Earth Gravitational Models (EGMs) including the GOCE only models (GO_CONS_GCF_2_TIM_R3 (GO_TIM_R3), GRACE only models ITG-Grace2010s, combined satellite gravity field models (GO_CONS_GCF_2_DIR_R3 (GO_DIR_R3), GOCO03S, DGM-1S, EIGEN-5S, EIGEN-6S), and combined gravity field models (EIGEN-51C, EIGEN-6C, GIF48, EGM2008) from satellite observations and ground gravity data sets. The statistical results show that in mainland China the most precise model is EIGEN-6C with the standard deviation (STD) ± 0.183 m of the quasi-geoid height differences compared with the GPS/Leveling data and the STD ± 22.5 mGal of the gravity anomaly differences compared with the gridded mean gravity anomalies from observations. For EGM2008, they are ± 0.240 m and ± 24.0 mGal respectively. Among the satellite only gravity models from GRACE, GOCE and LAGEOS observations, GO_TIM_R3 is the best one in mainland China, and the STDs of the corresponding quasi-geoid differences and the gravity anomaly differences are ± 0.459 m and ± 31.3 mGal respectively, which are nearly at the same levels as the ones for the models EIGEN-6S, GOCO03S and GO_DIR_R3. This shows that the GOCE mission can recover more medium-short wavelength gravity signals in mainland China than former satellite gravity missions.

Keywords

GPS/leveling • Gravity anomaly • Geoid • Evaluation • Gravity field model

1 Introduction

Since the successful implementation of the satellite gravity missions (CHAMP, GRACE, GOCE) early this century, many new global Earth Gravitational Models (EGMs) were released by different research institutes and organizations in the world (see http://icgem.gfz-potsdam.de/ICGEM). In recent 3 years, the GOCE-related EGMs, which include GOCE only models, combined satellite gravity field models and combined satellite-ground gravity field models, were released successively. Generally, GOCE models are determined by three different approaches: direct approach (DIR), time-wise approach (TIM), and space-wise approach (SPW)

J. Li (✉) • X. Zou • X. Xu • W. Shen
School of Geodesy and Geomatics, Wuhan University, Wuhan, China

Key Laboratory of Geospace Environment and Geodesy, Ministry of Education, Wuhan, China
e-mail: jcli@whu.edu.cn

W. Jiang
School of Geodesy and Geomatics, Wuhan University, Wuhan, China

Key Laboratory of Geospace Environment and Geodesy, Ministry of Education, Wuhan, China

GNSS Research Center, Wuhan University, Wuhan, China

U. Marti (ed.), *Gravity, Geoid and Height Systems*, International Association of Geodesy Symposia 141,
DOI 10.1007/978-3-319-10837-7_9,

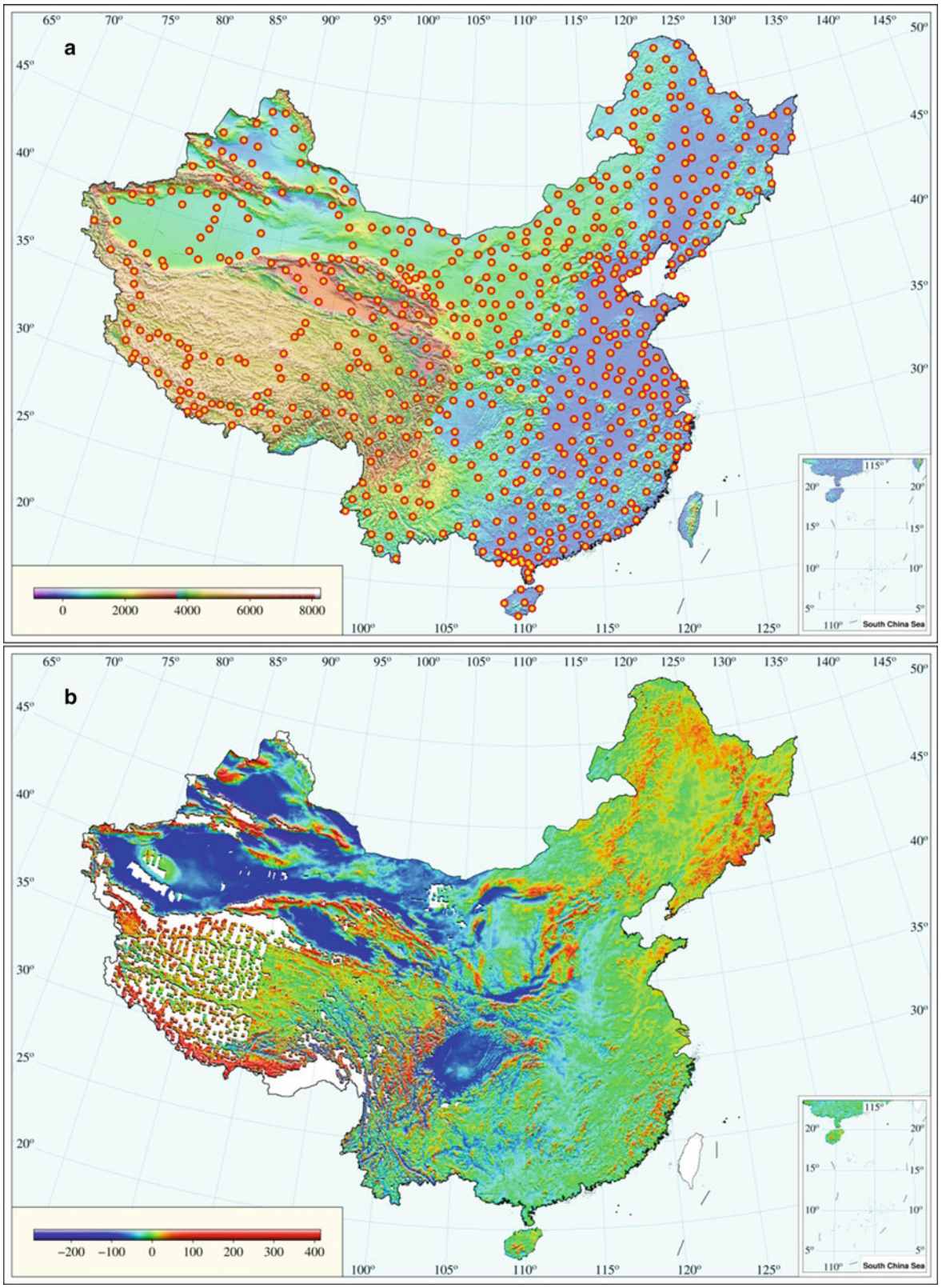

Fig. 1 (**a**) The point distribution of the order B GPS/Leveling, and (**b**) the $2' \times 2'$ free-air gravity anomaly grid, with *white areas* denoting the gaps without gravity anomalies (mGal)

(Pail et al. 2011). The third generation models by the first two approaches (GO_DIR_R3 and GO_TIM_R3) and the second generation model by the last approach (GO_SPW_R2) were released by ESA (2011). Comparing to the second generation model from DIR approach, GO_DIR_R3 is a combined model based on GRACE and GOCE observations. GO_SPW_R2 model is not a GOCE only model, because EGM2008 is used for degree variance modelling and for error calibration of the estimated gravitational potential along track. GO_TIM_R3 is the GOCE only model. At the same time, some other combined satellite gravity models recovered from GRACE and GOCE were also published, such as GOCE03S, DGM-1S, EIGEN-6S (Mayer-Gürr et al. 2012; Hashemi Farahani et al. 2013; Förste et al. 2011). EIGEN-6C is a new high degree and order model based on satellite and ground gravity data, complete to degree/order 1420.

This paper provides the results of the evaluation of those global gravity field models based on the GPS/Leveling and gravity data distributed in mainland China. For the purpose of the evaluation, the GRACE only model ITG-Grace2010s (Mayer-Gürr et al. 2010) and the benchmark global gravity model EGM08 (Pavlis et al. 2012) up to the degree 2190 are also compared with the datasets for references.

2 Data Used for the Evaluation

2.1 GPS/Leveling Data

For the evaluation of those gravity field models mentioned above, 649 GPS/Leveling points (Li et al. 2009) within the Chinese national B-order GPS networks (mainland China) are used, the distribution of which is shown in Fig. 1. The GPS coordinates are referred to WGS84 under the frame of the International Terrestrial Reference Frame (ITRF93) at epoch 1996.365, and the leveling at the GPS points is referred to the China Yellow Mean Sea Level 1985 Datum. The mean accuracy of the height anomalies derived from the GPS/Leveling is at the level of 0.14 m (Li et al. 2009).

2.2 Gravity Anomaly Data

The $2' \times 2'$ gridded free-air gravity anomalies (Li 2012) are generated from ground gravity data in China, which are shown in Fig. 1. The data in the west of China are sparse and there exist many data gaps, while the data in the east of China are much denser. In this study, by choosing the interpolation radius 16 km, there are 78811 grid points at which there are no gravity anomalies, and these grid points (e.g. in Taiwan) are not included in the comparisons. The total number of the gridded points for the evaluation is 799897 (see Fig. 1).

2.3 CNGG2011 Model

The Chinese National Gravimetric quasi-Geoid 2011 (CNGG2011) is a digital gravimetric quasi-geoid model for the National Height Datum 1985 of China, which is computed by using the Stokes-Helmert method with EIGEN-CG03C as the reference model. Its spatial resolution is $2' \times 2'$. The standard deviation (STD) of CNGG2011 when compared to 649 GPS/Leveling points is ± 0.126 m. The average accuracy of CNGG2011 is ± 0.07 m and ± 0.14 m in eastern and western China, respectively. For detailed information of the model CNGG2011, it is referred to Li (2012).

3 Quasi-geoid Comparisons

The observed quasi-geoid heights are computed at all the testing points in national B-order GPS/Leveling networks, and the corresponding values are derived from the recently

Table 1 The statistics of the differences among the CNGG2011 as well as the quasi-geoid heights derived from different EGMs and those at the 649 GPS/leveling points (unit: m)

Model	Degree	Max	Min	Bias	RMS	Std. D (GPS-L)	Std. D (CNGG)
CNGG2011	–	0.246	−0.746	−0.161	±0.205	±0.126	–
EGM2008	2190	1.319	−1.938	−0.171	±0.295	±0.240	±0.391
EIGEN-6C	1420	0.531	−1.074	−0.172	±0.251	±0.183	±0.342
GIF48	360	0.525	−2.262	−0.279	±0.434	±0.332	±0.376
DGM-1S	250	1.430	−2.666	−0.348	±0.588	±0.474	±0.527
EIGEN-5S	150	3.652	−4.063	−0.395	±0.874	±0.780	±0.903
EIGEN-6S	240	1.201	−2.731	−0.345	±0.597	±0.488	±0.541
GOCO03S	250	1.472	−2.528	−0.348	±0.579	±0.462	±0.516
EIGEN-51C	359	0.689	−2.496	−0.281	±0.457	±0.360	±0.419
ITG-GRACE2010S	180	3.363	−3.750	−0.368	±0.749	±0.653	±0.737
GO_DIR_R3	240	1.439	−2.540	−0.350	±0.587	±0.471	±0.528
GO_TIM_R3	250	1.377	−2.479	−0.340	±0.571	±0.459	±0.514

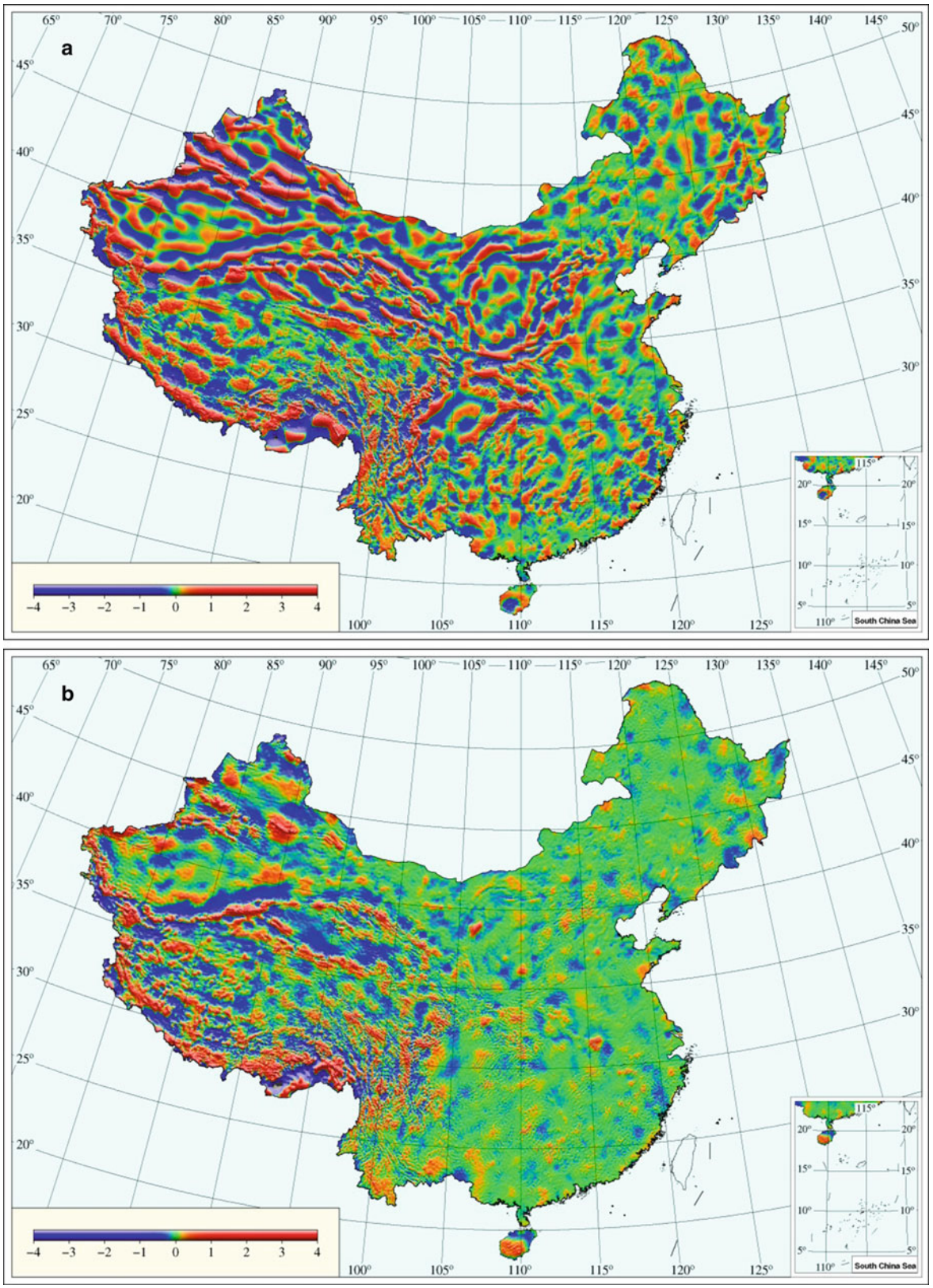

Fig. 2 The quasi-geoid height differences between (**a**) CNG2011 and GOCE only model GO_TIM_R3, and (**b**) CNG2011 and the combined model EIGEN-6C estimated by GRACE, GOCE and ground gravity data (unit: m)

released GOCE models and other EGMs. The statistical results of the comparisons between the observed and the model values are tabulated in Table 1, where the differences between CNGG2011 and the observed quasi-geoid heights are also given. The last column lists the STD of the differences between CNGG2011 and the values estimated from EGMs. From Table 1, we can see that the minimum STD of the differences between the observed and model values is ±0.183 m, which is corresponding to the model EIGEN-6C. The best GOCE only model is GO_TIM_R3, which performs better than the combined satellite gravity models GOCO03S, EIGEN-6S and DGM-1S. The accuracy of the regional model CNGG2011 is better than all the global gravity field models. As examples, Fig. 2 show respectively the quasi-geoid height differences between CNGG2011 and EIGEN-6C, GO_TIM_R3 in mainland China. One can see that large differences appear in the mountain areas in western China.

4 Gravity Anomaly Comparisons

The gridded free-air gravity anomalies from the gravity field models are computed and then compared with the corresponding gridded mean gravity anomalies derived from the observed gravity data. The statistics of their comparison differences are listed in Table 2, from which we can see that EIGEN-6C has the smallest RMS and STD. Thus one may conclude that EIGEN-6C is better fitted to the local gravity data in China and consequently it is more suitable as a reference model in the local geoid modeling (in our knowledge we don't know whether EIGEN-6C uses the ground gravity in China). The average biases of all the recent gravity field models are about 4.0 mGal, which indicates that the differences of the datum/reference of these models are negligible compared with RMS. Among the satellite only gravity field models, the STD of the differences between the observed gravity anomalies and the corresponding GO_TIM_R3 model ones is nearly identical to those between the observed gravity anomalies and the model values corresponding to EIGEN-6S, GOCO03S and GO_DIR_R3, respectively.

Table 2 The statistics of the comparison differences between the gravity anomalies derived from different EGMs and the 799897 $2' \times 2'$ gridded mean gravity anomalies in China (unit: mGal)

Model	Degree	Max	Min	Bias	RMS	Std. D
EGM2008	2190	375.8	−266.9	2.8	±24.2	±24.0
EIGEN-6C	1420	296.5	−221.0	2.7	±22.7	±22.5
GIF48	360	342.6	−236.2	3.7	±28.7	±28.4
DGM-1S	250	345.9	−282.8	4.3	±31.8	±31.5
EIGEN-5S	150	316.4	−319.6	4.9	±36.5	±36.2
EIGEN-6S	240	348.2	−283.5	4.3	±32.1	±31.8
GOCO03S	250	346.1	−281.5	4.3	±31.6	±31.3
EIGEN-51C	359	378.1	−221.6	3.7	±29.6	±29.3
ITG-GRACE2010S	180	346.4	−311.1	4.6	±34.9	±34.6
GO_DIR_R3	240	342.4	−278.0	4.3	±31.8	±31.5
GO_TIM_R3	250	347.5	−281.4	4.2	±31.6	±31.3

Figure 3 show, respectively, the differences among the observed gridded mean free-air gravity anomalies and the corresponding model values via EIGEN-6C, EGM08, GO_TIM_R3 and GOCO03S. Large differences appear in western China, which means that the above models cannot well represent the high frequency gravity signals in the mountainous areas of western China. The high degree model EIGEN-6C and ultra-high degree EGM08 perform better than the satellite only models GO_TIM_R3 and GOCO03S in both the west and east of China.

Conclusions

From the evaluation results of the recently released gravity field models using China GPS/Leveling and gravity datasets, we find that EIGEN-6C is the most precise model in mainland China region. The STD of the quasi-geoid height differences and that of the gravity anomaly differences are ±0.183 m and ±22.5 mGal respectively. The satellite only models GO_TIM_R3, GO_DIR_R3, EIGEN-6S and GOCO03S are nearly at the same accuracy level in mainland China, and are better than the satellite only models (e.g., EIGEN-5S, ITG-Grace2010s) without GOCE observations. This suggests that GOCE mission provides effective improvements in detecting the medium frequency gravity signals.

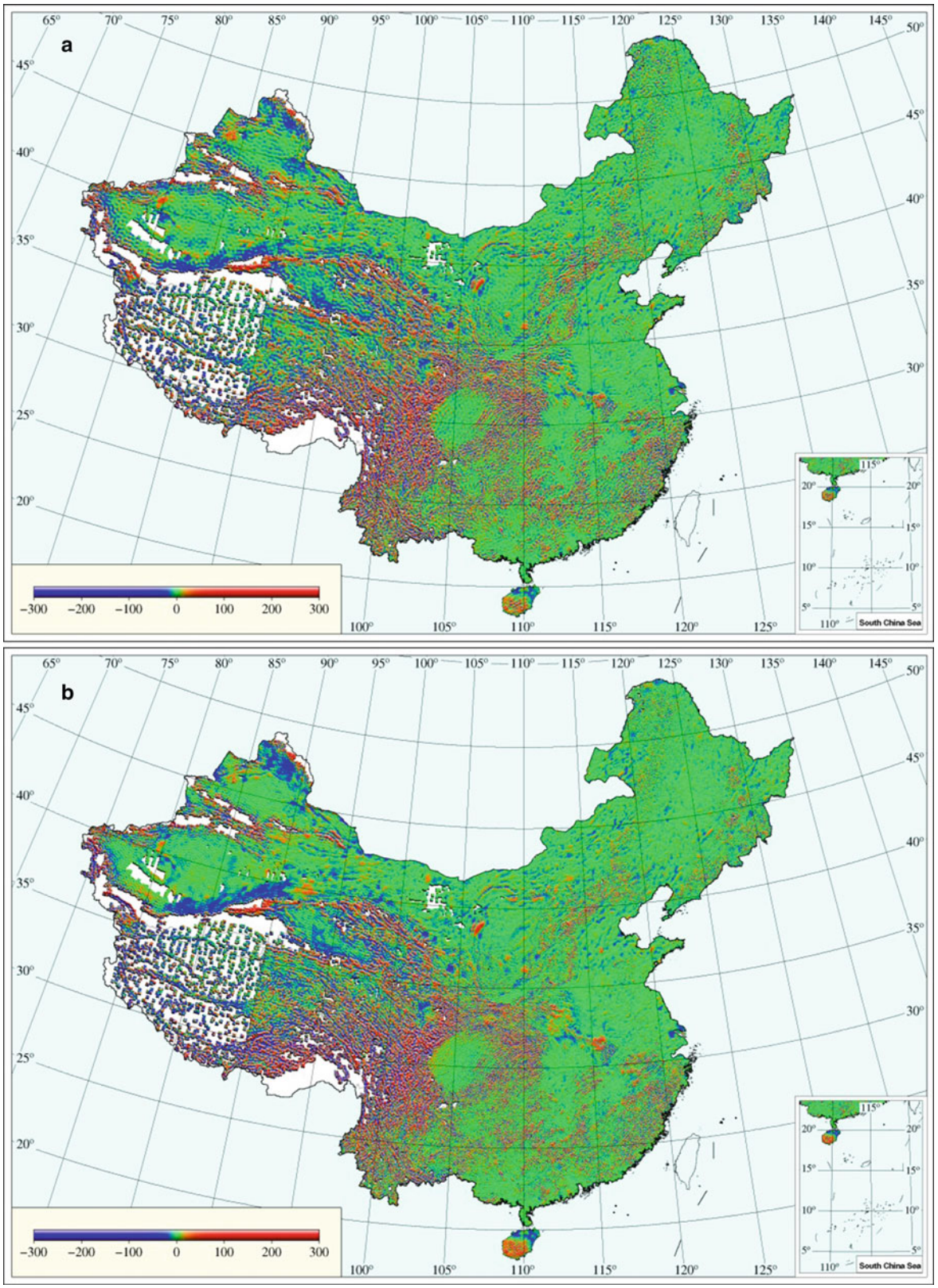

Fig. 3 (continued)

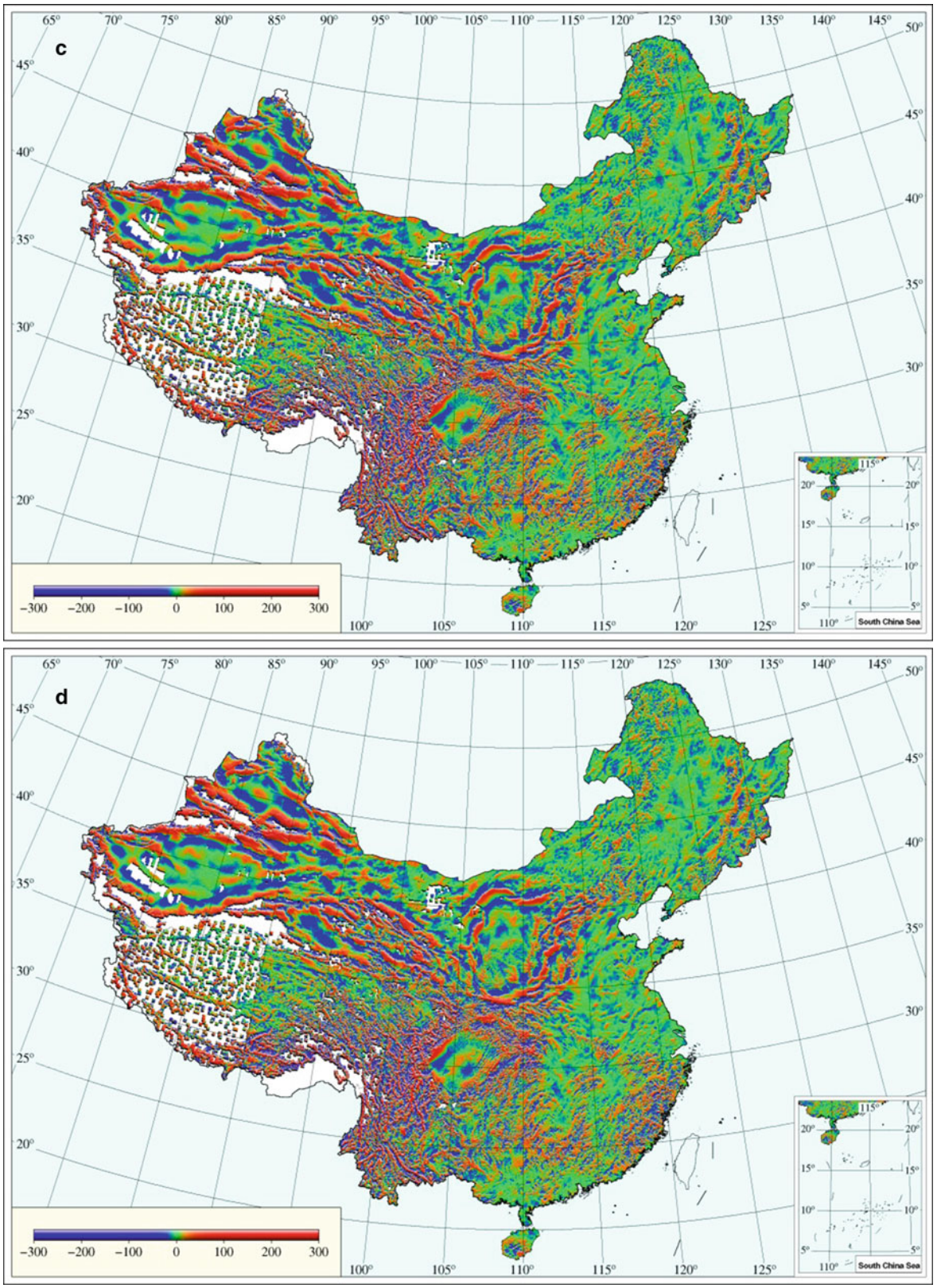

Fig. 3 (continued) The differences between the observed gridded mean free-air gravity anomalies and the corresponding model values computed by the (**a**) EIGEN-6C, (**b**) EGM08, (**c**) GO_TIM_R3, and (**d**) GOCO03S (unit: mGal)

Acknowledgements This study is funded by Natural Science Foundation China (grant No. 41210006), the National 973 Program China (grant No. 2013CB733301), and the Funds for Creative Research Groups of NSFC (grant No. 41021061).

References

ESA (2011) ESA's gravity mission. GOCE Newsletter, Issue 3, December 2011

FörsteC, Bruinsma S, Shako R, Marty J, Flechtner F et al (2011) EIGEN-6 – a new combined global gravity field model including GOCE data from the collaboration of GFZ-Potsdam and GRGS-Toulouse. Geophysical Research Abstracts, Vol. 13, EGU2011-3242-2, EGU General Assembly

HashemiFarahani H, Ditmar P, Klees R, Liu XL, Zhao QL, Guo J (2013) The static gravity field model DGM-1S from GRACE and GOCE data: computation, validation and an analysis of GOCE mission's added value. J Geod 87(9):843–867

Li JC (2012) The recent Chinese terrestrial digital height datum model: gravimetric quasi-geoid CNGG2011. Acta Geodaetica et Cartographica Sinica 41(5):651–660, in Chinese

Li JC, Ning JSH, Chao DB, Jiang WP (2009) Evaluation of the Earth Gravitational Model 2008 using GPS-leveling and gravity data in China. Newton's Bull 4:252–275

Mayer-Gürr T, Kurtenbach E, Eicker A (2010) ITG-Grace2010 gravity field model. www.igg.uni-bonn.de/apmg/index.php.

Mayer-Gürr T, Rieser D, Hoeck E, Brockmann JM, Schuh WD et al (2012) The new combined satellite only model GOCO03S. Presentation at GGHS 2012, Venice, October 2012

Pail R, Bruinsma S, Migliaccio F, Foerste C, Goiginger H, Schuh WD et al (2011) First GOCE gravity field models derived by three different approaches. J Geod 85(11):819–843

Pavlis NK, Holmes SA, Kenyon SC, Factor JK (2012) The development and evaluation of the Earth Gravitational Model 2008 (EGM2008). J Geophys Res 117, B04406. doi:10.1029/2011JB008916

Evaluation of GOCE/GRACE Derived Global Geopotential Models over Argentina with Collocated GPS/Levelling Observations

C. Tocho, G.S. Vergos, and M.C. Pacino

Abstract

This paper presents the results of the evaluation of recent GOCE/GRACE Global Geopotential Models (GGMs) over Argentina. Since the Gravity and steady state Ocean Circulation Explorer (GOCE) dedicated satellite gravity field mission was launched in March 2009, several global geopotential models have been computed and released. GOCE's mission was designed to provide models of the Earth's gravity field on a global scale with high-accuracy in the medium wavelength spectral band (maximum degree/order 200–250). Comparisons of geoid heights derived from different GGMs with GPS/Levelling derived geoid heights over Argentina have been carried out in both absolute and relative sense, to assess and validate the accuracy of GGM models over the entire country. The analysis has been carried out with actual GOCE-only, GOCE/GRACE and combined global gravity field models. In all cases, EGM2008 has been used as the baseline model, since it provides the overall best results. From the results, it was concluded that the latest Release 3 GOCE-only, TIM and SPW, GGMs provide improved accuracies by 1–4 cm compared to the Release 1 models. As far as the combined GOCE/GRACE models, GOCO and DIR, are concerned, the overall best results come from the Release 1 of the DIR model, probably due to the a-priori information from EIGEN5C used in its development. The Release 3 version of the GOCO GGMs improves the Release 1 model by 4 cm, while the same level of improvement is found between the Release 3 and Release 2 of the DIR GGMs.

Keywords

GOCE/GRACE GGMs • GPS/Levelling data • Absolute and relative differences • Argentina

1 Introduction

The main focus of this paper is the evaluation of the GOCE-only and GRACE-GOCE combined satellite-only models against GPS/Levelling observations in Argentina. GPS/Levelling-derived geoid heights are used as independent (external) control for the assessment of the GGM geoid heights on a network of 542 GPS/Levelling benchmarks (BMs) over Argentina.

The dedicated gravity field satellite missions CHAMP, GRACE, and GOCE have contributed significantly to improve the representation of the Earth's gravity field and its

C. Tocho (✉)
Facultad de Ciencias Astronómicas y Geofísicas, Universidad Nacional de La Plata, La Plata, Argentina
e-mail: ctocho@fcaglp.unlp.edu.ar

G.S. Vergos
Department of Geodesy and Surveying, School of Rural and Surveying Engineering, Aristotle University of Thessaloniki, Thessaloniki, Greece
e-mail: vergos@topo.auth.gr

M.C. Pacino
Facultad de Ciencias Exactas, Ingeniería y Agrimensura, Universidad Nacional de Rosario, Rosario, Argentina

U. Marti (ed.), *Gravity, Geoid and Height Systems*, International Association of Geodesy Symposia 141,
DOI 10.1007/978-3-319-10837-7_10,

temporal variations. The European Space Agency launched the GOCE (Gravity-field and steady-state Ocean Circulation Explorer) mission in March 17, 2009. The objective of the mission is to map gravity field features with ±1–2 cm accuracy for geoid undulations and ±1 mGal for gravity at spatial scales down to 120–140 km (degree/order 250). The measurement principle of the GOCE satellite is based on a combination of satellite gravity gradiometry (SGG) and Satellite-to-Satellite Tracking in high-low mode (SST-hl) (Drinkwater et al. 2007).

2 Methodology for Validation

2.1 Evaluation of Global Geopotential Models

The evaluation of GGMs can be performed by an external comparison to geoid heights calculated from GPS and spirit levelling over collocated BMs. Hereafter, we call these geoid heights as the geometric geoid heights for brevity keeping in mind that it is not a strict term. GPS-derived ellipsoidal heights and orthometric heights referenced to a local datum constitute an important type of dataset in order to determine discrete precise geoid undulations by the geometrical approach. Geometric geoid undulation on land can be determined both in an absolute and relative sense (height differences between two benchmarks points i and j) according to the following equations:

$$N^{GPS/Levelling} = h_i - H_i \tag{1}$$

$$\begin{aligned} N_j^{GPS/Levelling} - N_i^{GPS/Levelling} &= \Delta N_{ij}^{GPS/Levelling} \\ &= \Delta h_{ij} - \Delta H_{ij} \end{aligned} \tag{2}$$

where h is the ellipsoidal height from GPS and H is the orthometric height. However, the use of Eq. (1) has some limitations due to systematic and random errors in the derived heights h and H. There are systematic and gross errors in levelling, especially at higher altitudes. Levelling points are often difficult to access and they are sometimes covered by vegetation or destroyed. Other limitations include the assumptions and theoretical approximations made in the normal/orthometric correction; the effect of not taking into account the differences between the ellipsoidal normal and the plumb line (deflection of the vertical), which can cause an error in the geometric geoid determination. The latter is of the order of 0.08–0.1 mm for the GPS/Leveling BMs over the Andes, where the deflection of the vertical takes values greater than 29 arcsec and the BMs ellipsoidal heights are of the order of 3,500–4,000 m. Therefore, it should be kept in mind that even for the BMs at high altitudes, this error is insignificant, while on the other hand, since actual measurements of the deflection of the vertical and the GPS/Leveling BMs are not available, a rigorous error propagation cannot be carried out. The geometric geoid heights cannot be derived at sea, given that the Mean Dynamic Ocean Topography (MDOT) should be known, so interpolation is difficult near the coast. The main errors in ellipsoidal height determination come from satellite or orbits, signal propagation and receiver errors; spirit leveling height determination is mainly affected, especially with today's digital levels, by the length of the leveling baselines, total height difference to be determined, collimation and rod errors, atmospheric refraction and Earth's curvature (Tocho 2006). Despite systematic errors, geometric geoid heights can be derived with a high relative and absolute accuracy over reasonable distances. GPS/Levelling data have a poor spatial distribution.

The computation of GGM geoid undulations (N^{GGM}) has been carried out as (Heiskanen and Moritz 1967, Eqs. 8.100–8.102):

$$N^{GGM} = \zeta + N_0 + \frac{\Delta g_B}{\overline{\gamma}} H \tag{3}$$

where H is the orthometric height, Δg_B is the Bouguer gravity anomaly and ζ represents the height anomaly. The height anomaly has been computed from spherical harmonic series expansions based on the spherical harmonic coefficients of each model and the Geodetic Reference System 1980 (GRS80) normal gravity field parameters by the following expression:

$$\begin{aligned} \zeta(r,\ \theta,\ \lambda) = \frac{GM}{\gamma r} \sum_{n=2}^{n_{\max}} \left(\frac{a}{r}\right)^n \sum_{m=0}^{n} \Big(\overline{\Delta C}_{nm} \cos m\lambda \\ + \overline{\Delta S}_{nm} \sin m\lambda\Big) \overline{P}_{nm}(\cos\theta) \end{aligned} \tag{4}$$

Degree of the GGM expansion used, $\overline{P}_{nm}$ denotes the fully normalized associated Legendre functions and $\overline{\Delta C}_{nm}$ and $\Delta\overline{S}_{nm}$ are the differences of the fully normalized potential coefficients of the gravitational potential minus the coefficients of the normal gravity potential. The third term in Eq. (3) is to convert the height anomaly to a geoid height. The Bouguer correction is determined within the *harm_synth* software (Pavlis et al. 2012) using the spherical harmonics expansion of the DTM2006 model to represent Earth's topography. N_0 represents the contribution of the zero-degree harmonic to the GGM geoid undulations with respect to a specific reference ellipsoid. It has been computed according to the formula (Heiskanen and Moritz 1967, Eq. 2.182):

$$N_0 = \frac{GM - GM_0}{R\gamma} - \frac{W_0 - U_0}{\gamma} \tag{5}$$

where the parameters GM_o and U_o correspond to the geocentric gravitational constant of the reference ellipsoid and the normal gravity potential, respectively. The numerical values for the defining geocentric gravitational constant and the derived physical constant of the potential at the GRS80 ellipsoid (Moritz 2000) are: $GM_o = 398{,}600.5000 \times 10^9$ m^3 s^{-2} and $U_o = 62{,}636{,}860.850$ m^2 s^{-2}). The Earth's geocentric gravitational constant GM and the gravity potential at the geoid W_o have been set to $GM = 398{,}600.4418 \times 10^9$ m^3 s^{-2} and $W_o = 62{,}636{,}856.00$ m^2 s^{-2}, as given by the IERS Conventions (2010). Mean Earth's radius R has been taken equal to 6,371,008.7714 m and the normal gravity γ at the surface of the ellipsoid has been computed by the closed formula of Somigliana (Heiskanen and Moritz 1967). The mean value of N_0 in the area under study is −0.437 m.

All computations of the zero-degree term N_0 used in this study have been performed in the Tide Free (TF) system, so when a given GGM refers to the Zero Tide (ZT) system, the $\overline{C}_{20}$ coefficient is converted to TF using the following formula (Rapp et al. 1991):

$$C_{2,0}^{Tide-free} = C_{2,0}^{Zero-free} + 3.1108 \times 10^{-8} \frac{0.3}{\sqrt{5}} \tag{6}$$

2.2 Validation by Using GPS/Levelling-Derived Geoid Undulations in Absolute and Relative Sense

Geoid undulation (N^{GGM}) can be computed from a set of normalized coefficients in spherical harmonic approximation using Eq. (3). The quality of the GGM can then be evaluated by comparing these geoid undulations with those from GPS/Levelling ($N^{GPS/Levelling}$). Theoretically,

$$N^{GGM} - N^{GPS/Levelling} = 0 \tag{7}$$

but in practice, there are lots of factors that affect Eq. (7). These factors are described by Kotsakis and Sideris (1999), Tocho (2006) and Tziavos et al. (2012). Datum inconsistencies and systematic effects are the most important ones that cause discrepancies in Eq. (7).

Most of the geoid studies that use GPS/Levelling-derived geoid as an external evaluation are based one the following deterministic model to model their deviations:

$$l_i = h_i - H_i - N_i^{GGM} = a_i^T x + v_i \tag{8}$$

where x is a vector of unknown parameters, a_i is the design matrix of known coefficients, and v_i is the residual random noise term (Tziavos et al. 2012). The model of Eq. (8) is applied to all reliable GPS network points and the least squares adjusted values for the residuals give a realistic picture of the absolute level difference between the GGM geoid and the GPS/Levelling data, so that they are taken as the final external indication of the geoid accuracy (Tocho 2006; Vergos and Sideris 2002).

The most common parametric models used are the simplified four-parameter and five-parameter similarity transformation models (MODEL A and MODEL B, respectively) given by Heiskanen and Moritz (1967, see the discussion in Sect. 5.9 and Eq. 5.55):

$$a_i^T x = x_0 + x_1 \cos\varphi_i \cos\lambda_i + x_2 \cos\varphi_i \sin\lambda_i + x_3 \sin\varphi_i \tag{9}$$

$$a_i^T x = x_0 + x_1 \cos\varphi_i \cos\lambda_i + x_2 \cos\varphi_i \sin\lambda_i + x_3 \sin\varphi_i + x_4 \sin^2\varphi_i \tag{10}$$

where φ_i and λ_i are the latitude and longitude of the GPS/Levelling points, x_0 is the bias between the vertical datum implied by the GPS/Levelling data and the datum of the GGM, x_1, x_2, and x_3 are the translation parameters implied by the GPS/Levelling data and the geopotential model.

Some other, possible choices for the height combination problem, are to model the differences with a simple bias (μ) and two scale (δs_H and δs_N) factors. These models correspond to a height-dependent corrector surface in terms of the generalized equation (Kotsakis and Katsambalos 2010):

$$h_i - (1 + \delta s_H) H_i - (1 + \delta s_N) N_i = \mu + v_i \tag{11}$$

that can be further discomposed in the following parametric models (MODELS C, D and E, respectively):

$$a_i^T x = \mu + \delta s_H H_i + \delta s_N N_i \tag{12}$$

$$a_i^T x = \mu + \delta s_H H_i \tag{13}$$

$$a_i^T x = \mu + \delta s_N N_i \tag{14}$$

To evaluate the relative accuracy of the GGM geoid models against the GPS/Levelling-derived geoid heights, relative geoid heights differences have been formed for all the baselines and plotted as a function of the baseline length in parts per million (ppm). The relative differences in ppm were formed after all outliers have been removed.

$$\Delta N_{ij} = \left(N_j^{GGM} - N_i^{GGM}\right) - \left(N_j^{GPS/Levelling} - N_i^{GPS/Levelling}\right) \tag{15}$$

$$\Delta N_{ij}\,[\text{ppm}] = \frac{\Delta N_{ij}\,[\text{mm}]}{S_{ij}\,[\text{km}]} \tag{16}$$

where the spherical distance in degrees is evaluated, and then converted to km by assuming that 1° is ∼110 km, as:

$$S_{ij} = a\cos\left(\sin\varphi_i \sin\varphi_j + \cos\varphi_i \cos\varphi_j \cos\left(\lambda_i - \lambda_j\right)\right) \tag{17}$$

3 Data Used for GGM Validation

3.1 GPS/Levelling Data

GPS/Levelling height information on 567 points across Argentina has been collected through the National Geographic Institute of Argentina (IGN). From this database, we selected all GNSS stations on benchmarks. The geodetic coordinates (ϕ, λ, h) are referred to the POSgAR 07 (POSiciones Geodesicas ARgentinas) datum. POSgAR 07 is Argentina's official geodetic system and it was established through GPS measurements to realize the WGS84 (G1150) reference system in the country. The geocentric Cartesian coordinates of all stations were determined in ITRF2005 (epoch: 2006.632) and the ellipsoidal heights are given in the Tide Free system. GPS/Levelling networks like the POSgAR07 and some province geodetic networks have been used for the external evaluation of the GGMs geoid accuracy.

The levelling heights H correspond to the National Altimetric Network, which was measured by the Military Geographic Instituto (IGM), today National Geographic Institute (IGN), using spirit and/or trigonometric levelling techniques. Their values refer to the equipotential surface of Earth's gravity field that coincides with mean sea level at the Vertical Datum fundamental tide-gauge reference station located in the city of Mar del Plata, with unknown W_o value. Most countries do not make any luni-solar correction for precise levelling, so that their orthometric heights refer to the Mean Tide system (MT). Therefore, orthometric heights needed to be converted from the MT to the TF with the expression (Ekman 1989):

$$H^{TF} = H^{MT} - 0.68\left(0.099 - 0.296\sin^2\varphi\right) \tag{18}$$

It is not possible to define the orthometric height accuracy, since the network was not uniformly adjusted and no gravity corrections have been applied. Therefore its formal accuracy is largely unknown, even though we can assume that lowland stations have been determined with higher accuracy compared to stations at higher elevations. As far as the geodetic coordinates are concerned, their mean errors are at $\sigma_x = \pm 0.005$ m, $\sigma_y = \pm 0.005$ m and $\sigma z = \pm 0.005$ m. These GPS/Levelling points are located in area with varying topography, and their distribution is shown in Fig. 1.

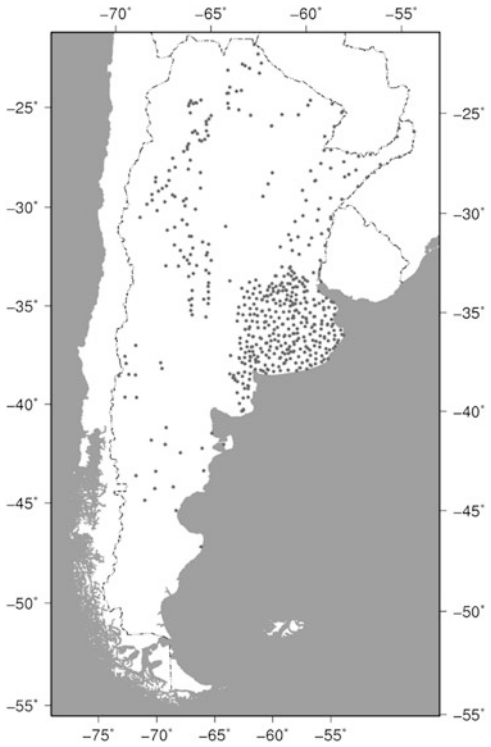

Fig. 1 Geographical distribution of the GPS/Levelling benchmarks in Argentina

3.2 Global Geopotential Models

Since 2010, ESA and the GOCE-related research teams have released three generations of GOCE GGMs. Models from the first, second and third release (R1, R2 and R3) are based on 2, 8, and 12 months of data, respectively. Each generation includes three solutions using different approaches for gravity field recovery, the direct approach (DIR, the time-wise approach (TIM) and the space-wise approach (SPW).

Geoid undulations have been computed at the 542 GPS/Levelling benchmarks using the 15 GGMs shown in Table 1.

Table 1 gives an overview of their resolution, which depends on the maximum spherical harmonic degree, and the data used to derive them. The models used are the new combined global gravity field model including GOCE data from the collaboration of GFZ-Potsdam and GRGS-Toulouse EIGEN-6C, the GRACE only derived model ITG-GRACE2010S the Gravity Observation Combination (GOCO) GGMs GOCO01S, GOCO02S and GOCO03S, the pre-GOCE models EIGEN-51C and EGM2008 both of them combined ones using satellite, gravity and altimetry data.

DIR-R1, DIR-R2 and DIR-R3 are the three different releases of the direct approach GOCE GGMs. The three of

Table 1 GGMs used for evaluation

Models	n_{max}	Data	References
EGM2008	2, 190	S(GRACE), G, A	Pavlis et al. (2012)
EIGEN-51C	359	S(GRACE, CHAMP), G, A	Bruinsma et al. (2010)
EIGEN-6C	1, 420	S(GOCE, GRACE, LAGEOS), G, A	Förste et al. (2011)
GOCO01S	224	S(GOCE, GRACE)	Pail et al. (2010)
GOCO02S	250	S(GOCE, GRACE, CHAMP, SLR)	Goiginger et al. (2011)
GOCO03S	250	S(GOCE, GRACE, CHAMP, SLR)	Mayer-Gürr et al. (2012)
ITG-GRACE2010S	180	S(GRACE)	Mayer-Gürr et al. (2010)
DIR-R1	240	S(GOCE + background model EIGEN-51C)	Bruinsma et al. (2010)
DIR-R2	240	S(GOCE + background model ITG-GRACE2010S)	Bruinsma et al. (2010)
DIR-R3	240	S(GOCE, GRACE, LAGEOS)	Bruinsma et al. (2010)
TIM-R1	224	S(GOCE)	Pail et al. (2011)
TIM-R2	250	S(GOCE)	Pail et al. (2011)
TIM-R3	250	S(GOCE)	Pail et al. (2010)
SPW-R1	210	S(GOCE)	Migliaccio et al. (2010)
SPW-R2	240	S(GOCE)	Migliaccio et al. (2011)

Data: *S* satellite tracking data, *G* gravity data, *A* altimetry data, *GRACE* Gravity Recovery And Climate Experiment, *CHAMP* CHAllenging Minisatellite Payload, *GOCE* Gravity field and steady state Ocean Circulation Explorer, *LAGEOS* LAser GEOdynamics Satellite, *SLR* Satellite Laser Ranking

them are based on 2, 8, and 12 months of GOCE gravity gradients, attitude information, and gradiometer observations, respectively. They differ in the a-priori information used. DIR-R1 used EIGEN-5C (Förste et al. 2008) as a-priori gravity field information model up to degree/order 360 and also used reduced dynamic orbits. DIR-R2 used ITG-GRACE2010S up to degree/order 150 as a-priori information and kinematics orbits. DIR-R3 used the DIR-R2 up to degree/order 240 and kinematics orbits.

TIM-R1, TIM-R2 and TIM-R3 are the three different releases of the time-wise approach. No a-priori gravity field information has been applied. They differ in the number of months of GOCE data used which includes: gravity gradients, kinematics orbits, and attitude and gradiometer observations. SPW-R1 is the first release of the space-wise model. The first GOCE quick-look model and EGM2008 model are incorporated as a-priori models. The input data in this model includes: satellite tracking data derived from the on-board GPS, gravity gradients observed by the on-board electrostatic gradiometer, kinematics orbits with their error estimates are used for SST gravity field recovery while reduced dynamic orbits are used for geo-locating gravity gradients and attitude. The SPW_R2 was also investigated. GOCO (Combination of GOCE data with complementary gravity field information) is a project initiative with the objective to compute high-accuracy and high-resolution static global gravity field models based on data of the satellite gravity missions CHAMP, GRACE, and GOCE, satellite altimetry, and SLR data. The satellite-only model GOCO01S based on GOCE and GRACE was the first computed. The second solution, GOCO02S, was computed with 8 months of GOCE, 7 years of GRACE, 8 years of CHAMP and 5 years of five SLR satellites. The latest release is the GOCO03S was also used for comparison. ITG-GRACE2010S is an unconstrained static field from of GRACE data only. ITG-GRACE2010S is a mean field of the entire Earth including atmosphere and ocean masses. EIGEN-51C is a combined global gravity field model to degree/order 359. It consists of 6 years of CHAMP and GRACE data and the DNSC08 global gravity anomaly data set. Finally, EGM2008 is a spherical harmonic model of the Earth's gravitational potential complete to degree/order 2159 with some additional coefficients up to degree 2190 and order 2159. EGM2008 is a model that combines the ITG-GRACE03S gravitational model with free-air gravity anomalies defined on a 5 arc-minute equiangular grid. This grid was formed by merging terrestrial, altimetry-derived, and airborne gravity data.

4 GGM Validation on Collocated GPS/Leveling BMs

4.1 Absolute Differences Between GGMs and GPS/Levelling Data

Software *harmonic_synth_v02*, provided by the National Geospatial-Intelligence Agency (NGA), is used to compute the geoid values from the 15 GGMs. Table 2 shows the results in terms of mean value and standard deviation (std) of the absolute differences between GPS/Levelling geoidal heights and geoid heights of several GGMs evaluated in this paper for different degree and order of expansion (60, 80,

Table 2 Mean and standard deviation of the GPS/Levelling derived geoid minus geoid heights computed with GGMs up to various truncation degrees for whole Argentina (before any fit to the residuals). Unit: [m]

n_{max}	60	80	140	160	180	210	220	224	240	250	360	1,420	2,160	2,190
	Mean	Mean	Mean	Mean	Mean	Mean	Mean	Mean	Mean	Mean	Mean	Mean	Mean	Mean
# points:542	Std	Std	Std	Std	Std	Std	Std	Std	Std	Std	Std	Std	Std	Std
$N^{GPS} - N^{EGM2008}$	0.120	0.357	0.303	0.305	0.281	0.274	0.271	0.269	0.265	0.264	0.270	0.309	0.310	0.310
	±1.261	±0.981	±0.617	±0.574	±0.522	±0.451	±0.439	±0.439	±0.424	±0.409	±0.334	±0.245	±0.244	±0.244
$N^{GPS} - N^{EIGEN-51C}$	0.119	0.356	0.298	0.3	0.276		0.266				0.272			
	±1.261	±0.981	±0.616	±0.582	±0.528		±0.443				±0.394			
$N^{GPS} - N^{EIGEN-6C}$	0.117	0.354	0.299	0.302	0.280		0.267				0.269	0.306		
	±1.261	±0.980	±0.621	±0.575	±0.519		±0.439				±0.347	±0.252		
$N^{GPS} - N^{GOCO01S}$	0.117	0.354	0.300	0.305	0.293			0.283						
	±1.261	±0.980	±0.624	±0.580	±0.536			±0.486						
$N^{GPS} - N^{GOCO02S}$	0.117	0.354	0.300	0.302	0.282			0.265		0.261				
	±1.261	±0.980	±0.623	±0.575	±0.524			±0.453		±0.448				
$N^{GPS} - N^{GOCO03S}$	0.117	0.354	0.301	0.303	0.285			0.273		0.269				
	±1.261	±0.980	±0.623	±0.573	±0.523			±0.444		±0.440				
$N^{GPS} - N^{ITG-GRACE2010S}$	0.117	0.354	0.302	0.295	0.307									
	±1.261	±0.980	±0.626	±0.583	±0.577									
$N^{GPS} - N^{DIR-R1}$	0.127	0.364	0.307	0.310	0.289		0.278		0.273					
	±1.260	±0.981	±0.623	±0.579	±0.526		±0.439		±0.427					
$N^{GPS} - N^{DIR-R2}$	0.120	0.356	0.303	0.304	0.287		0.276		0.274					
	±1.261	±0.980	±0.623	±0.577	±0.527		±0.459		±0.489					
$N^{GPS} - N^{DIR-R3}$	0.119	0.355	0.301	0.299	0.281		0.271		0.268					
	±1.261	±0.980	±0.623	±0.569	±0.525		±0.441		±0.444					
$N^{GPS} - N^{TIM-R1}$	0.120	0.357	0.303	0.307	0.294			0.284						
	±1.263	±0.981	±0.622	±0.580	±0.537			±0.486						
$N^{GPS} - N^{TIM-R2}$	0.107	0.344	0.292	0.293	0.272		0.254			0.251				
	±1.263	±0.980	±0.624	±0.576	±0.524		±0.450			±0.449				
$N^{GPS} - N^{TIM-R3}$	0.114	0.350	0.297	0.299	0.279		0.267			0.263				
	±1.262	±0.981	±0.623	±0.573	±0.524		±0.443			±0.443				
$N^{GPS} - N^{SPW-R1}$	0.125	0.359	0.306	0.308	0.287	0.273								
	±1.259	±0.977	±0.622	±0.579	±0.540	±0.487								
$N^{GPS} - N^{SPW-R2}$	0.120	0.356	0.303	0.304	0.287	0.267			0.265					
	±1.261	±0.981	±0.624	±0.577	±0.529	±0.477			±0.474					

140, 180, 210, 220, 224, 240, 250, 360, 1420, 2160 and 2190). The statistics in Table 2 are before the fit of any parametric model mentioned in Sect. 2.2. Before applying such models, the GPS/Levelling points having large gross error in either the GPS or the levelling data were removed. The statistics shown in Table 2 have been computed after the removal of points with gross errors, applying a 3 std test using EGM2008 to degree/order 2160. The final GPS/Levelling dataset in Argentina, after removing 25 suspicious stations, consists of 542 stations.

From Table 2, EGM2008 with n_{max} 2,160 shows the overall best agreement with the GPS/Levelling-derived geoid for Argentina with a standard deviation of ±24 cm and a mean value of 31 cm. Considering the standard deviation as the main indicator of the agreement; EGM2008 is the best global geopotential model that represents the long wavelength gravity field in Argentina.

We can also observe that except for DIR-R2, DIR-R3 models the best standard deviation has been obtained with the highest maximum spherical harmonic degrees of the model expansion. The best GRACE/GOCE model is DIR-R1 which gives a standard deviation of ±42.7 cm to its maximum cut-off degree of n = 240. The latter is 15 cm better than the GRACE-only model GRACE2010S (to degree and order 180). This is due to the contribution of GOCE and LAGEOS data to DIR-R1, its higher degree of expansion and the a-priori information from EIGEN-5C used in its development. When compared for the same spectral band (degree and order 180) DIR-R1 is 5 cm better than GRACE2010S. It is interesting to notice that DIR-R1 provides the overall best results in Argentina, even compared to the Release 2 and Release 3 models which contain more GOCE observations. GPS/Levelling comparisons suggest a geoid agreement of 42–49 cm for the full GOCE-only model expansions (degree and order 240–250) and biases of about 30 cm. Among the GOCE-only models, the TIM-R3 GGM provides the best results with a std at the ±44.3 cm being 2 cm better than SPW-R2, even for lower spectral bands. The combined GOCE/GRACE models GOCO show an increasing improvement towards Release 3, which is better by 4 cm compared to Release 1. We can also see that for the same spectral bands, the GOCE/GRACE models perform equally well with EGM2008. So for the band between 160 and 250 the standard deviations of the differences for the R3 models is the same, within a couple mm, as that of EGM2008. It should be kept in mind that GOCE models were not expected to perform better than EGM2008, since extensive local gravity data over Argentina have been used in its development.

The available corrector surfaces have been first tested for the differences between GPS/Levelling geoid heights and the EGM2008 geoid model, so the one that performs the best, will be used to compute adjusted residuals with respect to the other GGMs geoidal undulations (see Table 3). From this evaluation, it was concluded that MODEL B, provides the best residuals after the fit, even though its performance is marginally better than that of MODEL A (1 cm in terms of the range).

Table 3 Statistics of the differences between GPS/Levelling and geoid heights from EGM2008 before and after fit of the residuals. Unit: [m]

n = 2,190	Max	Min	Mean	Std
Before fit	1.143	−0.820	0.310	±0.244
MODEL A	0.656	−1.026	0.000	±0.164
MODEL B	0.653	−1.022	0.000	±0.164
MODEL C	0.728	−1.133	0.000	±0.189
MODEL D	0.853	−1.142	0.000	±0.217
MODEL E	0.694	−1.136	0.000	±0.191

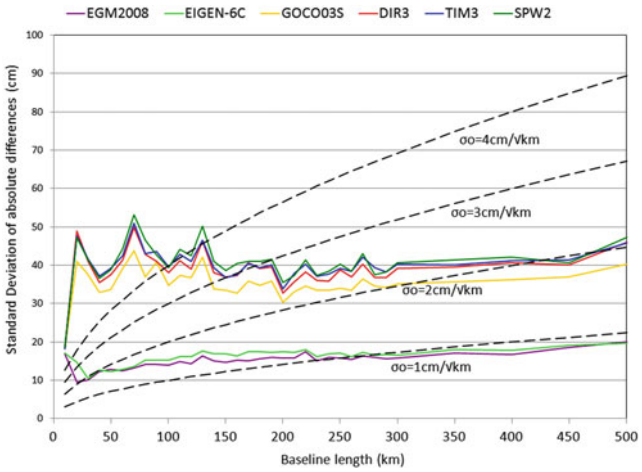

Fig. 2 Standard deviation of the absolute differences in the test network $\Delta N_{ij}^{GPS/Levelling} - \Delta N_{ij}^{GGM}$ of 542 GPS/Levelling benchmarks, as a function of the baseline length up to 500 km

4.2 Relative and Absolute Baselines Analysis

Figure 2 shows the standard deviation of the absolute geoid differences in the test network ($\Delta N_{ij}^{GPS/Levelling} - \Delta N_{ij}^{GGM}$) of 542 GPS/Levelling benchmarks, as a function of the baseline length (up to 500 km). For the evaluation of the relative accuracy of the GGMs with respect to the GPS/Levelling data, relative geoid differences have been formed for all the baselines and plotted as a function of the baseline length in ppm. The maximum spherical harmonic expansions of the GOCE-only models DIR-R3, TIM-R3, SPW-R2; the GRACE-GOCE combined satellite-only model GOCO03S, EIGEN-6C and EGM2008 have been used. The relative accuracy value at a certain distance is the average value of

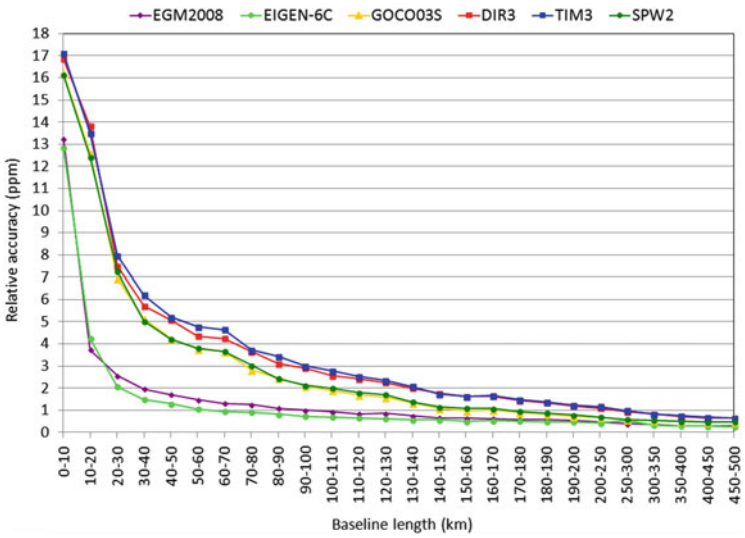

Fig. 3 Relative accuracy between GGMs models and GPS/Levelling derived geoid across Argentina (after a five-order similarity transformation model fit)

all the baselines distances, which have been computed with an increment of 10 km among all GPS/Levelling stations. Figure 3 shows the comparisons of the relative geoid undulation accuracy for the different GGMs after a five-order similarity transformation model was applied.

The results show that the GOCE models have a similar behavior to each other. EGM2008 and EIGEN-6C's relative accuracy is considerably better than the satellite-only models due to the contribution of the surface gravity data. The resolution of EIGEN-6C is about half of that of EGM2008. We can also see that the combined model EIGEN-6C outperforms EGM2008 for baselines of 20–170 km.

In Argentina, the statistics are computed using all 542 benchmarks. As seen in Fig. 3 for EGM2008 the relative geoid agreement is, 13–4 ppm for short baselines up to 20 km, 1–0.3 ppm over baselines of 100–500 km, meanwhile the GOCE-only models show a relative agreement of 8–16 ppm for short baselines of 20 km and 6–0.6 ppm over baselines of 100–500 km. The relative errors of the GOCE models show a slowly increasing trend with decreasing baseline until 40 km where a very sharp increase starts. On the contrary, the combined models show a slower deterioration of their relative accuracy for baselines smaller than 40 km. This disproportional increase indicates the fast deterioration of the GOCE models for baselines shorter than 40 km due to the limited satellite resolution. EIGEN-6C model outperforms EGM2008 and the SPW2 and GOCO03S models are better than the latest version of the DIR and TIM models. The average relative accuracies is achieved for baselines up to 80 km.

Conclusions

From the evaluation of the differences between GPS/Lev and GGM geoid heights, on a network of 542 stations over Argentina, it can be concluded that the GOCE/GRACE GGMs provide comparable, to EGM2008, agreement within the satellite spectral band (80–250). The latter is of course superior overall due its high maximum degree and order of expansion and the inclusion of local gravity data. In terms of the relative accuracies achieved, EIGEN-6C outperforms EGM2008, which can be due to the contribution of GOCE data used in its development. DIR-R1 provides the overall best results among the GOCE/GRACE GGMs, in terms of the absolute accuracy, due to the a-priori information from EIGEN-5C used in its development. In the relative case, GOCO03S and SPW-R2 outperform by 0.5–1 ppm TIM-R3 and DIR-R3 for baselines between 20 and 160 km.

Acknowledgements Claudia Tocho received financial support from the University of La Plata and gratefully acknowledges the generous hospitality of Dr. George S. Vergos at the Department of Geodesy and Surveying, Aristotle University of Thessaloniki, Thessaloniki, Greece. The authors are very grateful to the editors and reviewers for their comments and suggestions that improved the final manuscript.

References

Bruinsma SL, Marty JC, Balmino G, Biancale R, Förste C, Abrikosov O, Neumayer H (2010) GOCE gravity field recovery by means of the direct numerical method. In: Lacoste-Francis H (ed) Proceedings of the ESA living planet symposium, ESA Publication SP-686. ESA/ESTEC. ISBN 978-92-9221-250-6, ISSN 1609-042X

Drinkwater MR, Haagmans R, Muzi D, Popescu A, Floberghagen R, Kern M, Fehringer M (2007) The GOCE gravity mission: ESA's first core earth explorer. In: Proceedings of 3rd international GOCE user workshop, Frascati, Italy, 6–8 November 2006. ESA SP-627. ISBN 92-9092-938-3, pp 1–8

Ekman M (1989) Impacts of geodynamic phenomena on systems for height and gravity. Bull Géodésique 63(3):281–296

Förste C, Flechtner F, Schmidt R, Stubenvoll R, Rothacher M, Kusche J, Neumayer KH, Biancale R, Lemoine JM, Barthelmes F, Bruinsma S, König R, Meyer U (2008) EIGEN-GL05C—a new global combined high-resolution GRACE-based gravity field model

of the GFZ-GRGS cooperation. Geophysical Research Abstracts, vol 10, EGU2008-A-03426, SRef-ID: 16077962/gra/EGU2008-A-03426

Förste C, Bruinsma S, Shako R, Marty JC, Flechtner F, Abrikosov O, Dahle C, Lemoine JM, Neumayer KH, Biancale R, Barthelmes F, König R, Balmino G (2011) EIGEN-6—a new combined global gravity field model including GOCE data from the collaboration of GFZ-Potsdam and GRGS-Toulouse. Geophysical Research Abstracts, vol 13, EGU2011-3242-2, EGU General Assembly

Goiginger H, Höck E, Rieser D, Mayer-Gürr T, Maier A, Krauss S, Pail R, Fecher T, Gruber T, Brockmann JM, Krasbutter I, Schuh WD, Jäggi A, Prange L, Hausleitner W, Baur O, Kusche J (2011) The combined satellite-only global gravity field model GOCO02S. In: Presented at the 2011 General Assembly of the European Geosciences Union, Vienna, Austria, 4–8 April

Heiskanen WA, Moritz H (1967) Physical geodesy. W. H. Freeman, San Francisco, CA

IERS Conventions (2010) In: Petit G, Luzum B (eds) IERS Technical Note; 36. Frankfurt am Main: Verlag des Bundesamts für Kartographie und Geodäsie, 179 pp. ISBN 3-89888-989-6

Kotsakis C, Katsambalos K (2010) Quality analysis of global geopotential models at 1542 GPS/levelling benchmarks over the Hellenic mainland. Surv Rev 42(318):327–344

Kotsakis C, Sideris MG (1999) On the adjustment of combined GPS/levelling/geoid networks. J Geod 73(8):412–421

Mayer-Gürr T, Kurtenbach E, Eicker A (2010) GRACE-only gravity field model ITG-Grace2010s. http://www.igg.uni-bonn.de/apmg/index.php?id=itg-grace2010

Mayer-Gürr T, Rieser D, Höck E, Brockmann JM, Schuh W-D, Krasbutter I, Kusche J, Maier A, Krauss S, Hausleitner W, Baur O, Jäggi A, Meyer U, Prange L, Pail R, Fecher T, Gruber T (2012) The new combined satellite only model GOCO03S. Abstract submitted to GGHS2012, Venice

Migliaccio F, Reguzzoni M, Sansò F, Tscherning CC, Veicherts M (2010) GOCE data analysis: the space-wise approach and the first space-wise gravity field model. In: Lacoste-Francis H (ed) Proceedings of the ESA living planet symposium. ESA Publication SP-686, ESA/ESTEC. ISBN 978-92-9221-250-6

Migliaccio G, Reguzzoni M, Gatti A, Sanso F, Herceg M (2011) A GOCE-only global gravity field model by the space-wise approach. In: Ouwehand (Ed.) Proceedings of the 4th International GOCE User Workshop, ESA Publication 696, ESA/ESTEC. ISBN 978-92-9092-260-5.

Moritz H (2000) Geodetic reference system 1980. J Geod 4(1):128–162

Pail R, Goiginger H, Schuh WD, Hock E, Brockmann M, Fecher T, Gruber T, Mayer-Gurr T, Kusche J, Jaggi A, Rieser D (2010) Combined satellite gravity field model GOCO01S derived from GOCE and GRACE. Geophysical Research Letters, vol 37, EID L20314, American Geophysical Union. ISSN 0094-8276, doi: 10.1029/2010GL044906

Pail R, Bruinsma S, Migliaccio F, Förste C, Goiginger H, Schuh WD, Höck E, Reguzzoni M, Brockmann JM, Abrikosov O, Veicherts M, Fecher T, Mayrhofer R, Krasbutter I, Sansò F, Tscherning CC (2011) First GOCE gravity field models derived by three different approaches. J Geod 85(11):819–843. doi:10.1007/s00190-011-0467-x

Pavlis NK, Holmes SA, Kenyon SC, Factor JK (2012) The development and evaluation of the Earth Gravitational Model 2008 (EGM2008). J Geophys Res 117, B04406. doi:10.1029/2011JB008916

Rapp RH, Nerem RS, Shum CK, Klosko SM, Williamson RG (1991) Consideration of permanent tidal deformation in the orbit determination and data analysis for the Topex/Poseidon mission. NASA TM 100775, Goddard Space Flight Center, Greenbelt, MD

Tocho C (2006) A gravimetric geoid modelling. Tesis Doctoral, Facultad de Ciencias Astronómicas y Geofísicas, Universidad Nacional de La Plata

Tziavos IN, Vergos GS, Grigoriadis VN, Andritsanos VD (2012) Adjustment of collocated GPS, geoid and orthometric height observations in Greece. Geoid or orthometric height improvement? IAG Symp 136: 477–484

Vergos GS, Sideris MG (2002) Evaluation of geoid models and validation of geoid and GPS/leveling undulations in Canada. IGeS Bull 12:3–17

Evaluation of GOCE/GRACE Global Geopotential Models over Greece with Collocated GPS/Levelling Observations and Local Gravity Data

G.S. Vergos, V.N. Grigoriadis, I.N. Tziavos, and C. Kotsakis

Abstract

The advent of the GOCE and GRACE missions during the last decade have brought new insights and promising results both in the static and time-variable representation of the Earth's gravity field. The focus of this work is directed to the evaluation of most available Global Geopotential Models (GGMs) from GOCE and GRACE, both satellite only as well as combined ones. The evaluation is carried out over an extensive network of collocated GPS/Levelling benchmarks (BMs) which covers the entire part of continental Greece and with respect to the reductions the GGMs provide in existing gravity data in order to assess their performance in a scenario that a remove-compute-restore procedure would be followed for geoid determination. From the evaluation with GPS/Levelling BMs, it was concluded that the GOCE/GRACE GGMs provide an absolute accuracy at the 12–15 cm level, up to degree and order (d/o) 250, when considering the geoid omission error. This is comparable and in some cases better than the performance of EGM2008 in Greece. Moreover, the latest (Release 3) versions of the GGMs provide considerably better results compared to the earlier version by 1–5 cm. In terms of relative errors, GOCE/GRACE GGMs reach the 1 cm level for baselines between 50 and 60 km, while for longer ones, 80–90 km, their performance is analogous to the local geoid model and the ultra-high degree combined GGMs. Finally, GOCE/GRACE GGMs manage to provide the same, as EGM2008, level of reduction to the local gravity anomalies, with a std at the 26.7–27.8 mGal level, when evaluated up to d/o 250.

Keywords

Global geopotential models • validation • GOCE • GPS/Levelling BMs • GRACE • Gravity reduction

1 Introduction

The advent of the Gravity field and Ocean Circulation Explorer (GOCE) and Gravity Recovery and Climate Experiment (GRACE) missions during the last decade has brought new insights, promising results and improved accuracies in the representation of the Earth's gravity field within the spectral band up to d/o 160–220 (∼90–130 km) as far as GOCE and GOCE/GRACE models are concerned. Recent results from the evaluation of GOCE/GRACE based GGMs with terrestrial gravity data and deflections of the vertical (Hirt et al. 2011) show that GOCE offers improved results between d/o 160 and 185, since for larger degrees of expansion signal loss is experienced. The same results have been acquired by Šprlák et al. (2012) over Norway, evaluating the GGMs with terrestrial gravity data. The R1 versions of the GGMs have a std up to 4.5 mGal up to d/o 160–170 which increases to 180 for GO-DIR-R1. The R2

G.S. Vergos (✉) • V.N. Grigoriadis • I.N. Tziavos • C. Kotsakis
Department of Geodesy and Surveying, Aristotle University of Thessaloniki, University Box 440, 54124 Thessaloniki, Greece
e-mail: vergos@topo.auth.gr

U. Marti (ed.), *Gravity, Geoid and Height Systems*, International Association of Geodesy Symposia 141,
DOI 10.1007/978-3-319-10837-7_11,

and R3 versions of the GGMs improve this performance, especially up to d/o 180–200 and 225–240 respectively. The only exception is the GO-DIR-R2 model which provides worse results compared to its R1 version. Gruber et al. (2011) evaluated the first release of GOCE/GRACE GGMs and concluded that the spectral band improved by GRACE data is up to d/o 170 (ITG-GRACE2010s model) while GOCE data (GO-TIM mainly) manage to boost this up to d/o 190. The best results in terms of the rms of the differences (mean of all models), after removing the bias, were achieved for the German dataset (3.5 cm), while the ones for Japan and Canada where at ∼10 cm. Likewise, the focus of this work refers to the evaluation over Greece of available GGMs from GOCE, GOCE/GRACE and combined ones, to conclude on the improvements they bring to gravity field and geoid modelling.

2 Validation Methodology, GGMs and Local Data Availability

2.1 Methodology for GGM Validation

For the evaluation of the GOCE/GRACE and combined models, first the GGM spectrum has been validated in terms of the by-degree and cumulative geoid signal and error. This was based on the formal GGM degree and error variances, the former indicating the geoid signal at various degrees and the latter the geoid error.

The second step of the GGM evaluation refers to comparisons with collocated GPS/Levelling BMs, which cover the entire part of continental Greece. In all cases, band-limited versions of EGM2008 (Pavlis et al. 2012) to the GOCE/GRACE GGM d/o of expansion are used for the evaluation, while a local LSC-based gravimetric geoid model (N^{LSC}) is used as ground-truth (Tziavos et al. 2012, 2013), for the ultra-high degree models. Geoid heights were determined in the Tide-Free (TF) system from the various GGMs through their spherical harmonic coefficients (Pavlis et al. 2012), using GRS80 as the normal field (Heiskanen and Moritz 1967). All computations have been harmonized as to the ellipsoid used and the tide system, given that some GGMs were referenced to other ellipsoids and the Zero-Tide (ZT), rather than the TF, system (Ekman 1989). Note that the above approach guarantees the consistency of the compared GGMs, so that biases and/or errors due to differences in the reference ellipsoid, tide conventions and geoid reference are minimized.

When evaluating the absolute differences between collocated GPS, levelling and gravimetric geoid heights it has to be considered that the GPS/Levelling data represent the complete geoid spectrum whereas the GGMs are limited to their maximum degree of expansion and/or truncation. Therefore, the geoid omission error due to the GGMs truncation should be accounted for. Consequently, the geoid omission error was determined using Kaula's power law (Kaula 1966) and the Tscherning and Rapp (1974) degree variance model (see Table 1). Finally, the spectral range of the terrestrial data dictated by the area under study should be considered. The terrestrial data cover the entire part of continental Greece, an area roughly $6° \times 7°$ in latitude and longitude respectively. The spatial extent of the area under study means that both long-wavelength signal and errors in the GGMs up to d/o ∼30–40 (half-wavelength) cannot be accounted for, so that they may appear as biases in the validation. Given that, the GGM evaluation is performed for d/o 60 and above. Moreover, the relative accuracy of the GGM and gravimetric geoid models was evaluated as a function of the baseline length (spherical distance S_{ij} in km). The final part of the GGM validation, refers to their evaluation with respect to the reduction they provide in existing gravity data, simulating a remove-compute-restore procedure for geoid determination (Tziavos et al. 2013).

Table 1 Geoid omission error rms values for various maximum degrees of GGM expansion. Maximum degree in the summation 500,000.Unit: [cm]

	180	210	220	224	240	250	359	1420	1949	2159
Kaula	35.6	30.5	29.1	28.6	26.7	25.6	17.8	4.5	3.3	2.9
Tsch. /Rapp	46.7	38.3	36.0	35.2	32.1	30.3	22.9	6.6	2.8	2.0

2.2 GGM and Terrestrial Data Sets

Within the present work, most available GGMs based on GOCE/GRACE data have been evaluated. Depending on the releases of GOCE gradients various solutions became available, a.k.a. GOCE Release 1, GOCE Release 2 and GOCE Release 3 models based on 2, 6 and 12 months of GOCE observations respectively. These will be denoted as GO-xxx-R1, GO-xxx-R2 and GO-xxx-R3 in the sequel. Depending on the processing strategy four classes of models can be distinguished as (a) the TIM models using the time-wise approach (Pail et al. 2011), (b) the DIR models using the direct approach (Bruinsma et al. 2010), (c) the SPW models using the space-wise approach (Migliaccio et al. 2010) and (d) combined models (GOCO0xx and DGM-1S) where both GOCE, GRACE and other satellite data are used (Goiginger et al. 2011; Hashemi et al. 2013; Mayer-Guerr et al. 2010; Pail et al. 2010). The GO-DIR models are not pure GOCE ones since (a) for the R1 version a-priori information from EIGEN-5c was used, (b) for R2 a-priori information from ITG-GRACE20120S was used, while (c) for R3 a-priori information from the GO-DIR-R2 was used along with SLR

and GRACE data. Apart from the aforementioned GGMs, EGM2008 (Pavlis et al. 2012), EIGEN-51C (Bruinsma et al. 2010), the GRACE only model ITG-GRACE2010S (Mayer-Guerr et al. 2010) and the latest EIGEN-6S, EIGEN-6C (Förste et al. 2011) and EIGEN-6C2 (Förste et al. 2012) have been used as well, with the latest EIGEN combined models including GOCE Release 2 data.

The local data used, refer to GPS/Levelling observations (1,542 BMs) covering the entire part of continental Greece (cf. Kotsakis and Katsambalos 2010). This set of collocated GPS and Levelling data is based on historical orthometric heights from the HMGS (Hellenic Military Geographic Service) measured during the establishment of the Hellenic Vertical Datum (HVD) and ellipsoidal heights collected within the HEPOS (Hellenic Positioning System) project (Gianniou 2008). The HVD in principle models the physical heights as Helmert orthometric heights, while their tie is to the tide-gauge station situated at Piraeus harbor, so that the HVD origin is relative to a MSL determined with measurements for the period 1933–1978. Today, the true accuracy of the HVD is unknown, since (a) it was not uniformly adjusted, (b) it is not maintained by HMGS, and (c) the formal errors provided by HMGS are ambiguous and over optimistic (Kotsakis and Katsambalos 2010; Tziavos et al. 2012). As far as the ellipsoidal heights from the HEPOS project (www.hepos.gr) are concerned, they all refer to BMs belonging to the Hellenic trigonometric network (Gianniou 2008). All data were determined in ITRF00 (epoch t = 2,007.236) with their horizontal and vertical accuracy being estimated from the analysis of the original GPS observations to 1–4 cm (1σ) and 2–5 cm (1σ), respectively (Gianniou 2008; Kotsakis and Katsambalos 2010). It should be noted that the orthometric heights refer to the mean-tide (MT) system, so their conversion to the TF system has been performed according to Ekman (1989). Finally, the GGM evaluation with gravity data is performed using a local gravity database that has been compiled in the frame of the determination of a new Greek geoid model (Tziavos et al. 2012, 2013). This set comprises a number of 294,777 irregular point gravity observations (cf. Tziavos et al. 2010) covering the entire Hellenic territory (islands included) as well as parts of the neighbouring Balkan countries.

Given the availability of the GOCE/GRACE GGMs, first a spectral evaluation in terms of the formal/calibrated degree and error degree variances of their coefficients has been performed. From this evaluation it was concluded that GOCO03s provides the overall best results with smaller errors up to degree n ∼ 175, w.r.t. EGM2008, compared to n ∼ 153 and n ∼ 166 for GOCO01S and GOCO02S, respectively. The GOCE-DIR-R3 model has smaller formal errors compared to its earlier releases (R1 and R2), by 2–3 orders of magnitude and is better than EGM2008 to degree n ∼ 188. A general conclusion is that the R1 and R2 GOCE-only and GOCE/GRACE GGMs (TIM, DIR and SPW) are better than GRACE-based ones above n ∼ 140 due to the few GOCE observations used. Note that most models are based on a few months of GOCE data contrary to ∼7 years of GRACE observations. This situation changes completely with the R3 models which incorporate about 1 year of GOCE data. The DIR-R3 error spectrum is improved by ∼4 orders of magnitude compared to R1 and R2, while TIM-R3 by about 1–2 orders of magnitude. The improvement brought by including more GOCE data is evident when comparing the ITG-GRACE2010s model and GOCO02s, where GOCE data in the latter boost its error degree variances to be smaller than those of EGM2008 up to degree n = 175 contrary to n = 142 for the former. The Release 3 versions of GOCE-TIM, GOCE-DIR and GOCO are better than the first and second releases, since they have smaller errors to higher degrees. This is due to the use of more GOCE data (12 months) in the R3 releases and as far as the DIR models are concerned, the use of ITG-GRACE2010s as a reference for the R3 model contrary to EIGEN-51c for R1. In terms of the cumulative geoid errors, GOCO-01S, 02S, and 03S reach the 1 cm geoid error up to d/o 143, 159 and 190 respectively, while TIM-R1, TIM-R2 and TIM-R3 up to d/o 30, 36 and 56. The improvement brought by more GOCE data is evidenced in the DIR models as well, since the 1 cm error is reached up to d/o 48, 27 and 127 for the DIR-R1, DIR-R2 and DIR-R3 models. ITG-GRACE2010S reaches the 1 cm error up to d/o 138, hence the improved cumulative errors in the GOCO-03 s model compared to TIM-R3 and the significant improvement of the DIR-R3 to the earlier releases. It is clear that the inclusion of more GOCE data in the R3 models, offers a significant boost to the reduction of the formal geoid errors. As it will be presented below in the external evaluation with GPS/Levelling data, this improvement by 3 orders in the total cumulative geoid error of the GGMs to their maximum d/o of expansion, e.g., from 15.6 cm to 5.4 cm between GOCO01S and GOCO03S, is not depicted. The latter is due to their limited maximum degree of expansion, so that the GGM geoid omission error above d/o 250 counteracts any improvement in the cumulative geoid error, along with the limited and unknown accuracy of the levelling data.

3 Validation Results with GPS/Levelling and Gravity Data

In terms of the absolute differences between the GGMs and the GPS/Levelling geoid heights, the evaluation was performed for various degrees of expansion between d/o 60 and up to their n_{max}. The geoid omission error has been considered with Kaula's (1966) power law and the Tscherning and Rapp (1974) degree variance model, given that the former over- and underestimates the geoid power

at low and high frequencies, respectively. Table 1 presents the so determined geoid omission errors for all available degrees that the GGMs were either truncated or reached their n_{max} and Table 2 summarizes the differences between the available GPS/Levelling and GGM geoid heights. As far as the national gravimetric geoid model is concerned, its std is at the 14 cm, so it will provide the basis for the evaluation of the ultra-high degree GGMs. One point that needs attention is the mean of the differences and the rms, being at −39.2 cm and ±41.6 cm. The development of this model was based on EGM2008 as a reference field and free-air gravity anomalies reduced to a global geopotential level tied to the nominal *Wo* value of 62,636,856.00 m^2/s^2. Therefore, this bias indicates the offset between the HVD and the W_o^{LVD} realized by the TG station at Piraeus harbor and a global geopotential level as used in the gravimetric geoid development. From the GPS/Levelling geoid height differences with the available GGMs, the improvement offered by the GOCE-based R3 models, w.r.t. the earlier releases is evident. For the GOCO models, the std of the differences drops by 3.7 cm between R1 and R3 (to d/o 220), 2.8 cm for the TIM models (to d/o 220) and 2.5 cm for the DIR ones (to d/o 240). The improvement for the DIR is marginal given that its R1 model provided an accuracy equal to that of the R2 for GOCO and TIM. This is due to the a-priori information from EIGEN-5C used in the development of GO-DIR-R1.

Regarding the GOCE/GRACE models, their performance is equivalent to that of EGM2008, when truncated to d/o 250, being inferior by just 1–2 cm for the latest, R3, releases. This shows the great improvement offered by the inclusion of more GOCE data, especially in view of the fact that EGM2008 contains detailed local gravity data over Greece even at that d/o. The mean offset between the GPS/Levelling data and all used GGMs is consistent and at the ∼35 cm level, signaling an offset between the Greek local vertical datum and a global vertical datum. This is monitored by all GOCE models, even the ones where no a-priori information and/or GRACE data are used, and it is very close to the mean offset with EGM2008 up to d/o 2159 (37 cm). This is a valuable conclusion for GOCE-only models towards the unification of the local/national vertical datums (LVD) to a global one. It provides good evidence that even a medium wavelength gravity field representation by GOCE to say d/o 250 can indeed determine 95 % of the mean offsets of LVD so that their link to a global one can be rigorously modeled. Comparing the performance of GRACE- and GOCE-based models, ITG-GRACE2010s provides better results up to d/o 160 compared to all GGMs where GOCE data have been used, either solely or in combination with GRACE. The former is 2–3 cm better than the GOCE and GOCE/GRACE GGMs, while the turning point is d/o 170–180 where the improvement by GOCE inclusion is at the 2–6 cm level. GOCE and GOCE/GRACE GGMs retain their signal strength up to d/o 220–230 since for higher degrees the improvement offered is marginal (few mm) and hence statistically insignificant.

In terms of absolute errors, the GGMs seem to provide expected results when taking into account the geoid omission error. GOCO03s has a std of 49.6 cm up to d/o 250, so considering the geoid omission error of 30.3 cm and the GOCO03s cumulative geoid error of 15.5 cm an un-modeled error of ∼36 cm remains. This may stem from the quality of, mainly, the orthometric heights within the HVD, which are known to be of low, yet unknown, accuracy. These can be as many as 10 cm or more (Tziavos et al. 2012), so the rest can be attributed to errors in GOCO03s not depicted in its formal error degree variances. The same results are derived for the other combined GGMs, such as GO-DIR-R3 which has a std with the GPS/Levelling geoid heights at 48.2 cm (d/o 240), with a geoid omission error of 32.1 cm and a formal cumulative geoid error of only 5.6 cm. The latter may signals that the formal error degree variances are optimistic, so that proper error modeling would require external information for validation. On the other hand, when the same models are evaluated over reliable Levelling networks, e.g., in Germany (Gruber et al. 2011) the std of the differences is at the 3.5 cm level, i.e., within the formal cumulative geoid error of the GGMs. Thus, the remaining un-modelled error can be largely attributed the (bad) quality of the HVD, so that a spectral enhancement approach should be followed in the future for the evaluation of GOCE GGMs over Greece. As far as GO-TIM-R3 and GO-SPW-R2 are concerned, the former is superior by ∼2.8 cm, while the Release3 version of the GO-TIM model provides the same level of accuracy as the GOCO03 and GO-DIR-R3 models, which is quite significant as to the value of GOCE data given that GO-TIM is a pure GOCE model, whereas the latter two incorporate GRACE data as well. Some useful conclusions can be drawn from the ultra-high degree models EIGEN6C and EIGEN6C2 as well, where gravity data are included. Especially the latter, being a revised version of EIGEN6C, provides better agreement with the GPS/Levelling data in Greece (13.7 cm) for lower n_{max} compared to EGM2008 (14.1 cm). This is a marginal improvement, but it signals that the satellite mission data can indeed boost the achievable accuracy by GGM representations of the Earth's gravity field. These levels of accuracy are practically the same as that achieved by the gravimetric geoid model, therefore the local data seem not to provide more information, which is expected since the Hellenic database has been included in the EGM2008 development.

Table 3 depicts the relative accuracies for the local gravimetric geoid model, EGM2008, EIGEN6C, EIGEN6C2, EIGEN6S and the Release3 versions of the TIM, DIR, and GOCO GGMs. For short baselines, up to 10 km, the contribution of local gravity data to the LSC-based geoid is clear, since it is better by 2 ppm compared to EGM2008, EIGEN6C and EIGEN6C2. This is due to the fact that even

Table 2 Statistics (mean and std) of the differences between GPS/levelling and geoid heights from the GGMs for various degrees. Unit: [m]

Model		60	80	140	160	180	220	240	250	360	1420	1949	2159
EGM2008	Mean	0.349	0.036	−0.297	−0.284	−0.288	−0.318	−0.332	−0.343	−0.331	−0.375	−0.374	−0.374
	Std	1.733	1.387	0.724	0.724	0.642	0.529	0.497	0.472	0.369	0.152	0.142	0.141
EIGEN-51C(n_{max}=359)	Mean	0.351	0.045	−0.292	−0.273	−0.275	−0.308			0.309			
	Std	1.734	1.388	0.709	0.724	0.644	0.537			0.403			
EIGEN-6C	Mean	0.350	0.042	−0.304	−0.298	−0.303	−0.337		−0.361	−0.349	−0.394		
	Std	1.733	1.386	0.714	0.727	0.651	0.524		0.478	0.379	0.161		
EIGEN-6C2	Mean	0.350	0.041	−0.303	−0.296	−0.302	−0.356		−0.356	−0.344	−0.389	−0.388	
	Std	1.733	1.386	0.715	0.727	0.651	0.525		0.475	0.374	0.149	0.137	
EIGEN-6S	Mean	0.350	0.042	−0.302	−0.300	−0.307	−0.344	−0.358					
	Std	1.733	1.386	0.716	0.722	0.646	0.508	0.512					
ITG-GRACE2010S	Mean	0.349	0.041	−0.304	−0.308	−0.299							
	Std	1.734	1.386	0.716	0.692	0.690							
DGM-1S	Mean	0.349	0.041	−0.304	−0.298	−0.303	−0.341	−0.363					
	Std	1.734	1.386	0.716	0.720	0.647	0.527	0.515					
GOCO01S(n_{max}=224)	Mean	0.349	0.041	−0.303	−0.301	−0.305	−0.341						
	Std	1.734	1.386	0.716	0.714	0.661	0.547						
GOCO02S	Mean	0.349	0.041	−0.305	−0.300	−0.305	−0.341		−0.358				
	std	1.734	1.386	0.716	0.718	0.643	0.522		0.501				
GOCO03S	Mean	0.349	0.041	−0.304	−0.299	−0.303	−0.335		−0.353				
	Std	1.733	1.386	0.717	0.717	0.645	0.510		0.496				
GO-DIR-R1	Mean	0.347	0.042	−0.297	−0.292	−0.298	−0.330	−0.344					
	Std	1.733	1.385	0.714	0.725	0.656	0.535	0.507					
GO-DIR-R2	Mean	0.351	0.043	−0.302	−0.298	−0.306	−0.347	−0.357					
	Std	1.734	1.386	0.713	0.719	0.644	0.505	0.510					
GO-DIR-R3	Mean	0.350	0.042	−0.302	−0.295	−0.301	−0.341	−0.352					
	Std	1.734	1.386	0.716	0.722	0.645	0.496	0.482					
GO-TIM-R1(n_{max}=224)	Mean	0.343	0.037	−0.307	−0.305	−0.310	0.348						
	Std	1.734	1.383	0.716	0.720	0.663	0.544						
GO-TIM-R2	Mean	0.345	0.038	−0.305	−0.301	−0.306	−0.345		−0.360				
	Std	1.733	1.384	0.716	0.720	0.644	0.525		0.502				
GO-TIM-R3	Mean	0.347	0.010	−0.304	−0.298	−0.303	−0.337		−0.356				
	Std	1.734	1.386	0.718	0.720	0.647	0.516		0.494				
GO-SPW-R1(n_{max}=210)	Mean	0.345	0.042	−0.300	−0.297	−0.303	−0.371						
	Std	1.735	1.388	0.714	0.725	0.675	0.586						
GO-SPW-R2	Mean	0.338	0.029	−0.312	−0.309	−0.315	−0.347	−0.345					
	Std	1.732	1.384	0.716	0.719	0.642	0.539	0.537					
N^{LSC}	Max		Min			Mean			Rms			Std	
	0.119		−1.033			−0.392			±0.416			0.140	

Table 3 Relative accuracies for the local geoid model and GOCE/GRACE GGMs. Unit: [ppm]

Baselines (km)	0–10	10–20	20–30	30–40	40–50	50–60	60–70	70–80	80–90	90–100	>100
N^{LSC}	10.4	6.5	4.4	3.3	2.7	2.2	1.9	1.7	1.5	1.4	0.6
EGM2008 (2159)	12.2	7.2	4.8	3.7	3.1	2.6	2.2	2.0	1.8	1.6	0.7
EGM2008 (250)	23.8	20.7	16.6	14.0	12.1	10.6	9.4	8.3	7.4	6.6	2.6
EIGEN6S (240)	23.9	20.9	16.9	14.3	12.3	10.8	9.6	8.6	7.6	6.7	2.6
EIGEN6C (250)	23.7	20.6	16.4	13.8	11.7	10.1	8.8	7.8	6.9	6.1	2.4
EIGEN6C (1420)	13.9	8.6	5.3	4.2	3.4	2.9	2.5	2.3	2.0	1.9	0.8
EIGEN6C2 (250)	23.7	20.6	16.4	13.8	11.7	10.1	8.8	7.8	6.9	6.0	2.4
EIGEN6C2 (1949)	12.4	7.3	4.8	3.7	3.0	2.5	2.2	1.9	1.7	1.6	0.6
GOCO03S (250)	23.7	20.6	16.5	13.9	11.9	10.5	9.2	8.1	7.2	6.4	2.5
GO-DIR-R3 (240)	23.7	20.6	16.5	13.8	11.8	10.2	8.9	7.9	6.9	6.2	2.4
GO-TIM-R3 (250)	23.6	20.6	16.5	13.9	11.9	10.4	9.2	8.1	7.2	6.4	2.5

Table 4 Statistics of the original free-air gravity anomalies over Greece, contribution of the various GGMs (normal lettering) and reduced fields (italics). Unit: [mGal]

	Max	Min	Mean	Rms	Std
Δgf (original)	269.93	−236.10	−22.73	±77.52	74.11
EGM2008 (2159)	213.98	−236.87	−22.45	±77.58	74.26
Δg red EGM2008	*92.08*	*−147.41*	*−0.28*	*±5.87*	*5.86*
EGM2008 (250)	117.06	−192.91	−18.46	±73.35	70.99
Δg red EGM2008	*210.26*	*−138.39*	*−4.27*	*±27.07*	*26.74*
EIGEN6s (240)	113.71	−189.64	−18.64	±73.56	71.15
Δg red EIGEN6s	219.29	*−134.89*	*−4.07*	*±28.27*	*27.97*
EIEGN6c (250)	116.69	−194.28	−18.58	±73.46	71.07
Δg red EIGEN6C	211.25	*−137.17*	*−4.15*	*±27.07*	*26.75*
EIGEN6c (1420)	190.35	−242.27	−22.17	±77.64	74.40
Δg red EIGEN6c	118.96	*−137.87*	*−0.57*	*±9.36*	*9.34*
EIEGN6c2 (250)	115.19	−193.78	−18.59	±73.43	71.04
Δg red EIGEN6C2	210.37	*−135.02*	*−4.14*	*±27.07*	*26.76*
EIGEN6c2 (1949)	209.43	−238.29	−22.52	±77.68	74.35
Δg red EIGEN6c2	94.97	*−149.20*	*−0.22*	*±6.73*	*6.73*
GOCO03S (250)	107.50	−191.92	−18.31	±73.03	70.69
Δg red GOCO03s	*224.65*	*−132.06*	*−4.42*	*±27.78*	*27.43*
GO-DIR-R3 (240)	106.05	−190.98	−18.39	±73.14	70.80
Δg red GO-DIR-R3	*223.69*	*−129.92*	*−4.34*	*±28.10*	*27.76*
GO-TIM-R3 (250)	109.49	−192.80	−18.39	±73.16	70.81
Δg red GO-TIM-R3	*223.57*	*−133.43*	*−4.35*	*±27.68*	*27nn34*

though local gravity data are used in the development of ultra-high degree GGMs, their contribution is attenuated given the use of satellite data, neighbouring gravity data, lower spatial resolution of the final model and a global, rather than local, error modelling. As expected the GOCE and GOCE/GRACE GGMs have inferior performance for small baselines by as much as 13–15 ppm. This is resolved for longer baselines, e.g., >40–50 km, where the satellite only GGMs provide an error close to the 1 cm level, in the relative sense. After the 80–90 km benchmark, corresponding to the satellite GGM resolution, their performance can be regarded as approximately the same with the local model and high-degree GGMs. Compared to EGM2008 when truncated up to d/o 250, the GOCE and GOCE/GRACE GGMs are superior, even at the sub-ppm level for baselines larger than 50 km, This is clearly due to the use of GOCE data, while the largest improvement (0.5 ppm) is found for baselines between 80 and 90 km. This is clearly marginal, but it indicates the maximum spectral band (80 km correspond up to d/o ∼230) that the Release3 GGMs manage to improve.

The final set of tests for the evaluation of the GOCE/GRACE GGMs is related to the reduction they provide over a database of irregularly distributed free-air gravity anomalies covering Greece nationwide. Within

this test, the original field of Δg_f has been reduced using all available GGMs and the resulting fields have been investigated as to the mean and std reduction that each GGM offers. This simulates the first remove step within the well-known remove-compute-restore procedure for geoid determination. Table 4 summarizes the statistics of the original free-air gravity anomalies, the GGM contribution and the reduced fields, only for EGM2008, the latest EIGEN6 models and the Release3 versions of the GOCE/GRACE GGMs. As expected the overall best reduction is achieved with EGM2008 when used up to d/o 2,159, with the std of the reduced field at the ±5.8 mGal level and the mean close to zero, something expected due to the inclusion of terrestrial gravity data in that model. EIGEN6C and EIGEN6C2 are quite close, with the latter being less than 0.5 mGal, in terms of the std, better than EGM2008. In order to validate the performance of the GOCE/GRACE GGMs, it is worth comparing them with the reduced field when using EGM2008 up to d/o 250. For the latter case the performance of all GGMs is comparable, with EGM2008 offering a, statistically insignificant, improvement at the sub-mGal level. The reduction that the GOCE/GRACE GGMs offer is approximately the same, with the std reduced at the ±26.6 to ±27.8 mGal and the mean to −4.3 mGal. It should be mentioned again that the GOCE/GRACE GGMs use only satellite data and achieve the same performance as EGM2008 (up to d/o 250), while the latter employs gravity and altimetry data well, hence its performance is subject to correlations with the local terrestrial gravity data.

Conclusions

A detailed evaluation has been carried out for all available releases of the GOCE and GOCE/GRACE GGMs (R1, R2, and R3) each of them employing an increasing number of GOCE observations. From the results acquired, the improvement of incorporating more GOCE data in the GGMs is evident, ranging from 2.5 to 3.7 cm in terms of geoid height differences w.r.t. the GPS/Levelling data and the few mGal level when compared with the free-air gravity anomaly field. The latest (Release3) versions of the GOCE/GRACE GGMs manage to provide a 1 cm relative accuracy for baselines larger than 40–50 km, which is quite encouraging for their use in medium-wavelength geoid related studies. Comparing the performance of GRACE- and GOCE-based models, the former provides better results up to d/o 160–170 while the improvement by GOCE is found from d/o 170–180 up to d/o 220–230 for the Release3 models. The latest combined GGMs EIGEN6C and especially EIGEN6C2 provide slightly better results compared to EGM2008 even for lower maximum degrees of expansion. Therefore, combined GGMs, employing all available GOCE, GRACE, gravity and altimetry observations can now be determined with increased accuracy. This is the direction of our future work for GOCE GGM evaluation, where a spectral enhancement approach will be followed while national /regional high-resolution geoid solution based on GOCE GGMs will be sought.

Acknowledgements The first three of the authors wish to acknowledge the funding provided for this work by the European Space Agency in the frame of the ESA-PRODEX GOCESeaComb project (C4000106380).

References

Bruinsma SL et al (2010) GOCE gravity field recovery by means of the direct numerical method. Presented at the ESA living planet symposium, Bergen, Norway, 27 June–2 July

Ekman M (1989) Impacts of geodynamic phenomena on systems for height and gravity. Bull Geod 63(3):281–296

Förste Ch et al (2011) EIGEN-6—a new combined global gravity field model including GOCE data from the collaboration of GFZ-Potsdam and GRGS-Toulouse. In: Geophysical Research Abstracts, vol 13, EGU General Assembly 2011, EGU2011-3242-2

Förste C et al (2012) A preliminary update of the direct approach GOCE processing and a new release of EIGEN-6C. Presented at the AGU fall meeting, San Francisco, CA, 3–7 December 2012, Abstract No. G31B-0923

Goiginger H et al. (2011) The combined satellite-only global gravity field model GOCO02S. In: Presented at the 2011 general assembly of the European Geosciences Union, Vienna, Austria, 4–8 April

Gianniou M (2008) HEPOS: designing and implementing an RTK network. Geoinformatics 11(1):10–13

Heiskanen WA, Moritz H (1967) Physical geodesy. W. H. Freeman, San Francisco, CA

Gruber T, Visser PNAM, Ackermann C, Hosse M (2011) Validation of GOCE gravity field models by means of orbit residuals and geoid comparisons. J Geod 85(11):845–860

Hashemi FH, Ditmar P, Klees R, Liu X, Zhao Q, Guo J (2013) The static gravity field model DGM-1S from GRACE and GOCE data: computation, validation and an analysis of GOCE mission's added value. J Geod 87(9):843–867. doi:10.1007/s00190-013-0650-3

Hirt C, Gruber T, Featherstone WE (2011) Evaluation of the first GOCE static gravity field models using terrestrial gravity, vertical deflections and EGM2008 quasigeoid heights. J Geod 85(10):723–740

Kaula WM (1966) Theory of satellite geodesy. Dover, Mineola, NY

Kotsakis C, Katsambalos K (2010) Quality analysis of global geopotential models at 1542 GPS/levelling benchmarks over the Hellenic mainland. Surv Rev 42(318):327–344

Mayer-Guerr T, Kurtenbach E, Eicker A (2010) The GRACE-only gravity field model ITG-Grace2010s. http://www.igg.uni-bonn.de/apmg/index.php?id=itg-grace2010

Migliaccio F, Reguzzoni M, Sansò F, Tscherning CC, Veicherts M (2010) GOCE data analysis: the space-wise approach and the first space-wise gravity field model. In: Proceedings of the ESA living planet symposium, Bergen, Norway, 28 June–2 July

Pail R et al (2010) Combined satellite gravity field model GOCO01S derived from GOCE and GRACE. Geophys Res Lett 37, L20314. doi:10.1029/2010GL044906

Pail R et al (2011) First GOCE gravity field models derived by three different approaches. J Geod 85(11):819–843

Pavlis NK, Holmes SA, Kenyon SC, Factor JK (2012) The development and evaluation of the Earth Gravitational Model 2008 (EGM2008). J Geophys Res 117, B04406. doi:10.1029/2011JB008916

Šprlák M, Gerlach C, Pettersen PR (2012) Validation of GOCE global gravity field models using terrestrial gravity data in Norway. J Geod Science 2(2):134–143

Tscherning CC, Rapp RH (1974) Closed covariance expressions for gravity anomalies, geoid undulations, and deflections of the vertical implied by anomaly degree-variance models. The Ohio State University, Reports of the Department of Geodetic Science, Report 208, Columbus, Ohiod

Tziavos IN, Vergos GS, Grigoriadis VN (2010) Investigation of topographic reductions and aliasing effects to gravity and the geoid over Greece based on various digital terrain models. Surv Geophys 31(3): 23–67. doi:10.1007/s10712-009-9085-z

Tziavos IN, Vergos GS, Grigoriadis VN, Andritsanos VD (2012) Adjustment of collocated GPS, geoid and orthometric height observations in Greece. Geoid or orthometric height improvement? In: Kenyon S, Pacino C, Marti U (eds) Geodesy for planet Earth, international association of geodesy symposia, vol 136. Springer, Heidelberg, pp 481–488

Tziavos IN, Vergos GS, Mertikas SP, Daskalakis A, Grigoriadis VN, Tripolitsiotis A (2013) The contribution of local gravimetric geoid models to the calibration of satellite altimetry data and an outlook of the latest GOCE GGM performance in GAVDOS. Adv Space Res 51(8):1502–1522. doi:10.1016/j.asr.2012.06.013

Evaluation of the GOCE-Based Gravity Field Models in Turkey

E.S. Ince, B. Erol, and M.G. Sideris

Abstract

The recent GOCE-based global gravity field models are tested in Turkey and in two sub-regions, the Istanbul and Sakarya territories, by means of geoid undulations. Global gravity field model computed geoid undulations are compared with different sets of GPS/leveling-derived geoid undulations for different spherical harmonic degree expansions. High frequency components of the geoid undulations are estimated from EGM2008 and are removed from the GPS/leveling-derived geoid undulations. Therefore, model-based and GPS/leveling-derived geoid undulations are reduced to about the same gravity spectral band. The comparisons between the two geoid undulations are performed directly on the same benchmark points and also between the benchmark points by means of geoid slope differences. The comparison results suggest that GOCE-based as well as GRACE and GOCE combined satellite-only models provide better agreement with GPS/leveling-derived geoid than EGM2008 by up to a few centimeters for medium wavelength gravity components. Based on the results obtained in this study, current and upcoming satellite-based gravity models are expected to improve the regional geoid, as well as the regional gravity prediction from such models. Turkey is currently discussing the options for height system modernization. The investigations performed in this study will be useful for the height modernization project of Turkey and will help the development of an accurate geoid model and improvement of the current vertical datum in the regions.

Keywords

Turkey geoid • GOCE • Gravity field • EGM2008

1 Introduction

Turkey has been working towards a new, modernized height system. The latest improvements in geoid modeling (due to, e.g., the dedicated gravity satellite missions) have led scientists to consider developing an upgraded height system based on an accurate geoid model which can be derived from the improved data sets. The recent GOCE-based, GRACE and GOCE combined, and GRACE-based satellite-only static gravity field solutions are used in the computation of geoid undulations in Turkey and two sub-regions. Three GOCE-only models developed based on three independent approaches, namely the direct-approach, the time-wise ap-

E.S. Ince (✉)
Department of Earth and Space Science and Engineering, Lassonde School of Engineering, York University, Toronto, ON, Canada

Department of Geomatics Engineering, Schulich School of Engineering, University of Calgary, Calgary, AB, Canada
e-mail: seince@yorku.ca

B. Erol
Civil Engineering Faculty, Department of Geomatics Engineering, Istanbul Technical University, Istanbul, Turkey

M.G. Sideris
Department of Geomatics Engineering, Schulich School of Engineering, University of Calgary, Calgary, AB, Canada

U. Marti (ed.), *Gravity, Geoid and Height Systems*, International Association of Geodesy Symposia 141,
DOI 10.1007/978-3-319-10837-7_12,

Table 1 Global gravitational models used in the investigations

Model	Max d/o	Description and data used	Data period	Reference
DS03	240	Direct solution, a-priori model ITG2010S is applied	18 months GOCE	Bruinsma et al. (2010)
TW03	250	Time-wise solution, developed from GOCE-only data	18 months GOCE	Pail et al. (2010)
SW02	240	Space-wise solution, developed from GOCE data and EGM2008	8 months GOCE	Migliaccio et al. (2010)
GOCO02S	250	GRACE and GOCE combined satellite-only model. ITG2010S, GOCE SST, GOCE SGG, CHAMP, and SLR data are used, Kaula regularization is applied	8 months GOCE SGG, 7.5 years GRACE, 12 months SST, 8 years CHAMP, 5 years SLR	Goiginger et al. (2011)
ITG2010S	180	GRACE-only model	7 years GRACE	Mayer-Gurr et al. (2011)
EGM2008	2190	Combined model from satellite, altimetry and terrestrial data	GRACE, terrestrial gravity, altimetry-derived gravity	Pavlis et al. (2012)

proach, and the space-wise approach, are included in the investigations. Moreover, a combined satellite-only model developed based on the datasets obtained from GOCE and GRACE is investigated. Besides these models, one GRACE-only model is included in the comparisons to provide an additional perspective in order to make a judgment on the differences and possible improvements coming from the GOCE models as compared to the GRACE models and to the EGM2008 model (Pavlis et al. 2012).

The global geopotential model (GGM) obtained geoid undulations for different spherical harmonic degree expansions are compared with independent low-pass filtered GPS/leveling-derived geoid undulations on benchmarks. Higher frequency components (from the truncation degree of the GGM used to the highest available degree of EGM2008) of GPS/leveling-derived geoid undulations are estimated by using EGM2008 and removed from the GPS/leveling geoid undulations. This procedure ensures comparison of undulations having the same spectral content. The results provide information on the precision of the GGMs in different wavelength bands based on GPS/leveling data. Moreover, comparisons are performed between the benchmark points in terms of the differences in geoid slopes which are more sensitive to medium and high frequency signal variations of the geoid undulations. The results are expected to provide information on the solution of existing problems and shortcomings of the currently used height reference system in Turkey and the sub-regions. Also, the results would be indicative of whether GOCE models provide any improvement in the representation of the gravity field in Turkey or not.

2 Data Used

2.1 Global Geopotential Models

Two third-generation GOCE models developed based on the direct approach, DS03 (GO_CONS_GCF_2_DIR_R3) (Bruinsma et al. 2010) and the time-wise approach, TW03 (GO_CONS_GCF_2_TIM_R3) (Pail et al. 2010), and one second-generation GOCE model developed based on space-wise approach, SW02 (GO_CONS_GCF_2_SPW_R2) (Migliaccio et al. 2010), are included in the assessments. The latest GRACE and GOCE combined solutions, GOCO02S (Goiginger et al. 2011) and GOCO03S (Mayer-Guerr et al. 2012), and GRACE-only solution, ITG2010S (ITG-Grace2010s) (Mayer-Gurr et al. 2011), have been considered in the comparisons in order to indicate the differences and improvements coming from GOCE and GRACE data for different wavelengths of the gravity signal. The third-generation space-wise solution was not released at the time of the preparation of this study. Also, GOCO03S comparisons indicate similar results with the ones derived from GOCO02S up to spherical harmonic degrees (shd) 200–220; therefore, due to lack of space, the results derived from GOCO03S are not included in this paper. Besides satellite-only models, the EGM2008 is also included in the investigations. The descriptions of the GGMs used in our investigations are summarized in Table 1.

2.2 GPS/Leveling Data

There are three sets of GPS/leveling data made available for this study, comprising 30 points in Turkey and 109 and 450 points in the Sakarya and Istanbul regions, and shown in Figs. 1 and 2, respectively. The measurements of the two local networks were performed independently during different time periods and adjusted and analyzed separately from each other. Therefore, even though benchmarks cover neighboring regions, comparisons are processed separately.

The official datum for the fundamental GPS network in Turkey is ITRF96. The ITRF96 coordinates of GPS/leveling benchmarks for Turkey are obtained from Yilmaz and Karaali (2010), whereas the GPS/leveling data for Istanbul

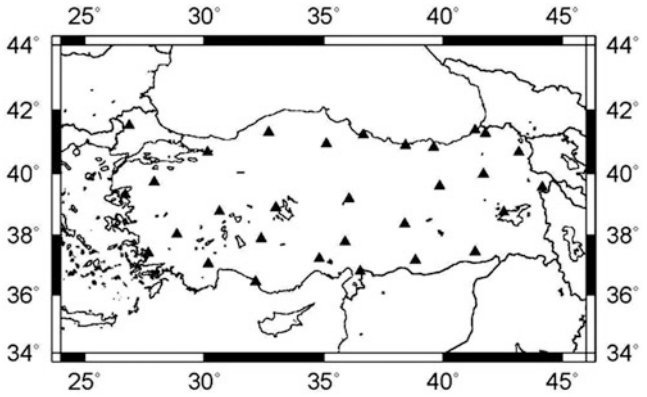

Fig. 1 The 30 GPS/leveling benchmarks (*black triangles*) used in the geoid comparisons in Turkey (Color figure online)

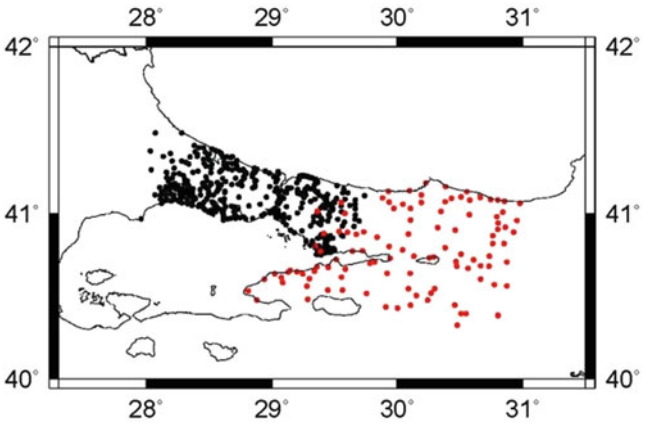

Fig. 2 The 109 and 450 GPS/leveling benchmarks used in the geoid comparisons in the Sakarya and Istanbul regions, in *red* and *black markers*, respectively (Color figure online)

and Sakarya are provided by the Istanbul GPS Triangulation Network (IGNA) and the Geodetic Infrastructure for Marmara Earthquake Region Land Information System (MERLIS) projects, respectively, in ITRF96 as well (Ayan et al. 1999; Çelik et al. 2002). The leveling benchmarks are classified as third and fourth order. The Helmert orthometric heights of the benchmarks are provided in the TUDKA99 (Turkish National Vertical Control Network of 1999) datum (Ayhan et al. 2002; Erol 2007; Erol et al. 2008).

The 30 benchmark points are homogenously distributed all over the country and the average distance among the points is around 200 km. The GPS/leveling benchmark points create dense networks, with 1 point per 165 km^2 in the Sakarya and 1 point per 32 km^2 in the Istanbul regions (see Erol 2007). In the Istanbul region, elevations range from 1 to 585 m. The 2D accuracy of GPS coordinates is estimated to be ±1.0 cm, the accuracy of GPS heights is ±2.0 cm and the accuracy of leveling is ±2.0 cm. In the Sakarya region, elevations range between 1 and 2,458 m. The 2D accuracy of GPS coordinates is ±1.5 cm whereas the accuracy for

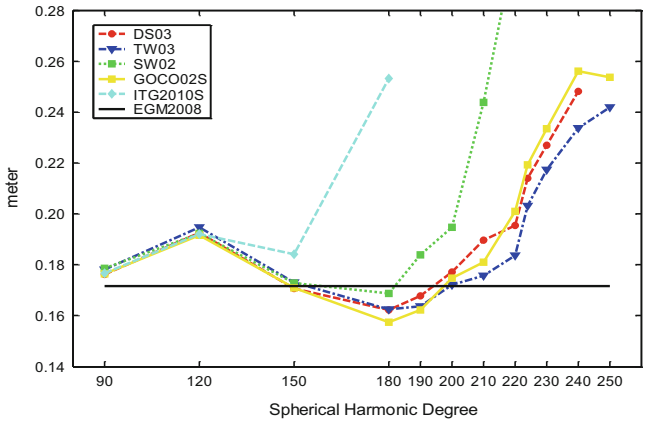

Fig. 3 Std values of the comparisons of the recent GGMs in Turkey with GPS/leveling-derived geoid undulations on 30 benchmarks

GPS heights is ±3.0 cm. The relative accuracy of the precise leveling performed in this region is 0.2 ppm (Erol 2007; Çelik et al. 2002).

3 Results

The comparison results between the GGMs described in Sect. 2.1 and Table 1 and GPS/leveling-derived geoid undulations are performed in absolute and relative sense and presented in this section.

3.1 Absolute Agreement Results

The validation of the absolute agreement is performed based on the well-known formula:

$$\delta N = (h_{GPS} - H) - N_{GGM} \quad (1)$$

where δN denotes the difference in geoids obtained from the two independent solutions, H is the orthometric height, h_{GPS} is the geometric height derived from GPS observations, and N_{GGM} is the GGM-based geoid undulation. According to Rapp (1997), height anomalies calculated from GGMs are converted into geoid heights by applying a correction, which is a function of the Bouguer gravity anomaly and elevations. The file Zeta_to_N_to2160_egm2008 provided by NGA is used for the calculation of the corrections. The absolute agreement comparison results for different spherical harmonic degree expansions for Turkey, Sakarya and Istanbul are depicted in Figs. 3, 4 and 5, respectively. The spherical harmonic degree expansion is set to 90, 120, 150, 180, 190, 200, 210, 220, 224, 230, 240 and 250. All GPS heights are referenced to the GRS80 reference ellipsoid.

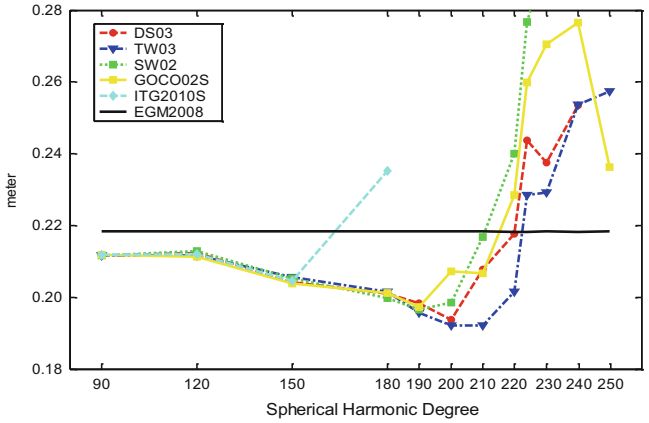

Fig. 4 Std values of the comparisons of the recent GGMs in Sakarya with GPS/leveling-derived geoid undulations on 109 benchmarks

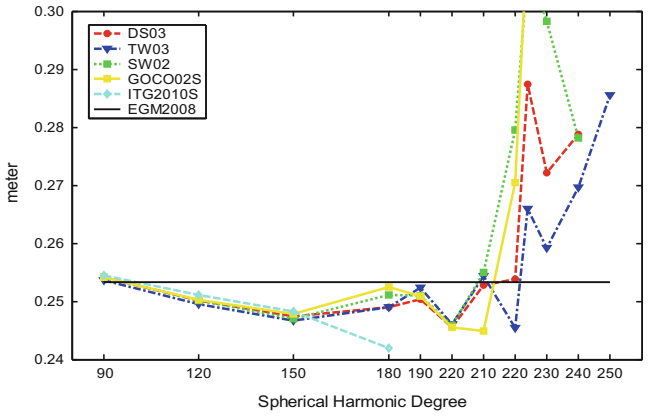

Fig. 5 Std values of the comparisons of the recent GGMs in Istanbul with GPS/leveling-derived geoid undulations on 450 benchmarks

Figure 3 shows the standard deviation (std) values of the differences of the geoid undulations on the 30 benchmark points in Turkey. In general, all satellite-only models except ITG2010S show improved agreement with GPS/leveling-derived geoid undulations between spherical harmonic degrees 150 and 180–190 compared to EGM2008. Beyond spherical harmonic degree 180–200, EGM2008's agreement is better than all the rest of the models due to the contribution of the terrestrial data and the loss of the GOCE signal. All GOCE-based models show compatible results with each other. It requires more investigations why ITG2010's behaviour differs from EGM2008 considerably in the spectral band between degrees 130 and 180.

Figure 4 shows the std values of the comparison results for the area of Sakarya. Comparisons are made in absolute sense on 109 benchmark points. In general, all GOCE-based models computed geoid undulations agree with GPS/leveling-derived geoid undulations better than EGM2008 up to spherical harmonic degree 200–220. This is a fair indicator, which illustrates that the improvement in this part of the spectrum comes from GOCE data. In general, GOCE models are compatible with each other up to spherical harmonic degree 180–190 and above degree 190 they show increasing commission error. The GRACE-only model ITG2010S shows comparable results with GOCE-based solutions up to degree 150 and, as expected, it shows increasing commission error after degree 150.

Figure 5 depicts std values of the comparison results for the region of Istanbul. Assessments have been performed by using the GPS/leveling-derived geoid undulations at 450 benchmark points. As it is the case for the Sakarya region, GOCE-based models show an improvement over EGM2008 up to degree 210–220 also in this region. It is observed that GOCE models are comparable with each other in the region and follow similar behaviour. In the spherical harmonic degree interval between 150 and 180, ITG2010S shows better agreement with GPS/leveling-derived geoid undulations than the rest of the models. The reason of this behaviour requires more investigations.

In Figs. 3, 4, and 5, the black line indicates the standard deviation of the differences between the GPS/leveling-derived geoid undulations (where the high frequency components from n + 1 truncation degree to 2190 are calculated from EGM2008 and removed) and GGM-derived geoid undulations (expanded up to n truncation degree). In other words, it is assumed that the entire spectra of the geoid undulations derived from GPS/leveling can be represented by using EGM2008 from degree 2 to 2190 and thus the contributions above degree 2190 are neglected in the comparisons. Similar studies performed for Canada and Germany can be found in Gruber (2009), Ince (2011), and Ince et al. (2012). In the three regions, based on the comparison results with GPS/leveling-derived geoid, it is observed that the GOCE-based models provide an improvement to the geoid of the order of 2–3 cm.

3.2 Relative Agreement Results

The comparisons are performed based on:

$$\delta\Delta N_{ij} = \left(N_{GPS/leveling(j)} - N_{GPS/leveling(i)}\right) - \left(N_{GGM(j)} - N_{GGM(i)}\right) \quad (2)$$

where $\delta\Delta N_{ij}$ is the difference of the geoid height difference between two benchmarks i and j computed from GPS/leveling and from a GGM, $N_{GPS/leveling}$ is the GPS/leveling-derived geoid undulation and N_{GGM} is the GGM-computed geoid undulation. The comparisons made in this section have been performed for four different truncation degrees (150, 180, 210 and the highest degree of each GGM). The mean values of the differences for the sub-regions are shown in Figs. 6 and 7. The general behavior of the

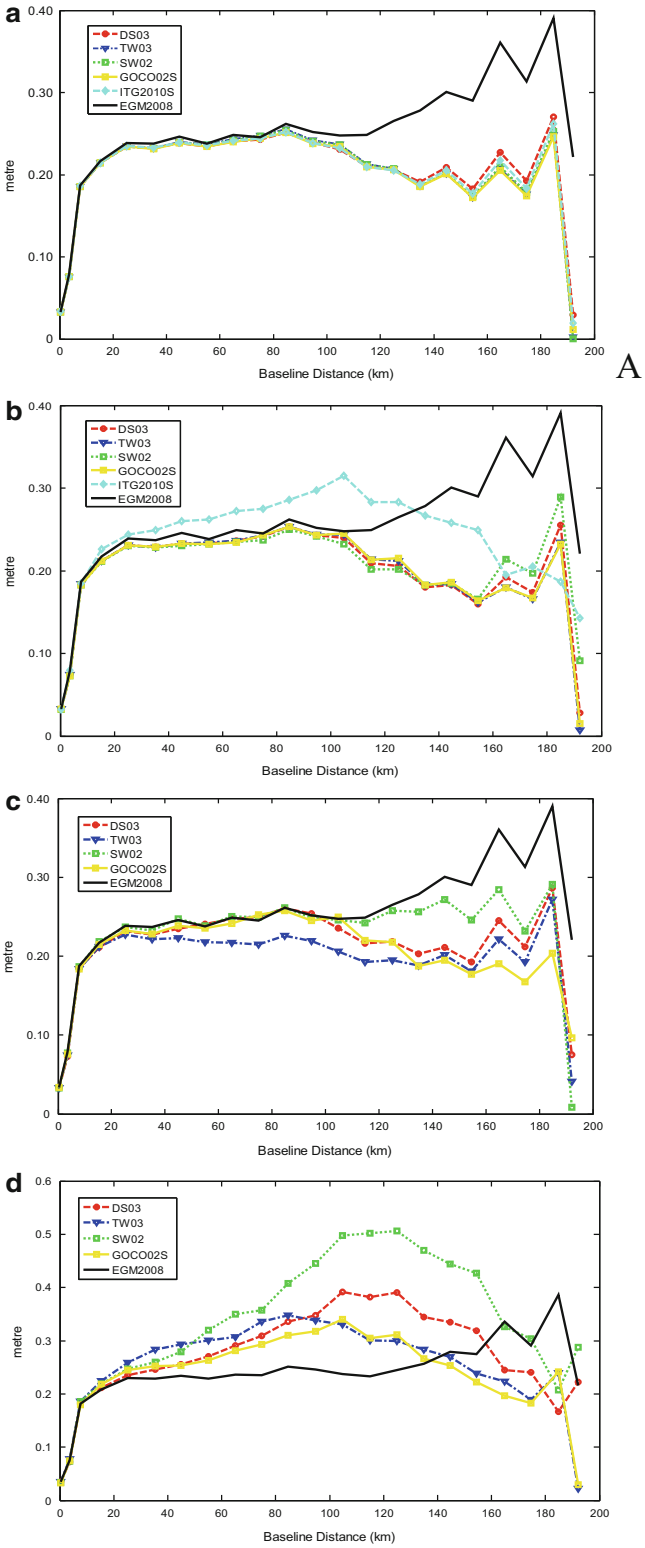

Fig. 6 Mean values of the relative agreement of the geoid undulation differences computed for Sakarya on 109 points (**a**) at truncation degree 150; (**b**) at truncation degree 180. Note that ITG2010S is at its max degree/order; (**c**) at truncation degree 210; (**d**) at models highest expansion degrees

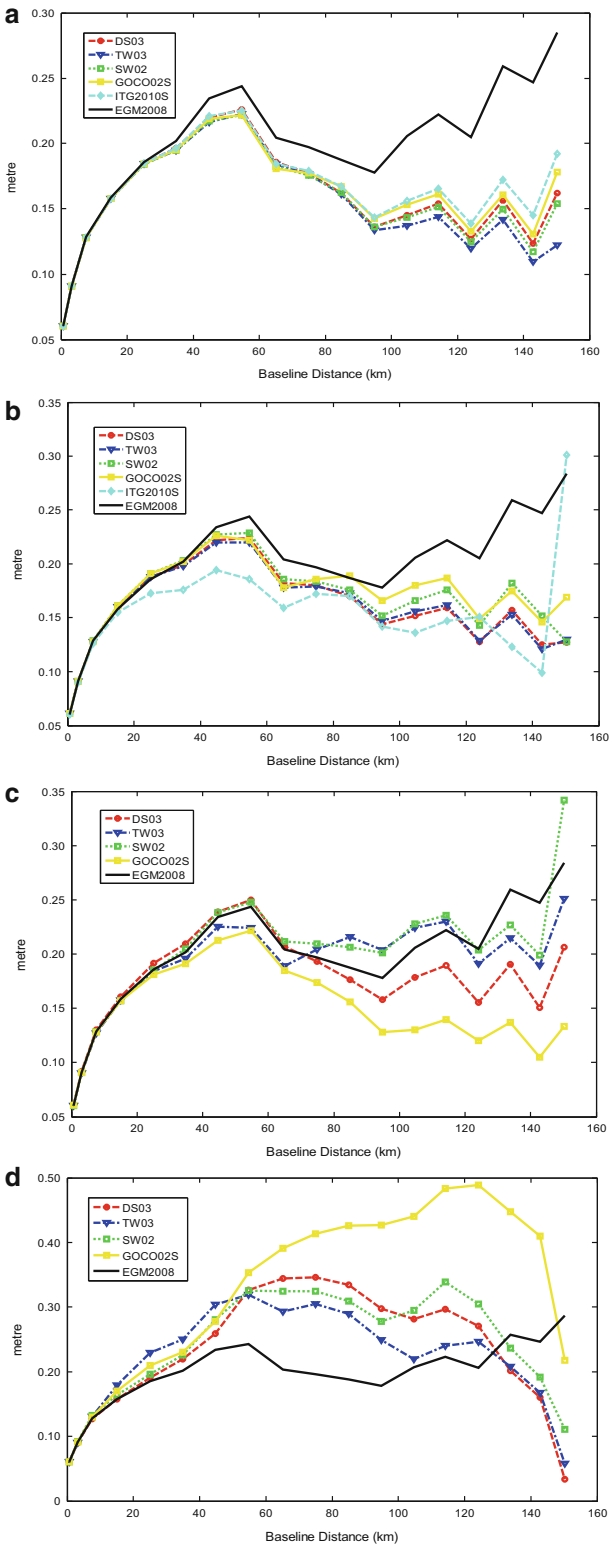

Fig. 7 Mean values of the relative agreement of the geoid undulation differences computed for Istanbul on 450 points (**a**) at truncation degree 150; (**b**) at truncation degree 180. Note that ITG2010S is at its max degree/order; (**c**) at truncation degree 210; (**d**) at models highest expansion degrees

models and the loss of the signal in different models (such as ITG2010S) can be observed in these comparisons as well. It should be noted that the relative agreement assessments are more sensitive to the medium to high frequency variations of the geoid undulations.

Figures 6a and 7a show the mean values of the agreement results for the truncation degree 150 for Sakarya and Istanbul, respectively. Moreover, Fig. 6b–d and 7b–d show the same comparison results for the truncation degrees 180, 210 and the highest expansion degree of each model, respectively (See Table 1). The mean values are derived from fixed distance intervals with an increase of 10 km. As seen in Fig. 6a–c referring to truncation degrees 150, 180 and 210, the GOCE-based models outperform EGM2008, especially above baseline distances of 100–120 km. One can observe the signal loss of ITG2010 comparing Fig. 6a and b. For the truncation degree 210, the model developed with the time-wise approach shows better results than all other GOCE-based models as well as EGM2008. The investigations performed for the highest truncation degree expansions of the models show that EGM2008's agreement is better than the rest of the satellite-only models due to the contribution of the terrestrial datasets included in its development.

The results presented for the region of Sakarya are similar to those for the Istanbul region. GOCE-based models are comparable with each other and agree better than EGM2008 with the GPS/leveling-derived geoid undulations in relative sense for truncation degrees of 150, 180 and 210. It is interesting to observe that GOCO02S shows better agreement in truncation degree 210 whereas TW03's results become better for the highest spherical harmonic degree expansion, which is 250 for both models. As mentioned in the previous paragraph, EGM2008 results get better whereas GOCE-based model results become worse at the highest expansion spherical harmonic degrees of the models, 2190 for EGM2008 and 240/250 for GOCE-based models. Note that ITG2010S is not included in the Figs. 6c, d and 7c, d as its maximum degree is 180.

Conclusions

The latest satellite-only geoids derived from the GOCE- and GRACE-based GGMs and their combinations were evaluated by comparing them with EGM2008 and GPS/leveling-derived geoids in Turkey and two local areas. The comparisons were performed in absolute and relative sense. According to the results obtained:

- GOCE GGMs are a significant source of possible improvement to the existing regional models for the medium wavelength geoid components in Turkey. These models are expected to increase the accuracy of the current geoid models and EGM2008 at least up to 2–3 cm.
- Considering the absolute agreement test results, GOCE-only models fit well to the terrestrial data within the spectral band of spherical harmonic degrees 90–180; however, they seem to deteriorate beyond degree 200.
- The GRACE-based model provides consistent results with GOCE-based satellite only models up to spherical harmonic degree 150; however, it deteriorates after degree 150 and reveals poor performance in comparisons against the GPS/leveling data in the whole country and in Sakarya.
- The combined satellite-only model GOCO02S provides slightly improved performance compared to the GOCE- and GRACE-only models in the whole country. This illustrates the superiority of the combined solutions from the two satellite gravity missions. Therefore, it is suggested that the satellite model to be used in a combined regional geoid model for Turkey should be a combined product of GRACE, GOCE and other geodetic techniques (e.g., SLR), rather than a GOCE-only model.
- Relative agreement comparison results confirm the conclusions from the absolute agreement tests and reveal slightly improved results from the new GGMs compared to EGM2008 on the fit of the tested models and the GPS/leveling-derived geoids.
- Finally, as expected, EGM2008's agreement is superior above spherical harmonic degree 200–220 in both absolute and relative sense due to the inclusion of the terrestrial data used in its development.

The modernization of the height system in Turkey will most likely be implemented by adopting a geoid-based vertical datum satisfying the requirements of the GNSS era. The new accurate geoid model will rely on the latest improved GGMs and terrestrial datasets. From this point of view, the outcome of this study is believed to provide valuable input to the discussions. As seen from the numerical results, the performance tests of GOCE-only and combined satellite-only models in Turkey are quite promising. Moreover, in collaboration with quality terrestrial data in the territory, they can indeed lead to a precise geoid-based vertical datum definition. Such a datum will provide a fast and economic approach to height determination for all geospatial data applications in Turkey. Moreover, a geoid-based national datum will provide a connection to the World Height System as soon as such a system/datum will be defined and realized.

Acknowledgement This research was supported by grants from the GEOIDE NCE in Canada, and SERC in Turkey. The GPS/levelling data of sub-regions used in this study were provided by ITU, Geodesy

Division. Figures presented in this paper were created by using the Generic Mapping Tools (GMT) and Matlab Tools.

References

Ayan T, Aksoy A, Deniz R, Arslan E, Çelik RN, Özşamlı C, Denli HH, Erol S, Erol Özöner B (1999) İstanbul GPS Nirengi Ağı (IGNA). Istanbul Technical University Report, ITU 1997/3882, Istanbul (in Turkish)

Ayhan ME, Demir C, Lenk O, Kilicoglu A, Aktug B, Acikgoz M, Firat O, Sengun YS, Cingoz A, Gurdal MA, Kurt AI, Ocak M, Turkezer A, Yildiz H, Bayazit N, Ata M, Caglar Y Ozerkan A (2002) Turkish national fundamental GPS network–1999 report. Mapping Journal Special Edition, 16, General Command of Mapping, Ankara, Turkey, pp 43–46

Bruinsma SL, Marty JC, Balmino G, Biancale R, Förste C, Abrikosov O, Neumayer H (2010) GOCE gravity field recovery by means of the direct numerical method. Presented at the ESA living planet symposium, Bergen, Norway, 27 June–2 July 2010. See also: earth.esa.int/GOCE

Çelik RN, Ayan T, Erol B (2002) Geodetic infrastructure project of Marmara earthquake region land information system (MERLIS). Istanbul Technical University Report, ITU 2002/06/20, Istanbul (in Turkish)

Erol B (2007) Investigations on local geoids for geodetic applications. Ph.D. Dissertation, Istanbul Technical University, Turkey

Erol B, Erol S, Çelik RN (2008) Height transformation using regional geoids and GPS/levelling in Turkey. Surv Rev 40(307):2–18

Goiginger H, Rieser D, Mayer-Guerr T, Pail R, Fecher T, Gruber T, Albertella A, Maier A, Hock E, Krauss S, Hausleitner W, Baur O, Jäggi A, Meyer U, Brockmann JM, Schuh W-D, Krasbutter I, Kusche J (2011) The combined satellite-only global gravity field model GOCO02S. European Geosciences Union General Assembly 2011, Wien, 4 April 2011

Gruber T (2009) Evaluation of the EGM2008 gravity field by means of GPS-levelling and sea surface topography solutions. Newton-Bulletin 4:3–17

Ince ES (2011) Geoid investigations for the new vertical datum in Canada. M.Sc. Thesis, UCGE Reports 20344, University of Calgary, Canada. http://www.ucalgary.ca/engo_webdocs/MGS/11.20344_ElmasInce.pdf

Ince ES, Sideris MG, Huang J, Véronneau M (2012) Assessment of GOCE-based global gravity field models in Canada. Geomatica 66–2:125–140

Mayer-Gurr T, Kurtenbach E, Eicker A, Kusche J (2011) The ITG-Grace2010 gravity field model. Geophys Res Lett, submitted. http://www.igg.uni-bonn.de/apmg/index.php?id=itggrace2010

Mayer-Gurr T, Rieser D, Höck E, Brockmann JM, Schuh W-D, Krasbutter I, Kusche J, Maier A, Krauss S, Hausleitner W, Baur O, Jäggi A, Meyer U, Prange L, Pail R, Fecher T, Gruber T (2012) The new combined satellite only model GOCO03s. Abstract submitted to GGHS2012, Venice (Poster)

Migliaccio F, Reguzzoni M, Sanso F, Tscherning CC, Veicherts M (2010) GOCE data analysis: the space-wise approach and the first space-wise gravity field model. In: Proceedings of the ESA living planet symposium, Bergen, Norway, 28 June–2 July 2010

Pail R, Goiginger H, Mayrhofer R, Schuh W, Brockmann JM, Krasbutter I, Hoeck E, Fecher T (2010) GOCE gravity field model derived from orbit and gradiometry data applying the time-wise method. In: Proceedings of the ESA living planet symposium, Bergen, Norway, 28 June–2 July 2010. See also: earth.esa.int/GOCE

Pavlis NK, Holmes SA, Kenyon SC, Factor JK (2012) The development and evaluation of the Earth Gravitational Model 2008 (EGM2008). J Geophys Res 117, B04406. doi:10.1029/2011JB008916

Rapp RH (1997) Use of potential coefficient models for geoid undulation determinations using a spherical harmonic representation of the height anomaly/geoid undulation difference. J Geod 71(5):282–289

Yilmaz N, Karaali C (2010) Comparison of global and local gravimetric geoid models in Turkey. Sci Res Essays 5(14):1829–1839

A Stokesian Approach for the Comparative Analysis of Satellite Gravity Models and Terrestrial Gravity Data

Jianliang Huang and Marc Véronneau

Abstract

A Stokesian approach is formulated to update the geoid model for a specific spherical harmonic band by spectrally combining a GOCE-based satellite global geopotential model with terrestrial gravity data. A simulation test shows that the GOCE-based model can be combined into a geoid solution with an accuracy better than 3 mm for the band between degrees 90 and 180. A comparison of the GOCE-based model GOCO03S and the Canadian terrestrial gravity data for the spherical harmonic band between degrees 90 and 180 shows that the geoid update by GOCO03S reaches 1.6 cm in RMS in the Yukon Territory, 1.8 cm in northern British Columbia, and 1.6 cm in the Maritimes. This may suggest a slight improvement of the GOCE model over the Canadian gravity data considering the standard deviation of 1.0 cm given by GOCO03S. However the analysis indicates comparable accuracy between the terrestrial gravity data and GOCE models for the rest of Canada where topography is relatively flat. The comparisons at the GPS-levelling points suggest that GOCE has improved our existing knowledge of the Earth's gravity field for wavelength components longer than 200 km over the Yukon Territory, northern British Columbia, the Maritimes, and Newfoundland.

Keywords

Satellite gravity model • Stokes integral • Terrestrial gravity data

1 Introduction

The Global Geopotential Models (GGMs) from GRACE and GOCE satellite missions are updating our knowledge on the Earth's gravity field and advancing a number of fronts in the Earth's sciences (Tapley et al. 2004; Rummel 2011). In order to use these models optimally, a realistic assessment on their quality is essential, and can be made by a direct comparison with terrestrial gravity data. However this comparison is affected by large omission errors from the satellite models, which pose a major problem when assessing the quality of either dataset (Huang et al. 2008). A common approach to deal with this problem is extending GRACE and GOCE models by an ultra-high global geopotential model such as EGM2008 (Pavlis et al. 2012, 2013) or EIGEN6C (Förste et al. 2011), and/or by forward topographical modelling (Hirt et al. 2010; Gruber et al. 2011; Ince et al. 2012). While EGM2008 and EIGEN6C represent the two best models of the Earth's gravity field in terms of spatial resolution, the approach prevents a direct comparison between the satellite models and local/regional terrestrial gravity data that may not be optimally incorporated into these ultra-high degree models.

In this study, we present an alternative approach that uses the Stokes integral with spectrally modified kernels to compare the satellite models with the terrestrial gravity data band-wise in terms of the resulting geoid difference. First a numerical simulation procedure is designed and performed to test this approach. Second this approach is used

J. Huang (✉) • M. Véronneau
Canadian Geodetic Survey, Surveyor General Branch, Natural Resources Canada, 615 Booth Street, Ottawa, ON, Canada K1A 0E9
e-mail: jianhuan@nrcan.gc.ca; marcv@nrcan.gc.ca

U. Marti (ed.), *Gravity, Geoid and Height Systems*, International Association of Geodesy Symposia 141,
DOI 10.1007/978-3-319-10837-7_13,

to compare GOCO03S with the Canadian terrestrial gravity data. The differences between GOCO03S and terrestrial gravity data are estimated for the spherical harmonic band between degrees 90 and 180 in which GOCE contributes to the improvement of GRACE satellite gravity models (Mayer-Güerr et al. 2012). Third the assessment of three release-3 GOCE-based models has been made by a comparison between the resulting gravimetric geoid models and independent geoid heights from GPS-levelling data on benchmarks to determine which datasets (satellite or terrestrial) provide better accuracy for the spectral band of study from region to region within Canada.

2 Mathematical Formulation

The remove-compute-restore Stokes-Helmert scheme for the determination of geoid can be formulated as (e.g. Huang and Véronneau 2013)

$$N(\Omega) = N_{\mathrm{GGM}}(\Omega) + \frac{R}{4\pi\gamma}\int_{\sigma_0} S_{\mathrm{MDB}}(\psi)\, dg(\Omega')d\sigma + \delta N_{\mathrm{T}} \tag{1}$$

where the term N_{GGM} is the geoid height computed from a global geopotential model (GGM). R is the mean radius of the Earth; γ is the normal gravity on the reference ellipsoid; σ_0 is the integration domain defined by a spherical cap with an angular radius ψ_0. The second term of the integral in Eq. (1) gives the Helmert-geoid residual. The third term is the sum of the direct and primary indirect topographical effects on the geoid. We have simplified Eq. (1) on purpose to focus discussions on the spectral combination of GGM and terrestrial gravity data. The details on the Stokes-Helmert scheme can be found in Ellmann and Vaníček (2007). The function $S_{\mathrm{MDB}}(\psi)$ is the modified degree-banded Stokes kernel, and can be expressed as

$$S_{\mathrm{MDB}}(\psi) = \sum_{n=L-u}^{M+v} \kappa_n(L,M)\frac{2n+1}{n-1}P_n(\cos\psi) \tag{2}$$

where κ_n are the spherical harmonic (SH) degree-dependent spectral transfer coefficients (Wenzel 1982). P_n are Legendre's polynomials. A simple modification can be realized by defining κ_n as a cosine function which increases from 0 at degree $n = L - u$ to 1 at degree $n = L$, and decreases from 1 at $n = M$ to 0 at $n = M + v$. The parameter L is the maximum SH degree up to which the GGM components are spectrally combined into the geoid model. The parameter M is the maximum SH degree of the geoid model spectrally corresponding to the spatial resolution of the surface gravity anomalies.

The Helmert gravity anomaly residual dg on the geoid is computed by

$$dg(\Omega) = \Delta g(\Omega) - \Delta g_{\mathrm{GGM}}(\Omega) \tag{3}$$

where Δg is the Helmert gravity anomaly on the geoid computed from the terrestrial gravity data. The term Δg_{GGM} is the Helmert gravity anomaly on the reference ellipsoid computed from the same global geopotential as for N_{GGM}.

The residual dg can be expanded into the SH form as

$$dg(\Omega) = dg_0 + \sum_{n=2}^{M+v} dg_n(\Omega) \tag{4}$$

The dg_n components below the maximum SH degree of GGM represent the differences between the terrestrial and GGM data for SH degree n, while the components above the maximum SH degree represent the omission errors of GGM.

Similarly the geoid residual given by the integral in Eq. (1) can be also expanded into spherical harmonics as

$$dN(\Omega) = -\beta_0 R\frac{dg_0}{\gamma} + \frac{R}{\gamma}\sum_{n=2}^{M+v}\beta_n\frac{dg_n(\Omega)}{n-1} \tag{5}$$

where

$$\beta_n(L,M) = \kappa_n(L,M) - \frac{n-1}{2}Q_n^{\mathrm{MDB}} \tag{6}$$

and

$$Q_n^{\mathrm{MDB}}(\psi_0) = \int_{\psi_0}^{\pi} S_{\mathrm{MDB}}(\psi)P_n(\cos\psi)\sin\psi d\psi \tag{7}$$

β_n are called the effective spectral transfer coefficients for the truncated Stokes integral. From Eq. (6), it can be seen that β_n are equal to the coefficients κ_n when $\psi_0 = \pi$, i.e. the Stokes integral is evaluated globally covering the entire sphere. On the other hand, when the Stokes integration covers only a spherical cap, β_n effect as the spectral transfer coefficients. Figure 1 shows β_n for $L = 150$ and 180. We can see that the β_n provides a close approximation to κ_n even though the Stokes integral is performed within a spherical cap. The larger the spherical cap is, the better β_n approximate κ_n.

Similar to the gravity anomaly residual components in Eq. (4), the geoid residual components given by Eq. (5) represent the β_n-scaled differences between the terrestrial and GGM data below the maximum SH degree of GGM, and the omission errors above the maximum degree in geoid height. For the comparison between the terrestrial and GGM data, we are interested in estimating their difference within

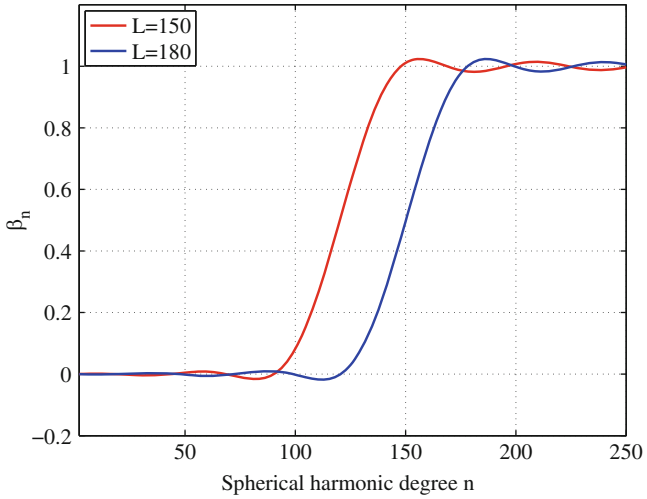

Fig. 1 The effective spectral transfer coefficients β_n for $L = 150$ and 180. $\psi_0 = \pi/30$

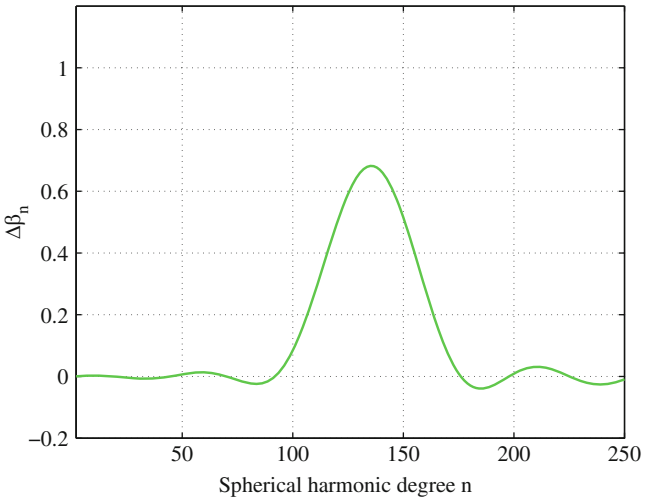

Fig. 2 The spectral transfer coefficient differences $\Delta\beta_n$ between $L = 150$ and 180

a specific SH band between $n = p - u$ and $n = q$ by differentiating the two geoid models for the modification degrees $L = p$ and q. The geoid difference can be expressed mathematically by the differential Stokes integral as

$$\Delta N(\Omega) = \frac{R}{4\pi\gamma}\int_{\sigma_0} \Delta S_{\mathrm{MDB}}(\psi)\, dg(\Omega')\, d\sigma \tag{8}$$

where

$$\Delta S_{\mathrm{MDB}}(\psi) = \sum_{n=p-u}^{q} [\kappa_n(p, M) - \kappa_n(q, M)]\, \frac{2n+1}{n-1} P_n(\cos\psi) \tag{9}$$

It can be written into the SH form as

$$\Delta N(\Omega) = -\Delta\beta_0 R \frac{dg_0}{\gamma} + \frac{R}{\gamma}\sum_{n=2}^{M+v} \Delta\beta_n \frac{dg_n(\Omega)}{n-1} \tag{10}$$

where

$$\Delta\beta_n = \beta_n(p, M) - \beta_n(q, M) \tag{11}$$

Equation (10) suggests that the geoid difference largely reflects the effect of the $\Delta\beta_n$-scaled difference between the terrestrial gravity and GGM data for the SH degree band of p to q, therefore gives a band-wise comparison between the terrestrial and GGM data when canceling most of the omission error associated with GGM. Figure 2 shows $\Delta\beta_n$ for the case of $p = 150$ and $q = 180$.

3 Simulation Test

Numerical performance of the Stokesian comparison method is analyzed by a simulation test over the study region. EGM2008 (Pavlis et al. 2012, 2013) is used to generate a simulated terrestrial gravity field from SH degrees 2 to 2,190 on the geoid predicted from EGM2008 while GOCO03S (Pail et al. 2011) is used as a GGM to generate a satellite gravity field from SH degrees 2 to 250 on the reference ellipsoid. The maximum numerical error of the geoid difference by the Stokesian method is estimated at 3 mm when comparing the Stokesian geoid difference with the one from the spherical harmonic synthesis using Eq. (10).

Figure 3 shows the $\Delta\beta_n$-scaled geoid difference between EGM2008 and GOCO03S for the SH band of degrees $L = 90$ to 180 with $u = 60$ by Eq. (10). The difference ranges from −13.8 to 12.5 cm with an RMS of 2.3 cm for the entire region. The difference is more significant over northern-eastern part than the rest of the region. The RMS difference decreases to 1.4 cm when the region is limited south of latitude 60°N.

4 Case Studies in Canada

The Stokesian geoid difference has been estimated for the SH band of degrees 90 to 180 using GOCO03S and the Canadian terrestrial gravity data. The result is shown in Fig. 4. It is similar to the difference shown in Fig. 3 mainly because the Canadian terrestrial gravity data have been used in the

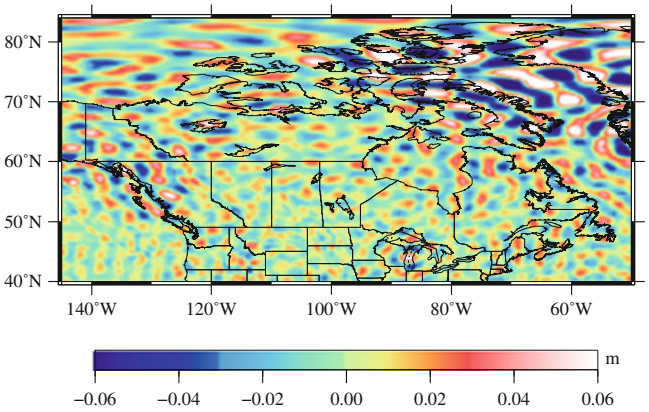

Fig. 3 The $\Delta\beta_n$-scaled geoid difference between GOCO03S and EGM2008 for the spherical harmonic band of degrees 90–180

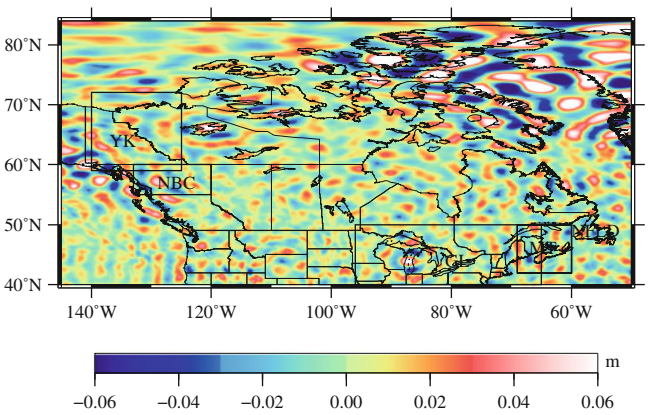

Fig. 4 The $\Delta\beta_n$-scaled geoid difference inferred from the difference between the gravity anomaly predicted from GOCO03S and the Canadian terrestrial gravity data for the SH band of degrees 90–180

development of EGM2008 (Pavlis et al. 2012, 2013). The difference is relatively larger over the Yukon Territory (YK), northern British Columbia (NBC), the Great Lakes (GL), the Maritimes (MT), Newfoundland (NFLD), and the Arctic region than the rest of Canada.

Table 1 shows statistics of the geoid difference over the study region and its sub-regions. This difference quantifies the level of agreement between the Canadian terrestrial gravity data and GOCO03S for the SH band of study. The RMS difference north of 60°N is 2.5 cm in contrast to 1.4 cm south of 60°N. A few areas showing large differences are attributed to poor or lack of terrestrial gravity data such as the Great Bear Lake (62°N; 120°W) and Lake Michigan (43°N; 87°W). It suggests that GOCE contributes to the improvement of the geoid models over these areas. The fact that the accuracy of GOCO03S is homogeneous across the study region suggests any large geoid differences can be considered as an improvement.

Table 1 Statistics of the $\Delta\beta_n$-scaled geoid difference by the Stokesian method over all and sub-regions (Unit: cm)

Region	Min	Max	Mean	RMS
All	−10.7	13.4	0.2	2.1
North of 60°N	−10.7	13.4	0.2	2.5
South of 60°N	−6.9	10.0	0.1	1.4
YK	−5.9	8.3	0.1	1.6
NBC	−4.2	5.2	−0.1	1.8
GL	−5.8	7.4	0.1	1.4
MT	−4.4	3.5	0.0	1.6
NFLD	−3.6	3.9	0.0	1.3

To examine the significance of the geoid difference, the $\Delta\beta_n$-scaled standard deviation has been estimated from GOCO03S's standard deviation coefficients because the full co-variance matrix is not available. It ranges from 0.9 to 1.0 cm in contrast to 3.2–3.8 cm for EGM2008 for the region of study. Assuming that the Canadian terrestrial gravity data are as accurate as GOCO03S, the standard deviation of the geoid difference would be about 1.4 cm. If the geoid difference is greater than this critical value of 1.4 cm, GOCO03S is statistically more precise than the terrestrial data, thus the improvement from GOCO03S over the terrestrial data is significant at the confidence level greater than 0.67. A comparison of the geoid difference with the GOCO03S's standard deviation implies significant improvement north of 60°N, and no improvement south of 60°N by increasing the modification degree from $L = 150$ to 180. In addition, the standard deviation from EGM2008 appears somewhat pessimistic when being compared with the RMS geoid difference shown in Table 1 considering the same terrestrial gravity data have been used for EGM2008.

5 GPS-Levelling Test

To further validate the improvement of GOCO03S over the terrestrial gravity data for different SH bands, the geoid models have been developed by increasing the modification degree of the Stokes kernel from $L = 150$ to 240. Two other GOCE-based models of release-3 have been used for comparisons: TIM03S (Mayer-Güerr et al. 2012), and DIR03S (Bruinsma et al. 2011). Results from the GPS-levelling test are shown in Fig. 5. The most significant improvements are in Newfoundland followed by the Yukon Territory and the Maritimes when comparing the cases of $L = 180$ and 150. These regions also correspond to relatively large geoid update by GOCO03S as shown in Table 1. Only a marginal improvement is seen over mainland Canada.

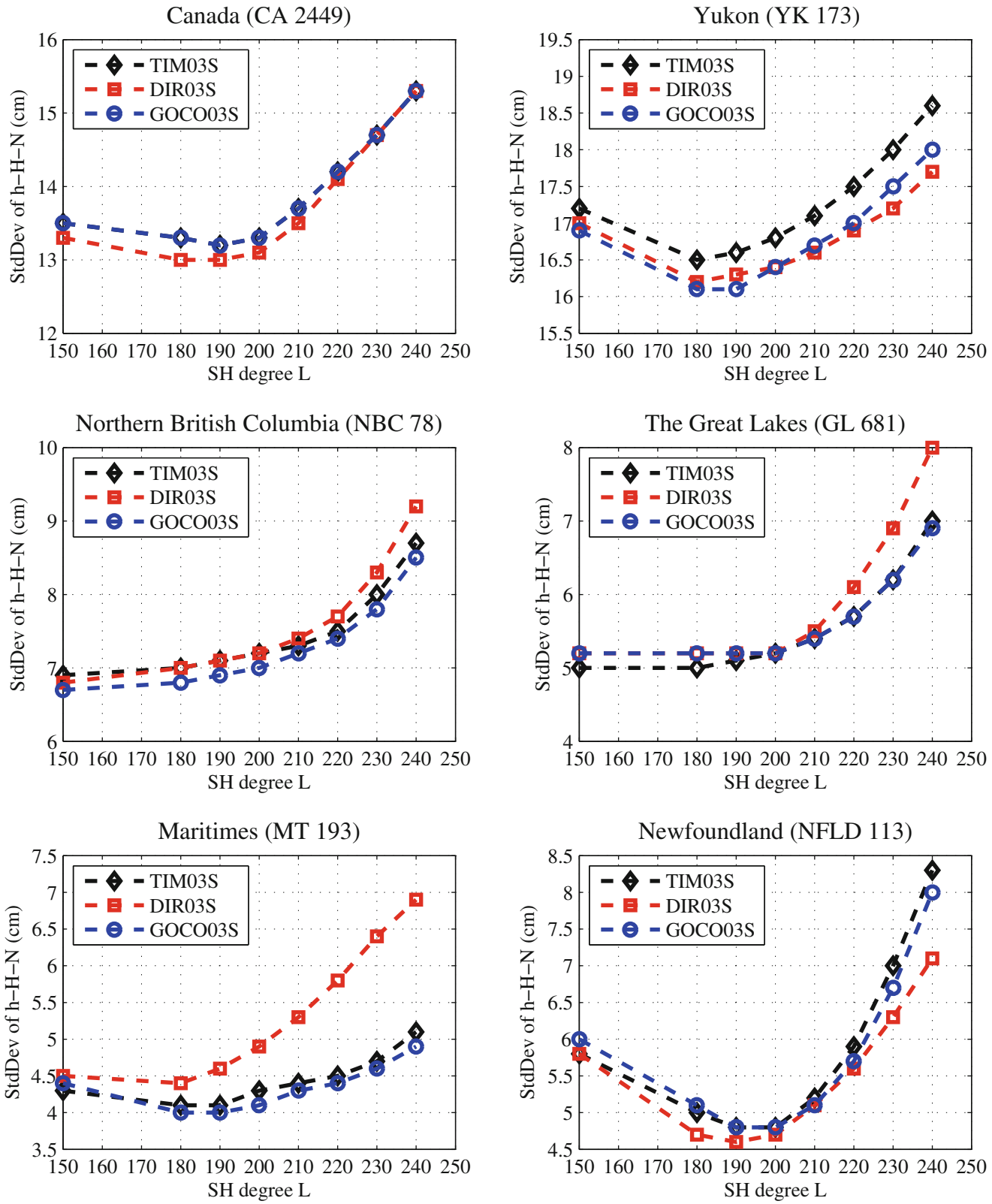

Fig. 5 The standard deviations of GPS-levelling-geoid ($h - H - N$) for mainland Canada (CA) and five regions: the Yukon Territory (YK), northern British Columbia (NBC), the Great Lakes (GL), the Maritimes (MT), and Newfoundland (NFLD). Numbers of GPS-levelling points are given between *round brackets* for each region (Unit: cm)

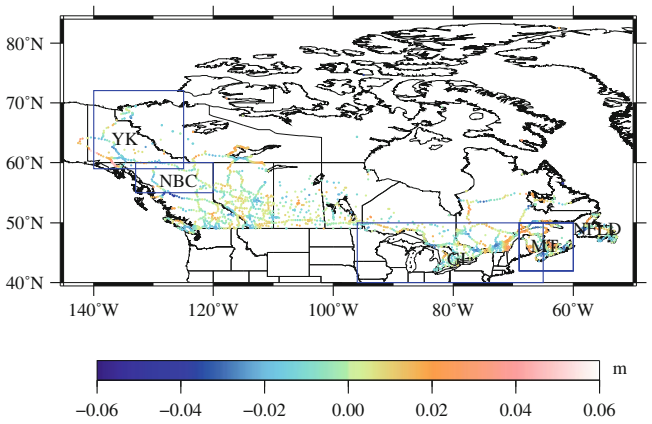

Fig. 6 The $\Delta\beta_n$-scaled geoid difference on the GPS-levelling points inferred from the difference between the gravity anomaly predicted from GOCO03S and the Canadian terrestrial gravity data for the SH band of degrees 90–180

The improvement continues till degree 200 (equivalent to a wavelength of 200 km) with respect to degree 150. With the increasing modification degree from $L = 210$ to 240, the agreement between the GPS-levelling data and the geoid models becomes worse reflecting rapid increase of GOCE model errors at higher degrees.

One exception is northern British Columbia where the large geoid update shown in Table 1 does not improve the agreement in the GPS-levelling comparison. In order to understand the reason, the RMS geoid difference on the GPS-levelling points between the cases of $L = 150$ and 180 is computed and shown in Fig. 6. It is 1.0 cm in contrast to 1.8 cm for all grid points in this region. Thus the RMS difference on the GPS-levelling points is neither representative, nor significant for this region when compared with the critical standard deviation of 1.4 cm. On the other hand, the RMS differences on the GPS-levelling points are relatively larger in other regions. They are 1.3 cm for mainland Canada, 1.9 cm for the Yukon Territory, 1.4 cm for the Great Lakes, 1.5 cm for the Maritimes, and 1.5 cm for Newfoundland. The RMS difference on the GPS-levelling points in the Great Lakes region is representative because of the homogeneous distribution of the GPS-levelling points in this region (see Fig. 6). However this difference is not significant enough to lead to a better agreement in the GPS-levelling comparison.

Among the three GOCE-based models, DIR03S performs the best in the GPS-levelling comparisons in mainland Canada and Newfoundland while GOCO03S is the best in the other sub-regions. This inconsistency makes it difficult to choose a model for the determination of the geoid in Canada. However the differences among GOCE-based models from each development team are expected to decrease with upcoming releases of GOCE models, and hopefully show further improvement in the GPS-levelling test.

Note that the GPS-levelling comparison is also affected by errors in the GPS and levelling data. The GPS ellipsoidal heights generally have an accuracy of 1–2 cm at most of the points, but can have an error of more than 10 cm for the GPS observations conducted before 1994. The levelling orthometric heights are as accurate as a few millimeters locally, but show a systematic error of about 30 cm from the eastern to western coasts. A further study is required to quantify the limit of the GPS-levelling data in validating the geoid improvement.

6 Summary

The comparison of the satellite model with terrestrial gravity data is an essential step to understand the quality of a satellite model, thereby enabling an optimal combination of the two data sets for regional geoid modelling. In this study, a Stokesian integral approach is suggested to compare the GOCE model with the Canadian terrestrial gravity data for a selected spherical harmonic band in terms of geoid height without being affected by the omission error of GOCE. A simulation test suggests that the geoid difference resulting from the two data sets can be estimated at the accuracy of 3 mm for the SH band of degrees 90 to 180, which is accurate enough for the comparison of interest.

As a case study, GOCO03S has been compared to the Canadian terrestrial gravity data for the spherical harmonic band between degrees 90 to 180. The resulting RMS geoid difference is 2.1 cm over Canada, which is significant when comparing it to the corresponding geoid standard deviation of about 1.0 cm from GOCO03S. The difference is larger north of 60°N (2.5 cm) than south of 60°N (1.4 cm). Similar results are given when using other GOCE-based models: TIM03S and DIR03S. These results suggest that the GOCE model improves the Canadian geoid model north of 60°N , but not south of 60°N when being used up to spherical harmonic degree as high as 180.

The GPS-levelling test shows that the better agreement can be achieved in the Yukon Territory, the Maritimes, and Newfoundland when using the GOCE-based models up to spherical harmonic degree 180. However it does not confirm any better agreement over the rest of Canada due to the limited sensitivity of the GPS-levelling data and the high quality of the Canadian terrestrial gravity data for the spherical harmonic band beyond degree 150. It is worth noting that the differences among the GOCE models of release-3 are still significant.

Acknowledgements This is the Earth Science Sector contribution 20120315 of Natural Resources Canada. We want to thank Pascal Willis and three anonymous reviewers for their constructive comments. The Generic Mapping Tools (GMT) were used to produce Figs. 3, 4 and 6 (Wessel and Smith 1998).

References

Bruinsma SL, Marty JC, Balmino G et al. (2011) GOCE gravity field recovery by means of the direct numerical method. Presented at the ESA Living Planet Symposium, 27th June–2nd July 2010, Bergen. See also earth.esa.int/GOCE

Ellmann A, Vanícěk P (2007) UNB application of Stokes-Helmert's approach to geoid computation. J Geodyn 43:200–213

Förste C, Bruinsma S, Shako R et al. (2011) A new combined global gravity field model including GOCE data from the collaboration of GFZ-Potsdam and GRGS-Toulouse. In: EGU General Assembly 2011, 3–8th April

Gruber T, Visser P, Ackermann C, Hosse M (2011) Validation of GOCE gravity field models by means of orbit residuals and geoid comparisons. J Geod 85:845–860. doi:10.1007/s00190-011-0486-7

Hirt C, Featherstone WE, Marti U (2010) Combining EGM2008 and SRTM/DTM2006.0 residual terrain model data to improve quasi-geoid computations in mountainous areas devoid of gravity data. J Geod 84(9):557–567. doi:10.1007/s00190-010-0395-1

Huang J, Véronneau M (2013) Canadian gravimetric geoid model 2010. J Geod 87(8):771–790

Huang J, Véronneau M, Mainville A (2008) Assessment of systematic errors in the surface gravity anomalies over North America using the GRACE gravity model. Geophys J Int 175:46–54. doi:10.1111/j.1365-246X.2008.03924.x

Ince ES, Sideris MG, Huang J, Véronneau M (2012) Assessment of the GOCE global gravity models in Canada. Geomatica 66(2):125–140

Mayer-Güerr T, Rieser D, Höck E et al. (2012) The new combined satellite only model GOCO03s. In: GGHS 2012, Venice. See also http://www.goco.eu/

Pail R, Bruinsma S, Migliaccio F et al. (2011) First GOCE gravity field models derived by three different approaches. J Geod 85:819–843. doi:10.1007/s00190-011-0467-x

Pavlis NK, Holmes SA, Kenyon SC, Factor JK (2012) The development and evaluation of the Earth Gravitational Model 2008 (EGM2008). J Geophys Res 117(B04406). doi:10.1029/2011JB008916

Pavlis NK, Holmes SA, Kenyon SC, Factor JK (2013) Correction to the development and evaluation of the earth gravitational model 2008 (EGM2008). J Geophys Res. doi:10.1002/jgrb.50167

Rummel R (2011) Preface. J Geod 85:747. doi:10.1007/s00190-011-0499-2

Tapley BD, Bettadpur S, Watkins M, Reigber C (2004) The gravity recovery and climate experiment: mission overview and early results. Geophys Res Lett 31(9):L09607. doi:10.1029/2004GL019920

Wenzel HG (1982) Geoid computation by least-squares spectral combination using integration kernels. In: Nakagawa I, Kasahara K, Tanaka T (eds) Proceedings of IAG general meeting, The Geodetic Society of Japan, Tokyo, pp 438–453

Wessel P, Smith WHF (1998) New, improved version of the generic mapping tools released, Eos Trans AGU 79(47):579. doi:10.1029/98EO00426

Part III

Future Gravity Field Missions

New Approach to Estimate Time Variable Gravity Fields from High-Low Satellite Tracking Data

N. Zehentner and T. Mayer-Gürr

Abstract

Estimating the time-variable gravity field signal has become an important task in climate research. Different scientific communities rely on the produced time series of gravity field information to investigate for example ice melting, changes in water storage or the effects of heavy earthquakes. Today the only measurement system which can provide these gravity field solutions without any constraints is the satellite mission GRACE (Gravity Recovery and Climate Experiment). Therefore it would be of interest to prolong the current time series by another technology. A method to estimate the gravity field is based on the kinematic orbit positions of a satellite. These positions are determined using the Global Positioning System. This method is well known and is widely used as a supplement to other measurement technologies. But present orbit estimates are degraded by systematic effects which affect the long-wavelength components of the gravity field estimation. Especially these frequencies are of concern for investigating variations in the Earth's gravity field. If these systematic effects are reduced it should be possible to generate a time series of gravity field solutions similar to those available today. To improve the orbit accuracy we introduce a new approach to estimate kinematic orbit positions based on raw observations. This contribution presents this method and first results based on real data.

Keywords

Kinematic orbit • Precise orbit determination • Raw observations • Time variable gravity field

1 Introduction

Mass variations in the system earth are of special interest for climate research, see e.g. Frappart and Ramillien (2012), Güntner (2008), Ramillien et al. (2008), or Kusche et al. (2012). Therefore a continuous time series of gravity field estimations is needed. Currently the GRACE (Gravity Recovery And Climate Experiment) (Tapley et al. 2004) satellite mission provides a continuous time series of monthly gravity fields. GRACE is in orbit for more than a decade and has outlived the originally planned mission life-time. A follow-on mission is under preparation, but a second method to observe variations in the earth's gravity field would be highly interesting. GRACE relies on the highly accurate microwave measurements between the two satellites. A different method to estimate the gravity field is based on kinematic orbit positions. Different approaches exist, see for example Beutler et al. (2010), Mayer-Gürr (2006), Gerlach et al. (2003) and Reubelt et al. (2003). These methods were used for the former satellite mission CHAMP (Challenging Minisatellite Payload) (Reigber et al. 2002) and are still used as supplement technology in case of GRACE and GOCE (Gravity Field and Steady-State Ocean Circulation Explorer) (Drinkwater et al. 2006). This method is therefore well established and investigated. It is

N. Zehentner (✉) • T. Mayer-Gürr
Institute of Theoretical Geodesy and Satellite Geodesy, Graz University of Technology, Steyrergasse 30/III, 8010 Graz, Austria
e-mail: zehentner@tugraz.at; mayer-guerr@tugraz.at

U. Marti (ed.), *Gravity, Geoid and Height Systems*, International Association of Geodesy Symposia 141,
DOI 10.1007/978-3-319-10837-7_14,

especially suited for estimating the long wavelength terms of the Earth's gravity field which are of special interest concerning their variations. But the accuracy of solutions merely based on kinematic orbit information is not sufficient to extract time variations on short time scales like weeks or months without constraints. The reasons for this are mainly unmodeled systematic effects which affect the estimation of positions. The position determination is done by using GNSS (Global Navigation Satellite System) observations, e.g. from the Global Positioning System (GPS). In combination with precise GPS satellite orbits and clock information these observations are then used to compute the orbit of the LEO (low earth orbiter) satellite. Currently used methods are in general based on observation combinations. On the one hand different observation types are linearly combined to e.g. the ionosphere-free and on the other hand differences are formed between transmitters, receivers or epochs. These combinations are formed to account for different systematic effects.

With this work we introduce a new approach which is based on the principle to directly use the observations as they are collected by the receiver. All measurements are included in a least-squares adjustment and all influences are either corrected beforehand by using state-of-the art models or additional parameters are added to the observation equation. The mathematical formulation of the approach is presented along with some first results based on GRACE data. Our results show the actual state of research and give a promising outlook for the future.

2 Current Situation

We have used GOCE precise kinematic orbits to produce monthly gravity field estimates. These orbits are generated at the Astronomical Institute of the University of Bern (AIUB) (Bock et al. 2011) and published as official orbit product in the frame of ESA's (European Space Agency) GOCE High-level Processing Facility (EGG-C 2010). All gravity field estimations were conducted using the acceleration approach (Reubelt et al. 2003). The solution displayed in Fig. 1 is based on a dataset for October 2010.

From Fig. 1 it can be seen that there are some major deviations in the equatorial region, obviously related to the earth's geomagnetic equator. The cause for this deviations is not yet clear and must be examined separately. But at this point we only want to show that there are systematic deficiencies in current orbit products. This fact currently prevents the estimation of time variable gravity fields from satellite-to-satellite tracking in high-low mode (SST-hl). If the GOCE

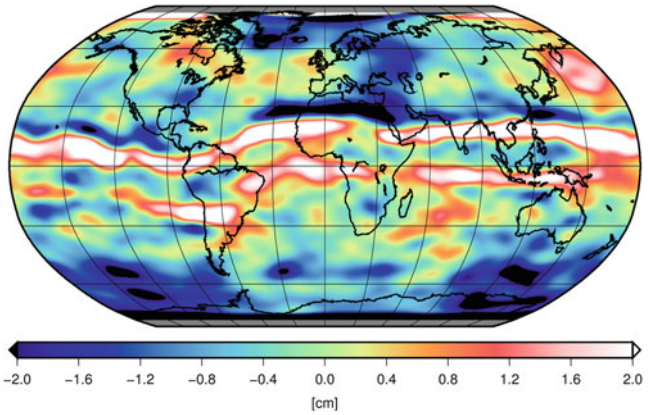

Fig. 1 Difference of GOCE monthly gravity field estimation for October 2010 with respect to the static gravity field GOCO02S (Goiginger et al. 2011). The differences are filtered with a Gaussian filter with a radius of 500 km

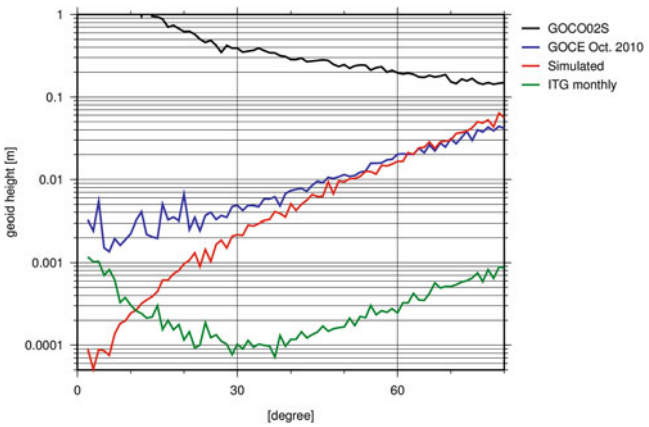

Fig. 2 Degree variances of GOCE monthly solution for October 2010 (*blue*), simulated monthly solution (*red*) and ITG-GRACE monthly (ITG-GRACE 2010) for October 2010 (*green*) (Color figure online)

monthly solution is displayed in terms of degree variances, compared to a simulation and the monthly gravity field signal derived from GRACE, these deficiencies are visible. This comparison is shown in Fig. 2.

Especially for low frequencies, for example up to degree ~25, the discrepancies between simulated and real data results are quite big. For the simulation only white noise, with a standard deviation of 5 mm, was assumed. In real case kinematic orbit positions are correlated in time but this fact can not fully explain the large differences between simulation and real data analysis, see also Jäggi et al. (2011). This indicates that there is the potential to improve current solutions. If this can be achieved monthly solutions will reach an accuracy regime which enables the resolution of time variable gravity field information.

3 Methods

3.1 Basic Concept

In principle the introduced approach is based on four basic rules:

– directly use all available observations
– no formation of differences or linear combinations
– correct all known influences beforehand
– include remaining influences as additional parameters

The first principle means that all available observations, including code- and phase-observations, are used in one least squares adjustment. The second principle addresses the usage of linear combinations or differences between observations. Today most approaches rely on the so-called ionosphere-free linear combination to reduce the influence of the ionosphere on the measurements. Or they use observation differences, in general single- or double-differences. By forming differences several errors are reduced. But both, linear combination and differencing of observations, have drawbacks, the measurement noise is increased and the number of available observations is reduced. The third point says that all known influences shall be corrected beforehand by using state-of-the-art models. This includes corrections for relativistic effects, phase wind-up, curved space time, antenna offsets and more (Kouba 2009; Hoffmann-Wellenhof et al. 2008). According to the fourth principle all other influences are included as additional parameters in the least-squares adjustment. This encloses parameters for the receiver position and clock error for each epoch, ionosphere, antenna center variations (ACV) and others.

Starting with the classical formulation of the observation equations for GPS measurements (Hoffmann-Wellenhof et al. 2008)

$$R = \rho + c\delta t \tag{1}$$

$$\Phi = \rho + c\delta t + \lambda N \tag{2}$$

where R denotes the code range, Φ the phase range, ρ the distance between receiver and transmitter, δt the receiver clock error, N the unknown number of ambiguities, λ the wavelength of the carrier frequency and c the light velocity. These equations can be extended to fulfill the four mentioned basic principles. The equations are now related to one receiver and one transmitter in particular, indicated by the indices i and j. Additional parameters are added for the ionospheric influence and for ACV for code- and phase-observations. As already mentioned all known influences are corrected beforehand, e.g. transmitter clock error. This modifications feature the following observation equations

$$R_i^j = \rho_i^j + c\delta t_i + I_i^j + CCV_i + CCV^j \tag{3}$$

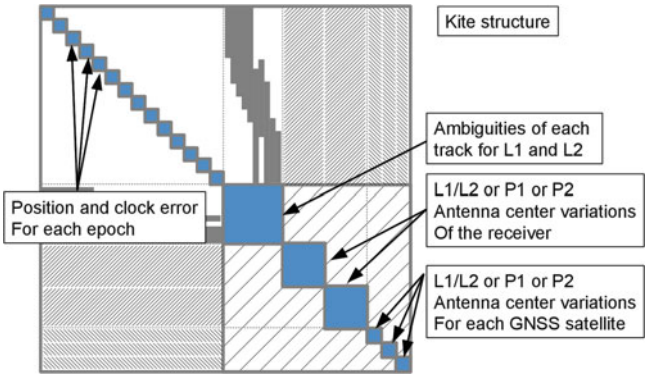

Fig. 3 Normal equation matrix with ACV added

$$\Phi_i^j = \rho_i^j + c\delta t_i + \lambda N - I_i^j + PCV_i + PCV^j. \tag{4}$$

The parameter I represents the ionospheric influence and is represented in terms of the TEC (total electron content) along the line of sight between a receiver and one transmitter per epoch, according to Hoffmann-Wellenhof et al. (2008).

Additional parameters added in Eqs. (3) and (4) are the *CCV* (code center variations) and the *PCV* (phase center variations). These two parameters account for the fact that the electronic center of the receiver antenna as well as for the transmitter antenna are not a physically defined point inside the antenna. Moreover this center depends on the direction of reception or transmission. For sake of completeness it should be mentioned that ρ contains the unknown coordinates of the receiver.

Based on Eqs. (3) and (4) the system of normal equations can be set up. To keep the dimension of the normal equation matrix small the ionosphere parameter I is eliminated beforehand by means of parameter elimination on the basis of the design matrix. If the parameters are sorted in a sense that epoch dependent ones are grouped and non-epoch dependent are grouped this features a normal equation matrix with a so-called kite structure. If additionally to the epoch parameters and the two ambiguities ACV are included the structure is extended by additional blocks on the right side of the matrix as shown in Fig. 3.

3.2 Parametrization of Receiver ACV

Receiver ACV are known in the context of precise point positioning or global reference networks. They are represented as azimuth and elevation dependent corrections given on a regular grid with e.g. a 1° spacing. We want to include the estimation of ACV into the least squares adjustment with a homogenous parametrization. Due to the fact that the reception area of a receiver antenna is more or less a

hemisphere it is possible to use spherical harmonics to model the variations.

$$ACV(\alpha, E) = \sum_{n=2}^{N} \sum_{m=0}^{n} (c_{nm} \cos(m\alpha) P_{nm}(\cos E) + \\ + s_{nm} \sin(m\alpha) P_{nm}(\cos E)). \quad (5)$$

Due to the fact that only one hemisphere is covered with observations the expansion must be restricted to harmonics symmetric to the equator. This can be formulated by the relation that $n-m$ must be an even number. According to (5) ACV depend on the azimuth α and the elevation E. P_{nm} are the associated Legendre polynomials and c_{nm} and s_{nm} are the corresponding coefficients which are estimated. The first summation starts with $n = 2$ due to the fact that degree 0 and 1 are not estimable, because they correspond to a constant value fully correlated to the receiver clock error respectively to an unchanged coordinate origin which is equivalent to a change in satellite position. In contrast to the representation by corrections on a regular grid this parametrization features a constant spatial resolution for the whole hemisphere.

3.3 Parametrization of Transmitter ACV

Similar to ACV for receivers also the transmitting antenna has an electronic center to which the measurements are related. But again this electronic center is not a physically defined point inside the antenna. It also depends on the direction of signal emission given as azimuth and nadir angle. A big difference however is the field of view. In case of a GPS satellite the field of view is restricted to a view angle of approximately 17° around the nadir direction. 14° is sufficient for receivers on the earth's surface, but in case of LEOs the field of view extends to ~17°, depending on the orbit altitude of the LEO. There are ACV for GPS satellites provided by the IGS (International GNSS Service) (Dow et al. 2009; Schmid et al. 2007), but they are only given as nadir dependent values. Additionally these corrections are only given up to a nadir angle of 14° and only Block specific values are available. We want to include the estimation of these variations into the least squares adjustment. In this case a representation by spherical harmonics is not applicable, because the area covered with observations is too small for a spherical harmonic expansion. We choose radial basis functions on a regular grid. First of all they can be scaled to fit the desired resolution and secondly by using a regular distribution the amount of parameters can be minimized. The whole expansion is given as

$$ACV(\alpha, E) = \sum_{i=1}^{I} a_i \Phi_i(\cos\psi). \quad (6)$$

The radial basis functions are given by

$$\Phi_i(\cos\psi) = \sum_{n=2}^{N} \sqrt{2n+1} \cdot P_n(\cos\psi). \quad (7)$$

a_i denotes the estimated parameters each associated to one basis function which are named Φ_i and are based on the Legendre polynomials P_n up to a maximum degree N. ψ denotes the spherical distance between the center of a basis function Φ_i and the actual direction represented by azimuth α and nadir angle E. The distribution type for localization of the basis functions can be chosen arbitrarily. We choose the so called triangle vertex grid as described by Eicker (2008).

3.4 Raw Observation Zero Difference Approach

In Sect. 3.1 a new approach for kinematic position estimation is introduced. This concept differs from currently used approaches in a few aspects.

1. All observation types are used directly in one least squares adjustment.
2. Ambiguities are estimated for each track of phase observations, e.g. for L1 and L2 individually. Integer nature of the ambiguities is preserved and suited for fixing.
3. Antenna center variations are estimated not only for phase observations but also for code observations.
4. New observation types can be included by just setting up the observation equation.

4 Results

Based on GPS observation data from the two GRACE satellites orbit positions were estimated and subsequently used to estimate monthly gravity fields covering the period from May until December 2008. The exemplary presented solution is May 2008. The raw observation data was taken from the GRACE level 1B dataset (Case et al. 2010). As precise GPS orbit and clock information the final precise orbit and clock corrections from CODE (Dach et al. 2009) were used. The orbit positions are given in a 15 min interval and the clock corrections are given at a 5 s sampling. Based on these input data, orbit positions were estimated for each day with a sampling of 0.1 Hz. In a first step the solutions were estimated along with the parameters for ACV for receivers as well as transmitters. For estimating the ACV epoch dependent parameters were eliminated and then the individual daily solutions were accumulated on the basis of normal equations for the time span of May-December 2008. Individual ACV were estimated for the two receivers and each GPS satellite.

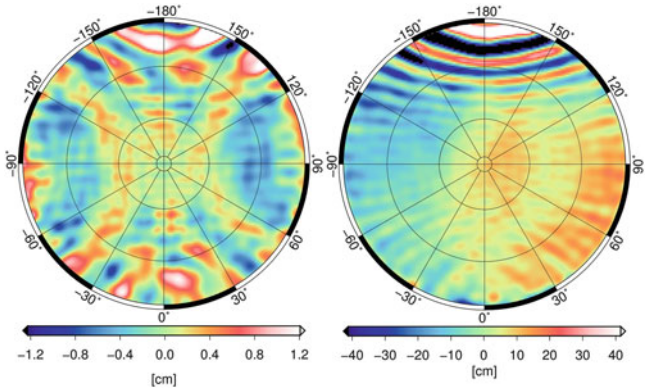

Fig. 4 Antenna center variations for receiver on-board of GRACE A with elevation above 10°. L1 and L2 common phase observation correction (*left*) and P1 code observation correction (*right*)

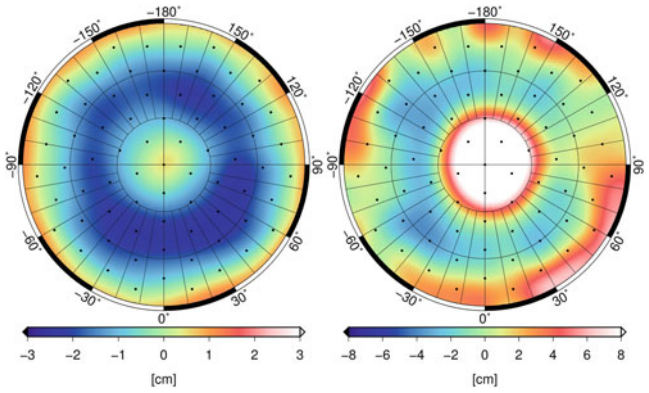

Fig. 5 Antenna center variations for GPS satellite PRN 23 (Block IIR-B) with a nadir angle <15°. Common L1 and L2 phase observation correction (*left*) and P1 code observation correction (*right*). *Black dots* show the locations of the used radial basis functions

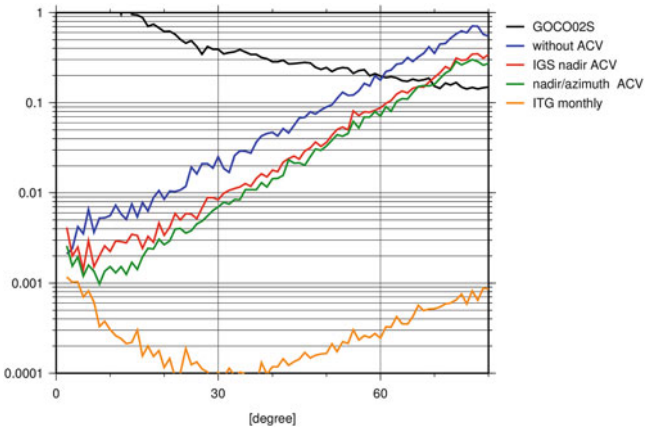

Fig. 6 Degree error variances of ITSG solution May 2008, without any ACV (*blue*), with receiver ACV and IGS nadir dependent transmitter ACV (*red*) and with receiver ACV and nadir-azimuth dependent transmitter ACV (*green*) applied. For comparison ITG-GRACE monthly for May 2008 (*orange*) is displayed to show the expected time variable gravity field signal (Color figure online)

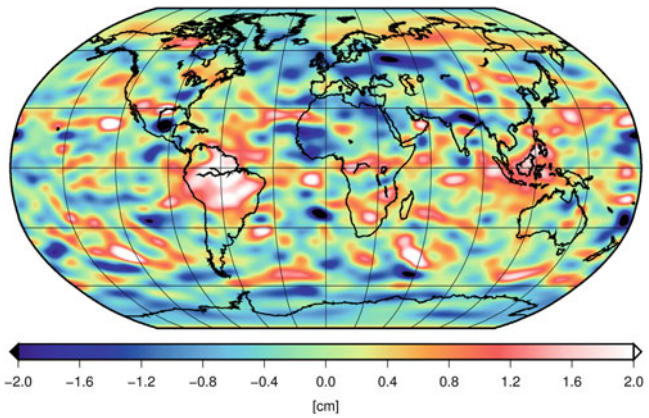

Fig. 7 Difference of ITSG solution May 2008 to GOCO02S in terms of geoid height. Gaussian filter with a radius of 500 km applied

In particular a combined parameter set for L1 and L2 phase observation was estimated as well as individual sets for P1 and P2 code observations. For L1 and L2 only a common correction can be estimated. Due to the high correlation of parameters a separate estimation of ACVs gives unreasonable results. By iteration these corrections were refined four times. With the gained corrections for receivers and transmitters the final orbit estimation was computed. An important part of the estimation process is weighting of the individual observations. Therefore a modified M-Huber estimator (Koch 1999) was used to determine the weight for code and phase observations separately for each epoch and each observed transmitter. The weight of an observation is changed if the estimated standard deviation exceeds the 3-sigma level. Due to the used weighting method no explicit outlier detection has to be done. Exemplary results of ACV are displayed in Fig. 4 for the receiver of GRACE A and in Fig. 5 for the GPS transmitter antenna of satellite PRN 23.

The final solution includes ACV for receivers and transmitters. Additionally a solution with application of IGS nadir-dependent receiver ACV was produced to see the impact on the final gravity field estimation. Figure 6 shows degree error variances of these two solutions along with a solution without any ACV applied. From Fig. 6 it can be seen that the introduction of receiver ACV has a huge effect on the accuracy of the gravity field estimation. The introduction of azimuth-nadir-dependent transmitter ACVs further improves the solution, especially in the low degrees.

For degrees 2–8 the comparison shows that the degree variances of the solution are in the same regime as the expected signal strength. This fact gets even more obvious when looking at the solution in spatial domain as shown in Fig. 7. From this comparison with a static gravity field it can be seen that the most prominent time variable gravity field signal, the amazon river basin, is visible. Besides the amazon basin no other known signal is visible. This is due to the fact that they all have lower amplitudes and are therefore covered

by the noise of the solution. This problem could be reduced by using more observations e.g. data from several satellite missions like the upcoming SWARM satellites. Also the orbit estimation based on the introduced method is not yet mature. But the presented results give a good perspective how the introduced method could bring us to the goal of estimating time variable gravity field solutions based simply on orbit positions. This approach could then be a possibility to close the gap between GRACE and a GRACE follow-on mission.

5 Discussion and Outlook

We presented a new approach to estimate kinematic orbit positions for LEO satellites. The idea is to fully exploit the available observations without forming linear combinations or differences. Sources of influence are included in the estimation by adding additional parameters. The proposed method is well suited for upcoming challenges in the context of a modernized GNSS signal structure. We also presented first results with GRACE data, which give an impression on what can be achieved with this method.

References

Beutler G, Jäggi A, Mervart L, Meyer U (2010) The celestial mechanics approach: application to data of the GRACE mission. J Geod 84:661–681. doi:10.1007/s00190-010-0402-6

Bock H, Jäggi A, Meyer U, Visser P, van den IJssel J, van Helleputte T, Heinze M, Hugentobler U (2011) GPS-derived orbits for the GOCE satellite. J Geod 85:807–818. doi:10.1007/s00190-011-0484-9

Case K, Kruizinga G, Wu S (2010) GRACE level 1B data product user handbook. Jet Propulsion Laboratory, California Institute of Technology. http://podaac.jpl.nasa.gov/gravity/grace-documentation

Dach R, Brockmann E, Schaer S, Beutler G, Meindl M, Prange L, Bock H, Jäggi A, Ostini L (2009) GNSS processing at CODE: status report. J Geod 83:353–365. doi:10.1007/s00190-008-0281-2

Drinkwater MR, Haagmans R, Muzi D, Popescu A, Floberghagen R, Kern M, Fehringer M (2006) The GOCE gravity mission: ESA'S first core earth explorer. In: Proceedings of the 3rd international GOCE user workshop, ESA Special Publication, SP-627, Frascati, pp. 1–8. ISBN 92-9092-938-3

Dow J, Neilan RE, Rizos C (2009) The international GNSS service in a changing landscape of global navigation satellite systems. J Geod 83(3–4):191–198. doi:10.1007/s00190-008-0300-3

EGG-C (2010) GOCE level 2 product data handbook. European GOCE gravity consortium. https://earth.esa.int/web/guest/missions

Eicker A (2008) Gravity field refinement by radial basis functions from in-situ satellite data. University of Bonn. http://hss.ulb.uni-bonn.de

Frappart R, Ramillien G (2012) Contribution of GRACE satellite gravimetry in global and regional hydrology and in ice sheet mass balance. In: Nayak P (ed) Water resources management and modeling. InTech Publishing, Crotia, ISBN 978-953-51-0246-5

Gerlach Ch, Sneeuw N, Visser P, Svehla D (2003) CHAMP gravity field recovery using the energy balance approach. In: Advances in geoscience, vol 1. Springer, Berlin, pp 73–80

Goiginger H, Rieser D, Mayer-Guerr T, Pail R, Fecher T, Gruber T, Albertella A, Maier A, Höck E, Krauss S, Hausleitner W, Baur O, Jäggi A, Meyer U, Brockmann JM, Schuh WD, Krasbutter I, Kusche J (2011) The satellite-only global gravity field model GOCO02S. EGU - General Assembly 2011. www.goco.eu

Güntner A (2008) Improvements of global hydrological models using GRACE data. In: Surveys in geophysics, vol 29. Springer, Netherland, pp 375–397. doi:10.1007/s10712-008-9038-y

Hoffmann-Wellenhof B, Lichtenegger H, Wasle E (2008) GNSS - Global navigation satellite systems. Springer, Vienna. ISBN 978-3-211-73012-6

ITG-GRACE (2010). http://www.igg.uni-bonn.de/apmg Universität Bonn - IGG

Jäggi A, Prange L, Hugentobler U (2011) Impact of covariance information of kinematic positions on orbit reconstruction and gravity field recovery. In: Advances in space research, vol 47. Elsevier B.V., Amsterdam, pp 1472–1479. doi:10.1016/j.asr.2010.12.009

Koch KR (1999) Parameter estimation and hypothesis testing in linear models. Springer, Berlin. ISBN 3-540-65257-4

Kouba J (2009) A guide to using International GNSS Service (IGS) products. Geodetic Survey Division, Natural Resources Canada. http://igscb.jpl.nasa.gov/components/usage.html

Kusche J, Klemann V, Bosch W (2012) Mass distribution and mass transport in the Earth system. J Geodyn 59–60:1–8. doi:10.1016/j.jog.2012.03.003

Mayer-Gürr T (2006) Gravitationsfeldbestimmung aus der Analyse kurzer Bahnbögen am Beispiel der Satellitenmissionen CHAMP und GRACE. University of Bonn. http://hss.ulb.uni-bonn.de

Ramillien G, Bouhours S, Lombard A, Cazenave A, Flechtner F, Schmidt R (2008) Land water storage contribution to sea level from GRACE geoid data over 2003–2006. In: Global and planetary change, vol 60. Elsevier B.V., Amsterdam, pp 381–392. doi:10.1016/j.gloplacha.2007.04.002

Reigber Ch, Lühr H, Schwintzer P (2002) CHAMP mission status. In: Advances in space research. vol 30. Elsevier B.V., Amsterdam, pp 129–134. doi:10.1016/S0273-1177(02)00276-4

Reubelt T, Austen G, Grafarend E.W. (2003) Harmonic analysis of the Earth's gravitational field by means of semi-continuous ephemerides of a low Earth orbiting GPS-tracked satellite. Case study: CHAMP. J Geod 77:257–278. doi:10.1007/s00190-003-0322-9

Schmid R, Steigenberger P, Gendt G, Ge M, Rothacher M (2007) Generation of a consistent absolute phase center correction model for GPS receiver and satellite antennas. J Geod 81:781–798. doi:10.1007/s00190-007-0148-y

Tapley BD, Bettadpur S, Watkins M, Reigber C (2004) The gravity recovery and climate experiment: Mission overview and early results. Geophys Res Lett 31(9). doi:10.1029/2004GL019920

Status of the GRACE Follow-On Mission

Frank Flechtner, Phil Morton, Mike Watkins, and Frank Webb

Abstract

The Gravity Recovery and Climate Mission (GRACE) has been so far the only satellite mission capable of monitoring mass variations in the Earth system and has made many breakthroughs in the understanding of Earth system dynamics. The mission has been operating for over 10 years at the time of this paper. Expected end of mission is dependent on future solar activity, instrument conditions and—most likely—on the battery health. Due to the extreme success of GRACE in many Earth science disciplines there was a long-standing strong request by the user community to launch a GRACE Follow-On (GRACE-FO) mission as soon as possible to extend the GRACE mass transport time series with the minimum practical data gap between both missions. GRACE-FO has in fact been approved by the NASA and German ministries BMBF (Federal Ministry of Education and Research) and BMWi (Federal Ministry of Economics and Technology), and will be implemented under US-German partnership. GRACE-FO entered Phase-A in January 2012 and Phase-B in September 2012. The current target launch date is August 2017. This paper summarizes the status of the various mission elements.

Keywords

GRACE • GRACE-FO • Time-variable gravity field • Mass transport

1 Background

The Gravity Recovery and Climate Experiment (GRACE) US/German twin satellite constellation (Tapley et al. 2004) has been so far the only mission capable of monitoring mass variations in the Earth system. GRACE provides monthly gravity field models down to a spatial resolution of about 400 km. During its primary mission and continuing now in its extended mission, the analysis and interpretation of GRACE data have led to many breakthroughs in the understanding of the dynamics in the Earth system (Cazenave and Chen 2010; Zlotnicki et al. 2013). Prominent examples include

- Observation of the continental water storage change, which results from the sum of precipitation, evaporation, runoff and infiltration. This enabled the monitoring of the season-dependent changes in the major river basins, as well as huge groundwater extraction due to irrigation e.g. in India or California.
- Quantification of the polar ice-sheet and mountain glacier mass balance and their contribution to global sea-level rise. In particular, GRACE measurements have confirmed the substantial ice mass loss of the Greenland and West Antarctica ice-sheets. Additionally, the determination of ocean mass change (due to ice melt) allowed separation of steric (due to global warming) sea-level change from the total sea-level measured by satellite radar altimetry, although these results are still influenced by global isostatic adjustment (GIA) uncertainties.

F. Flechtner (✉)
GFZ German Research Centre for Geosciences, c/o DLR Oberpfaffenhofen, 82230 Wessling, Germany
e-mail: flechtne@gfz-potsdam.de

P. Morton • M. Watkins • F. Webb
Jet Propulsion Laboratory, California Institute of Technology, Pasadena, CA, USA

U. Marti (ed.), *Gravity, Geoid and Height Systems*, International Association of Geodesy Symposia 141,
DOI 10.1007/978-3-319-10837-7_15,

- Observation of surface and deep ocean currents, which—in combination with the sea surface topography derived from satellite altimetry—has brought a much better understanding of the global ocean circulation and thus the heat transport from the equator toward the poles.
- Observation and geophysical interpretation of co-/post-seismic deformation in the solid Earth following large earthquakes, including the Sumatra-Andaman (2004), Chilean Maule (2010) and Japan Tohoku-Oki (2011).

These results are based on the 10+ year time series of monthly estimates of the global gravity field of the Earth. All GRACE instruments are still producing nominal high quality observation data, the solar activity is still moderate and the fuel consumption is still better than predicted. Therefore, a mission lifetime of GRACE could in principle be through 2015 or beyond, but unfortunately, the batteries on both satellites are degrading and as a consequence the accelerometer (to observe non-gravitational forces such as atmospheric drag or solar radiation pressure), Instrument Control Units, and the Microwave Assembly (part of the K-band inter-satellite ranging system) have to be powered off during the maximum eclipse season, thus interrupting the nominal science data flow every 161 days for a period of approximately 3–4 weeks. Further information on the GRACE mission status is provided at http://www.csr.utexas.edu/grace/operations/mission_status.

Due to the tremendous success of GRACE data in many Earth science disciplines there has always been a long standing strong request by the international user community to launch a GRACE Follow-On (GRACE-FO) mission as fast as possible to extend the mass flux time series with the minimum practical data gap between both missions. GRACE-FO has been approved to be implemented under US-German partnership. The overall mission management and satellite and instrument responsibility is by the Jet Propulsion Laboratory (JPL) which will procure the satellite buses and accelerometers, provide the microwave instrument, the GNSS receiver, and a significant portion of a joint laser ranging interferometer (LRI). Germany will provide the launch vehicle, perform mission operations, participate in the joint Science Data System (SDS) and will provide major contributions to the joint LRI. All German contributions are managed by the German Research Centre for Geosciences (GFZ). The NASA/GFZ partnership will be described in a Memorandum of Understanding (MOU) and the roles and responsibilities in a Cooperative Project Plan (CPP). GRACE-FO passed the Mission Concept Review (MCR) in October 2011 and entered Phase-A in January 2012. A combined System Requirements Review and Mission Design Review (SRR/MDR) was successfully passed in July 2012 enabling entry into Phase B in September 2012. The Preliminary Design Review will be in January 2014. The technical baseline for the spacecrafts and the instruments has been refined and is in place, major suppliers are on contract and all inheritance reviews have been completed. In the following the status of the various mission elements is summarized.

2 GRACE-FO Mission Objectives

The primary objective of the GRACE-FO mission is to continue the record of climate change observations established by GRACE by extending the time series of high-resolution monthly global models of the Earth's gravity field for an additional 5 years. The current target launch date is August 2017.

The secondary GRACE-FO objectives are to

a) demonstrate the effectiveness of a laser ranging interferometer (LRI) in improving low-low SST (satellite-to-satellite tracking) measurement performance which is directly linked to the accuracy of the derived gravity field models. The LRI (see also below) will be the first ever inter-spacecraft laser interferometer and should lead to improved spatial and temporal resolution for future gravity missions, such as GRACE-II, although the final resolution will depend on aliasing or number of satellite pairs, and
b) continue measurements of GRACE radio occultations for operational provision of e.g. vertical temperature or humidity profiles to numerical weather services.

3 Satellite Bus

The twin satellites will be built again by Astrium GmbH (Friedrichshafen/Germany) and are based on GRACE and SWARM [Friis-Christensen et al. 2007] heritage (third generation flex bus system). A combination of the natural improvements in the flex bus line, plus targeted modifications to the thermal control system and reduction in satellite seismicity together should make the GRACE-FO bus platform significantly better than the GRACE one and will likely translate into more accurate SST observations for GRACE-FO.

4 Instruments

To reach the primary mission objectives, the GRACE-FO instrumentation (see Fig. 1) is based on GRACE heritage with slight modifications due to both "lessons learned from GRACE", which includes an improved star camera configuration, a more reliable IMU, improved thermal control, and reduced spacecraft seismisity; and evolutionary heritage and technical modernization of the microwave instrument from

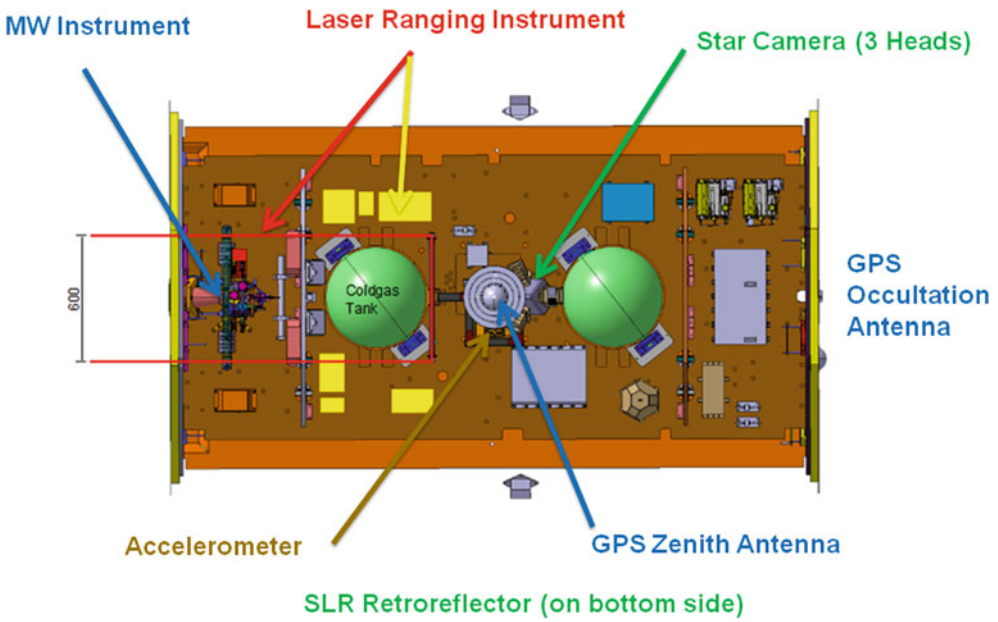

Fig. 1 The GRACE-FO satellite and instruments (shown from top, SLR retroreflector is located on the bottom of the spacecraft and is not shown)

GRAIL (Gravity Recovery and Interior Laboratory) (Zuber et al. 2012). This "baseline instrumentation" consists of

- a GNSS receiver, capable to track GPS and Galileo signals, for geo-location of measurements and long-wavelength gravity field determination,
- a SuperSTAR accelerometer as for GRACE procured at ONERA (France) to observe the non-gravitational forces,
- a Star Camera System as for GRACE procured at DTU (Denmark) for attitude determination. To improve GRACE-FO attitude determination, GRACE-FO will carry three (instead of only two in case of GRACE) star camera heads (see Fig. 1) and
- a third generation Microwave Instrument to produce the highly accurate inter-satellite ranging measurements using K- and Ka-band cross-links.

Additionally GFZ will provide Laser Retro-Reflectors (LRR) for each satellite for independent orbit determination and validation.

As stated above, the secondary mission objective is to operate a laser ranging interferometer (LRI) which shall be operated in parallel with the microwave ranging instrument. The LRI design is based on a so called "race track configuration" and is described in detail in (Sheard et al. 2012). The minimum instrument requirements ("mission success criteria") are a frequency dependent SST measurement noise σSST(f) of 500 nm/$\sqrt{Hz}$•NSF(f) (noise shape function) for a frequency bandwidth between 10 mHz and 100 mHz. The minimum operation time shall be 1 year. The goal is to decrease σSST(f) to 50 nm/$\sqrt{Hz}$•NSF(f) for a frequency bandwidth between 0.2 mHz and 100 mHz and to operate the LRI much longer than a year. As a result, the LRI would increase the K-band SST measurement accuracy by a factor of 5 and 50, respectively (see Fig. 2). For completeness the expected performance of the Laser Interferometer Space Antenna (LISA (ESA 2011)) is shown.

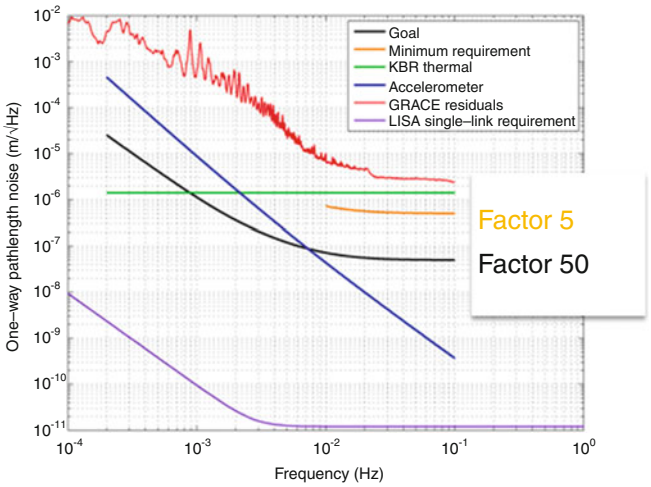

Fig. 2 Laser ranging instrument performance

5 Science Data

The GRACE-FO Level-0 science and housekeeping data will be routinely (2/day) provided by the Mission Operations Raw Data Center (RDC) to the Science Data System (SDS) in a rolling archive. As for GRACE, the GRACE-FO SDS will be implemented in a joint US/German collaboration

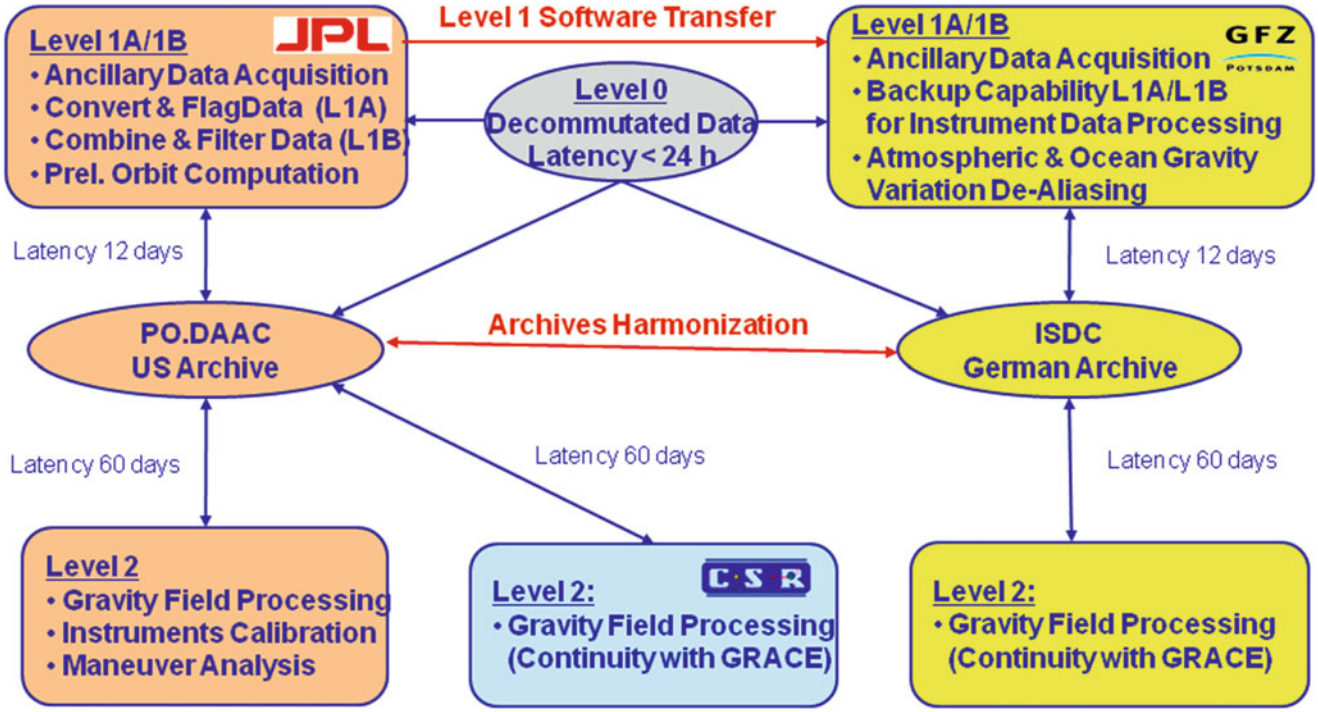

Fig. 3 GRACE FO science data system: overview and responsibilities

between JPL, UTCSR (University of Texas, Center for Space Research) and GFZ.

Figure 3 shows the overall approximate responsibilities to and the nominal time delay for Level-1 and Level-2 product generation. In contrast with GRACE, all Level-0 to Level-2 data will be made available (after validation) to the user community and will again be archived for long-term data preservation at JPL/PO.DAAC (Physical Oceanography Distributed Active Archive Center) and GFZ/ISDC (Information System and Data Center).

6 Launcher and Orbit

The GRACE-FO mission is due for launch in August 2017 into a target circular orbit with 490 km initial altitude and an inclination of 89°. Same as GRACE, the orbital parameters will not be maintained during the mission to allow for a varying ground track pattern. The launcher shall be either a ROCKOT (GRACE heritage) or a DNEPR depending on technical and budgetary constraints. A final decision is expected for Spring 2013.

7 Summary

The GRACE Follow-On mission will continue the high-resolution monthly global models of the Earth's gravity field of the original GRACE mission. Additionally it will carry a Laser Ranging Interferometer demonstrator to improve the inter-satellite distance measurement and consequently the accuracy and spatial resolution of the original GRACE gravity models. GRACE-FO is again jointly implemented in a US-German partnership. All major reviews have been successfully passed to this point and the project is currently on track for launch in 2017.

Acknowledgements The authors thank BMBF, BMWi, HGF (German Helmholtz Foundation) and DLR (German Aerospace Center) for providing funding and in kind contribution for the German GRACE-FO mission elements. (Part of) The research was carried out at the Jet Propulsion Laboratory, California Institute of Technology, under a contract with the National Aeronautics and Space Administration.

References

Cazenave A, Chen J (2010) Time-variable gravity from space and present-day mass redistribution in the Earth system. Earth Planet Sci Lett 298:263–274. doi:10.1016/j.epsl.2010.07.035

European Space Agency (2011) LISA – unveiling a hidden universe, assessment study report (Yellow Book), ESA/SRE(2011), 141 pp. http://sci.esa.int/science-e/www/object/index.cfm?fobjectid=48364#. Accessed 15 Mar 2013

Friis-Christensen E, Lühr H, Knudsen D, Haagmans R (2007) Swarm – an Earth observation mission investigating geospace. Adv Space Res 41:210–216. doi:10.1016/j.asr.2006.10.008

Sheard BS, Heinzel G, Danzmann K, Shaddock DA, Klipstein WM, Folkner WM (2012) Intersatellite laser ranging instrument for the GRACE follow-on mission. J Geod 86:1083–1095. doi:10.1007/s00190-012-0566-3

Tapley BD, Bettadpur S, Watkins MM, Reigber C (2004) The gravity recovery and climate experiment: mission overview and early results. Geophys Res Lett 31:9607–9613. doi:10.1029/2004GL019920

Zlotnicki V, Bettadpur S, Landerer FW, Watkins MM (2013) Gravity recovery and climate experiment (GRACE): detection of ice mass loss, terrestrial mass changes, and ocean mass gains. In: Orcutt J (ed) Earth system monitoring. Springer Science+Business Media, New York, NY, pp 123–152

Zuber MT, Smith DE, Lehman DH, Hoffman TL, Asmar SW, Watkins MM (2012) Gravity Recovery and Interior Laboratory (GRAIL): mapping the lunar interior from crust to core. Space Sci Rev. doi:10.1007/s11214-012-9952-7

Feasibility Study of a Future Satellite Gravity Mission Using GEO-LEO Line-of-Sight Observations

Jakob Schlie, Michael Murböck, and Roland Pail

Abstract

In this article the feasibility of gravity field determination with very high-low satellite-to-satellite tracking, as intended as part of the GETRIS ("Geodesy and Time Reference in Space") mission concept, is investigated. For this purpose several geostationary satellites (GEOs) are positioned around the Earth. A microwave system is used to determine the relative position between satellites in low Earth orbits (LEOs) and GEOs with very high accuracy, from which the gravity field of the Earth can be estimated.

This concept is simulated to retrieve the time-variable gravity field caused by temporal changes in continental hydrology. The simulation is based on simplified assumptions, taking only errors of the ranging instrument into account. The gravity field is recovered in a closed-loop environment from the simulated observations. Furthermore, the possibility of enhancing GRACE results with GEO-LEO tracking is investigated.

Overall the results show that the GEO-LEO concept is very promising, since it possibly reduces some of the weaknesses of the LEO-LEO tracking concept and measures the radial component of the Earth's gravity field. Due to the option of multi-satellite tracking, the time-variable gravity field might be observed within shorter time periods than with a single GRACE-like mission. However, more detailed simulations are required to draw final conclusions on the exact magnitude of benefit.

Keywords

Future gravity mission • GETRIS • GRACE destriping • Satellite geodesy • Satellite-to-satellite tracking • Time variable gravity

1 Introduction

For more than 10 years GRACE (Tapley et al. 2007) is providing time variable gravity fields to the scientific community. With these data significant scientific progress was possible in the field of Earth system sciences. GRACE helped to get a more precise understanding of the different processes of mass transport in system Earth and the energy exchange among the different domains of the Earth system (see, e.g., Ramillien et al. 2004; Tapley et al. 2004; Horwath and Dietrich 2009).

The GRACE battery capacity decreased during the long time in orbit, so that GRACE is not fully operational during long shadow passes. To provide continuity in the time variable gravity field data, a GRACE Follow-On satellite mission is scheduled for August 2017, and a wide range of possible future gravity mission concepts for the time following is under investigation.

The main disadvantage of a GRACE-like mission design is that the precise measurements are only taken in one direction, namely the line-of-sight, which is nearly the flight direction. This leads to the typical GRACE error structure

J. Schlie • M. Murböck • R. Pail (✉)
Institut für Astronomische und Physikalische Geodäsie
Technische Universität München, Munich, Germany
e-mail: j.schlie@tum.de; murboeck@bv.tu-muenchen.de; pail@bv.tum.de

U. Marti (ed.), *Gravity, Geoid and Height Systems*, International Association of Geodesy Symposia 141,
DOI 10.1007/978-3-319-10837-7_16,

as shown in Fig. 5. There are numerous filtering tools to reduce these errors and to extract as much signal as possible (see, e.g., Swenson and Wahr 2006; Werth et al. 2009), but filtering always causes a loss of information. Mission designs of future gravity missions consider modifications of the low-low SST (ll-SST) concept. One possible mission design is based on GRACE ll-SST, but with a periodic change of the relative satellite positions to get across-track measurements of the gravity field. However, this mission design of the so-called Pendulum configuration is more challenging from a technological point of view. Another design strategy is the so-called Peter-Bender configuration (Bender et al. 2008). It consists of two pairs of satellites with different inclinations. The combination of observations from both pairs provides results with reduced striping error structures compared to a single pair. Investigations are ongoing to find the best orbit parameters of the two pairs of satellites (Wiese et al. 2012).

This article is based on a different concept of SST, i.e. distance measurements from GEOs to LEOs with GRACE-like performance. To be able to measure the distance to a LEO at all times, a minimum of two GEOs located at opposite sides of the Earth is needed. From these distance measurements the time variable gravity field can be derived. This principle is the basis of the gravity field determination in the frame of the "geodesy and time reference in space" mission, whose main goals and mission architecture are described in the next section.

2 Mission Concept, Simulation Environment and Data

2.1 The GETRIS Mission

The GETRIS mission was proposed in response to the ESA invitation to tender (AO/1-6311-2010/F/WE). Main goals of the mission are:

- Provision of an accurate Space-based Geodesy Reference System with Navigation support to LEO Satellites
- Provision of an extremely accurate Time- and Frequency reference to space and ground users

at an unprecedented level of performance, with continuous availability at a significant lifetime.

To fulfill these objectives, several GEOs with a wide range of approved and new technologies on board shall be located around the Earth. Figure 1 shows the outlined mission architecture.

One main component on board the geostationary GETRIS satellites is the ACES module ("Atomic Clock Ensemble in Space"; Cacciapuoti and Salomon 2009; Hess et al. 2011). It consist of two atomic clocks and a microwave link for time transfer. With this module the time and frequency reference shall be realized.

Another main component of the GETRIS satellites is the distance measurement device. The range is measured by a microwave link or by the Laser Communication Terminal "Ranging and Time Transfer add-on Box" (LCT). This module is the basis for the GEO-LEO distance measurements, and thereby the basis for the gravity field determination. LCT shall allow distance measurements with a GRACE-like accuracy of 1 μm over nearly 30,000 km. A corresponding module is also needed on board the LEO satellites, and with a weight of only 5 kg and only 5 W power consumption it could easily be attached to various LEO missions.

2.2 Mission Simulation Environment

The simulations were done with a closed-loop simulator developed by Pail and Mayrhofer (2009). Figure 2 shows the working principle of the simulator. The input data are described in detail in Sect. 2.3. We based our studies on simplified Keplerian repeat orbits with eccentricity equal to zero and 10 s sampling. Detailed numerical studies (not presented here) have shown that this simplifying assumption has no major impact on the results and conclusions of this study. As input gravity field signals, arbitrary static and time-varying tidal and non-tidal gravity signal time series can be generated. In this study continental hydrology is considered as the target signal.

Several observation types can be simulated, such as high-low and low-low satellite to satellite tracking observations, and gravity gradients. In our case, the SST observations are implemented as gravitational acceleration differences between the GEO and LEO projected onto the line-of-sight, and thus as linear functionals of the disturbing potential and correspondingly unknown spherical harmonic (SH) coefficients. Therefore, neither iteration nor short arcs are needed, enabling fast solutions. Arbitrary colored noise time series can be added to the observations, and a consistent stochastic model can be introduced by applying digital recursive filters of ARMA type both, to the observations and the columns of the design matrix. In our study, we restricted ourselves to white noise behavior.

The SH coefficients are recovered by a least squares adjustment based on full normal equations (NEQs). The NEQs are fully populated, resulting from the non-continuous observation time series when the Earth is blocking the line-of-sight between GEO and LEO. Therefore, a minimum of two GEOs is needed to be able to get always line-of-sight measurements from at least one GEO to a LEO and thus global coverage. The NEQ are assembled for each GEO-LEO link separately, then added, and finally solved as a combined system. The resulting gravity field coefficients are compared with the input gravity field, from which the remaining mission specific errors can be derived. Input signals

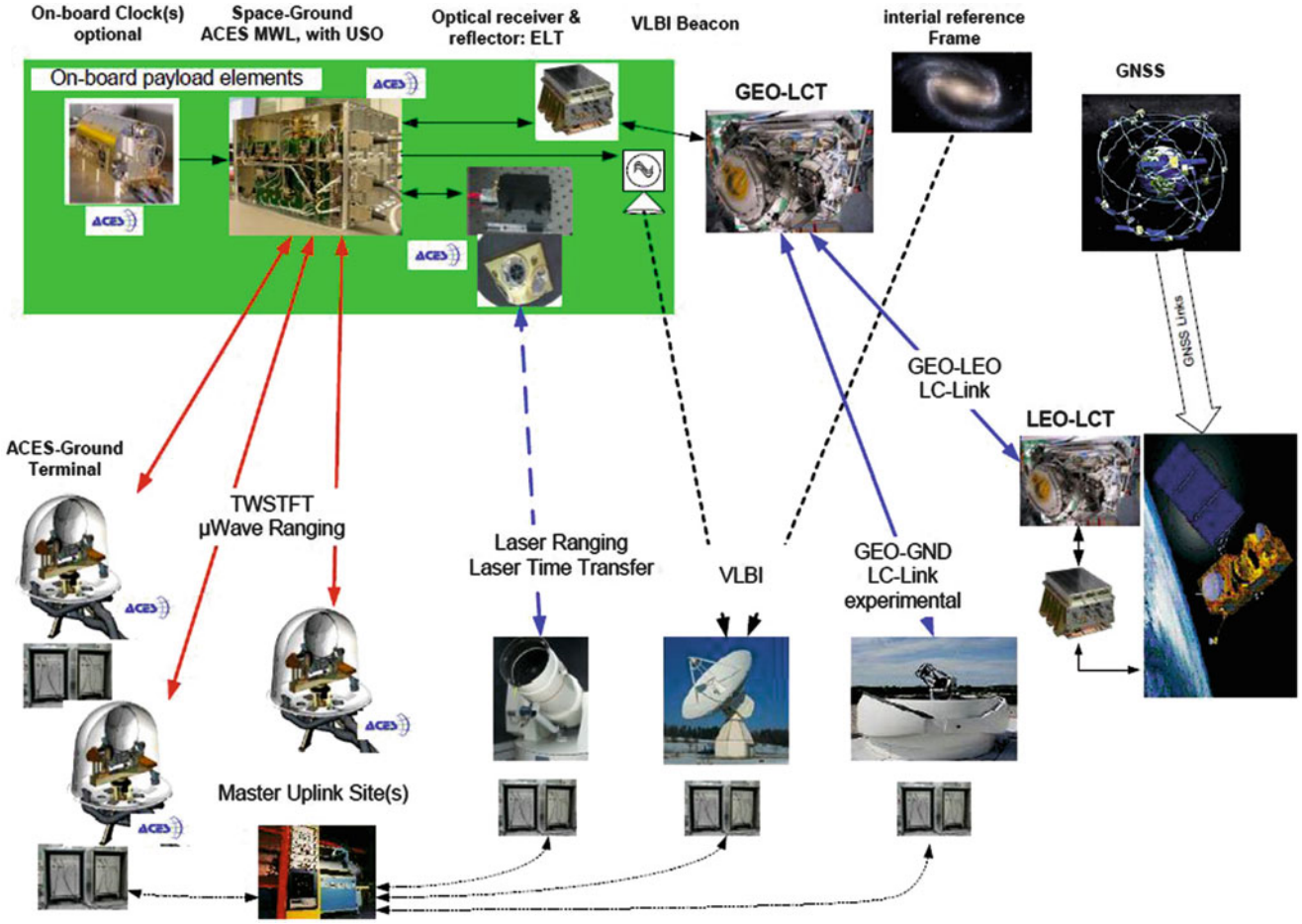

Fig. 1 Outline of GETRIS architecture (see Acknowledgments)

and recovered temporal gravity field models are consistently resolved up to degree and order $n_{max} = 60$, which covers the dominant components of the hydrological signal.

2.3 Input Data

As input data for the simulations a static gravity field, temporal gravity variations, satellite orbits and observation noise are needed (cf. Fig. 2).

The combined satellite-only model GOCO02S (Pail et al. 2010) up to maximum degree/order 60 was used as static gravity field. However the use of a static model is not crucial, because linear observation equations are used, and thus no need for linearization or a background model exists.

For the time varying part of the gravity field data compiled in the ESA study "Monitoring and Modeling individual Sources of Mass distribution and Transport in the Earth System by Means of Satellites" (Gruber et al. 2011) were used. In this study time variable gravity fields were derived from geophysical models and ECMWF climate data up to degree and order 180 in 6 hour resolution. A linear interpolation between the 6 hourly data was done for the simulation. The time period for this study is January 2001. The hydrological data is based on the PCR-GLOBWB model

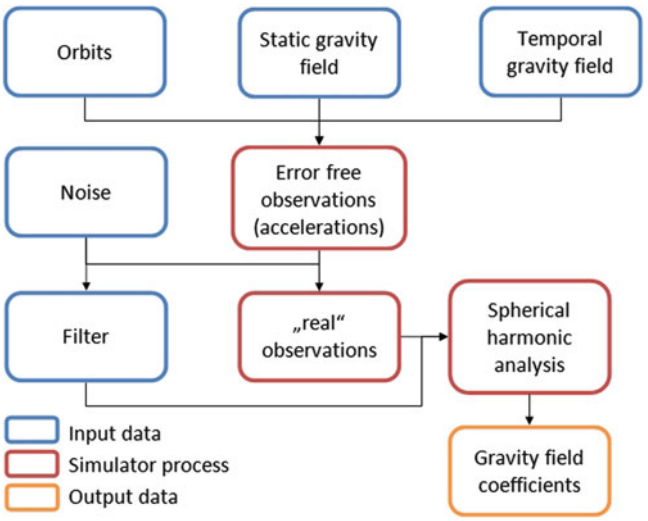

Fig. 2 Schematic representation of the simulator

(Van Beek and Bierkens 2008) with interactions between the different domains of the Earth system and ECMWF data used as forcing. We chose the continental hydrology for this study, because it is a rather clean and relatively slowly varying signal which causes only small temporal aliasing effects. This allows getting a clear picture of the specific features of the mission concept regarding the propagation of the measurement errors and the effect of the mission configuration and geometry (cf. Sects. 3.1 and 3.2). The impact of aliasing for this mission configuration is investigated by adding ocean tide and atmospheric signals (cf. Sect. 3.3).

As a reference, a GRACE-like mission scenario was simulated for comparison (orbit inclination 89°, orbit height 470 km, satellites separated by 200 km in along-track direction, 27 days repeat time). In this simulation study, also the GRACE-like mission is analyzed on the basis of accelerations differences, and not on ranges or range-rates as usually done in real GRACE data analysis. As test case for GEO-LEO tracking, one LEO in a GRACE-like orbit was chosen (orbit parameters like above), observed by two GEOs at longitudes of 0° and 180°.

Finally, noise was added to the error free simulated observations. The noise level strongly depends on the measurement equipment that is not exactly known so far. A white noise level of $5 \cdot 10^{-9}$ m/s^2 for the acceleration differences was derived. This was done by comparing semi-analytic simulations, focusing on the relevant frequency range where the interesting hydrological signals are located. In order to guarantee comparability, the same noise time series have been applied to the GRACE-like and the GEO-LEO mission scenario. In this study we consider only noise of the main ranging instrument, assuming that other error sources such as orbit, accelerometer and attitude errors affect both mission concepts in a similar way, and that the precision of the orbit knowledge does not influence the gravity recovery. Consequently, this study mainly investigates the noise propagation of the main instrument to the gravity field solution as well as the effect of different observation geometries. The effects of more realistic error assumptions for the ranging instrument and the accelerometers as well as the impact of orbit errors (Vonbun et al. 1978) and non-adjusted parameters (Douglas et al. 1980) will be investigated in the frame of a full-scale simulation in the future.

3 Simulation Results

3.1 Monthly Solutions

Based on the above-mentioned assumptions, the simulation results show, that with a mission duration of 27 days the time variable gravity field can be determined more accurately than with the GRACE-like mission for most parts of the spherical harmonic spectrum. Figure 3 shows the formal errors of the recovered gravity field coefficients for the simulated GRACE-like mission (top) and the GEO-LEO mission (bottom). The top part of Fig. 3 shows the typical GRACE error distribution with low zonal errors. This error distribution is caused by the ll-SST principle and the precise measurement mainly in along-track direction. The bottom part of Fig. 3 shows a totally different behavior. The formal errors of nearly all coefficients are significantly smaller than those of the GRACE-like solution. They show an isotropic error structure, with a slight degradation with increasing harmonic degree.

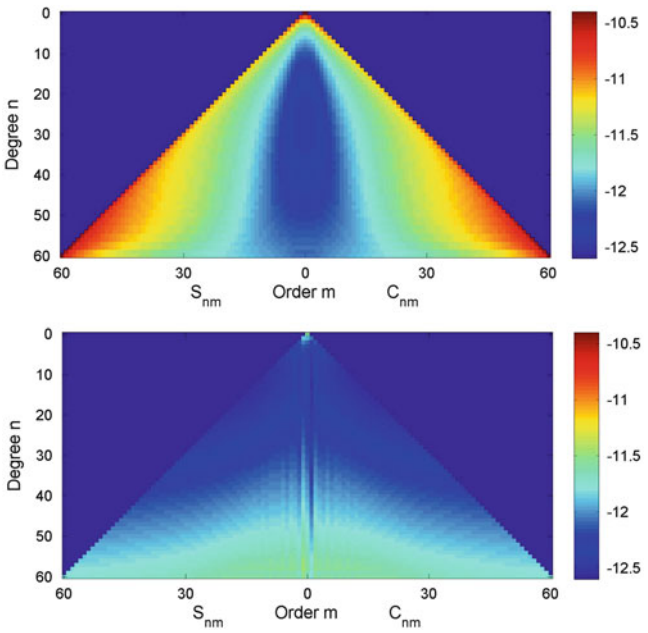

Fig. 3 Formal error of the simulated gravity field coefficients, *top*: GRACE result, *bottom*: GEO-LEO tracking result with one LEO observed by two GEOs

Noticeable are some vertical lines that occur at low orders. Further simulations showed that these lines result from the specific positions of the GEOs. They could be traced back to the relative position of the GEOs and their connection to the spherical harmonic base functions. If all GEOs are directly above a zero-crossing of a spherical harmonic base function, the corresponding coefficient cannot be determined exactly. It can be shown that in reality, if the GEOs were not exactly separated by 180°, or if three or more GEOs were used, these features would not show up.

Figure 4 shows the mean temporal field for the 27 day period derived from the 6 hourly time series described in Sect. 2.3. The main signal of the continental hydrology occurs in the equatorial regions, especially in the rain forest regions. Figure 5 and the upper part of Fig. 6 give an overview of the spatial distribution of the reconstructed mean temporal gravity field caused by the continental hydrology

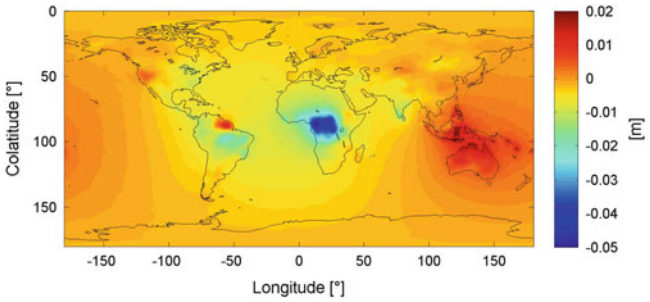

Fig. 4 Mean temporal variable gravity field expressed in terms of geoid heights [m] caused by the hydrology, 27 days (input data)

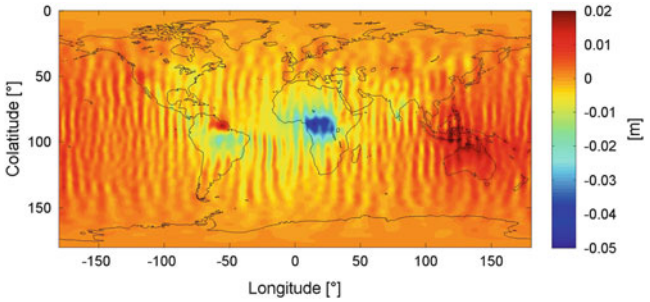

Fig. 5 Mean temporal gravity field (27 days) in terms of geoid heights [m] recovered from GRACE-like scenario

over 27 days. Figure 5 shows the simulated results of the GRACE-like mission which can be considered as the state of the art. Typical GRACE error stripes are part of the estimated temporal gravity field. The GRACE results need to be filtered afterwards to destripe the solutions.

The GEO-LEO tracking result in the top of Fig. 6 shows that the temporal gravity field can be recovered with much smaller errors compared to the GRACE-like scenario. Also the anisotropy of the error structure is much smaller in this case, which makes filtering in the post processing less important than in the GRACE case. To get a closer look at the error structure of GEO-LEO tracking, the bottom part of Fig. 6 shows the difference between Fig. 4 and the upper part of Fig. 6.

The error structure is now clearly visible with errors getting larger near the boundary of the field of view of the two GEOs. The geostationary satellites are located at longitudes of 0° and 180°, which leads to more precise measurements of the radial gravity field component at these longitudes. Figure 7 shows the combination of the GRACE-like observations and GEO-LEO tracking. This combination decreases the typical error structures of both measurement principles and leads to a solution with an isotropic error structure.

Table 1 shows the mission performance in terms of latitudinally weighted Root-Mean-Square (RMS) of the geoid errors. The RMS calculated for the GEO-LEO solution is by

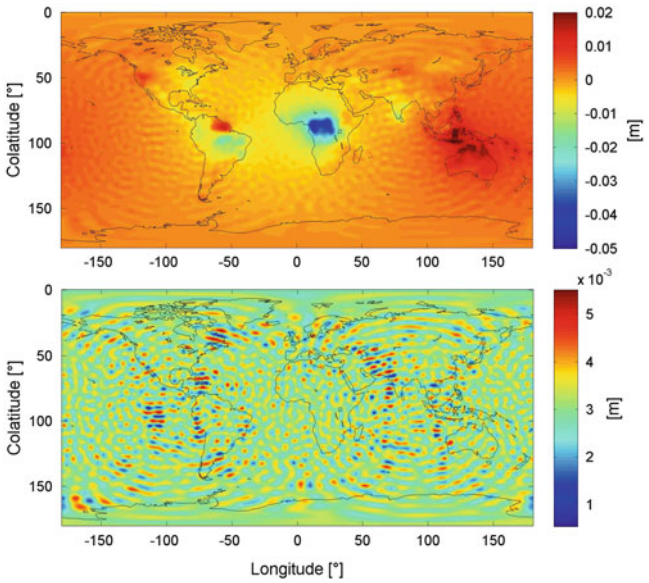

Fig. 6 Mean temporal gravity field (27 days) in terms of geoid heights [m], *top*: recovered from GEO-LEO tracking scenario, *bottom*: top minus mean temporal variable field (input data)

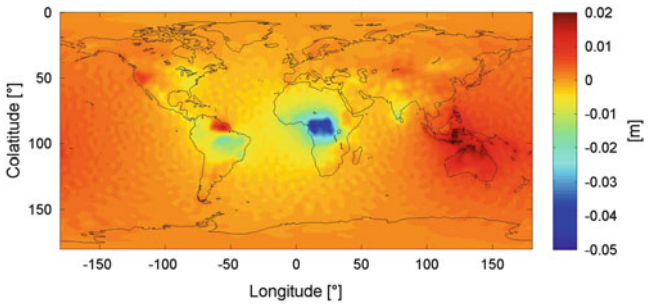

Fig. 7 Mean temporal gravity field (27 days) in terms of geoid heights [m] recovered from the combination of GRACE and GEO-LEO tracking

Table 1 RMS [mm] of the geoid heights for the temporal gravity recovery errors for different mission scenarios

GRACE-like	GEO-LEO	GRACE-like + GEO-LEO
2.237	0.508	0.316

a factor of 4 smaller than that of the GRACE-like result, and a combination of these two scenarios leads to a reduction by a factor of 7 compared to the GRACE-like results.

As a summary picture, Fig. 8 shows the degree RMS in terms of geoid heights in meter of the mean hydrological signal (black), the coefficient differences of the GRACE-like (blue) and the GEO-LEO (green) solutions, as well as their formal error estimates (red and cyan, respectively). The consistency of the coefficient differences and the formal errors demonstrate, that the applied ranging noise is the dominant error source in these simulations, while hydrological aliasing

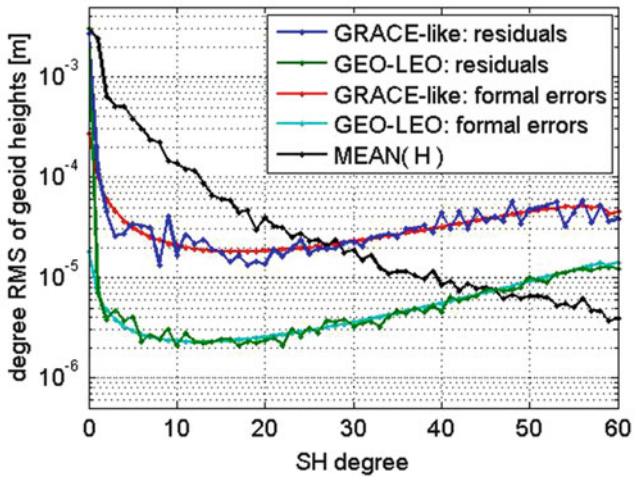

Fig. 8 Degree RMS of geoid heights in [m] of the average hydrological signal, coefficient differences and formal error estimates of the GRACE-like and the GEO-LEO concepts

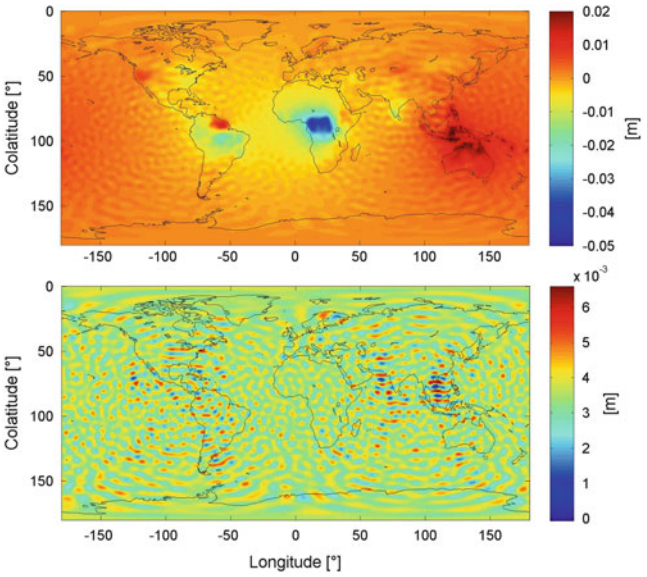

Fig. 9 Mean temporal gravity field (5 days) in terms of geoid heights [m], *top*: recovered from GEO-LEO tracking scenario with five LEOs, *bottom*: top minus mean temporal variable field (input data)

plays only a minor role. Again, the superiority of the GEO-LEO concept becomes visible.

3.2 Five-Day Solutions

Five LEOs, evenly distributed in ascending node, have simultaneously been observed by two GEO satellites for 5 days in this simulation. Figure 9 shows the results, applying the same noise assumptions as in the 27 day scenario. The upper part of Fig. 9 shows that the 5 day mean temporal gravity field can be recovered very well. After subtracting the mean temporal input field, the errors displayed in the bottom part of Fig. 9

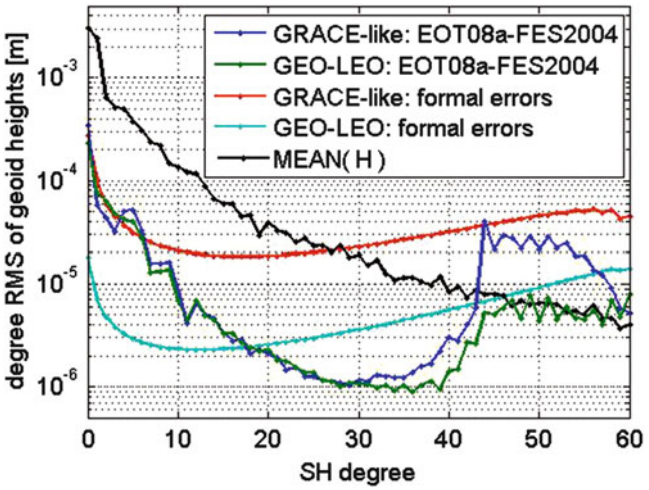

Fig. 10 Degree RMS in terms of geoid heights in [m] of results including ocean tide aliasing

show a similar distribution as shown for the 27 day scenario in Fig. 6. The amplitude of the errors is still very low with a geoid height RMS of 0.583 mm.

3.3 Ocean Tide and Atmospheric Aliasing

Up to now, only the main stochastic error component, i.e., the noise of the ranging system, has been considered. The main systematic error component of a future gravity field mission, however, will be related to temporal aliasing, which results from non-modeled high-frequency temporal variation signals which cannot be resolved by the satellite. In the case of GRACE, it results in a characteristic North-South striping pattern. The effect of temporal aliasing in the frame of the GEO-LEO concept is currently studied in systematical manner, and the results will be published in a separate paper. First preliminary results are presented here.

For this purpose, ocean tide and atmosphere/ocean signals have been superimposed to the measurement time series. In order to show the pure aliasing affect, no ranging errors have been applied in this case. (A combined simulation of applying both ranging errors and aliasing signals shows that also the effects in the gravity field solutions sum up.)

To simulate realistically unmodelled ocean tide errors, the difference of the two ocean tide models EOT08a (Savcenko and Bosch 2008) and FES2004 (Lyard et al. 2006) have been generated for the 27-day orbit period based on the eight main semi-diurnal and diurnal tidal constituents, consistently for the GEO-LEO concept and the GRACE-like reference scenario. Figure 10 shows the results for the two scenarios in terms of degree RMS of geoid heights. The GEO-LEO concept (green) shows significantly lower errors than the GRACE-like scenario (blue) above degree 30. As a reference, again the amplitude of the mean hydrological signal is

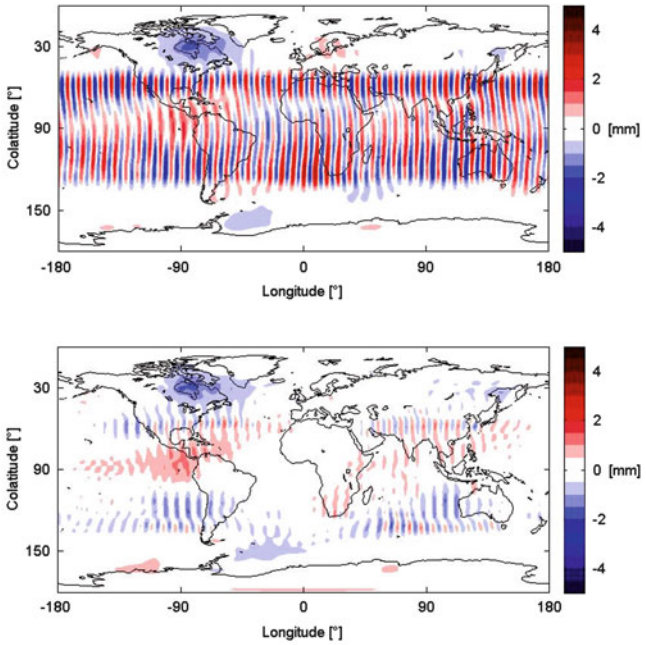

Fig. 11 Geoid height errors [mm] due to ocean tide aliasing for the GRACE-like (*top*) and the GEO-LEO (*bottom*) concept

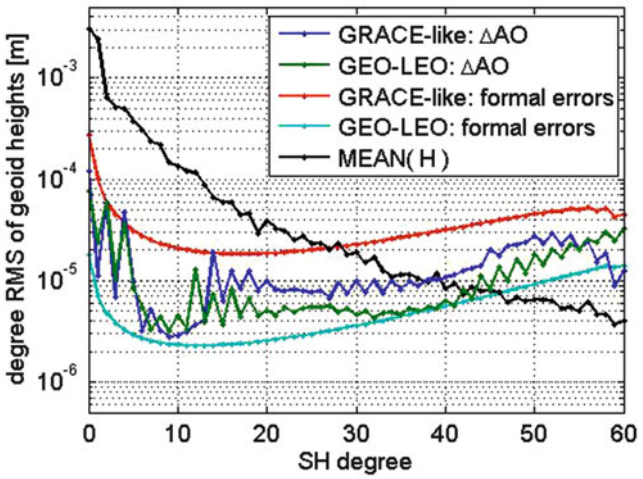

Fig. 12 Degree RMS of geoid heights in [m] of results including atmosphere/ocean aliasing

shown, demonstrating that in this simulation the ocean tide aliasing error of the GEO-LEO solution stays slightly below the hydrology signal until the maximum degree 60. In the case of aliasing, it is particularly interesting to analyze the spatial error structure. Therefore, Fig. 11 illustrates the effect of ocean tide aliasing in terms of geoid height errors, for the GRACE-like scenario (top) and the GEO-LEO concept (bottom). The errors of the GRACE-like scenario with an RMS of 1 mm are larger than those of the GEO-LEO concepts with 0.4 mm.

Finally, instead of the ocean tide difference signals, non-tidal signal of atmosphere and ocean have been applied. For the purpose of comparing the two concepts regarding non-tidal aliasing the signals are computed from the non-tidal atmospheric and oceanic part of the ESA model (Gruber et al. 2011) and after adjustment the mean signal was subtracted. Figure 12 demonstrates that also here the GEO-LEO simulation shows a slightly better performance than the GRACE-like scenario. In contrast to the ocean tide aliasing study, the differences among the two scenarios occur almost over the whole spectral range. The rms of corresponding geoid height errors amount to 1 mm (GRACE-like) and 0.9 mm (GEO-LEO).

At this point it shall be emphasized again, that these results concerning temporal aliasing should be understood as preliminary. Detail analyses will show if the GEO-LEO concept is generally performing better than the GRACE-like scenario, and have to give a generalized answer to the spatial and spectral characteristics of the resulting error structures.

Conclusions

In this study the specific features of the GEO-LEO tracking concept, especially concerning its observation geometry, have been investigated and compared with a GRACE-like scenario. It has been shown that the concept of very high-low satellite-to-satellite tracking with geostationary satellites is a geometrically favorable method for determining the Earth's temporal gravity field.

It shall be emphasized that this study is based on a number of simplifications, such as a white-noise assumption of the ranging instrument, and neglecting orbit and accelerometer errors. The same simplifications and ranging noise assumptions have been applied to both the GEO-LEO tracking and the GRACE scenario, assuming that the neglected error sources affect both concepts in a similar way. Under these conditions, the simulations with 27 days mission period showed that the combination of two geostationary satellites and one satellite in a low GRACE-like orbit shows a better performance of temporal gravity recovery than the GRACE-like reference mission, which is mainly due to the observation geometry. Especially the large GRACE error structures (stripes) resulting from the along-track ll-SST measurement principle do not occur for the GEO-LEO mission design. However, some smaller errors appeared particularly at the boundary of the GEO field of view, leading to slightly increased errors in these regions in case only two GEO satellites are available.

The combination of GRACE-like and GEO-LEO tracking provides very good results where only minor post processing (filtering) would be necessary. The 5 day solution with five LEOs observed by two GEO satellites has shown a similar behavior. The shorter mission duration is

compensated by an increased number of LEO satellites which leads to a similar number of total observations. The error structure is nearly the same, but could in both cases be avoided by using three or more GEO satellites to reduce the vertical lines shown in Fig. 3. With three or more GEO satellites the accuracy would also increase because of the increased number of observations, and because of more precise measurements of the radial component of the Earth's gravity field. Compared to GRACE, the radial measurements are one of the main advantages of the GEO-LEO concept. Due to the fact that an LCT box (and an accelerometer) could be mounted on several LEO satellites which much lower costs than for a dedicated gravity field mission, compared to a single GRACE-like mission the temporal resolution could be increased significantly.

Further investigations have to show which quality could be achieved with upcoming technical specifications for the instrumental accuracy and thus the observation noise. The impact of colored observation noise, errors in the background models as well as the required target accuracy of GEO orbit determination and of the observation of non-conservative forces on LEO and GEO satellites will have to be investigated in the future.

First studies of temporal aliasing seem to indicate that also here the GEO-LEO concept could be an interesting alternative to GRACE-like missions. When including high-frequency ocean tide or atmosphere/ocean aliasing signals in our simulations, the GEO-LEO concept performed generally better. Further studies based on various alternative orbit configurations have to show if this is a general promising feature of this mission type, and the resulting spatio-temporal error will have to be analyzed in detail.

Present investigations in the field of laser distance measurement techniques show an increasing precision, which could lead to further improvements of the results. However, the main disadvantage of a realization of the laser concept instead of the microwave ranging is, that the option of multi-directional tracking, and thus observing several LEOs in parallel by one LEO, gets lost. Thus the capability to significantly improve the temporal resolution by a multi-mission LEO tracking is reduced. Yet the concept is worth to be further investigated regarding both, its technical feasibility and its potential for improved temporal gravity field modeling for determining mass changes in the Earth system.

Acknowledgements This study was inspired by the ESA project "Geodesy and Time Reference in Space" (GETRIS), contract no. 4000103328/2011/NL/WE.

We thank Dr. W. Schäfer for providing us with detailed information on technical issues, and Fig. 1 of this paper.

References

Bender PL, Wiese DN, Nerem RS (2008) A possible dual-GRACE mission with 90° degree and 63° degree inclination orbits. In: Proceedings of the third international symposium on formation flying, missions and technologies. ESA/ESTEC, Noordwijk (ESA SP-654, June 2008), pp 1–6. ISBN 978-92-9221-218-6

Cacciapuoti L, Salomon Ch (2009) Space clocks and fundamental tests: The ACES experiment. Eur Phys J Special Topics 172:57–68

Douglas B, Goad CC, Morrison FF (1980) Determination of the geopotential from satellite to satellite tracking data. J Geophys Res 85(NB10):5471–5480. doi:10.1029/JB085iB10p05471

Gruber T, Bamber JL, Bierkens MFP, Dobslaw H, Murböck M, Thomas M et al (2011) Simulation of the time-variable gravity field by means of coupled geophysical models. Earth Syst Sci Data 3(1):19–35

Hess MP, Kehrer J, Kufner M, Durand S, Hejc G, Fruhauf H, et al (2011) ACES MWL status and test results. In: 2011 Joint Conference of the IEEE international frequency control and the European frequency and time forum (FCS), pp 1–8. doi:10.1109/FCS.2011.5977727

Horwath M, Dietrich R (2009) Signal and error in mass change inferences from GRACE: the case of Antarctica. Geophys J Int 177(3):849–864

Lyard F, Lefevre F, Letellier T, Francis O (2006) Modelling the global ocean tides: a modern insight from FES2004. Ocean Dyn 56:394–415

Pail R, Mayrhofer R (2009) Satellite formations for the reduction of temporal (tidal) aliasing effects. Presented at IAG 2009, Geodesy for Planet Earth, Buenos Aires, August 31, 2009. http://www.iapg.bv.tum.de/mediadb/5505990/5505991/20090831_Poster_MISSION SIM_OTIDE_IAG20...pdf Accessed 16 Apr 2013

Pail R, Goiginger H, Schuh W-D, Höck E, Brockmann JM, Fecher T, Gruber T, Mayer-Gürr T, Kusche J, Jäggi A, Rieser D (2010) Combined satellite gravity field model GOCO01S derived from GOCE and GRACE. Geophysical Research Letters EID L20314, vol 37. American Geophysical Union. doi:10.1029/2010GL044906. ISSN 0094-8276

Ramillien G, Cazenava A, Brunau O (2004) Global time variations of hydrological signals from GRACE satellite gravimetry. Geophys J Int 158(3):813–826

Savcenko R, Bosch W (2008) EOT08a-empirical ocean tide model from multi-mission satellite altimetry. Report No. 81. German Geodetic Research Institute, Munich

Swenson S, Wahr J (2006), Post-processing removal of correlated errors in GRACE. Geophys Res Lett 33:L08402. doi:10.1029/2005GL025285

Tapley BD, Bettadpur S, Ries JC, Thompson PF, Watkins MM (2004), GRACE measurements of mass variability in the earth system. Science 305:1503–1505

Tapley BD, Ries J, Bettadpur S, Chambers D, Cheng M, Condi F, Poole S (2007) The GGM03 mean earth gravity model from GRACE. Eos Trans, AGU, 88(52), Fall Meeting Suppl., Abstract G42A-03

Van Beek LPH, Bierkens MFP (2008) The Global Hydrological Model PCR-GLOBWB: Conceptualization, Parameterization and Verification. Report, Department of Physical Geography, Utrecht University, Utrecht, The Netherlands, http://vanbeek.geo.uu.nl/suppinfo/vanbeekbierkens2009.pdf. Accessed 26 February 2013

Vonbun FO, Argentiero PD, Schmid PE (1978) Orbit determination accuracies using satellite-to-satellite tracking. IEEE Trans Aerospace and Electronic Syst 14(6):834–842. doi:10.1109/TAES.1978.308547

Werth S, Güntner A, Schmidt R, Kusche J (2009) Evaluation of GRACE filter tools from a hydrological perspective. Geophys J Int 179(3):1499–1515

Wiese DN, Nerem RS, Lemoine FG (2012) Design considerations for a dedicated gravity recovery satellite mission consisting of two pairs of satellites. J Geodesy 86(2):81–98

Part IV

Advances in Precise Local and Regional High-Resolution Geoid Modeling

GOCE Data for Local Geoid Enhancement

Matija Herceg, Per Knudsen, and Carl Christian Tscherning

Abstract

The GOCE gradients, having a spatially dense data distribution, may potentially provide better predictions of the regional gravity field than those obtained using a spherical harmonic Earth Geopotential Model. The aim of this study is to develop a methodology to improve the use of GOCE gradients and to determine the Earth's gravity field with better accuracy than by using global models, which have been truncated at a specific harmonic degree and order. The method makes use of all available GOCE gradient data in addition to the global models and aims at improving the determination of Earth's gravitational field in regional areas. Subsequently, the calculated geoid is used together with measurements of sea surface height in a calculation of the Mean Dynamic Topography.

In regional geoid recovery from GOCE gradients, two methods are used, one of them being Least-Squares Collocation (LSC). The second method is developed as a part of this study, and it is based on the Reduced Point Mass (RPM) response. The results show that the RPM method and LSC method give very similar results when using the same data, i.e. the difference is insignificant when compared to the EGM2008 results. However, when all of the available GOCE gradient data are used with the RPM method, an improvement in the gravitational field determination is achieved. The enhanced geoid by the RPM method is then used for the improvement of the MDT in the North Atlantic region.

Keywords

Collocation • GOCE gradients • Geoid • Reduced point mass

1 Introduction

The success of the Gravity field and steady state Ocean Circulation Explorer (GOCE) is depending on adequate methodologies for extracting the gravity field from its observations and for combining the gravity field with information from other sources.

GOCE is the first satellite mission to observe gravity gradients in space; these are primarily to be used for the determination of high precision global gravity field models. The advantage of a dense distribution of the GOCE gradients may potentially provide better predictions of the regional gravity field than those obtained using a global spherical harmonic Earth Geopotential Model (EGM).

Gravity field recovery from GOCE gradient data using Least-Squares Collocation (LSC) in different areas of the Earth was recently investigated by Tscherning and Arabelos (2011) and Yildiz (2012). This LSC investigation confirm that short wavelengths of the gravity field, beyond maximal

M. Herceg (✉)
IGG, University of Copenhagen, Øster Voldgade 10, 1350 Copenhagen K, Denmark
e-mail: matija.herceg@geo.ku.dk

P. Knudsen
DTU Space, Technical University of Denmark, Elektrovej, Building 328, 2800 Kgs. Lyngby, Denmark

C.C. Tscherning
Niels Bohr Institute, Juliane Maries Vej 30, 2100 Copenhagen Ø, Denmark

U. Marti (ed.), *Gravity, Geoid and Height Systems*, International Association of Geodesy Symposia 141,
DOI 10.1007/978-3-319-10837-7_17,

degree of the global GOCE EGM, is present in the GOCE gradient measurements.

In Knudsen et al. (2011) the potential of using GOCE for studying the ocean circulation was confirmed. The aim of this study is to improve the methodology for using GOCE gradients by development of the Reduced Point Mass (RPM) method, and to possibly extract more signal in local areas than the one produced by GOCE global models. This may lead to geoid enhancement and improvement of the Mean Dynamic Topography (MDT).

The results presented in this study are based on all available GOCE gradient data in the Geoid and Ocean Circulation in the North Atlantic (GOCINA) region (Knudsen 2005), i.e. 18 months of observations.

2 Methodology

2.1 Least-Squares Collocation

LSC enables the use of many types of observables (Krarup 1969) for the estimation of gravity field quantities and theirs errors.

The basic observation equation for LSC is

$$y_i = L_i T_{LSC} + e_i + A_i^T X \tag{1}$$

where X are parameters, A_i is a vector connecting parameters and the observations and e_i the error contribution. Here the contribution from a datum transformation and a EGM must have been subtracted from the anomalous potential T.

The estimate of T_{LSC} is obtained by

$$\tilde{T}_{LSC}(P) = \{C_{Pi}\}^T \bar{C}^{-1} \{y - A^T X\} \tag{2}$$

where $\bar{C} = \{C_{ij} + \sigma_{ij}\}$, and σ_{ij} is the variance-covariance of the errors.

The estimates of the parameters are obtained by

$$\tilde{X} = (A^T C^{-1} A + W)^{-1} (A^T C^{-1} y) \tag{3}$$

W is the matrix of contributions from observations only related to parameters such as the differences between geodetic coordinates in a geocentric and non-geocentric datum (Tscherning and Veicherts 2007).

Analytic covariance models are used in LSC. By fitting an analytic model to empirically determined values, obtained using the program *EMPCOV* (Forsberg and Tscherning 2008) on data in a certain region, a covariance function optimal for this region is selected. To fit empirical covariance functions to isotropic analytic models, the Fortran program *covfit.f* from *GRAVSOFT* package was used (Knudsen 1987). The parameters obtained by fitting the covariance function were used for collocation prediction and reduced point mass solution.

2.2 Reduced Point Mass Method

There are different implementations of the point mass methodology for geoid determination, and they are already described in many publications (Sjogren et al. 1971; Vermeer 1982, 1990, 1992, 1995; Hauck and Lelgemann 1985; Marchenko et al. 2001; Chanfang et al. 2011).

Point-mass functions or multipole base-functions are harmonic functions, which may be used to represent T either globally or locally. The functions may be expressed by closed expressions or as sums of Legendre series. In both cases at least the two first terms must be removed since they are not present in T, i.e. zero-degree ($l=0$) harmonic terms cancel each other out and the first degree harmonics ($l=1$) are equal to zero since the origin of the coordinate system is chosen to coincide with the geocentre. For local applications the effect of a global gravity model is generally removed and later on restored. Then, more terms need to be removed or substituted by terms similar to the error-degree variances.

The anomalous gravity field, T, at point Q is modeled by a set of base functions, each obtained as the anomalous gravity potential from each point mass m_i located at the position P_i on the surface with radius R_M. This radius is smaller than that of the Earth, R_E.

$$T(Q) = \sum_i T_i(Q) \quad \text{and} \quad T_i(Q) = V_i(Q) - U_i(Q) \tag{4}$$

where V and U are Earth's gravity potential and normal potential respectively.

Normally a gravitational potential function is related to the position in terms of spherical coordinates (ϕ, λ, r). The spatial derivatives of interest in connection with the output from a satellite gradiometer are all second partial derivatives with respect to a local Cartesian coordinate system at an arbitrary point in the near Earth space. As the derivatives of the potential have tensorial properties, the required transformations are conveniently derived by the methods of tensor calculus.

A geocentric system is presented by $x^p = (x, y, z)$ and in spherical coordinates by $u^p = (\lambda, \phi, r)$. The local coordinate system is described by the basis e_p with vectors in triad (e_1, e_2, e_3) that are not unit vectors. Here, a local rectangular coordinate system (η, ξ, ζ) is defined by the e_p basis, Reed (1973).

The position vector of an arbitrary point P in space is given in terms of the geocentric Cartesian coordinates by:

$$r = x^P i_P = x\hat{i}_1 + y\hat{i}_2 + z\hat{i}_3 \tag{5}$$

Geocentric coordinates are functionally related to the spherical coordinates by:

$$x^P = x^P(u^P) \tag{6}$$

which is given by:

$$\begin{aligned} x &= r\cos\varphi\cos\lambda \\ y &= r\cos\varphi\sin\lambda \\ z &= r\sin\varphi \end{aligned} \tag{7}$$

If the potential is considered, $V = V(u^P) = V(\lambda, \varphi, r)$, the gradient of V is defined in the (x, y, z) or (η, ξ, ζ) Cartesian coordinate system in the normalized basis as (see Herceg 2012):

$$\nabla V = \frac{1}{r\cos\varphi} V_\lambda \hat{e}_1 + \frac{1}{r} V_\varphi \hat{e}_2 + V_r \hat{e}_3 \tag{8}$$

The symmetric second order derivatives in the local (η, ξ, ζ) system are:

$$\begin{aligned} V_{\eta\eta} &= \frac{1}{r^2\cos^2\varphi}\frac{\partial^2 V}{\partial\lambda^2} - \frac{\tan\varphi}{r^2}\frac{\partial V}{\partial\varphi} + \frac{1}{r}\frac{\partial V}{\partial r} \\ V_{\xi\xi} &= \frac{1}{r^2}\frac{\partial^2 V}{\partial\varphi^2} + \frac{1}{r}\frac{\partial V}{\partial r} \\ V_{\zeta\zeta} &= \frac{\partial^2 V}{\partial r^2} \end{aligned} \tag{9}$$

To expand Eq. (9) completely, a derivation of the cosine of the spherical distance with respect to the longitude and latitude needs to be carried out. Finally, expressions for the second order derivatives of the potential (and closed expressions for gravity gradients when using point masses) in the (η, ξ, ζ) system, are (Herceg 2012):

$$V_{\eta\eta} = 3\frac{r_q^2}{l^5}\cos^2\varphi_q \sin^2(\Delta\lambda) - \frac{1}{l^3} \tag{10}$$

$$V_{\xi\xi} = 3\frac{r_q^2}{l^5}\left[\cos\varphi_P \sin\varphi_q - \sin\varphi_P\cos\varphi_q\cos(\Delta\lambda)\right]^2 - \\ - \frac{1}{l^3} \tag{11}$$

$$V_{\zeta\zeta} = \frac{\partial^2 V}{\partial r_P^2} = -\frac{1}{l^3} + 3\frac{(r_P - r_q t)^2}{l^5} \tag{12}$$

where the partial differential equation of second order satisfies *Laplacian differential equation*, $\Delta V = 0$.

For the expressions of gravity gradients, when using reduced point masses, the derivative of the sum of a finite Legendre series is used:

$$S = \sum_{m=0}^{n} a_l s^{m+1} P_m(t) \tag{13}$$

which can be computed easily using a recursion algorithm (Tscherning and Rapp 1974). Where m is degree of Legendre polynomial, s are parameters of anomaly degree variance model and t is cosine of spherical distance ψ between two points. The derivatives of S with respect to t are then computed by recursion algorithm obtained from Tscherning (1976). Then, the expressions for the second order derivatives of the gravitational potential in η, ξ, and ζ direction are (Herceg 2012):

$$V_{\eta\eta} = \frac{1}{r_P^2\cos^2\varphi_P}\left[\frac{\partial V}{\partial t}\frac{\partial^2 t}{\partial\lambda_P^2} + \frac{\partial^2 V}{\partial t^2}\left(\frac{\partial t}{\partial\lambda_P}\right)^2\right] - \\ - \frac{\tan\varphi_P}{r_P^2}\frac{\partial t}{\partial\varphi_P}\frac{\partial V}{\partial t} + \frac{1}{r_P}\frac{\partial V}{\partial r_P} \tag{14}$$

$$V_{\xi\xi} = \frac{1}{r_P^2}\left[\frac{\partial V}{\partial t}\frac{\partial^2 t}{\partial\varphi_P^2} + \frac{\partial^2 V}{\partial t^2}\left(\frac{\partial t}{\partial\varphi_P}\right)^2\right] + \frac{1}{r_P}\frac{\partial V}{\partial r_P} \tag{15}$$

$$V_{\zeta\zeta} = \frac{\partial^2 V}{\partial r_P^2} \tag{16}$$

where partial derivatives of the spherical distance ψ with respect to the latitude and longitude are expressed through cosine of spherical distance t, as in Herceg (2012):

$$\frac{\partial t}{\partial\varphi_P} = \cos\varphi_P\sin\varphi_q - \sin\varphi_P\cos\varphi_q\cos(\Delta\lambda) \tag{17}$$

$$\begin{aligned} \frac{\partial t}{\partial\lambda_P} &= -\cos\varphi_P\cos\varphi_q\sin(\Delta\lambda) \\ \frac{\partial^2 t}{\partial\varphi_P^2} &= -t \\ \frac{\partial^2 t}{\partial\lambda_P^2} &= -\cos\varphi_P\cos\varphi_q\cos(\Delta\lambda) \end{aligned} \tag{18}$$

This approach is able to tailor the algorithm for point mass depth and grid spacing relations. The method provides the calculation of full gravity field quantities or reduced by using either full or reduced point masses. Gravity and geoid determination by means of the reduced point masses can be used as an alternative method to the conventional ones for geoid determination.

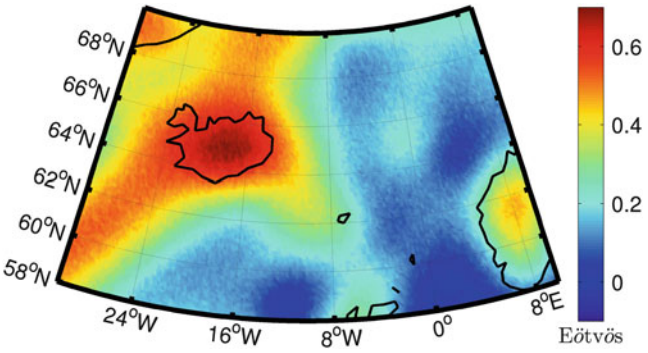

Fig. 1 GOCE T_{zz} gradient at satellite altitude (209,282 observation)

3 Truncation of the Long Wavelength Part Of the Gravity Field Quantities

In this study, only GOCE observation from the North Atlantic region were used (209,282 observations). Figure 1 shows the dense distribution of T_{zz} GOCE gradients in the GOCINA region and its value in E*ö*tv*ö*s units.

Truncation of the long wavelength part of the gravity field in local gravity field modelling ensures that the contribution of the masses outside the area can be neglected. Another purpose of truncation of the long wavelength is to allow us to use planar Fast Fourier Transform (FFT). In order to produce the gravity anomaly, and geoid height anomaly grid in GOCINA region, the long wavelength part of the gravity field must be subtracted from these gravity field quantities. When removing the long wavelength part of the gravity field for the collocation solution, the program *GEOCOL* from the Gravsoft package is used (Tscherning 2005). Both geoid height and gravity anomaly are calculated by the use of the Earth's Gravitational Model 2008 (EGM2008) spherical harmonics set up to degree and order 2190 (Pavlis et al. 2012) and the GOCE Direct release 3 spherical harmonic set up to the degree and order 240 (Bruinsma et al. 2010). The long wavelength part of the gravity field, corresponding to the spherical harmonic degree and order 0–100, was truncated from GOCE gradients, geoid height and gravity anomaly. Even though GOCE Direct release 3 does not include information in high frequencies, as model EGM2008, here comparison is made to see if there is information in GOCE gradients that exceeds resolution of GOCE Direct release 3 spherical harmonics set.

It is clear from Fig. 2 that the geoid height anomalies based on the EGM2008 global gravitational model contain details not present in the GOCE based solution. This is not a surprise, since the EGM2008 incorporates shipborne, airborne, and satellite altimetry derived gravity anomalies (Pavlis et al. 2012). It also includes satellite based solutions from the Gravity Recovery and Climate Experiment

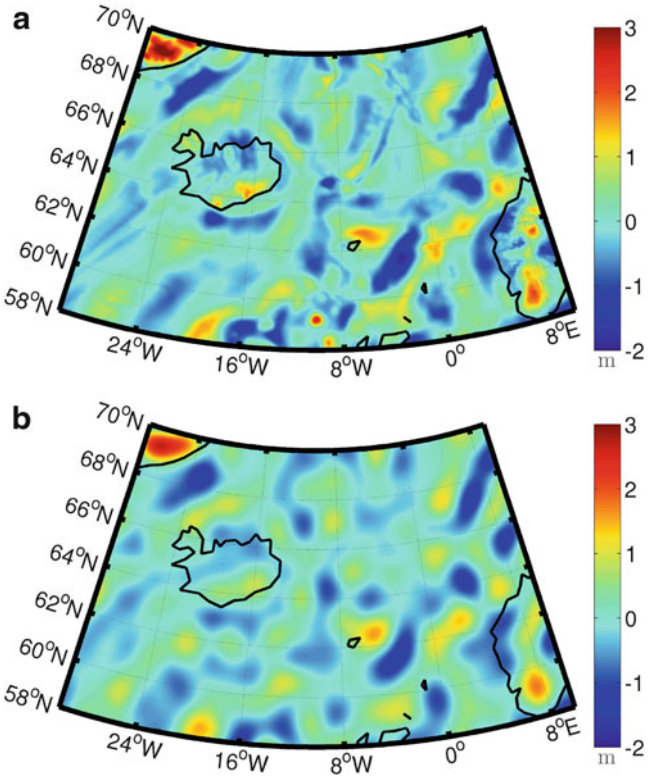

Fig. 2 Geoid height anomalies derived from two global geopotential models, i.e. EGM2008 up to spherical harmonic degree 2190 and GOCE Direct release 3 up to spherical harmonic degree 240. From both datasets, contribution from spherical harmonic set EGM2008 up to harmonic degree and order 100 is subtracted. (**a**) Geoid height anomalies based on EGM2008 geopotential model. (**b**) Geoid height anomalies based on GOCE Direct release 3 geopotential model

(GRACE) mission, i.e. 57-month period from September 2002 to April 2007 (Mayer-Guerr 2007). While the GOCE model presented here is based on only 18 months of data, i.e. from first of November 2009 until 17th of April 2011.

4 Results of Prediction of Gravity Anomaly and Geoid in GOCINA Region

To investigate if a higher accuracy could be obtained by the direct use of GOCE satellite gradients, prediction of gravity anomaly residuals and geoid height anomaly data, using LSC and RPM methods, with GOCE T_{zz} gradients were made.

The determination of the appropriate depth of the point masses, when using RPM method, is done by fitting the function of different gravity field quantities, i.e. geoid heights and gravity anomalies, to the previously calculated empirical covariance function. The function of different gravity field quantities, based on the reduced point masses is shown in Fig. 3.

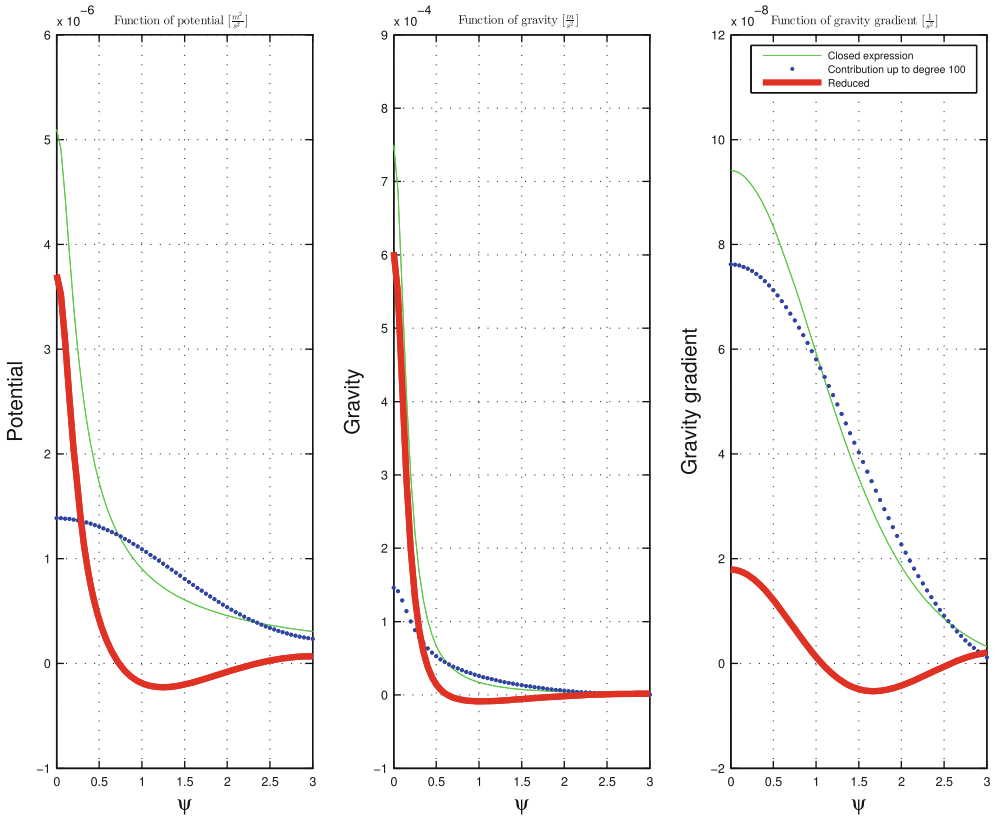

Fig. 3 The different gravity field quantities as a function of spherical distance ψ: the gravitational potential $[\frac{m^2}{s^2}]$, the gravity anomaly $[\frac{m}{s^2}]$ and the gravity gradients $[\frac{m^2}{s^2}]$. The function shows the quantities when using point masses solution for the closed expression, for the contribution up to harmonic degree and order 100, and for the reduced point masses

Fitting of the function for different gravity field quantities to the empirical covariance function was done by comparing empirical covariance estimations based on the GOCE T_{zz} gradient anomalies to the function of reduced gravity gradients shown on Fig. 3 (right hand side of the plot). Numerous tests with different point mass depths showed that the best results are achieved when the R_M is 20 km smaller than the mean radius of the Earth (6,370 km), i.e. when the depth of the point masses is 20 km.

The other issue with the RPM method is the point mass spacing. The grid of point masses should be dense enough to represent fine details of the gravity field as good as possible, and at the same time far enough to prevent large correlation from adjacent point masses. This correlation can cause singularities in the calculations. The spacing of the point masses depends on the content of the residual field which needs to be predicted. Thus, the higher the harmonic degree and order of the reference field that is removed from the observations in the remove-restore method, the closer the point masses can be spaced without causing problems due to the large correlation.

Both methods presented here show good agreement in prediction of both the gravity anomaly residuals and the geoid height anomaly, which are shown on the Fig. 4, in the first and second column respectively. Compared to the LSC method, the RPM method needs less time for calculation by using a thinned gradient dataset, i.e. a selection of values closest to the nods of the $0.1° \times 0.2°$ grid. The predicted gravity anomaly residuals have a standard deviation of around 11 mGal at the surface for both methods (Table 1: the third and fifth column). The same agreement can be noticed in the prediction of the geoid height anomaly, where the standard deviation is around 0.51 m for both methods. Statistics of the differences between prediction by RPM and LSC of gravity anomaly residuals and geoid height anomaly is shown in the sixth column of Table 1.

Since LSC requires the solution of as many linear equations as the number of data, and this large amount of data was not feasible in GEOCOL at the time when calculation was carried out, the GOCE gradient data is thinned prior to applying the method. The observations closest to the knots of a $0.1° \times 0.2°$ grid are selected and used in the further calculation. The selected dataset for GEOCOL collocation solution contains 24,116 observations.

This is not the case for the RPM, where the number of equations we want to solve depends on the number of point mass grid points.

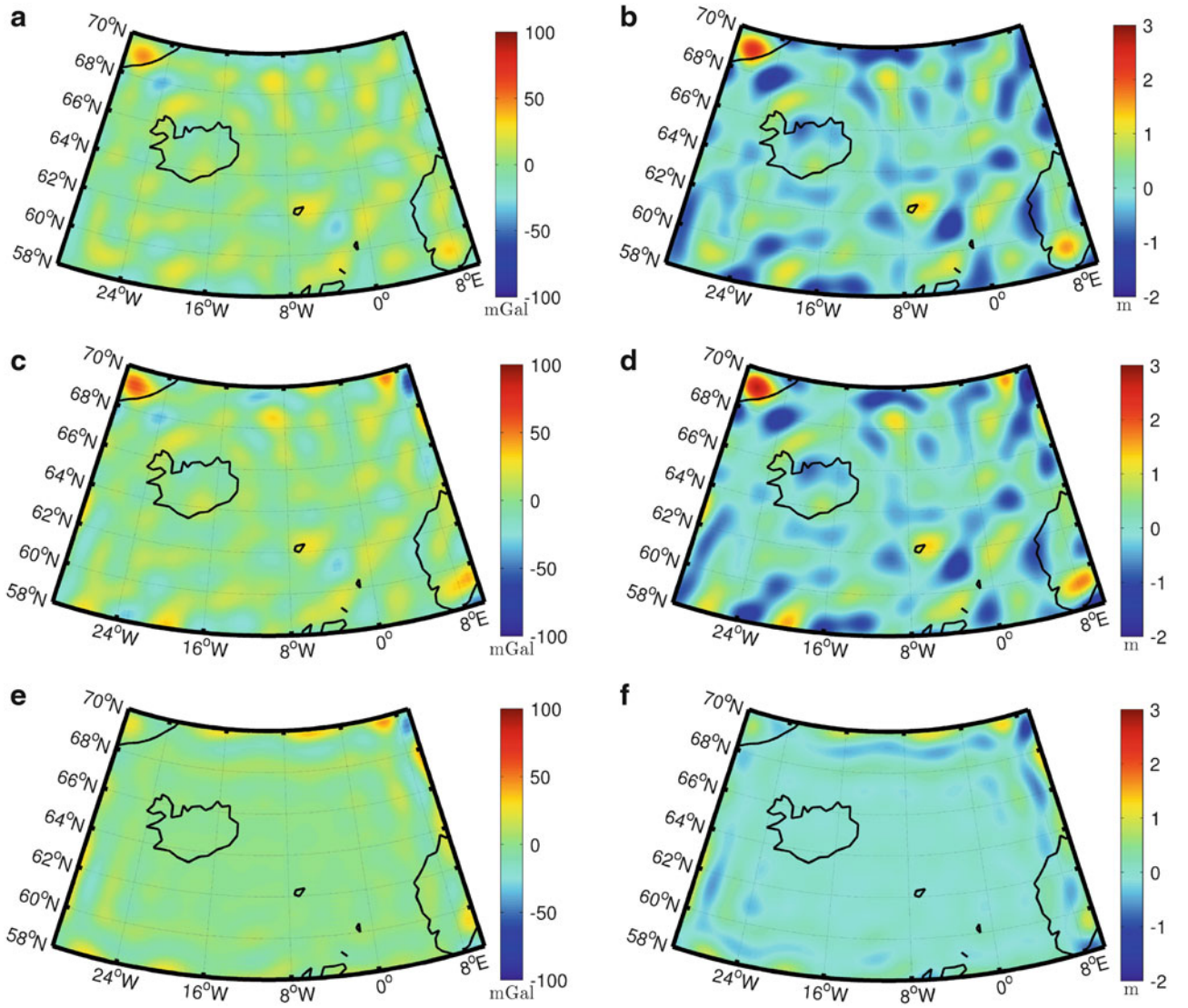

Fig. 4 Comparison between the gravity anomaly residuals [mGal] and geoid height anomaly [m] predicted using the LSC and the RPM method (**a**) Gravity anomaly residuals predicted by collocation. (**b**) Geoid height anomaly predicted by collocation. (**c**) Gravity anomaly residuals predicted by reduced point mass method. (**d**) Geoid height anomaly predicted by reduced point mass method. (**e**) Gravity anomaly residual difference. (**f**) Geoid height anomaly difference

Table 1 Statistics of gravity anomaly residuals [mGal] and geoid height anomaly [m] predicted from global geopotential EGM2008 and GOCE Direct release 3, and by RPM and LSC methods (when selected $0.1° \times 0.2°$ T_{zz} dataset is used), and by RPM (when all available T_{zz} gradient anomalies are used)

		GOCE				
	EGM08	DIR R3	RPM	RPM_{ALL}	LSC	LSC-RPM
Gravity anomaly residuals [mGal]						
Mean	0.3761	0.2813	−0.1218	0.3643	−0.6802	−0.5584
StD dev	20.0414	11.8893	11.9745	15.9469	10.8674	7.4811
Geoid height anomaly [m]						
Mean	0.0172	0.0097	−0.0027	0.0188	−0.0341	−0.0314
StD	0.5780	0.5240	0.5211	0.5922	0.5037	0.2393

With RPM there is the possibility of using all gravity gradients available (209,282 observations). In that case, the standard deviation increases from 11.97 to 15.95 mGal in the case of gravity anomaly residuals and from 0.52 to 0.59 m when it comes to the geoid height anomaly, see Table 1.

One could say that increasing the standard deviation does not mean that the prediction is made any better—in fact, it could imply that it is insignificant. However, in these cases, where the standard deviations increase and it actually goes closer to the standard deviation of the EGM2008 (see the first column in the Table 1), it can be implied that there is an improvement in the prediction. This is not fully confirmed

Table 2 Geoid height anomaly [m] prediction difference by RPM and LSC (when selected 0.1° ×0.2° GOCE T_{zz} dateset is used), and by RPM (when all T_{zz} gradient anomalies are used)

	EGM08-LSC	EGM08-RPM	EGM08-RPM$_{ALL}$
Geoid height anomaly [m]			
Mean	0.0514	0.0200	0.0197
StD	0.4022	0.4049	0.4072

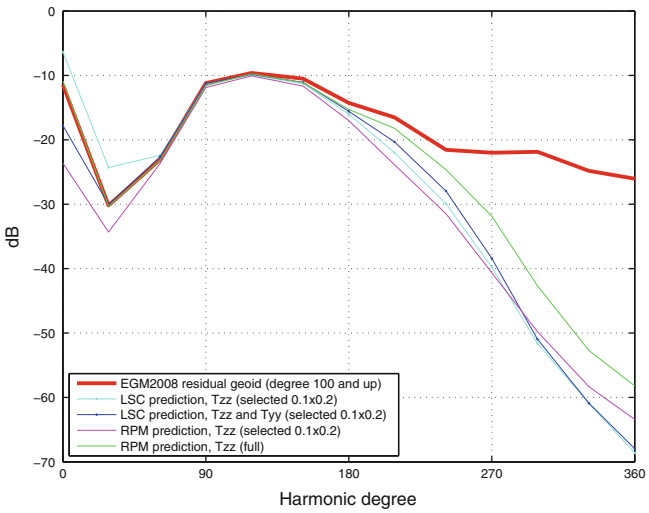

Fig. 5 Power spectrum calculated by planar FFT of the geoid height anomaly prediction when EGM2008 up to spherical harmonic degree and order 100 is subtracted. The prediction is done by the LSC and the RPM methods with different datasets. Power below spherical harmonic degree 100 is present because of the spectral leakage and imperfection of the reference model. Units are in *decibel* [dB]

if we look in statistic difference Table 2, where mean value of the differences are decreasing but standard deviations are slightly increasing when RPM is used.

Figure 5 shows a power spectra in *decibel* [dB][1] computed by regional FFT (Forsberg 1984), of the geoid height anomaly predicted by the LSC and the RPM methods. A comparison is shown between the prediction using only T_{zz} or both T_{zz} and T_{yy} GOCE gradients by the use of the LSC method. T_{xx} GOCE gradient component is not used because the error of T_{xx} and T_{yy} is approximately at the level of the requirement for the gravitational gradient trace in upper measurement bandwidth, while T_{zz} is two to three times above that level for higher frequencies.

For the RPM method, two different power spectra of geoid height anomaly solutions are shown. The first power spectrum shows the RPM solution in which the selected GOCE gradient dataset is used for the prediction, while the second shows the solution when all available GOCE gravity

[1]The *decibel* [*dB*] is a logarithmic unit that indicates the geoid power. A decibel is ten times the logarithm to the base 10 (10 log_{10}), i.e. a change in power by a factor of 10 is a 10 dB change. Unit of 0 dB equals to the $1m^2 Degree^2$ in the case of geoid heights and MDT (Forsberg 1984).

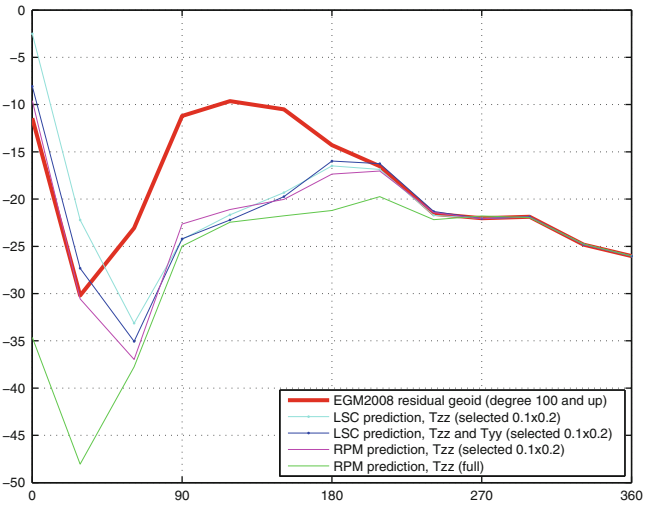

Fig. 6 Power spectrum calculated by planar FFT of the difference between geoid height anomaly prediction (when EGM2008 up to spherical harmonic degree and order 100 is subtracted) and EGM2008 based geoid height anomaly. Units are in *decibel* [dB]

gradient observations are used. From Fig. 5 it can be seen that adding the T_{yy} GOCE gradients component provides marginal improvements to the results obtained when using only T_{zz}. The same conclusion can be found in the investigation of Tscherning and Arabelos (2011). However, using more GOCE gradient T_{zz} observations does improve the solution, i.e. the power spectrum shows more signal in the RPM solution when all available GOCE gradients are used comparing to the results obtained when using only selected T_{zz} GOCE gradients.

When taking the difference from the reference, i.e. the EGM2008 based geoid height anomaly, it can be seen in Fig. 6 that both solutions, by the LSC and the RPM methods, give similar results when the selected GOCE gradient dataset is used. This is not the case for the RPM prediction when all available GOCE gradients are used, where an improvement of the geoid height anomaly prediction in the spectrum band from harmonic degree 120 to 140 can be seen. Hence, the improvement in the geoid height anomaly prediction by the use of the RPM method and all available GOCE gravity gradients in the GOCINA region may lead to better geoid determination.

The geoid height anomaly produced by the RPM method shown in Fig. 4 is then used to enhance the geoid produced by the GOCE Direct Release 3 spherical harmonic set.

4.1 Merging Enhanced Geoid Heights with Mean Sea Surface

The MDT is the small residual of two larger fields, the geoid and the Mean Sea Surface (MSS). The MDT in the GOCINA

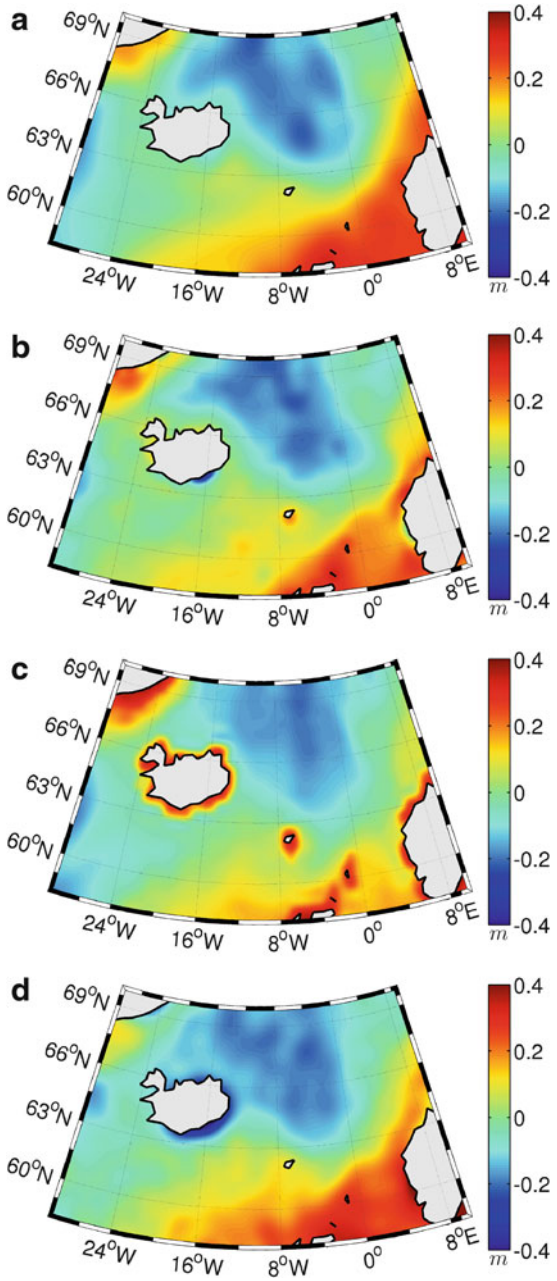

Fig. 7 Different mean dynamic topography in GOCINA region [m]) (**a**) DTU10 MDT, (**b**) GOCINA project MDT, (**c**) Maximenko MDT, (**d**) GOCE Direct enhanced MDT

region is calculated as the difference between DTU10 MSS (Andersen 2011) and enhanced geoid produced by the RPM method and GOCE Direct Release 3 spherical harmonic set.

In this analysis, a GOCE Direct enhanced MDT, filtered by Gaussian with a 1.5° width, is presented as the final MDT. For the estimation of the quality of the GOCE Direct enhanced MDT (filtered by Gaussian with a 1.5° width) a comparison with the different MDT's is presented, see Fig. 7.

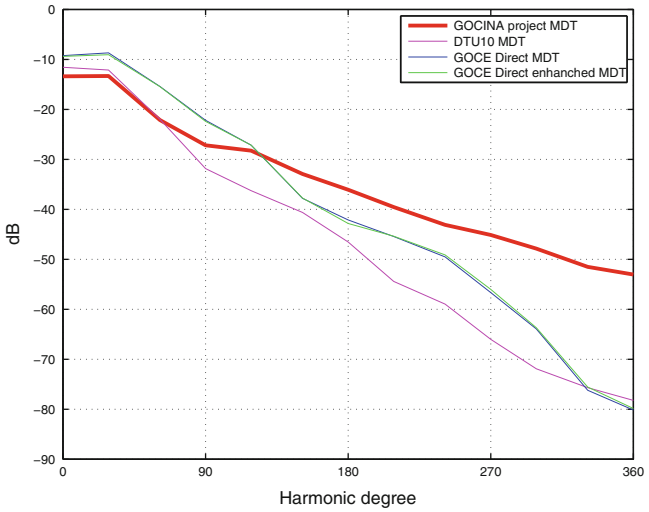

Fig. 8 Power spectra calculated by planar FFT of different MDT estimates. Units are in *decibel* [dB]

The Maximenko MDT (Maximenko et al. 2009) incorporates the GRACE satellite and drifting buoy data, and should show the most detailed oceanographic content. However, it doesn't reveal more information than the MDT calculated in the GOCINA project. This can be seen especially in the coastal areas, where synergy of low resolution Maximenko MDT grid and land proximity shows an unreliable signal.

From Fig. 8 it can be seen that the GOCE Direct MDT has higher signal in the spectrum band from harmonic degree 0 to 140 than the MDT calculated in the GOCINA project. However, the signal contained in the wavelengths shorter than harmonic degrees 140 in the GOCE Direct MDT slowly attenuates. The DTU10 MDT shows significantly less signal than the GOCE Direct MDT.

Even though GOCE data provides a better estimation of the MDT in the GOCINA region than any previously obtained using only satellite observations, it could not be concluded whether the regionally enhanced geoid model estimated using GOCE gradients contribute to a further improvement of the determination of the MDT in the GOCINA area (where ground and airborne data have been used as mentioned above).

Once the MDT has been calculated, it can be used to determine the surface geostrophic currents, which are associated with the slope of the MDT. Figure 9 shows the calculated current speeds from different mean dynamic topography. Here, the current speed reaches a maximum of 0.77 m/s, calculated by the GOCINA project MDT. In case of GOCE Direct enhanced MDT current speeds, the maximum is 0.46 m/s, and in case of the DTU10 MDT current speed the magnitude and the details of the circulation features are far from expected, i.e. the maximum current speed of 0.18 m/s. Whereas the MDT calculated in GOCINA project shows

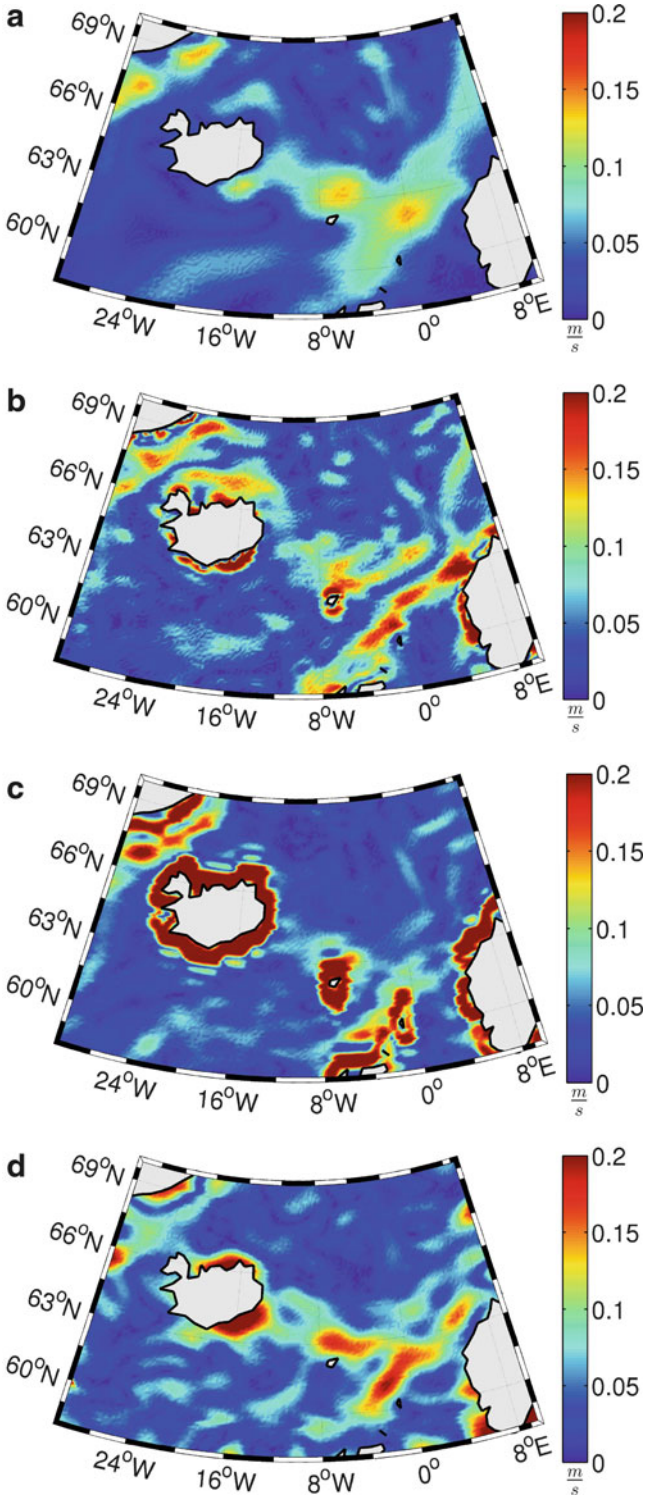

Fig. 9 Current speed calculated from different mean dynamic topography in the GOCINA region [$\frac{m}{s}$]. (**a**) DTU10 MDT current speed. (**b**) GOCINA project MDT current speed. (**c**) Maximenko MDT current speed. (**d**) GOCE Direct enhanced MDT current speed

smallest scale details. Maximenko MDT current speeds solution with in-situ drifter data gives quite reasonable results, however the low resolution hides general circulation features in this region.

Calculation of the geostrophic surface currents from the GOCE Direct MDT reveals continuation of the North Atlantic current, i.e. Norwegian current, as well as the East Greenland Current. Therefore, the model estimates similar current speeds to the ones from the GOCINA project MDT, showing the ability to resolve the fine scale features of the ocean circulation.

Conclusions

The results presented in this study are based on all available GOCE gradient data in the GOCINA region, i.e. 18 months of observations, which is not presented in any other previous investigation.

A comparison of the solutions from LSC and RPM methods shows that adding the T_{yy} component to the input file marginally changes the result in gravity filed quantities prediction. However, using more GOCE gradient T_{zz} observations does improve the solution.

When taking the difference from the reference field, i.e. the EGM2008 based geoid height anomaly, it can be seen that the solutions from both the LSC and RPM methods give similar results when the selected GOCE gradient dataset is used. When all available GOCE gradients are used, an improvement of the geoid height anomaly prediction in the spectrum band from harmonic degree 120 to 140 can be seen.

Even though GOCE data provides a better estimation of the MDT in the GOCINA region than any previously obtained using only satellite observations, it could not be concluded whether the regionally enhanced geoid model estimated using GOCE gradients contribute to a further improvement of the determination of the MDT in the GOCINA area. The surface geostrophic currents calculated from the GOCE Direct MDT current speeds reveal all of the gross features of the general circulation in the region. However, the MDT calculated in the GOCINA project shows the smallest scale details, which makes it the best ocean circulation representation in this region.

The resulting RPM technique can supplement the available collection of tools for the MDT determination, and can be applied to other regions of the world oceans where gravity data of high quality and spatial distribution is not available. Also, in the regions with higher gravity anomaly signal oscillations, i.e. mountain regions, GOCE

gradients can possibly provide even higher geoid enhancements than the ones shown here in an ocean region.

References

Andersen OB (2011) The DTU10 Global Gravity field and Mean Sea Surface-improvements in the Arctic. In: Second international symposium of the international gravity field service, Fairbanks, Alaska

Bruinsma S, Marty J, Balmino G, Biancale R, Boerste C, Abrikosov O, Neumayer H (2010) GOCE gravity field recovery by means of the direct numerical method. Presented at the ESA living planet symposium, Bergen, 27th June–2nd July

Chanfang S, Fei L, Weifeng H (2011) Geoid, quasigeoid fitting based on equivalent point masses. Geomatics and Information Science of Wuhan University

Forsberg R (1984) A study of terrain reductions, density anomalies and geophysical inversion methods in gravity field modelling. Reports of the department of geodetic science No 5, The Ohio State University, Columbus

Forsberg R, Tscherning CC (2008) An overview manual for the GRAVSOFT, geodetic gravity field modelling programs, 2nd edn. http://cct.gfy.ku.dk/publ_cct/cct1936.pdf

Hauck H, Lelgemann D (1985) Regional gravity field approximation with buried masses using least-norm collocation. Manuscri Geodaet 10(1):50–58

Herceg M (2012) GOCE data for ocean modelling. PhD Thesis, DTU Space, National Space Institute, Technical University of Denmark. http://curis.ku.dk/ws/files/40299176/HercegThesis2012.pdf. ISBN: 978-87-92477-12-5

Knudsen P (1987) Estimation and modelling of the local empirical covariance function using gravity and satellite altimeter data. Bull Geodesique 61:145–160

Knudsen P (2005) GOCINA: geoid and ocean circulation in the North Atlantic. Technical Report No. 5. Danish National Space Center

Knudsen P, Bingham R, Andersen OB, Rio MH (2011) A global mean dynamic topography and ocean circulation estimation using a preliminary GOCE gravity model. J Geodesy 85:861–879. doi:10.1007/s00190-011-0485-8

Krarup T (1969) A contribution to the mathematical foundation of physical geodesy. Meddelelse no 44. Geodaetisk Institut, Koebenhavn

Marchenko A, Barthelmes F, Meyer U, Schwintzer P (2001) Regional geoid determination: An application to airborne gravity data in the Skagerrak. Scientific Technical Report STR01/07. GFZ Potsdam

Maximenko N, Niiler P, Rio MH, Melnichenko O, Centurioni L, Chambers D, Zlotnicki V, Galperin B (2009) Mean dynamic topography of the ocean derived from satellite and drifting buoy data using three different techniques. J Atmos Oceanic Tech 26(9):1910–1919

Mayer-Guerr T (2007) ITG-Grace03s: The latest GRACE gravity field solution computed in Bonn. Presentation at GSTM+SPP, Potsdam, 15–17 October 2007

Pavlis E, Holmes S, Kenyon S, Factor J (2012) The development and evaluation of the Earth Gravitational Model 2008 (EGM2008). J Geophys Res 117:38. doi:10.1029/2011JB008916

Reed GB (1973) Application of kinematical geodesy for determining the short wave length components of the gravity field by satellite gradiometry. Reports of the Department of Geodetic Science no 201. The Ohio State University, Columbus

Sjogren W, Muller P, Gottlieb P, Wong L, Buechler G, Downs W, Prislin R (1971) Lunar surface mass distribution from dynamical point-mass solution. Moon 2:338–353. doi:10.1007/BF00561885. http://dx.doi.org/10.1007/BF00561885

Tscherning CC (1976) Covariance expressions for second and lower order derivatives of the anomalous potential. Reports of the Department of Geodetic Science no 225. The Ohio State University, Columbus

Tscherning CC (2005) Program GEOCOL - A FORTRAN program for gravity field approximation by collocation. Geophysical Institute, University of Copenhagen. http://cct.gfy.ku.dk/geocol.pdf

Tscherning CC, Arabelos D (2011) Gravity anomaly and gradient recovery from GOCE gradient data using LSC and comparisons with known ground data. In: Proceedings 4th international GOCE user workshop. ESA Publications Division, Nordwijk

Tscherning CC, Rapp RH (1974) closed covariance expressions for gravity anomalies, geoid undulations, and deflections of the vertical implied by anomaly degree-variance models. Reports of the Department of Geodetic Science No 208. The Ohio State University, Columbus

Tscherning CC, Veicherts M (2007) Optimization of gradient prediction. http://cct.gfy.ku.dk/publ_cct/cct1912.pdf

Vermeer M (1982) The use of mass point models for describing the Finnish gravity field. In: Proceedings, 9th meeting nordic geodetic commission, Gaevle

Vermeer M (1990) Work on satellite gravity gradiometry using a burried masses grid representation. Study on Precise gravity field determination methods and mission requirements (Phase 2). Final Report, Part 510B, pp 1–18

Vermeer M (1992) Geoid determination with mass point frequency domain inversion in the Mediterranean. Mare Nostrum 2, GEOMED report, Madrid, pp 109–119

Vermeer M (1995) Mass point geopotential modelling using fast spectral techniques. Manuscr Geodaet 20(5):362–378

Yildiz H (2012) A study of regional gravity field recovery from GOCE vertical gravity gradient data in the Auvergne test area using collocation. Stud Geophys Geod 56:171–184. doi:10.1007/s11200-011-9030-8

Investigation of Gravity Data Requirements for a 5 mm-Quasigeoid Model over Sweden

Jonas Ågren and Lars E. Sjöberg

Abstract

When GNSS height determination improves in the future, users will ask for increasingly better geoid models. It is not unlikely that a standard error of 5 mm will more or less be required in a couple of years. The main purpose of this paper is to investigate the gravity data requirements to compute a Swedish gravimetric quasigeoid model to that order. The propagation of errors in the terrestrial gravity observations and the Earth Gravitational Model (EGM) are studied using both variance-covariance analysis in the spectral domain and least squares collocation. These errors are also checked by computing a new gravimetric quasigeoid model and comparing it with GNSS/levelling height anomalies. It is concluded that it will be possible to compute a 5 mm model over Sweden in the case that the gravity data set is updated to fulfil the following requirements: the resolution should be at least 5 km and there should be no data gaps nearby. Finally, the standard errors of the uncorrelated and correlated gravity anomaly noises should be below 0.5 and 0.1 mGal, respectively.

Keywords

Geoid • Quasigeoid • Gravity

1 Introduction

For a long time the geoid community has been aiming for the "1 cm geoid" (e.g., Saleh et al. 2012). This is definitely a tough goal, especially in mountainous areas, but it is nevertheless questionable whether it will be sufficient for the future. Today, GNSS height determination is replacing levelling in an increasing number of practical applications, even though the accuracy of real time GNSS methods is still not sufficient for the most demanding surveying tasks. The state of the art standard error of Network RTK is presently (2013) around 10–25 mm for the height above the ellipsoid, depending on the distance between the reference stations (Emardson et al. 2009). To this we should then add the error contribution of the geoid model. For instance, the standard error of the official Swedish quasigeoid model SWEN08_RH2000 is estimated to 10–15 mm (Ågren 2009).

However, as is shown by Emardson et al. (2009), there is room for improvement of the real time GNSS methods, and it is not unrealistic that a standard error of 5 mm will be achieved for the height above the ellipsoid. Of course, it is uncertain how rapid this development will be, but a reasonable guess is that this high accuracy will be reached within 10–20 years. If (or when) this happens, GNSS users will more or less require the corresponding accuracy for the geoid model.

To be able to meet such high demands, it is important to know already now in what cases it will actually be realistic to compute a 5 mm geoid, what kind of computation methods that are required and what data (gravity, DEM, etc.) that

J. Ågren (✉)
Division of Geodesy and Geoinformatics, Org Name: Royal Institute of Technology (KTH), Post-Code: 100 44 City: Stockholm, Country: Sweden

Lantmäteriet, The Swedish Mapping, Cadastre and Registry Authority, Post-Code: 801 82 City: Gävle, Country: Sweden

L.E. Sjöberg
Division of Geodesy and Geoinformatics, Royal Institute of Technology (KTH), 100 44 Stockholm, Sweden

U. Marti (ed.), *Gravity, Geoid and Height Systems*, International Association of Geodesy Symposia 141,
DOI 10.1007/978-3-319-10837-7_18, © Springer International Publishing Switzerland 2014

should be available. Since it takes a long time and much work to improve some of the data sets, especially terrestrial gravity, it is important to consider the above questions now. It might be the case that we have to start to measure relative gravity today to be able to compute a 5 mm model in 20 years. To answer the above and similar questions, a new project has been created by the Nordic Geodetic Commission (NKG).

The main purpose of this paper is to study the gravity *data requirements* to determine a gravimetric quasigeoid model with 5 mm standard error (in the relative sense) over Sweden. This should be seen as an initial contribution to the above mentioned NKG project. The project will then continue with similar investigations in the other Nordic countries and also with treatments of various modelling aspects.

The paper is organised as follows: The terrestrial gravity data now available over Sweden and surrounding areas is briefly summarised in Sect. 2. It is then investigated how the standard errors in the gravity anomalies and in the Earth Gravitational Model (EGM) propagate to the quasigeoid. The methods used are both direct variance-covariance analyses in the spectral domain (Sect. 3) and least squares collocation (Sect. 4). To check the results, a new quasigeoid model is compared with GNSS/levelling height anomalies in Sect. 5. The GOCO03S EGM (Mayer-Gürr et al. 2012) is used in all the above error propagations as well as in the computation of the new gravimetric quasigeoid model.

The main purpose of the stochastic error propagations in Sects. 3 and 4 is to find out what requirements have to be put on the Swedish gravity data to be able to compute a quasigeoid model with 5 mm standard error. It might of course be a serious practical problem how to ascertain whether the gravity anomaly data really fulfils these requirements. It is also a problem that methodological limitations might introduce additional errors. However, this does not diminish the value of the error propagations. Based on the results we might say: *if* the data in question fulfils the requirements of the error propagations, and *if* no additional methodological errors are involved, *then* it will be possible to compute a gravimetric quasigeoid model to 5 mm standard error. This is valuable information. We can then work on improving the gravity data to fulfil the data requirements in question. At the same time, we should also work on theoretical and methodological improvements, but this is not the purpose of this paper.

2 The Swedish and Nordic Gravity Data

In the error propagations we will start from the present gravity data situation. We will then need as realistic standard errors as possible for the gravity anomalies. This section will present the available gravity anomalies and an estimate of their approximate standard errors.

The observations in the Swedish gravity database are stored with standard errors for the gravity values and the normal heights (σ_g and σ_H). It is difficult to judge how realistic these standard errors are, but they seem to have been assigned in a comparatively careful way, as judged by what can be expected from the specified instruments, methods, etc. The standard error of the gravity anomaly (Δg) is then computed using the standard law of error propagation (i.e., $\sigma_{\Delta g} = \sqrt{\sigma_g^2 + 0.3086^2\sigma_H^2}$).

For the non-Swedish data, the gravity anomaly standard errors are taken directly from the NKG database of the Nordic Geodetic Commission (NKG). Here the standard errors are given in a more schematic way, usually using the same standard errors for large groups of observations, mainly in order to weight them relative to each other. Sometimes a very high standard error is assumed just to indicate that a group is unreliable and that another group should be preferred instead, etc. Since we are only interested in the Swedish quasigeoid, the NKG standard errors are considered as sufficient for the gravity data *outside* Sweden. The standard errors for the gravity anomalies in and around Sweden are illustrated in Fig. 1.

The resolution of the Swedish data is approximately 5 km. It can be seen in Fig. 1 that the gravity anomaly standard errors for these data are below 0.5 mGal in the majority of areas (purple/blue areas), but in some places they are larger (green areas). It can further be seen that there are a number of areas with no observations at all. Most important are the data gaps in Lake Vättern and along many of the coastlines as well as the low resolution in the NW of the country.

3 Variance-Covariance Propagation in the Spectral Domain

Here we present the stochastic error propagations made based on the assumptions of *homogeneous* and *isotropic* signal and error covariance functions. We study how the standard error of the height anomaly depends on the error covariance functions of the gravity anomalies and the EGM.

3.1 Basic Formulas and Assumptions

It is assumed that a suitable regional quasigeoid determination method is used to estimate the height anomaly, and that the only error sources are the stochastic errors of the EGM and the terrestrial gravity anomalies. The height anomaly is assumed to be computed by a remove-compute-restore (r-c-r) estimator using a modification of Stokes' formula with the terrestrial gravity anomalies in a spherical cap. Both the terrestrial gravity anomaly and the EGM contributions are corrected for the direct topographic effect, and the indirect

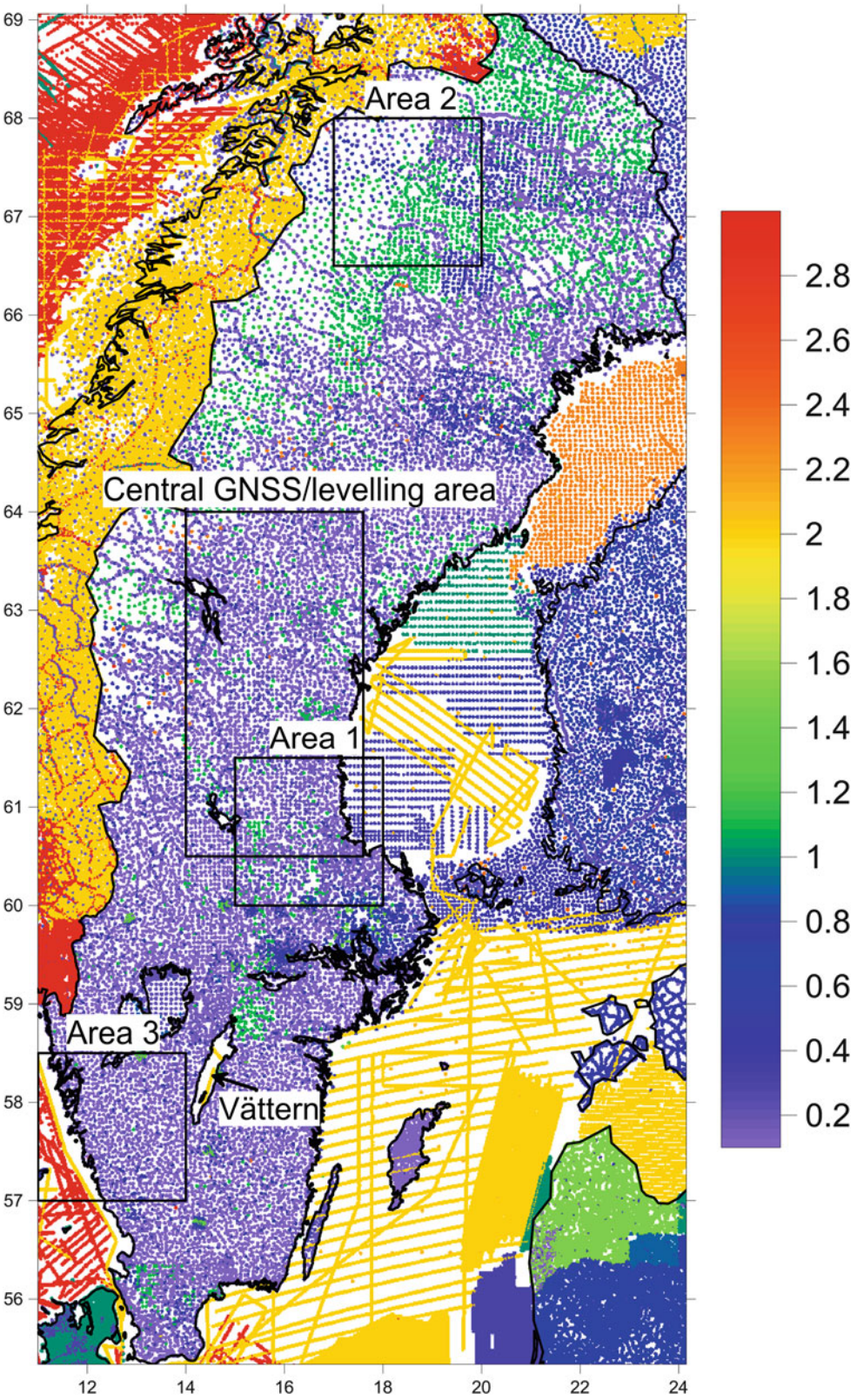

Fig. 1 The gravity anomaly standard errors used in the error propagations in Sect. 4. All observations with standard errors larger than 3 mGal are plotted as *red*. The three areas studied in Sect. 4 are also illustrated together with the central area used in the GNSS/levelling comparison of Sect. 5. Unit: mGal. (colour figure online)

topographic effect is finally added to the height anomaly; see e.g. Forsberg (1984a).

The gravity anomaly error degree variances for the terrestrial gravity anomaly and the EGM are denoted by $\sigma_n^{\Delta g}$ and σ_n^{EGM}, respectively, while the signal gravity anomaly degree variances for the *reduced field* are denoted c_n. If the degree variances at point level are taken as identical to those at sea level, which is a good approximation for the rather low topography of Sweden (Ågren 2004), then the expected global mean square error becomes (Sjöberg 1991; Ågren 2004):

$$\begin{aligned}\delta\overline{\zeta}^2 \approx \delta\overline{N}^2 = \left(\tfrac{R}{2\gamma}\right)^2 \sum_{n=2}^{M} \Bigg[\left(\frac{2}{n-1} - s_n - Q_n^M\right)^2 \sigma_{n,\Delta g}^2 \\ + \left(s_n + Q_n^M\right)^2 \sigma_{n,EGM}^2 \Bigg] \\ + \left(\tfrac{R}{2\gamma}\right)^2 \sum_{n=M+1}^{n_0} \Bigg[\left(\frac{2}{n-1} - Q_n^M\right)^2 \sigma_{n,\Delta g}^2 \\ + \left(Q_n^M\right)^2 c_n \Bigg] \\ + \left(\tfrac{R}{2\gamma}\right)^2 \sum_{n=n_0+1}^{\infty} \left(\frac{2}{n-1}\right)^2 c_n \end{aligned} \tag{1}$$

where R is the mean Earth radius, γ is the mean normal gravity at sea level, n is the spherical harmonic degree, M is the maximum degree of the EGM, Q_n^M are the Molodensky truncation coefficients for the modified Stokes' kernel with modification parameters s_n and n_0 is the Nyquist degree of the terrestrial gravity anomalies. In this section the propagated expected global RMS height anomaly error $\delta\overline{\zeta}$ is studied for various signal and error degree variances.

It should be pointed out that the above results are also relevant for the technique of Least Squares Modification of Stokes formula with Additive corrections (LSMSA) (see Sect. 5) even though the unreduced gravity anomaly is then used. This is the case as long as the LSMSA method is applied using a r-c-r strategy in the gravity anomaly gridding phase, and this is the standard way to apply this method (e.g., Ågren et al. 2009).

3.2 Selection of Degree Variances

It is naturally important to use as representative degree variances as possible. Here we first deal with the estimation of the reduced signal degree variances and then with the choice of error degree variances for the EGM and the terrestrial gravity anomalies.

3.2.1 Signal Degree Variances

The reduced signal degree variances are computed empirically from the reduced gravity anomalies over Sweden, computed by subtracting the following effects from the surface gravity anomalies:

- The EGM effect computed by GOCO03S (Mayer-Gürr et al. 2012) with maximum degree $M = 200$.
- The high-frequency part of the topographic effect computed by the RTM method with a smooth reference surface (corresponding to M). The TC and TCFOUR programs in GRAVSOFT (Forsberg 2003) are applied for this task using a $0.001° \times 0.002°$ DEM, computed based on the Swedish photogrammetric 50 m × 50 m DEM.

The local empirical covariance function is computed by numerical integration in more or less the standard way described in Knudsen (1987). A Tscherning and Rapp (1974) analytical covariance function (model 4) is used to represent the covariance function. The following gravity anomaly degree variance model is assumed:

$$c_n = \sigma_{n,\,\mathrm{GOCO03S}}^2 \qquad \mathrm{n} \le 200 \tag{2a}$$

$$c_n = \alpha \frac{(n-1)}{(n-2)\,(n+4)} \left(\frac{(R-D)^2}{R^2}\right)^{n+2} \qquad n > 200 \tag{2b}$$

The local empirical covariance function is computed both for the whole of Sweden and for several small $1° \times 2°$ areas. The purpose of using a number of small areas is to get a good estimate of how the highest frequencies vary with the location (cf. Forsberg 1984b). Two different analytical covariance functions are finally chosen for use in the error propagations: The first (with $\alpha = 240$ mGal^2 and $D = 3.5$ km) is representative for the areas with the roughest high frequency variation in Sweden, while the second (with $\alpha = 100$ mGal^2, $D = 5.0$ km) is representative for the smoothest areas. The second model is close to the average for the whole of Sweden.

3.2.2 Error Degree Variances

As mentioned in the introduction, the GOCO03S EGM with $M = 200$ is used in all computations. The EGM error degree variances are then derived from the formal degree-order standard deviations. It is considered as sufficient to use degree variances here. Since the EGM is combined with terrestrial gravity in a least squares sense, the propagated height anomaly standard error is not sensitive to small changes in the error model of the EGM.

The Swedish gravity data were presented in Sect. 2. The present average resolution, 5 km, is chosen in order to

investigate whether this is sufficient or not. The error degree variances for the gravity anomalies are assumed to be a combination of two independent parts:

- Band-limited white noise with the Nyquist harmonic degree 3960 (corresponding to 5 km).
- Correlated noise following the reciprocal distance covariance function (Moritz 1980) with a certain correlation length.

It might be objected that the reciprocal distance model is not limited to degrees below the Nyquist limit. However, if the correlation length is chosen longer than about 0.2°, the power above the Nyquist degree becomes very close to zero.

The idea here is to use one covariance function for correlated noise stemming predominantly from the errors in the underlying gravity network/system and to combine it with a white noise covariance function describing the uncorrelated errors in the gravimeter measurements at the station, errors in the height measurements, etc. This stochastic model is, of course, an approximation. For the present purpose, though, we can learn a lot by studying the propagated height anomaly RMS error for different variances (standard errors) and correlation lengths. Since the present Swedish gravity network has one station approximately every 50 km, it is reasonable to assume a correlation length around 0.25°, but also other values have been tested (not presented here).

3.3 Propagated Quasigeoid Height RMS Errors

Based on the assumptions of Sects. 3.1 and 3.2, the results of a selection of error propagations computed according to Eq. (1) are presented in Table 1. A 3-degree spherical Stokes integration cap is assumed in combination with the least squares (stochastic) kernel modification with correct weighting. In reality we do not know the correct weighting (signal and error degree variances), which will increase the height anomaly error. However, this is not considered as depending on the quality of the data, which is what we study here. It should also be mentioned that both the rough and the smooth signal degree variance models have been tested, but since the obtained results are very similar, only the results for the rough case are presented in Table 1. The table shows that the propagated height anomaly RMS error is much more affected by the correlated noise than by the band-limited white noise. If the correlated noise is zero, a standard error of 5 mm can be obtained with a white noise standard error as high as 1.0 mGal. For the reciprocal distance model, the corresponding standard error is 0.2 mGal. In reality, there will be a combination of white and coloured noise. The third error propagation (with the RMS error 5.2 mm) shows a situation that could possibly be fulfilled already now for the best areas of Sweden (the purple/blue areas of Fig. 1).

Table 1 Propagated expected global RMS error for the height anomaly. The rough signal degree variance model, a spherical cap with radius 3 degrees and the Nyquist degree 3960 are used

Gravity anomaly noise model	Std Err. (mGal)	Corr. length (deg)	Expected global RMS error (mm)
White	1.0	–	4.7
Reciprocal dist.	0.0	0.25	
White	0.0	–	4.9
Reciprocal dist.	0.2	0.25	
White	0.5	–	5.2
Reciprocal dist.	0.2	0.25	
White	0.5	–	3.6
Reciprocal dist.	0.1	0.25	
White	0.2	–	3.0
Reciprocal dist.	0.1	0.25	

It should be noted that the results in Table 1 are dependent on the type of covariance function that is assumed for the correlated noise, and it is extremely difficult to ascertain exactly what type of correlated noise that is involved in a specific case. The only reliable way to do this is to repeat all measurements in a way that results in very close to uncorrelated gravity anomalies. However, what we can say based on Table 1 is that, *if* the gravity anomalies are very close to being uncorrelated (within a standard error of 0.1 mGal, to be on the safe side), then it will be possible to compute a quasigeoid model with 5 mm standard error over Sweden in case one has uniform data with 5 km resolution and a white noise standard error below approximately 0.5 mGal.

4 Error Propagation by Least Squares Collocation

In the error propagations in Sect. 3, the gravity anomaly error covariance function was assumed to be homogeneous and isotropic. Here we test how the error propagations are affected by using the more realistic data distribution and the individual standard errors in Fig. 1. The method used is Least Squares Collocation (e.g. Moritz 1980, pp. 124–128), by which the propagated standard errors are obtained by taking the square root of

$$\sigma_\zeta^2 = C_{\zeta\zeta} - \mathbf{C}_{\xi\Delta g}\left(\mathbf{C}_{\Delta g\Delta g} + \mathbf{D}\right)^{-1}\mathbf{C}_{\Delta g\zeta}, \qquad (3)$$

where $\mathbf{C}$ and $\mathbf{D}$ are the signal and error variance-covariance matrices, respectively. The latter matrix is taken as consisting of two independent parts: The uncorrelated part is computed based on the individual standard errors of Fig. 1. The correlated part is again given by the reciprocal distance model (same as in Sect. 3) with the standard error 0.1 mGal

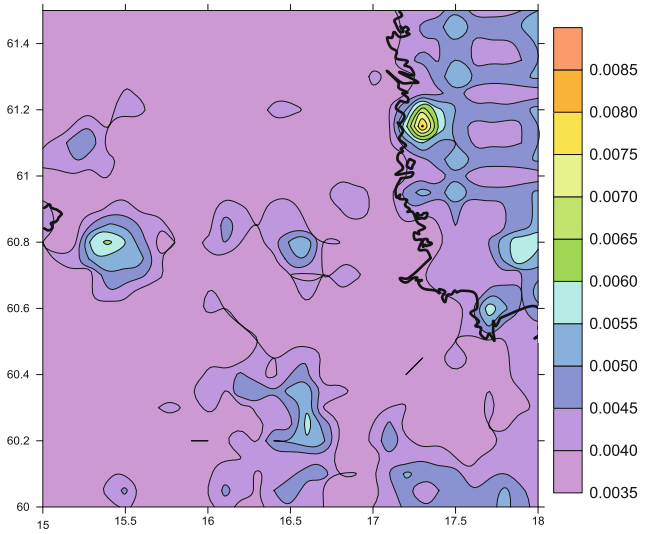

Fig. 2 Propagated height anomaly standard errors in *area 1* computed by Least Squares Collocation. Unit: m. (colour figure online)

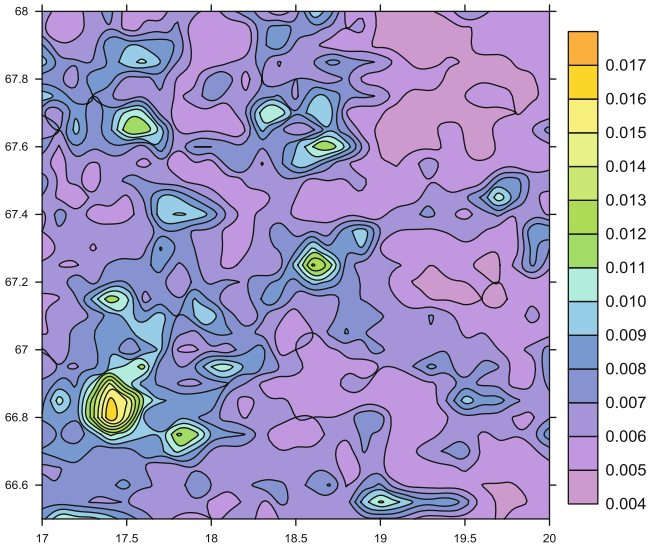

Fig. 3 Propagated height anomaly standard errors in *area 2* computed by Least Squares Collocation. Unit: m. (colour figure online)

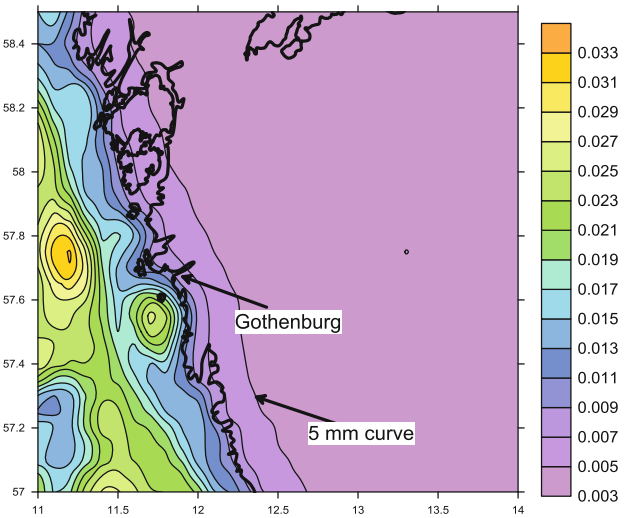

Fig. 4 Propagated height anomaly standard errors in *area 3* computed by Least Squares Collocation. Unit: m. (colour figure online)

and the correlation length 0.25°. The chosen error model corresponds to the fourth and fifth rows of Table 1. It should further be mentioned that a strict covariance propagation with a correct dependence on heights is considered, taking advantage of the closed formulas derived by Tscherning and Rapp (1974). The error propagations were made using Eq. (3) in three test areas, which are illustrated in Fig. 1. The smooth signal covariance function model is used in areas 1 and 3, while the rough model is applied in area 2. The chosen models agree well with the local empirical covariance function in all three areas. The data has been slightly smoothed by selecting only one observation per 5 km × 5 km. Furthermore, the gravity observations cover a larger area, obtained by extending the height anomaly area with 110 km in the east, west, north and south directions. The propagated height anomaly standard errors are illustrated for areas 1–3 in Figs. 2, 3, and 4, respectively. Some statistics for all three areas are presented in Table 2.

By comparing Fig. 1 with Figs. 2, 3, and 4 it can be seen that the requirement of 5 mm height anomaly standard error can be reached in the areas with 5 km resolution, no data gaps and a white noise standard error below approximately 0.5 mGal. In such areas (e.g. most parts of area 1 in Fig. 2) the results agree well with the corresponding error propagations in Table 1. It should especially be noted that the data gaps are problematic. Not only does the gap outside the west coast of Sweden in Fig. 4 yield a maximum error of about 3 cm at sea, but it also affects the height anomaly standard error on land, near to the sea. In Gothenburg, for instance, a standard error around 8 mm is obtained. It is concluded that it is of highest priority to close the gaps, e.g. the gaps around the coasts and in Lake Vättern (see Fig. 1). Furthermore, Fig. 3 shows that it is difficult to reach 5 mm in the rough area 2. This is also due to the lower resolution (around 7–10 km) utilised in this rough, mountainous part of Sweden.

Table 2 Statistics for the height anomaly standard errors propagated using Least Squares Collocation. Unit: m

Area	# of pts	Min	Max	Mean
1	961	0.0035	0.0081	0.0040
2	961	0.0044	0.0170	0.0067
3	961	0.0035	0.0332	0.0080

Table 3 Comparison of the new gravimetric model with GNSS/levelling. Statistics for the GNSS/levelling residuals without a fit and after a 1 and a 4 parameter fit. Unit: m

Area	Fit	# pts	Min	Max	Mean	StdDev
Whole Sweden	No fit	197	−0.699	−0.564	−0.641	0.021
	1-par.	197	−0.058	0.076	0.000	0.021
	4-par.	197	−0.055	0.083	0.000	0.020
Central area	No fit	28	−0.651	−0.608	−0.632	0.012
	1-par	28	−0.018	0.024	0.000	0.012
	4-par.	28	−0.013	0.017	0.000	0.009

5 Comparison with GNSS/Levelling

The above error propagations are made under a number of assumptions. In order to check that they are reasonably realistic, a new gravimetric quasigeoid model has been computed by the LSMSA method, applied in almost the same way as in Ågren et al. (2009). The only differences to Ågren et al. (ibid.) are that the GOCO03S model is used here, and that the weighting of the least squares (stochastic) kernel modification is made using the error model in the third row of Table 1. This error model is thus *not* chosen to optimise the fit to GNSS/levelling (even though the choice in question yields a good fit).

The results are compared with 197 high accuracy GNSS/levelling height anomalies. Except for one new observation, this data set is described in detail in Ågren et al. (2009, Sect. 5). The relative standard error for the GNSS/levelling height anomalies, $\sigma_{GNSS/lev}$, is here taken to be approximately 15 mm over long distances (inside Sweden) and about 7 mm over short distances (below 100–200 km).

The statistics of the residuals after 1- and 4-parameter fits are presented in Table 3. A fit is also made in the small, central area illustrated in Fig. 1, where the gravity data is particularly good (except for one gap to the east). Statistics for the corresponding fits are also given in Table 3. The differences between the GNSS/levelling height anomalies and the gravimetric model without a fit are also presented in Table 3.

Since the fit residuals contain errors in the gravimetric model, in the GNSS heights and in the levelled heights, the standard error of the gravimetric quasigeoid model is then estimated using the standard law of error propagation,

$$\sigma_{quasigeoid} = \sqrt{\sigma^2_{4-par.\,fit} - \sigma^2_{GNSS} - \sigma^2_{levelling}} = \sqrt{\sigma^2_{4-par.\,fit} - \sigma^2_{GNSS/lev}} \quad (4)$$

For the GNSS/levelling standard errors ($\sigma^2_{GNSS/lev}$) mentioned above, we then obtain a quasigeoid standard error of 13 mm over longer distances and around 5 mm in the central area. The latter result is close to the results of the error propagations in areas without data gaps and where the gravity anomaly standard errors are below 0.5 mGal. This yields support to the error propagations of Sects. 3 and 4.

Conclusions

The error propagations presented in Sects. 3 and 4 have shown that it is possible to compute a gravimetric quasigeoid model with 5 mm standard error over Sweden in case the following data requirements are fulfilled:

- The gravity anomaly resolution should be at least 5 km. (This has also been confirmed with 1 km gravity data in a few test areas in Sweden, but these results are not presented here.)
- There should be no gravity data gaps in the "5 mm quasigeoid area" or in its vicinity.
- The standard error of the uncorrelated (white) noise should be lower than approximately 0.5 mGal for the gravity anomaly.
- The systematic errors should be as low as possible. For the assumed reciprocal distance function with 0.25° correlation length, the standard error has to be lower than about 0.2 mGal. In reality the covariance function is more complex and not precisely known. To be on the safe side, the correlated standard error should be below 0.1 mGal. To achieve this we need to do everything we can to reduce all kind of systematic effects.

Work is presently under way to improve the Swedish gravity data by filling-in the data gaps, by replacing bad gravity observations and by checking about 10 % of the good observations. Also, a new Swedish gravity system (RG 2000) is under construction, to which existing and new data will be connected. It is the intention that these efforts will result in gravity anomalies that are very nearly uncorrelated and that fulfil the above requirements. The gravity system RG 2000 will primarily be realised by gravity determined by Absolute Gravimetry (FG5 or A10) in about 100 stations, but relative gravity observations will also be utilised. The system will be defined as far as possible according to international conventions and is planned for release in 2015 (Lantmäteriet 2010).

References

Ågren J (2004) Regional geoid determination methods for the era of satellite gravimetry – numerical investigations using synthetic earth gravity models. Doctoral Dissertation (PhD thesis) in Geodesy Report No 1062, Royal Institute of Technology, Stockholm

Ågren J (2009) Beskrivning av de nationella geoidmodellerna SWEN08_RH2000 och SWEN08_RH70. Reports in Geodesy and Geographic Information Systems, 2009:1, Gävle, Sweden

Ågren J, Sjöberg LE, Kiamehr R (2009) The new gravimetric quasi-geoid model KTH08 over Sweden. J Appl Geod 3:143–153

Emardson R, Jarlemark P, Bergstrand S, Nilsson T, Johansson J (2009) Measurement accuracy in Network-RTK. SP report 2009:23, Borås, Sweden

Forsberg R (1984a) A study of terrain reductions, density anomalies and geophysical inversion methods in gravity field modelling. Rep 355, Dept Geod Sci, Ohio State Univ, Columbus

Forsberg R (1984b) Local covariance functions and density distributions. Rep No 356, Dept Geod Sci, Ohio State Univ, Columbus

Forsberg R (2003) An overview manual for the GRAVSOFT geodetic gravity field modelling programs, report, 1st edn. Kort & Matrikelstyrelsen, Copenhagen

Kuudsen P (1987) Estimation and Modelling of the local empirical covariance function using gravity and satellite altimetter data. Bull Gèod 61:145–160

Lantmäteriet (2010) A strategic plan for Lantmäteriet's geodetic activities 2011–2020. Report, Lantmäteriet, Gävle

Mayer-Gürr T et al (2012) The new combined satellite only model GOCO03S. Poster presentation at GGHS2012, Venice, Italy, 9–12 October 2012

Moritz H (1980) Advanced physical geodesy. Wichmann, Karlsruhe

Saleh J, Xiaopeng L, Wang YM, Roman DR, Smith DA (2012) Error analysis of the NGS' surface gravity database. J Geod 87:203–221. doi:10.1007/s00190-012-0589-9

Sjöberg LE (1991) Refined least squares modification of Stokes' formula. Manuscr Geod 16:367–375

Tscherning CC, Rapp RH (1974) Closed covariance expressions for gravity anomalies, geoid undulations, and deflections of the vertical implied by anomaly degree variance models. Rep 208, Dept Geod Sci, Ohio State Univ, Columbus

Consistent Combination of Satellite and Terrestrial Gravity Field Observations in Regional Geoid Modeling: A Case Study for Austria

Christian Pock, Torsten Mayer-Guerr, and Norbert Kuehtreiber

Abstract

In this investigation a consistent combination of the complementary data types of satellite observations and the available terrestrial gravity field measurements in Austria is considered. For this purpose, the well known Remove-Compute-Restore technique is adapted to perform long- and short-wavelength signal reductions. The long-wavelength effect is represented by a global satellite-only model in terms of spherical harmonics. The short-wavelength are modeled by topographic masses in the spatial domain. As the topographic reduction contains also long-wavelength effects a possible double consideration has to be avoided. Alternatively to Least Squares Collocation (LSC) method (Moritz 1980a) a least squares approach with parametrization as Radial Basis Functions (RBF) is applied. The RBF approach has the advantage that an increasing number of observations can be included in the calculations and a downsampling of the available data, as it is required in LSC, will no longer be necessary. Another advantage is that RBF is to able to handle an inhomogeneous input data distribution. The very first outcomes are verified by comparing with independent GPS/leveling observations.

Keywords

GPS/leveling observations • Radial basis functions (RBF) • Regional geoid modeling • Remove-compute-restore technique

1 Introduction

The determination of the Earth's gravity field can take place on different spatial scales. Dedicated satellite missions like CHAMP (CHAllenging Minisatellite Payload) (Reigber et al. 2002), GRACE (Gravity Recovery And Climate Experiment) (Tapley et al. 2002) or GOCE (Gravity field and steady-state Ocean Circulation Explorer) (Drinkwater et al. 2003) detect the global gravity field with high accuracy. For instance, with the GOCE mission it is possible to derive a global gravity field model parametrized in terms of a spherical harmonic series expansion up to a degree and order (D/O) of 250 corresponding to a spatial resolution of approximately 80 km half wavelength. The accuracy in terms of geoid height with 100 km spatial resolution is 1–2 cm (Drinkwater et al. 2008). However, for regional applications the spatial resolution of a satellite-only gravity field model is insufficient. Many local and regional applications require a much higher spatial resolution than a satellite-only model can provide.

On the other hand, local gravity field models derived from terrestrial and airborne gravity field data e.g. gravity anomalies or deflections of the vertical reflect the small scale features better as the satellite data but lack from long-wavelength information. Therefore a pure gravimetric geoid solution is affected by long-wavelength errors (Pail et al. 2009).

C. Pock (✉) • T. Mayer-Guerr
Institute of Theoretical Geodesy and Satellite Geodesy, Steyrergasse 30/III, 8010 Graz, Austria
e-mail: christian.pock@tugraz.at; mayer-guerr@tugraz.at

N. Kuehtreiber
Institute of Navigation, Steyrergasse 30/III, 8010 Graz, Austria
e-mail: norbert.kuehtreiber@tugraz.at

U. Marti (ed.), *Gravity, Geoid and Height Systems*, International Association of Geodesy Symposia 141,
DOI 10.1007/978-3-319-10837-7_19,

So an consistent combination of satellite derived global gravity field models with complementary local gravity field data suggests itself. Recently two research projects GEO-nAUT (Pail et al. 2008) and GEOID + (Kuehtreiber et al. 2011) were carried out at Graz University of Technology. By combining heterogeneous data the precision of the Austrian geoid has improved to sub-decimeter level. The computation was based on the Remove-Compute-Restore technique. In the remove step a global satellite only model has been used to represent the long-wavelength components as well as a topographic reduction has been carried out to remove the topographic short-wavelength components from the measured gravity. For geoid computation the LSC approach was used and furthermore all removed components have been restored afterwards. Nevertheless, the present Austrian geoid solution (Pail et al. 2008) shows long wavelength errors when compared to the GPS/leveling observations which is supposed to be a problem of the combination of the satellite derived gravity field models and the terrestrial gravity data. A common practical approach to handle this problem is to introduce a non-physical correction surface. The need of such a correction surface for practical applications was tried to be avoided by combinations with global satellite-only models of different D/O. However, these attempts were not successful and a correction surface is still required. The main goal of this investigation is to discover a proper way for the combination of the satellite derived global gravity field models with the complementary terrestrial data with the result, that the computed geoid can be directly validated with GPS/leveling observations and a correction surface is not needed anymore.

2 Data

2.1 Gravity Dataset

The achieved results are based on a gravity dataset spanning Central Europe. This database was established by Norbert Kuehtreiber during the last decades and the gravity measurements have been provided by several project partners (e.g. Federal Office of Meteorology and Surveying (BEV), Institute of Geophysics (Mining University Leoben) or the Austrian Mineral Oil Administration (OMV). Including Austrian data and data from neighbouring countries there are currently almost 123,000 measurements available. For these first investigations only 28,212 gravity measurements within Austria have been used to avoid datum problems. In the future all available data will be incorporated. The spatial distribution of the data is about 1 to 15 km and quite inhomogeneous. In mountainous regions measurements are spare whereas in valleys and flatland a huge amount of measurements is available. The gravity data consists of global WGS-84 coordinates and the heights are related to the official Austrian orthometric height system. In Fig. 1 the data sample is shown.

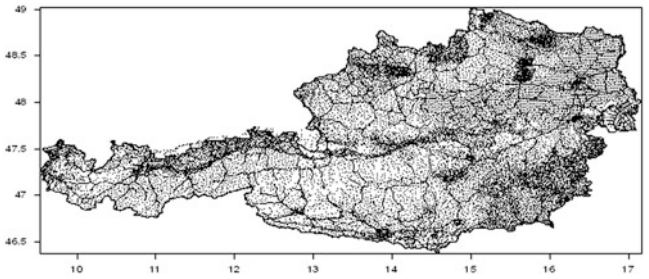

Fig. 1 Sample of 28212 gravity measurements

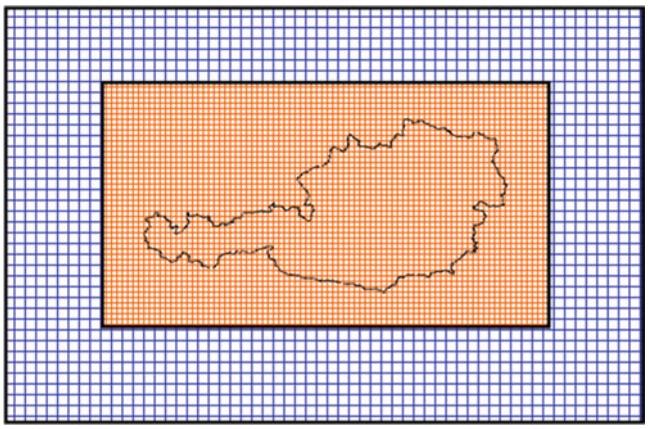

Fig. 2 Combination of the two DTMs in the Central European region-coarse (*blue*), dense (*red*)

2.2 Digital Terrain Model (DTM)

The topographic reduction which is representing the short-wavelengths components of the gravity field is based on two DTMs established by the BEV. The resolution for the coarse DTM is $11.25'' \times 18.75''$. For the dense DTM a uniform resolution of $1.40625'' \times 2.34375''$ is provided. Both DTMs cover the Central European area. Further information concerning the development of the height models can be found in Graf (1996) or Ruess (1983). The DTMs have to be combined in the calculation. Therefore the coarse DTM covers the whole area. In the area nearby Austria the coarse grid is refined by a residual dense grid which contains not the complete topography but only the corrections to the coarse grid (Fig. 2).

2.3 GPS/Leveling Observations

The GPS/leveling observations have been used to check the quality of the computed geoid solution. Currently 192 points

with measured geoid heights are available within Austria. This set is composed of points from the Austrian Reference Frame-net (AREF-net) and GPS permanent stations provided by the BEV. The precision of the observed geoid heights is assumed to be a few centimeter.

3 Consistent Reduction

3.1 Remove Step

The remove procedure is used to smooth the measured gravity field quantities to permit the continuation and interpolation to the generating geoid. Therefore the measured data on Earth surface has to be reduced by long- and short wavelength components. The long wavelength part is known by means of a given global satellite model which is expressed in terms of spherical harmonic expansion. The short wavelength part is a function of the mass and density distribution of the topography and can be approximated by the DTM. The effect of the topography is represented by prism integrated in the spatial domain and contains in principle all frequencies and also some long-wavelength part which is already considered in the satellite data. Therefore the effect of the DTM have to be reduced by this long-wavelength part and is expressed as a spherical harmonic expansion limited by the maximum degree of the satellite derived global gravity field model. The topographic coefficients are obtained by:

$$\begin{pmatrix} c_{nm} \\ s_{nm} \end{pmatrix} = \frac{1}{M(2n+1)} \iiint_{\Omega} \left(\frac{r'}{R}\right)^n \begin{pmatrix} C_{nm}(\theta', \lambda') \\ S_{nm}(\theta', \lambda') \end{pmatrix} \rho(r') d\Omega, \tag{1}$$

where in Eq. (1) the C_{nm} and S_{nm} are representing the spherical harmonics as defined

$$\begin{pmatrix} C_{nm} \\ S_{nm} \end{pmatrix} = P_{nm}(cos\vartheta) \begin{pmatrix} cos\, m\lambda \\ sin\, m\lambda \end{pmatrix}. \tag{2}$$

The Earth mass is denoted with M. The ρ stands for the standard crustal density. For this investigation a crustal density of $\rho = 2{,}670\,\mathrm{kg/m^3}$ was chosen. More details about the modeling of the topographic effects in spectral domain can be found in (Rummel et al. 1988). To sum up, the topographic reduction by prism is reduced of long wavelength parts represented by spherical harmonics [Eq. (3)]. The same reduction has to be done for both used DTMs (see Sect. 2.2).

3.2 Realization of Reduction

The input gravity dataset consists of 28,212 gravity measurements as described in Sect. 2.1. The long-wavelength part is represented by the latest Gravity Observation Combination

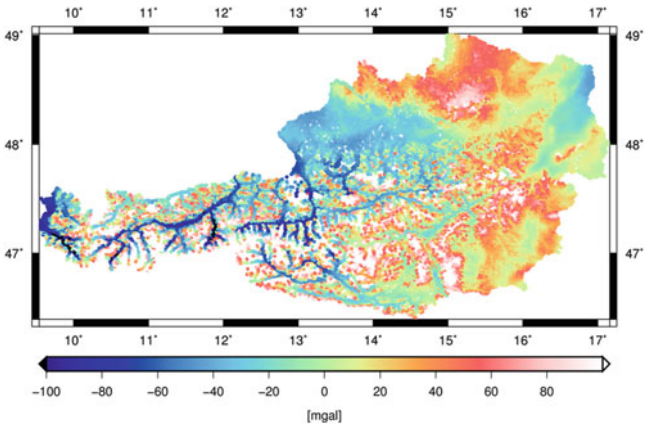

Fig. 3 Free air anomalies g_{abs}-γ; rms = 41.56 mgal

(GOCO) model GOCO03s (Mayer-Guerr et al. 2012) up to the full degree of 250. For short wavelength reduction the well known prism formula (Wild-Pfeiffer 2007) has been used. The reduction is done without any isostatic compensation. We expect the isostatic part as information which is already included in the global satellite models characterized by the long-wavelength. The reduced gravity Δg_{red} is computed by

$$\Delta g_{red} = g_{abs} - \gamma - [\Delta g_{global} - (g_{Coarse} - g_{CoarseSHM}) - (g_{Dense} - g_{DenseSHM})]. \tag{3}$$

The parameter g_{abs} represents the measured absolute gravity on Earth surface. In a first step the normal gravity γ which belongs to the GRS80 (Moritz 1980b) is subtracted from measured gravity data. For the absolute gravity the orthometric height above the geoid is known and the normal gravity is computed at height above the ellipsoid. Therefore the differences are the classical free air anomalies Δg_{fa} shown in Fig. 3.

In a next step the long-wavelength reduction Δg_{global} using the GOCO03s global gravity field model has been carried out. The spherical harmonic expansion was performed up to the full degree $n = 250$. The rms is now increasing to 47.26 mgal and the remaining topographic parts are clearly show up and can be seen in Fig. 4. This fact is attributable to the spatial distribution of the measured gravity observations. They are mostly measured in valleys and not in mountainous regions and the global model can not resolve the sharp structure of the valleys.

The remaining notations in Eq. (3) are all related to the DTM. The g_{Coarse}, g_{Dense} parts are representing the topographic reduction and the $g_{CoarseSHM}$, $g_{DenseSHM}$ terms are the corrections obtained from the spherical harmonic expansion of the DTM. In Fig. 5 the impact of the coarse grid is taken into account. In this illustration and in Table 1 the

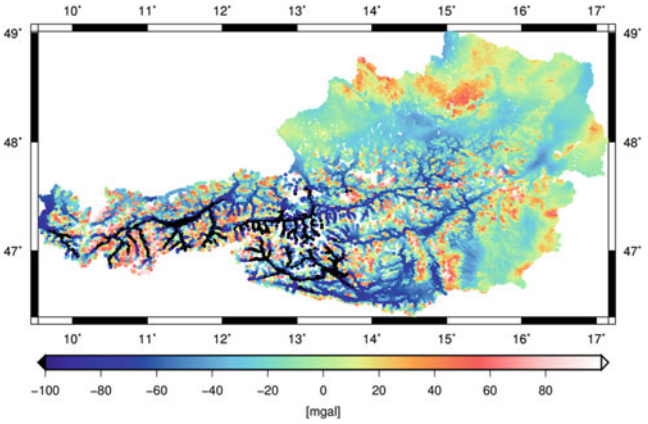

Fig. 4 Additionally reduced by the global part using the GOCO03s model; g_{abs}-γ- Δg_{global} ; rms = 47.26 mgal

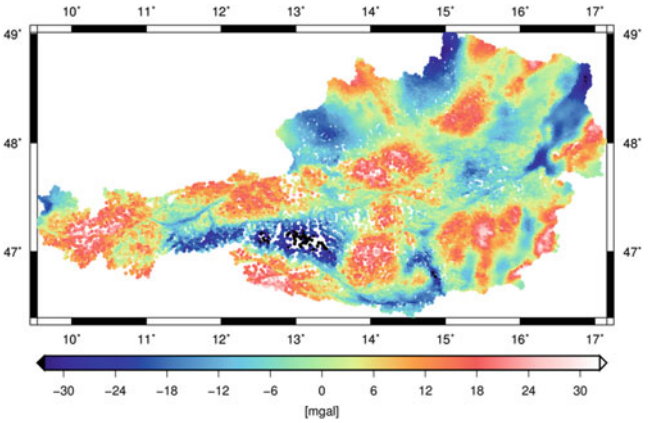

Fig. 5 Additionally reduced by the coarse topographic parts; g_{abs}-γ - Δg_{global}-(g_{Coarse}-$g_{CoarseSHM}$); rms = 11.25 mgal

Table 1 Statistics of reduction-adding another reduction step subsequently

	Min [mgal]	Max [mgal]	Mean [mgal]	rms [mgal]
Δg_{fa}	−123.78	205.42	5.84	41.56
Δg_{global}	−186.82	134.16	−23.57	47.26
g_{coarse}	−44.64	41.39	−1.32	11.25
g_{dense}	−48.71	38.11	−1.21	11.06

effect of the topographic reduction g_{Coarse} is shown together with the associated coarse DTM derived gravity correction $g_{CoarseSHM}$ which is computed with help of Eq. (1). The rms is now decreasing to 11.25 mgal. In Fig. 6 the impact of the reduction steps using the dense DTM can be seen. In fact, it is rather low compared to Fig. 5 because the dense DTM can be seen as an improvement to the coarse DTM in the overlapping area (see Sect. 2.2). The rms is slightly decreasing to 11.06 mgal.

Finally the reduced gravity [see Eq. (3)] is obtained using a proper combination of global and local data and is representing the remaining part from measured absolute

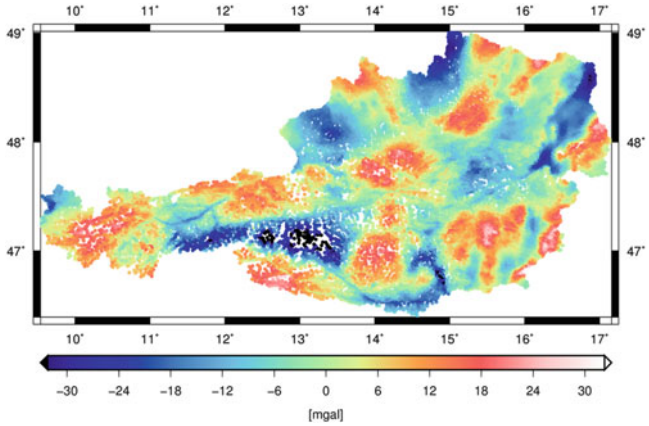

Fig. 6 Reduced gravity Δg_{red} after the final reduction step; rms = 11.06 mgal

gravity on Earth surface within Austria. To give an overview about the impact of every single reduction step the statistical results are summarized in Table 1.

4 Computation Step: Radial Basis Functions (RBF)

For the computation step a least squares approach (Gauss-Markov model) in association with radial basis functions is introduced. This procedure enables the possibility to estimate the residual parts as supplements to the satellite model. Applying this approach for regional geoid modeling which is based on (Eicker 2008) the gravity anomalies can be represented as series expansion of radial basis functions

$$\Delta g_{red} = \sum_{i=1}^{N} a_i \phi(x, x_i), \tag{4}$$

where a_i are the unknown scaling coefficients to determine, x denotes the evaluation point and the x_i stands for the centers of the basis function. The radial symmetric basis functions ϕ which are representing the deviations of the achieved solution compared to a GOCO based solution in turn can be expressed by a sum of Legendre polynomials

$$\phi(x, x_i) = \frac{GM}{R} \sum_{n=2}^{\infty} \sum_{m=-n}^{n} \left(\frac{n-1}{R} \right) k_n Y_{nm}(x) Y_{nm}(x_i). \tag{5}$$

The spherical harmonics are denoted as Y_{nm}. The shape of the function is controlled by the coefficients k_n

$$k_n = \frac{\sigma_n}{\sqrt{2n+1}}. \tag{6}$$

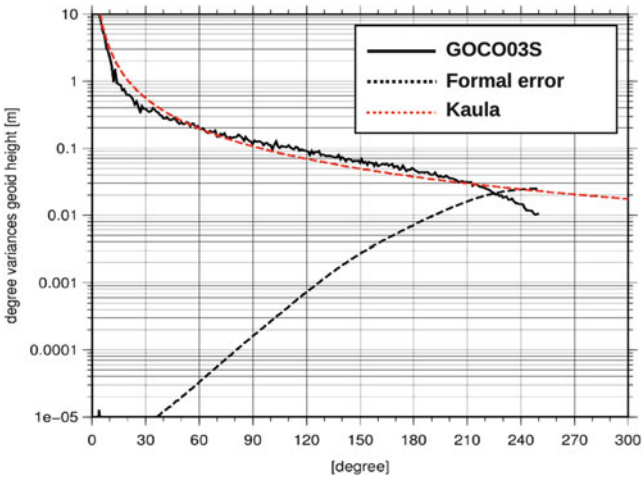

Fig. 7 Transition between the GOCO formal errors and the full signal of the high frequencies using Kaula's rule

For the coefficient up to degree $n = 250$ the formal errors of the GOCO03s model have been used. Beyond this degree the coefficients are padded by Kaula's rule:

$$k_n = \frac{1}{n^2}. \tag{7}$$

This choice of the shape functions consider the fact, that the satellite model does not affords the full spectral power in the high degrees but provide a high accuracy in the long wavelength and increasingly weaker accuracy with increasing degree. Beyond D/O 250 the high frequencies are still containing the full signal expressed by Kaula's rule. This approach is shown in Fig. 7.

For the spatial distribution of the RBF a global triangle vertex (Schmidt 1981) has been used. The point distribution of the RBF is essential for the outcomes and was chosen homogeneously. In case of regional geoid modeling RBF are situated within Austria and 10 km beyond Austrian borders to reduce edge effects. To achieve a proper RBF representation a similar spatial resolution as the input data should be ensured. This means that the k_n for this investigation are given up to $n = 6{,}000$. This degree corresponds to a point distance of approximately 3 km on Earth surface and results in 7,091 unknowns.

5 Results: Restore Step

In the restore step the operations of the remove step described in Sect. 3.2 have to be reversed. An advantage of the used least squares approach is the overdetermination, which allows the analysis of the residuals and furthermore an a-posteriori variance can be estimated. In Fig. 8 the computed residuals between the reduced input gravity and the estimated gravity based on RBF parametrization can be seen. Apart from a few outliers the quality of the input data is quite good. Additionally the point distance of the RBF is still insufficient and a densification is needed. In Table 2 the statistics of the residuals is shown. For this first investigation the outliers have not been eliminated and are still contained in the computed gravimetric geoid solution.

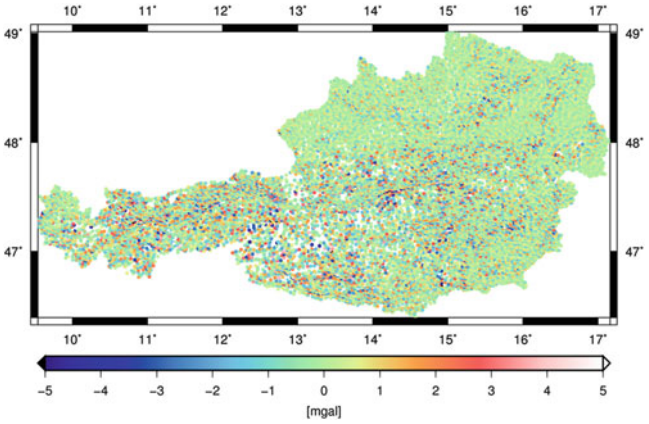

Fig. 8 Residuals between reduced input gravity and estimated gravity based on RBF parametrization; rms = 1.12 mgal

Table 2 Statistics of 28,212 residuals

	Min [mgal]	Max [mgal]	Mean [mgal]	rms [mgal]
$v_{\Delta g_{red}}$	−5.77	12.14	−0.01	1.12

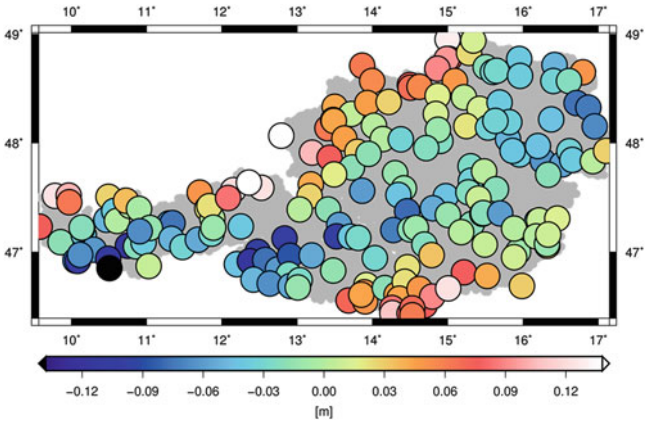

Fig. 9 Residuals between the computed gravimetric geoid and GPS/leveling observations; rms = 5.8 cm

To check the quality of the pure gravimetric geoid solution GPS/leveling observation with measured geoid heights have been used (see Sect. 2.3). The resulting rms is lower than 6 cm. It has to be remarked that the huge residuals are located near Austrian borders as shown in Fig. 9. This has to be expected due to edge effects and suggests that additional gravity data from neighbouring countries have to be taken into account to sustain the solution in these areas.

Table 3 Statistics of 192 geoid height residuals-mean value was subtracted beforehand

	Min [cm]	Max [cm]	Mean [cm]	rms [cm]
v_N	−15.11	24.52	0.00	5.80

The statistics of the geoidal height residuals can be seen in Table 3.

6 Summary and Outlook

The methodological improvements in Remove Compute Restore procedure result in a consistent combination of satellite and terrestrial data. Relative to previous Austrian geoid computation the long-wavelength errors of the gravimetric geoid are reduced compared to GPS/leveling observations and a correction surface is not needed anymore. An additional benefit results from the fact that the inhomogeneous distribution of the observations is not crucial compared to LSC and the full information provided by the GOCO model is incorporated. It has to be pointed out that the achieved results are at an early stage of computation and further improvement have to be done. This improvements are in particular:

- applying atmospheric corrections to measured gravity field quantities
- use of global DTM model (e.g. DTM 2006)
- use additional gravity data from neighbouring countries

The atmospheric correction of the measured gravity data will contribute to a slightly improvement of the reduced quantities. The use of a global DTM in addition to the currently available data will ensure a global DTM coverage and hence a global representation of DTM derived spherical harmonics. Additional data from neighbouring countries will sustain the solution and help to avoid edge effects. Furthermore a combined solution with deflections of the vertical ξ,η is intended to achieve improvements. The optimum weighting between the observation groups will be performed by variance component estimation (Koch and Kusche 2002).

References

Drinkwater M, Floberghagen R, Haagmans R, Muzi D, Popescu A (2003) GOCE: ESAs first earth explorer core mission. Space sciences series of ISSI, vol 18. Kluwer Academic, Boston, pp 419–432. ISBN 1-4020-1408-2

Drinkwater M, Floberghagen R, Haagmans R, Muzi D, Kern M (2008) GOCE: Obtaining a portrait of earth's most intimate features. ESA Bull 133:4–13

Eicker A (2008) Gravity field refinement by radial basis functions from in-situ satellite data. Dissertation, Universitaet Bonn, Bonn

Graf J (1996) Das digitale Gelaendemodell fuer Geoidberechnungen und Schwerereduktionen in Oesterreich. In: Proceedings of the 7th international meeting on alpine gravimetry-Heft 14, Wien, pp 121–136. ISSN 1016-6254

Koch K, Kusche J (2002) Regularization of geopotential determination from satellite data by variance components. J Geodesy 76:259–268 (Bonn)

Kuehtreiber N, Pail R, Wasle B, Pock C, Wirnsberger H, Hofmann-Wellenhof B, Steinbach O, Hoeggerl N, Imrek E, Ruess D, Ullrich C (2011) Improved Austrian geoid solution combining terrestrial and satellite gravity data (GEOID+). ASAP Phase VI Project-Final Report. https://online.tugraz.at, Graz

Mayer-Guerr T, Rieser D, Hoeck E, Brockmann J, Schuh WD, Krasbutter I, Kusche J, Maier A, Krauss S, Hausleitner W, Baur O, Jaeggi A, Meyer U, Prange L, Pail R, Fecher T, Gruber T (2012) The new combined satellite only model GOCO03s. In: Proceedings of the international symposium on gravity geoid and height systems GGHS 2012, Venice, Presentation-www.goco.eu

Moritz H (1980a) Advanced physical geodesy. Herbert Wichmann Verlag, Karlsruhe

Moritz H (1980b) Geodetic reference system 1980. Bull Geodes 55:395–405

Pail R, Kuehtreiber N, Wiesenhofer B, Hofmann-Wellenhof B, Of G, Steinbach O, Hoeggerl N, Ruess D, Ullrich C (2008) The new Austrian geoid solution (GEOnAUT). In: Gravity geoid and Earth observation 2008-International Association of Geodesy (IAG). https://online.tugraz.at

Pail R, Kuehtreiber N, Wiesenhofer B, Hofmann-Wellenhof B, Ullrich C, Hoeggerl N, Imrek E, Ruess D (2009) The official Austrian geoid solution 2008: data method and results. EGU General Assembly. https://online.tugraz.at, Vienna

Reigber C, Luehr H, Schwintzer P (2002) CHAMP mission status. Adv Space Res 30(2):129–134. doi:10.1016/S0273-1177(02)00276-4

Ruess D (1983) Ein digitales Höhenmodell von Österreich. Geodätische Arbeiten Österreichs für die internationale Erdmessung, Band III, Wien, pp 153–157

Rummel R, Rapp RH, Suenkel H, Tscherning CC (1988) Comparisons of global topographic/isostatic models to the Earth's observed gravity field. Department of Geodetic Science and Surveying Rep. No 388. The Ohio State University Columbus, Columbus

Schmidt H (1981) Sampling function and finite element method representation of the gravity field. Rev Geophys 19(3):421–436. doi:10.1029/RG019i003p00421

Tapley B, Bettadpur S, Watkins M, Reigber C (2002) The gravity recovery and climate experiment. Mission overview and early results. Geophys Res Lett 31:L09607. doi:10.1029/2004GL019920

Wild-Pfeiffer F (2007) Auswirkungen topographisch-isostatischer Massen auf die Satellitengradiometrie. Dissertation zu Karlsruhe Karlsruhe. ISBN 3769650423

Modelling the Influence of Terraced Landforms to the Earth's Gravity Field

Silja Märdla, Tõnis Oja, Artu Ellmann, and Harli Jürgenson

Abstract

Medium resolution (1–3 arc-min) gravity anomaly grids do not reflect reality very accurately over terraced landforms, which in turn may affect the uncertainty of subsequent geoid modelling. This inaccuracy is due to many factors. The gravimetric datasets used in the gridding of gravity field models have a varying accuracy and coverage, especially in terraced and coastal areas. Further, the resolution of the terrain model used in the modelling of anomaly grids is usually too low to capture the complete gravimetric attraction of terraced landforms.

Since the values of free-air anomalies are strongly correlated with terrain heights, it is difficult to model the gridded surface over terraced landforms. Depending on the quality of existing gravity data and terrain height models, different procedures should be used. In the case of a terraced area that is densely covered by gravity data, if an accurate terrain model exists, free-air anomaly grids should be calculated on high resolution ($6'' \times 12''$) and using Bouguer anomaly values on grid nodes. If gridding is proceeded without Bouguer anomalies, triangulation based gridding methods should be preferred.

Keywords

Gravity • Anomalies • Gridding • Terrace • North-Estonian Klint

1 Introduction

The Earth's gravity field is varying, especially in areas of changing terrain surface. Today the global, long-wavelength features of the gravity field are relatively well known thanks to dedicated gravimetric satellite missions. A recent combined Earth's geopotential model EGM08 (Pavlis et al. 2012) has a resolution of 5 arc-min (corresponding to 9 km). Although it could correspond well with local gravity data within gravimetrically well studied areas (see e.g. Ellmann 2010), its spatial resolution or accuracy is still not sufficient for engineering applications, where 1–2 cm accuracy of geoid model is needed. Having better knowledge about the local nature of the gravity field would allow for more accurate regional geoid models, calculation of which is aided by the SRTM global topography model (Farr et al. 2007). In many countries, even more accurate airborne LIDAR-acquired data exist. Apparently, availability of detailed terrain heights helps improve gravity anomaly data.

The conventional and still often used source data for calculating a geoid model are the gravity free-air anomalies (FAA) deduced from gravity measurements. For some geoid computation methods (fast Fourier transform or Stokesian integration), anomalies need to be calculated into regular grids. This arises many questions about areas with sparse data, see e.g. Kirby et al. (1997), Goos et al. (2003) and references therein.

S. Märdla (✉) • A. Ellmann
Tallinn University of Technology, Tallinn, Estonia
e-mail: silja.mardla@ttu.ee

T. Oja
Tallinn University of Technology, Tallinn, Estonia

Estonian Land Board, Tallinn, Estonia

H. Jürgenson
Estonian University of Life Sciences, Tartu, Estonia

U. Marti (ed.), *Gravity, Geoid and Height Systems*, International Association of Geodesy Symposia 141,
DOI 10.1007/978-3-319-10837-7_20,

Usually, when compiling gravity anomaly models, no distinction is made between gridding over different landforms. It is, often optimistically, assumed that the selected gridding algorithm is universally suited for all landforms within the area of interest. In the past such simplification was often justified by computational constraints. In this study however, emphasis is on developing optimum gridding algorithms for areas with contrasting landforms.

The question arose since discrepancies between the results of different gridding methods seem to be especially large in areas with terraced landforms. Therefore, the behaviour of the gravity field in terraced areas, different methods for calculating gravity anomaly grids (without prior removal of any frequency based information such as EGM-based long-wavelength contribution) and the evaluation of the resulting models of gravity anomaly fields are discussed in this contribution.

First, different methods of gridding gravity data are introduced. Then, a numerical case study is described to evaluate these methods. The most suitable algorithm is found for gridding gravity data in the terraced study area. Obtained results are compared with existing models: the anomaly grids used for the latest Estonian gravimetric geoid calculation are evaluated. A discussion on practical uses of high resolution anomaly grids concludes this contribution.

2 Methods of Gridding Gravity Data

Gridding of gravity anomalies is a critical issue in geoid modelling, because any error committed at this stage will propagate into the geoid solution. There are a number of commonly used gridding methods. These include continuous curvature, triangulation or neighbouring points' based algorithms, among others. These are programmed into many software packages, including the free and open source Generic Mapping Tools (GMT; Wessel and Smith 1998), often used by geoscientists.

Continuous curvature is an algorithm that fits a curved surface between data points, allowing for a smooth and in a specific case even harmonic surface that either does or does not pass through all data points. Nearest Neighbour is an algorithm that considers only the very neighbouring points when calculating values. Triangulation gives a solution where the resulting surface passes through all data points. A grid can be produced from a triangulated surface by interpolation.

Due to free-air anomalies being strongly correlated with terrain heights, the FAA values can change quite rapidly in terraced areas. Therefore free-air anomalies are not very suitable for gridding. As discussed by many, e.g. Janák and Vaníček (2005), there are a number of different methods for compiling FAA grids, yielding remarkable differences in resulting anomaly models.

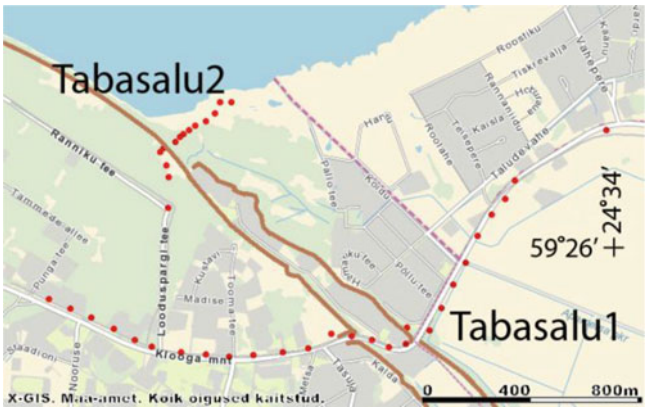

Fig. 1 Detailed gravity measurement profiles Tabasalu1 and Tabasalu2 (depicted by *red dots*) crossing the North-Estonian Klint (depicted by the *brown line*) near seashore (Color figure online)

Instead of directly gridding the FAA values, the FAA grids can also be obtained through simple or complete Bouguer anomalies (denoted correspondingly as SBA and CBA) that have a much smoother behaviour in most cases. The grid is obtained by using a terrain model to calculate FAA values at every grid node of the Bouguer anomaly grid. Note that accurate height information at every grid node is needed for such a gridding approach. If heights are not well known, the free-air anomalies cannot be derived accurately through Bouguer anomaly grids.

Over the Canadian Rocky Mountains Janák and Vaníček (2005) calculated free-air anomalies through SBA and CBA. Systematic errors up to 20 mGal between corresponding FAA grids and 2 m in subsequent geoid models were detected. Therefore it is reasonable to believe that, in a terraced area, in addition to the gridding method, the way of obtaining free-air anomaly grids is also important.

3 Gravity and Terrain Data Within the Study Area

For the evaluation of gravity anomaly grids, detailed gravity surveys were conducted at a terraced area in Tabasalu, some 10 km west from Tallinn, the capital of Estonia. It is an area on the seashore with the North-Estonian Klint passing through, having a height of about 30 m there. Two gravity profiles (Tabasalu1 and Tabasalu2) were measured almost perpendicularly to the Klint, see Fig. 1.

Gravity data were measured about every 100 m with uncertainty of ±0.07 mGal. Coordinates and heights were deduced from GPS measurements with maximum uncertainty of about ±5–10 cm.

For the modelling of the gravity field, an existing gravity anomaly database of Estonia was used. The gravity data available in the study area mostly consist of gravity values with uniform uncertainty estimates (about ± 0.2 mGal) from the surveys of Geological Survey of Estonia. For more details on the database, the evaluation of the gravity data in question and earlier use of the data see Ellmann et al. (2009) and references therein. Average gravity data density within the selected study area is 0.25 km in the North-south direction and 1 km in the East-west direction (see Fig. 5 for gravity points' placement).

From the gravity data measured, free-air, simple and complete Bouguer anomalies were calculated. For calculation of spherical terrain correction (e.g. Janák and Vaníček 2005) values, a LIDAR and SRTM combined digital terrain model (A. Gruno, *pers. comm.*) with $3'' \times 3''$ (approximately 90×45 m^2 in the study area) resolution was used. Discrepancies between the DTM and heights measured on profile points were found to reach up to 10 m. Apparently, even the $3'' \times 3''$ DTM does not have a high enough resolution or precise enough source data to reflect actual heights very accurately near a terrace.

Since the calculated spherical terrain corrections are less than 0.25 mGal the complete Bouguer anomaly values do not differ much from the simple Bouguer anomaly values. As the anomalies behave similarly, often no distinction is made between SBA and CBA in further discussion. Also, since both profiles showed similar gravity field behaviour, only Tabasalu1 is discussed hereafter.

As expected, the gravity increases with the height decreasing. Free-air anomalies are clearly correlated with height values with the change up to 6 mGal over the terrace. Bouguer anomalies (BA) however are smooth and not correlated with height values. Slight changes in the BA field near the terrace may be explained by complex variations of ground density underneath the terrace. See Talvik (2012) for a more detailed description of the gravity field in the area.

4 The Optimal Gridding Algorithm

As discussed in Sect. 2, there are many ways for gridding gravity anomalies. For this study, six different approaches were used to generate regular grids from the gravity anomaly database:

- GMT module *surface*, tension factors 0.25 and 1;
- GMT *triangulate*;
- Matlab *griddata*;
- GMT *nearneighbour* with $1'$ search radius and four sectors (NN4);
- GMT *nearneighbour* with $1'$ search radius and eight sectors out of which at least four must contain a point with a value that is not NaN (NN4/8).

Each time free-air anomalies were in turn calculated by the three different options described in Sect. 2. The resulting anomaly grids were denoted as following: FAAv (direct), FAAs (through SBA) and FAAc (through CBA).

In addition, six different grid resolutions were tested: $1' \times 2'$, $0.5' \times 1'$, $15'' \times 30''$, $6'' \times 12''$, $3'' \times 6''$ and $1.5'' \times 3''$. The lowest, $1' \times 2'$ (about 1.8×1.8 km^2) resolution corresponds to the resolution of the contemporary geoid and corresponding gravity (anomaly) field models of Estonia. The highest, $1.5'' \times 3''$ (about 45×45 m^2) resolution corresponds to the shortest distances between gravity points in the database and roughly to the distance between profile points.

The optimal gridding algorithm for the given terraced area proved to be the GMT *triangulate* with grid resolution of $6'' \times 12''$. This was determined by comparing the gridded anomaly data to the values obtained from the measurements on the profiles. For this, gravity anomaly values were interpolated from all the different grids to the profile points. Differences of the interpolated values and the measured values were depicted on one-dimensional profile graphs. The mean, root mean square (RMS), minimal and maximal discrepancies were found for each profile. The best algorithm was then chosen by the statistics of discrepancies.

The explanation to the optimal resolution lies in the average density of input gravity data in N-S direction (250 m $\approx 8''$). The advantage of the *triangulate* method is its ability to better reflect rapid changes in the modelled quantity, in this case, the anomaly field near the terrace's edge. Out of the modules available in GMT, the NN4 appeared to be almost as good as *triangulate* whereas the NN4/8 option was unable to estimate a value to many grid nodes. The GMT module *surface* with tension factor 0.25 distorts the gridded model unreasonably on resolutions higher than $6'' \times 12''$, which is something to take note of. When the tension factor was increased to 1, which gives a harmonic surface, the model was no longer distorted, statistical indicators however were still not as good as for the *triangulate* results.

Differences between methods were smaller for Bouguer anomaly fields as these have a much smoother behaviour. The best results were reached with the *surface* method, with other methods differing only by 0.1–0.2 mGal.

Discrepancies between the measured and interpolated (from the optimal *triangulate* $6'' \times 12''$ grid) anomaly values are shown on Fig. 2. The statistics of discrepancies between free-air anomalies are shown in Table 1, left hand side. On $6'' \times 12''$ resolution the free-air anomalies are considerably more accurate when gridded through Bouguer anomalies compared to when gridded directly.

In fact, the scheme of calculating the FAA grid through Bouguer anomalies instead of direct gridding yields a more

Table 1 Discrepancies of different type (FAA/FAAc) free-air anomaly grids from the profile data; units mGal

	Optimal ($6'' \times 12''$)				GRAV-GEOID2011 ($1' \times 2'$)			
Profile	Min	Max	Mean	RMS	Min	Max	Mean	RMS
Free-air anomaly (directly gridded)								
Tabasalu1	−1.74	+0.70	−0.34	±0.74	−1.02	+1.33	+0.10	±0.79
Tabasalu2	−2.06	+1.50	−0.41	±1.21	−1.65	+2.13	−0.16	±1.38
Free-air anomaly (using CBA)								
Tabasalu1	−0.39	+0.30	−0.04	±0.18	−0.95	+1.55	+0.28	±0.93
Tabasalu2	−1.17	+1.87	+0.29	±0.77	−1.22	+2.58	+0.25	±1.40

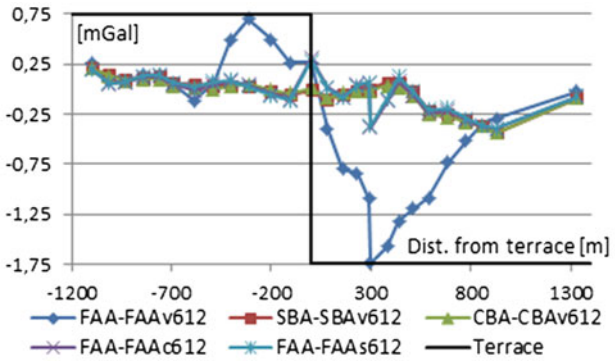

Fig. 2 Discrepancies between the gravity free-air (FAAv, FAAs and FAAc), simple Bouguer (SBA) and complete Bouguer (CBA) anomaly values calculated for the Tabasalu1 profile and interpolated from the optimal $6'' \times 12''$ *triangulate* grid (with suffix 612); the terrace is illustratively depicted by the *black line* (Color figure online)

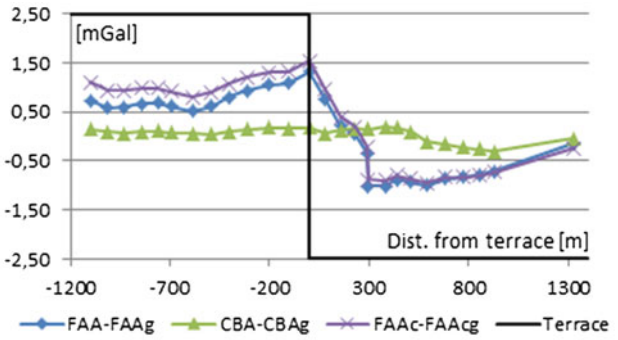

Fig. 3 Discrepancies between the free-air (FAA and FAAc) or complete Bouguer anomalies (CBA) used for the GRAV-GEOID2011 (with suffix _g) and the profile measurements on Tabasalu1

accurate FAA grid only if the DTM resolution is as high as the resolution of the BA grid. If the DTM resolution is much lower than that of the BA grid, the resulting FAA grid is actually less accurate, which was noticed in the case of $1' \times 2'$ resolution (for calculations on each resolution the DTM was also sampled to that resolution).

5 Comparisons with Existing High-Resolution Gravity Anomaly Grids

The latest gravimetric geoid model of Estonia is GRAV-GEOID2011 (Ellmann et al. 2011). It has a resolution of $1' \times 2'$, which was also tested in this study. The free-air anomaly grids used for the geoid modelling had also been calculated directly from FAA values and through SBA or CBA.

The anomaly grids used for GRAV-GEOID2011 were compared to the profile measurements (Fig. 3). Discrepancies of the free-air anomaly values used for the GRAV-GEOID2011 from the measured data are shown in Table 1, right-hand side. As mentioned, on low resolutions, gridding FAA through BA leads to no improvement of the FAA grid. That is why in case of the geoid modelling data, free-air anomalies obtained by gridding through CBA do not show a better agreement with the profile values.

Comparison of discrepancy graphs (cf. Figs. 2 and 3) and the statistics in Table 1 reveal that the $6'' \times 12''$ optimal grid corresponds better to profile measurements than the grids used for the geoid model.

Since the optimal $6'' \times 12''$ triangulate grids were found to have smaller discrepancies from the measured gravity anomaly values than those of the GRAV-GEOID2011, free-air anomaly grids of the geoid model were also compared to the corresponding optimal grids of the present study. To compare the free-air anomaly grids of GRAV-GEOID2011 to the optimal grid, the resolution of the first was increased to $6'' \times 12''$ by bicubic interpolation. Discrepancies between directly gridded free-air anomaly models did not exceed ±0.5 mGal and did not reveal any specific pattern.

However, discrepancies in free-air anomaly models obtained by gridding through complete Bouguer anomalies show a clear pattern with the optimal grid giving larger values on top of the terrace and smaller values on the foot than the grids used for the gravimetric geoid model (Fig. 4).

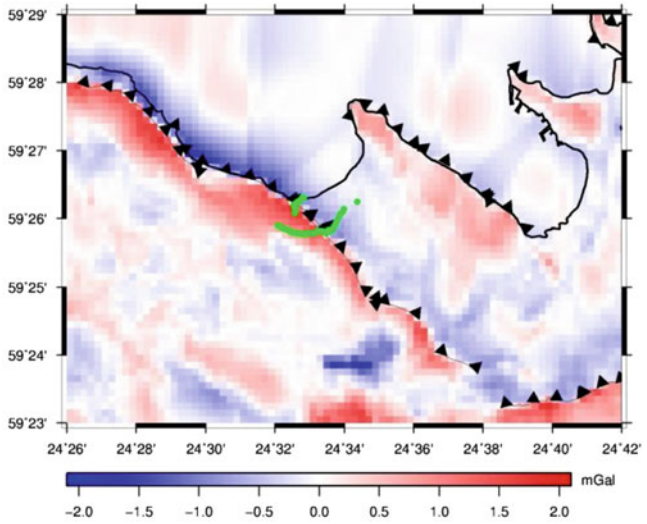

Fig. 4 Comparison of free-air anomalies gridded through complete Bouguer anomalies used for the GRAV-GEOID2011 model to the corresponding optimal $6'' \times 12''$ *triangulate* grid (optimal minus GRAV-GEOID); profiles depicted in *green*, the terrace by the aligned *black triangles* (Color figure online)

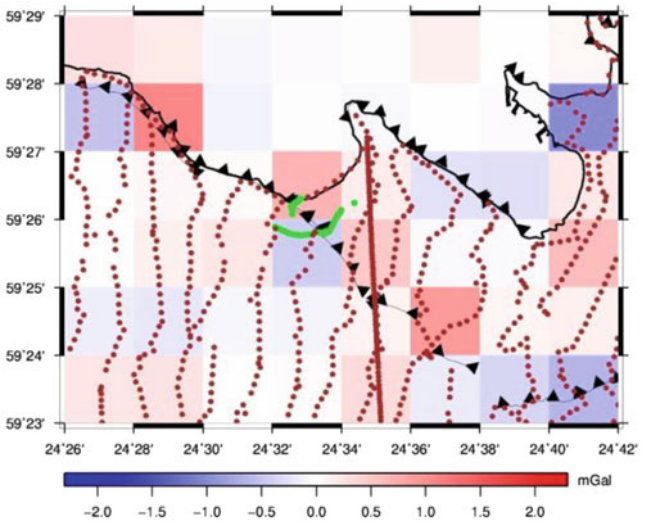

Fig. 5 Differences between the $1' \times 2'$ *triangulate* FAA grid and the $6'' \times 12''$ *triangulate* FAA grid averaged to $1' \times 2'$; profiles depicted in *green*, gravity data points in *brown* (Color figure online)

6 Averaging the Optimal 6″ × 12″ Anomaly Grid to 1′ × 2′ Resolution

Using the optimal resolution of $6'' \times 12''$ in regional geoid modelling is computationally quite demanding (the number of cells increases two magnitude orders when using the resolution of $6'' \times 12''$ instead of $1' \times 2'$). Therefore, the reasonability of extracting areas that need specific attention, for example by selecting all cells that contain data points with height difference of more than 15 m or have a certain RMS value of heights within the grid cell, was investigated. In such areas, high-resolution gridding could be used. These grids could later be averaged back to $1' \times 2'$ resolution and substituted to the initial ($1' \times 2'$) anomaly grid.

In this study, $6'' \times 12''$ grid averaged to $1' \times 2'$ does not show superiority over the initial model calculated directly on $1' \times 2'$ resolution. This was determined by comparing the $6'' \times 12''$ *triangulate* grid averaged to $1' \times 2'$ resolution with the original $1' \times 2'$ *triangulate* grid (Fig. 5). Differences between free-air anomaly grids are not very significant (average difference is 0.06 ± 0.20 mGal), yet larger discrepancies occur near the terrace. Study of a longer strip along the coastline may reveal a clearer pattern.

Comparison of the averaged grid to profile values yields that the averaged grid is not necessarily more accurate than the original one; the discrepancies are just the same or slightly larger even. Similar results are seen for the free-air anomaly grids calculated using Bouguer anomalies.

Discussion and Conclusions

The $1' \times 2'$ resolution used for the gravimetric geoid model calculation appears to be too low to reflect short-wavelength changes in the gravity anomaly field near the terrace. One cell of the grid covers both the top and the foot of the terrace, thus assigning both the same gravity anomaly value which is a weighted average of the actual values, depending on the position of the cell. This implies that the magnitude of discrepancies from the actual value on top of or on the foot of the terrace may reach up to half of the actual change in the gravity (anomaly) field values on the terrace.

To reduce errors in the anomaly field models in terraced areas, the use of triangulation based gridding methods for free-air anomalies can be the most suitable approach. It would be best to increase the resolution of these models according to the average density of gravity data to get the most out of existing data. In case of North Estonia that would be up to $6'' \times 12''$. A significant improvement can be achieved in high resolution free-air anomaly grids if these are calculated using Bouguer anomalies which include height information via a DTM.

Within the study area the anomaly values were best reflected in the $6'' \times 12''$ resolution *triangulate* grid. Even if gravity data are gridded using the optimal algorithm, the result has some discrepancies from the measured data in terraced areas (cf. Fig. 2 and Table 1). This is due to the low resolution of both gravity data and the used DTM. It is therefore expected that LIDAR data will soon find its way into gravity anomaly field gridding, terrain correction calculation and geoid modelling [like the Stokes-Helmert

geoid determination approach, where estimation of related topographical effects may be quite demanding, for a review see Ellmann and Vaníček (2007)]. Discrepancies between gridded (using the optimal algorithm) and actual (measured) data may be larger in other areas (since gravity data as dense as data in the study area are rare both in Estonia and elsewhere), especially areas with much higher terraces.

The discrepancies between different models and also errors in the models (discrepancies of the models from the measured data) have a systematic pattern (cf. Figs. 2, 3 and 4). From the edge of the terrace to the bottom, the differences change sign. It is obvious that the terrace has a significant but short (1–2 km) wavelength effect on the gravity field and its models. In Estonia, the terraced Klint areas are narrow, but they continue along the coast for about a 100 km. These may cause noticeable errors in gravity anomaly models which may propagate to subsequent geoid models. Therefore it is necessary to note the existence of such areas, although the magnitude of the effect on geoid modelling needs to be tested in further studies.

It can be argued that gravity data with average distance of 5 km between data points is sufficient for a 5 mm quasigeoid solution (Ågren and Sjöberg 2012). In this study we have seen that gravity field models can be improved by using appropriate gridding methods, however in terraced areas the discrepancies are still significant (up to 0.8 mGal). If the terraces are high and their effect to gravity anomaly field models should also affect the geoid solution, some additional gravity data may be needed.

For gridding free-air anomalies directly, there is no remarkable difference between the optimal $6'' \times 12''$ *triangulate* grid and the $1' \times 2'$ grid used for the GRAVGEOID2011. For gridding free-air anomalies through (simple or complete) Bouguer anomalies, the $6'' \times 12''$ grid is much more accurate than the grid used for the geoid model (cf. Table 1) confirming that anomaly grids can be calculated more accurately.

As the differences between the original $1' \times 2'$ grid and the $6'' \times 12''$ grid averaged to $1' \times 2'$ were insignificant (cf. Fig. 5), it can be concluded that using the optimal method is reasonable only if the gravity field model (and if necessary, the subsequent geoid model) can also be presented with the same resolution as the optimal one. If this is too demanding, an option of calculating one general model on a lower resolution and additional models on higher resolutions for specific areas could be considered.

The results of this study can also be applied to gridding the gravity field in other areas with terraced landforms. Much higher terraces are found in Europe and elsewhere, reaching more than 1,000 m. In these areas the effect of the terrace certainly demands attention. Gridding methods discussed here are well applicable to other areas; the optimal model resolutions however are dependent on existing gravity data density.

Acknowledgements The authors are thankful for three anonymous reviewers for their constructive comments. This research has been supported by Estonian Science Foundation Grant No. 7356 and 8749 and Estonian Land Board. The DTM used was generated within the frames of the Archimedes Foundation project KESTA ERMAS (3.2.0802.11-0043).

References

Ågren J, Sjöberg LE (2015) Investigations of the requirements for a future 5 mm quasigeoid model over Sweden. In: Gravity, geoid and height systems. IAG symposia 141. Springer International Publishing Switzerland

Ellmann A (2010) Validation of the new Earth Gravitational Model EGM08 over the Baltic countries. In: Mertikas SP (ed) Gravity, geoid and Earth observation. IAG symposia, vol 135, pp 489–496

Ellmann A, Vaníček P (2007) UNB application of Stokes–Helmert's approach to geoid computation. J Geodyn 43:200–213

Ellmann A, All T, Oja T (2009) Toward unification of terrestrial gravity data sets in Estonia. Est J Earth Sci 58:229–245

Ellmann A, Oja T, Jürgenson H (2011) Application of space technologies to improve geoid and gravity field models over Estonia [in Estonian]. Geodeet 41:22–25

Farr TG, Rosen PA, Caro E, Crippen R, Duren R, Hensley S, Kobrick M, Paller M, Rodriguez E, Roth L, Seal D, Shaffer S (2007) The Shuttle Radar Topography Mission. Rev Geophys 45

Goos JM, Featherstone WE, Kirby JF, Holmes SA (2003) Experiments with two different approaches to gridding terrestrial gravity anomalies and their effect on regional geoid computation. Surv Rev 37(288):92–112

Janák J, Vaníček P (2005) Mean free-air gravity anomalies in the mountains. Studia Geophysica et Geodaetica 49:31–42

Kirby JF, Feathersdtone WE, Kearsley AHW (1997) Geoid computations using ring integration: gridded vs. point data. Geomatics Res Aust 67:33–46

Pavlis NK, Holmes SA, Kenyon SC, Factor JK (2012) The development and evaluation of the Earth Gravitational Model 2008 (EGM2008). J Geophys Res 117, B04406

Talvik Silja (2012) Influence of terraced landforms to the Earth's gravity field and precise levelling results, with application to the North-Estonian Klint. Tallinn University of Technology. MSc. thesis. [in Estonian]

Wessel P, Smith WHF (1998) New, improved version of the Generic Mapping Tools released. EOS Trans AGU 79:579

Accurate Geoid Height Differences Computation from GNSS Data and Modern Astrogeodetic Observations

Evangelia Lambrou

Abstract

This work presents the revival of the astrogeodetic observation procedure by means of modern instrumentation and processing. The determination of astronomical coordinates Φ, Λ and the components ξ and η of the deflection of the vertical is achieved with an accuracy that reaches $\pm 0.01''$.

The used method brings to the fore the classical geodetic astronomy actually aided by modern technology. The system of NTUA is used [Lambrou (Development of a methodology for astrogeodetic determinations, using digital geodetic instruments. Ph.D. Thesis, 2003)]. This system consists of a first order total station connected with a GNSS receiver in order to register time with 1 ms.

The same method is applied by changing the instrumentation. An advanced "imaging" total station is used, providing a direct connection to the internet, to a world time server, in order to obtain the necessary accurate time information. This total station runs windows CE and moreover it allows carrying out the observations on a digital screen, as the telescope is not deemed essential anymore. The sightings may be also carried out remotely via a PC's screen situated anywhere and connected to the internet.

Alternatively, in order to bypass the need of accurate time information, the Laplace equation can be used. Thus the determination of η is achieved. As a limitation, this procedure requires visibility between the points.

By using the corresponding geodetic coordinates φ, λ and azimuth, which are all provided by the GNSS measurements, the deflection of the vertical components (ξ and η) are computed. Thereinafter the geoid undulation differences ΔN are calculated, with few mm accuracy.

By following this procedure, the results are independent from the definition of the local height datum. For this reason, it can improve the global geoid models as it enriches their data in areas characterized by large geoid variations due to rough topography. Finally, this

E. Lambrou (✉)
School of Rural and Surveying Engineering, National Technical
University of Athens, Athens, Greece
e-mail: litsal@central.ntua.gr

U. Marti (ed.), *Gravity, Geoid and Height Systems*, International Association of Geodesy Symposia 141,
DOI 10.1007/978-3-319-10837-7_21, © Springer International Publishing Switzerland 2014

procedure could be used for the unification or the definition of a unified height datum, for a country.

Keywords
Astrogeodetic determination • Imaging total station • Geoid • Astronomical coordinates • Deflection of the vertical

1 Introduction

Today the GNSS positioning is widely used for many applications. The main goal of surveyors for many years is the easy determination of orthometric heights, via GNSS measurements.

The global geoid models are continuously being improved but they can't reach the adequate accuracy needed for the surveyors' fieldwork. The EGM2008 geopotential model (complete to degree and order 2190) totally presents differences of some centimeters in USA, about 25 cm in Australia and about 10 cm over the world, in comparison to the direct calculated N derived from orthometric heights and GPS leveling. (Pavlis et al. 2008, 2012). Especially in Greece the respective differences vary from +54 cm to −44 cm (Kotsakis et al. 2008).

Also the unification of a height datum over a country and beyond requires height connections between remote points. The transfer of the orthometric height doesn't seem to be an easy task.

Height connections between remote points, (i.e. points between islands, points from both sides of large earth openings (gaps) over the sea or river banks, or points between mountains), cannot be performed by using the classical methods of spirit leveling or one side trigonometric heighting. In addition, the one side trigonometric heighting isn't accurate enough due to the influence of the refraction, which adds a significant uncertainty to the final ΔH. The application of reciprocal trigonometric heighting of substantial kilometers, leads to better results but the accuracy threshold of some cm remains (Ceylan et al. 2005).

Nowadays, the wide use of GNSS provides effortless the geometric height differences. Nevertheless, the determination of the accurate orthometric height differences ΔH between two points on the earth's surface, via the geometric height differences Δh, is a real challenge. The well-known formula (1) may be used, under the presupposition that the geoid undulation N or ΔN has been previously precisely calculated.

$$h = H + N \quad \text{or} \quad \Delta h = \Delta H + \Delta N \tag{1}$$

Several remarkable methods have been developed for the independent calculation of the components $\boldsymbol{\xi}$ and $\boldsymbol{\eta}$ of the deflection of the vertical. The system of the digital zenith camera TZK2-D, which provides the deflection components by an external accuracy of $\pm 0.10''$ to $\pm 0.15''$ (Hirt et al. 2005). Moreover its combination with a high-resolution digital terrain model may determine the quasi geoid profile by ±1–2 mm (Hirt and Flury 2008). Furthermore other procedures are tested via zenith angles observations (Soycan and Soycan 2005) or via leveling measurements (Ceylan 2009).

Probably it's the time for the revival of the classical method of astrogeodetic leveling which accurately determines the slope of the geoid surface relative to the ellipsoid (Bomford 1971; Torge 1980).

Three alternative modern ways to perform astrogeodetic observations with the use of high-end instrumentation and developed software are proposed. The combination of the classical measurement methodologies with numerous gathered data and their thorough statistical processing, can lead quickly and easily to reliable and accurate results.

2 The Basic Concept

The components $\boldsymbol{\xi}$ (along the meridian) and $\boldsymbol{\eta}$ (along the prime vertical) of the deflection of the vertical $\boldsymbol{\varepsilon}$ at a point A, can be calculated from the following formulae, assuming that the minor axis of the ellipsoid is parallel to the mean spin axis of the earth's rotation.

$$\xi_A = \Phi_A - \varphi_A \qquad \eta_A = (\Lambda_A - \lambda_A) \cdot \cos \varphi_A \tag{2}$$

where: Φ_A, Λ_A, φ_A, λ_A the astronomical and geodetic coordinates respectively of point A. Thus σ_ξ and σ_η can be estimated as follows

$$\sigma_\xi = \pm\sqrt{\sigma_\Phi^2 + \sigma_\varphi^2} \text{ and } \sigma_\eta = \pm \cos\varphi \cdot \sqrt{\sigma_\Lambda^2 + \sigma_\lambda^2} \tag{3}$$

An alternative procedure may be applied in order to determine the $\boldsymbol{\eta}$ component by using the Laplace equation (Bomford 1971; Torge 1980):

$$\eta = \frac{\Delta A}{\tan \varphi} \tag{4}$$

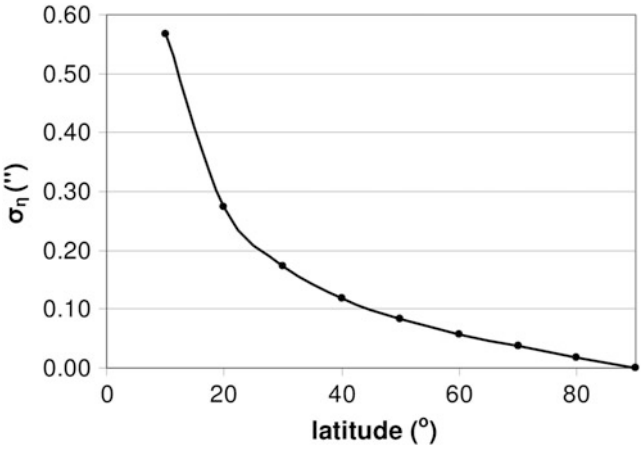

Fig. 1 The change of σ_η with respect to the latitude

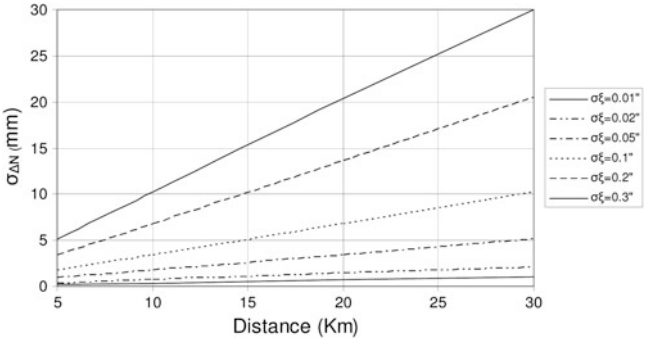

Fig. 2 Accuracy of ΔN in relation to $\sigma_\xi = \sigma_\eta$, and the distance between the points

where $\Delta A = A_{AB} - \alpha_{AB}$, A_{AB}, α_{AB} the astronomical and geodetic azimuth respectively

Assuming that $\sigma_{A_{AB}} = \pm 0.1''$ and $\sigma_{\alpha_{AB}} = \pm 0.01''$, the difference ΔA has a determination error equal to:

$$\sigma_{\Delta A} = \pm\sqrt{\sigma^2_{A_{AB}} + \sigma^2_{\alpha_{AB}}} = \pm 0.1'' \tag{5}$$

Applying the variance covariance propagation to the formula (4) the σ_η can be calculated

$$\sigma_\eta = \pm\sqrt{\cot^2\varphi \cdot \sigma^2_{\Delta A} + \left(\frac{\Delta A}{\sin^2\varphi}\right)^2 \cdot \sigma^2_\varphi} \tag{6}$$

Figure 1 illustrates the change of σ_η with respect to the geodetic latitude, for $\sigma_{\Delta A} = \pm 0.1''$ and $\sigma_\varphi = \pm 0.001''$. According to the diagram, σ_η has a mean value of the order of $\pm 0.1''$ for mean latitudes. The factor ΔA doesn't influence the result.

The determination of the variation of the geoid undulation ΔN between two points A and B is given by the following equation (Bomford 1971, p. 361–362; Torge 1980):

$$\Delta N_{AB} = N_B - N_A = \frac{1}{2} \cdot \left(\Psi''_A + \Psi''_B\right) \cdot S_{AB} \cdot \sin 1'' \tag{7}$$

where

$$\Psi = -\left(\xi \cdot \cos A_{AB} + \eta \cdot \sin A_{AB}\right) \tag{8}$$

Combining the Eqs. (7) and (8), the geoidal undulation difference ΔN is given by the formula:

$$\Delta N_{AB} = -\left[\frac{\xi_A + \xi_B}{2} \cdot \cos A_{AB} + \frac{\eta_A + \eta_B}{2} \cdot \sin A_{AB}\right] \cdot S_{AB} \tag{9}$$

where:

ξ_A, η_A, ξ_B, η_B = the components of the deflection of the vertical at the points A and B, in arcsec.

S_{AB} = the horizontal distance between the points

Equation (9) gives accurate results if the mean of deflections at the end points is equal to the mean along the whole line (integral of the deflections) and also, in the assumption that ground level deviations are equal to those of geoid level. Otherwise the reduction of the components to sea level must be applied. The appropriate equations are used for the correction of the systematic part of this error. The random part is below the mm level, therefore insignificant (Bomford 1971, pp. 365–366).

This procedure gives reliable results for distances up to 30 km as for greater intervals such as 100 or 200 km thickening of the profile with gravity measurements is needed (Bomford 1971, p. 362). Otherwise a high-resolution digital terrain model as Hirt and Flury (2008) propose is necessary.

Assuming that, $\sigma_{\xi_A} = \sigma_{\xi_B} = \sigma_\xi = \sigma_{\eta_A} = \sigma_{\eta_B} = \sigma_\eta$, by applying the variance-covariance propagation to formula (9) the uncertainty of ΔN is calculated, in relation to the distance between the points (Fig. 2).

$$\begin{aligned}\sigma_{\Delta N_{AB}} &= \pm \cdot \sqrt{\tfrac{1}{2} \cdot \left(\cos^2 A_{AB} + \cdot \sin^2 A_{AB}\right) \cdot \sigma^2_\xi \cdot {S_{AB}}^2 +} \\ &+ \sqrt{\left(\tfrac{\xi_A + \xi_B}{2} \cdot \cos A_{AB} + \tfrac{\eta_A + \eta_B}{2} \cdot \sin A_{AB}\right)^2 \cdot \sigma^2{}_{S_{AB}}} \approx \\ &\approx S_{AB} \sqrt{\tfrac{1}{2} \cdot \left(\cos^2 A_{AB} + \cdot \sin^2 A_{AB}\right) \cdot \sigma^2_\xi} \quad \approx S_{AB} \cdot \tfrac{\sqrt{2}}{2} \cdot \sigma_\xi\end{aligned} \tag{10}$$

Considering the maximum distance error $\sigma_S = \pm 5$ cm and ξ, η of the order of $10''$ then the contribution of the factor $\left(\frac{\xi_A + \xi_B}{2} \cdot \cos A_{AB} + \frac{\eta_A + \eta_B}{2} \cdot \sin A_{AB}\right)^2 \cdot \sigma^2{}_{S_{AB}}$ in the error budget is $< 5 \cdot 10^{-3}$ mm, namely insignificant.

As nowadays **ξ** and **η** components are calculated easily with an accuracy of $\pm 0.1''$, it is pointed out by the diagram that uncertainty less than ±1 cm is feasible for distance up to

30 km between the points. So the distance may be extended for quite smooth geoid profiles.

As the GNSS can provide the Δh by a corresponding uncertainty, thus the ΔH can be calculated, applying the variance covariance propagation to the Eq. (1) with few centimeters uncertainty. This meets the requirements of a wide range of modern projects and applications in surveying and geodesy.

3 Modern Astrogeodetic Observations

3.1 By Using the System of NTUA

The advanced system, which was developed at NTUA (Lambrou 2003; Balodimos et al. 2003) provides the astronomical coordinates Φ, Λ of a point with an accuracy of $\pm 0.01''$. The system consists of the first order total station, Leica DTM 5000, connected with the GNSS receiver, Trimble 4000 DL, for the time registration.

The instrument reading direction error is eliminated to $\pm 0.5''$. The determination of the coordinates is based on observations of stars around their meridian transit. The transit zenith distances of several pairs of stars are used for the determination of latitude (Sterneck method), while the transit times of the same stars are used for the determination of longitude (Mayer method). Despite that the two methods are using different selection criteria, they might be combined using special written software in a careful and thorough procedure, (Kakoliris 2006). The selected stars can be used in both methods, in order to make the system time efficient.

Observations of 3–5 star-pairs, which can be performed in about 1 h, are enough for the determination. The horizontal and vertical angles as well as the time are registered, as about 80–100 sightings are carried out for each star. An adaptation of fourth and third degree polynomial respectively is performed in order to extract the value of the transit zenith angle and the transit time (Lambrou 2003). Additionally a data snooping test is performed in order to detect and reject the observations, which include gross errors (Baarda 1968).

The refraction influence is eliminated, as the Sterneck method is used (Mueller 1969; Mackie 1971; Lambrou 2003; Lambrou et al. 2003). This method was based on the symmetry and observation of stars at small zenith distances in order to efface the astronomical refraction influence. This is valid, if the atmospheric conditions remain the same during the observations of a stars' pair. Actually this is not true. As Hirt (2012) refers, in an in depth analysis and detailed bibliographical flashback, the anomalous atmospheric refraction error remains and influences the computations about $\pm 0.1''$. On the other hand, Vondrak et al. (2003) concluded that the astronomical refraction could be eliminated not to impair the result of measurements. Also Panou (2009) concluded that there is no model that can describe and correct accurately the effect of anomalous refraction. Thus the only way is the repetition of measurements and the corresponding adjustment through the least square errors method, which leads to a result that has the maximum likelihood to reach the accurate value of the unknown.

The presented methodology uses stars in small zenith distances (10^g–25^g) that ensure a regular description of the optical beam. The observations of both stars in each pair last about 10 min. In this time interval the atmospheric conditions cannot change dramatically. Additionally the data possessing is based on two adjustments. The first one is used for the determination of the transit vertical angle and the transit time. The second one leads to the determination of the Φ and Λ respectively. Additionaly the numerous measurements permit the application of all the statistical tests. Thus the supposed unknown remaining part of the anomalous refraction may be effaced or at last be eliminated in an insignificant quantity.

Additionally thoroughly corrections are applied concerning the precision and the stability of the instrument's clock as well as the personal equation of the observer. As it came out of many experiments, there is an average delay of 0.3 s at the registration time of each sighting (Lambrou 2003). It should be noted that the celestial coordinates, right ascension and declination as well as other astrometric data for each star, are taken from the Tycho2 catalogue (ESA 1997). This catalogue provides positions (ICRS, epoch J2000) of 2.5 million stars to a mean accuracy of ± 7 milliarcsec (for stars brighter than magnitude 9) and proper motions to a mean accuracy of ± 2.5 mas/year. Also a portable data logger is used to register the atmospheric temperature by ± 0.05 °C and pressure by ± 0.1 mbar, using digital sensors during the observations.

Consequently under the above presuppositions the NTUA's system is used successfully for the last decade.

The reliability of the system is proved by six sets of observations, which were carried out at a pillar of which the geodetic coordinates are $\varphi = 37°58'30.5015'' \pm 0.001''$ and $\lambda = 23°46'48.7905'' \pm 0.001''$ (ITRF89 epoch 2001). These sets are uncorrelated to each other as they are performed on different dates, observing different stars, performed by different observers, at different seasons, with different atmospheric conditions, using different instruments (Lambrou 2003; Tzoumaka 2007). Apart from that the repeated adjustments insure the minimization of the influence of the anomalous refraction as the value with the minimum covariance comes out.

As it is shown in the Table 1, the standard deviations of the results vary from $\pm 0.004''$ to $\pm 0.025''$.

The standard deviation of the mean reaches almost the $\pm 0.01''$ as it is computed by using the simple covariance propagation law.

Considering the less precise observation i.e. the one having a standard deviation of $\pm 0.025'' = \sigma_\Phi = \sigma_\Lambda$

Table 1 The results of six astrogeodetic observation sets

Date	Φ	Star pairs	Λ	Stars
29/1/2002	37°58′29.655″ ± 0.010″	7	23°46′39.543″ ± 0.018″	17
16/5/2002	37°58′29.669″ ± 0.018″	6	23°46′39.544″ ± 0.015″	18
24/6/2006	37°58′29.651″ ± 0.006″	5	23°46′39.554″ ± 0.004″	10
27/6/2006	37°58′29.657″ ± 0.010″	5	23°46′39.553″ ± 0.011″	10
7/11/2006	37°58′29.650″ ± 0.009″	3	23°46′39.556″ ± 0.014″	7
13/05/2010	37°58′29.663″ ± 0.020″	5	23°46′39.560″ ± 0.025″	10
Mean value	37°58′29.658″ ± 0.01″		23°46′39.552″ ± 0.01″	

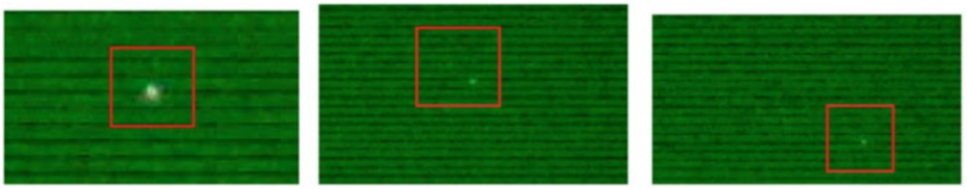

Fig. 3 Polaris and stars of magnitude 4 and 5 on the instrument's display

Table 2 The astronomical coordinates by using an imaging station

Date	Φ	Star pairs	Λ	stars
24/04/2007	37°58′29.590″ ± 0.06″	4	23°46′39.460″ ± 0.06″	8

and $\sigma_\varphi = \sigma_\lambda = \pm 0.001''$ then, according to Eq. (3), $\sigma_\xi = \sigma_\eta = \pm 0.025''$, which according to formula (10) and Fig. 2 gives $\sigma_{\Delta N} = \pm 2.5$ mm at 30 km, which is really satisfying.

3.2 By Using Imaging Total Stations

In 2005 a new generation of total stations was born. They are called "imaging" total stations. They incorporate inside their telescope at least one digital CCD camera. This serves for the transfer of the instrument's field of view to their display or to a computer device. Also they are able to communicate with other peripherals with the use of USB cable, Bluetooth and/or WiFi cards. Finally the Windows CE that they have on board allows them to work as a portable PC.

For the execution of astrogeodetic observations the simultaneous use of the instrument's most advanced technological features, such as wireless connection via Bluetooth™ and wireless connection to the Internet at a free Wi-Fi area, was indispensable. Also the connection may be realized everywhere by using a Smartphone, which supports the GSM profile and uses the GPRS service for fast data transmission, or a laptop using a wireless internet stick. This makes feasible the connection with an available and reliable world time server, for the station's clock synchronization with UTC time every second by 0.001 s.

The astronomical coordinates Φ, Λ are calculated by following the procedure of Sect. 3.1, as the astronomical Azimuth A by following the procedure, which will be refered on Sect. 3.3.

It is notable that all the sightings to the stars are carried out manually by the observer through the display of the instrument and not through the telescope. This means that all the essential corrections, which are mentioned in Sect. 3.1, as the personal equation of the observer, are applied. Although it is under research the exploitation of the captured images for the extraction of the angles along to the star's path. Additionally, the main advantage of the use of such total station is that the observation may be carried out remotely via a PC's display in an office or elsewhere, as the total station may be handled by a PC's keyboard (Lambrou 2014). Figure 3 presents the images of the Polaris and two other stars, of magnitude 4 and 5 respectively, on the instrument's display.

Table 2 presents the results of the observations that were carried out at the same pillar as in Sect. 3.1 (Tsonakas 2007).

3.3 By Using the Laplace Equation

The most difficult aspect in the previous determination is the required accuracy for the time registration that reaches the ±0.001 s and the complicated connections of peripherals for the determination of astronomical Λ.

Therefore, an alternative procedure may be applied in order to determine η component without the need of high accuracy in the time registration, by using Eq. (4).

Assuming that two points A and B have visible contact, the astronomical azimuth A_{AB} between them can be determined. This determination needs time information with accuracy of the order of 4–5 s (Lambrou and Pantazis 2008)

Table 3 The results by using the Laplace equation

Date	Φ	Star pairs	η
15/06/2010	$37°58'29.649'' \pm 0.02''$	5	$-7.41'' \pm 0.25''$

Table 4 The comparison of the results

Instrumentation	Φ	ξ	Λ	η
NTUA's system	$37°58'29.66'' \pm 0.01''$	$-0.84'' \pm 0.01''$	$23°46'39.55'' \pm 0.01''$	$-7.28'' \pm 0.01''$
"Imaging" station	$37°58'29.59'' \pm 0.06''$	$-0.91'' \pm 0.06''$	$23°46'39.46'' \pm 0.06''$	$-7.35'' \pm 0.06''$
Laplace Method	$37°58'29.65'' \pm 0.02''$	$-0.85'' \pm 0.02''$	–	$-7.41'' \pm 0.25''$

and Polaris can be used for this purpose on the northern hemisphere. The method of the hour angle is used (Mueller 1969; Mackie 1971) and about 60–80 sightings to Polaris can be performed within 10 min. Also the geodetic azimuth α_{AB} between the points can be determined using GNSS measurements.

The astronomical latitude Φ is measured and calculated independently following the procedure of the Sect. 3.1. Therefore **ξ** is calculated according to Eq. (2).

An application was carried out, by using a high-end total station ($\pm 0.5''$), between the same pillar as in Sect. 3.1 and one other at a distance of 3 km. The results of the measurements are presented in Table 3.

3.4 Comparison of the Results

Table 4 summarizes the results of the used methodologies. As depicted, the values of Φ and Λ are statistically compatible, which means that they differ within their uncertainties for confidence level 95 %. So the three independent methodologies used prove to be reliable for the ξ and η calculation.

Conclusions

As Bomford (1971) mentions one of the ultimate aims of geodesy is to cover the land surface of the earth with a network of accurate geoid profiles, and thereby to get a direct measure of the form of the geoid.

The contribution of this work to the aforementioned aim is the revival of the method of astrogeodetic leveling by means of high-end instrumentation and software. This offers an independent procedure for the geoid differences' determination. It is considered as a contribution to the improvement of local geoid models and also to a country's height datum definition, and unification.

Combining GNSS measurements (for the determination of coordinates φ, λ and also the geometric height differences Δh) and astrogeodetic measurements (for the determination of astronomical coordinates Φ, Λ), the **ξ** and **η** components can be determined accurately. Then the determination of ΔN with few mm accuracy is feasible for distance of 30 km between the points; as the interval may be lengthen for quite smooth geoid profiles.

The modern astrogeodetic observations are easy to apply today by using modern instrumentation and fast mathematical calculations via appropriate software. About 1 h is adequate for the measurements.

The use of the NTUA's system ensures external accuracy of the order of $\pm 0.01''$ for Φ and Λ determination leading to under cm definition of ΔN. Bear in mind that the 1 ms is essential for the time registration.

On the other hand the use of the Laplace equation via the astronomical azimuth determination is free of the accurate UTC time registration. However, the method requires visibility between the points and independent calculation of Φ otherwise. It may result to ΔN determination of the order of ± 2 cm due to **η** determination accuracy not better than $\pm 0.2''$.

Eventually, the use of "imaging" total stations is the most innovative method towards the future. Besides all it gives the opportunity of remote observations via a PC's screen. So it rejects the great disadvantage of the astrogeodetic measurements namely the remaining of the observer in harsh environmental conditions. Additionally, it meets the standards of the required time registration. Until now, due to the resolution of the incorporated camera, 1.3 Mpixels it ensures accuracy of the order of $\pm 0.05''$ for the Φ and Λ determination namely ±1 cm for ΔN definition.

The method may be applied between the GNSS Reference Stations of a country's permanent network, where there is accurate determination of the geodetic coordinates φ and λ as well as reliable determination of Δh.

Consequently the independently calculated ΔN can be used for the:

- Creation of a precise local geoid map of large areas
- Height connections between remote points (banks, gaps, mountains etc.)
- Overseas height connections between islands or countries, within the distance limits of the method, in order to refer to a common height datum. (For insular countries like Greece)

- Enrichment of the data of the global geoid models in areas with large geoid variations due to rough topography
- Reliable height determination, applying the RTK method, combining GNSS systems and permanent reference stations

References

Baarda W (1968) A testing procedure for use in geodetic networks. New Series, vol 2, No 5. Netherlands Geodetic Commission, Delft

Balodimos DD, Korakitis R, Lambrou E, Pantazis G (2003) Fast and accurate determination of astronomical coordinates Φ, Λ and Azimuth, using a total station and GPS receiver. Surv Rev 37(290):269–275

Bomford G (1971) Geodesy, 3rd edn. Oxford University Press/Clarendon, Oxford. ISBN 0198519192 9780198519195

Ceylan A (2009) Determination of the deflection of vertical components, via GPS and leveling measurement: a case study of a GPS test network in Konya Turkey. Sci Res Essay 4(12):1438–1444

Ceylan A, Inal C, Sanlioglu I (2005) Modern height determination techniques and comparison of accuracies. From Pharaohs to Geoinformatics FIG Working Week 2005 and GSDI-8 Cairo, Egypt

ESA (1997) The Hipparcos and Tycho catalogues. ESA SP-1200, France

Hirt C (2012) Anomalous atmospheric refraction and comments on "fast and accurate determination of astronomical coordinates ..." (Balodimos et al. 2003, Survey Review 37(290):269–275). Surv Rev 44, 327. doi:10.1179/1752270612Y.0000000006

Hirt C, Flury J (2008) Astronomical-topographic levelling using high-precision astrogeodetic vertical deflections and digital terrain model data. J Geod 82:231–248

Hirt C, Reese B, Enslin H (2005) On the accuracy of vertical deflection measurements using the high-precision digital zenith camera system TZK2-D. Gravity, geoid and space missions. Int Assoc Geodes Symp 129(3):197–201. doi:10.1007/3-540-26932-0_34

Kakoliris D (2006) Software development for the best selection of stars' pairs for meridian transit observations. Diploma thesis (In Greek), School of Rural and Surveying Engineers of NTUA

Kotsakis C, Katsabalos K, Ampatzidis D, Gianniou M (2008) Evaluation of EGM08 using GPS and leveling heights in Greece. In: IAG international symposium gravity, geoid and earth observation 2008, Chania, Crete, Greece

Lambrou E (2003) Development of a methodology for astrogeodetic determinations, using digital geodetic instruments. Ph.D. Thesis, School of Rural and Surveying Engineering, NTUA (In Greek)

Lambrou E (2014) Remote survey. An alternative method for capturing data. J Surv Eng 140(1):60–64

Lambrou E, Pantazis G (2008) Astronomical azimuth determination by the hour angle of Polaris using ordinary total stations. Surv Rev 40(308):164–172

Lambrou E, Pantazis G, Balodimos DD (2003) Accurate determination of the geoidal undulation N. EGS–AGU–EUG Joint Assembly, Nice. Reports on Geodesy, Institute of Geodesy and Geodetic Astronomy, Warsaw University of Technology, vol 1 (64), pp. 165–172

Mackie JB (1971) The elements of astronomy for surveyors, 7th edn. Charles Griffin, London

Mueller I (1969) Spherical and practical astronomy as applied to geodesy. Frederick Ungar, New York, NY

Panou G (2009) Astronomical latitude determination by using the autocalibration method. Diploma Thesis (In Greek), School of Rural and Surveying Engineers of NTUA

Pavlis NK, Holmes SA, Kenyon SC and Factor JK (2008) An Earth gravitational model to degree 2160: EGM2008. In: Presented at the 2008 general assembly of the European geosciences union, Vienna, Austria

Pavlis NK, Holmes SA, Kenyon SC, Factor JK (2012) The development and evaluation of the Earth Gravitational Model 2008 (EGM2008). J Geophys Res 117(B4), CiteID B04406. doi:10.1029/2011JB008916

Soycan M, Soycan A (2005) Geoid heights computation from GPS data and classical terrestrial zenith angle observations. From Pharaohs to Geoinformatics, FIG Working Week 2005 and GSDI-8 Cairo, Egypt

Torge W (1980) Geodesy. Walter de Gruyter, Berlin. ISBN 3110170728

Tsonakas N (2007) Metrological tests, analysis, development and evaluation of the capabilities of the imaging total station Topcon GPT – 7000i. Diploma Thesis (In Greek), School of Rural and Surveying Engineers of NTUA

Tzoumaka V (2007) Hypsometric connection of the sea opening between Chios and Innouses islands (Aegean Sea) by using modern total stations. Diploma Thesis (In Greek), School of Rural and Surveying Engineers of NTUA

Vondrak J, Machotka R, Podstavek J (2003) Testing of mathematical models for astronomical refraction elimination. Electronic Journal of Polish Agricultural Universities, Geodesy and Cartography 6(2). http://www.ejpau.media.pl

Improving the Swedish Quasigeoid by Gravity Observations on the Ice of Lake Vänern

Jonas Ågren, Lars E. Engberg, Linda Alm, Fredrik Dahlström, Andreas Engfeldt, and Martin Lidberg

Abstract

One of the key activities in *Geodesy 2010*, the Swedish strategic plan for geodetic activities during the period 2011–2020, is the restoration of the gravity network and data in order to improve the accuracy of the national quasigeoid model. One weak point has been that very few gravity observations have been available over Lake Vänern, Sweden's largest lake. During the extremely cold winters 2010 and 2011, the ice became sufficiently thick to make ice observation of gravity. The main purpose of this paper is to present the 2011 ice gravity campaign, summarise the experiences made and investigate how much the new ice observations improve the computed quasigeoid model in the area. This is investigated under the assumption that a modern Earth Gravitational Model based on GRACE and GOCE is used. It is found that new ice measurements improve the quasigeoid with a RMS of about 2–3 cm in and around the lake with a maximum improvement of 7 cm.

Keywords

Geoid • Gravity • Ice • Lake Vänern • GOCE

1 Introduction

The official Swedish quasigeoid model SWEN08_RH2000 was derived by fitting the gravimetric model KTH08 to a large number of GNSS/levelling height anomalies using a smooth corrector surface (Ågren 2009). The gravimetric quasigeoid model KTH08 (Ågren et al. 2009) was computed by Least Squares Modification of Stokes' formula with Additive corrections (LSMSA- or KTH-method); see for instance Sjöberg (1991, 2003). The standard error of SWEN08_RH2000 has been estimated to 10–15 mm in the mainland of Sweden, where good gravity data and high quality GNSS/levelling observations are available. However, the standard error is expected to be significantly higher in the highest mountains to the North West, in the largest lakes and at sea. This is mainly due to that the gravity observations are not as dense in these areas. The ship gravity observations at sea are also often of bad quality, mainly due to that the connection to a gravity network has been made in a questionable way. At the same time, there are no GNSS/levelling observations available to improve or check the situation.

One of the key activities in Geodesy 2010, the strategic plan for Swedish Geodesy in the time period 2011–2020, is the improvement of the gravity situation with the main goal of improving the accuracy of the national quasigeoid model. One especially weak point has been the lack of gravity observations in Lake Vänern, Sweden's largest lake. Fortunately, during the extremely cold winters 2010 and 2011, the ice became sufficiently thick to make ice observation of gravity. In 2010, the Geological Survey of Sweden started by observing a small area in the northernmost part of the lake.

J. Ågren (✉)
Lantmäteriet, the Swedish Mapping, Cadastre and Registry Authority, 801 82 Gävle, Sweden

Division of Geodesy and Geoinformatics, Royal Institute of Technology (KTH), 100 44 Stockholm, Sweden
e-mail: jonas.agren@lm.se

L.E. Engberg • L. Alm • F. Dahlström • A. Engfeldt • M. Lidberg
Lantmäteriet, the Swedish Mapping, Cadastre and Registry Authority, 801 82 Gävle, Sweden

U. Marti (ed.), *Gravity, Geoid and Height Systems*, International Association of Geodesy Symposia 141,
DOI 10.1007/978-3-319-10837-7_22,

In 2011, Lantmäteriet (the Swedish mapping, cadastre and registry authority) conducted a large ice gravity campaign, in which gravity was determined over almost the whole lake with 5 km resolution (Alm et al. 2011).

It is the main purpose of this paper to present the large 2011 ice gravity campaign, discuss some practical experiences and investigate how much the new ice gravity data improve the official Swedish quasigeoid model. It is also studied how much the sparse NKG Baltic 99 airborne gravity observations (Arne Olesen, personal communication), which is what was available over Lake Vänern before the ice campaigns, improve the situation. In all computations, the GOCO03S (Mayer-Gürr et al. 2012) Earth Gravitational Model (EGM) is used together with the LSMSA-method.

The paper is organised as follows: the 2011 ice gravity campaign is described and discussed in Sect. 2. All the now available gravity observations in and around Lake Vänern are then summarised in Sect. 3. This is followed by an investigation of how much the new ice and old air gravity observations mean for the computed quasigeoid model (Sect. 4). In Sect. 5, we take a look at how well the new quasigeoid model, computed by taking advantage of the ice gravity data, agrees with GNSS/levelling. Another external evaluation is made by studying the horizontality of the GNSS determined normal heights of the ice surface when the new quasigeoid model has been used for conversion from the heights above the ellipsoid.

2 The 2011 Ice Gravity Campaign

The 2011 ice gravity campaign was carried out by Lantmäteriet 4–17 March 2011. All ice transports were made with the hovercraft Griffon 2000 TDX, which was leased from the Vänertjänst Company together with a driver and a mechanic (see Fig. 1). The hovercraft was a prerequisite for the whole expedition. It would not have been practically possible to measure the whole of Lake Vänern without it: the hovercraft made it possible to cross areas with weak ice safely and provided a fast and convenient transportation on the ice.

The gravity observations were carried out with the Scintrex CG-5 Autograv™ gravimeter. A minimum of five 60-s sessions were collected. If the estimated standard deviation for the 60-s sessions was higher than approximately 0.1 mGal, or if the tilt changed too much, then five more 60-s sessions were observed. The approximate 0.1 mGal limit was chosen high enough to work under normal wind vibrations and low enough to get a standard error of the mean that was judged negligible in geoid determination (≈0.05 mGal).

The special wooden tripod illustrated in Fig. 2 was used to make observations directly on the ice, which efficiently limited the sinking of the instrument into the ice. When the ice was covered with snow, a standard Lacoste & Romberg metallic plate was utilised, which also worked well. The small wind shelter in Fig. 2 was also constructed especially for the purpose.

Fig. 1 The hovercraft Griffon 2000 TDX operated by Vänertjänst

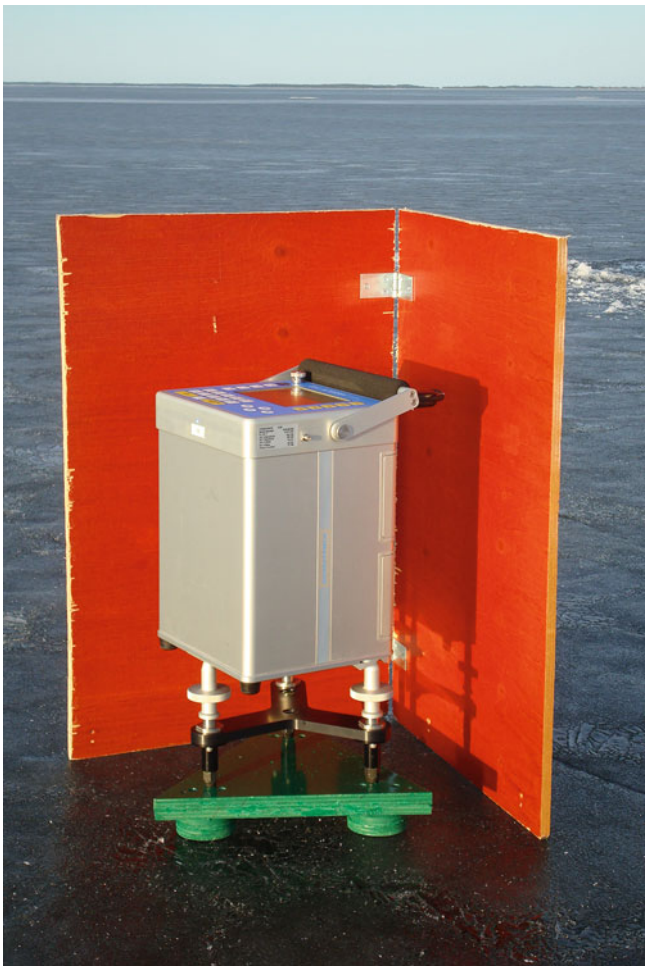

Fig. 2 Measurements on the ice with a Scintrex CG-5 gravimeter using a special wooden tripod and a wind shelter

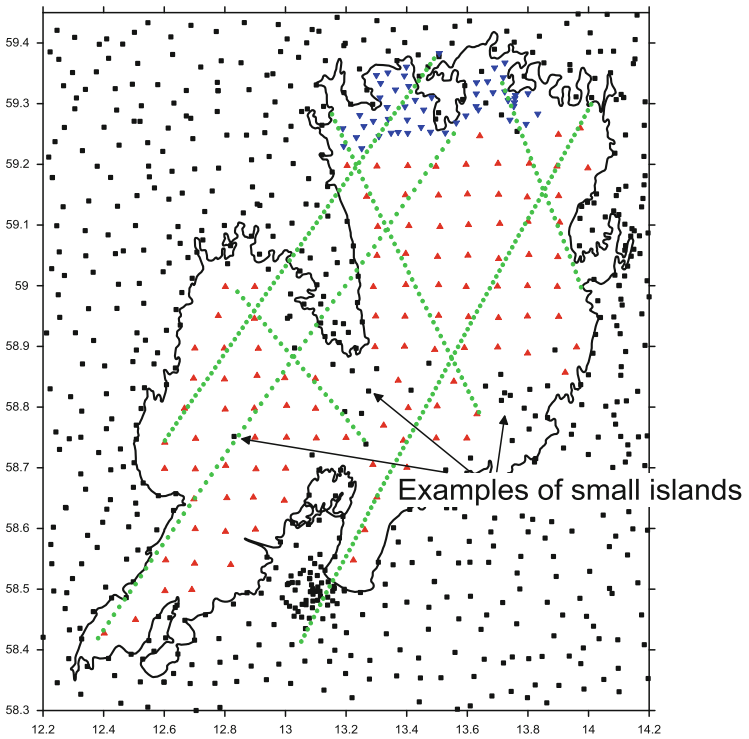

Fig. 3 Gravity observations in and around Lake Vänern. *Black squares* indicate the land gravity observations, *red triangles* the 2011 ice campaign observations, *blue upside-down triangles* the 2010 ice campaign observations and *green dots* the NKG Baltic 99 airborne gravity observations from 1999. (Colour figure online)

Four base points were established on stable ground close to the ice. These points were later connected to the Swedish national gravity network and determined in the National gravity system RG 82 (Haller and Ekman 1988). Each day started and ended by connecting to two of the base points.

The horizontal position and height were determined by GNSS relative to the Swedish network of permanent reference stations, SWEPOS, using Network RTK (Sunna et al. 2010). The following quantities were also measured:

- Ice thickness
- Water depth using echo sounding
- Atmospheric pressure and temperature

More details can be found in Alm et al. (2011).

Even though ice gravity measurements were made by our organization (Lantmäteriet) in the Gulf of Bothnia some 30 years ago, we had to learn many practical things from scratch, based on our own experiences on the ice. It was for instance found that the vibrations caused by the wind are extremely critical. After some experimentation, it was discovered that the best results were obtained by parking the hovercraft with the wind in the stern and by placing the instrument in front of the hovercraft. Luckily, the weather was nice with comparatively calm winds during the whole 2011 campaign. This is rare over such a long time span. Another problem was the gradual tilting of the gravimeter that is caused by the weight of the parked hovercraft. This problem, which is larger for thin ice, could be handled reasonably well by using of the automatic tilt correction of the CG-5 gravimeter. A more thorough description of the practical experiences can be found in Alm et al. (2011).

Overall, the 2011 ice gravity campaign was a success. The weather conditions were favourable and we managed to measure 112 out of the 114 planned points. The standard error of gravity in RG 82 has been estimated to better than 0.2 mGal. The standard error of the height above the ellipsoid is approximately 20–25 mm (Sunna et al. 2010).

3 Summary of the Available Gravity Observations in and Around Lake Vänern

The gravity observations determined in the 2011 campaign are plotted using red triangles in Fig. 3. The resolution is approximately 5 km. The blue upside-down triangles show the result of the 2010 ice gravity campaign in the northern part of the lake. As can be seen, the resolution is higher there.

The black squares in Fig. 3 show the location of the land gravity observations in Lantmäteriet's database, which have mostly been observed using Lacoste & Romberg gravimeters. The average resolution is 5 km and the standard errors are mainly in the interval 0.1–0.5 mGal, but the situation is a little diverse. It should be noticed that a few of the land observations are located on small islands in Lake Vänern.

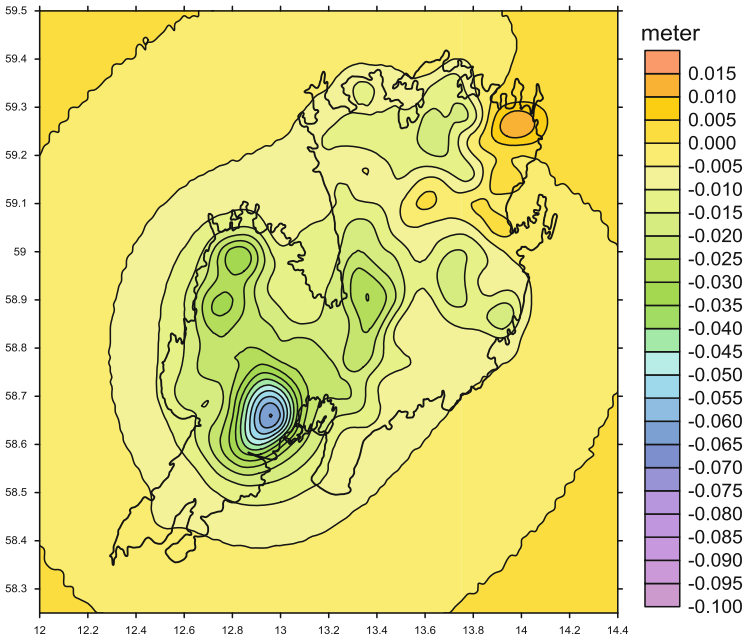

Fig. 4 Height anomaly differences between using the new ice observations and the old airborne gravity over Lake Vänern in the computation of the gravimetric quasigeoid model. Unit: meter. (Colour figure online)

As mentioned in the introduction, there are also a few lines of air gravity measured in connection with the NKG Baltic 99 airborne gravity project. The air gravity lines are plotted as green dots in Fig. 3. Before the 2010 and 2011 ice gravity campaigns, the green lines were the only observations available over Lake Vänern (except for some occasional land gravity observations on a few small islands). The approximate standard error of the airborne observations is about 2 mGal (René Forsberg, personal communication).

4 Influence of the Ice and Air Gravity Data on the Gravimetric Quasigeoid Model

In the last section the gravity observations available in the Lake Vänern area were summarised. Here it is investigated how much the new 2010 and 2011 ice gravity observations improve the computed gravimetric quasigeoid model, as compared to relying on the airborne gravity observations over Lake Vänern. In both cases, all the land gravity observations are used in combination with the new GOCO03S (Mayer-Gürr et al. 2012) EGM, which takes advantage of both GRACE and GOCE.

A comparison is also made between using the ice data and no ice/air gravity at all for Lake Vänern (except for land gravity on islands). The latter investigation is made to judge the value of the airborne gravity measurements.

To compute the gravimetric quasigeoid models, the Least Squares Modification of Stokes' formula with Additive corrections method (LSMSA-method) is applied in the same way as is described in detail in Ågren et al. (2009). Exactly the same data sets are used, except for that different observations are here tested over Lake Vänern and that GOCO03S is used with the maximum degree 200. The only methodological difference compared to Ågren et al. (2009) is that the weighting of the stochastic kernel modification is made a bit differently, now assuming the following stochastic error model (cf. Table 1 in Ågren et al. 2009):

- The error degree variances for GOCO03S are applied without rescaling.
- For the terrestrial gravity anomaly error, a combination of the reciprocal distance and band limited white noise models is used. The band limited white noise part is specified by the standard error 0.5 mGal and the spherical harmonic Nyquist degree 3960. The reciprocal distance part is specified by the standard error 0.2 mGal and the correlation length 0.25°.

The height anomaly differences between using the new ice observations and the old airborne gravity for Lake Vänern are presented in Fig. 4.

The table shows that the maximum improvement in the Lake Vänern area is 7 cm. The corresponding RMS value is around 2–3 cm, depending on how large an area one considers. This comparison shows the benefit of the new ice gravity data in case a modern EGM is used that is based on GRACE and GOCE. The magnitude of Lake Vänern is a little too small to be reliably determined by GOCE. The parts of the lake without gravity data corresponds to a bulge with a geocentric angle of about 0.5° in the south-east to north-west (diagonal) direction, corresponding to a spherical harmonic degree of about 360.

Next, we investigate how large the improvement would have been in case the NKG Baltic 99 airborne gravity

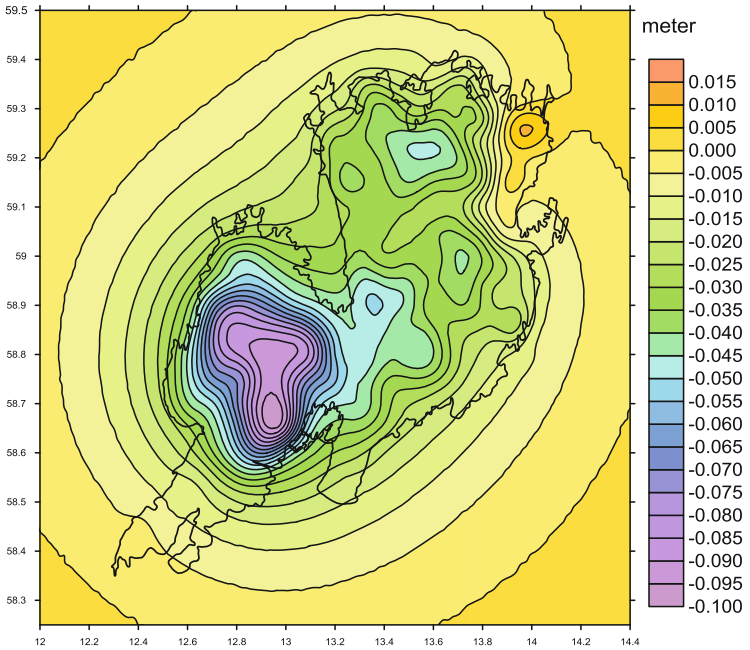

Fig. 5 Height anomaly differences between using the new ice observations and no gravity at all for Lake Vänern (except for land observations) in the computation of the gravimetric quasigeoid model. Unit: meter. (Colour figure online)

observations had not been available over Lake Vänern. The height anomaly differences between using the new ice data and using neither air nor ice data are illustrated in Fig. 5.

It can be seen that the differences are considerably larger in Fig. 5 than in Fig. 4. It is thus clear that also the NKG Baltic 99 airborne gravity observations help significantly, even though they are sparsely distributed along only six lines (see Fig. 3).

5 External Evaluation of the New Gravimetric Model

Here we present two external evaluations of the new gravimetric quasigeoid model computed as described in Sect. 4 using the new ice gravity data for Lake Vänern. First, a comparison is made with respect to GNSS/levelling height anomalies. Second, the horizontality of the GNSS determined normal heights of the ice surface is studied.

The GNSS/levelling height anomalies are of a very high quality (Ågren et al. 2009) and are computed as the difference between the heights above the ellipsoid in the Swedish three dimensional reference frame SWEREF 99 and the normal heights in the new Swedish height system RH 2000. The GNSS observations are either permanent GNSS stations in the SWEPOS™ network or have been determined relative to SWEPOS using 48 h of static observations with the same antenna type as on the SWEPOS stations (Dorne Margolin T). The processing is made in the Bernese software. We estimate the relative standard errors of the heights above the ellipsoid to 10 mm over the whole of Sweden. The relative standard errors of the normal heights of RH 2000 were estimated to about 10–15 mm within Sweden in the final RH 2000 adjustment. See Ågren et al. (2009) for further details and references.

The GNSS/levelling residuals after a standard four-parameter fit/transformation of the gravimetric model are presented in Fig. 6 for the Southern part of Sweden.

It is clear that the agreement to GNSS/levelling around Lake Vänern is now very good, with residuals smaller than 1–2 cm. Naturally, this does not tell us anything about the accuracy in the middle of the lake, only about the quality along the shores. However, this is also important information. If we take a look at the GNSS/levelling residuals around the big Lake Vättern to the east of Lake Vänern, then we see that the agreement is not as good. This presumably depends on the lack of gravity data over this lake.

In order to get some kind of external evaluation of the new quasigeoid model over the whole Lake Vänern, we now make use of the height of the ice determined by Network RTK during the 2011 ice gravity campaign. The heights above the ellipsoid are here transformed to normal heights in RH 2000 using the new four-parameter transformed gravimetric model (computed with ice data). The normal heights of the ice surface are illustrated in Fig. 7 and the corresponding statistics are given in Table 1. Two observations have been excluded since they were made on small islands and not on the surface of the ice.

It can be seen that the determined normal heights agree surprisingly well with each other. There are several reasons for that the normal height of the ice should not be constant for all points measured during the 2011 campaign. The ice height depends, for instance, on winds, ice dynamics, ice thickness

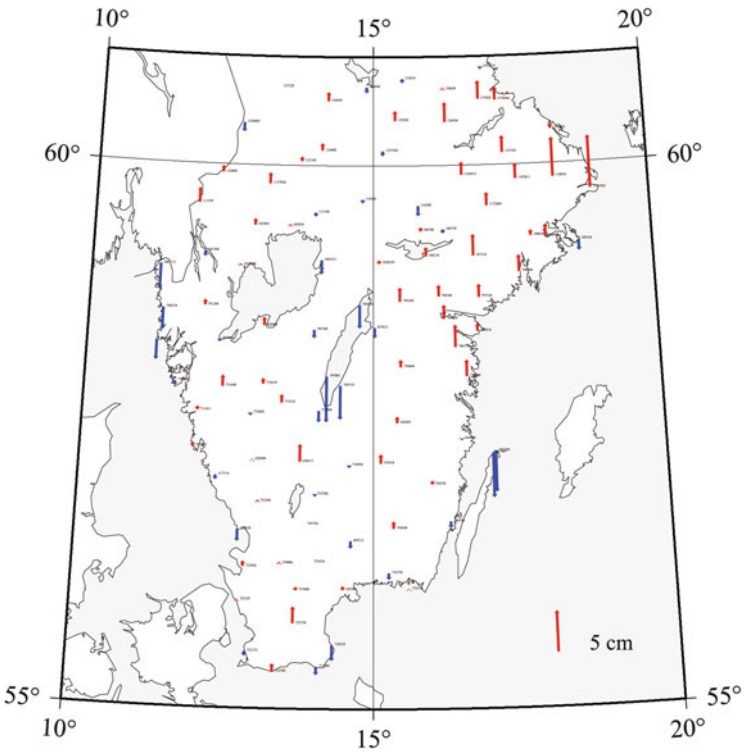

Fig. 6 GNSS/levelling residuals for the new gravimetric model after a four-parameter transformation. The new ice gravity measurements are utilised over Lake Vänern. The scale is given by the 5 cm arrow to the South-East. (Colour figure online)

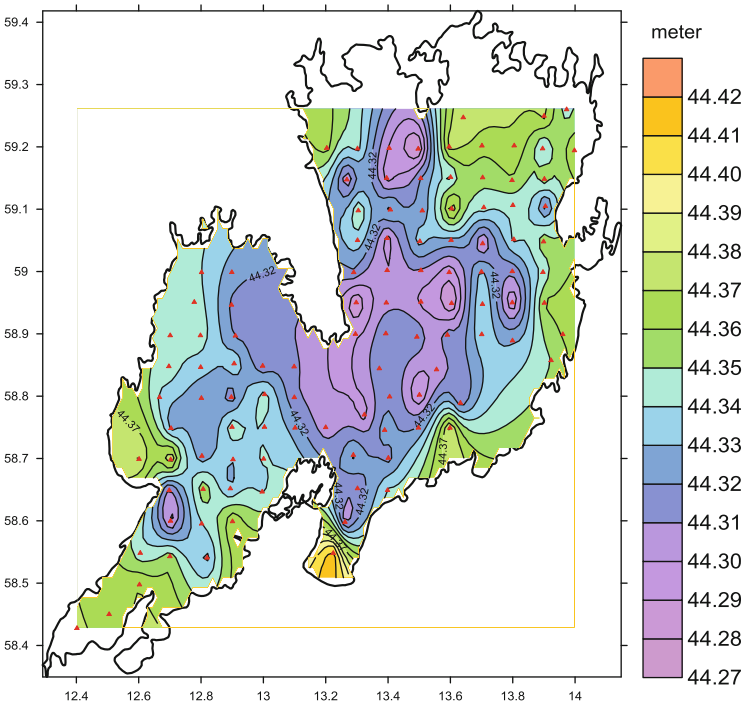

Fig. 7 Normal heights of the ice surface in RH 2000 determined during the 2011 ice gravity campaign using Network RTK and converted by the new four-parameter transformed gravimetric quasigeoid model. (Colour figure online)

Table 1 Statistics for the normal heights of the ice determined during the 2011 ice campaign using Network RTK and the new gravimetric quasigeoid model (after a four-parameter transformation)

Quantity	# pts	Min	Max	Mean	StdDev
Height of the ice	110	44.277	44.417	44.332	0.027
Height minus mean	110	−0.055	0.085	0.000	0.027

and distance to the shore. Besides this, the standard error for Network RTK is specified to 20–25 mm (Sunna et al. 2010). The obtained standard deviation (27 mm) is therefore extraordinary small. Considering the specified standard error of Network RTK and the other effects mentioned above, it can be concluded that the quasigeoid standard error is on the 1 cm-level.

Conclusions and Recommendations

The main purpose of this paper has been to present the experience from the 2011 ice gravity campaign and to analyse the results. In contrast to Alm et al (2011), which concentrated only on the practical implementation, we have focused mainly on how much the collected ice gravity data improve the quasigeoid model in the area. The main conclusion has been that the ice data improve the quasigeoid significantly, with a RMS of about 2–3 cm in and a maximum value of 7 cm (Fig. 4). In case the few NKG Baltic 99 airborne gravity observations had not been available, the improvement would have been even larger (Fig. 5). The external comparisons in Sect. 5 have further shown that the new quasigeoid model is of very high quality in the area. It is concluded that ice measurements is a viable method for accurate gravity determination over lakes, but the method requires good (calm) weather and sufficiently thick ice, which is rare large lakes.

It should finally be mentioned that we have not investigated the extent to which the large error bulge over the southern part of the lake (cf. Fig. 5) is dependent on the bathymetry. Could it for instance have been avoided simply by taking the bathymetry into consideration? These investigations have been left for the future, mainly since it has not been possible for us to get access to depth data.

References

Ågren J (2009) Beskrivning av de nationella geoidmodell-erna SWEN08_RH2000 och SWEN08_RH70. Reports in Geodesy and Geographic Information Systems, 2009:1, Gävle, Sweden

Ågren J, Sjöberg LE, Kiamehr R (2009) The new gravimetric quasigeoid model KTH08 over Sweden. J Appl Geod 3:143–153

Alm L, Engberg LE, Dahlström F, Ågren J, Engfeldt A, Lidberg M (2011) Relative gravity measurements on the ice of the lake Vänern. Report of the Symposium of the IAG Subcommission for Europe (EUREF) held in Chisinau, Moldova, 25–28 May 2011

Haller L-Å, Ekman M (1988) The fundamental gravity network of Sweden. Lantmäteriet, Reports in Geodesy and Geographic Information Systems, 1988:16, Gävle, Sweden

Mayer-Gürr T et al (2012) The new combined satellite only model GOCO03S. Poster presentation at GGHS2012, Venice, Italy, 9–12 October 2012

Sjöberg LE (1991) Refined least squares modification of Stokes' formula. Manuscr Geod 16:367–375

Sjöberg LE (2003) A computational scheme to model the geoid by the modified Stokes' formula without gravity reductions. J Geod 77:423–432

Sunna J, Jämtnäs L, Jonsson B (2010) Improving RTK positioning with SWEPOS™ – lessons from theory and practice. Nordic Geodetic Commission (NKG), 16th General Assembly, Sundvolden, Norway, 27–30 September 2010

Geoid Model and Altitude at Mount Aconcagua Region (Argentina) from Airborne Gravity Survey

M. Cristina Pacino, Eric Jäger, René Forsberg, Arne Olesen, Silvia Miranda, and Luis Lenzano

Abstract

Aconcagua is part of the Southern Andes in the Argentine Province of Mendoza and it is the highest mountain in the Americas. The Aconcagua region is mostly inaccessible for land surveys. The existing gravity data are sparsely distributed, and mainly along the route currently used to climb the mountain. Gravity data are needed for applications such as geoid modeling, vertical datum determination and geological study. In 2010, a high-altitude survey (between 7,000 and 8,000 m above sea level), covering the entire area of Aconcagua was performed. This survey was done within the framework of IAG Project "Gravity and Geoid in South America". Free Air anomalies were computed and compared to Earth Gravitational Model 2008 (EGM08), degree 2190 at the flight altitude. The residuals can be attributed to the fact that the airborne data carries a lot of new gravity information not represented in the EGM08 model. A geoid model was computed from those airborne gravity anomalies and land gravimetry data. A remove-restore method was used for terrain and global spherical harmonic reference models, with the residual gravity field signal downward continued by least-squares collocation, and the geoid and quasi-geoid computed by spherical Fourier methods. The N value at Aconcagua's summit was combined with the ellipsoidal height observed at the summit GPS station to obtain the orthometric height above sea level, confirming the most recent triangulated summit height of 6,960 m.

Keywords

Geoid • Aconcagua • Airborne gravity

1 Introduction

The airborne gravity technology is important to Argentina because for the Andean region, where gravity data are sparse or not available at all (Pacino et al. 2005). Consequently, the determination of a precise geoid model at centimeter level accuracy for any Andean zone has been hampered or made impossible by the lack of gravity data. Precise knowledge of the geoid is of particular interest for GPS-leveling applications, engineering, and in support of the future height modernization initiative of the country.

In 2010, the National Space Institute, Technical University of Denmark, carried out a high-altitude survey (in altitudes ranging from 7,000 to 8,000 m above sea level) covering the entire area of Aconcagua (Fig. 1).

M.C. Pacino (✉) • E. Jäger
Facultad de Cs. Exactas, Ingeniería y Agrimensura (UNR), Pellegrini 250, 2000 Rosario, Argentina
e-mail: mpacino@fceia.unr.edu.ar

R. Forsberg • A. Olesen
National Space Institute, Technical University of Denmark, Elektrovej 327, 2800 Lyngby, Denmark
e-mail: rf@space.dtu.dk

S. Miranda
Universidad Nacional de San Juan, San Juan, Argentina
e-mail: s_mirandaar@yahoo.com

L. Lenzano
IANIGLA - CRICYT, Universidad Nacional de Cuyo, Mendoza, Argentina
e-mail: llenzano@lab.cricyt.edu.ar

U. Marti (ed.), *Gravity, Geoid and Height Systems*, International Association of Geodesy Symposia 141,
DOI 10.1007/978-3-319-10837-7_23,

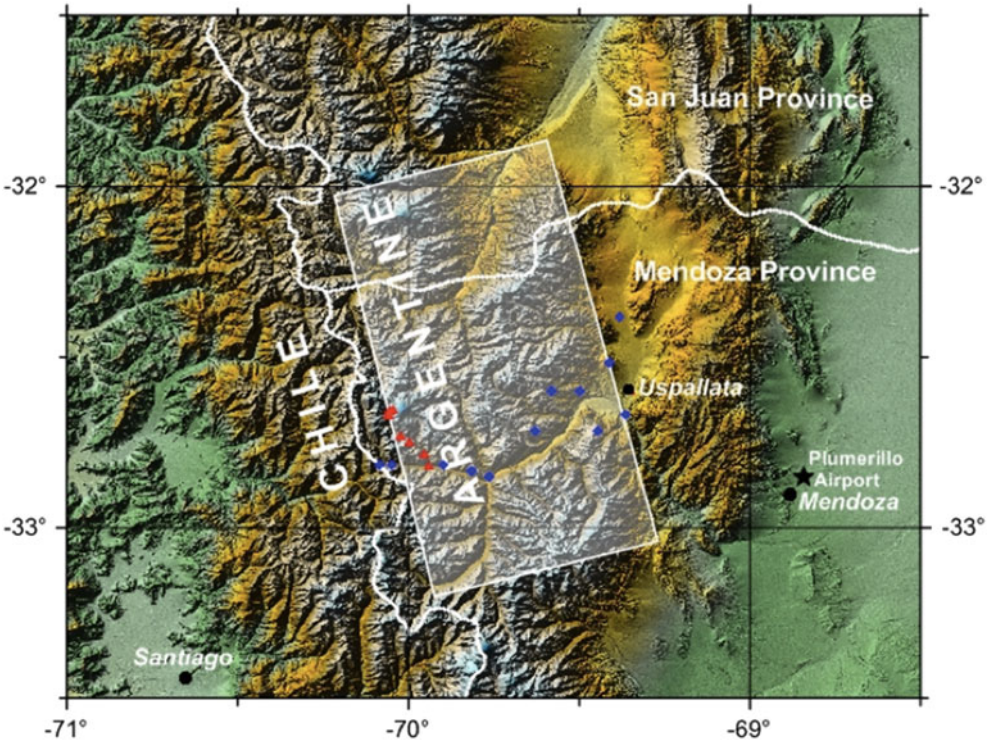

Fig. 1 Location map of the study region of Mount Aconcagua (*rectangle* in *white*). The summit is located about 5 km from San Juan Province and 15 km from the international border with Chile. *Star* shows the Plumerillo Airport where the Basler DC3 aircraft is based and the reference GPS station is settled. *Filled red triangles* show the gravity stations on ground re-measured in 2009–2011. *Filled blue diamonds* are ground gravity stations from Argentine gravity database (Color figure online)

The Aconcagua airborne gravity survey was flown on February 19, 2010, using a Kenn Borek Aviation Basler DC3 aircraft (Fig. 2), enroute from survey operations in Antarctica. The flight originate and ended at Mendoza Airport. Flight altitude was 8,000 m above sea level for most survey lines; this was at the service ceiling for the Basler, and required oxygen for the aircraft crew and scientists. Total airborne time was 6 h 10 min. Weather conditions were reasonable with good visibility but quite some wind at altitude. This wind generated considerable turbulence in some places, which could potentially affect the quality of the collected data.

The airborne gravity data have been acquired using a Lacoste & Romberg Air/Sea S-99 gravimeter, with a number of Javad geodetic GPS receivers onboard the aircraft and on ground providing the necessary kinematic positioning. The kinematic GPS solutions are essential for determining the aircraft vertical accelerations and the Eötvös corrections, and are filtered together with the measured gravity values to produce free-air anomalies at altitude. Details of the airborne gravity survey principles are given in Forsberg and Olesen (2010), and also outlined below.

For references, the receiver of the GPS reference station on ground was located in the Mendoza airport. Its coordinates are: 32°50′37.3483″ South Latitude, 68°47′46.8001″ West Longitude and ellipsoidal height h = 727.575 m. Coordinates for the reference station were obtained from the AUSPOS GPS service provided by Geoscience Australia. Coordinates are given in ITRF2008 frame, see http://www.ga.gov.au/bin/gps.pl. Aircraft trajectory was computed with the WayPoint software package from NovAtel (Calgary, Canada) using precise ephemerides from International GNSS

Fig. 2 Basler DC3 aircraft used for the 2010 survey at Plumerillo Airport (Mendoza)

Service (http://igscb.jpl.nasa.gov/). The Lacoste & Romberg gravimeter is a relative instrument, and the airborne measurements are tied to ground gravity values through stationary base readings in the airport. A land gravimeter Lacoste & Romberg (LCR G 069) has been used to tie to the Argentine National gravity net. Apron base readings were performed before and after the flight in order to make a proper connection of airborne readings to IGNS71. The measured apron gravity reference value was determined at 9.7921328 m/s^2 (979,213.28 mGal).

2 Airborne Gravity Concept

The principle of gravity measurement at aircraft altitude is given as:

$$\mathbf{g} = \mathrm{f_z} - \mathrm{f_{z_0}} - \dot{\mathrm{h}} + \delta \mathrm{g_{Eotvos}} + \delta \mathrm{g_{tilt}} + \mathrm{g_0} \tag{1}$$

Where $\mathrm{f_z}$ is the airborne gravimeter reading, $\mathrm{f_{z0}}$ is the corresponding apron base reading, $\dot{\mathrm{h}}$ is the vertical GPS acceleration, $\mathrm{dg_{Eotvos}}$ is the Eötvös correction, $\mathrm{dg_{tilt}}$ is the platform off-level correction, and $\mathrm{g_0}$ the airport reference gravity value. Equation (1) cannot be used to recover the gravity directly; because of the noise in the measurement of both gravity and GPS accelerations, it is necessary to apply a low-pass filter to Eq. (1). Because gravity **g** varies strongly with height, gravity anomalies are in practice the fundamental primary output from an airborne gravity. Either gravity disturbance (i.e., using GPS ellipsoidal heights) or classical (free-air) gravity anomalies (i.e., aircraft GPS heights are reduced for an apriori geoid, such as the EGM08) can be used. For the sake of ease of comparisons and merging of the airborne data with existing data sets, gravity free-air anomalies are chosen to be the final product. The full reduction scheme for the airborne readings is therefore given by the following fundamental equation:

$$\begin{aligned}\Delta g = {} & f_z - f_{z_0} - \dot{h} + \delta g_{Eotvos} + \delta g_{tilt} + g_0 \\ & - \left(\gamma_0 + \tfrac{\partial \gamma}{\partial h}(h - N_{EGM08}) + \tfrac{\partial^2 \gamma}{\partial h^2}(h - N_{EGM08})^2\right)\end{aligned} \tag{2}$$

Here Δg is the derived free air gravity anomaly, γ_0 is the normal gravity, h is the GPS ellipsoidal height, and N_{EGM08} is the EGM08 geoid undulation. Note that second order height effects must be taken into account in computing a sufficiently accurate free-air anomaly, except for surveys at low elevations, for details see (Heiskanen and Moritz 1967). Note that in Eq. (2) use of an approximate N value, such us that from EGM08 is sufficient, giving the expected error in the airborne gravity at several mGal under the challenging survey conditions. Since the EGM08 geoid fits most parts of the world better than 20–30 cm (Pavlis et al. 2012), the error in the geoid gives an effect below 0.1×10^{-5} m/s^2 on gravity anomaly, and it can therefore be neglected.

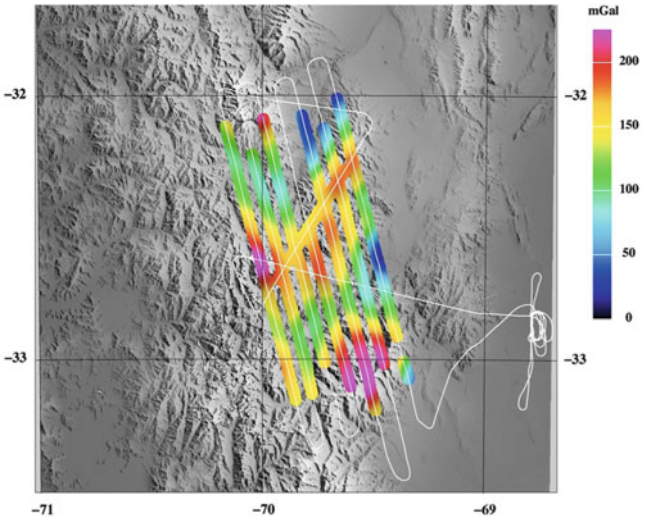

Fig. 3 Free Air Anomalies in 10^{-5} m/s^2 at flight altitude from airborne gravity survey. Tracks of flight lines are shown in *white trace* (Color figure online)

3 Data Validation

Resulting free air anomalies at flight altitude is shown in Fig. 3. Some parts of the flight were unfortunately too heavily affected by turbulence and aircraft maneuvers to yield reliable gravity data. The accepted part of the airborne data comprises the shown lines, with a total of five line intersections. The RMS value of the misfit in the crossing points is 10.3×10^{-5} m/s^2 indicating a noise level around 7×10^{-5} m/s^2; however, since the crossing are not at the same level this statistics could be misleading. The first survey line was flown at 7,000 m altitude whereas the remainder was flown at 8,000 m altitude; restricting the cross over analysis to the four intersections at approximately same altitude (8,000 m) reduces the RMS misfit to 8.5×10^{-5} m/s^2 and thus suggest a noise level around 6×10^{-5} m/s^2. This accuracy level is much higher than usually obtained accuracies with the DTU-Space aerogravity system, and is due to the challenging, turbulent flight conditions.

No cross-over adjustment is performed in the final data set, as such process may be a source of aliasing, and is not necessary due to excellent stability of the used LCR gravimeter (Olesen 2003).

A comparison to EGM08 (degree 2190 at altitude) shows a mean difference of -18.4×10^{-5} m/s^2 and a standard deviation of 26.7×10^{-5} m/s^2 (Table 1). These quite big residuals mean that the airborne data carries a lot of gravity informa-

Table 1 Statistics of the residuals (in 10^{-5} m/s^2) between EGM08 anomalies and raw airborne gravity anomalies

Statistics (10^{-5} m/s^2)	Mean	Min.	Max.	Std. dev.
Original data (pointfile)	141.214	18.000	242.500	45.453
Grid interpolation results	159.632	25.298	264.347	49.841
Predicted values output	−18.418	−86.118	42.844	26.716

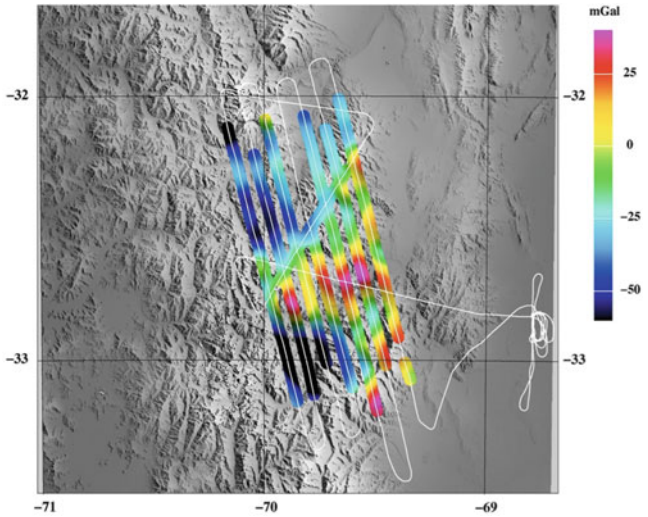

Fig. 4 EGM08 residuals at flight altitude ($\times 10^{-5}$ m/s^2)

tion not represented in the EGM08 model. The residuals are also shown in Fig. 4.

4 Geoid Computation

Although the cm-geoid could be derived in numerous cases in lowland areas with sufficiently dense gravity data coverage, so far no convincing case of attaining a cm-level geoid in mountainous regions has been reported. This is a consequence of both insufficient gravity data coverage, the rough gravity field, theoretical shortcomings, and insufficient quality of the leveling data used to compute "groundtruth" geoid (or quasi-geoid) values (Yildiz et al. 2012).

The most commonly adopted and applied approach to regional gravimetric geoid determination today is probably the remove- compute-restore (RCR) technique (e.g., Schwarz et al. 1990). In the remove step, a long-wavelength part (predicted by a global gravity field model) and a short-wavelength part (predicted by topography) are removed from the original gravity data. In the compute step, the obtained band-pass filtered gravity anomalies are transformed into geoid or quasi-geoid heights either using Stokes' integration methods, 2-D spherical Fast Fourier Transform (FFT) methods, or using Least Squares Collocation (LSC). After having carried out the compute step, the long-wavelength and short-wavelength parts of the field are restored to yield either the quasi-geoid or geoid, depending on the exact implementation of the methods. The methods need in practice to be combined with modified Stokes function kernels (e.g., Wong and Gore 1969), to avoid modifying accurate long-wavelength gravity field information from satellites (GRACE, GOCE).

Alternative methods for estimating the geoid include the optimized modified kernel methods of Sjöberg (2005), which treat the reference field and terrain removal in different ways, but ultimately giving nearly equivalent results. We have therefore in the Aconcagua geoid determination decided to use the FFT remove-restore technique for the determination of the quasigeoid, which is subsequently transformed to the classical geoid using the standard formula outlined in Heiskanen and Moritz (1967). Terrain effects are computed using the prism integration method, and filtered along-track to match the airborne gravity filter. For details of the applied method see Forsberg and Olesen (2010).

4.1 Downward Continuation of Airborne Data and Merging with Surface Data

In this study, the limited surface gravity data (Fig. 5) was merged with downward continued airborne gravity data, yielding the final geoid model shown in Fig. 6. The harmonic downward continuation of airborne gravity data is a classical unstable operation which can be regularized by applying the collocation approach or stabilized Fourier methods (Forsberg 2002). Because of the mix of airborne and surface data, and the varying flight altitudes, we use the method of least squares collocation for the downward continuation.

All processing has been done using the remove-restore method, where the gravity anomalies have been split into three terms

$$\Delta g = \Delta g_1 + \Delta g_2 + \Delta g_3 \tag{3}$$

where the first term is a spherical harmonic reference field, the second term the terrain effects, and the third part the residual gravity. As outlined above, only the residual gravity is downward continued by collocation, and subsequently transformed to the geoid; the other terms are computed at the surface of the topography in the "restore" step of the RCR method. For the spherical harmonic reference field, a composite model of GOCE coefficients to degree 180 (Pail et al. 2011) and EGM08 to degree 720 has been used.

Table 2 Statistics on reduction of gravity data for geoid calculation

		Free-air anom. Δg		Δg—GOCE/EGM08		Δg-Ref.—RTM	
Statistics (10^{-5} m/s^2)	Points	Mean	Std. dev.	Mean	Std. dev.	Mean	Std. dev.
Surface gravity (Argentina)	2, 122	−24.6	33.9	−9.0	25.1	−4.0	13.7
Aconcagua profile	17	124.1	102.3	−51.0	57.6	−6.4	10.3
Airborne free-air at altitude	966	141.2	45.5	1.7	40.7	−4.8	28.8

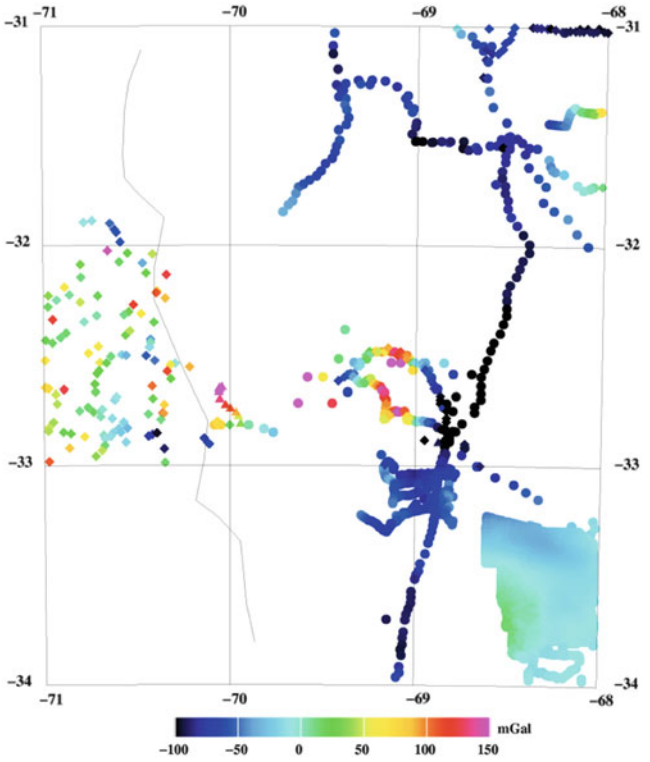

Fig. 5 Available surface gravity data ($\times 10^{-5}$ m/s^2)

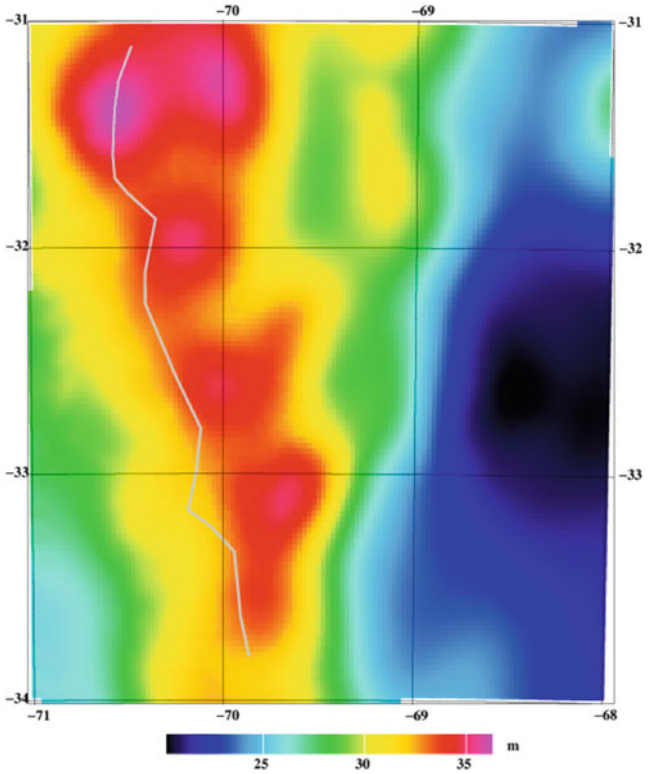

Fig. 6 Final geoid model

Because of the extreme topography, the direct use of gravity terrain effects in the downward continuation process is necessary. Terrain reductions will—if properly applied—reduce the short-wavelength information in the gravity data, and thus make the problem more stable. In the Aconcagua region we used SRTM elevation data, averaged to 15″ resolution as the basic terrain data. These data were used to compute residual terrain effects Δg_2 on all surface and airborne data, relative to a smooth mean elevation surface of about 25 km resolution. The terrain effects were computed by prism integration using the TC program (Forsberg 1984), assuming a constant density of 2.67 g/cm^3 for all topography. Statistics on reduction of gravity data for the GOCE/EGM08 reference field and the RTM terrain effects can be found at Table 2. The large residual bias expresses likely primarily the errors in EGM08 in this region.

4.2 FFT Geoid Computation

Using the reduced gravity data, gravimetric geoid models were computed by spherical FFT methods. In the used multi-band FFT method (Forsberg and Sideris 1993), the fundamental Stokes' formula is transformed into a spherical convolution in latitude and longitude (φ, λ) for a given reference parallel φ_{ref}, and by utilization of a number of bands a virtually exact convolution expression may be obtained by a suitable linear combination of the bands. For each band the convolution expressions are evaluated by

$$\begin{aligned} \zeta_3 &= S_{ref}(\Delta\varphi, \Delta\lambda) * [\Delta g_3(\varphi, \lambda) \sin\varphi] \\ &= F^{-1}[F(S_{ref})\, F(\Delta g \sin\varphi)] \end{aligned} \tag{4}$$

where S_{ref} is a (modified) Stokes' kernel function, and * and F are thetwo-dimensional convolution and Fourier transform,

respectively. In the actual implementation of the method, the data are gridded by least-squares collocation, and a 100 % zero padding is used to limit the periodicity errors of FFT. After the FFT transformation to the (residual) quasigeoid, the geoid terrain effects and the spherical harmonic terrain effects, computed at the level of the topography, are restored to give the final geoid. The final gravimetric geoid model is shown in Fig. 6. Because the gravimetric geoid model is based on the long-wavelength gravity field information underlying EGM08, the corresponding height system for the geoid is in a global height system, with a W_0-value corresponding to EGM08 (termed loosely as a "World Height System", although no formal World Height System has yet been adopted by the IAG). The error estimation of the geoid is difficult, since the accuracy of the underlying EGM08 model is unknown, the relatively high error and limited coverage of the airborne data, and the errors of downward continuation and estimation of the classical geoid (with its inherent density assumptions). A conservative estimate of the geoid error is likely at the 30–50 cm level, based on experience from similar geoid computation projects.

5 Altitude Computation of Aconcagua

In 1969, the Geodesy Institute of the National University of Buenos Aires carried out the first gravity measurements in Mount Aconcagua (Baglietto 1969). These surveys were performed using a relative Worden gravimeter to measure the gravity, and classical leveling for heights determination, deriving a height value of 6,959.6 m in the national Argentinean height datum, based on Atlantic sea level at Mar del Plata. The new measurement using GPS and geoid, is a contribution to the SIGMA project (Mount Aconcagua GPS Research System), an effort toward the scientific-technologic development within the Aconcagua National Park, that link natural and anthropogenic processes with the variables to be developed for controlling the environment (Lenzano et al. 2008). The SIGMA project comprises a research in the fields of geodesy and geophysics and will develop basic knowledge for the programming and development of the management of mountain ecosystems, leading to preservation and restoration to alleviate natural hazards. A permanent GPS station, named ACON and a meteorological station were installed at the Aconcagua summit in 2006 as part of this project.

The coordinates at ACON GPS station are −32°39′13″.141924 South Latitude, −70°00′43″.383210 West Longitude, 6,984.41 m (ellipsoidal height at the GPS antenna), while the summit's ellipsoidal height is 6,995.10 m. These coordinates are listed in POSGAR07, which is the national reference frame in Argentina.

From the new geoid computation results, we obtain a GOCE/EGM quasigeoid at the summit of 35.91 m, a gravimetric quasigeoid value of 36.14 m, and a gravimetric geoid of 34.67 m. This last value yield a new GPS-based orthometric height of 6,960.4 m of the Aconcagua summit. This value refers to the EGM08-based global vertical datum (the current de-facto "World Height System"). The offset between the "World Height System", and the Argentinean height system, is not known in the Aconcagua region. However, a similar GPS-geoid project in the San Juan province, close to the Aconcagua region, indicates an offset in the two system of about 1 m, yielding a corresponding (lower) altitude of around 6,959.4 m. The GPS height determination therefore confirms (at the 1 m-level) the official height value of Aconcagua. A final confirmation of the Aconcagua height in the Argentine system awaits additional GPS of levelling benchmarks close to Aconcagua, but within an error bar of about a half metre the rounded value can be given at 6,960 m. Many international values of the summit elevation quote widely different values (up to 10 m different), which can now be confirmed to be in error.

Conclusions

For the purposes of geodetic and geophysical applications, new gravity measurements were undertaken in Aconcagua Mount area by means of ground and airborne surveys. The airborne survey over Aconcagua provided, despite challenging conditions, new valuable gravity data over the region. Internal noise estimate is around 6×10^{-5} m/s^2, but this value is quite unreliable because it is based on few crossing points. Experience from surveys under comparable conditions suggests a somewhat lower noise level. A comparison to EGM08 (degree 2190 at 8,000 m) shows a mean difference of -18.4×10^{-5} m/s^2 and a standard deviation of 26.7×10^{-5} m/s^2. These quite big residuals mean that the airborne data carries a lot of gravity information not represented in the EGM08 model.

Geoid computation plus coordinates derived from ACON GPS station yield to a new height of 6,960.4 m for Mount Aconcagua in the EGM08-inferred global height system, and a confirms the officially adopted Argentinean height value of 6,959.6 m within a half-meter error bar.

Acknowledgements This work was partially supported by PICT-0899 (ANPCyT). The authors acknowledge the invaluable technical support given by CRICyT, SIGMA Project and "Dirección de Recursos Naturales, Mendoza", specially to guard parks at "Parque Provincial Aconcagua".

References

Baglietto EE (1969) Determination de la pesanteur au sommet de la Montagne Aconcagua, 6959,6 ms.n.m., Association Internationale de Geodesie—Bureau Gravimetrique International, Bulletin 20

Forsberg R (1984) A study of terrain reductions, density anomalies and geophysical inversion methods in gravity field modelling. Reports of the Department of Geodetic Science and Surveying, No. 355, The Ohio State University, Columbus, Ohio

Forsberg R (2002) Downward continuation of airborne gravity—an Arctic case story. In: Proceedings of the international gravity and geoid commission meeting, Thessaloniki

Forsberg R, Olesen A (2010) Airborne gravity field determination. In: Xu G (ed) Sciences of geodesy. Springer, Berlin, pp 83–104

Forsberg R, Sideris MG (1993) Geoid computations by the multi-band spherical FFT approach. Manuscripta Geodaetica 18:82–90

Heiskanen WA, Moritz H (1967) Physical geodesy. Freeman, San Francisco, CA

Lenzano L, Mackern MV, Lenzano MG, Robín AM, Cabrera G, Barón J (2008) Estación Permanente GPS ACON. Instalación y funcionamiento. Monte Aconcagua. Mendoza, Argentina. GEOACTA, vol 33, pp 137–141 (In Spanish)

Olesen AV (2003) Improved airborne scalar gravimetry for regional gravity field mapping and geoid determination. Technical Report no 24, Kort og Matrikeldstyrelsen, Copenhagen

Pacino MC, Del Cogliano D, Font G, Moirano J, Natalí P, Lauría E, Ramos R, Miranda S (2005) Activities related to the materialization of a new vertical system for Argentina. Dynamic planet, IAG symposium, vol 130. Springer, pp 671–676

Pail R, Bruinsma S, Migliaccio F, Foerste C, Goiginger H, Schuh W-D, Hoeck E, Reguzzoni M, Brockmann JM, Abrikosov O, Veicherts M, Fecher T, Mayrhofer R, Krasbutter I, Sanso F, Tscherning CC (2011) First GOCE gravity field models derived by three different approaches. J Geod 85:819–843

Pavlis N, Holmes S, Kenyon S, Factor J (2012) The development and evaluation of the Earth Gravitational Model 2008 (EGM2008). J Geophys Res 117(B16):4406. doi:10.1029/2011JB008916

Schwarz KP, Sideris MG, Forsberg R (1990) Use of FFT methods in physical geodesy. Geophys J Int 100:485–514

Sjöberg LE (2005) A discussion on the approximations made in the practical implementation of the remove-compute-restore technique in regional geoid modeling. J Geod 78:645–653

Wong L, Gore R (1969) Accuracy of geoid heights from modified Stokes kernels. Geophys J R Astron Soc 18:81–91

Yildiz H, Forsberg R, Ågren J, Tscherning C, Sjöberg L (2012) Comparison of remove-compute-restore and least squares modification of Stokes' formula techniques to quasi-geoid determination over the Auvergne test area. J Geod Sci 2(1):53–64

HRG2009: New High Resolution Geoid Model for Croatia

Tomislav Bašić and Olga Bjelotomić

Abstract

Using an updated Earth´s gravity field data set widely available and applying the least square collocation calculation technique, a new Croatian geoid model HRG2009 was calculated. Significant accuracy improvements have been achieved regarding the previous national geoid model HRG2000; four times better resolution and 69 % better absolute accuracy of the model. The following data sets were used: great number of new measured terrestrial gravity data and data obtained from satellite altimetry for the area of the Adriatic Sea, along with geoid undulations at discrete points measured by GNSS/leveling on almost 500 stations all over the mainland, futhermore long and mediumwave field structures taken from the latest detailed global geopotential model EGM2008 and high frequencies field structures modeled with the help of $3'' \times 3''$ Shuttle Radar DEM's. Absolute accuracy assessment made on 59 GNSS/leveling control stations, that were not used in calculations, have resulted with 69 % improvement of new national geoid model regarding the previous one, with standard deviation of 3.5 cm on overall computation area. It is significantly more reliable surface as compared to the earlier HRG2000 solution with standard deviation of 11.4 cm.

The new geoid surface has been used for different purposes, primary in the precise height definition using modern GNSS technology. Therefore, the Croatian Positioning System CROPOS was upgraded in 2011 with the new service which enables the real time transformation of ellipsoidal heights to the (normal) orthometric heights using HRG2009 geoid GRID and Trimble Transformation Generator software for more than 440 surveying and geoinformation companies in Croatia.

Keywords

External accuracy • Least square collocation • New national geoid

1 Introduction

Several significant studies (Denker et al. 2009; Bašić and Hećimović 2006; Grgić et al. 2010) have preceded the computation of the new national geoid HRG2009.

Firstly, the analysis (Liker et al. 2010) of recent global geopotential models based on CHAMP (Prange et al. 2010) , GRACE (Mayer-Gürr et al. 2010) and GOCE (Pail et al. 2011) mission as well as testing of EGM2008 model (Denker et al. 2008) have been conducted. Secondly, great number of additional gravity data for the area of interest was gathered. Furthermore, a $3'' \times 3''$ DTM model from SRTM data for the calculation of the Earth's gravity field topographic effects was developed (Bašić and Buble 2007). Regarding terrestrial data, it was of great significance that the Basic Gravimetric Network (Barišić et al. 2008) was established that was used together with EUVN and EUVN_DA data (Grgić et al.

T. Bašić • O. Bjelotomić (✉)
Faculty of Geodesy, University of Zagreb, Kačićeva 26, 10000 Zagreb, Croatia
e-mail: tomislav.basic@geof.hr; olga.bjelotomic@geof.hr

U. Marti (ed.), *Gravity, Geoid and Height Systems*, International Association of Geodesy Symposia 141,
DOI 10.1007/978-3-319-10837-7_24,

2009) for independent control of the HRG2009. And finally, the analysis of new and previous national height datum was made, as well as the establishment of more than 500 GNSS/levelling points regularly distributed over the Croatian territory for the purpose of geoid orientation and independent control of previous HRG2000 geoid model.

The determination of the local high-resolution gravity field is divided in three parts regarding the different wavelenghts of the observed gravity field structures. The long-wavelenght part is derived from global geopotential model (EGM2008 in this case), the medium-wavelenght part originates in terrestrial point gravity filed observations, and the short-wavelenght part is taken from the high-resolution digital terrain model. In the simple remove-restore technique, the reduced observations are thus written as linear functional of the anomalous gravity potential (Bašić 1989):

$$x_i = L_i(T) - L_i(T_{EGM}) - L_i(T_{RTM}) + n_i \qquad (1)$$

The least square collocation (Moritz 1980) results in predictions $L_j(\tilde{T}')$. To obtain the desired results, the effect of the anomalous masses and the effect of the geopotential model needs to be added later on in the "restore" procedure:

$$L_j(\tilde{T}) = L_j(\tilde{T}') + L_j(T_{EGM}) + L_j(T_{RTM}) \qquad (2)$$

We decided to use the least square collocation because it has shown to be most suitable with regard to the relatively small area of the territory of Croatia, so that large and extensive numerical operations could be carried out more easily in just one-step due to their flexibility in handling irregularly distributed heterogeneous data. In addition, we preferred to have the error estimates of predicted quantities. The calculation area covers the entire territory of Croatia spreading between the area 42–46.6° in latitude, and 13.0–19.5° in longitude.

The calculation was carried out in a regular grid of 30″ × 45″ resolution (approximately 1 × 1 km), which is four times better resolution then the one of the previous national geoid HRG2000 (Bašić et al. 1999). Consequently, the number of calculating residual points increased from 72297 with HRG2000 to 288113 with HRG2009 solution.

2 Analysis

In Table 1, the main statistical indicators of the original gravity anomalies, EGM2008 and RTM effects as well as residual field are presented.

In performing the residual terrain modelling, the following grids have been used: (a) the DTM of 4″ × 5″ (approximately 120 × 110 m), obtained from 3″ × 3″ SRTM data, covering the area from 40° to 48° in latitude, and 10° to 22° in longitude, (b) the coarse 1′ × 1′ grid of relief height covering the bigger area from 36° to 52° in latitude and from 5° to 27° in longitude, and (c) 5′ × 5′ RTM reference grid of the same area as the coarse one.

Table 1 Statistical indicators of gravity anomalies in the *remove* procedure, in [mGal]

N = 29330	Δg_GRS80	Δg_EGM2008	Δg_RTM	Δg_RES
Mean	11.58	15.45	−4.14	0.276
Standard deviation	29.20	28.55	13.18	5.491
Min	−130.71	−102.79	−142.69	−14.994
Max	166.47	163.12	62.58	14.996

The effect of the applied "remove" procedure is evident in decreasing standard deviation, which drops from 29.20 mGal for the observed anomalies to 5.49 mGal for the residuals (Δg_GRS80–Δg_EGM2008–Δg_RTM). A significant reduction of the mean value from 11.58 mGal to 0.28 mGal (good centered data) can also be recognized (1 mGal = 10^{-5} ms^{-2}).

A-priori information about the variation of the local gravity field is introduced through the empirical covariance function calculated using 29330 residual gravity anomalies (Fig. 1, right). In this study the variance of the empirical covariance function has the value of only 30.03 mgal^2 and the first zero-value occurs already at 9 km distance (covariance graph on Fig. 1 right).

For the purpose of correcting the absolute orientation of the calculated geoid surface, a significant number (495) of GNSS/leveling points distributed across Croatia has been used. The statistical indicators are presented in Table 2, where an apparent residual bias effect is present again, but it should be noted that the value of the mean N_RES = -1.024 m, most likely originates from the discrepancy between the used EGM2008 model and the definition of national vertical datum that relates to five tide gauges.

3 Quality Assessment

The assessment of the HRG2009 quality was done in two ways. Firstly, its internal accuracy was evaluated through the analysis conducted on 495 points, on which measured GNSS/leveling undulations were compared with calculated undulations form HRG2009 geoid model. Internal accuracy analysis has shown a remarkably high mutual compatibility, giving the standard deviation of 2.7 cm and the mean difference almost zero (Table 3). These internal control indicators obtained with GNSS/leveling undulations used for computation of new geoid surface, verified well-chosen methodology and conducted computation, implicating on high reliability of the new geoid solution of 2–3 cm over most of the Croatian mainland (Fig. 2, left).

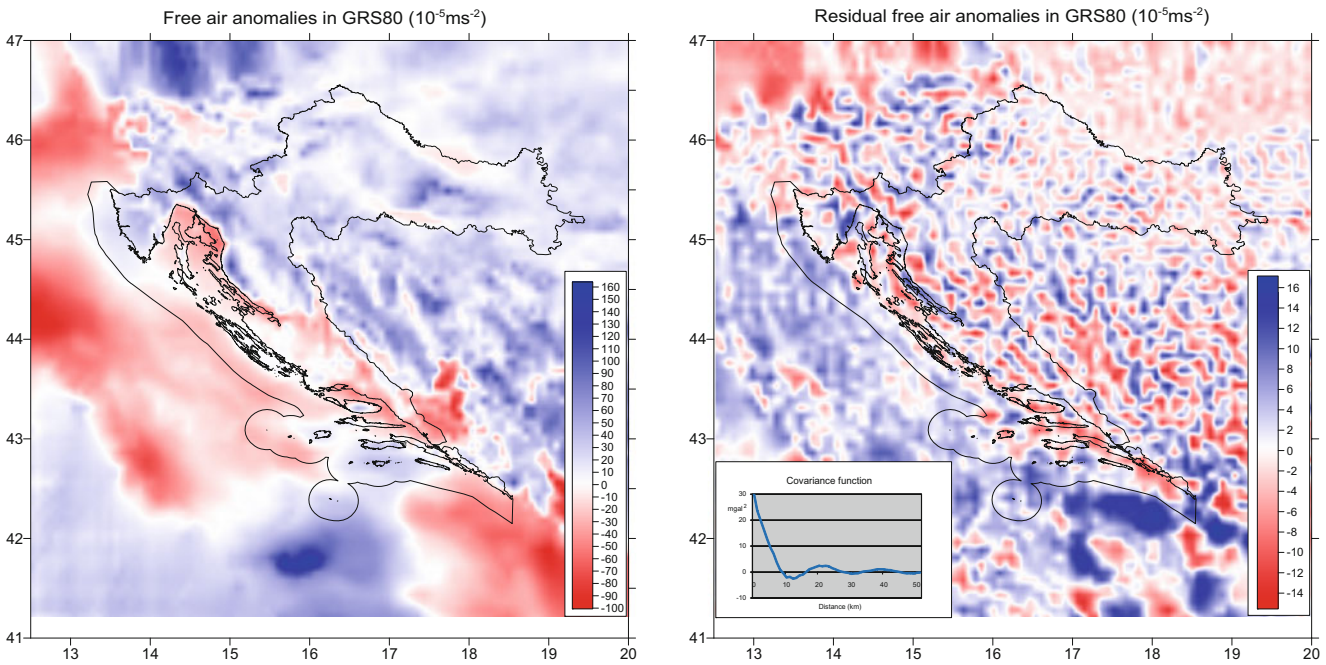

Fig. 1 Gravity anomaly field obtained in *remove* procedure: (*left*) free air anomalies (*right*) residual free air anomalies

Table 2 Indicators of the geoid reduction effect in 495 GNSS/leveling points, in [m]

	N_GNSS/LEV.	N_EGM2008	N_RTM	N_RES
Mean	44.548	45.438	0.134	−1.024
Standard deviation	1.100	1.081	0.030	0.062
Min	40.414	41.429	0.089	−1.271
Max	46.666	45.517	0.247	−0.899

Table 3 Internal (495 points) and external (59 points) accuracy indicators, in meters

Internal control	Min	Max	Average	Standard deviation
HRG2009–495 GNSS/lev.	−0.071	0.059	−0.004	0.027
Absolute (external) control				
HRG2009–59 GNSS/lev.	−0.078	0.058	−0.012	0.035
HRG2000–59 GNSS/lev.	−0.275	0.242	−0.024	0.114

Beside the internal accuracy, we made an external independent quality assessment on 59 stations that were not used in the computation procedure (Bašić 2009). Comparison was made between 59 GNSS/leveling undulations measured for external geoid control and calculated HRG2009 undulations for these stations. This comparison confirmed that there was an enviable good absolute accuracy of the new national geoid, especially considering the obtained standard deviation of 3.5 cm (Table 3) and the mean difference of almost zero, absolutely confirming high reliability of this solution (Fig. 2, right).

The improvement of the HRG2009 with respect to the previous HRG2000 geoid model is analysed on 59 control stations which were neither used in HRG2000 computations so unambiguous comparison could be made. External control conducted on 59 GNSS/levelling points gave the standard deviation of 11 cm for HRG2000 solution while for new geoid solution HRG2009 it amounts 3.5 cm. Therefore, the improvement of the new national geoid HRG2009 with respect to the previous geoid model resulted with 69 % better compatibility to the Earth's surface.

New national high-resolution geoid model HRG2009 (Bašić 2009) is shown on Fig. 3. Its average geoid undulation equals 44.151 m with standard deviation of 2.055 m, while minimum and maximum are 36.807 and 50.262 m respectively.

4 HRG2009 Versus EGG2008

The comparison between HRG2009 and EGG2008 (Denker et al. 2008) geoid model has been done for all points of 30″ × 45″ grid, within the solution area for Croatia, meaning 42–46.6°N and 13–19.5°E. The comparison has shown the mean surface difference of 24.1 cm, which is consequent of different height datum surfaces, i.e. Croatian geoid model refers to HVRS71 mean sea level surface,

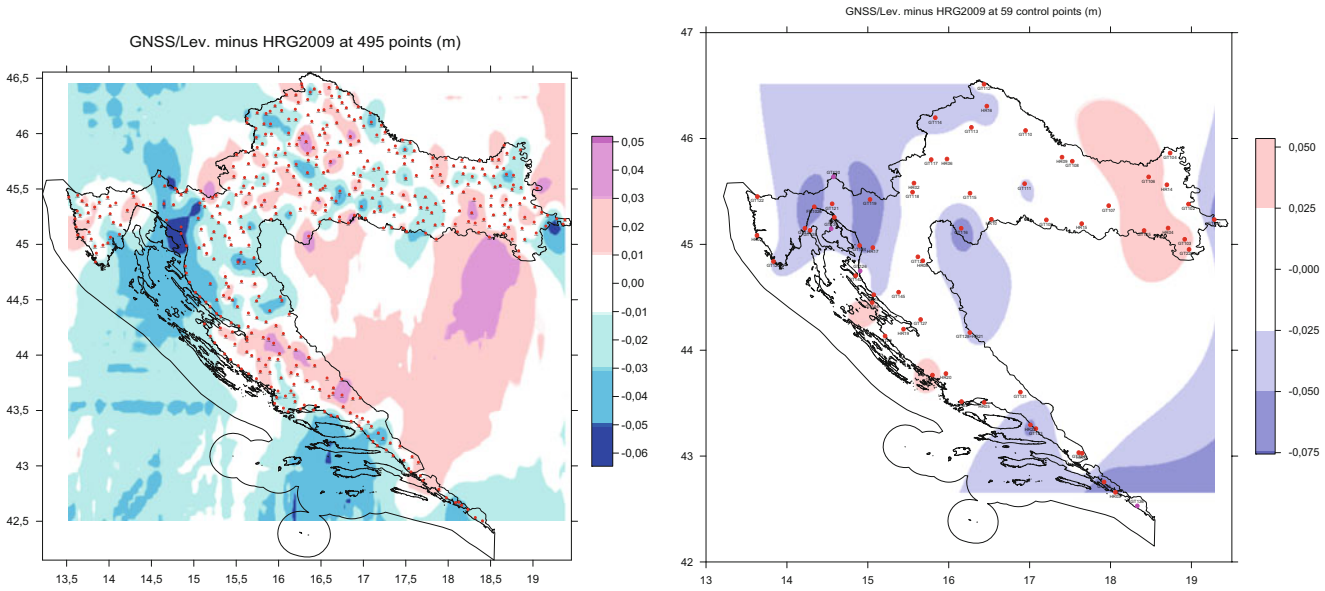

Fig. 2 Quality of the HRG2009 geoid: (*left*) internal accuracy, (*right*) absolute accuracy

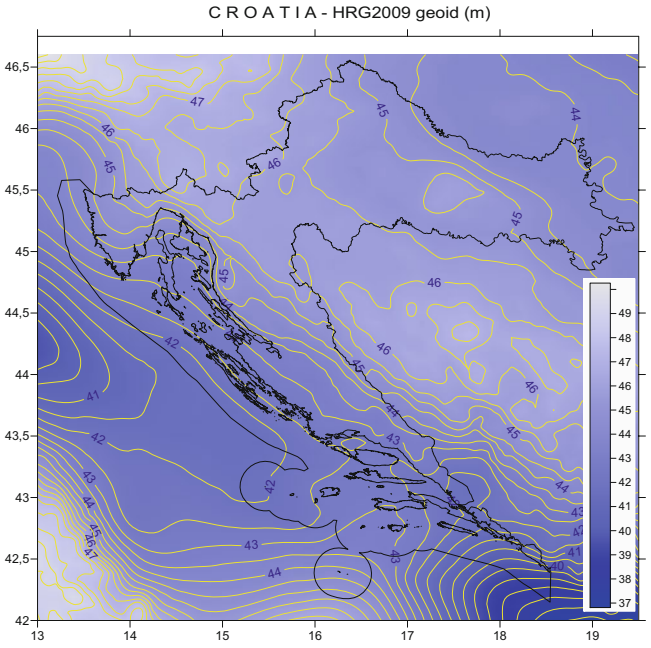

Fig. 3 New high-resolution geoid model HRG2009

while EGG2008 refers to Amsterdam MSL. Furthermore, the standard deviation is 17.0 cm, while the range varies from the minimum of −1.214 m to the maximum of 0.452 m (Denker and Bašić 2011). Greater disagreements can be found outside the Croatian borders, due to different data used, different methods, as well as border effects.

The comparison between EGG2008 and 495 GNSS/lev. points was made and it has shown good mutual matching after removing the mean difference of an 22.8 cm (Table 4).

Table 4 Quasigeoid differences regarding the EGG2008, in [m]

Quasigeoid differences	Min	Max	Average	Standard deviation
GNSS/lev.–EGG2008	−0.175	0.095	−0.228	0.039
HRG2009–EGG2008	−0.155	0.064	−0.223	0.026

After the mean difference of 24.1 cm (height datum difference) had been removed, HRG2009 was compared with EGG2008 over the 495 GNSS/leveled points. The results obtained gave very good indicators for land areas, with the standard deviation of 2.6 cm (Table 4).

There are several areas with differences between 10 and 15 cm, but they are all on the borders with Monte Negro, Italy close to Trieste, and the area of Rijeka and Bakar bay.

Quality assessment of the EGG2008 made on Croatian territory has confirmed good reliability of European quasi-geoid on a larger part of territory. Neglecting problematic border areas discussed above, EGG2008 geoid model fits to the continental part within 3–5 cm.

5 HRG2009 Implementation in Online GNSS Service

By the Decision on determining the official geodetic datum and map projections of Republic of Croatia (8 August 2004) passed by Croatian State Geodetic Administration, regulations on the transfer from the old to the new geodetic national datum have been determined. Consequently, in collaboration with Faculty of Geodesy unique transformation model T7D based on GRID transformation procedure has

been developed. It consists of 7 parameter transformation and $30'' \times 45''$ regular grid of predicted distorsion for height and positional coordinates and it provides both transformation within $+/-0.06$ m on the national land area.

The implementation of the Decision has resulted further in implementing the new geoid HRG2009 within the T7D model to the online service of national positioning system-CROPOS for real time height transfer.

The online service is in its full operation since January 03, 2011, which allows CROPOS users to select easily CROPOS_VRS_HTRS96 service online on their instruments and obtain orthometric heights in real time in the new official height datum HVRS71, through implemented HRG2009. Also, the same service allows immediate online transformation for horizontal positioning. For that matter, user is provided by ellipsoidal coordinates in new national datum HTRS96 with option to use the new official map projection HTRS96/TM and display them directly on the field.

Prior to release, CROPOS_VRS_HTRS96 service was successfully tested on 604 control points through out the whole Croatian territory.

Conclusion

As shown in this study, a new national high-resolution geoid solution HRG2009 has been calculated, showing an accuracy of few (2–3) cm for the predominant part of Croatia, especially in land areas. At the same time, regional quasigeoid EGG2008 fits very well at GNSS/leveling points over a large part of continental Croatia, varying just 3–5 cm, apart from few problematic areas, mostly on the borders to Monte Negro and Italy, where consistency varies from 10 to 15 cm. Due to these facts, along with the newest GOCE results, there is a clear need for a more precise overlap of the European and Croatian geoid model to be achieved in the forthcoming years. Better fitting new solutions are needed both at regional and local levels. As the new GOCE data are expected to be of even better resolution, the integration of the Croatian geoid model with GOCE data is expected to be further developed and improved.

References

Barišić B, Repanić M, Grgić I, Bašić T, Liker M, Lučić M, Markovinović D (2008) Gravity measurements on the territory of the Republic of Croatia past, current and future gravity networks. In: Proceedings of the IAG international symposium on terrestrial gravimetry: static and mobile measurements (TG-SMM2007), pp 197–202. ISBN 978-5-900780-76-4

Bašić T (1989) Research aimed at regional determination of geoid with decimenter accuracy (PhD thesis, in German). Wissenschaftliche Arbeiten der Fachrichtung Vermessungswesen der Universitat Hannover, vol 157. Universitat Hannover, Hannover, pp 1–131

Bašić T, Brkić M, Snkel H (1999) A new, more accurate geoid for Croatia. Phys Chem Earth: A Solid Earth Geod 24(1):67–72. doi:10.1016/S1464-1895(98)00012-X. ISSN: 1464–1895

Bašić T, Buble G (2007) Comparison of SRTM3 Global heights model with existing digital terrain models on the territory of croatia (in Croatian). Geodetski List 61(2):93–111 (Zagreb)

Bašić T, Hećimović Ž (2006) Latest geoid determinations for the Republic of Croatia. Newton's Bull 3:83–92. ISSN 1810-8547

Bašić T (2009) The unique transformation model and a new Croatian geoid model (in Croatian). Reports of scientific and professional projects for 2006–2008. State Geodetic Administration, Zagreb, pp 5–21

Denker H, Bašić T (2011) European gravimetric geoid EGG2008 and Croatian geoid HRG2009 (in Croatian). In: Proceedings of the 2nd CROPOS conference, Zagreb, pp 59–69. ISSN 1847-4098

Denker H, Barriot J-P, Barzaghi R, Fairhead D, Forsberg R, Ihde J, Kenyeres A, Marti U, Sarrailh M, Tziavos IN (2009) The development of the European gravimetric geoid model EGG07. In: Proceedings of the 2007 IAG general assembly, vol 133. Springer, NewYork, pp 177–186

Denker H, Barzaghi R, Fairhead D, Forsberg R, Ihde J, Kenyeres A, Marti U, Sarrailh M, Tziavos IN (2008) A new European gravimetric quasigeoid EGG2008. In: IAG international symposium on "Gravity, Geoid and Earth Observation 2008", Crete (Poster)

Grgić I, Barišić B, Bašić T, Lučić M, Repanić M, Liker M (2009) Fundamental gravity network of the republic of croatia in the function of control and improving of National and European Geoid Model. In: Proceedings of the symposium of the IAG, pp 300–307. ISSN 1436-3445

Grgić I, Lučić M, Repanić M, Bjelotomić O, Liker M, Markovinović D, Bašić T (2010) Preliminary works on creation of the new croatian geoid model HRG2009. Bollettino di Geodesia e Scienze Affini LXIX(2-3):165–177. ISSN 0006-6710

Liker M, Lučić M, Barišić B, Repanić M, Grgić I, Bašić T (2010) Analysis of recent global geopotential models over the croatian territory. In: IAG symposia, vol 135. Springer, Berlin, pp 283–228. ISBN 978-3-540-85425-8

Mayer-Gürr T, Eicker A, Kurtenbach E, Ilk K-H (2010) ITG-GRACE: global static and temporal gravity field models from GRACE Data. System earth via geodetic-geophysical space techniques advanced technologies in Earth sciences. Springer, Berlin, pp 159–168

Moritz H (1980) Advanced physical geodesy. Herbert Wichmann Verlag, Karlsruhe

Pail R, Bruinsma S, Migliaccio F, Förste C, Goiginger H, Schuh W-D, Höck E, Reguzzoni M, Brockmann JM, Abrikosov O, Veicherts M, Fecher T, Mayrhofer R, Krasbutter I, Sansò F, Tscherning CC (2011) First GOCE gravity field models derived by three different approaches. J Geodesy 85(11):819–843

Prange L, Jäggi A, Dach R, Bock H, Beutler G, Mervart L (2010) The AIUB-CHAMP02S and the influence of GNSS model changes on gravity field recovery using spaceborne GPS. Adv Space Res 45(2):215–224

Validation of Regional Geoid Models for Saudi Arabia Using GPS/Levelling Data and GOCE Models

A. Alothman, J. Bouman, T. Gruber, V. Lieb, M. Alsubaei, A. Alomar, M. Fuchs, and M. Schmidt

Abstract

To meet increased demands in mapping, surveying, geodesy, and large infrastructure projects, an accurate national geoid model for Saudi Arabia is required to transform ellipsoid heights to orthometric heights. The lack of data and the nature of the topography make the computation of a geoid model in Saudi Arabia a difficult task. Two regional geoids were developed for the Kingdom of Saudi Arabia (KSA): (1) the KSA geoid developed by the General Directorate of Survey (GDS); and (2) a geoid developed by the Ministry of Municipality and Rural Affairs (MOMRA). The KSA model was developed using a remove and restore technique and over 5,000 observations of Global Positioning System (GPS) ellipsoidal heights on leveling benchmarks (GPS/BM). The MOMRA geoid was estimated from 861GPS/Levelling with a kriging approach. A GPS/Levelling test campaign (T campaign) was carried out in 2010 by re-observing about 391 BM stations common to the two geoid models. The two geoid models are first compared against each other and EGM2008 at the 391 BM stations from the T campaign. The absolute differences between models may reach several meters, whereas the standard deviation of the differences ranges between 0.5 and 1.5 m. Analysis revealed that KSA and MOMRA geoids seem not to coincide. Both are biased (means of 0.46 m) and highly scattered (standard deviation is ± 0.72 m). Next, geoid models developed using GOCE satellite data are used to validate the T campaign data.

Keywords

Geoid • GPS • Levelling • Benchmark • GOCE • EGM2008 • Residuals

1 Introduction

In geodesy, one of the primary tasks is to determine the position of points on the Earth's surface uniquely and accurately. The definition of points requires knowledge of geodetic latitude, longitude, and ellipsoidal height. The orthometric height (H) is measured along the curved plumb line which starts from the geoid realized by the mean sea level at a reference point (e.g. a tide gauge). The ellipsoidal height (h) is a geometric quantity and differs from the orthometric height (H) by the geoid undulation (or geoid height) (N). The relation between the three quantities can be represented by the following formula (Heiskanen and

A. Alothman (✉)
King Abdulaziz City for Science and Technology (KACST), Riyadh, Saudi Arabia
e-mail: aalothman@kacst.edu.sa

J. Bouman • V. Lieb • M. Fuchs • M. Schmidt
Deutsches Geodätisches Forschungsinstitut (DGFI), Munich, Germany

T. Gruber
Institut für Astronomische und Physikalische Geodäsie (IAPG), Technical University Munich, Munich, Germany

M. Alsubaei
General Directorate of Survey (GDS), Riyadh, Saudi Arabia

A. Alomar
Ministry of Municipality and Rural Affairs (MOMRA), Riyadh, Saudi Arabia

U. Marti (ed.), *Gravity, Geoid and Height Systems*, International Association of Geodesy Symposia 141,
DOI 10.1007/978-3-319-10837-7_25,

Moritz 1967):

$$h = H + N. \tag{1}$$

Geoid undulations are of significant importance when high accuracy orthometric heights are required for GPS-derived ellipsoidal heights. Advances in space technology and the launch of CHAMP (CHAllenging Minisatellite Payload), GRACE (Gravity Recovery and Climate Experiment), and GOCE (Gravity Field and Steady-State Ocean Circulation Explorer) satellite missions have revolutionized the nature of recovering the Earth's gravity field because they allow for the first time to derive global gravity field models with homogeneous accuracy and spatial and temporal resolution (Reigber et al. 2002; Tapley et al. 2004; Rummel et al. 2012). Specifically with data from the GRACE and GOCE missions, global gravity field models with an accuracy of a few cm with 100 km spatial resolution can be obtained (Gruber et al. 2011). Especially regions with poor or no terrestrial gravity data benefit from the detailed gravity information that GOCE provides (e.g. Bouman et al. 2011).

Saudi Arabia is located on the Arabian tectonic plate with high terrain topography in the western part of the kingdom, where the Arabian shield is dominating, and the geoid is expected to have high frequency components, whereas in the east the topography is flat with low features. In this paper we first will investigate the geoid models available for Saudi Arabia. Secondly, the geoid models will be tested and evaluated by comparing them with the recently observed GPS/Levelling geoid heights (T campaign) and the global geoid model EGM2008 (Pavlis et al. 2012). Finally, we will directly compare GOCE geoids and the GPS/Levelling data at different spatial resolutions in order to validate the GPS/Levelling data.

2 Global Geoid Models

The global gravitational model EGM2008 is derived from a GRACE satellite-only solution, satellite altimeter observations over the oceans and mean surface gravity observations over land, and has a resolution of $5' \times 5'$ (Pavlis et al. 2012). EGM2008 is today's state-of-the-art high resolution global gravity field model and is widely used but suffers some deficiencies in particular in regions where poor or no terrestrial gravity data are available, such as KSA. For some geodetic applications, this model still is not accurate enough and not necessarily coincides with mean sea level at the reference tide gauge. Furthermore, some areas of the globe lack data coverage necessary for this model and it is limited by the truncation of the spherical harmonics expansion series. This truncation is expected to introduce errors in the high frequency geoid signal. Due to the high terrain topography and tectonic activities, in the western region of the Saudi Arabia, high frequency components of the geoid are expected.

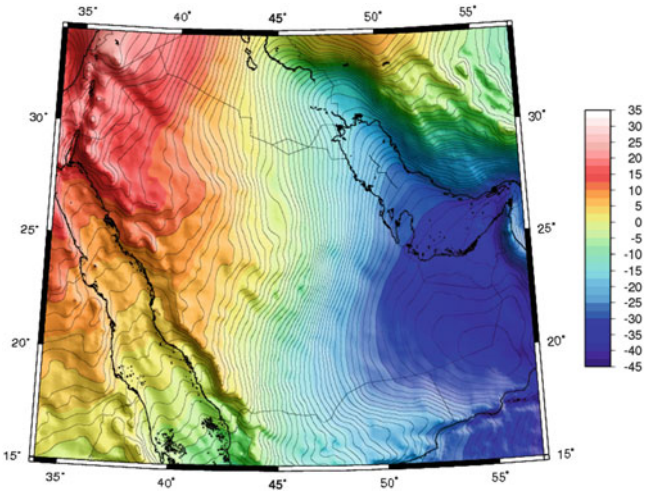

Fig. 1 EGM2008 geoid model (Pavlis et al. 2012) over the Kingdom, in meter

This model aimed to provide a geoid accuracy of 15 cm RMS worldwide. Pavlis et al. (2012) have reported RMS of 10 cm for geoid heights when globally tested with GPS/Levelling geoid heights. Figure 1 shows the EGM2008 geoid within and around the Kingdom, by using coefficients complete to degree 2190 and order 2159. It can be seen that the EGM2008 geoid estimates are higher particularly over mountainous area in the west of the Arabian Peninsula.

Today's state-of-the-art satellite-only global gravity field models are based on GRACE and/or GOCE measurements. GRACE-only models for the static gravity field, such as ITG-GRACE2010s, are solved up to spherical harmonic degree and order 180, whereas GOCE-only or GOCE/GRACE models, e.g. GOCO03S, typically have spherical harmonic coefficients up to degree and order 250 (Mayer-Gürr et al. 2010, 2012). Whereas GRACE is more sensitive to the long wavelengths of the gravity field, GOCE is more sensitive to the medium wavelengths and complements terrestrial gravity data especially in regions where these data are poor or unavailable.

3 Regional Geoid Models for Saudi Arabia

Two recent geoid models for Saudi Arabia exist. The first model is known as the KSA geoid (Ngiboglu 2008) and was computed by the General Directorate of Survey (GDS). The second model is known as the MOMRA geoid 2009 (Alrajhi et al. 2009) and was established by the Ministry of Municipality and Rural Affairs (MOMRA).

The *KSA geoid* is based on GPS/Levelling, i.e. using Global Positioning System (GPS) observations along with levelling Bench Marks (BM). About 5898 Bench Marks (BM) of the Arabian-American Oil Company (ARAMCO) network, distributed over the whole country, were observed with GPS. The levelling network is dense in the east while in other regions, especially the western parts of the country, it is very sparse. The vertical datum is based on the mean sea level (MSL) at the RasTanura Tidal BM at the east coast of Saudi Arabia (i.e. in the Arabian Gulf). The vertical datum of GDS was based on an old version of Saudi ARAMCO Vertical Datum SAVD 71 at Ain Al Abd-1970. ARAMCO BM network is based on two geodetic datums: WGS84 and SAVD78. The ellipsoidal heights and the vertical datum are corrected for datum differences by computing transformation parameters between the ARAMCO (WGS84 and SAVD78) and GDS datums (ITRF2000 and SAVD71). GDS vertical datum (SAVD71) is based on tide gauge observations at the Jeddah tide gauge, which not necessarily coincides with the global geoid model EGM2008. The global EGM2008 model was adopted and corrections have been applied: (1) long-wavelength biases to mean sea level at the Jeddah tide gauge BM need to be applied and (2) high frequency biases due to truncation of the spherical harmonics expansions in the global model have to be removed. The mathematical model representing these errors can be written as:

$$N_{BG} + r = N_{EGM} + b + c \tag{2}$$

where N_{BG} is the observed geoid height at a BM/GPS station, r is the random observation error in the observed geoid height, N_{EGM} is the EGM2008 geoid height at the station, b is the long-wavelength bias in EGM2008 geoid (commission error), and c is the high frequency correction to EGM2008 at the station (omission error).

Least squares collocation (LSC) was used to model the high frequency correction part of the model. LSC may be applied assuming that the Earth's gravity field, including geoid undulations, gravity anomalies, and the deflections of the vertical can be modeled as a stationary, isotropic stochastic process (Moritz 1980; Torge and Denker 1991). The long wavelength correction was modeled as a shift of the center of the EGM2008 geoid to the center of ARAMCO local datum SAVD71. Least squares techniques have been used to estimate the shift parameters. Then collocation filtering was used to separate signal from noise in the local geoid observations. Furthermore, LSC has been applied to estimate the geoid heights for the whole country. The procedures were applied in an iterative manner.

The *MOMRA geoid* facilitates surveying applications by making orthometric heights available. MOMRA has produced its geoid for large scale maps for about 220 cities in Saudi Arabia. Ellipsoidal heights of about 861 BMs, of

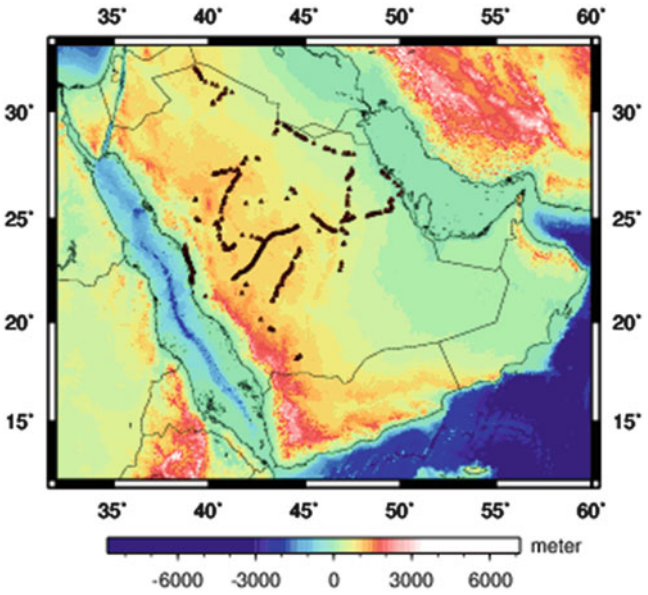

Fig. 2 Location of the GPS/BM stations used in the test campaign (T campaign). The topography and bathymetry are shown as well

first order vertical control network established in 1970s by spirit levelling based on tidal gauges along the Red Sea and Arabian Gulf, were observed by GPS in the ITRF2000 frame, GRS80 ellipsoid (Moritz 1992). The global geoid model EGM2008 was adopted as reference surface to determine the long wavelength effect of the geoid surface. Residuals are interpolated using the Kriging statistical approach (Davis 1986). The nominal RMS of the MOMRA geoid was ±10 cm at the observed GPS/BMs and ±20 cm at random locations respectively (Alrajhi et al. 2009). Details of the computation of this model are not available for this investigation.

4 Analysis of GPS/Levelling, KSA, MOMRA, and EGM2008 Geoid Models over Saudi Arabia

Validation of geoid models over the continents can be performed by GPS techniques, by which the orthometric height is algebraically subtracted from the derived GPS ellipsoidal height (e.g. Yun 1999; Featherstone 2001). A GPS/Levelling test campaign (T campaign) was made by GDS in 2009 observing about 391 BMs stations using geodetic GPS receivers. The GPS/Levelling stations used in the T campaign were discrete and located loop-wise along main roads as shown in Fig. 2. The orthometric heights of these BM stations are based on SAVD1 vertical datum and ITRF2000 (Altamimi et al. 2002) reference frame, whereas the GPS ellipsoidal heights are based on WGS84 and ITRF2005 (Altamimi et al. 2007). Since no more details are available

Table 1 Computed statistics for geoid differences at 391 GPS/Levelling points (T campaign). Units: m

Residual (dN)	Max.	Min.	Mean	S.D.	Range
KSA-GPS/BM	−2.45	2.86	−0.11	0.54	5.31
MOMRA-GPS/BM	−7.18	11.71	−0.44	1.54	18.89
EGM2008-GPS/BM	−3.15	2.08	−0.58	0.53	5.23
EGM2008-MOMRA	−0.28	3.08	0.57	0.67	3.36
EGM2008-KSA	−1.60	1.28	−0.47	0.38	2.88
KSA-MOMRA	−2.03	3.28	0.46	0.72	5.31

to describe all data sets, corrections on height between these datums were neglected assuming very small differences.

In order to validate the KSA, MOMRA, EGM2008 geoids over Saudi Arabia, geoid heights (N) at each T campaign station were computed and used for analysis of these geoid models. In addition, GPS/Levelling geoid heights have been computed according to Eq. (1) from observed ellipsoidal and orthometric heights at the T campaign stations. Residuals ΔN of these four data sets were computed at each T campaign station. Statistics (maximum, minimum, mean, standard deviation, and range) for the residuals between the KSA, MOMRA, EGM2008, and GPS/Levelling (T Campaign) geoids are shown in Table 1.

The frequency distribution of the residual geoidal heights is shown in Fig. 4. It shows that the ΔN of KSA geoid and T Campaign are ranging from −2.45 m to 2.86 m with large standard deviation of 0.54 m. The large differences of KSA geoid may be due to the accuracy of the geoid or the observed geoid undulations. Residuals of MOMRA geoid 2009 and the T campaign are very high, ranging from −7.18 m to 11.71 m with large standard deviation of 1.54 m. The large statistics may be caused by the kriging algorithm used in residual geoid estimation and the number and distribution of the BMs used in MOMRA geoid computation.

Residuals ΔN of EGM2008 geoid and T Campaign reveal that the EGM2008 geoid seems to be biased with −0.58 m and scattered relative to test points. This bias may be caused by the SAD71 vertical datum definition of normal orthometric heights at Jeddah MSL on the Red Sea coast. This difference has been investigated and it has been discovered that at one tide gauge station at the coast of the Arabian Gulf, the MSL is by 0.79 m lower than the Jeddah datum (communication and discussion with Prof. S.M. Nagiboglu). The standard deviation of the residuals of the EGM2008 and GPS/Levelling points is 45 cm.

Analysis of differences between the KSA and MOMRA geoids revealed that the two geoids seem to be inconsistent and biased, with mean residuals of 46 cm, and are highly scattered with a standard deviation of 72 cm. Figure 3 shows that the frequency distributions of the differences with respect to the MOMRA geoid are not normally distributed, but rather have a bimodal distribution. Comparison of the standard deviation of the residuals of the four data sets revealed that when the MOMRA geoid is involved, the standard deviation is always larger than for any of the other residuals. One may conclude that the MOMRA geoid is not the best one to be applied in KSA. Obviously, the KSA geoid gives the best fit to the GPS/Levelling data compared with the other geoid models, where it has to be noted that the KSA geoid was also based on GPS/Levelling data at the same points from an earlier measurement campaign.

It can be seen from Fig. 3, that the frequency distribution of the residuals between GPS/Levelling and both the KSA and the EGM2008 geoid are almost normally distributed with similar standard deviations. It can be concluded that the KSA and EGM geoids have similar geoid details over the test area. Although these two geoids are biased with about half a meter, they are consistent with each other. In general, frequency distributions of EGM2008 and KSA geoid are similar and almost normally distributed, whereas the frequency distribution of the residuals of MOMRA geoid is not normally distributed.

5 Correlation Analysis

In order to evaluate these different geoids over KSA, correlation analysis may be used. Assuming that the residuals obtained by differencing two geoid data sets are normally distributed, linear correlation coefficients between a pair of vector data can be estimated. Because of the bimodal distribution of the residuals with respect to the MOMRA geoid, these correlation coefficients need to be interpreted with care. Correlation coefficients were computed using the following formula:

$$r = \frac{\sum_m \sum_n \left(A_{mn} - \overline{A}\right)\left(B_{nm} - \overline{B}\right)}{\sqrt{\sum_m \sum_n \left(A_{mn} - \overline{A}\right)^2 \left(\sum_m \sum_n \left(B_{nm} - \overline{B}\right)\right)^2}} \quad (3)$$

where A_{mn} and B_{nm} are geoid estimates matrices, and $\overline{A}$ and $\overline{B}$ are mean of the corresponding A_{mn} and B_{nm} respectively (Mathworks 2004). Table 2, shows the correlation coefficients between different data sets obtained by removing orthometric heights of GPS/Levelling and EGM2008 geoids from KSA and MOMRA geoids. It can be seen that the highest correlation coefficients is 0.96, between GPS/Levelling and KSA geoids, while the MOMRA geoid gave 0.91. Removing MOMRA geoid from both KSA and EGM2008 indicates a high negative correlation coefficient (−0.85).

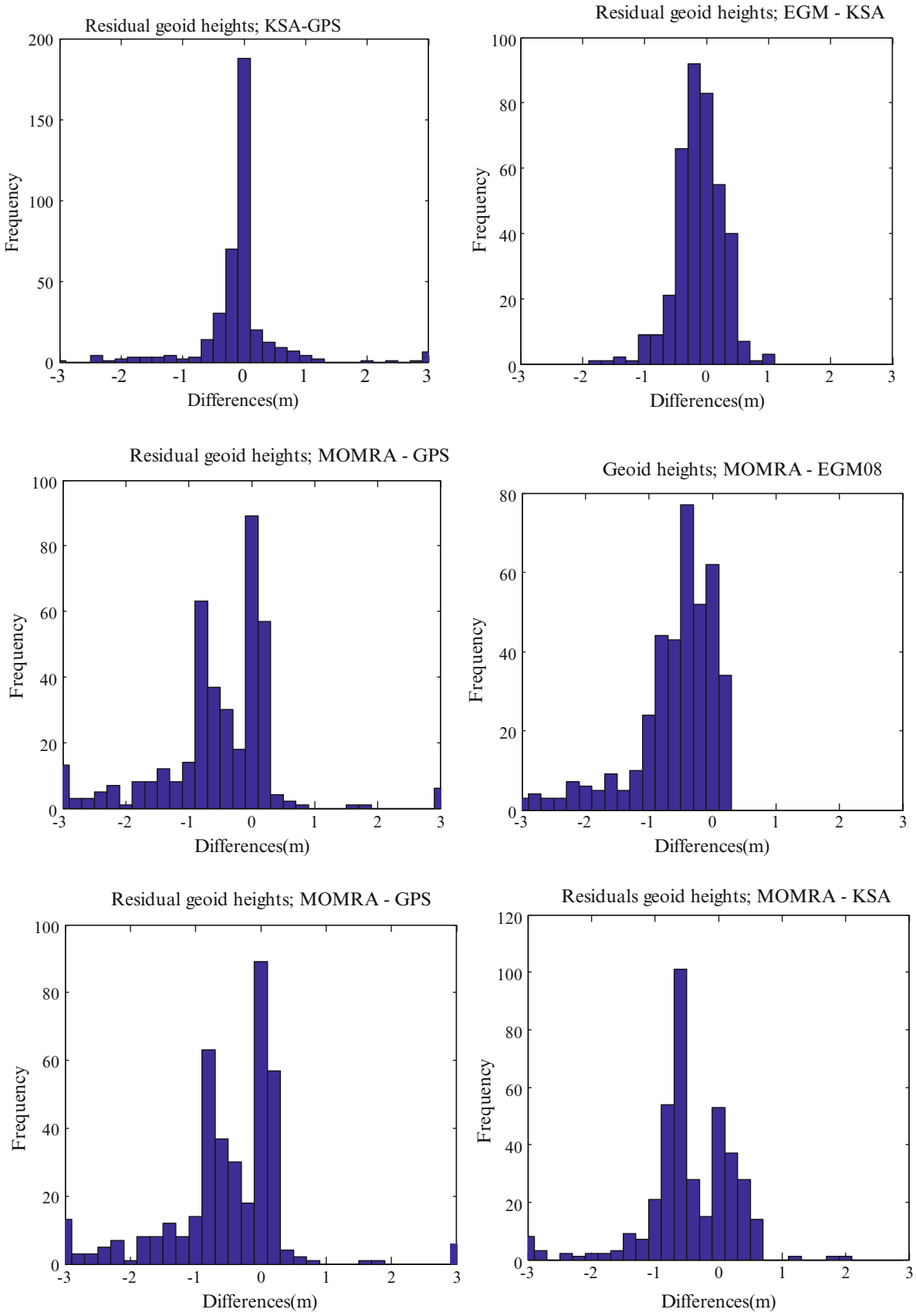

Fig. 3 Frequency distribution histograms of geoid height residuals *Left column*: removing GPS/Levelling data from KSA, EGM2008, and MOMRA respectively. *Right column*: residuals between KSA, EGM2008 and MOMRA 2009 geoids. Values are in meter

Table 2 Correlation coefficients between different residual data of geoids

Residuals	KSA-GPS/BM	EGM2008-GPS/BM	MOMRA-GPS/BM	EGM2008-KSA	EGM2008-MOMRA	KSA-MOMRA
KSA-GPS	1					
EGM2008-GPS/BM	0.96	1				
MOMRA-GPS/BM	0.88	0.91	1			
EGM2008-KSA	0.16	−0.11	−0.04	1		
EGM2008-MOMRA	0.04	0.001	0.43	0.14	1	
KSA-MOMRA	0.06	−0.06	−0.42	0.40	−0.85	1

6 Validation Using a Combined GRACE/GOCE Satellite Model

With the advances in satellite gravimetry geoid models derived from those missions are a new tool for validation and improvement of regional geoid models. By such an approach, the space based observations of CHAMP, GRACE, and GOCE satellites are implemented in conjunction with in situ (ground) observations.

The best combination of GRACE and GOCE is the GOCO03S model. It was taken up to degree 180 and complemented with EGM2008 from degree 181 to 2190 in order to reduce the omission error. Both models are converted to the tide free system in order to be consistent with the GPS/Levelling geoid heights. After conversion to a common reference system (WGS84), differences of model and GPS/Levelling geoid heights have been computed for the study area, as shown in Fig. 4 (Gruber et al. 2011). Root Mean Squares (RMS) of differences for the complete data set have been computed for truncation degrees in steps of 10 from 10 to 250. The result shows that the regional geoids for Saudi Arabia can be improved using GOCE satellite data for the study area compared to EGM2008. This means that EGM2008 obviously performs not as good as the GRACE/GOCE models plus the residual geoid from EGM2008. In order to correctly interpret the differences it would be required to identify the individual error contributions. As it was shown in other studies (e.g. Gruber et al. 2011) the GOCE commission error up to degree 180 is at a level of 6–8 cm. In addition, one should be aware that by combining coefficients from different global models additional inconsistencies could be introduced. These inconsistencies are estimated to be far below the error level of the other observations involved. It is also a fair assumption that the GPS ellipsoidal heights are at least as good as the GOCE geoid. This implies that the largest error stems from the national levelling network. From the differences shown in Fig. 4 one can estimate the levelling error at a level of several decimeters up to half a meter leading to RMS values of the differences between 53 and 54 cm.

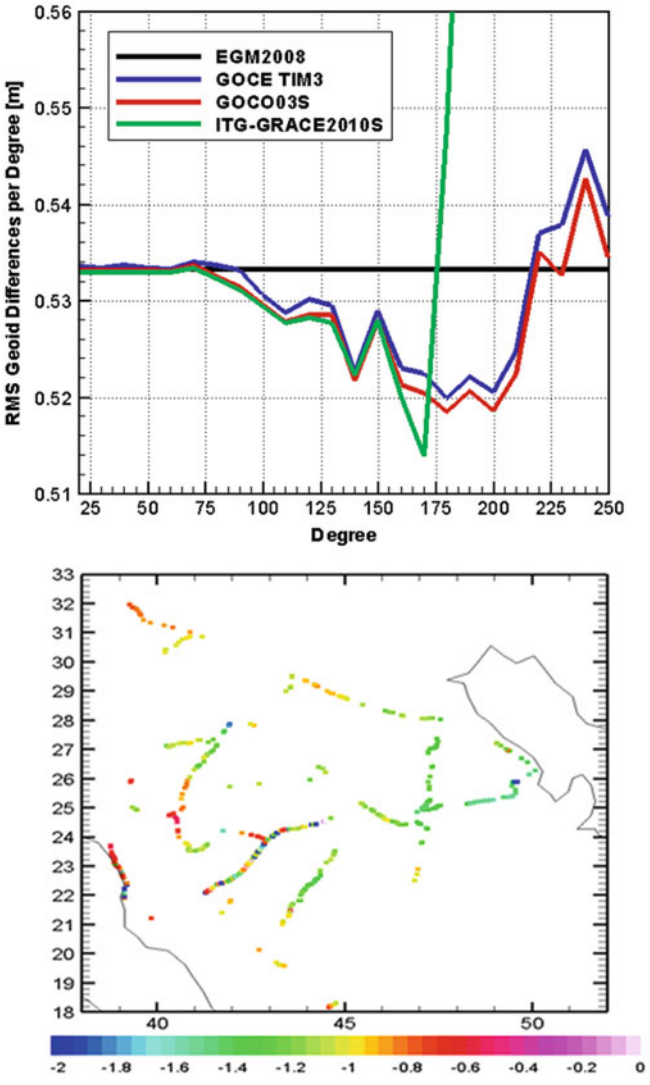

Fig. 4 Differences of GPS Levelling geoid and extended GRACE/GOCE model (GOCO03) in meter (*bottom*) and RMS of differences per truncation degree for a pure GRACE (ITG-GRACE2010), a pure GOCE (GOCE TIM3), a GRACE/GOCE combined model (GOCO03S) and for EGM2008 (*top*)

Conclusions

Geoid models in Saudi Arabia have been evaluated based on comparison with GPS/Levelling orthometric heights. Large residuals of MOMRA and GPS/Levelling geoids may be due to the kriging algorithms used in residual geoid estimation. The global geoid model, EGM2008, has shown a high bias of −0.58 m and scattered relative to test points. This could be due to the different datum definition of normal orthometric heights at Jeddah MSL. Residuals of KSA and MOMRA geoids revealed that the two geoids seem to be inconsistent and both biased, highly scattered, and not normally distributed. Comparison of the standard deviations of the residuals of the four data sets revealed that these are always large when the MOMRA geoid is involved. One may conclude that the MOMRA geoid may not be the best one to apply in Saudi Arabia. The KSA and EGM2008 geoids give the best fit to the GPS/Levelling data.

Residuals of both KSA and EGM2008 geoids are biased with about half a meter, coincident with each other, and have similar geoid details over the test area. In general, frequency distributions of EGM2008 and KSA geoid are similar and almost normally distributed, whereas the frequency distribution of the residuals of MOMRA geoid is not normally distributed. This may result in datum shift and systematic errors in MOMRA geoid. MOMRA-GPS and MOMRA-KSA residuals are almost the same. This emphasizes the conclusion that KSA and GPS geoids are consistent with each other.

Correlation analysis has shown that the highest correlation coefficient is 0.96, obtained between GPS/Levelling and KSA geoids. The MOMRA geoid gave a relatively high correlation, 0.91, but lower than one obtained from KSA. This indicates that both geoids are in general agreement with GPS/Levelling and EGM2008 geoids. The results obtained from the comparison of the GPS/Levelling geoid heights with those from the combined GRACE/GOCE model (GOCO03S) are promising. It can be expected that by using such a model for future regional geoid computations further improvements for the KSA geoid can be expected.

Acknowledgements The authors acknowledge King Abdulaziz City for Science and Technology, KACST, for the support to publish this paper. Professor S.M. Naqiboglu and Dr. M.E. Ayhan are acknowledged for their suggestions and computation and analyses. Also, General Directorate of Survey (GDS), Ministry of Municipality and Rural Affairs (MOMRA), and ARAMCO are acknowledged for providing the data and their cooperation.

References

Alrajhi M, Yanar R, Hawarey M, Alomar A (2009) Refinement of Geoid in Saudi Arabia using GPS/Benchmark data with EGM1996 and EGM2008. Geophysical Research Abstracts, vol 11, EGU2009-4385, European Geosciences Union. Presented at EGU general assembly 2009, Vienna, Austria, April 2009

Altamimi Z, Sillard P, Boucher C (2002) ITRF2000: a new release of the international terrestrial reference frame for earth science applications. J Geophys Res 107(B10):2214. doi:10.1029/2001JB000561

Altamimi Z, Collilieux X, Legrand J, Garayt B, Boucher C (2007) ITRF2005: a new release of the international terrestrial reference frame based on time series of station positions and Earth Orientation Parameters. J Geophys Res 112, B09401. doi:10.1029/2007JB004949

Bouman J, Fiorot S, Fuchs M, Gruber T, Schrama E, Tscherning CC, Veicherts M, Visser P (2011) GOCE gravitational gradients along the orbit. J Geod 85:791–805. doi:10.1007/s00190-011-0464-0

Davis JC (1986) Statistics and data analysis in geology. John Wiley, New York, NY

Featherstone WE (2001) Absolute and relative testing of gravimetric geoid models using Global Positioning System and orthometric height data. Comput Geosci 27:807–814

Gruber Th, Visser PN, Ackermann Ch, Hosse M (2011) Validation of GOCE gravity field models by means of orbit residuals and geoid comparisons. J Geod 85:845–860. doi:10.1007ls00190-011-0486-7

Heiskanen WA, Moritz H (1967) Physical geodesy. W. H. Freeman, San Francisco, CA

Mathworks (2004) MATLAB: the language of technical computing, version 7.0. Mathworks, Inc., 3 Apple Hill Drive, Natick, MA, 01760-2098, USA

Mayer-Gürr T, Kurtenbach E, Eicker A (2010) ITG-Grace2010. http://www.igg.uni-bonn.de/apmg/index.php?id=itg-grace2010

Mayer-Gürr T et al (2012) The new combined satellite only model GOCO03s. Abstract submitted to GGHS2012, Venice (Poster)

Moritz H (1992) Geodetic reference system 1980. Bull Geod 62(2):187–192

Moritz H (1980) Advanced physical geodesy. Abacus, Kent, 500 pp

Ngiboglu SM (2008) Final report on the determination of the geoid for the Kingdom of Saudi Arabia, General Directorate of Military Survey, GDMS, 2008, Riyadh, Saudi Arabia, Internal Document

Pavlis NK, Holmes SA, Kenyon SC, Factor JK (2012) The development and evaluation of the Earth Gravitational Model 2008 (EGM2008). J Geophys Res 117:38. doi:10.1029/2011JB008916

Reigber Ch, Balmino G, Schwintzer P, Biancale R, Bode A, Lemoine J-M, Koenig R, Loyer S, Neumayer H, Marty J-C, Barthelmes F, Perosanz F, Zhu SY (2002) A high quality global gravity field model from CHAMP GPS tracking data and accelerometry (EIGEN-1S). Geophys Res Lett 29(14). doi:10.1029/2002GL015064

Rummel R, Gruber Th, Yi W, Albertella A (2012) GOCE: its principles and science. In: Schuh H, Böhm J, Nilsson T, Capitaine N (eds) Proceedings of the Journées 2011 "Systèmes de référence spatio-temporels". Vienna University of Technology

Tapley BD, Bettadpur S, Watkins M, Reigber C (2004) The gravity recovery and climate experiment: mission overview and early results. Geophys Res Lett 31(9), L09607. doi:10.1029/2004GL019920

Torge W, Denker H (1991) Possible improvements of the existing European geoid. In: Rapp R, Sanso F (eds) Determination of the geoid. International association of geodesy symposia, no 106. Springer, New York, NYx

Yun HS (1999) Precision geoid determination by spherical FFT in and around the Korean peninsula. Earth Planets Space 51:13–18

Part V

Establishment and Unification of Vertical Reference Systems

W_0 Estimates in the Frame of the GGOS Working Group on Vertical Datum Standardisation

L. Sánchez, N. Dayoub, R. Čunderlík, Z. Minarechová, K. Mikula, V. Vatrt, M. Vojtíšková, and Z. Šíma

Abstract

During the 2011 IUGG General Assembly, GGOS, the IAG Commissions 1 (Reference Frames) and 2 (Gravity Field) and the IGFS established a joint working group devoted to the *Vertical Datum Standardisation*. This working group supports the activities of GGOS Theme 1 *Unified Height System;* in particular, to recommend a reliable geopotential value W_0 to be introduced as the conventional reference level for the realisation of the GGOS Vertical Reference System. At present, the most commonly accepted W_0 value corresponds to the best estimate available in 2004; however, this value presents discrepancies of about 2 m^2 s^{-2} with respect to recent computations based on the latest Earth's surface and gravity field models. According to this, as a first approach, four different teams working on the computation of a global W_0 value were brought together in order to compare methodologies and models, and to establish the reliability of the individual computations. Results of this comparison show that the four individual estimates present a maximum discrepancy of about 0.5 m^2 s^{-2}. They also confirm that the W_0 value declared as the best estimate in 2004 corresponds to an equipotential surface located about 17 cm beneath the sea surface scanned by satellite altimetry, while the potential value U_0 of the GRS80 ellipsoid realises an equipotential surface located about 67 cm lower. In this context, the need to provide a new better estimate of W_0 is evident.

1 Introduction

The *Global Geodetic Observing System* (GGOS) (Plag and Pearlman 2009) of the *International Association of Geodesy* (IAG) established during its Planning Meeting 2010 (February 1–3, Miami/Florida, USA) the GGOS Theme 1: *Unified Height System*. The main purpose is to provide a global gravity field-related vertical reference system that (1) supports a highly-precise (at cm-level) combination of physical and geometric heights worldwide, (2) allows the unification of all existing local height datums, and (3) guarantees vertical coordinates with global consistency (the same accuracy everywhere) and long-term stability (the same order of accuracy at any time) (Kutterer et al. 2012). Activities to be undertaken under the umbrella of the GGOS Theme 1 are understood as the continuation of the work started by the 2007–2011 *IAG Inter-Commission Project 1.2 Vertical*

L. Sánchez (✉)
Deutsches Geodätisches Forschungsinstitut (DGFI), Alfons-Goppel-Str. 11, 80539 Munich, Germany
e-mail: sanchez@dgfi.badw.de

N. Dayoub
Faculty of Civil Engineering, Department of Topography, Tishreen University, P. O. Box 2230, Latakia, Syria

R. Čunderlík • Z. Minarechová • K. Mikula
Faculty of Civil Engineering, Department of Mathematics and Descriptive Geometry, Slovak University of Technology in Bratislava, Bratislava, Slovakia

V. Vatrt • M. Vojtíšková
Geographic Service of the Czech Armed Forces, Military Geographic and Hydrometeorologic Office, Dobruška, Czech Republic

Z. Šíma
Astronomical Institute, Academy of Sciences, Prague, Czech Republic

U. Marti (ed.), *Gravity, Geoid and Height Systems*, International Association of Geodesy Symposia 141,
DOI 10.1007/978-3-319-10837-7_26,

Reference Frames (IAG ICP1.2, Ihde 2007). The main result of the IAG ICP1.2 is the document *Conventions for the Definition and Realisation of a Conventional Vertical Reference System*—CVRS (Ihde et al. 2007). These conventions describe the fundamentals to be taken into consideration for the establishment of a vertical reference system fulfilling the requirements outlined by GGOS. According to CVRS and Kutterer et al. (2012), the global vertical datum shall correspond to a level surface of the Earth's gravity field with a given potential value $W_0 = const.$ and, consequently, a formal recommendation about the W_0 value to be adopted is a main objective of GGOS Theme 1 (cf. *GGOS 2020 Action Plans 2011–2015*, unpublished). The agreed value of W_0 must also be promoted as a defining parameter for a new reference ellipsoid and as a reference value for the estimation of the constant L_G, which is necessary for the transformation between Terrestrial Time (TT) and Geocentric Coordinate Time (GCT) (Petit and Luzum 2010).

It is well-known that any W_0 value can be arbitrarily appointed for the determination of vertical coordinates (e.g., Heck and Rummel 1990; Heck 2004). However, the establishment of a vertical reference system with global consistency demands that the selected W_0 value be realisable with high-precision at any time and at any place around the world. With this, the real problem is not the selection of the value W_0, but its realisation, i.e., the estimation of the position and geometry of the equipotential surface that W_0 is defining, namely the geoid. To get correspondence between W_0 and the global geoid, it is necessary that both be estimated from the same geodetic observations and that they be consistent with other defining parameters of geometric and physical models of the Earth. Consequently, like any reference system, W_0 should be based on some adopted conventions, which guarantee its uniqueness, reliability and repeatability. Otherwise there would be as many W_0 reference values (i.e., global zero-height surfaces) as there are groups evaluating it.

The responsibility of outlining the necessary standards and conventions for the determination and realisation of a reference W_0 value was given to the *Working Group on Vertical Datum Standardisation*. It was established for a period of 4 years (2011–2015) as a common initiative of GGOS Theme 1, IAG Commissions 1 (*Reference Frames*) and 2 (*Gravity Field*), and the *International Gravity Field Service* (IGFS). According to IAG nomenclature (Drewes et al. 2012), it is called *Joint Working Group JWG 0.1.1*. The first activities faced by JWG 0.1.1 concentrate on (1) making an inventory about the published W_0 computations to identify methodologies, conventions, standards, and models presently applied (cf. Sánchez 2012) and (2) bringing together the different groups working on the determination of a global W_0 in order to coordinate these individual initiatives for a unified computation. Once these aims are achieved, the next steps relate to the preparation of a proposal for a formal IAG/GGOS convention about W_0 and to provide a roadmap for the usage of W_0 in the unification (linkage) of the local height systems into the global datum. This paper discusses the first W_0 estimations performed in the frame of this JWG 0.1.1.

2 Empirical Determination of W_0

The empirical estimation of W_0 is strongly related to the concept of "geoid". The most accepted definition of this is understood to be the equipotential surface coinciding, in the sense of the least squares, with the mean sea surface at rest worldwide (Gauss 1876, p. 32). Since this "ideal" cannot be satisfied, the realisation of this definition has been refined over time depending on the geodetic observations and analysis strategies available for geoid modelling (e.g., Mather 1978; Heck and Rummel 1990; Heck 2004). In particular, Mather (1978), based on the availability of satellite altimetry techniques and the possibility to estimate the dynamic ocean topography (*DOT*), indicates that the geoid represents that level surface with respect to the average of the *DOT* is zero when sampled over all oceans (S), i.e.,

$$\int_S DOT^2 \mathrm{d}s \;=\; \min \tag{1}$$

The *DOT* at any point $j(\varphi,\lambda,h)$ located at the sea surface can be written as:

$$DOT_j \;=\; \left[h_S - r_j - N_j\right] = \frac{W_0 \;-\; W_j}{\gamma_j} \tag{2}$$

Here, (φ,λ,h) are the ellipsoidal coordinates latitude, longitude and height of j, h_S is the height of the satellite with respect to a reference ellipsoid; r_j is the range measurement representing the distance between the satellite and j; and N_j, γ_j and W_j denote geoid undulation, normal gravity and gravity potential at j. To satisfy Eq. (2) it is assumed that γ_j is computed from the same ellipsoid to which h_S and N_j are referred. In this way, for consistency, it is expected that the values $N_j(\varphi,\lambda)$, defined geometrically, describe the equipotential surface defined by W_0 (cf. Sánchez 2012). According to this, the minimum condition in Eq. (1) can be re-written as (cf. Sacerdorte and Sansò 2001):

$$\frac{\partial}{\partial W_0}\int_S DOT^2\,\mathrm{d}s \;=\; \frac{\partial}{\partial W_0}\int_S\left[\frac{W_0-W_j}{\gamma_j}\right]^2\mathrm{d}s \;=\; 0\;;$$
$$W_0 \;=\; \frac{\int_S \frac{W_j}{\gamma_j^2}\,\mathrm{d}s}{\int_S \frac{1}{\gamma_j^2}\,\mathrm{d}s} \tag{3}$$

Equation (3) is, in general, the basic approach most applied during the last two decades for the empirical estimation of a global W_0 value (e.g., Burša et al. 2002; Sánchez 2007; Dayoub et al. 2012). The geometry of the sea surface is assumed to be described by the coordinates contained in a mean sea surface model (MSS) and the potential values W_j are derived from a global gravitational model (GGM) expressed normally as a spherical harmonic expansion (e.g., Heiskanen and Moritz 1967, p. 57).

Dayoub et al. (2012) propose the reduction of the sea surface heights by an oceanographic mean dynamic topography model (MDT) in order to get a level surface closer to the geoid, i.e.,

$$N_j\,(\varphi,\lambda) \;=\; h_j\,(\varphi,\lambda) - MDT_j\,(\varphi,\lambda) \tag{4}$$

Basically, *DOT* and *MDT* are representing the same, but, in this context, the first one is derived from satellite altimetry in combination with a gravimetric geoid, and the second one is obtained from ocean circulation analysis. Hence, the MDT model is independent of pre-given gravimetric geoid models. Dayoub et al. (2012) base their computations on the ECCO2 model (Menemenlis et al. 2008).

Another approach applied presently for the estimation of a global W_0 is the solution of the geodetic boundary value problem. In this case, an additional unknown ($\Delta W_0 = W_0 - U_0$) representing the difference between the Earth's gravity potential W_0 and the normal potential U_0 introduced for the linearization of the boundary conditions is included in the observation equations (e.g., Sacerdote and Sansò 2004), Heck and Rummel 1990). As U_0 is known, the determination of ΔW_0 allows the estimation of W_0. In general, the observables building the boundary conditions (i.e., geopotential numbers and physical heights used for the estimation of gravity anomalies) refer to different vertical datums, and therefore, there shall be as many ΔW_0 unknowns as existing i datums: ($\Delta W_0^i = W_0^i - U_0$) (e.g., Rummel and Teunissen 1988; Heck and Rummel 1990; Sacerdorte and Sansò 2004). According to this, the geodetic boundary value problem in linear and spherical approximation can be formulated as:

$$\nabla^2 T \;=\; 0, \quad \text{outside } \Sigma \tag{5a}$$

$$-\frac{\partial T}{\partial r} - \frac{2}{R}T \;=\; g_j - \frac{2}{R}\Delta W_0^i, \;\text{ on } \Sigma \tag{5b}$$

$$T \to 0, \;\text{ at } \infty \tag{5c}$$

Σ is the boundary surface, T is the anomalous potential, and function g_j represents the observational data included in the boundary conditions. The multiple vertical datum dependence in (5b) can be avoided if the boundary conditions are given as a function of only one kind of data ($j=1$), depending on only one vertical datum ($i=1$). For instance, taking into consideration only ocean areas and by applying exclusively satellite altimetry data and satellite-only global gravity models, there will be only one ΔW_0^i ($i=1$) and the W_0 obtained can be thus conventionally assumed as the global reference level (Sánchez 2008). In this case, g_j in Eq. (5b) corresponds to the gravity disturbance at the sea surface:

$$\delta g_P \;=\; g_P \;-\; \gamma_P \tag{6}$$

Some empirical evaluations of this approach utilize as input data sea surface heights of a MSS model (assumed as the geometrical representation of the boundary surface Σ) and gravity disturbances derived from a GGM in combination with the normal gravity of the GRS80 ellipsoid (e.g. Sánchez 2008; Čunderlík and Mikula 2009). In particular, Čunderlík and Mikula (2009) extend the computations to land areas, where the geometry of the boundary surface is represented by means of an SRTM model (specifically the SRTM_PLUS V1.0, Becker and Sandwel 2003). Nevertheless, ΔW_0 takes different values depending on the continent, and consequently, authors recommend adoption of a value computed over the ocean areas only.

3 Current W_0 Estimates

At present, there are four groups working on the estimation of a global W_0 value (local estimations, i.e., based on data distributed within limited geographical areas have not been considered). The group with the largest experience, called in the following the *Prague Group*, started this kind of computations in the early 1990s (e.g., Burša et al. 1992,

1997). Then, in the first decade of the 2000s, some related computations were published by the *Munich Group* (e.g., Sánchez 2007, 2008), and the *Bratislava Group* (e.g., Čunderlík et al. 2008; Čunderlík and Mikula 2009). Finally, the most recent contribution to the global W_0 estimation was produced by the *Latakia(/Newcastle) Group* (e.g., Dayoub 2010; Dayoub et al. 2012).

The four groups apply in general different methodologies and different input models of the sea surface and the Earth's gravity field. The Prague Group (e.g., Burša et al. 2007a) and the Latakia Group (e.g., Dayoub et al. 2012) solve Eq. (3) using an equal-area weighting function for the estimation of the averaged potential value. The Bratislava Group (e.g., Čunderlík and Mikula 2009) and the Munich Group (e.g., Sánchez 2008) prefer the solution of the geodetic boundary value problem (Eq. 5). The computations of the Bratislava Group are based on the boundary element method, while the computations of the Munich Group are based on an analytical solution of the boundary value problem. Furthermore, the Prague Group uses its own sea surface models, derived from TOPEX/Poseidon and Jason 1 data (e.g., Burša et al. 1998, 2001, 2002, 2007a), while the other groups (e.g., Čunderlík et al. 2008; Čunderlík and Mikula 2009; Sánchez 2007, 2009; Dayoub et al. 2012) also apply models already published by other specialists, such as CLS01 (Hernandes and Schaeffer 2001), KMS04 (Andersen et al. 2006) or DNSC08 (Andersen and Knudsen 2009). Further analyses (e.g., Burša et al. 2007a; Sánchez 2007; Dayoub et al. 2012) are also devoted to estimating time variations of W_0 (by taking into consideration yearly sea surface models) and to identifying the dependence of the W_0 estimation on the GGM spectral resolution, the MSS spatial resolution, and the MSS latitude coverage. As expected, this mixture of strategies, MSS and GGM models produces different W_0 values, which are very similar (Fig. 1), but with discrepancies larger than the expected realisation accuracy, i.e., >1 m^2 s^{-2} ($\sim$10 cm).

At present, the most commonly accepted W_0 value is that included in the IERS Conventions ($W_0 = 62{,}636{,}856.0 \pm 0.5$ m^2 s^{-2}, Petit and Luzum 2010, Table 1.1). The objective there is not to provide a vertical reference level but to explain the value assigned to the constant $L_G (= W_0/c^2)$ (Resolution B1.9 of the XXIV General Assembly of the International Astronomical Union, 2000). This W_0 value was recommended by Groten (2004) as the "best estimate" available at that time and its computation is explained by Burša et al. (1999).

Before this kind of computations could be performed, the procedure to obtain a global W_0 value was the determination of a reference ellipsoid and to assume $W_0 = U_0$ by definition. U_0 corresponds to the normal potential at the surface of the reference (biaxial geocentric) ellipsoid and can be computed from the ellipsoid parameters, e.g., Somigliana theory (cf. Heiskanen and Moritz 1967, p. 67). Today, the GRS80 ellipsoid is used (Moritz 2000).

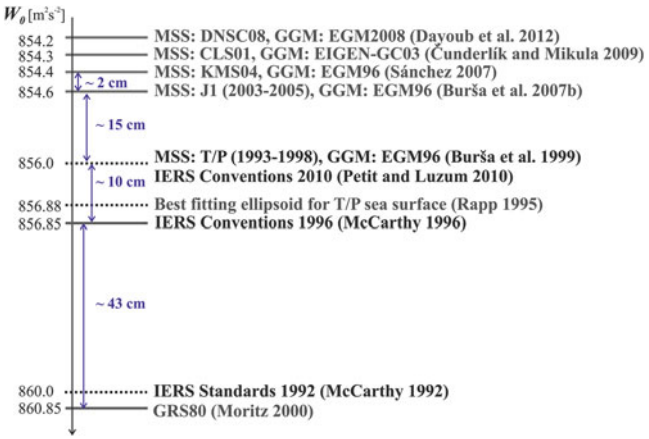

Fig. 1 Examples of W_0 values computed after the publication of the GRS80 ellipsoid. The values included in the IERS conventions are also represented. The value 62,636,000 m^2 s^{-2} must be added. Credits for GGMs applied in the different computations: EGM96 (Lemoine et al. 1998), EIGEN-GC03 (Förste et al. 2005), EGM2008 (Pavlis et al. 2012)

4 Towards a Unified W_0 Estimation

In the frame of JWG 0.1.1, it was agreed by the four groups to perform a new W_0 computation applying their own methodologies, but introducing the same input models in order to identify possible inconsistencies between the individual procedures. The MSS's selected at this first step are MSS_CNES_CLS11 (Schaeffer et al. 2012) and DTU10 (Andersen 2010). With respect to the reference time period adopted in the computation of each model, it is assumed that the corresponding sea surface heights are given at epoch 1996.0 in the CLS11 model and at epoch 2001.0 in the DTU10 model. The Latakia and Munich Groups referred the data to the mean tide system, while the Bratislava Group used the tide-free system. The Prague Group continues working with its own MSSs, but in this study, only Jason 1 data are considered. The usage of data referring to different tide systems shall not influence the obtained W_0 values, as already demonstrated by Burša et al. (1999) and Dayoub et al. (2012).

The four groups utilised the GGMs EGM2008 (Pavlis et al. 2012), EIGEN-6C (Förste et al. 2011) and GOCO03S (Mayer-Gürr et al. 2012), which were evaluated considering degree/order up to 250 and the complete expansion, i.e., EGM2008 up to 2160 and EIGEN-6C up to 1420. The GGMs were referenced to epoch 1996.0 when using the CLS11 model and to epoch 2001.0 for the DTU10 model. In addition, their coefficient $C_{2,0}$ was transformed to the same tide system in which the MSS were represented.

Results show that the higher degree coefficients of the GGM do not influence the global estimation of W_0: from $n = 10$ to $n = 20$ W_0 changes by -1.46 m^2 s^{-2}, from $n = 20$ to $n = 30$ it varies -0.52 m^2 s^{-2}. In general, when the

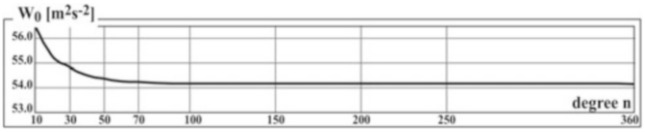

Fig. 2 W_0 dependence on the GGM's harmonic degree n (GGM: EGM2008, MSS: CLS11). Value 62,636,800 $m^2\ s^{-2}$ should be added

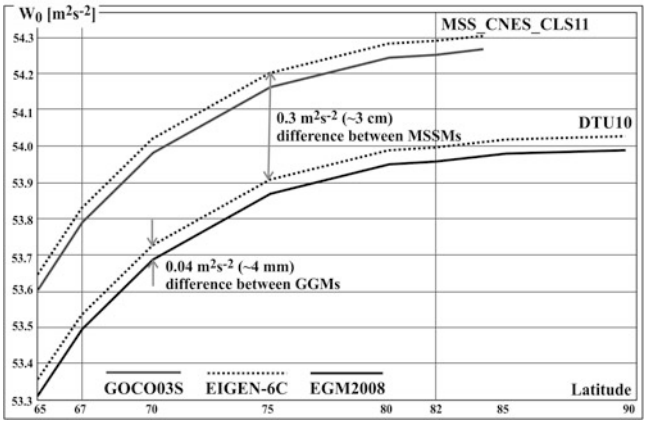

Fig. 3 W_0 dependence on the MSS latitudinal coverage. Estimates applying CLS11 and DTU10 in combination with GOCO03S, EIGEN-6C and EGM-2008. Value 62,636,800 $m^2\ s^{-2}$ should be added

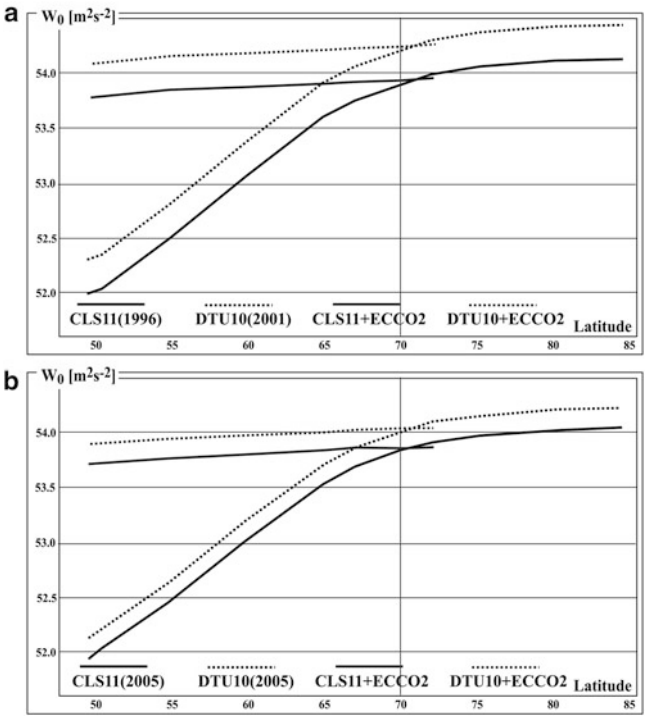

Fig. 4 W_0 estimates after adding the oceanographic mean dynamic topography model ECCO2 to the sea surfaces models CLS11 and DTU10. (**a**) CLS11 at 1996.0 and DTU10 at 2001.0. (**b**) CLS11 and DTU10 at 2005.0. Value 62,636,800 $m^2\ s^{-2}$ should be added

retained harmonic degree n grows, the difference between the corresponding W_0 values decreases. Nevertheless, up to $n = 120$ the variation of W_0 is smaller than 0.001 $m^2\ s^{-2}$. This proves that the dependence of W_0 on the harmonics $n > 120$ is negligible (Fig. 2).

The choice of GGM has insignificant effects on W_0 causing maximum differences of about 0.04 $m^2\ s^{-2}$ in the final estimates (Fig. 3). The effects of the MSS are, by contrast, larger. The comparison between the W_0 values obtained after applying CLS11 and DTU10 reveals a constant offset of 0.30 $m^2\ s^{-2}$. This can be understood as a difference of about 3 cm in the mean height of the models. In fact, after comparing both MSS models, positive differences larger than +10 cm in the Indian Ocean and the western equatorial part of the Pacific Ocean as well as negative differences less than −5 cm in the Tasman Sea and the Antarctic Ocean are found. The mean value of these discrepancies is +3.0 cm with a standard deviation ±7.3 cm. This could be attributable to differences in the processing of the altimetry data as well as in the corrections applied to each model; for more details about the computation of these models see: Andersen (2010) and Schaeffer et al. (2012). In addition, as mentioned above, it is assumed that CLS11 refers to epoch 1996.0 and DTU10 to 2001.0, so it would be necessary to refer both sets of sea surface heights to the same epoch. To investigate this issue, a common date at 2005.0 was adopted; and results from both models were shifted to this date using the value of $dW_0/dt = -0.027\ m^2\ s^{-2}\ year^{-1}$ from Dayoub et al. (2012). Results show that the offset is reduced by almost 0.2 $m^2\ s^{-2}$ (Fig. 4).

The estimate also strongly depends on the latitudinal limits covered by the MSS. If the area is increased from $\varphi = 60°$N/S to $\varphi = 80°$N/S, W_0 changes by more than 1 $m^2\ s^{-2}$ (cf. Sánchez 2007; Dayoub et al. 2012). If the same experiment is done varying the limits from $\varphi = 50°$N/S to $\varphi = 84°$N/S, it is evident that the largest influence on W_0 from the data coverage is happening between $\varphi = 50°$N/S and $\varphi = 70°$N/S, while after $\varphi = 70°$N/S the change becomes less noticeable (Fig. 4). Following Dayoub et al. (2012), the sea surface heights included in the models CLS11 and DTU10 were reduced by the MDT values of the ECCO2 model (Menemenlis et al. 2008). This considerably decreases the W_0 dependence on the latitudinal coverage (Fig. 4).

Concluding Remarks and Outlook

The W_0 estimations obtained by the four groups in this first attempt are very similar (Table 1), especially those values based on the same models and the same latitudinal coverage (cf. estimations of the Bratislava, Latakia and Munich groups). However, there are discrepancies of about 0.5 $m^2\ s^{-2}$, which can be caused by the usage of different MSS models (cf. values of the Prague Group

Table 1 Summary of the W_0 estimates delivered by the four groups working on the W_0 determination in the frame of the JWG 0.1.1

Group	MSS	Area	GOCO03S	EIGEN-6C	EGM2008
Prague	Jason 1	67°N/S	54.28	54.25	54.24
		60°N/S	53.75	53.73	53.96
Bratislava	DTU10	82°N/S	54.00	53.95	53.96
		67°N/S	53.53	53.49	53.49
	CLS11	82°N/S	54.30	54.26	54.26
		67°N/S	53.82	53.79	53.79
Latakia	DTU10	80°N/S	54.11	54.11	54.11
		70°N/S	53.91	53.92	53.92
		60°N/S	53.07	53.08	53.07
	CLS11	80°N/S	54.42	54.43	54.43
		70°N/S	54.23	54.24	54.23
		60°N/S	53.38	53.40	53.39
	DTU10 + ECCO2	70°N/S	53.94	53.95	53.95
		60°N/S	53.87	53.88	53.87
	CLS11 + ECCO2	70°N/S	54.26	54.27	54.26
		60°N/S	54.18	54.20	54.19
Munich	DTU10	82°N/S	54.02	53.98	53.97
		67°N/S	53.55	53.53	53.53
		60°N/S	53.11	53.12	53.12
	CLS11	82°N/S	54.31	54.29	54.30
		67°N/S	53.86	53.82	53.83
		60°N/S	53.44	53.41	53.40

The values are given in [$m^2\ s^{-2}$] and the constant 62,636,800 should be added. Applied methodologies are described in Burša et al. (1999), Čunderlik and Mikula (2009), Dayoub et al. (2012) and Sánchez (2009), respectively

with the others in Table 1). To evaluate if these differences are significant, the next step is to perform a formal error propagation analysis that allows us to establish the uncertainty in W_0. In parallel, it is necessary to start selecting some conventions for a formal recommendation on W_0. To do this, some open questions that need to be answered first are listed in the following:

- The Gaussian definition for the geoid is based on the sea surface sampled globally. At present, we are restricted to the range of the satellite altimetry measurements (i.e. $\varphi = \sim 82°$N/S). Under this perspective—should the polar regions be integrated in the W_0 computation?
- The sea surface should be *quasi-stationary*, i.e., it should not show any significant temporal variations detectable in the satellite altimetry data. Normally, most of these effects (tides, sea state bias, etc.) are reduced, but how should the seasonal variations be considered, especially those generated by the sea ice cycle and glaciations and melting effects in the polar regions?
- The precision of the satellite altimetry data degrades in coastal areas. Should they be excluded from the global W_0 computation? If not, how can their reliability be improved?
- The continental surfaces can be considered, together with the sea surface, as a part of the known boundary surface in the solution of the geodetic boundary value problem. Can the existing topography surface models refine/improve the W_0 computation?
- Since both the Earth's surface and gravity field vary with time, should W_0 also be defined to vary with time? Which strategy should be followed to estimate the variation of W_0 through time? How should the reference epoch be appointed and how often should the datum be updated?
- Which tide system should be selected for the W_0 realisation?

Independently of the answers to these questions, it is clear that the potential value U_0 of the GRS80 ellipsoid and the W_0 value included in the IERS conventions differ considerably from the recent W_0 computations: the former corresponds to an equipotential surface located about 67 cm beneath the sea surface scanned by satellite altimetry, while the latter is located about 17 cm lower. Although *any* of these values could be introduced as a vertical reference level (as could any other value), the reliability of their realisation cannot be guaranteed, since

the most recent geodetic models describing the geometry and physics of the Earth yield other values. In this respect, the need to provide a new "better estimate" of W_0 is urgent.

Acknowledgments The authors would like to thank the reviewers whose comments helped to improve the paper. The Prague Group specially recognizes the support of the grant N62909-12-1-7037, ACO: N62927 ONRG LTR 7037. The work of the Bratislava Group has been supported by the grants APVV-0072-11 and VEGA 1/1063/11.

References

Andersen OB (2010) The DTU10 gravity field and mean sea surface. Presented at second international symposium of the gravity field of the Earth (IGFS2), Fairbanks, Alaska

Andersen OB, Knudsen P (2009) DNSC08 mean sea surface and mean dynamic topography models. J Geophys Res 114, C11001. doi: 10.1029/2008JC005179

Andersen OB, Vest AL, Knudsen P (2006) The KMS04 multi-mission mean sea surface. In: Knudsen P, Johannessen J, Gruber T, Stammer S, van Dam T (eds) GOCINA: improving modelling of ocean transport and climate prediction in the north atlantic region using GOCE gravimetry. Cahiers du Centre European de Geodynamique et de Seimologie, Séismologie (ECGS) 2006, vol 25. ISBN: 2-9599804-2-5. http://gocinascience.spacecenter.dk/publications/4_1_kmss04-lux.pdf

Becker J, Sandwel D (2003) Accuracy and resolution of shuttle radar topography mission data. Geosphys Res Lett 30(9), 1467. doi:10.1029/2002GL016643

Burša M, Šíma Z, Kostelecky J (1992) Determination of the geopotential scale factor from satellite altimetry. Studia geoph et geod 36:101–109

Burša M, Radej K, Šíma Z, True S, Vatrt V (1997) Determination of the geopotential scale factor from Topex/Poseidon satellite altimetry. Studia geoph et geod 41:203–215

Burša M, Kouba J, Radej K, True S, Vatrt V, Vojtíšková M (1998) Monitoring geoidal potential on the basis of Topex/Poseidon altimeter data and EGM96. IAG Symp 119:352–358

Burša M, Kouba J, Kumar M, Müller A, Raděj K, True SA, Vatrt V, Vojtíšková M (1999) Geoidal geopotential and world height system. Studia geoph et geod 43:327–337

Burša M, Kouba J, Radej K, Vatrt V, Vojtíšková M (2001) Geopotential at tide gauge stations used for specifying a world height system. Geographic service of the army of the Czech Republic. Acta Geodaetica 1:87–96

Burša M, Groten E, Kenyon S, Kouba J, Radej K, Vatrt V, Vojtíšková M (2002) Earth's dimension specified by geoidal geopotential. Studia geoph et geod 46:1–8

Burša M, Kenyon S, Kouba J, Šíma Z, Vatrt V, Vitek V, Vojtíšková M (2007a) The geopotential value *Wo* for specifying the relativistic atomic time scale and a global vertical reference system. J Geod 81:103–110

Burša M, Šíma Z, Kenyon S, Kouba J, Vatrt V, Vojtíšková M (2007b) Twelve years of developments: geoidal geopotential *Wo* for the establishment of a world height system – present and future. In: Proceedings of the 1st international symposium of the international gravity field service, Istanbul, pp 121–123

Čunderlík R, Mikula K (2009) Numerical solution of the fixed altimetry-gravimetry BVP using the direct BEM formulation. IAG Symp 133:229–236

Čunderlík R, Mikula K, Mojzeš M (2008) Numerical solution of the linearized fixed gravimetric boundary-value problem. J Geod 82:15–29. doi:10.1007/s00190-007-0154-0

Dayoub N (2010) The Gauss-Listing gravitational parameter *W0* and its time variation from analysis of the sea levels and GRACE. PhD thesis, Geomatics, University of Newcastle

Dayoub N, Edwards SJ, Moore P (2012) The Gauss-Listing potential value *Wo* and its rate from altimetric mean sea level and GRACE. J Geod 86(9):681–694. doi:10.1007/s00190-012-1547-6

Drewes H, Hornik H, Ádám J, Rózsa S (eds) (2012) The geodesist's handbook 2012. J Geod 86(10). doi:10.1007/s00190-012-0584-1

Förste C, Flechtner F, Schmidt R, Meyer U, Stubenvoll R, Barthelmes F, König R, Neumayer KH, Rothacher M, Reigber Ch, Biancale R, Bruinsma S, Lemoine J-M, Raimondo JC (2005) A new high resolution global gravity field model derived from combination of GRACE and CHAMP mission and altimetry/gravimetry surface gravity data. Poster g004_EGU05-A-04561.pdf (316 KB) presented at EGU General Assembly 2005, Vienna, Austria, 24–29 April 2005

Förste C, Bruinsma S, Shako R, Marty JC, Flechtner F, Abrikosov O, Dahle C, Lemoine JM, Neumayer H, Biancale R, Barthelmes F, König R, Balmino G (2011) EIGEN-6 – a new combined global gravity field model including GOCE data from the collaboration of GFZ-Potsdam and GRGS-Toulouse. Geophys Res Abstr 13, EGU2011-3242-2, EGU2011

Gauss CF (1876) Trigonometrischen und polygonometrischen Rechnungen in der Feldmesskunst. Halle, a. S. Verlag von Eugen Strien.Bestimmung des Breitenunterschiedes zwischen den Sternwarten von Göttingen und Altona durch Beobachtungen am ramsdenschen Zenithsektor. In: Carl Friedrich Gauss Werke, neunter Band. Königlichen Gesellschaft der Wissenschaften zu Göttingen (1903) (in German)

Groten E (2004) Fundamental parameters and current (2004) best estimates of the parameters of common relevance to astronomy, geodesy and geodynamics. J Geod 77:724–731. doi:10.1007/s00190-003-0373y

Heck B (2004) Problems in the definition of vertical reference frames. IAG Symp 127:164–173

Heck B, Rummel R (1990) Strategies for solving the vertical datum problem using terrestrial and satellite geodetic data. IAG Symp 104:116–128

Heiskanen WA, Moritz H (1967) Physical geodesy. W.H. Freeman, San Francisco, CA

Hernandes F, Schaeffer Ph (2001) The CLS01 mean sea surface: a validation with the GFSC00.1 surface. www.cls.fr/html/oceano/projects/mss/cls_01_en.html

Ihde J (2007) Inter-Commission project 1.2: vertical reference frames. Final report for the period 2003–2007. In: IAG Commission 1 – Reference Frames, Report 2003–2007. DGFI, Munich. Bulletin No 20:57–59

Ihde J, Amos M, Heck B, Kearsley W, Schöne T, Sánchez L, Drewes H (2007) Conventions for the definitions and realisation of a conventional vertical reference system (CVRS). http://whs.dgfi.badw.de/fileadmin/user_upload/CVRS_conventions_final_20070629.pdf

Kutterer H, Neilan R, Bianco G (2012) Global geodetic observing system (GGOS). In: Drewes H, Hornik H, Ádám J, Rózsa S (eds) The geodesist's handbook 2012. J Geod 86(10):915–926. doi:10.1007/s00190-012-0584-1

Lemoine F, Kenyon S, Factor J, Trimmer R, Pavlis N, Chinn D, Cox C, Kloslo S, Luthcke S, Torrence M, Wang Y, Williamson R, Pavlis E, Rapp R, Olson T (1998) The development of the joint NASA GSFC and the National Imagery and Mapping Agency (NIMA) geopotential model EGM96. NASA, Goddard Space Flight Center, Greenbelt

Mather RS (1978) The role of the geoid in four-dimensional geodesy. Mar Geod 1:217–252

Mayer-Gürr T, Rieser D, Hoeck E, Brockmann JM, Schuh WD, Krasbutter I, Kusche J, Maier A, Krauss S, Hausleitner W, Baur O, Jäggi A, Meyer U, Prange L, Pail R, Fecher T, Gruber Th (2012) The new combined satellite only model GOCO03S. Presented at the international symposium on gravity, geoid and height systems GGHS 2012, Venice

McCarthy DD (1992) IERS standards (1992). IERS Technical Note 13. Central Bureau of IERS – Observatoire de Paris

McCarthy DD (1996) IERS conventions (1992). IERS Technical Note 21. Central Bureau of IERS – Observatoire de Paris

Menemenlis D, Campin J, Heimbach P, Hill C, Lee T, Nguyen A, Schodlock M, Zhang H (2008) ECCO2: high resolution global ocean and sea ice data synthesis. Mercator Ocean Quarterly Newsletter 31:13–21

Moritz H (2000) Geodetic reference system 1980. J Geod 74:128–133

Pavlis N-K, Holmes SA, Kenyon SC, Factor JK (2012) The development of the Earth Gravitational Model 2008 (EGM2008). J Geophys Res 117, B04406. doi:10.1029/2011JB008916

Petit G, Luzum B (eds) (2010) IERS conventions 2010. IERS Technical Note 36. Verlag des Bundesamtes für Kartographie und Geodäsie, Frankfurt a.M.

Plag H-P, Pearlman M (2009) Global geodetic observing system: meeting the requirements of a global society. Springer, Berlin

Rapp R (1995) Equatorial radius estimates from Topex altimeter data. Publication dedicated to Erwin Groten on the occasion of his 60th anniversary. Publication of the Institute of Geodesy and Navigation (IfEN), University FAF Munich. pp 90–97

Rummel R, Teunissen P (1988) Height datum definiton, height datum connection and the role of the geodetic boundary value problem. Bull Géod 62:477–498

Sacerdorte F, Sansò F (2001) *Wo*: a story of the height datum problem. In: Wissenschaftliche Arbeiten der Fachrichtung Vermessungswesen der Universität Hannover. Nr. 241:49–56

Sacerdorte F, Sansò F (2004) Geodetic boundary-value problems and the height datum problem. IAG Symp 127:174–178

Sánchez L (2007) Definition and realization of the SIRGAS vertical reference system within a globally unified height system. IAG Symp 130:638–645

Sánchez L (2008) Approach for the establishment of a global vertical reference level. IAG Symp 132:119–125

Sánchez L (2009) Strategy to establish a global vertical reference system. IAG Symp 134:273–278. doi:10.1007/978-642-3-00860-3-42

Sánchez L (2012) Towards a vertical datum standardisation under the umbrella of Global Geodetic Observing System. Journal of Geodetic Science 2(4):325–342. doi:10.2478/v10156-012-0002-x

Schaeffer P, Faugére Y, Legeais JF, Ollivier A, Guinle T, Picot N (2012) The CNES_CLS11 global mean sea surface computed from 16 years of satellite altimeter data. Mar Geod 35(1):3–19. doi:10.1080/01490419.2012.718231

Realization of WHS Based on the Static Gravity Field Observed by GOCE

Róbert Čunderlík, Zuzana Minarechová, and Karol Mikula

Abstract

The paper deals with a determination of W_0 as well as testing of geoid candidates for a realization of the World Height System using the GOCO03S satellite-only geopotential model. The W_0 values are estimated for two different altimetric mean sea surface models (DTU10_MSS and MSS_CNES_CLS2011) using four different global geopotential models (GGMs), namely GOCE-DIR2 or GOCO03S satellite-only GGMs, and EGM2008 or EIGEN-6C combined GGMs. In all cases the impact of including polar regions into the integration area is presented.

The second part studies how the high-degree combined GGMs or local gravimetric geoid models correspond to the static gravity field observed by GOCE. The nonlinear diffusion filtering is used to reduce the stripping noise of the geopotential evaluated from the GOCO03S model up to degree 250. On lands, the geopotential is evaluated at 3D positions of the local (national) gravimetric-only geoid models, namely USGG-2012 in USA, CGG-2010 in Canada, AGQG-2009 in Australia, and NZGeoid09 in New Zealand, otherwise at 3D positions of the EIGEN-6C or EGM-2008 geoid models. At oceans, the geopotential is filtered on the DTU10 mean sea surface whose 3D position is precisely provided by satellite altimetry. Apart from high mountainous areas, the smoothed geopotential on the considered geoid models shows good agreement with GOCO03S, i.e. with the low-frequency part of the gravity field precisely observed by GRACE/GOCE. At the same time the filtered satellite-only mean dynamic topography is provided specifying its relation to the geoid models at coastal areas.

Keywords

World height system • Geopotential • W_0 estimates • Satellite-only geopotential models • Nonlinear diffusion filtering • Testing of geoid models

1 Introduction

A realization of the World Height System (WHS) is usually performed on basis of global geopotential models (GGMs), cf. (Burša et al. 1999, 2004, 2007; Sánchez 2008, 2009; Ihde 2011). The GOCE satellite mission has brought a significant improvement in modelling of the low-frequency (or rather medium-frequency) part of the Earth's static gravity field. Its objective "*to determine the geoid with an accuracy of 1–2 cm at a spatial resolution better than 100 km*" (Drinkwater et al. 2007) is promising for purposes of a unification of local vertical datums (LVDs). An advantage is that satellite-only GGMs are fully independent from LVDs. On the other hand, new precise GRACE/GOCE satellite-only GGMs are still considerably affected by a stripping noise due to the omission and commission errors. Consequently, for many geodetic

R. Čunderlík (✉) • Z. Minarechová • K. Mikula
Faculty of Civil Engineering, Department of Mathematics and Descriptive Geometry, Slovak University of Technology in Bratislava, Bratislava, Slovakia
e-mail: cunderli@svf.stuba.sk; faskova@math.sk; mikula@math.sk

U. Marti (ed.), *Gravity, Geoid and Height Systems*, International Association of Geodesy Symposia 141,
DOI 10.1007/978-3-319-10837-7_27, © Springer International Publishing Switzerland 2014

purposes it is practically inevitable to model also high-frequency part, especially at zones where long-wavelength terms are not able to capture sufficiently abrupt changes of the gravity field, see e.g. (Čunderlík et al. 2014). However, the terrestrial gravity data are usually related to LVDs and suffer from deficiencies of local vertical networks. This can yield additional biases that can mislead precise gravity field modeling.

The objective of this paper is to utilize information of the low-frequency part of the Earth's static gravity field precisely observed by GOCE and to analyse how it agrees with detailed geoid models that include also high-frequencies. The paper consists of two parts. The first part deals with a determination of W_0 as a reference value of the geopotential on the geoid using two mean sea surface (MSS) models and four different GGMs. In the second part we present testing of global or local geoid candidates for the realization of WHS using the GOCO03S satellite-only geopotential model (Mayer-Gürr et al. 2012). For such purposes the geopotential is evaluated from GOCO03S up to degree 250 at 3D position of the tested geoid models on land and on the MSS models over oceans. In order to reduce the stripping noise, the geopotential is filtered using the nonlinear diffusion filtering on the Earth's surface (Čunderlík et al. 2013). In such a way the filtered geopotential on geoid models over land areas should tend to a constant value (removing the bias of the regional geoid models) while at oceans it should result in the filtered satellite-only mean dynamic topography (MDT). The nonlinear diffusion filtering using the regularized surface Perona-Malik model preserves gradients at coastal areas that can be useful to detect consistency between the precise geoid models and the satellite-only MDT.

2 Determination of W_0

In our approach for determination of W_0 as a reference value for the establishment of WHS we use weighted averaging of the geopotential evaluated on two MSS models provided by satellite altimetry, namely DTU10_MSS (Andersen 2010) (Fig. 1) and MSS_CNES_CLS2011 (Schaeffer et al. 2012). In both cases we have created a regular grid 5×5 arc min from the original datasets. Our weighting function depends on the surface areas that correspond to the grid points on the ellipsoid. The transformations from the Topex/Posseidon ellipsoid to WGS84 and from the mean tide to tide free system have been performed using the GOCE User Toolbox (ESA 2011). To evaluate the geopotential at precise 3D positions of the grid points, we have used (i) two satellite-only GGMs: GOCE-DIR2 up to degree 240 (Bruinsma et al. 2010) and GOCO03S up to degree 250, and (ii) two combined GGMs: EGM-2008 up to degree 2160 (Pavlis et al. 2012) and EIGEN-6C up to degree 1420 (Förste et al. 2011). For all GGMs we have considered the full set of coefficients and the $J_{2,0}$ coefficient in the tide-

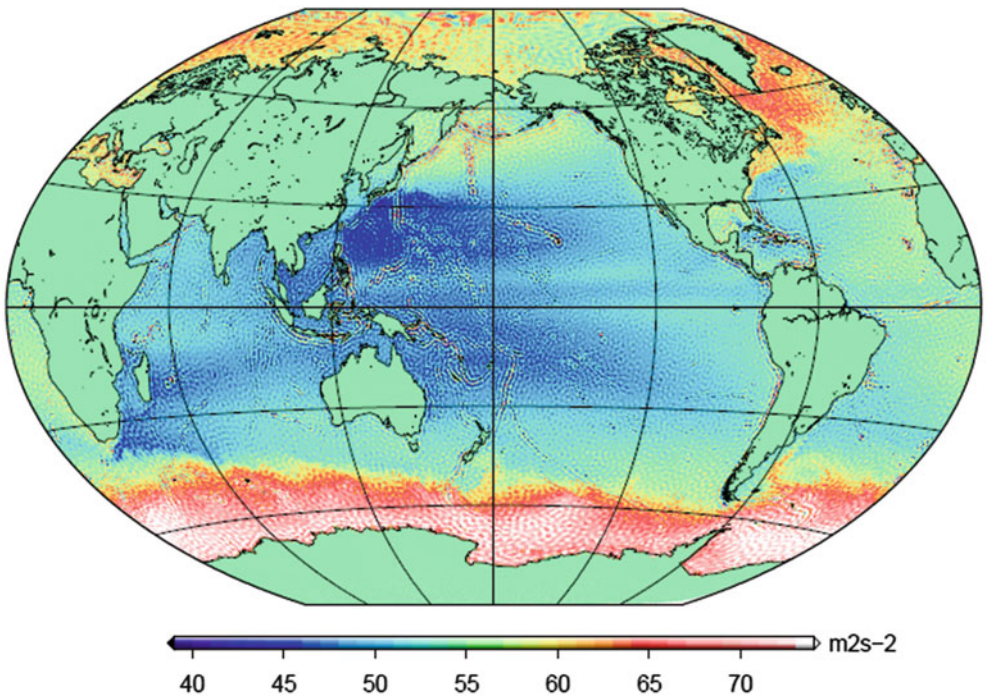

Fig. 1 Geopotential on the DTU10 mean sea surface evaluated from the GOCO03S geopotential model up to degree 250 (the constant 62,636,800.0 m^2s^{-2} is subtracted). On lands, $W_0 = 62{,}636{,}854.0$ m^2s^{-2} is prescribed

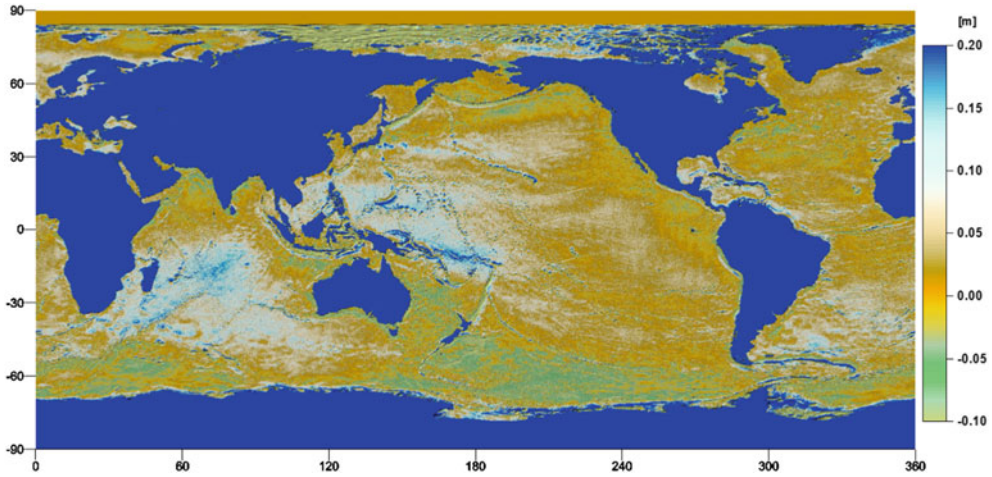

Fig. 2 Differences between DTU10_MSS and MSS_CNES_CLS2011

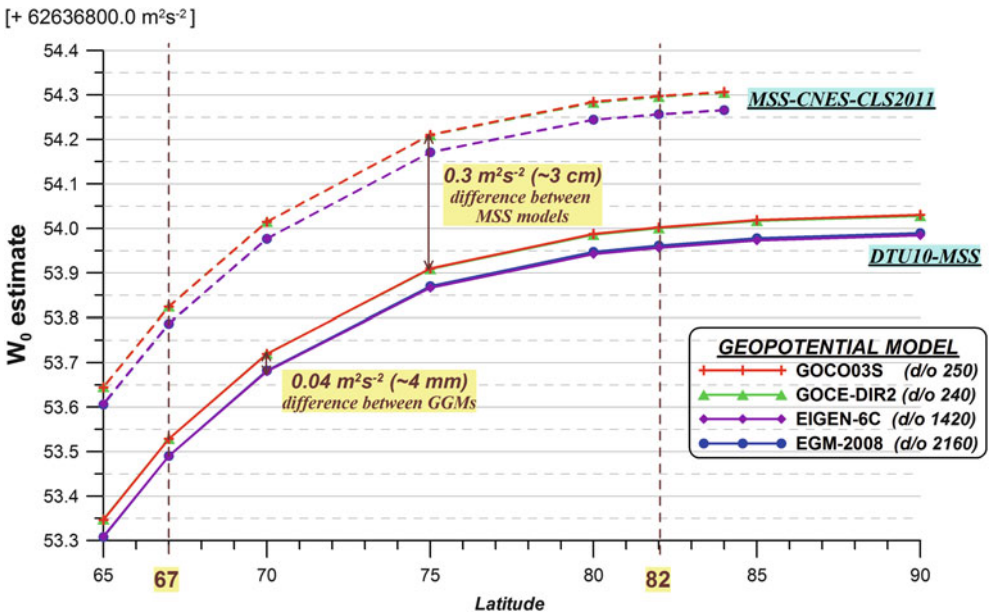

Fig. 3 W_0 estimates for two MSS models (DTU10_MSS and MSS_CNES_CLS2011) and four global geopotential models (GOCO03S, GOCE-DIR2, EIGEN-6C and EGM-2008) and the impact of including polar regions into the integrating area

free system referenced to the same epoch 2005.0. All grid points located at oceans and seas have been incorporated into the averaging, i.e. including coastal and shallow water regions.

Figure 2 depicts differences between the DTU10_MSS and MSS_CNES_CLS2011 models. It shows high positive differences more than +10 cm in the Indian Ocean or in the western equatorial part of the Pacific Ocean, and high negative differences less than −5 cm in the Tasman Sea and the Antarctic Ocean. The mean value of these differences is +3.0 cm and the standard deviation is 7.3 cm. Such quite large differences between both MSS models obviously yield different W_0 estimates. This discrepancy is probably due to the different time periods of processed altimetry data and their reference periods, respectively. Namely, for DTU10_MSS the whole period 1993–2009 (17 years) represents the reference period while in case of MSS_CNES_CLS2011 16 years (1993–2008) of altimetry data are referenced to the period 1993–1999 using the GDR-C standard (Schaeffer et al. 2012).

An impact of including polar regions (Fig. 1) into the integration area is also essential for averaging, cf. (Sánchez 2009) or (Dayoub et al. 2012). Figure 3 shows how the W_0 estimates are changing for different latitude limits of the integration area. For example, excluding the polar regions above 67°N/S leads to an average that is 0.5 m^2s^{-2} (≈5 cm) smaller than when considering the whole polar regions. A difference about 0.3 m^2s^{-2} between both MSS models corresponds to

Table 1 W_0 estimates for two MSS models (DTU10_MSS and MSS_CNES_CLS2011) and four global geopotential models (GOCO03S, GOCE-DIR2, EIGEN-6C and EGM-2008) (units: m^2s^{-2}, the constant 62,636,800.0 m^2s^{-2} is subtracted)

MSS model	Area	GOCO03S (d/o 250)	GOCE-Dir2 (d/o 240)	EIGEN-6C (d/o 1420)	EGM-2008 (d/o 2160)
DTU10_MSS	82°S–82°N	54.00	54.00	53.95	53.96
	67°S–67°N	53.53	53.53	53.49	53.49
CNES_CLS2011	82°S–82°N	54.30	54.29	54.26	54.26
	67°S–67°N	53.82	53.82	53.79	53.79

the aforementioned mean value of their differences +3 cm. An influence of using different GGMs with the different degrees of coefficients is less than 0.04 m^2s^{-2} (≈4 mm). Table 1 summarizes our W_0 estimates for two integration areas, namely 67°S–67°N and 82°S–82°N. These results as well as the W_0 estimates provided by other research teams using the same datasets are presented in the report paper published in this volume by Sánchez et al. (2015).

3 Smoothed Geopotential from GOCO03S on Tested Geoid Models

There are basically two main strategies for a realization of WHS using GGMs. The first one is based on a precise evaluation of the geopotential W_P at any point P on the Earth's surface, whose 3D position is precisely obtained by GNSS. It can be easily transformed to the geopotential numbers $c_P = -(W_P - W_0)$ that are globally consistent and represent a basis for all types of heights, namely the dynamic, orthometric, and normal Molodensky heights. Here the W_0 value plays a role of the reference number of the geopotential on the geoid without a necessity to know its 3D position.

In the second approach, the 3D position of the geoid as an equipotential surface for a selected W_0 needs to be determined. Then offsets of LVDs with respect to this W_0 geoid can be estimated from an approximate relation (Sánchez 2009)

$$h^{GNSS} - H^{Orth} - N \cong dN, \tag{1}$$

where h^{GNSS} is the ellipsoidal height, H^{Orth} is the orthometric height and N is the geoidal height above a chosen reference ellipsoid. The term δN represents the offset of the LVD reference surface to the global W_0 geoid. To get a correct 3D position of the global W_0 geoid it is important to consider properly the zero-degree term

$$N_0 = -\frac{(W_0 - U_0)}{\gamma}, \tag{2}$$

where U_0 is the normal equipotential on the surface of the reference ellipsoid and γ is the mean value of the normal gravity over this ellipsoid. In general, U_0 differs from the geopotential W_0 defining the reference geoid. Hence the zero-degree term N_0 represents a bias of the geoid model with respect to the reference ellipsoid and it should be considered in the geoidal height N in Eq. (1).

The goal of this paper is to test how chosen geoid candidates for the realization of WHS agree with the low frequency part obtained from the GOCO03S satellite-only GGM. We focus on detailed geoid models in which the high-frequency part is also modeled using terrestrial or airborne gravimetric data. In this way we validate (i) the local (national) geoid models: USGG-2012 in USA (NGS 2012), CGG-2010 in Canada (Huang and Véronneau 2013), AGQG-2009 as a gravimetric-only version of AUSGeoid09 in Australia (Featherstone et al. 2011), and NZGeoid09 in New Zealand (Amos and Featherstone 2009), or (ii) the combined GGMs namely EGM-2008 up to degree 2160 or EIGEN-6C up to degree 1420.

In case of the quasigeoid models (i.e. AGQG-2009, NZGeoid09 and EIGEN-6C) we transform the quasigeoid height ζ into the geoidal height N using the approximate relation

$$N \cong \zeta + \frac{\Delta g_{BA}}{\overline{\gamma}} H^{Orth}, \tag{3}$$

where $\Delta g_{BA} = (\Delta g - 0.1119\, H^{Orth})$ is the Bouguer gravity anomaly computed from the free-air gravity anomaly Δg, and $\overline{\gamma}$ is the mean normal gravity along the plumbline. (Remark: there are more accurate expressions for the geoid-to-quasigeoid correction that require knowledge of the topographical mass density distribution, cf. (Tenzer et al. 2006)). To avoid undesirable biases we have to consider the zero-degree term N_0 in Eq. (2) for every geoid model tested.

From the definition, the geopotential should be constant everywhere on the true geoid although it is a complicated surface in 3D reflecting irregularities of the Earth's gravity field. Analogously, the geopotential on MSS, which is also complicated surface in 3D, should have smooth behaviour and it should correspond to MDT. Therefore we evaluate the geopotential from the GOCO03S model up to degree 250 at 3D positions of the tested geoid models on lands and on the DTU10_MSS model at oceans (Fig. 4a). After reducing the stripping noise (Fig. 4b) we test whether the

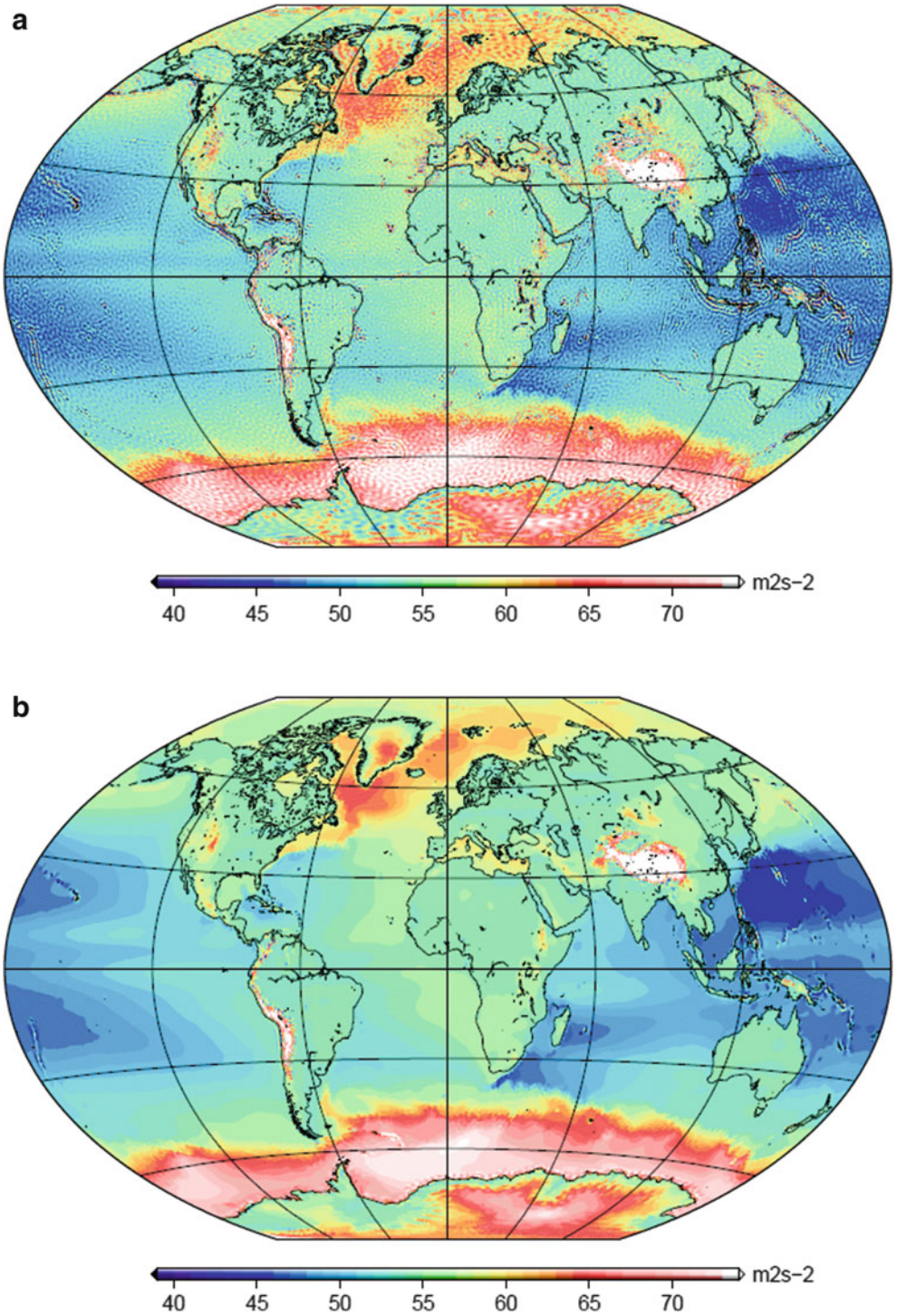

Fig. 4 (**a**) Initial data—the geopotential evaluated from GOCO03S up to degree 250 on the DTU10_MSS at oceans and on the EIGEN-6C geoid on lands, (**b**) the filtered geopotential after 25 iterations of the nonlinear diffusion filtering (the constant 62,636,800.0 m^2s^{-2} is subtracted)

smoothed geopotential tends to a constant value on land areas.

To reduce a significant stripping noise (Figs. 4a, 5a or 6a) we use the nonlinear diffusion equation on a closed surface based on the regularized surface Perona-Malik model (Čunderlík et al. 2013)

$$\frac{\partial W}{\partial t} - \nabla_S \cdot \left(G \left(|\nabla_S W^{\sigma}| \right) \nabla_S W \right) = 0, \tag{4}$$

where $\partial W/\partial t$ is the time derivative of the filtered geopotential W, ∇_S represents the surface gradient, and the function G is the so-called edge detector

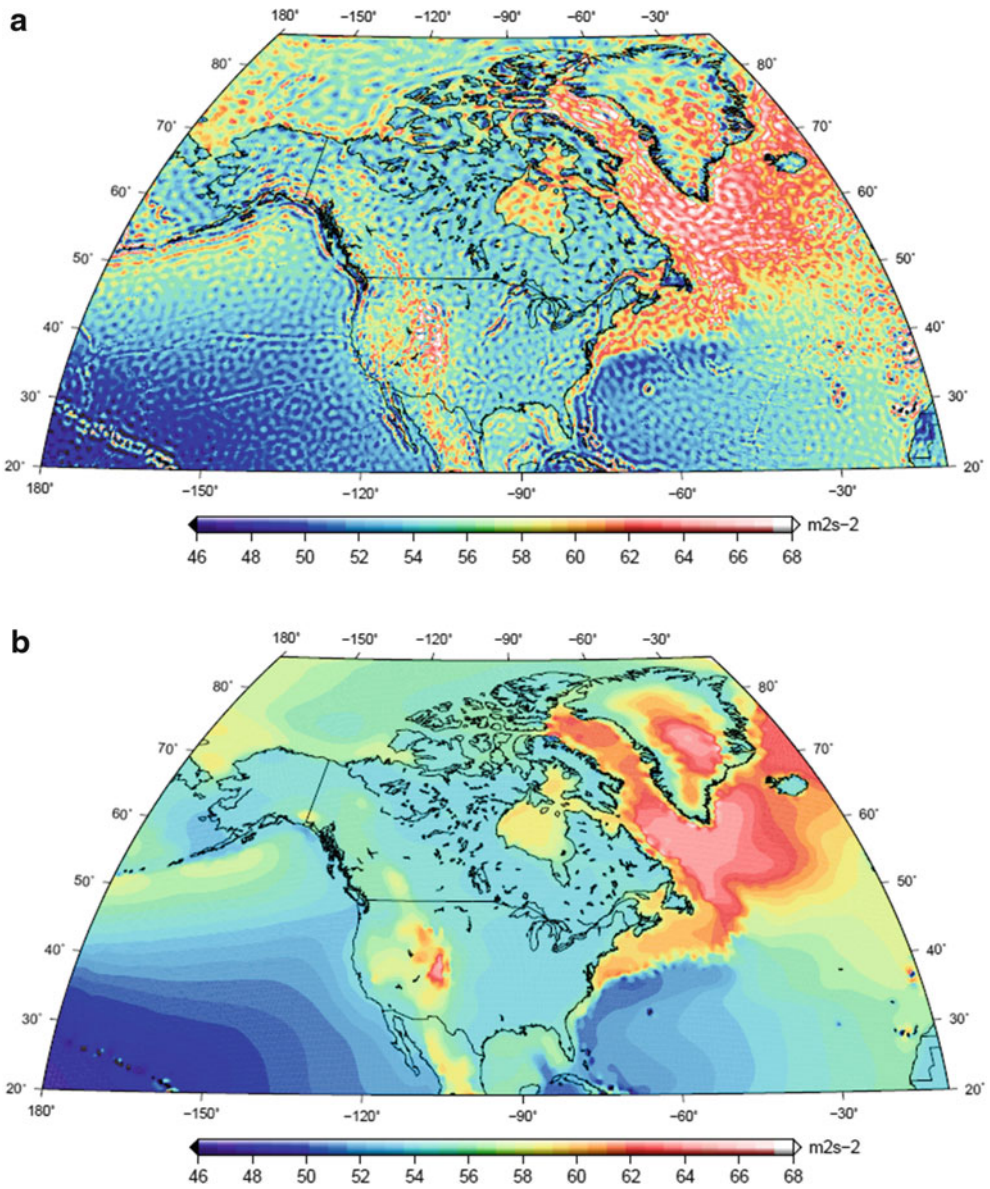

Fig. 5 (**a**) The geopotential evaluated from GOCO03S up to degree 250 on the DTU10_MSS at oceans and on the USGG-2012 geoid model in CONUS and ALASKA and on the CGG-2010 geoid model in Canada, Greenland and Island, (**b**) the filtered geopotential after 25 iterations of the nonlinear diffusion filtering (the constant 62,636,800.0 m^2s^{-2} is subtracted)

$$G\left(|\nabla_S W^{\sigma}|\right) = \frac{1}{1 + K|\nabla_S W^{\sigma}|^2}, \tag{5}$$

where K is the sensitivity parameter which needs to be tuned experimentally. The edge detector G depends on the surface gradients of the solution W^{σ} obtained from the previous filtering time step, which is slightly smoothed by the linear diffusion using the discrete time step σ, for more details see (Čunderlík et al. 2013).

Such nonlinear filtering preserves high gradients in the filtered data where smoothing is slower than in areas with small gradients. Obviously, the end time of the filtering is important. There are several possible techniques that can be taken into consideration; however to find an optimal end time is still an objective of mathematical investigations, c.f. (Capuzzo Dolcetta and Ferretti 2001). In these numerical experiments we use our subjective visual considerations. We try to find a compromise between the "almost" smoothed stripping noise in areas of high gradients while areas of small gradients are not over smoothed. Hence a number of iterations necessary for efficient reducing the stripping noise can differ for different regions.

Figure 4b shows the filtered geopotential after 25 iterations of the nonlinear diffusion filtering in case of the EIGEN-6C geoid model on lands and the DTU10_MSS

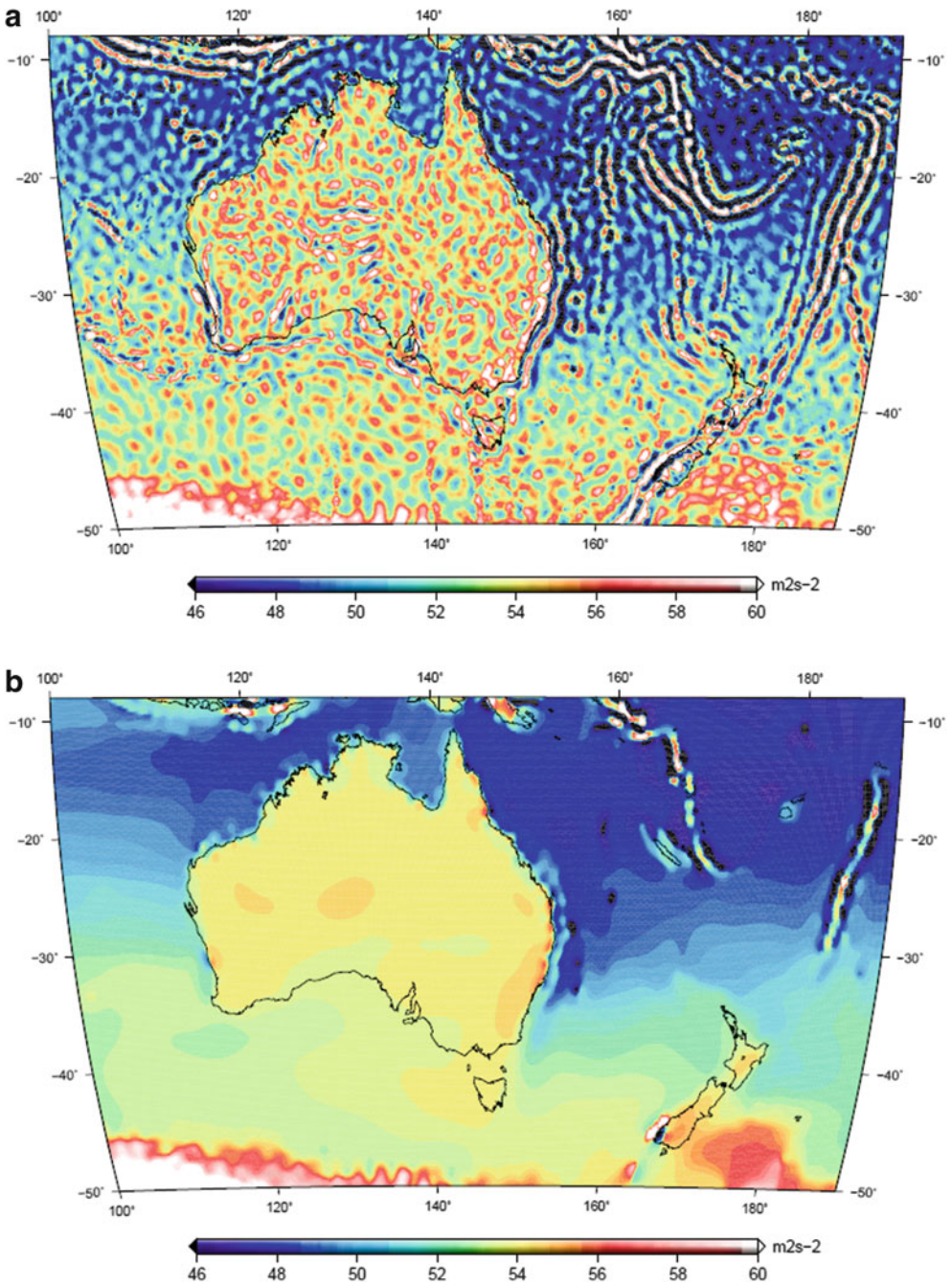

Fig. 6 (**a**) The geopotential evaluated from GOCO03S up to degree 250 on the DTU10_MSS at oceans and on the AGQG-2009 geoid model in Australia and on the NZGeoid09 geoid model in New Zealand, (**b**) the filtered geopotential after 20 iterations of the nonlinear diffusion filtering (the constant 62,636,800.0 m^2s^{-2} is subtracted)

model over oceans. Here the stripping noise is effectively reduced and the main gradients are preserved, e.g. at coastal areas or in zones of the ocean geostrophic surface currents. Such an approach allows us to indicate (i) how the smoothed geopotential on the tested geoid models on lands agree with the selected $W_0 = 62{,}636{,}854.0\ m^2s^{-2}$ as our candidate for a realization of WHS, and (ii) if there are some systematic tendencies like biases or tilts. At the same time the filtered satellite-only MDT is obtained. The preserved gradients at coastal areas provide useful information about relationships between the tested geoid models and the obtained MDT.

Figure 5 depicts the testing of the national geoid models in North America, namely USGG-2012 in "CONUS" (CONtinental US) and Alaska and CGG-2010 in Canada, Greenland and Iceland. It shows an agreement better than 10 cm in

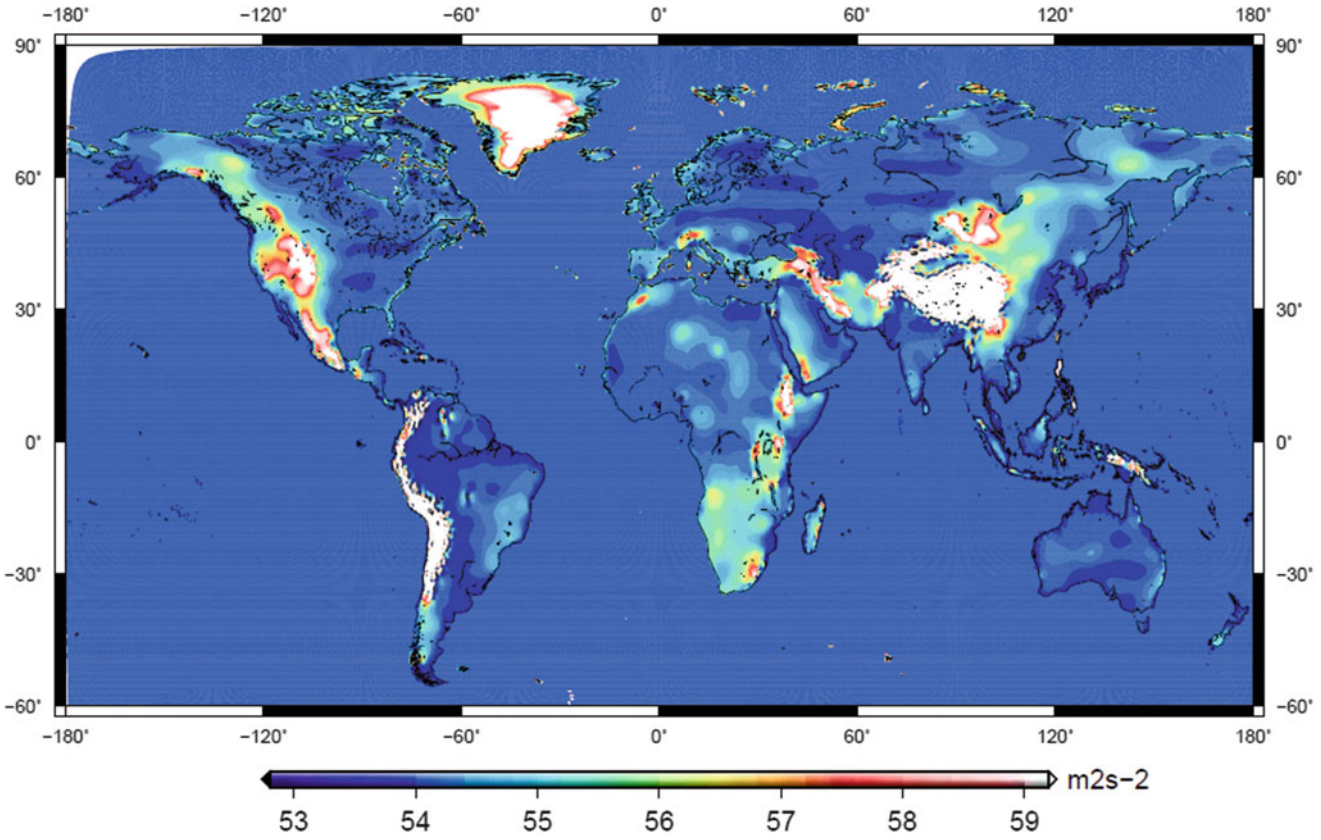

Fig. 7 Our estimate $W_0 = 62{,}636{,}854.0\ \mathrm{m^2 s^{-2}}$ prescribed at oceans and the filtered geopotential from GOCO03S on lands after 25 iterations of the nonlinear diffusion filtering considered at 3D position of the geoid models: USGG-2012 in USA, CGG-2010 in Canada, Greenland and Island, AGQG-2009 in Australia and NZGeoid09 in New Zealand, otherwise EIGEN-6C (the constant $62{,}636{,}800.0\ \mathrm{m^2 s^{-2}}$ is subtracted)

majority of areas, however in North American Cordillera differences are larger than 20 cm reaching up to 70 cm in the central part of Rocky Mountains. Even larger discrepancies are in Greenland (Figs. 5b and 7).

Figure 6 depicts the validation of AGQG-2009 in Australia and NZgeoid09 in New Zealand. An agreement better than 5 cm has been for almost the whole of Australia, but with a slightly worse agreement up to 10 cm in the southern part of the Great Dividing Range and in the Macdonell Ranges (Fig. 6b). Large stripping noise of the geopotential from GOCO03S in the area of New Zealand (Fig. 6a) confirms complicated gravity field along the edge of lithospheric plates. Not even 20 iterations of the nonlinear diffusion filtering are sufficient to reduce abrupt changes in the southwestern part of the Southern Island (Fig. 6b). In the rest of New Zealand our testing shows an agreement up to 10 cm however a slight tilt in the Southern Island can be detected, cf. (Čunderlík et al. 2014).

Finally, Figure 7 depicts the filtered geopotential from GOCO03S on the tested geoid models, i.e. on four national models, otherwise on EIGEN-6C where the high-frequency part is derived using the DTU10 gravity anomalies (Andersen 2010). At oceans, the value $W_0 = 62{,}636{,}854.0\ \mathrm{m^2 s^{-2}}$ as our candidate for the realization of WHS is prescribed. A smaller interval of the colour scale aims to emphasize the differences from the selected W_0 value. One can see that negative differences vary only up to $-0.5\ \mathrm{m^2 s^{-2}}$ (~ -5 cm) while positive ones exceed $+5\ \mathrm{m^2 s^{-2}}$ (~ 50 cm) in areas of high mountains, mainly in the Himalayas, Andes, Greenland and Rocky Mountains (see white areas in Fig. 7). In our opinion, these high discrepancies in mountainous areas are mainly due to the omission/commission errors of GOCO03S and partly due to the decreasing accuracy of the quasigeoid-to-geoid correction term (Eq. 3) in high mountains. In addition, the real accuracy of the tested geoid models in mountainous areas can likely reach dm level due to a lack of reliable terrestrial or airborne gravimetric data in extremely complicated terrain. Apart from these high mountainous regions, the smoothed geopotential from GOCO03S varies within ± 10 cm without significant biases or tilts (Fig. 7). This demonstrates that the tested geoid models, in which the high-frequency part is also modelled, are suitable for the realization of WHS providing that they are related to the adopted W_0 value.

Summary and Conclusions

An improvement in modelling of the low-frequency part of the Earth's static gravity field achieved by the GOCE satellite mission is promising for purposes of the realization of WHS. The new GRACE/GOCE satellite-only GGMs, e.g. GOCO03S, provides a suitable basis for a unification of LVDs on different continents. The nonlinear diffusion filtering of the geopotential evaluated from GOCO03S on the tested geoid models shows good agreement with the selected W_0 value. In many places differences are smaller than 1 m^2s^{-2} ($\sim$10 cm). Larger differences exceeding 2 m^2s^{-2} ($\sim$20 cm) are mostly in high mountainous regions (Fig. 7) and they are probably due to the omission/commission errors of GOCO03S. The results indicate zones where the national geoids or combined GGMs precisely determine 3D position of the W_0 global geoid as a reference surface. Here they are suitable for the realization of WHS, e.g. estimating LVD offsets using Eq. (1). We note that the tested detailed geoid models also include the high-frequency terms modelled from terrestrial or airborne gravimetric measurements, which is, in our opinion, essential for a precise unification of LVDs.

Over oceans, the filtered geopotential on the DTU10_MSS model corresponds to the filtered satellite-only MDT (Fig. 4b). The gradients preserved at coastal areas provide useful information about relationships between the tested geoid models and the obtained MDT (Figs. 4b, 5, and 6b). The filtering process has practically no impact on the W_0 estimation since the regularized Perona-Malik model preserves a mean value of the geopotential. Our analysis shows that W_0 estimates are mainly influenced by limits of the integration area in polar regions and can vary by more than 0.5 m^2s^{-2} ($\approx$5 cm). Differences between both MSS models yield a disagreement about 0.3 m^2s^{-2} ($\approx$3 cm). An influence of using different GGMs with the different degrees of coefficients is less than 0.04 m^2s^{-2} ($\approx$4 mm) (Fig. 3, Table 1).

Before recommending the best W_0 estimate, it would be useful (i) to make a common decision about the integration area (e.g. if including polar zones or coastal and shallow water areas), and (ii) to ensure consistency between time periods for the processed datasets, i.e. MSS models provided by satellite altimetry and satellite-only GGMs. In our opinion, once we are able to model MSS in the North Pole area (e.g. as in DTU10_MSS), although less precise, there is no reason to remove this region from averaging. Regarding the time consistency of the datasets, it would be helpful to develop the MSS models purely from altimetry data that correspond to time periods of GRACE/GOCE satellite-only GGMs.

Acknowledgements The work has been supported by the grant VEGA 1/1063/11 and the project APVV-0072-11.

References

Amos MJ, Featherstone WE (2009) Unification of New Zealand's local vertical datums: iterative gravimetric quasigeoid computations. J Geod 83(1):57–68

Andersen OB (2010) The DTU10 gravity field and mean sea surface. Presented at the second international symposium of the gravity field of the Earth (IGFS2), Fairbanks, Alaska

Bruinsma SL, Marty JC, Balmino G, Biancale R, Foerste C, Abrikosov O, Neumayer H (2010) GOCE gravity field recovery by means of the direct numerical method. Presented at the ESA living planet symposium, Bergen, Norway, 27 June–2 July 2010 (see also: earth.esa.int/GOCE)

Burša M, Kouba J, Kumar M, Muller A, Radej K, True SA, Vatrt V, Vojtišková M (1999) Geoidal geopotential and World Height System. Stud Geophys Geod 43:327–337

Burša M, Kenyon S, Kouba J, Šíma Z, Vatrt V, Vojtíšková M (2004) A global vertical reference frame based on four regional vertical datums. Stud Geophys Geod 48(3):493–502

Burša M, Kenyon S, Kouba J, Šíma Z, Vatrt V, Vítek V, Vojtíšková M (2007) The geopotential value W0 for specifying the relativistic atomic time scale and a global vertical reference system. J Geod 81(2):103–110

Capuzzo Dolcetta I, Ferretti R (2001) Optimal stopping time formulation of adaptive image filtering. Appl Math Optim 43(3):245–258

Čunderlík R, Tenzer R, Mikula K (2014) Realization of WHS based on gravity field models free of dependencies on local vertical datums. In: Earth on the Edge: Science for a Sustainable Planet, IAG Symposia, Vol. 139, pp. 551–559

Čunderlík R, Mikula K, Tunega M (2013) Nonlinear diffusion filtering of data on the Earth's surface. J Geod 87:143–160. doi:10.1007/s00190-012-0587-y

Dayoub N, Edwards SJ, Moore P (2012) The Gauss-Listing potential value W0 and its rate from altimetric mean sea level and GRACE. J Geod 86:681–694. doi:10.1007/s00190-012-1547-6

Drinkwater MR, Haagmans R, Muzi D, Popescu A, Floberghagen R, Kern M, Fehringer M (2007) The GOCE gravity mission: ESA's first core earth explorer. In: Proceedings of 3rd international GOCE user workshop, Frascati, Italy, 6–8 November 2006. ESA SP-627, ISBN 92-9092-938-3, pp 1–8

ESA (2011) The GOCE user toolbox, version 2.0. http://earth.esa.int/gut

Featherstone WE, Kirby JF, Hirt C, Filmer MS, Claessens SJ, Brown NJ, Hu G, Johnston GM (2011) The AUSGeoid09 model of the Australian height datum. J Geod 85(3):133–150

Förste C et al (2011) EIGEN-6: a new combined global gravity field model including GOCE data from the collaboration of GFZ-Potsdam and GRGS-Toulouse. Presented at the 2011 general assembly of EGU, Vienna, Austria, 3–8 April 2011

Huang J, Véronneau M (2013) Canadian gravimetric geoid model 2010. J Geod 87:771–790. doi:10.1007/s00190-013-0645-0

Ihde J (2011) Inter-commission project 1.2: vertical reference frames. Report of the International Association of Geodesy 2007–2011. http://iag.ign.fr/uploads/media/IC-P1.2.pdf

Mayer-Gürr T, Rieser D, Hoeck E, Brockmann M, Schuh WD, Krasbutter I, Kusche J, Maier A, Krauss S, Hausleitner W, Baur O, Jaeggi A, Meyer U, Prange L, Pail R, Fecher T, Gruber T (2012) The new combined satellite only model GOCO03s. Presented at the GGHS-2012 in Venice, Italy, 9–12 October 2012

NGS (2012) USGG2012 – a refined gravimetric model of the geoid in the United States and other territories. The National Geodetic Survey. http://www.ngs.noaa.gov/GEOID/USGG2012/

Pavlis NK, Holmes SA, Kenyon SC, Factor JK (2012) The development of the Earth Gravitational Model 2008 (EGM2008). J Geophys Res 117, B04406. doi:10.1029/2011JB008916

Sánchez L (2008) Approach for the establishment of a global vertical reference level. IAG Symp 132:119–124

Sánchez L (2009) Strategy to establish a global vertical reference system. In: Drewes H (ed) Geodetic reference systems. Springer, Berlin. IAG Symp 134:273–278

Sánchez L, Dayoub N, Čunderlík R, Minarechová Z, Mikula K, Vatrt V, Vojtíšková M, Šíma M (2015) W0 Estimates in the Frame of the GGOS Working Group on Vertical Datum Standardisation. In: Proc. of the International Symposium on Gravity, Geoid and Height Systems, IAG Symposia, Vol. 141, DOI 10.1007/978-3-319-10837-7__26

Schaeffer P, Faugére Y, Legeais JF, Ollivier A, Guinle T, Picot N (2012) The CNES_CLS11 global mean sea surface computed from 16 years of satellite altimeter data. Mar Geod 35(*Jason*-2):3–19. doi:10.1080/01490419.2012.718231

Tenzer R, Novak P, Moore P, Kuhn M, Vanicek P (2006) Explicit formula for the geoid-quasigeoid separation. Stud Geophys Geod 50(4):607–618

First Results on Height System Unification in North America Using GOCE

M.G. Sideris, E. Rangelova, and B. Amjadiparvar

Abstract

We study the impact of GOCE on the North American height system unification by assessing different factors: the performance of the GOCE global geopotential models, the models' omission error and its effect on the computed mean height datum offsets, and the effect of the biased local gravity data. Depending on the distribution of the data points, the omission error of the third release time-wise GOCE model used up to degree and order 180 contributes 13–15 cm to the computed mean offset of CGVD28 in Canada and only 2 cm to the mean offset of NAVD88 in the USA. The effect of the biased local gravity anomalies on the datum offsets is assessed by means of Stokes's integration with the original and residual kernels in a regional simulation scenario. This effect is found to be negligible when GOCE geopotential models are used in the computation of the geoid heights.

Keywords

GOCE • Height system unification • Vertical datum

1 Introduction

North America is characterized by two official height datums: CGVD28 (Canadian Geodetic Vertical Datum of 1928; Cannon 1929) in Canada and NAVD88 (North American Vertical Datum of 1988; Zilkoski et al. 1992) in the USA and Mexico. In addition, orthometric heights from the last, unofficial adjustment Nov07 of the first-order levelling network in Canada are available and used primarily for validation of the regional gravimetric and global geoid models (Véronneau, personal communication). The levelling networks in Canada and the USA are considered outdated, with large systematic errors accumulated from coast to coast (e.g., NAVD88 and to a lesser degree Nov07) and large regional distortions (CGVD28). Benchmarks are subject to rapid accuracy degradation due to the crustal motion from postglacial rebound, earthquakes, subsidence, frost heave, and local instabilities of the monuments.

These continental-size, levelling-based height datums will soon be replaced by geoid-based national and international height datums (Véronneau et al. 2006; NGS 2008). The zero height level surface of such a modern height datum will be defined by the regionally representative value $W_o = 62{,}636{,}856.00\ \mathrm{m}^2/\mathrm{s}^2$ of the geopotential determined at North American tide gauges (Roman and Weston 2012). The datum will be realized by means of a high resolution and accuracy gravimetric geoid model based on combined GRACE/GOCE global geopotential models and computed with improved local gravity and topographic data sets.

By providing improved medium wavelengths of the Earth's gravity field (ESA 1999), the GOCE mission initiated new studies of the regional and global unification of the existing over one hundred height systems worldwide. All datums can be connected using the global level surface defined by a GOCE-derived geoid model. In addition, GOCE provides a means for assessing systematic errors in the regional and national height datums, e.g., the large east-west tilt of NAVD88 in Canada. The determination of the North

M.G. Sideris • E. Rangelova (✉) • B. Amjadiparvar
Department of Geomatics Engineering, Schulich School of Engineering, University of Calgary, 2500 University Drive NW, Calgary, AB, Canada T2N 1N4
e-mail: evrangel@ucalgary.ca

U. Marti (ed.), *Gravity, Geoid and Height Systems*, International Association of Geodesy Symposia 141,
DOI 10.1007/978-3-319-10837-7_28,

American height datum offsets with respect to a global level surface is needed for analyzing the effect of the unified height systems on gravity and topography data sets used in regional geoid modeling, and for homogenization of these terrestrial data.

In this study, we follow the Geodetic Boundary Value Problem (GBVP) approach developed by Rummel and Teunissen (1988) for height system unification. Related to this approach, we study the effect of the omission error of the GOCE geopotential model on the height datum offsets. In addition, we study the magnitude of the so-called indirect bias term in the observation equation of the geoid height derived by means of the GBVP approach.

2 The GBVP Approach

It is assumed that the whole Earth (including the oceans) is covered by J non-overlapping vertical datum zones Ω^j, $j=0,\ldots,J$. At least one point P in each Ω^j should be given with its GNSS ellipsoidal height h_P and its orthometric height H^j_P. One arbitrary vertical datum zone Ω^o defined by the geopotential value W_o can be chosen as a (global) reference equipotential surface with respect to which the geopotential differences $\delta W^j_o = W_o - W^j_o$ and the offsets $\delta N^j = \delta W^j_o/\gamma$ can be computed, where W^j_o defines the reference potential of the datum zone Ω^j and γ is the normal gravity on the ellipsoid.

The solution to the GBVP at point P in terms of the anomalous potential T is

$$T_P = \frac{\delta GM}{R} + \frac{R}{4\pi}\iint_{\Omega} St\left(\psi_{PQ}\right)\left\{\Delta g^j_Q + 2\frac{\delta W^j_o}{R}\right\} d\Omega_Q, \tag{1}$$

where $\Delta g = \Delta g^j + 2\delta W^j_o/R$ is the gravity anomaly in the global datum, computed from the gravity anomaly

$$\Delta g^j = g_P - \frac{\partial g}{\partial h} H^j - \gamma_{P_o} \tag{2}$$

in the local datum zone Ω^j; g_P is the measured gravity at the topographic surface, $(\partial g/\partial h)H^j$ is the reduction to the zero height level in Ω^j, and γ_{P_o} is the normal gravity on the ellipsoid at point P_o. The term $2\delta W^j_o/R$ in Eq. (1) is interpreted as the "free-air" reduction used for reducing the gravity anomaly Δg^j from the local zero height level to the reference surface defined by the W_o value. R is the mean Earth's radius, δGM is the difference in the geocentric gravitational constant GM of the geoid and GM^e of the normal ellipsoid, and $St(\psi_{PQ})$ is Stokes's function computed with the spherical distance ψ_{PQ}.

Equation (1) is inserted in Bruns's equation

$$N^j_P = \left(T_P - \Delta W_o + \delta W^j_o\right)/\gamma, \tag{3}$$

and if δW^j_o is assumed to be a constant over the datum zone Ω^j, the geoid height is expressed as

$$\begin{aligned} N^j_P = &\left(\frac{\delta GM}{R\gamma} - \frac{\Delta W_o}{\gamma}\right) + \frac{\delta W^j_o}{\gamma} \\ &+ \frac{R}{4\pi\gamma}\iint_{\Omega} St\left(\psi_{PQ}\right)\Delta g^j_Q d\Omega_Q \\ &+ \sum_{i=1}^{J}\frac{1}{2\pi\gamma}\delta W^i_o \iint_{\Omega^i} St\left(\psi_{PQ}\right) d\Omega^i_Q. \end{aligned} \tag{4}$$

The constant term (Heiskanen and Mortiz 1967)

$$N_o = \delta GM/(R\gamma) - \Delta W_o/\gamma \tag{5}$$

contains $\Delta W_o = W_o - U_o$, computed with the potential of the normal ellipsoid U_o. The third term in Eq. (4) is Stokes's integral with the local gravity anomalies Δg^j as input:

$$N^j_{P_{Stokes}} = \frac{R}{4\pi\gamma}\iint_{\Omega} St\left(\psi_{PQ}\right)\Delta g^j_Q d\Omega_Q. \tag{6}$$

The fourth term in Eq. (4) is the so-called indirect bias term. With $S^i_P = (1/2\pi)\iint_{\Omega^i} St\left(\psi_{PQ}\right) d\Omega^i_Q$, the indirect bias term can be written as

$$\begin{aligned} N^{ind}_P &= \frac{1}{\gamma}S^j_P\delta W^j_o + \sum_{i=1, i\neq j}^{J}\frac{1}{\gamma}S^i_P\delta W^i_o \\ &= S^j_P\delta N^j + \sum_{i=1, i\neq j}^{J} S^i_P\delta N^i. \end{aligned} \tag{7}$$

This equation shows that the geoid height in the datum zone Ω^j is affected by the offsets of all datum zones. This excludes the reference datum zone Ω^o, for which the offset is zero by definition. With Eqs. (5)–(7), Eq. (4) can be written as

$$N^j_P = N_o + \delta N^j + N^j_{P_{Stokes}} + N^{ind}_P, \tag{8}$$

where δN^j is the datum offset. The local geoid height in the left hand side of Eq. (8) can be computed also as a difference of the GNSS ellipsoidal height and the orthometric height:

$$N^j_P = h_P - H^j_P \tag{9}$$

and used in the observation equation of the geoid height in the datum offset computational scheme in Fig. 1.

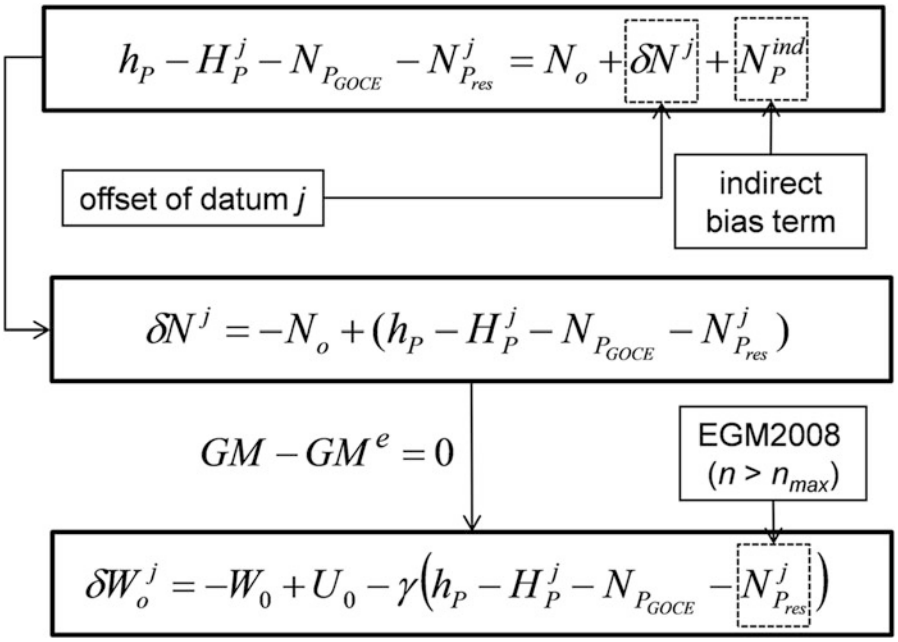

Fig. 1 Computational scheme of the vertical datum offset and geopotential difference

The local gravity anomalies in Eq. (2) used in Stokes's integration are biased because of the bias of the orthometric heights with respect to the reference datum. The use of the GOCE geoid can mitigate the effect of these biases and can simplify the computations in Eq. (8) and Fig. 1. The geoid height can be computed from a GOCE geopotential model and Stokes's integral in Eq. (4) with $\Delta g_{res}^j = \Delta g^j - \Delta g_{GOCE}$ to account for the omission error of the GOCE model. Therefore,

$$N_{P_{Stokes}}^j = N_{P_{GOCE}} + N_{P_{res}}^j. \tag{10}$$

The residual gravity anomalies Δg_{res}^j, which contain the gravity signal with frequencies higher than the maximum degree and order of the GOCE geopotential model $n_{\max}$, integrated by the residual Stokes's kernel (Gerlach and Rummel 2013)

$$St^{res}(\psi) = St(\psi) - St^{n_{\max}}(\psi) \tag{11}$$

provide $N_{P_{res}}^j$. The same kernel must also be used in Eq. (7).

It will be shown in Sect. 4.1 that the indirect bias term is below 1 cm in North America for degree larger than or equal to 70 ($n_{\max} \geq 70$). Therefore, the indirect bias term can be omitted in Eq. (8) for practical computations. In this case, the datum offset δN^j is computed as a (weighted) mean of the differences between the geometric geoid heights in Eq. (9) and the gravimetric geoid heights at the GNSS benchmarks. Figure 1 shows how the geopotential difference δW_o^j is computed. It also shows that the effect of the GOCE model omission error can be assessed by means of the EGM2008 geoid (Pavlis et al. 2012) for $n > n_{\max}$.

3 Data

The Canadian GNSS benchmarks data set consists of 2,579 data points obtained from the Geodetic Survey Division (GSD) of Natural Resources Canada. From this data set, 308 points are extracted that are benchmarks with orthometric heights computed in the Nov07 adjustment using the levelling data after 1981. In addition, CGVD28 normal-orthometric heights and NAVD88 orthometric heights are available for these GNSS benchmarks. The geodetic coordinates are determined in ITRF2005, epoch 2006. The 308 GNSS benchmarks in Fig. 2 represent well the coverage of the Canadian levelling network over the mainland, and they are used for computing the mean offset of the zero height levels of CGVD28, NAVD88 and Nov07. In addition, 95 GNSS tide gauge stations on the Atlantic and Pacific coasts are added to the GNSS benchmarks. The USA data set in Fig. 3 consists of 18,399 GNSS benchmarks with orthometric heights in NAVD88 and geodetic coordinates in ITRF2005, epoch 2006.0.

For height system unification with a centimetre accuracy, it is required that the GNSS ellipsoidal heights, orthometric heights and geoid heights (i) be given in one reference frame

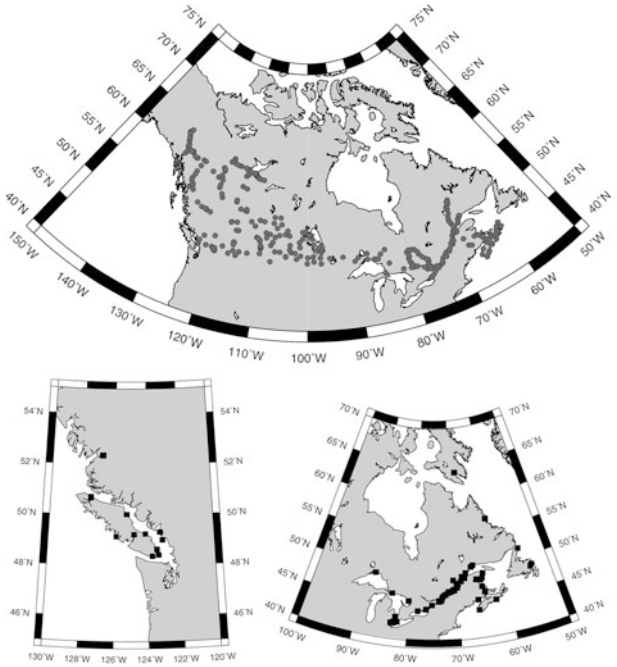

Fig. 2 A subset of 308 Canadian GNSS benchmarks and 95 tide gauges

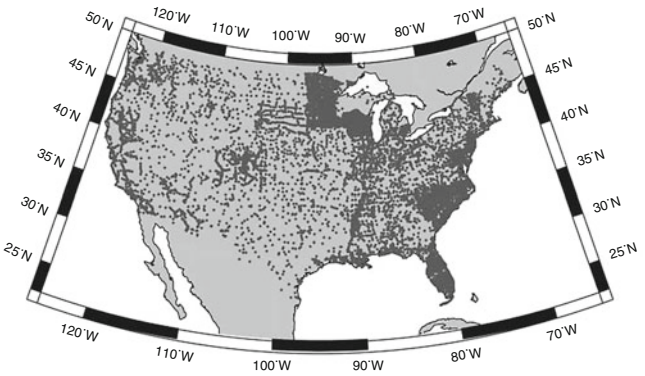

Fig. 3 GNSS benchmarks in the USA

and epoch, (ii) refer to the same reference ellipsoid, (iii) be in the same tidal system, and (iv) refer to the same epoch in areas with significant crustal motion and mass displacement. Our data sets satisfy the first three requirements. The fourth requirement cannot be easily fulfilled because it is not feasible to unify the epoch of the levelling measurements.

4 Analysis of Results

First, we discuss the effect of the indirect bias term in a simulation study for North America using rounded offset estimates of −30 cm for CGVD28 and −50 cm for NAVD88 (Amjadiparvar et al. 2012) with respect to the equipotential surface defined by $W_o = 62{,}636{,}856.00\ \mathrm{m}^2/\mathrm{s}^2$.

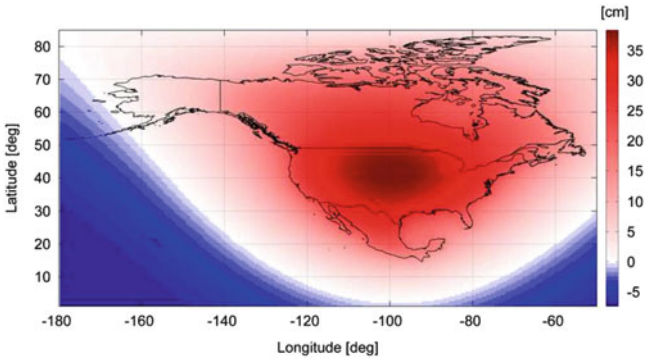

Fig. 4 Indirect bias term computed with the original Stokes's kernel

4.1 Effect of the Indirect Bias Term

The indirect bias term in Eq. (8) was evaluated with residual Stokes's kernels with $n_{\max} = 70$, 120, 150 and 200 related to the spectral resolution of existing satellite-only geopotential models; see Eq. (11). Figure 4 shows the indirect bias term over North America computed with the original Stokes's kernel. The maximum effect of 38 cm is located over the USA. Figure 5 shows the indirect bias term computed with the residual kernels. The maximum effect is less than 1 cm for all $n_{\max}$ values. Therefore, the indirect bias term can be omitted if a global geopotential model with $n_{\max} \geq 70$ is used.

4.2 Mean Datum Offsets

The computation of the mean datum offsets was performed with the GOCE model go_cons_gcf_2_tim_r3 (TIM3, Pail et al. 2011). Table 1 shows that this model has one of the smallest standard deviations of the geoid height differences at the Canadian and USA GNSS benchmarks among the 11 evaluated satellite-only geopotenial models. The difference between the standard deviations for TIM3 and EGM2008 shows the omission error of the GOCE model for its maximum degree and order (D/O) 250: 18.4 cm in Canada and 14.6 cm in the USA.

The mean datum offsets of CGVD28, NAVD88 and Nov07 are shown in Fig. 6. The offsets in Canada (CAN) are computed with the GNSS benchmarks (GNSS/BMs), GNSS tide gauges (GNSS/TGs) and the combined data set GNSS/BMs + GNSS/TGs. Two global geopotential models were used to compute the geoid heights: TIM3 up to D/O 180 and TIM3 expanded by means of EGM2008 from D/O 181 to 2190. The difference in the offsets computed by means of the two models provides an estimate of the effect of the omission error of TIM3 for the particular data point distribution. It can be expected that because the GNSS/BMs sample the

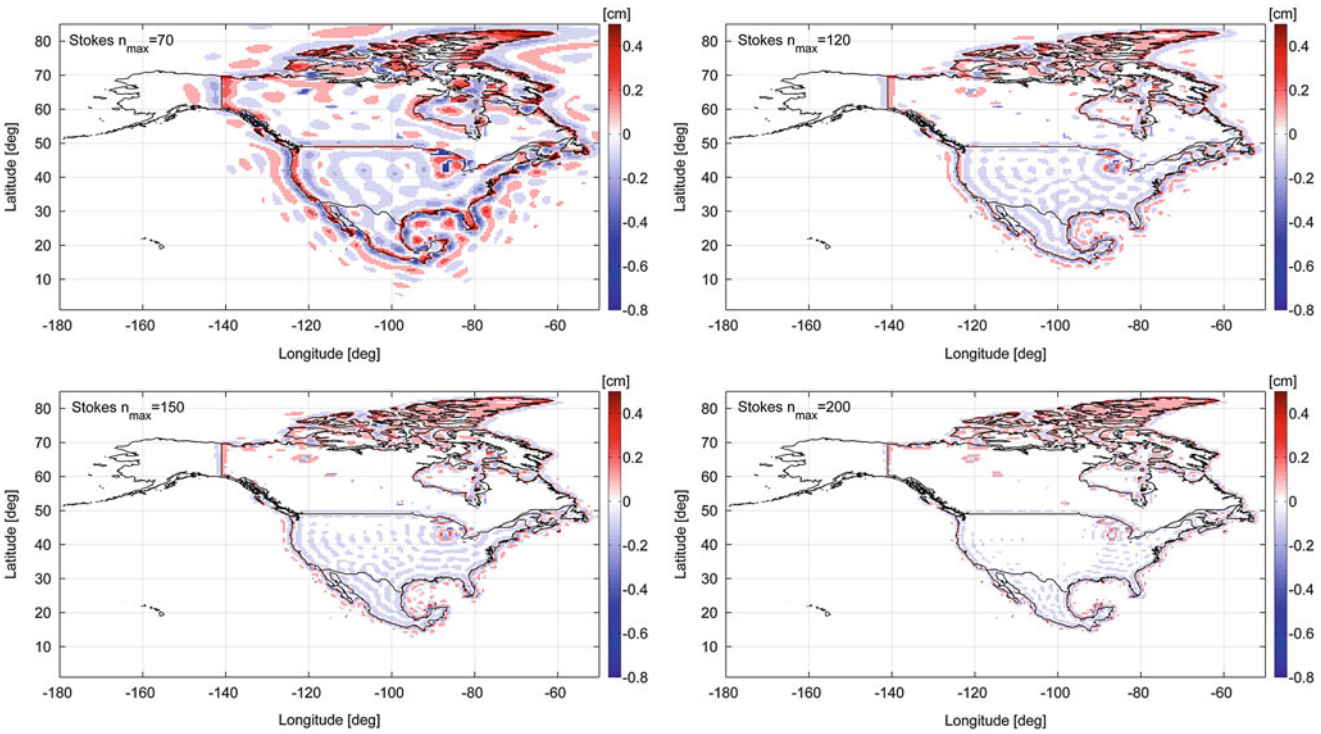

Fig. 5 The indirect bias term in North America computed with the residual Stokes's kernel with $n_{\max} = 70$, 120, 150 and 200

Table 1 Standard deviations of the geoid height differences for 11 satellite-only global geopotential models and EGM2008 evaluated in Canada and the USA; unit is cm

Model	D/O	Canada	USA
go_cons_gcf_2_dir_r3	240	32.6	45.0
go_cons_gcf_2_tim_r3	250	32.8	44.5
go_cons_gcf_2_dir_r2	240	35.1	46.3
go_cons_gcf_2_tim_r2	250	33.9	45.1
go_cons_gcf_2_tim_r1	224	36.1	47.0
eigen-6s	240	35.3	46.6
Goco03s	250	32.4	44.3
Goco02s	250	33.6	44.8
Goco01s	224	35.7	46.5
itg-grace2010s	180	43.9	57.3
eigen-5s	150	49.6	62.5
EGM2008	2190	14.2	30.4

landmasses better than the GNSS/TGs, the omission error will have a smaller effect on the offsets. This can be seen for all three offsets in Fig. 6. The difference of 13 cm between the values computed with TIM3 and TIM3 + EGM2008 using CAN GNSS/BMs is smaller than the corresponding difference of 15–21 cm computed with CAN GNSS/TGs. The USA NAVD88 offset is less affected by the omission error: the difference between the offsets computed with TIM3 and TIM3 + EGM2008 is only 2 cm. This small value is due to the much more regular and dense data coverage of the USA landmasses.

In addition to the GOCE model omission error, the systematic errors in the minimum constrained national levelling networks affect the computed offsets. NAVD88 has a very large 1.5 m tilt from the Atlantic to the Pacific coast of Canada, most likely due to the accumulation of errors in the first-order levelling network. This large tilt results in a large offset of the Canadian NAVD88 of −82 cm. The USA NAVD88 has accumulated errors in east-west and north-south directions (Wang et al. 2012) that compensate each other in the computed offset (e.g., Amjadiparvar et al. 2012). The USA NAVD88 offset is −48 cm. Nov07 is a minimum constrained datum but has a much smaller tilt because of the care taken by GSD to minimize the propagation of the levelling errors in the network adjustment. Nov07 is also defined by the mean sea level at the same fundamental tide gauge station at Rimouski, Québec, Canada. Although NAVD88 and Nov07 are defined by the same unique datum station, the computed mean offsets may not agree because NAVD88 and Nov07 are realized through different networks with different systematic levelling errors. The computed Nov07 offset is −46 cm.

The mean offset of the over-constrained CGVD28 (defined by the mean sea level at five tide gauges on the Atlantic and Pacific coasts) is affected by the regional distortions due to the piece-wise densification of the first-order lev-

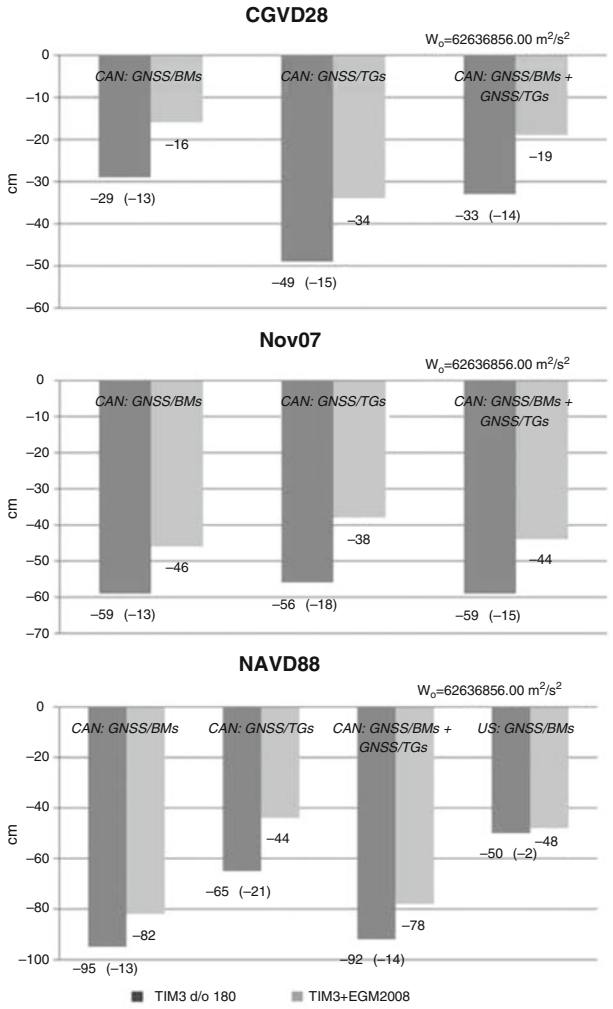

Fig. 6 Mean offsets of CGVD28, NAVD88 and Nov07 with respect to the level surface $W_o = 62{,}636{,}856.00\ \mathrm{m}^2/\mathrm{s}^2$, in cm

elling network over the years. These unknown distortions are sampled to a certain extent by the GNSS/BMs, but not by the GNSS/TGs. On the other hand, it has been shown that the mean sea level sampled by the Canadian tide gauges is approximately 20 cm above the reference surface of $W_o = 62{,}636{,}856.00\ \mathrm{m}^2/\mathrm{s}^2$ for the Pacific coast and approximately 40 cm below this surface for the Atlantic coast (Hayden et al. 2013) due to the dynamic ocean topography not taken into account in CGVD28. These differences will be reflected in the mean CGVD28 offset of −34 cm computed by means of the GNSS/TGs (see Fig. 6).

Finally, the effect of the commission error of the GOCE model of D/O 180 on the computed mean offsets is studied. This error together with the standard deviations of the GNSS ellipsoidal heights and orthometric heights comprise the stochastic information for the computation of the Nov07 offset. The inclusion of this stochastic information results in a 4 cm difference in the computed offset.

Conclusions

In this study, we presented the first results of the unification of the height datums in North America using a third generation GOCE geopotential model. Our investigations show that in North America the third generation GOCE models can be used up to degree and order 180. For this resolution, the model's performance is similar to EGM2008. The model's omission error, however, is significant. In a follow-on study, we will model the residual geoid signal using local gravity and topography information with a focus on the GNSS tide gauge stations. We will use these high-resolution geoid heights to study the regional biases of CGVD28 along the coasts with respect to the $W_o = 62{,}636{,}856.00\ \mathrm{m}^2/\mathrm{s}^2$ level surface.

Furthermore, we have shown that the indirect bias term can be omitted if a GOCE model of degree and order 180 is used in the datum offset computations. This is

because the use of a residual Stokes's kernel, which is employed since a global geopotential model provides the long wavelengths of the gravity anomalies and the geoid, diminishes the significance of the biased local gravity anomalies in the datum offset computations. As a consequence, the computational procedure is simplified enormously.

Acknowledgements This work is a contribution to the project STSE—GOCE+ Height System Unification with GOCE, funded by the European Space Agency. The Geodetic Survey Division of Natural Resources Canada, and the National Geodetic Survey, NOAA, USA, are acknowledged for the provided data sets and discussions. The satellite models are obtained from the International Centre for Global Earth Models http://icgem.gfz-potsdam.de/ICGEM/.

References

Amjadiparvar B, Rangelova EV, Sideris MG, Véronneau M (2012) North American height datums and their offsets: the effect of GOCE omission errors and systematic leveling effects. J Appl Geod 7(1):39–50. doi:10.1515/jag-2012-0034

Cannon JB (1929) Adjustment of the Precise Level Net of Canada 1928. Publication No. 28, Geodetic Survey Division, Earth Sciences Sector, Natural Resources Canada, Ottawa, Canada

European Space Agency, ESA (1999) Gravity field and steady-state ocean circulation mission. Report for mission selection of the four candidates Earth Explorer missions, ESA SP-1233(1)

Gerlach C, Rummel R (2013) Global height system unification with GOCE: a simulation study on the indirect bias term in the GBVP approach. J Geod 87:57–67. doi:10.1007/s00190-012-0579-y

Hayden T, Rangelova E, Sideris MG, Véronneau M (2014) Contribution of tide gauges for the determination of W_o in Canada, In: U. Marti (ed.), Gravity, Geoid and Height Systems, International Association of Geodesy Symposia 141, Springer International Publishing Switzerland 2014

Heiskanen WA, Mortiz H (1967) Physical geodesy. WH Freeman, San Francisco, CA. Reprint, Technical University, Graz, Austria, 1999

National Geodetic Survey, NGS (2008) The National Geodetic Survey ten-year plan: mission, vision, and strategy 2008–2018. Silver Spring, MD, U.S. Dept. of Commerce, National Oceanic and Atmospheric Administration, National Ocean Service

Pail R, Bruinsma S, Migliaccio F, Foerste C, Goiginger H, Schuh WD, Hoeck E, Reguzzoni M, Brockmann JM, Abrikosov O, Veicherts M, Fecher T, Mayrhofer R, Krasbutter I, Sanso F, Tscherning CC (2011) First GOCE gravity field models derived by three different approaches. J Geod 85:819–843

Pavlis NK, Holmes SA, Kenyon SC, Factor JK (2012) The development and evaluation of the Earth Gravitational Model 2008 (EGM2008). J Geophys Res 117, B04406. doi:10.1029/2011JB008916

Roman D, Weston ND (2012) Beyond GEOID12: implementing a new vertical datum for North America. FIG Proceedings 2012, Rome, Italy, 6–10 May 2012. http://www.fig.net/pub/fig2012/papers/ts04b/TS04B_weston_5691.pdf

Rummel R, Teunissen P (1988) Height datum definition, height datum connection and the role of the geodetic boundary value problem. Bulletin Géodésique 62:477–498

Véronneau M, Duval R, Huang J (2006) A gravimetric geoid model as a vertical datum for Canada. Geomatica 60(2):165–172

Wang YM, Saleh J, Li X, Roman DR (2012) The US Gravimetric Geoid of 2009 (USGG2009): model development and evaluation. J Geod 86:165–180. doi:10.1007/s00190-011-0506-7

Zilkoski D, Richards J, Young G (1992) Results of the general adjustment of the North American vertical datum of 1988. Surv Land Inform Syst 52(3):133–149

Using GOCE to Straighten and Sew European Local Geoids: Preliminary Study and First Results

M. Gilardoni, M. Reguzzoni, and D. Sampietro

Abstract

National geoids of neighbouring countries usually do not fit to each other along the borders. This problem is mainly due to inconsistencies between the national reference frames used to estimate local geoids: it is well known that a change in the height datum and in the reference ellipsoid causes systematic effects in terms of geoid undulation. Therefore, before merging national geoids, these effects should be estimated and removed. The availability of a global geoid coming from satellite data, such as one of the GOCE models or a GOCE-GRACE combined model, can be of great importance to solve this problem. In fact, these models are not affected by local biases since they do not make use of any ground gravity data and they are referred to a global geocentric ellipsoid. In the present work a merging strategy based on two steps is proposed. Firstly, the bias and the systematic effect due to an ellipsoidal centre variation are estimated for each national geoid by exploiting GOCE data; particular attention is dedicated to the covariance modelling of all involved quantities. Secondly, these straightened geoids are "sewn" to each other by applying a standard collocation procedure along the borders. In this way the final result is an unbiased geoid, joining in a optimal way the national models. The merging strategy is here applied to create a new geoid model for Spain, Portugal, France, Italy, Switzerland and part of the Mediterranean Sea.

Keywords

GOCE • Height datum problem • Local geoids

1 Introduction

The problem of geoid modelling is traditionally tackled in two different ways. A first approach is to define a global model in terms of coefficients of a spherical harmonic expansion (Heiskanen and Moritz 1967) describing the long wavelengths of the gravity field. This model can be based on data from satellite missions only (e.g. Mayer-Gürr 2006) or on a mixture among many data sources taken from ground, air-borne, ship-borne and space-borne gravimetry. Among the latter models, EGM2008 (Pavlis et al. 2012) is certainly the most widely used; since this model is complete up to degree and order 2159, corresponding to a spatial resolution of $5' \times 5'$, the statement that only long wavelengths are represented by global models is now questionable.

A second approach to geoid modelling is to produce local solutions (very often at a national level) based on a combination of ground gravity observations, a reference geopotential model and topographic effects, delivering grid values of geoid undulations. Sometimes a fitting to GPS-levelling data

M. Gilardoni (✉)
DICA, Politecnico di Milano, Polo Territoriale di Como,
Via Valleggio 11, 22100 Como, Italy
e-mail: maddalena.gilardoni@polimi.it

M. Reguzzoni
DICA, Politecnico di Milano,
Piazza Leonardo da Vinci 32, 20133 Milano, Italy
e-mail: mirko.reguzzoni@polimi.it

D. Sampietro
GReD, Via Valleggio 11, 22100 Como, Italy
e-mail: daniele.sampietro@g-red.eu

U. Marti (ed.), *Gravity, Geoid and Height Systems*, International Association of Geodesy Symposia 141,
DOI 10.1007/978-3-319-10837-7_29,

is performed too (Forsberg 2000) to tie the gravimetric geoid to a geometric one. In any case this solution depends on the chosen height datum, typically referred to a certain tide gauge. This choice has a direct effect on geoid values and an indirect effect on gravity observations. This inevitably implies that national geoids of neighboring countries based of different height datum definitions do not fit to each other along their borders (Rummel and Teunissen 1988; Sansó and Usai 1995; Sansó and Venuti 2002). Note that the differences cannot be attributed to the height datum only but also to the different reference ellipsoids, the different computation techniques, border effects, etc.

This height datum problem can be successfully solved using global geoids coming from satellite data only (Rummel 2002; Gerlach and Rummel 2013), because these global models are not based on any ground gravity data and are referred to a unique global geocentric ellipsoid. In particular one can use GOCE or GOCE-GRACE combined models (Pail et al. 2010, 2011) to estimate the systematic effects due to the adoption of different height datums and reference systems. Note that the same reasoning is not true in the case of EGM2008, being based on ground gravity data too; however its information can be also used in the bias determination (Gatti et al. 2013) to reduce the error estimate especially when the region under study is too small with respect to the GOCE geoid resolution, which is about 80 km.

The purpose of this work is to investigate a step-wise technique to straight (i.e. to correct long wavelength distortions) and to sew (i.e. to connect border values) local geoids into a unique one, also including the contribution of GOCE data (see also Gilardoni et al. 2013). As a matter of fact the "cleanest" way to do this merging is to correct the original ground gravity observations for height datum biases, to fix a unique reference ellipsoid and compute a geoid model using a unique processing technique. However, since original ground gravity data are not always publicly available and since this joint solution could be very heavy and lengthy from the computational point of view, the proposed strategy, though sub-optimal, is an answer to the problem of straightening and merging together already available local geoids. In particular the paper deals with the computation of a unique geoid model of Spain, Portugal, France, Italy, Switzerland and part of the Mediterranean Sea. EGM2008 geoid is used to get data outside these regions so as to limit border effects. The problem is faced from the methodological point of view in Sect. 2, while the application to real data is treated in Sect. 3. The results and the main difficulties met are summarized in the conclusions.

2 Mathematical Formulation of the Problem

In this section the two-step procedure to remove biases from local geoids and produce a unified merged model is presented. In order to work with the same quantities we decided to synthesize quasi-geoids from the global model spherical harmonic coefficients and, if necessary, to remove the topographic contribution (Heiskanen and Moritz 1967) from the available geoid models. The bias estimation is performed by applying a least-squares adjustment, while the merging of the unbiased quantities is done by means of collocation. In particular the bias B at a certain point of latitude φ and longitude λ can be modelled as (Heiskanen and Moritz 1967):

$$B(\varphi,\lambda) = c_1 + c_2 \cos\varphi \cos\lambda + c_3 \cos\varphi \sin\lambda + c_4 \sin\varphi \quad (1)$$

where c_1, c_2, c_3, c_4 are the unknown coefficients to be estimated. Note that c_1 takes into account a variation in the zero-degree term of the spherical harmonic expansion of the potential due to a variation between the actual mass of the Earth and the one of the reference ellipsoid, while c_2, c_3, c_4 represent a variation in the first degree harmonic due to the shift between the Earth and the reference ellipsoid centres.

The observations of the least-squares adjustment are the residuals r obtained by subtracting from each local quasi-geoid model ζ the unbiased low frequency contribution ζ_L coming from a satellite-only gravity model, like for example a GOCE-only solution up to a maximum degree N_L, and the high frequency contribution ζ_H coming from a high resolution global model like EGM2008:

$$r = \zeta - \zeta_L - \zeta_H \ . \quad (2)$$

In other words, representing the bias in Eq. (1) as the product between a design matrix A and the vector x of the unknown coefficients c_1, c_2, c_3, c_4, Eq. (2) becomes:

$$r = Ax + e_L + e_H + v \quad (3)$$

where e_L and e_H are the low frequency and the high frequency error respectively, while v is the noise of the local quasi-geoid model. Note that if the high frequency component is not removed from the data, then it can "hide" or somehow modify the discontinuities due to the different biases. On the other hand if the high frequency component is computed from a biased global model mainly based on ground gravity observations, we should introduce an additional systematic effect in Eq. (3). However it can be shown that this term is negligible if N_L is sufficiently high (Gatti et al. 2013).

Table 1 Characteristics of the local quasi-geoid models used in this study

Model	Author	Year	Source	Availability	Resolution
Ibergeo2008	M. J. Sevilla	2008	IGeS website	Public	$1.7' \times 1.7'$
French quasi-geoid	H. Duquenne	1997	IGeS website	On demand	$1.5' \times 1.5'$
CHGeo2004	U. Marti	2004	Swiss Topo	Private	$30'' \times 30''$
ITALGEO2005	R. Barzaghi	2005	Politecnico di Milano	Private	$3' \times 3'$
GEOMED	F. Sansó	1994	IGeS website	Public	$5' \times 5'$

In order to estimate the bias parameters vector x it is also important to properly model the stochastic structure of the residuals r:

$$C_r = C_{e_L} + C_{e_H} + C_v \tag{4}$$

where C_{e_L}, C_{e_H} and C_v are the error variance-covariance matrices of the low frequency part, the high frequency part and the local quasi-geoid model respectively, assuming that the three contributions are independent of one another.

In the absence of better information, the local quasi-geoid model error is assumed to be white noise and therefore C_v is a diagonal matrix. In order to calibrate the variance of this "fictitious" white noise a statistical chi-square test is set up requiring that the a posteriori scale factor of the variance-covariance matrix in Eq. (4) is equal to 1 with a certain significant level. Actually the hypothesis under test has been relaxed requiring that the a posteriori scale factor is smaller than 1.25, in this way accepting variations in the C_r matrix up to 25 %; these variations can be mainly attributed to omitted terms in the deterministic bias model of Eq. (1), because we assume that the error variance-covariance matrices of the global models are already calibrated. The white noise variance is then tentatively increased until the test is accepted. It has to be stressed that this white noise hypothesis is a strong simplification that leads to an overestimated error variance and affects the results as we will discuss in the next section.

The second step of the procedure consists in a standard collocation approach where the input data are now the residuals with respect of the satellite-only gravity model, corrected by the estimated biases:

$$s = \zeta - \zeta_L - A\hat{x} \; . \tag{5}$$

Differently from the bias estimation, here it is no more necessary to remove the contribution of the high frequency global model ζ_H. The variance-covariance matrix of s is therefore given by:

$$C_s = C_{\zeta_H} + C_{e_L} + C_v \tag{6}$$

where C_{ζ_H} is the high frequency signal variance-covariance matrix computed on the basis of a degree variance model, e.g. Kaula (1966) or Tscherning and Rapp (1974). In addition to producing an easier-to-use unified model, the goal of this step is to fully exploit the GOCE information that cannot be limited to the bias estimation but can be also used to "glue" the low frequencies of the local quasi-geoid models.

3 Case Study

The methodology has been applied to merge some available quasi-geoids in the South-West part of Europe, namely the quasi-geoid models of the Iberian peninsula, France, Switzerland, Italy and the Mediterranean Sea. The characteristics of these models are reported in Table 1. As for the global satellite-only unbiased model ζ_L we use a GOCE-only space-wise solution (Migliaccio et al. 2011) and we model C_{e_L} using an order-wise block covariance matrix. The high frequency signal, when required, is taken from EGM2008 and its error covariance C_{e_H} is modelled by using the spherical harmonic coefficient error variances and the point-wise geoid error variances that are publicly available in the EGM2008 website (Gilardoni et al. 2013).

By applying the procedure described in Sect. 2 we calibrate the white noise variances of each local quasi-geoid model and estimate the unknown coefficients of Eq. (1). The resulting systematic effects are shown in Fig. 1. Note that Corsica and Sardinia have been separately analysed because we assumed they have their own height datum.

Once the biases B have been estimated and removed from the original quasi-geoid observations, collocation has been applied to predict a merged geoid with resolution $3' \times 3'$. Due to computational problems the prediction area has been divided into 140 patches of $5.5° \times 5.5°$ size with 1.5° overlap. For each patch, grid values are predicted only for the central part of $2.5° \times 2.5°$ size obtaining the subdivision shown in Fig. 2. A synthesis from the EGM2008 model, up to its maximum degree, has been performed to have observations also in the area not covered by data and thus avoiding border effects. The resulting merged quasi-geoid model in South-West Europe is shown in Fig. 3, while its prediction error is displayed in Fig. 4.

To better visualize the effect of this straightening and merging procedure, the new unified quasi-geoid and the original local models are compared along some selected profiles; the comparison is performed in terms of residuals with respect to GOCE synthesized quasi-geoid values. For example, taking a profile along a parallel with latitude equal to 42° N

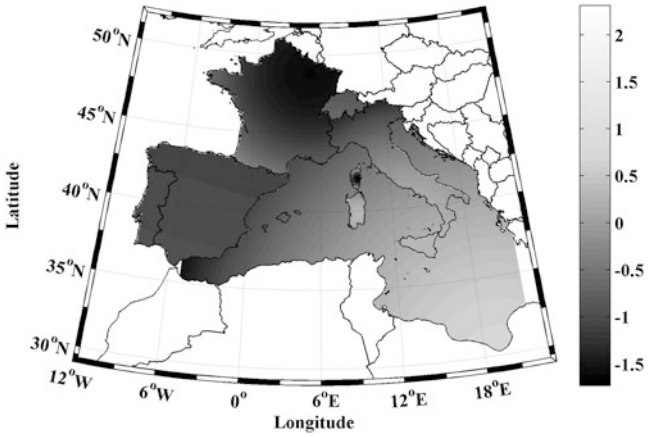

Fig. 1 Estimated systematic effects of each local quasi-geoid model in the region under study (units: m)

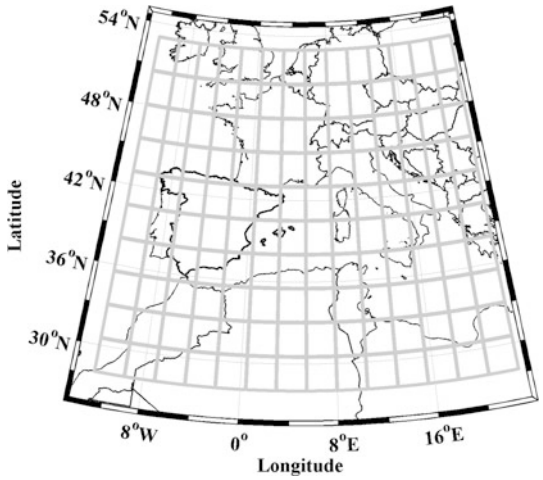

Fig. 2 Patches used for partitioning the area of interest

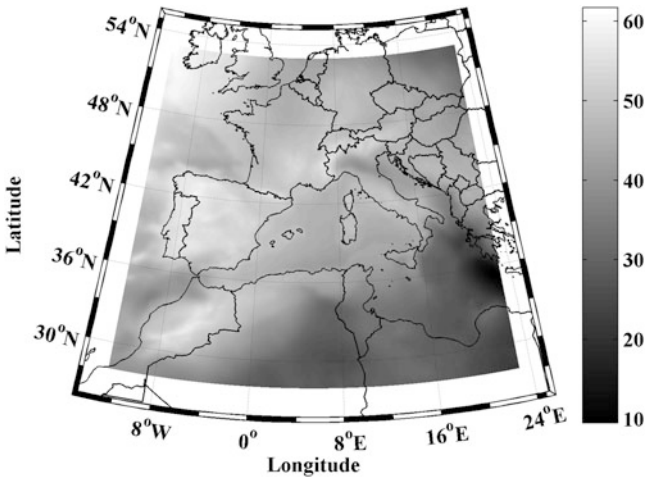

Fig. 3 The unified quasi-geoid (units: m)

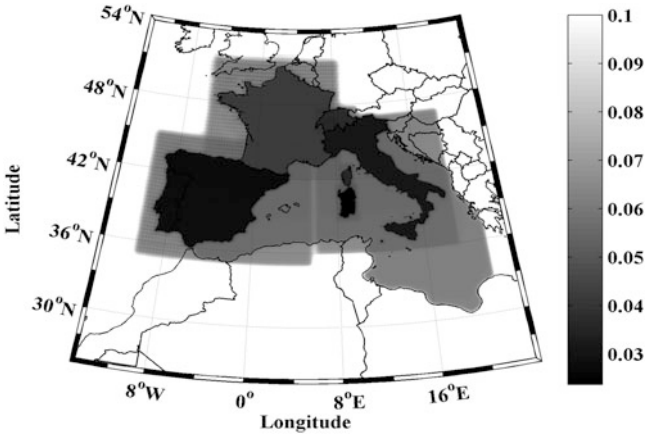

Fig. 4 The unified quasi-geoid accuracy in terms of standard deviation (units: m)

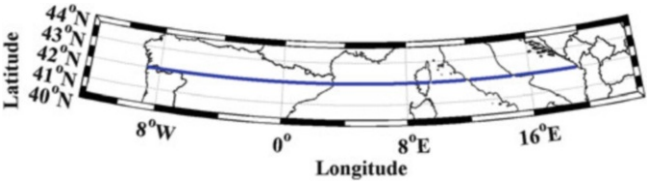

Fig. 5 Profile along a parallel with latitude equal to 42° N

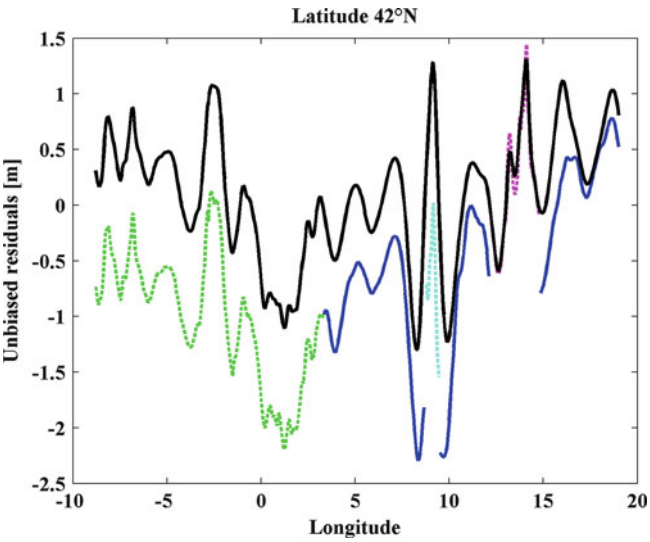

Fig. 6 Residuals with respect to GOCE data along the profile of Fig. 5. The merged solution is in *black* (solid line), while the local solutions are displayed with different colours: Ibergeo2008 is represented in *green* (dashed line), GEOMED in *blue* (solid line), ITALGEO2005 in *pink* (dashed line) and the residuals for Corsica in *cyan* (dashed line). (Color figure online)

(Fig. 5) one can immediately realize that the height datum of the Mediterranean Sea is quite consistent with the Iberian one but significantly different from the ones of Corsica and Italy, that by the way are different from each other (Fig. 6).

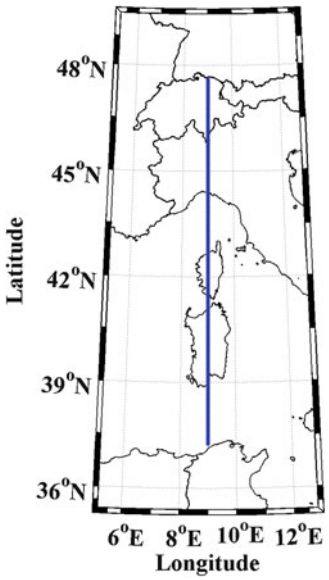

Fig. 7 Profile along a meridian with longitude equal to 9°E

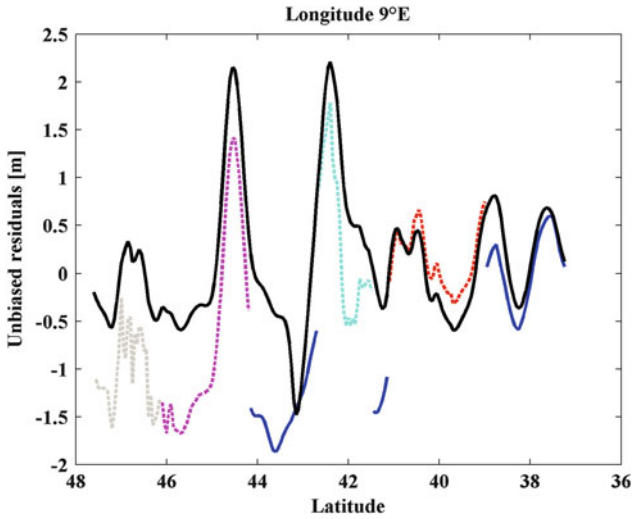

Fig. 8 Residuals with respect to GOCE data along the profile of Fig. 7. The merged solution is in *black* (solid line), while the local solutions are displayed with different colours: CHGeo2004 is represented in *gray* (dashed line), ITALGEO2005 in *pink* (dashed line), GEOMED in *blue* (solid line), the residuals for Corsica in *cyan* (dashed line) and the residuals for Sardinia in *red* (dashed line). (Color figure online)

Apart from removing discontinuities between local models, the new quasi-geoids is obtained by straightening the single solutions and this can be seen along the profile noting that the correction is decreasing from east to west.

Other interesting considerations can be drawn by taking a profile along a meridian with longitude equal to 9°E (Figs. 7 and 8). Apart from the already discussed bias and tilt corrections, here one can easily observe that the new unified quasi-geoid is smoother than the original ones. This is not expected because in principle low frequencies should be taken from GOCE, high frequencies should come from original local quasi-geoid data and the merging between the two should be controlled by the covariance modelling in the collocation procedure. As a consequence a strong approximation in the covariance modelling can lead to a non-optimal combination. Here the error of the local quasi-geoids has been modelled with a white noise (which is certainly not the case since the input quasi-geoids are not observed but processed data) and the chi-square test for calibrating their variances leads to sigma values of the order of 10 cm or even more. These values are obviously too high, giving rise to an over-regularization, and therefore an over-smoothing, in the collocation procedure used for the computation of the unified solution. On the other hand, taking for granted an a priori smaller error variance of the local quasi-geoids would preserve the high frequencies in the combined solution, but would have the side effect of penalizing too much the GOCE information which would not be able anymore to produce significant estimates of the bias coefficients. This dilemma cannot find a solution as long as the error of the local quasi-geoids is assumed to be white noise; a more accurate modelling is required in such a way that the different sources of information are properly weighted in the frequency spectrum.

Conclusions

In this work a first attempt to merge local geoids, without starting from the original ground gravity data and exploiting the additional information of a GOCE model to solve the height datum problem, has been performed. The proposed procedure basically comprises a first straightening of local geoids and a subsequent merging of them. However it has to be underlined that this study is still preliminary because many simplifications have been introduced; for instance only distortions due to a different height datum and a different reference ellipsoid have been taken into account. The main problem seems to be the modelling of the error covariance of the local geoids; the standard solution of using white noise looks too simplified and leads to a non optimal combination between data sources, as arises from the case study of the unbiased unified geoid of the south-western Europe.

As a conclusion one can state that the proposed method can provide a feasible solution from the computational point of view to the height datum problem at a local/regional level. In a future work a better description of the bias deterministic model and of the data covariance structure is however required to improve the quality of the results.

Acknowledgements The authors would like to thank Dr. Urs Marti and Prof. Riccardo Barzaghi for providing the Swiss and the Italian geoid models, respectively.

References

EGM2008 website: http://earth-info.nga.mil/GandG/wgs84/gravitymod/egm2008

Forsberg R (2000) Draping of geoids to GPS observations. IGeS Geoid School, Johor, Malaysia. IGeS Publications, Milan

Gatti A, Reguzzoni M, Venuti G (2013) The height datum problem and the role of satellite gravity models. J Geod 87(1):15–22. doi:10.1007/s00190-012-0574-3

Gerlach C, Rummel R (2013) Global height system unification with GOCE: a simulation study on the indirect bias term in the GBVP approach. J Geod 87(1):57–67. doi:10.1007/s00190-012-0579-y

Gilardoni M, Reguzzoni M, Sampietro D (2013) A least-squares collocation procedure to merge local geoids with the aid of satellite-only gravity models: The Italian-Swiss geoids case study. Boll Geofis Teor Appl 54(4):303–319

Gilardoni M, Reguzzoni M, Sampietro D, Sansò F (2013) Combining EGM2008 with GOCE gravity models. Boll Geofis Teor Appl 54(4):285–302

Heiskanen WA, Moritz H (1967) Physical geodesy. Freeman, San Francisco

IGeS website: http://www.iges.polimi.it

Kaula WM (1966) Theory of satellite geodesy. Blaisdell, Waltham

Mayer-Gürr T (2006) Gravitationsfeldbestimmung aus der Analyse kurzer Bahnbögen am Beispiel der Satellitenmissionen CHAMP und GRACE. PhD thesis, Universitäts-und Landesbibliothek Bonn

Migliaccio F, Reguzzoni M, Gatti A, Sansó F, Herceg M (2011) A GOCE-only global gravity field model by the space-wise approach. In: Proceedings of the 4th international GOCE user workshop, 31 March–1 April 2011, Munich, ESA SP-696. ISBN: 978-92-9092-260-5, ISSN: 1609-042X

Pail R, Goiginger H, Schuh WD, Höck E, Brockmann JM, Fecher T, Gruber T, Mayer-Gürr T, Kusche J, Jäggi A, Rieser D (2010) Combined satellite gravity field model GOCO01S derived from GOCE and GRACE. Geophys Res Lett 37(20):L20,314

Pail R, Bruinsma S, Migliaccio F, Förste C, Goiginger H, Schuh WD, Höck E, Reguzzoni M, Brockmann JM, Abrikosov O, Veicherts M, Fecher T, Mayerhofer R, Kransbutter I, Sansó F, Tscherning CC (2011) First GOCE gravity field models derived by three different approaches. J Geod 85(11):819–843. doi: 10.1007/s00190-011-0467-x

Pavlis NK, Holmes SA, Kenyon SC, Factor JK (2012) The development and evaluation of the Earth gravitational model 2008 (EGM2008). J Geophys Res 117(B04406). doi:10.1029/2011JB008916

Rummel R (2002) Global unification of height systems and GOCE. In: Sideris MG (ed) Gravity, geoid and geodynamics 2000. IAG symposia, vol 123. Springer, Berlin, pp 13–20

Rummel R, Teunissen P (1988) Height datum definition, height datum connection and the role of the geodetic boundary value problem. Bull Géod 62(4):477–498

Sansó F, Usai S (1995) Height datum and local geodetic datums in the theory of geodetic boundary value problems. Allgemeine Vermessung-Nachrichten (AVN) 102(8–9):343–355

Sansò F, Venuti G (2002) The height datum/geodetic datum problem. Geophys J Int 149(3):768–775

Tscherning CC, Rapp RH (1974) Closed covariance expressions for gravity anomalies, geoid undulations, and deflections of the vertical implied by anomaly degree-variance models. OSU Report No. 208, Columbus

Combination of Geometric and Orthometric Heights in the Presence of Geoid and Quasi-geoid Models

C. Kotsakis and I. Tsalis

Abstract

A generalization of the well-known relationship between geometric and orthometric heights is presented in this paper. The advantage of our revised formulation is that, instead of the non-determinable true orthometric heights, it employs the (most commonly used in geodetic practice) Helmert orthometric heights. Based on standard concepts from physical geodesy theory and straightforward analytical derivations, we obtain a set of linearized constraints relating the geometric and Helmert orthometric heights in the presence of a geoid or quasi-geoid model. These constraints should be theoretically satisfied in the case of errorless data and thus they provide a standard framework for the joint analysis and the quality testing of heterogeneous heights in a terrestrial network.

Keywords

Geoid • Quasi-geoid • Helmert orthometric heights • Vertical reference frame • Height transformation

1 Introduction

Since the advent of space-geodetic positioning techniques, the joint analysis of heterogeneous height data has become an important tool for many geodetic applications. The most prominent example is the combination of GPS derived geometric heights with spirit levelled orthometric heights in the presence of a geoid model, which has been a standard method for the quality testing of global geopotential models (or terrestrial leveling networks) and the implementation of unification schemes between traditional and geoid-based vertical datums (e.g. Rapp 1994; Pan and Sjöberg 1998; Burša et al. 2004; Sánchez 2007; Amos and Featherstone 2009; Kotsakis and Katsambalos 2010). The underlying principle relies on the low-order parameterization of the theoretical constraint (Heiskanen and Moritz 1967, p. 187)

$$h - N - H = 0 \tag{1}$$

and the assessment of the results from its least squares adjustment over a network of GPS/leveling benchmarks. For most applications the emphasis is given on the analysis of the adjusted residuals in terms of (i) their statistical characteristics that indicate the combined accuracy level of the different height types, and (ii) their spatial modeling that facilitates the identification of local systematic distortions in the geoid model and/or the leveled orthometric heights. The estimated parameters from the aforementioned adjustment do not usually carry any theoretical or practical relevance, other than providing the overall trend of the heterogeneous height differences in the underlying network due to hidden biases and long-wavelength data errors. Indeed, the trend modeling schemes that are used in practice for the analysis of the height differences *h-N-H* are mostly empirical (e.g. bias/tilt models, polynomial surfaces, Fotopoulos 2003) without considering

C. Kotsakis (✉) • I. Tsalis
Department of Geodesy and Surveying, Aristotle University of Thessaloniki, Thessaloniki, 541 24, Greece
e-mail: kotsaki@topo.auth.gr

U. Marti (ed.), *Gravity, Geoid and Height Systems*, International Association of Geodesy Symposia 141,
DOI 10.1007/978-3-319-10837-7_30,

any geodetically important principles for vertical reference systems and their realizations from different data sources. The aim of this paper is to revise the theoretical constraint between geometric, orthometric and geoid heights beyond the simplified form of Eq. (1), thus providing a general parametric model that can be used for the joint analysis of heterogeneous height data in terrestrial networks. Our treatment is confined to a theoretical discussion of the basic principles and the motivation for such a revised formulation in the context of the combination problem of Helmert-type orthometric heights not only with a geoid model (as it is usual case in the geodetic literature) but also with a quasi-geoid model.

2 Fundamental Relationship Between Geometric and Orthometric Heights

The theoretical equation relating the geometric and orthometric heights in the presence of a geoid model has the general form

$$h - N - H = \frac{\delta W_{\mathrm{o}}}{g^{(W_{\mathrm{o}})}} \tag{2}$$

where the meaning of each height type is shown in Fig. 1. The term δW_{o} refers to the geopotential difference between (i) the local vertical datum (LVD) defining the zero-height level of the orthometric heights and (ii) the equipotential surface which is realized by the geoid model, whereas $g^{(W_{\mathrm{o}})}$ denotes the gravity value on the geoid as depicted in Fig. 1.

Essentially the above formula quantifies, within a linear approximation, the vertical separation between the equipotential surfaces $W = W_{\mathrm{o}}^{\mathrm{LVD}}$ and $W = W_{\mathrm{o}}$ using three different types of geodetic "observables". Its linearization error is negligible provided that the two surfaces are not separated by more than few meters, a fact that can be ensured for any reasonable geoid model in relation with most existing vertical datums.[1] The non-parallelism of these equipotential surfaces is reflected through the presence of the non-constant gravity value $g^{(W_{\mathrm{o}})}$ in Eq. (2). In fact, the gravity variation on the geoid can cause an almost mm-level dispersion in the vertical offset *h-N-H*, mostly over very large distances (>10,000 km). For most practical applications, however, we may replace the geoidal gravity with a conventional mean gravity value (g or γ) without causing any notable modeling error in Eq. (2).

[1] If the geoid model does not include a zero-degree term then the W_{o} value is solely dictated by the normal gravity potential of the underlying reference ellipsoid and the mass difference between the actual Earth and the reference ellipsoid, i.e. $W_{\mathrm{o}} = f(U_{\mathrm{o}}, \delta M)$.

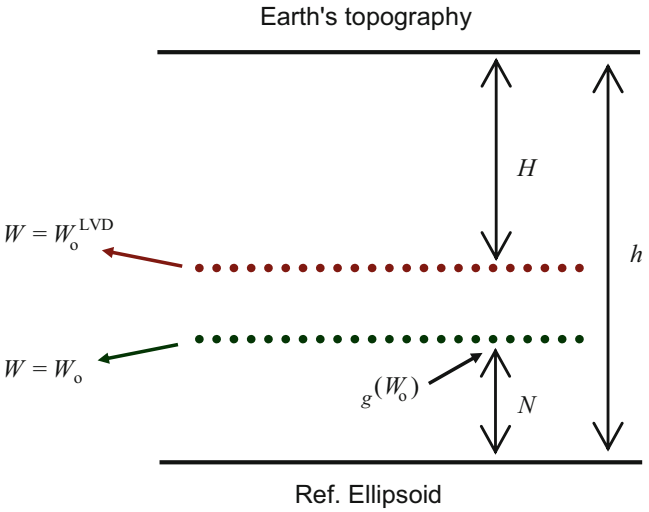

Fig. 1 The general relationship between the geometric and orthometric heights in the presence of a geoid model

The theoretical validity of the previous relationship relies on two basic assumptions. Firstly, the deflection of the vertical on the Earth's surface is ignored so that the geometric and orthometric heights can be treated as straight distances along the same normal direction. The approximation error in Eq. (2) due to this simplification remains below the mm level and it is thus negligible for most practical applications (Jekeli 2000, p. 15). Secondly, the geometric height and the geoid height should refer to a common geodetic reference system with respect to the same Earth reference ellipsoid so that Eq. (2) remains free of any datum related inconsistencies. This second assumption includes also the requirement that the permanent tide effect and other geophysical loading phenomena are treated and corrected in a consistent way among the heterogeneous height types.

3 Revised Theoretical Constraint for Geometric and Orthometric Heights

The (true) orthometric height is not a determinable physical quantity from geodetic measurements since it depends on the unknown mass distribution within the Earth. Therefore, it would be useful to replace Eq. (2) with a more realistic, yet equally rigorous, theoretical constraint which incorporates the operational type of Helmert orthometric heights.

Based on the definition of the true and Helmert orthometric heights (Heiskanen and Moritz 1967, Chap. 4), we have the following relationship between them

$$H = \left(\frac{\overline{g}^{\mathrm{helm}}}{\overline{g}} \right) H^{\mathrm{helm}} \tag{3}$$

where $\overline{g}$ denotes the average gravity along the actual plumb-line between the Earth's surface and the zero-height reference surface of the vertical datum (i.e. $W = W_o^{\mathrm{LVD}}$). The term $\overline{g}^{\mathrm{helm}}$ corresponds to a conventional approximation of $\overline{g}$ that is determined through the Poincare-Prey gravity reduction according to the general formula (ibid. p. 167)

$$\overline{g}^{\mathrm{helm}} = g + 0.0424\, H^{\mathrm{helm}} \tag{4}$$

where g is the gravity value on the Earth's surface given in Gal and H^{helm} is the Helmert orthometric height in km; for more details see also Jekeli (2000). From the combination of Eqs. (2) and (3) the following equation is obtained

$$h - N - H^{\mathrm{helm}} = \frac{\overline{g}^{\mathrm{helm}} - \overline{g}}{\overline{g}}\, H^{\mathrm{helm}} + \frac{\delta W_{\mathrm{o}}}{g^{(W_{\mathrm{o}})}} \tag{5}$$

which corresponds to the rigorous constraint for geometric and Helmert orthometric heights in the presence of a geoid model. Other conventional types of orthometric heights (e.g. Niethammer, Mader) may also be used with Eq. (5) by modifying appropriately the scale factor of Eq. (3).

The above constraint emulates a transformation model between different vertical reference frames (VRFs) in the following sense

$$H^{\mathrm{VRF2}} - H^{\mathrm{VRF1}} = \lambda\, H^{\mathrm{VRF1}} + \mu \tag{6}$$

where λ is a differential scale factor relating the two frames and μ is the vertical offset of their zero-height reference surfaces. In our case, the first frame (VRF1) refers to the Helmert orthometric heights in a local vertical datum while the second frame (VRF2) is realized through the GPS derived orthometric heights with respect to a geoid model. Further remarks on the VRF transformation aspects related to the rigorous constraint in Eq. (5) will be given in Sect. 5.

4 Theoretical Constraint for Geometric and Orthometric Heights in the Presence of a Quasi-geoid Model

Let us consider the well-known theoretical relationship between geoid and quasi-geoid heights (Heiskanen and Moritz 1967, p. 326)

$$N = \zeta + \frac{\overline{g}' - \overline{\gamma}}{\overline{\gamma}}\, H' \tag{7}$$

where the (true) orthometric height H' refers to the geoidal equipotential surface $W{=}W_{\mathrm{o}}$ and it should be distinguished from the (true) orthometric height H which was introduced in Eqs. (2)–(3) and refers to the equipotential surface $W = W_{\mathrm{o}}^{\mathrm{LVD}}$ of a local vertical datum (see Fig. 1). The term $\overline{g}'$ denotes the average gravity along the actual plumb-line between the Earth's surface and the geoidal equipotential surface, whereas $\overline{\gamma}$ is the average normal gravity along the normal plumb-line between the telluroid and the reference ellipsoid. For more details on the conversion between geoid and quasi-geoid heights, see Flury and Rummel (2009).

Starting from the rigorous integral expression that defines the average gravity $\overline{g}'$, we have

$$\begin{aligned}
\overline{g}' &= \tfrac{1}{H'} \int_{W=W_o}^{P} g\, dH \\
&= \left(\tfrac{1}{H'} \int_{W=W_o}^{W=W_o^{\mathrm{LVD}}} g\, dH \right) + \left(\tfrac{1}{H'} \int_{W=W_o^{\mathrm{LVD}}}^{P} g\, dH \right) \\
&= \tfrac{\delta W_{\mathrm{o}}/g^{(W_{\mathrm{o}})}}{H'} \left(\tfrac{1}{\delta W_{\mathrm{o}}/g^{(W_{\mathrm{o}})}} \int_{W=W_o}^{W=W_o^{\mathrm{LVD}}} g\, dH \right) \\
&\quad + \tfrac{H}{H'} \left(\tfrac{1}{H} \int_{W=W_o^{\mathrm{LVD}}}^{P} g\, dH \right) = \tfrac{\delta W_{\mathrm{o}}/g^{(W_{\mathrm{o}})}}{H'}\, \overline{g}^{(\delta W_{\mathrm{o}})} + \tfrac{H}{H'}\, \overline{g}
\end{aligned} \tag{8}$$

where $\overline{g}^{(\delta W_{\mathrm{o}})}$ denotes the average gravity along the vertical segment between the equipotential surfaces $W = W_{\mathrm{o}}$ and $W = W_{\mathrm{o}}^{\mathrm{LVD}}$ while the rest of the terms were already introduced in the previous sections.

Substituting the result of Eq. (8) into Eq. (7) and considering that the orthometric heights H and H' differ by the amount $\delta W_{\mathrm{o}}/g^{(W_{\mathrm{o}})}$ (within a linear approximation), we have

$$N = \zeta + \frac{\overline{g} - \overline{\gamma}}{\overline{\gamma}}\, H + \frac{\overline{g}^{(\delta W_o)} - \overline{\gamma}}{\overline{\gamma}}\, \frac{\delta W_o}{g^{(W_o)}} \tag{9}$$

and by replacing H according to Eq. (3), we obtain the relationship

$$N = \zeta + \frac{\overline{g}^{\mathrm{helm}}\,(\overline{g} - \overline{\gamma})}{\overline{g}\,\overline{\gamma}}\, H^{\mathrm{helm}} + \frac{\overline{g}^{(\delta W_o)} - \overline{\gamma}}{\overline{\gamma}}\, \frac{\delta W_{\mathrm{o}}}{g^{(W_{\mathrm{o}})}} \tag{10}$$

Finally, if we combine the last equation with Eq. (5) we get the result

$$h - \zeta - H^{\mathrm{helm}} = \frac{\overline{g}^{\mathrm{helm}} - \overline{\gamma}}{\overline{\gamma}}\, H^{\mathrm{helm}} + \frac{\overline{g}^{(\delta W_o)}}{\overline{\gamma}}\, \frac{\delta W_{\mathrm{o}}}{g^{(W_{\mathrm{o}})}} \tag{11}$$

Since the equipotential surfaces $W = W_{\mathrm{o}}$ and $W = W_{\mathrm{o}}^{\mathrm{LVD}}$ do not deviate by more than few meters, it is reasonable to assume that $\overline{g}^{(\delta W_o)} \simeq g^{(W_{\mathrm{o}})}$ without causing any notable error in the last equation. More specifically, we have that

$$\frac{\overline{g}^{(\delta W_o)}}{\overline{\gamma}}\, \frac{\delta W_{\mathrm{o}}}{g^{(W_{\mathrm{o}})}} = \left(\frac{\overline{g}^{(\delta W_o)} - g^{(W_{\mathrm{o}})}}{g^{(W_{\mathrm{o}})}} \right) \frac{\delta W_{\mathrm{o}}}{\overline{\gamma}} + \frac{\delta W_{\mathrm{o}}}{\overline{\gamma}} \simeq \frac{\delta W_{\mathrm{o}}}{\overline{\gamma}} \tag{12}$$

and thus Eq. (11) is practically equivalent to

$$h - \zeta - H^{\text{helm}} = \frac{\overline{g}^{\text{helm}} - \overline{\gamma}}{\overline{\gamma}} H^{\text{helm}} + \frac{\delta W_{\text{o}}}{\overline{\gamma}} \tag{13}$$

The above relationship corresponds to a theoretical constraint for geometric and Helmert orthometric heights *in the presence of a quasi-geoid model*. It resembles a frame transformation model for physical heights in a similar sense as Eq. (6), where the first frame (VRF1) refers to the Helmert orthometric heights in a local vertical datum while the second frame (VRF2) is realized through the GPS derived normal heights with respect to a quasi-geoid model.

Interestingly enough, the terms $\overline{g}$ and $g^{(W_{\text{o}})}$ which appear in the geoid-related constraint of Eq. (5) (see previous section) have been now replaced by the mean normal gravity $\overline{\gamma}$. The latter is a computable quantity in terms of a truncated power series expansion of the station's normal height H^* (Jekeli 2000, Eq. 29)

$$\overline{\gamma} = \gamma \left(1 - \left(1 + f + \frac{\omega^2 a^2 b}{GM} - 2f \sin^2\varphi\right) \frac{H^*}{a} + \left(\frac{H^*}{a}\right)^2 + \ldots\right) \tag{14}$$

where γ is the normal gravity on the reference ellipsoid at the geodetic latitude (φ) of the underlying station, a, b and f denote the length of the semi-major and semi-minor axes and the flattening of the reference ellipsoid, and finally ω and GM correspond to the rotational velocity and the gravitational constant of the normal gravity field. In the context of Eq. (13), the required normal height H^* for the implementation of the previous formula can be taken as the difference between the geometric height (h) and the height anomaly (ζ) from the available quasi-geoid model.

5 Discussion

A modification of the well-known theoretical relationship between geometric and orthometric heights (see Eq. (1)) was presented in the preceding sections. The advantage of our revised formulation is that, instead of the non-determinable true orthometric heights, it employs the (most commonly used) Helmert orthometric heights in conjunction with a gravimetric geoid or quasi-geoid model. The corresponding constraints given in Eqs. (5) and (13) should be theoretically satisfied in the case of errorless data, and thus they provide a standard modeling framework for the joint analysis of heterogeneous heights in a terrestrial network.

Evidently, the height residuals $h - N - H^{\text{helm}}$ or $h - \zeta - H^{\text{helm}}$ will always contain a terrain-correlated part due to the difference of the "vertical metric" that is associated with the physical heights H^{helm} and $h - N$ (or $h - \zeta$). In reality, though, the terrain-correlated part of these residuals should not be attributed solely to the different vertical metrics as implied by the respective constraints (5) and (13), but it is also caused by hidden systematic errors which inflict an additional scale discrepancy among the heterogeneous height data.

Both of the derived constraints resemble a 1D similarity-like transformation between different vertical frame realizations; see Eq. (6). However, the height transformation parameters which are implied by the analytic forms of these constraints are not spatially invariant and thus Eq. (6) represents only a simplified approximation of the rigorous transformation between the underlying VRFs. More specifically,

- the spatial variation of the translation terms $\delta W_{\text{o}}/g^{(W_{\text{o}})}$ and $\delta W_o/\overline{\gamma}$ is negligible even in large networks and their effect can be safely replaced by a mean vertical offset μ, but
- the spatial variation of the scaling factors $\left(\overline{g}^{\text{helm}} - \overline{g}\right)/\overline{g}$ and $\left(\overline{g}^{\text{helm}} - \overline{\gamma}\right)/\overline{\gamma}$ on the Earth's surface may have a considerable contribution to the respective height residuals $h - N - H^{\text{helm}}$ and $h - \zeta - H^{\text{helm}}$, and it can create a significant nonlinear systematic behavior in their values.

Nonetheless, the simplified model in Eq. (6) can be effectively used for the least squares de-trending of heterogeneous height data and the assessment of their low-order systematic differences. Depending on the particular type of gravity field information that we have available (i.e. geoid or quasi-geoid heights), the following alternative forms of "observation equations" can be devised:

$$\begin{Bmatrix} h_i - N_i - H_i^{\text{helm}} \\ h_i - \zeta_i - H_i^{\text{helm}} \end{Bmatrix} = \begin{Bmatrix} \lambda \\ \lambda' \end{Bmatrix} H_i^{\text{helm}} + \delta W_{\text{o}} \begin{Bmatrix} 1/g^{(W_{\text{o}})} \\ 1/\overline{\gamma}_i \end{Bmatrix} + \begin{Bmatrix} v_i \\ v_i' \end{Bmatrix} \tag{15}$$

which are deduced from Eqs. (5) and (13) by replacing the pointwise scaling factors with a "global" scale-change parameter. The terms v_i and v_i' contain the total data noise and other systematic effects (including of course the spatial irregularities of the scaling factors $\left(\overline{g}^{\text{helm}} - \overline{g}\right)/\overline{g}$ and $\left(\overline{g}^{\text{helm}} - \overline{\gamma}\right)/\overline{\gamma}$ over the test network) which cannot be absorbed by the unknown parameters λ, or alternatively λ', and δW_{o}. Note that the latter will absorb not only the actual offset of the involved reference surfaces (i.e. $W \neq W_{\text{o}}^{\text{LVD}}$) but it will also be strongly affected by data systematic errors in spatial wavelengths that overly exceed the coverage of the test area. Anyhow, the results from the least squares adjustment of either version of Eq. (15) can support the conventional quality testing of global or regional gravity field models in GPS/leveling networks, as well as the assessment of the vertical frame consistency between the Helmert orthometric heights and the GPS/geoid orthometric heights (or the

GPS/quasi-geoid normal heights) over a number of leveling benchmarks.

Conclusions

Our approach in this paper instigates a unified scheme with which the geometric and Helmert orthometric heights can be jointly analyzed and tested either with a geoid or quasi-geoid model. The second option may seem peculiar and in conflict with Molodensky's theoretical framework (Heiskanen and Moritz 1967, Chap. 8), yet it is fully justified on the basis of the fundamental constraint that was derived in Sect. 4. In fact, the direct combination of h, ζ and H^{helm} according to Eq. (13) besides being theoretically valid, it is also practically advantageous since it avoids the conversion of the initially known height anomalies to geoid undulations (or, alternatively, the conversion of the orthometric heights to normal heights).

The aforementioned height conversion has been a prerequisite step for the consistent use of a quasi-geoid model with orthometric heights while its rigorous implementation is a challenging task especially in mountainous regions (e.g. Flury and Rummel 2009). Nevertheless, if Helmert orthometric heights are to be used then their consistent combination with a quasi-geoid model can be based on the much simpler equation (13) which essentially requires only the knowledge of:

- the surface gravity g at each point (so that the term $\overline{g}^{\text{helm}}$ can be directly determined via Eq. (4)), and
- the geopotential difference δW_{o} between the local vertical datum of the Helmert orthometric heights and the W_{o} value which is implied in the zero-degree term of the quasi-geoid model.

Due to the limited extent of the current paper, it has not been possible to present some numerical examples related to the height modeling aspects that were discussed in the previous sections. A more thorough theoretical analysis, along with detailed examples using real data, will therefore be presented in a future journal paper.

References

Amos MJ, Featherstone WE (2009) Unification of New Zealand's local vertical datums: iterative gravimetric quasigeoid computations. J Geod 83:57–68

Burša M, Kenyon S, Kouba J, Šima Z, Vatrt V, Vojtišková M (2004) A global vertical reference frame based on four regional vertical datums. Stud Geophys Geod 48:493–502

Flury J, Rummel R (2009) On the geoid-quasigeoid separation in mountainous areas. J Geod 83:829–847

Fotopoulos G (2003) An analysis on the optimal combination of geoid, orthometric and ellipsoidal height data. PhD Thesis, UCGE Report No 20185, Department of Geomatics Engineering, University of Calgary, Calgary, Canada

Heiskanen W, Moritz H (1967) Physical geodesy. WH Freeman, San Francisco, CA

Jekeli C (2000) Heights, the geopotential and vertical datums. Department of Civil, Environmental Engineering and Geodetic Science, The Ohio State University, OSU Report No 459, Columbus, Ohio

Kotsakis C, Katsambalos K (2010) Quality analysis of global geopotential models at 1542 GPS/leveling benchmarks over the Hellenic mainland. Surv Rev 42(318):327–344

Pan M, Sjöberg LE (1998) Unification of vertical datums by GPS and gravimetric geoid models with application to Fennoscandia. J Geod 72:64–70

Rapp RH (1994) Separation between reference surfaces of selected vertical datums. Bull Geod 69:26–31

Sánchez L (2007) Definition and realization of the SIRGAS vertical reference system within a globally unified height system. In: Tregoning P, Rizos Ch (eds) Dynamic planet. Springer, Berlin. IAG Symp 130:638–645

Contribution of Tide Gauges for the Determination of W_0 in Canada

T. Hayden, E. Rangelova, M.G. Sideris, and M. Véronneau

Abstract

Canada plans to implement a geoid-based and GNSS-accessible vertical datum in 2013 in order to replace the existing Canadian Geodetic Vertical Datum of 1928, which no longer meets the needs of the modern user in terms of accuracy and accessibility. One of the primary concerns when realizing a geoid-based vertical datum is to determine the W_0 value that will represent the potential of the zero-height surface. Thus, the objective of this study is to determine W_0 by averaging the potential of points on the mean water surface by using Canadian tide gauge records and GOCE-based global geopotential models. The GOCE-based models are extended with the high-resolution gravity field model EGM2008 in order to assess the effect of the omission error on the computation of W_0. Similarly, the regional gravimetric geoid model CGG2010 is also used for the estimation of W_0 in order to assess the effect of higher frequency contributions of the gravity field, which are missing from the GOCE-based global geopotential models. Additionally, sea surface topography models are utilized in order to validate the W_0 results based on tide gauges and to estimate W_0 values for North America. The W_0 values obtained using Canadian tide gauges and high resolution gravity field and geoid models are not statistically different from the International Earth Rotation and Reference Systems Service 2010 global conventional value of 62,636,856.00 m^2/s^2.

Keywords

Geoid-based vertical datum • GOCE • Mean sea level • Sea surface topography • W_0

1 Introduction

The official vertical datum of Canada, i.e., the Canadian Geodetic Vertical Datum of 1928 (CGVD28), will be replaced with a geoid-based and GNSS-accessible vertical datum by November 2013 according to the Canadian Geodetic Survey (CGS) of Natural Resources Canada. The transition to a geoid-based vertical datum is motivated by the fact that CGVD28 does not satisfy the needs of the modern user in terms of accuracy and accessibility for precise height determination by the GNSS technique. Similarly, the U.S. National Geodetic Survey (NGS) also plans to implement a geoid-based vertical datum, but not before 2022. One of the primary concerns when realizing a geoid-based vertical datum is to determine the W_0 value that will represent the potential of the zero-height surface for the common datum that will be adopted by Canada and the USA. Generally, W_0 has been evaluated globally using satellite altimetry observations (e.g., Burša et al. 1998; Sánchez 2009; Dayoub et al. 2012; Yonghai and Jiancheng 2012) and, to a lesser

International Symposium on Gravity, Geoid and Height Systems, 9–12 October 2012, Venice, Italy

T. Hayden (✉) • E. Rangelova • M.G. Sideris
Department of Geomatics Engineering, University of Calgary, 2500 University Drive NW, Calgary, AB T2N 1N4, Canada
e-mail: tasnuva.hayden@stantec.com

M. Véronneau
Canadian Geodetic Survey, Natural Resources Canada, 615 Booth Street, Ottawa, ON, Canada K1A 0E9

U. Marti (ed.), *Gravity, Geoid and Height Systems*, International Association of Geodesy Symposia 141,
DOI 10.1007/978-3-319-10837-7_31,

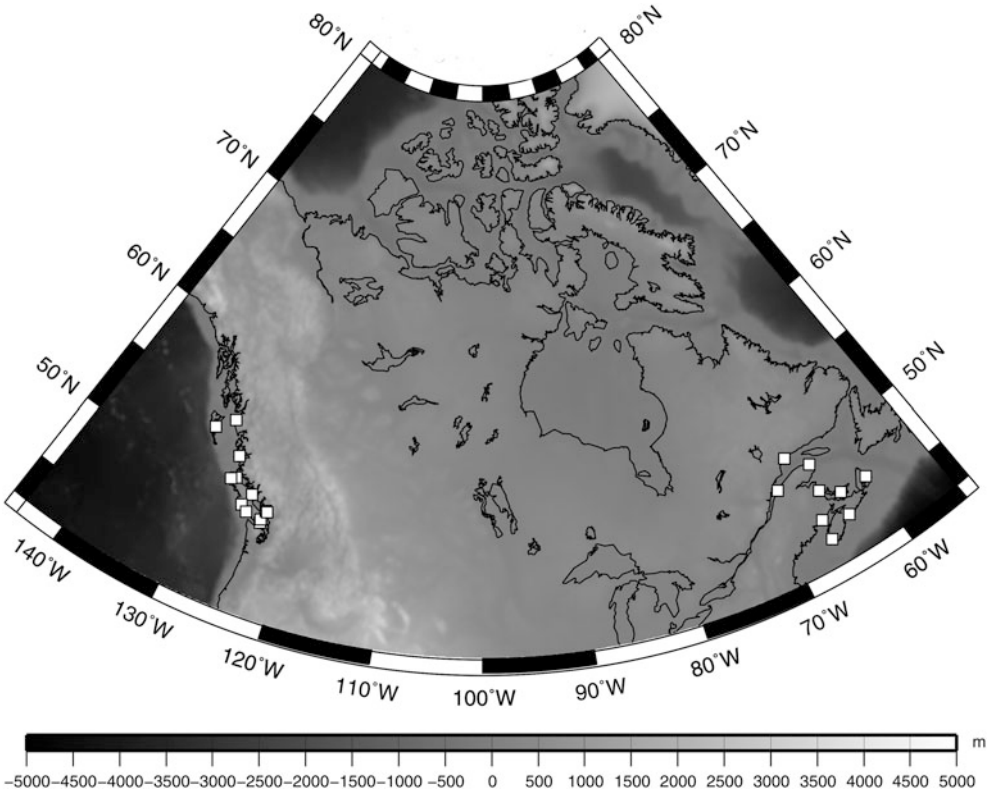

Fig. 1 Geographical distribution of the 22 tide gauges in Canada used in this study

extent, regionally using the geopotential at tide gauges (e.g., Grafarend and Ardalan 1997; Ardalan et al. 2002). CGS and NGS have agreed on the W_0 value of 62,636,856.00 m^2/s^2, which has been determined by averaging the potential values at selected North American tide gauges (CGS Pers. Comm. 2012). Coincidently, this value is the same as the global W_0 of the 2010 conventions adopted by the International Earth Rotation and Reference Systems Service (IERS; Petit and Luzum 2010).

When estimating W_0, it is preferable to use a satellite-only global geopotential model (GGM) in order to avoid inconsistencies coming from the terrestrial gravity data (e.g., datum issues). However, the omission error of the satellite-only GGM creates another source of error. Thus, the focus of this study is to assess the effect of the omission error of recent Gravity field and steady-state Ocean Circulation Explorer (GOCE; ESA 2011) GGMs when computing a regional W_0 with records at sparsely located tide gauge stations. In this context, the analysis makes use of Canadian tide gauges to which the potential of the mean water level is determined from a 19-year period (accounting for sea level rise and vertical land motion) and geoid models (global and regional). Furthermore, the study also includes the analysis of oceanographic sea surface topography (SST) models in order to independently validate the results obtained from the tide gauge records and geoid models.

2 Data Sets

2.1 Tide Gauges

Tide gauges have been selected based on the following three criteria:

- the tide gauge must have a corresponding benchmark which has been surveyed with GNSS;
- the tide gauge benchmark must be in good condition according to the Canadian Hydrographic Service (CHS); and
- the tide gauge must have a 19-year data record between 1992 and 2011 without significant recording gaps (i.e., no more than 2–3 years of missing data) in order to remove the lunar nodal tide of 18.6 years (Ardalan and Safari 2005).

The 22 tide gauges that meet the above requirements are shown in Fig. 1. Twelve gauges are located on the Pacific coast and ten gauges are located on the Atlantic coast. The daily water level data for these tide gauges are available

Table 1 Gravity field models used in the evaluation of the geoid height (N) at the tide gauges; n_{max} is the maximum degree of the GGM

Model	Model resolution	Data source
go_cons_gcf_2_tim_r3	$n_{max} = 250$	GOCE time-wise approach based on 18 months of data
goco03s	$n_{max} = 250$	Based on 18 months of GOCE data, 7 years of GRACE data, 8 years of CHAMP data and 5 years of SLR
EGM2008	$n_{max} = 2190$	Based on itg-grace03s global geopotential model, surface gravimetry, and altimetry
CGG2010	Gravimetric spatial resolution: 2′ by 2′	Based on terrestrial gravity data and global models goco01s and EGM2008

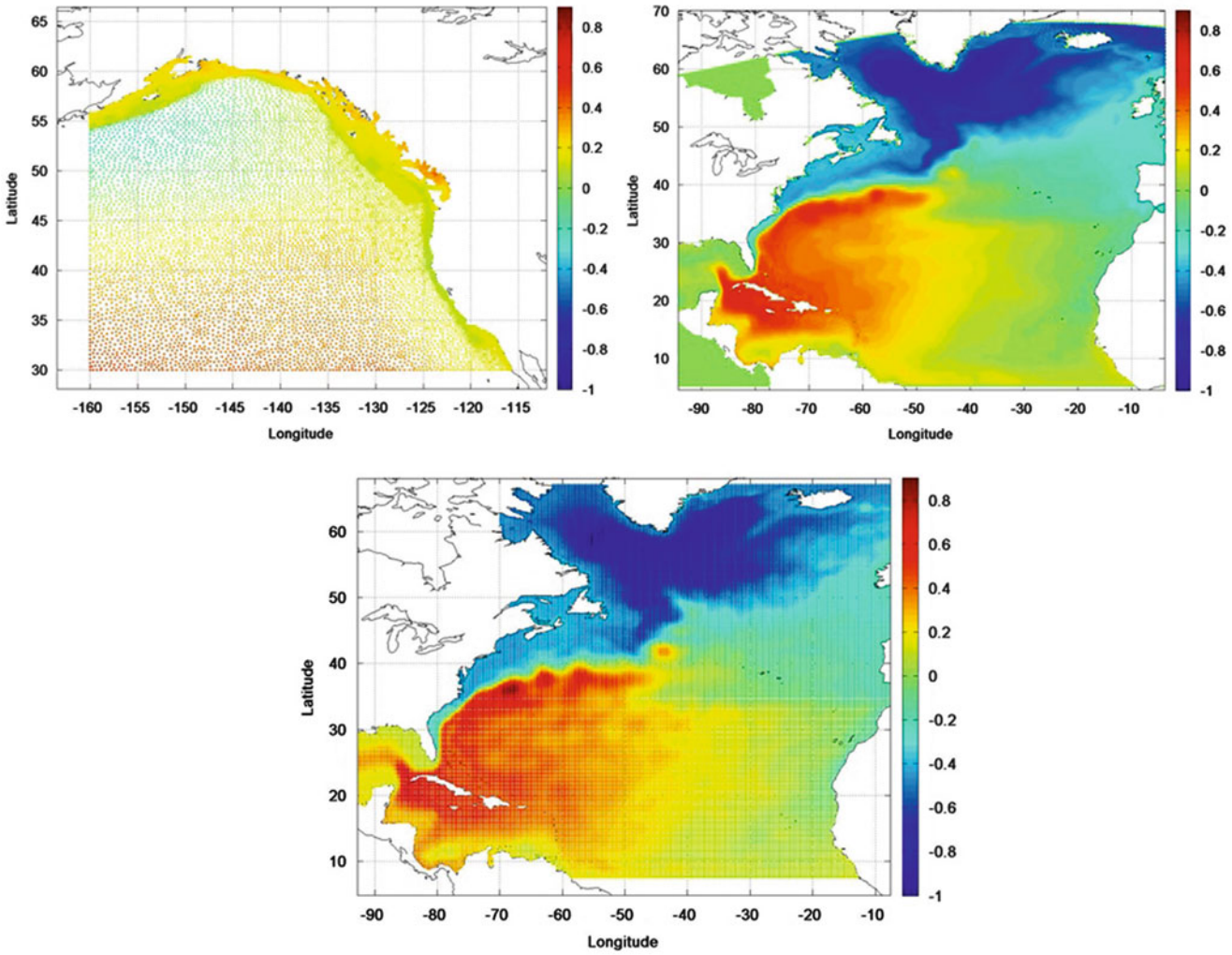

Fig. 2 Regional SST Models (in m); *Top Left*: Foreman; *Top Right*: Wright; *Bottom*: Thompson & Demirov

from the Integrated Science Data Management (ISDM) of Fisheries and Oceans Canada.

2.2 Gravity Field Models

Global geopotential models are required in order to obtain the gravity potential at the tide gauge sites. One of the main factors that affect the accuracy of spherical harmonic expansions is the omission error, i.e., the gravity field signal omitted from the GGM due to the use of a maximum degree of expansion. The omission error of the satellite-only GOCE gravity field models is not expected to average out over the limited number of tide gauges available. For that reason, the Canadian gravimetric geoid model CGG2010 (Huang and Véronneau 2013) and the high-resolution GGM EGM2008

(Pavlis et al. 2012) are included in order to assess the effect of the omission error of the GOCE-based GGMs. Table 1 describes the gravity field models utilized in this study. All models are in the conventional tide-free system. The GGMs are available from http://icgem.gfz-potsdam.de/ICGEM/ while the gravimetric geoid model CGG2010 is available from Natural Resources Canada.

2.3 Sea Surface Topography Models

Natural Resources Canada provided three regional SST models: Foreman's model for the Pacific (Foreman et al. 2008), Wright's model for the Atlantic developed at Fisheries and Oceans Canada, and Thompson's & Demirov's model for the Atlantic (Thompson and Demirov 2006). These three models are depicted in Fig. 2. In addition, the National Oceanography Centre (NOC) Liverpool made available ten global models: Maximenko, CLS, ECCO2 JPL, OCCAM12, GECCO, ECCO-godae, Liv Fine, Liv Coarse, GOCE-1, and GOCE-2. All of the SST models used in this study are given in the mean tide system. These SST models provide an independent approach for validating the W_0 results obtained from the tide gauges and gravity field models.

3 Methodology

The potential W_P of a point on the mean water surface is computed from the mean SST, which is referenced to an equipotential surface with a known potential W_N (see Fig. 3). The SST can be approximated by the following equation (Sánchez 2009):

$$SST_P = \frac{W_N - W_P}{\gamma_P}, \tag{1}$$

where γ_P is the normal gravity at the geoid computed with the latitude of the tide gauge station.

Figure 3 shows that the SST at a tide gauge can be determined geometrically from the ellipsoidal height h of the tidal benchmark, the geoid height N, the height of the tidal benchmark CD above the chart datum, and the height of the local mean sea level (MSL) Z_0 above the chart datum [see Fig. 4, Eq. (2)].

It should be noted that Z_0 can be corrected for SST in order to account for the discrepancy of the mean sea surface at the tide gauge and that of the deep ocean. For example, the tide gauges on the Atlantic coast located near the St. Lawrence River may be affected by river discharge (Bourgault and Koutitonsky 1999); therefore adjusting the local MSL (i.e., Z_0) for deep ocean SST can help to mitigate such effects. Thus, the SST shown in Fig. 3 is obtained from an

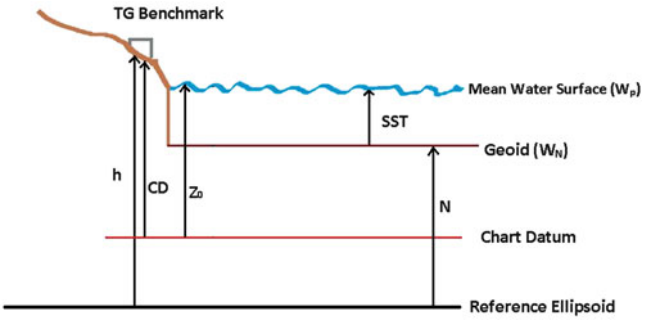

Fig. 3 Geometrical evaluation of sea surface topography at tide gauges

oceanic model, and the difference between the geometrical SST computed using geodetic data and the oceanic SST results in the correction to be applied to Z_0. An averaged oceanic SST at 50 km from the tide gauge location is used when evaluating the correction to be applied to Z_0 in order to avoid SST values near the coast, which are more likely to be erroneous due to the localized effects of the coastline. Moreover, if the oceanic model incorporates altimetry data, the altimetry signal is likely to be contaminated by the land portion of the coastline. This is especially applicable if using global SST models to obtain this correction. For this study we use the regional SST models for this correction as they have better coverage when compared to the global models of ocean regions near the coast. When using the regional SST model, a correction interpolated 50 km away from the tide gauges or one that is interpolated to the tide gauge locations, results in a difference in W_0 that is approximately at most 0.10 m^2/s^2 or 1 cm.

The methodology utilized to evaluate W_0 from tide gauges (also known as tide gauge averaging) and from oceanic SST models is summarized in Fig. 4.

Equation (2) in Fig. 4 can be evaluated using either a tide-free, mean-tide, or zero-tide system. In this study, we have opted to evaluate Eq. (2) using the conventional tide-free system. It is for this reason that SSTs obtained from oceanic models are converted from mean-tide to tide-free using Eq. (4) in order to make W_0 results obtained from these two different datasets comparable.

For this study, the ellipsoidal heights h are in ITRF 2008 epoch 2008.0. Thus, before the evaluation of Eq. (3) (see Fig. 4), the values for CD and Z_0 are also transformed to the common epoch of 2008.0 by taking into consideration the vertical velocity of the land and the sea level at each tide gauge. The ellipsoidal heights of the tidal benchmarks are corrected for the vertical land motion. The absolute sea level rate is the twentieth century average for North America: 1.8 mm/year ± 0.2 mm/year (Church et al. 2004; Snay et al. 2007; Mazzotti et al. 2008). For the Pacific region, the vertical land motion rates are mainly due to seismic variations, and these values are obtained from the GNSS-based rates

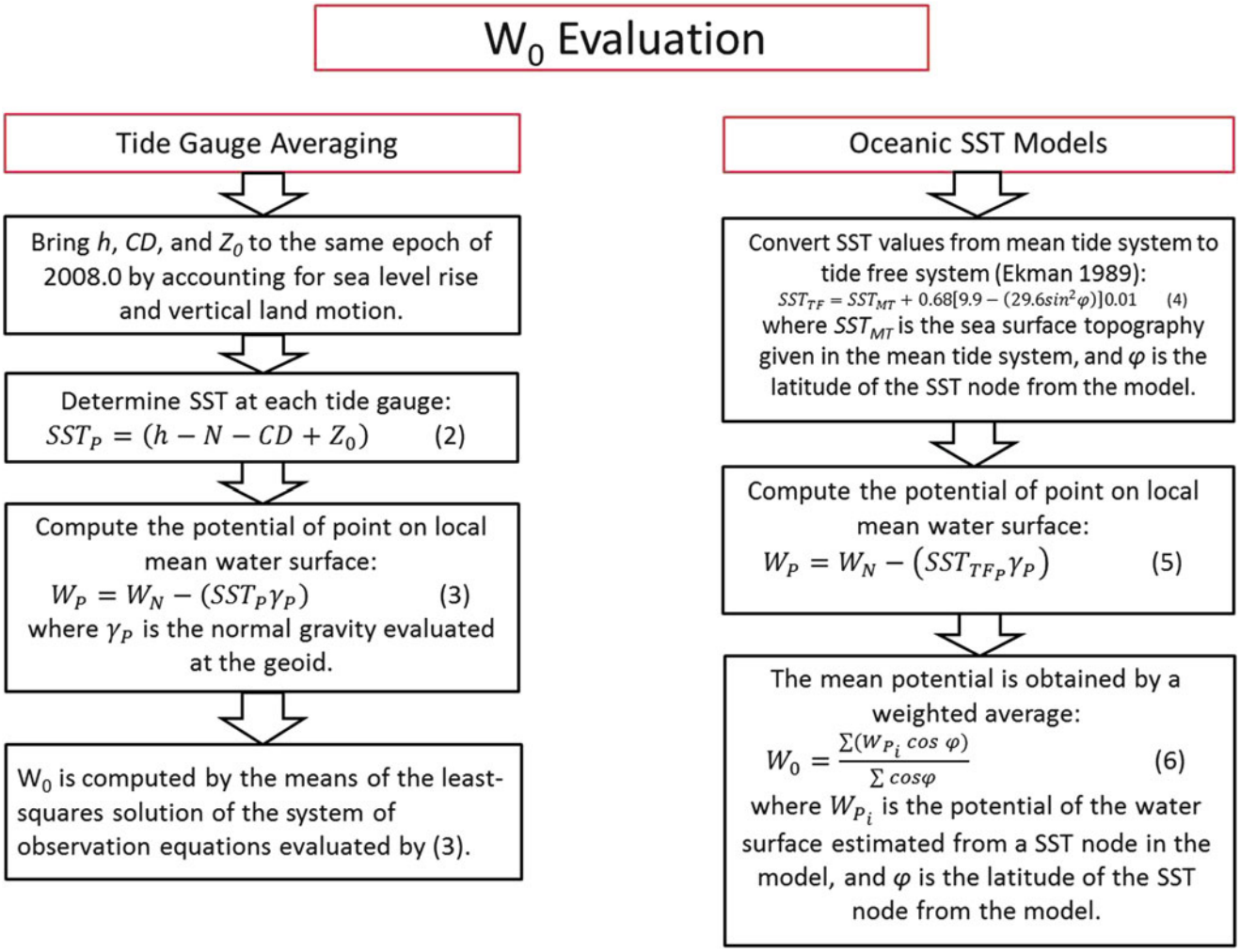

Fig. 4 Evaluation of W_0 using tide gauges and sea surface topography models

evaluated by Mazzotti et al. (2008). For the Atlantic region, the vertical land motion rates are primarily due to glacial isostatic adjustment, and these values are interpolated at the tide gauge locations from the GEODVEL1b GPS solution (Argus and Peltier 2010). As the velocity corrections are on the order of mm/year they add only a few millimetres to h, CD, and Z_0; thus these corrections do not have a significant effect on W_0 (Rangelova et al. 2012).

4 Results and Discussion

4.1 W_0 Results Obtained from Tide Gauge Averaging Using Gravity Field Models

The objective of this section is to study the effect of the omission error on the computed W_0 evaluated from GOCE-based GGMs. Previous studies indicate that the GOCE models perform the best up to degree and order 180 (e.g., Ince et al. 2012; Hirt et al. 2012). Therefore, two third-generation models that include GOCE data (go_cons_gcf_tim_r3 (tim_r3) and goco03s) are used up to degree and order 180 to determine mean potential values at tide gauges. In order to assess the effect of the omission error on the computation of W_0, these two models are extended to degree 2190 using EGM2008. The standard deviations in Table 2 are estimated by the a posteriori variance factor of the adjustment of Eq. (3) using a unit weight matrix; the error estimates in the table indicate only a formal statistical accuracy.

From the results in Table 2, we can determine that the effect of the omission error of the two GOCE models on W_0 is 1.28 m^2/s^2 (13 cm) with respect to their expanded versions. The effect of the omission error is only 0.18 m^2/s^2 or less than 2 cm when utilizing tim_r3 to its maximum expansion of degree and order 250. However, the commission error, i.e., the data errors that propagate into the spherical harmonic coefficients, increases after degree and order 180 for the GOCE-based GGMs. Therefore, the inclusion of the geoid

Table 2 W_0 values evaluated at tide gauges with different gravity field models (add 62,636,850.00 m^2/s^2 to values in the table)

Gravity field model expanded to degree and order n_{max}	W_0 using Z_0 without correction (m^2/s^2)	W_0 using Foreman and Wright corrected Z_0 (m^2/s^2)	W_0 using Foreman and Thompson & Demirov corrected Z_0 (m^2/s^2)
goco03s; n_{max}: 180	5.50 ± 1.39	5.52 ± 1.38	6.03 ± 1.43
goco03s + EGM2008; n_{max}: 180 + 181–2190	6.78 ± 0.56	6.81 ± 0.56	7.31 ± 0.65
go_cons_gcf_2_tim_r3; n_{max}: 180	5.44 ± 1.40	5.47 ± 1.38	5.97 ± 1.44
go_cons_gcf_2_tim_r3 + EGM2008; n_{max}: 180 + 181–2190	6.73 ± 0.56	6.75 ± 0.55	7.26 ± 0.65
go_cons_gcf_2_tim_r3; n_{max}: 250	6.18 ± 1.01	6.20 ± 0.99	6.71 ± 1.06
go_cons_gcf_2_tim_r3 + EGM2008; n_{max}: 250 + 251–2190	6.36 ± 0.69	6.38 ± 0.70	6.89 ± 0.76
CGG2010	6.71 ± 0.60	6.74 ± 0.59	7.24 ± 0.69

height accuracy information is necessary for a more accurate assessment of W_0.

The tim_r3 and goco03s models enhanced with EGM2008 to degree and order 2190 have similar results to CGG2010. The geometric difference is only 0.1 cm (62,636,856.75 m^2/s^2 and 62,636,856.74 m^2/s^2 for tim_r3 + EGM2008 and CGG2010, respectively). This is expected as CGG2010 and EGM2008 use basically the same Canadian terrestrial data to model the higher frequency contributions of the gravity field over North America.

The regional SST models are chosen to account for SST at the tide gauges since they model the SST in coastal regions better than the SST global models, with the exception of ECCO2 JPL. The geometrically derived SST [see Eq. (2)] at the tide gauges is used as a criterion for external validation of the SST models. The Foreman, Wright, and Thompson & Demirov regional models have the best agreement with the geometrically determined SST, respectively. Additionally, the Foreman model is very dense in the coastal region when compared with the global models, and is therefore less likely to be subject to interpolation errors. Correcting Z_0 for the SST of the deep ocean has an effect that is less than 1 cm when utilizing the Wright SST model. On the other hand, the contribution of this correction is approximately 5 cm when utilizing the Thompson & Demirov SST model. Thus, when using a small number of tide gauges, the variability between SST models can be an appreciable factor in W_0 estimation.

Table 3 W_0 values evaluated with SST interpolated from oceanic models at tide gauges

SST models	W_0 (m^2/s^2)
Local: Foreman and Wright	$62,636,856.75 \pm 2.73$
Local: Foreman and Thompson & Demirov	$62,636,857.15 \pm 3.15$
Maximenko	$62,636,857.29 \pm 2.15$
CLS	$62,636,856.74 \pm 2.70$
ECCO2 JPL	$62,636,857.28 \pm 2.89$
OCCAM12	$62,636,857.23 \pm 3.11$
GECCO	$62,636,856.94 \pm 3.26$
ECCO-godae	$62,636,857.33 \pm 3.54$
Liv Fine	$62,636,857.23 \pm 3.46$
Liv Coarse	$62,636,856.76 \pm 3.87$
GOCE1	$62,636,856.91 \pm 2.41$
GOCE2	$62,636,857.14 \pm 2.18$

4.2 W_0 Results Obtained from Oceanic Models with SST Interpolated at the Tide Gauges

W_0 is computed using various SST models with SST values interpolated to tide gauge locations (using 2-D linear interpolation) in order to validate the results from tide gauge averaging. The results are shown in Table 3. The standard deviations in Table 3 correspond to the distribution of the W_0 as computed by Eq. (6).

The W_0 results in Table 3 are overall in good agreement with results obtained using tide gauges and high resolution gravity field models (i.e., CGG2010 and the GOCE + EGM2008 models). When compared to the result obtained with CGG2010 (without correcting Z_0 for SST) in Table 2, the maximum difference is observed with the application of the ECCO-godae model, where the difference is 0.62 m^2/s^2 or approximately 6 cm.

4.3 W_0 Results Obtained from Oceanic Models for the Pacific and Atlantic Regions

Lastly, W_0 values are computed using the SST models described in Sect. 2.3 for the Pacific and Atlantic regions in order to estimate the average potential for North America. These results are shown in Table 4. The ten models obtained

Table 4 W_0 values evaluated for the Pacific and Atlantic oceans using SST models

SST models	Pacific W_0 (m^2/s^2) Latitude: 30°N to 60°N Longitude: 150°W to 115°W	Atlantic W_0 (m^2/s^2) Latitude: 30°N to 60°N Longitude: 80°W to 50°W
Tide gauges with CGG2010	*62,636,854.17 ± 0.19*	*62,636,860.70 ± 0.18*
Local: Foreman	62,636,854.25 ± 0.63	–
Local: Wright	–	62,636,857.28 ± 4.50
Local: Thompson & Demirov	–	62,636,857.11 ± 5.04
Maximenko	62,636,854.69 ± 1.03	62,636,859.61 ± 6.86
CLS	62,636,854.04 ± 0.65	62,636,859.99 ± 6.87
ECCO2 JPL	62,636,854.69 ± 0.29	62,636,860.84 ± 6.84
OCCAM12	62,636,854.24 ± 0.29	62,636,861.09 ± 6.75
GECCO	62,636,854.11 ± 0.24	62,636,861.08 ± 6.85
ECCO-godae	62,636,854.23 ± 0.37	62,636,861.77 ± 6.74
Liv Fine	62,636,854.15 ± 0.31	62,636,861.33 ± 6.75
Liv Coarse	62,636,853.32 ± 0.35	62,636,861.23 ± 6.72
GOCE1	62,636,854.33 ± 0.45	62,636,859.79 ± 6.85
GOCE2	62,636,854.75 ± 0.82	62,636,859.73 ± 6.86

Italicized entries are obtained with the tide gauge averaging method and non-italicized entries are results obtained using the SST models

from NOC are limited to the coastal region while the regional models include the deep oceans, extending from 130°W to 115°W for the Pacific and 80°W to 50°W for the Atlantic.

Based on the results in Table 4, it can be inferred that the SST is highly variable for the north Atlantic while it is relatively uniform for the northeast Pacific. The MSL of the Pacific is approximately 20 cm above the reference surface agreed on by CGS and NGS while the MSL of the Atlantic is approximately 40 cm below this surface. The Thompson & Demirov and Wright SST models in Table 4 yield a lower potential for the Atlantic than the other ten global SST models because these two models include the deep ocean part of the South Atlantic where warmer waters from the Gulf Stream create a positive SST (see Fig. 2). Thus, when utilizing the regional SST models in the evaluation of W_0 for North America, one expects a decrease in potential when compared to the Canadian case (e.g., Foreman + Wright yields 62,636,855.77 m^2/s^2 and Foreman + Thompson & Demirov yields 62,636,855.68 m^2/s^2) as the SST values off the Canadian east coast are mostly negative.

Conclusion

The truncation degree of GOCE-based GGMs and the distribution of the tide gauges are two important factors when estimating the potential W_0 of the regional MSL through tide gauge averaging. Ideally, a uniform distribution of tide gauges with up to date long-term time series, preferably up to one lunar nodal cycle (i.e., 18.6 years) is preferable. However, for Canada, only a small number of tide gauges actually have long-term time-series without significant data gaps. GOCE models truncated at degree and order 180 is not sufficient for an accurate determination of W_0 in Canada due to the limited number and scattered distribution of tide gauges available; the effect of the GOCE omission error on W_0 is at the decimetre level. Therefore, a high resolution geoid model such as CGG2010 or EGM2008 should be used when computing W_0 by the tide gauge averaging method in order to adequately model the high frequency components of the gravity field. Furthermore, it is recommended to use regional SST models (i.e., Wright and Foreman) for the determination of W_0, as they have the best agreement with the geometrically determined SSTs and adequately reflect the positive SST of the South Atlantic when compared with the global models.

Though the W_0 values obtained using the Canadian tide gauges represents a difference of approximately 1.00 m^2/s^2 or 10 cm with respect to the global conventional value adopted by CGS and NGS, these values cannot be considered statistically different from the IERS 2010 conventional value, as the difference between these W_0 values is less than three times their formal errors. The difference is due to the fact that the North American conventional value comes from an average that includes American tide gauges. Furthermore, it should be noted that our analysis lacks water level data and SST models for the Arctic region, leaving our W_0 results from tide gauge averaging for the Pacific and Atlantic coasts of southern Canada. However, when taking into account the entire region of North America, we expect the W_0 to decrease due to positive SST values in the southern Atlantic. Therefore, the adopted conventional value is a reasonable compromise between both countries since a common geoid-based vertical datum will be implemented by the two national geodetic agencies.

Acknowledgements This work is a contribution to the ESA STSE—GOCE + Height System Unification with GOCE project, and was also supported by NSERC and the GEOIDE Network of Centres of Excellence. The late D.G. Wright is acknowledged for the development of the regional Atlantic SST model used in this study. P. Woodworth and C. Hughes 'from NOC Liverpool' are also acknowledged for providing the global SST models.

References

Ardalan AA, Safari A (2005) Global height datum unification: a new approach in gravity potential space. J Geod 79:512–523. doi:10.1007/s00190-005-0001-0

Ardalan A, Grafaren E, Kakkuri J (2002) National height datum, the Gauss-Listing geoid level value w0 and its time variation (Baltic Sea Level Project: epochs 1990.8, 1993.8, 1997.4). J Geod 76:1–28

Argus DE, Peltier WR (2010) Constraining models of postglacial rebound using space geodesy: a detailed assessment of model ICE-5G (VM2) and its relatives. Geophys J Int 181:697–723. doi:10.1111/j.1365-246X.2010.04562.x

Bourgault D, Koutitonsky VG (1999) Real-time monitoring of the freshwater discharge at the head of the St. Lawrence Estuary. Atmosphere-Ocean 37(2):203–220

Burša M, Kouba J, Raděj K, True SA, Vatrt V, Vojtìšková M (1998) Mean Earth's equipotential surface from TOPEX/POSEIDON altimetry. Studia Geoph et Geod 42:459–466

Church JA, White NJ, Coleman R, Lambeck K, Mitrovica J (2004) Estimates of the regional distribution of sea level rise over the 1950-2000 period. J Clim 17:2609–2625

Dayoub N, Edwards SJ, Moore P (2012) The Gauss-Listing geopotential value W_0 and its rate from altimetric mean sea level and GRACE. J Geod 86(9):681–694

Ekman M (1989) Impacts of geodynamic phenomena on systems for height and gravity. Bull Geod 63:281–296

ESA (2011) ESA GOCE earth explorers. http://www.esa.int/esaLP/ESAYEK1VMOC_LPgoce_0.html

Foreman MGG, Crawford WR, Cherniawsky JY, Galbraith J (2008) Dynamic ocean topography for the northeast Pacific and its continental margins. Geophys Res Lett 35(22): L22606. doi:10.1029/2008GL035152

Grafarend EW, Ardalan AA (1997) W_0: an estimate in the Finnish Height Datum N60, epoch 1993.4 from twenty-five GPS points on the Baltic Sea Level Project. J Geod 71:673–679

Hirt C, Kuhn M, Featherstone WE, Göttl F (2012) Topographic/isostatic evaluation for new-generation GOCE gravity field models. J Geophys Res. doi:10.1029/2011JB00878

Huang J, Véronneau M (2013) Canadian gravimetric geoid model 2010. J Geod 87(8):771–790. doi:10.1007/s00190-013-0645-0

Ince ES, Sideris MG, Huang J, Véronneau M (2012) Assessment of the GOCE-based global gravity models in Canada. Geomatica 66(2):125–145

Mazzotti S, Jones C, Thomson RE (2008) Relative and absolute sea level rise in western Canada and northwestern United States from a combined tide gauge-GPS analysis. J Geophys Res. doi:10.1029/2008JC004835

Pavlis NK, Holmes SA, Kenyon SC, Factor JK (2012) The development and evaluation of the Earth Gravitational Model 2008 (EGM2008). J Geophys Res. doi:10.1029/2011JB008916

Petit G, Luzum B (2010) IERS convention 2010. IERS Technical Note 36, Verlag den Bundesamtes für Kartographie und Geodäsie, Frankfurt

Rangelova E, van der Wal W, Sideris MG (2012) How significant is the dynamic component of the North American vertical datum? J Geod Sci 2(4):281–289

Sánchez L (2009) Strategy to establish a global vertical reference system. In: Drewes H (ed) Geodetic reference frames. International association of geodesy symposia, vol 134, pp 273–278. doi:10.1007/978-3-642-00860-3_42

Snay R, Cline M, Dillinger W, Foote R, Hilla S, Kass W et al (2007) Using global positioning-system derived crustal velocities to estimate rates of absolute sea level change from North America tide gauge records. J Geophys Res. doi:10.1029/2006JB004606

Thompson KR, Demirov E (2006) Skewness of sea level variability of the world's oceans. J Geophys Res. doi:10.1029/2004JC002839

Yonghai C, Jiancheng L (2012) Determination of mean sea level geopotential from global gravity field model and global sea surface height model. J Geod Geodyn 32(5):58–62

Estimation of the Reference Geopotential Value for the Local Vertical Datum of Continental Greece Using EGM08 and GPS/Leveling Data

V.N. Grigoriadis, C. Kotsakis, I.N. Tziavos, and G.S. Vergos

Abstract

Estimation of the zero-height geopotential level represented by W_o^{LVD} in a local vertical datum (LVD) is a problem of main importance for a wide range of geodetic applications related to different height frames and plays a fundamental role in the connection of traditional height reference systems into a global height system or even a modern geoid-based vertical datum. This paper aims primarily at the estimation of W_o^{LVD} for the continental part of Greece, with the use of surface gravity data and geopotential values computed from EGM08 in conjunction with GPS and orthometric heights over an extensive network which covers sufficiently the test area. The method used focuses on the estimation of W_o^{LVD} from a least squares adjustment scheme that is applied on the Helmert model for orthometric heights, using surface geopotential and gravity values (as obtained from EGM08 and the known 3D geocentric coordinates of each benchmark) along with the local Helmert heights over all network stations. Moreover, an attempt is made towards the modeling and removal of any height correlated errors in the available data according to this adjustment procedure. Different weighting schemes are tested, and, finally, some conclusions are drawn considering the accuracy of the obtained results.

Keywords

Local vertical datum • Hellenic vertical datum • Helmert orthometric heights • Zero-height geopotential level

1 Introduction

The use of heights is of main importance for a wide range of geodetic, surveying and engineering applications. In the case of orthometric heights, i.e., heights above the geoid, differences are determined nationwide by conventional spirit leveling accompanied by gravity measurements along dedicated traverses. The orthometric heights of all established benchmarks are then obtained, through a Least-Squares (LS) adjustment of the entire vertical network, as height differences with respect to (w.r.t.) a selected benchmark (BM) that serves as the origin point of the country's vertical reference system. It has been customary for the origin point to coincide with a tide gauge (TG) station at which the local mean sea level (MSL) has been determined over a long period of time—the latter provides the primary realization of a zero-height reference surface w.r.t. which all orthometric heights are referred and measured thereafter. In this way, the orthometric height of a point P on the Earth's surface w.r.t. a local vertical datum (LVD) is obtained, in principle, through the geopotential difference between the Earth's gravity potential W_P at that point and the reference geopotential value W_o^{LVD} on the associated zero-height surface of the LVD divided by the mean gravity along the corresponding plumbline segment (Heiskanen and Moritz 1967, Sect. 4-4).

V.N. Grigoriadis (✉) • C. Kotsakis • I.N. Tziavos • G.S. Vergos
Department of Geodesy and Surveying, Aristotle University of Thessaloniki, University Box 440, 54124 Thessaloniki, Greece
e-mail: nezos@topo.auth.gr

U. Marti (ed.), *Gravity, Geoid and Height Systems*, International Association of Geodesy Symposia 141,
DOI 10.1007/978-3-319-10837-7_32,

Many studies have been carried out in the past decades towards the unification of independent realizations of height systems under a common vertical datum through a global reference value W_o. Moreover, vertical shifts between national vertical datums have been determined by various approaches in terms of height or geopotential differences of their corresponding zero-height reference surfaces. For example, Burša et al. (2001) computed geopotential differences among several LVDs and unified them into a World Height System (WHS) while Burša et al. (2002) demonstrated the practical realization of a WHS by determining geopotential values at TG stations and the geopotential differences between the LVDs and a global vertical datum. Ardalan et al. (2002) used GPS data, orthometric heights and a Global Geopotential Model (GGM) for deriving a zero-height geopotential value for TG stations located in the region of the Baltic Sea. Burša et al. (2004) determined a global vertical reference frame through the unification of the North American, Australian, French and Brazilian height datums. Sánchez (2007), after determining a global W_o value, attempted the unification of the South American height datums into a WHS. Ardalan et al. (2010) used potential and gravity differences for height datum unification within a test area in Southwest Finland.

The determination of the zero-height geopotential level of an existing vertical datum is considered of main importance for the connection of traditional height reference systems into a global height system or even a modern geoid-based vertical datum. Various methods have been used in practice for estimating the fundamental parameter W_o^{LVD} which can be broadly classified into two basic categories as described in Kotsakis et al. (2012). The first one is based on the combined adjustment of GGM and GPS/leveling data while the second one employs the formulation of a geodetic boundary value problem (GBVP) with the use of gravity anomaly data over different LVD zones. Both approaches have been extensively utilized by the scientific community but the present paper will focus only on the first approach.

In practice, the primary realization of most vertical datums is not accompanied by the specification or the determination of its associated W_o^{LVD} value. This is also the case for Greece, with the main problem being the existence of hundreds of islands, where no hydrostatic leveling has been applied to connect the orthometric heights of the reference BMs at the islands with the official origin of the Hellenic Vertical Datum (HVD), i.e. the TG reference station at Piraeus harbour. Apart from this difficulty, the HVD suffers also from local biases that can be attributed to the lack of a common adjustment of the whole vertical network (Tziavos et al. 2012). Under these conditions, estimates of the zero-height reference levels W_o^{LVD} for the independent vertical datums within the 16 largest Greek islands were derived by Kotsakis et al. (2012) while for the continental part the only available estimate has been given by Vatrt et al. (2009) from a combined processing of geoid heights with a limited number of GPS/leveling data.

The main objective of this study is to obtain a representative estimate W_o^{LVD} for the HVD zero-height level over the entire continental part of Greece using Helmert orthometric heights, GPS measurements and a high-resolution GGM. The used data provide an extremely dense coverage of the test area, and the accuracy of our final estimate is limited only by the GGM commission error over the spatial wavelengths that overly exceed the size of the country. In Europe there has been a significant amount of work towards the determination and the modernization of the European Vertical Reference System (EVRS) by combining several geodetic datasets from many different countries (Ihde et al. 2002). The absence of the Greek leveling (and other types of) data from such an effort and the practical exclusion of the country from the EVRS efforts give good evidence on the necessity of the present study.

2 Method for the Determination of W_o^{LVD}

The simplest approach for determining the unknown zero-height geopotential value W_o^{LVD} in a local vertical datum based on heterogeneous height data over a terrestrial network of m leveling BMs relies on the following LS estimator

$$\widehat{W}_o^{LVD} = W_o - \frac{\sum_1^m (h_i - H_i - N_i)\,\gamma_i}{m}, \qquad (1)$$

where h_i is the ellipsoidal height obtained from space geodetic techniques, N_i is the geoid height from a GGM or a regional geoid model, and H_i is the known orthometric height of each benchmark w.r.t. the underlying LVD. The term W_o specifies the equipotential surface that is realized by the GGM or the geoid model (i.e., as deduced by the zero-degree term in the known geoid heights N_i) while γ_i is the normal gravity on the reference ellipsoid computed through Somigliana's formula; for more details on the use of Eq. (1) see Jekeli (2000) and Kotsakis et al. (2012).

In our current study we devise an alternative estimator $\widehat{W}_o^{LVD}$ to be used in conjunction with orthometric heights and a high-resolution GGM, without the need to compute geoid heights at the leveling BMs. This is advantageous since it abolishes the effect of terrain modeling errors that are inherently present whenever geoid heights are determined through a spherical harmonic series expansion of Earth's disturbing gravity field (e.g., Rapp 1997; Smith 1998). Moreover, the approximate character of the orthometric heights used in geodetic practice (Helmert orthometric heights) is taken into account in our alternative estimator, thus avoiding any

errors due to their theoretical inconsistency with GPS/GGM derived orthometric heights (note that such errors are always present in the result of Eq. (1)).

Based on the definition of Helmert orthometric heights (Heiskanen and Moritz 1967, Chap. 4) we have the following equation:

$$H_i^{\text{helm}} = \frac{W_{\text{o}}^{\text{LVD}} - W_i}{\overline{g}_i}, \tag{2}$$

where H_i^{helm} is the known Helmert orthometric height w.r.t. the underlying LVD, $W_{\text{o}}^{\text{LVD}}$ is the (unknown) reference geopotential level of the LVD, W_i is the gravity potential at the leveling benchmark, and $\overline{g}_i$ is the mean gravity value along the plumb line between the LVD's zero-height equipotential reference surface and the Earth's surface according to the Poincare-Prey reduction scheme (ibid., Eqs. 4–24)

$$\overline{g}_i = g_i + 0.0424 H_i^{\text{helm}} \quad \left(g_i \text{ and } \overline{g}_i \text{ in mGal, } H_i^{\text{helm}} \text{ in m}\right). \tag{3}$$

Both terms W_i and $\overline{g}_i$ in Eq. (2) can be determined on the basis of a GGM and the knowledge of the spatial position of the leveling benchmark from space geodetic measurements (e.g., GPS). Specifically, the gravity potential W_i can be synthesized from a gravitational part obtained by the GGM spherical harmonic coefficients and a centrifugal part using the benchmark's known spatial position and the Earth's conventional rotational velocity (Petit and Luzum 2010), whereas the surface gravity value g_i in Eq. (3) can be simply reconstructed through the GGM-derived gravity disturbance as described in Filmer et al. (2010).

Hence, the implementation of Eq. (2) over a network of leveling BMs yields a system of "observation equations" with a single unknown parameter ($W_{\text{o}}^{\text{LVD}}$) which can be resolved in terms of the general weighted LS estimator

$$\widehat{W}_{\text{o}}^{\text{LVD}} = \frac{\sum_i p_i y_i}{\sum_i p_i} = \frac{\sum_i p_i \left(W_i + H_i^{\text{helm}} \overline{g}_i\right)}{\sum_i p_i}, \tag{4}$$

where p_i is a positive weight factor associated with each BM such that

$$\sum_i p_i \delta W_i^2 = \min. \tag{5}$$

(see Fig. 1 for a graphical description of the above estimation scheme). Note that the estimate $\widehat{W}_{\text{o}}^{\text{LVD}}$ according to Eq. (4) is rather insensitive to the uncertainty of the GGM-derived surface gravity values that are used for computing the terms $\overline{g}_i$ at the leveling BMs. Indeed, if we apply a straightforward error propagation to Eq. (4) and assuming for simplicity that $p_i = 1$, we have

$$\sigma_{\widehat{W}_{\text{o}}^{\text{LVD}}} = \frac{\sqrt{\sum_i^m \left(H_i^{\text{helm}}\right)^2}}{m} \sigma_g, \tag{6}$$

which implies an uncertainty less than 0.1 $\text{m}^2\ \text{s}^{-2}$ for the zero-height geopotential value even in mountainous test networks and surface gravity accuracy σ_g reaching up to 20 mGal.

3 Available Data

The Hellenic Vertical Datum (HVD) was established by the Hellenic Geographic Military Service within the period 1963–1986. In principle, the physical heights in the HVD were modeled as Helmert orthometric heights in the mean-tide system. They refer to the TG station at the Piraeus harbor, where local MSL was computed from sea level measurements over the period 1933–1978 (Takos 1989). The true accuracy of the HVD's leveling network is largely unknown. Additionally, a zero-height geopotential value was not originally associated with the HVD and hence is also considered as unknown.

In the present study, Helmert orthometric heights referring to the HVD along with GPS derived ellipsoidal heights at 1,629 control stations of the Hellenic geodetic network are used for estimating the unknown parameter $W_{\text{o}}^{\text{LVD}}$ of the HVD according to the methodology presented in Sect. 2. The ellipsoidal heights refer to the ITRF2000 frame (epoch t = 2007.236, tide-free system) and they were obtained from a number of GPS measurement campaigns which were performed over Greece for the establishment of the Hellenic Positioning (HEPOS) system (Gianniou 2008). All control stations used in our study are located in the mainland part of the country (see Fig. 2) and the horizontal and vertical accuracy of their GPS derived spatial positions is 1–4 cm (1σ) and 2–5 cm (1σ), respectively, whereas their orthometric heights had been computed by the Hellenic Geographic Military Service through spirit and/or trigonometric leveling ties with the primary national leveling network (Takos 1989). A total of 94 stations out of the 1,629 were rejected from our analysis (see next section) having failed to pass the standard outlier detection (3σ) test during the preliminary LS adjustment of Eq. (2) over our test network, most probably due to existing blunders in their HVD orthometric heights.

All required computations for our analysis have been carried out in the tide-free system. The conversion, given in meters, from mean-tide H_{MT} to tide-free H_{TF} orthometric heights was implemented according to the following

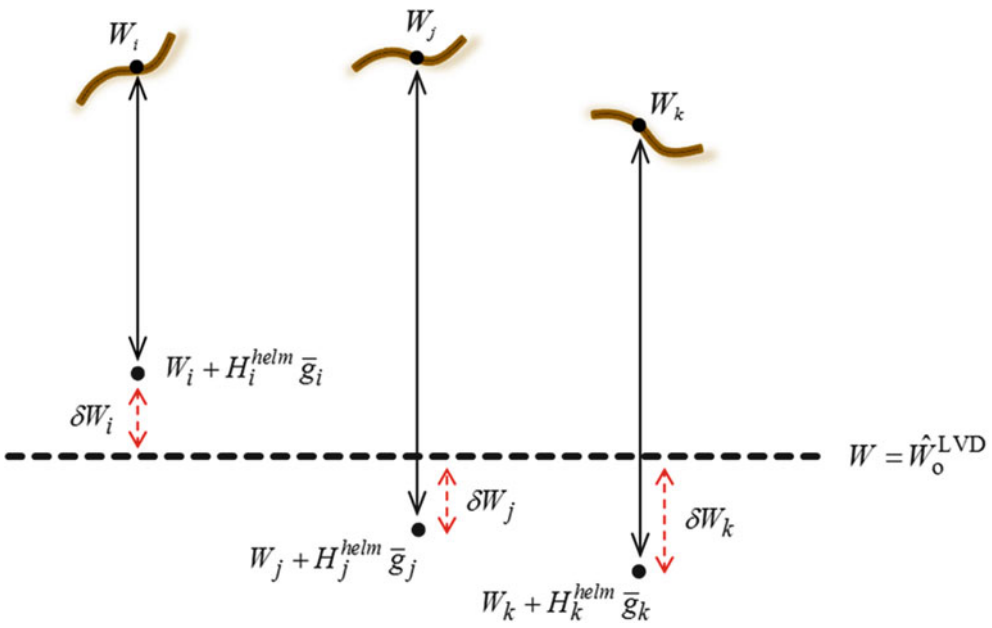

Fig. 1 Zero-height geopotential value determination from a network of stations

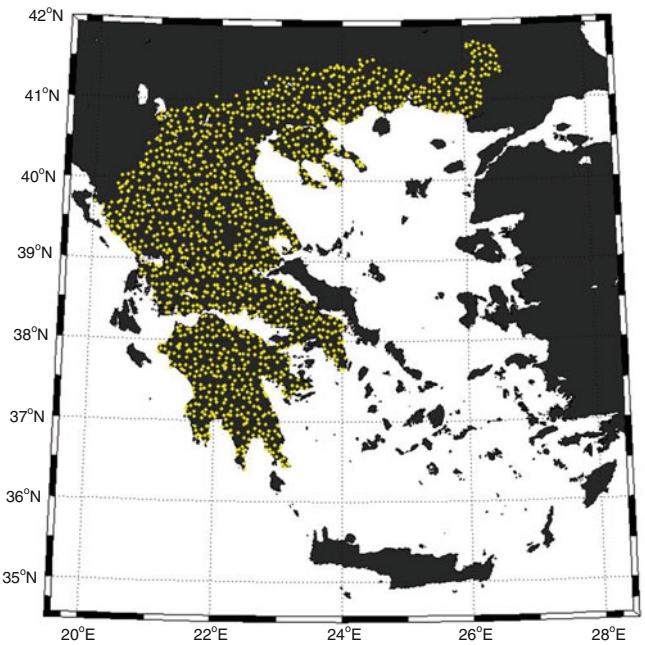

Fig. 2 Spatial distribution of the 1629 GPS/leveling control stations in continental Greece

formula, which is a combination of Eqs. 1, 6 and 7 found in Ekman (1989):

$$H_{\mathrm{TF}} - H_{\mathrm{MT}} = \left(29.6\sin^2\varphi - 9.9\right)\gamma \cdot 10^{-2}, \tag{7}$$

where φ is the geodetic latitude and γ is the elasticity factor of the Earth which was set equal to 0.68 (Ekman 1989).

The computation of the gravity potential values (W_i) at all control stations has been performed with the Earth Gravitational Model 2008 (EGM08) (Pavlis et al. 2012), complete to degree and order 2159, in the tide-free system using (for the gravitational part) the harmonic synthesis program of Holmes and Pavlis (2006) and (for the centrifugal part) the GPS derived spatial coordinates of each station. The surface gravity at each station, which is required for the computation of the mean gravity term $\bar{g}_i$ as per Eq. (3), was also determined through the EGM08-based gravity disturbances according to the following formula

$$g_{\mathrm{BM}} = \gamma_{\mathrm{BM}} - \frac{\partial T}{\partial r}, \tag{8}$$

where γ_{BM} is the normal gravity on the Earth's surface and $\partial T/\partial r$ is the radial derivative of the disturbing potential. Note that the GRS80 reference ellipsoid has been used for all related computations described in the previous paragraphs.

4 Numerical Results

The results for the estimation of W_o^{LVD} in the HVD using the method and datasets described in Sects. 2 and 3 are presented in Table 1. Both an un-weighted and a weighted LS adjustment of Eq. (2) were performed with empirically assigned weights p_i taken as the inverse Helmert orthometric heights of each station. The accuracy level of our results shown in Table 1 corresponds to the standard error (1σ) obtained from the LS estimation algorithm taking into account the a posteriori variance factor that was obtained in each case.

Table 1 Estimates of the zero-height geopotential value for continental Greece

	$\widehat{W}_{\mathrm{o}}^{\mathrm{LVD}}$ [m^2 s^{-2}]
Un-weighted LS	62,636,859.37 ± 0.04
Weighted LS ($p_i = 1/H_i^{\mathrm{helm}}$)	62,636,860.16 ± 0.03

Looking at the results of Table 1 we notice a significant difference between the un-weighted and the weighted estimate $\widehat{W}_{\mathrm{o}}^{\mathrm{LVD}}$ at the level of 0.79 m^2 s^{-2} (approximately 8 cm). The magnitude of this discrepancy, in conjunction with the high statistical precision of the two estimates, manifests the existence of a bias into our results due to height-dependent systematic errors within the available data. This effect was further investigated by performing additional LS adjustment tests using different subsets of the control stations according to a certain height threshold. The results of these tests are presented in Table 2 for the un-weighted and weighted solutions, respectively. It is evident that, as more stations with higher altitude are included in the LS adjustment, the un-weighted estimate of the zero-height level systematically increases by several cm while the corresponding weighted estimate remains practically unaffected (within a few mm). This implies the presence of a height-correlated bias in our data that originates mostly from the HVD physical heights and partially from EGM08 related systematic errors in the computed W_i values at the test stations. The empirical weighting scheme that was used during the estimation process managed to control the effect of these systematic errors and provided more robust estimates for the HVD's zero-height level $\widehat{W}_{\mathrm{o}}^{\mathrm{LVD}}$. The existence of a height-correlated bias in our data is clearly visible in the scatter plot of the adjusted height residuals

$$e_i = H_i^{\mathrm{helm}} - \frac{\widehat{W}_{\mathrm{o}}^{\mathrm{LVD}} - W_i}{\overline{g}_i}, \tag{9}$$

which were obtained from the un-weighted LS solution over the entire test network (1,535 BMs), see Fig. 3. The statistics of these residuals are presented in Table 3 indicating an average agreement among the GPS heights, the HVD Helmert orthometric heights and the EGM08 model at the level of 15 cm over the Hellenic mainland.

For the treatment of the data biases that were identified in our previous tests, we next employed an extended parametric model towards the LS estimation of the HVD's geopotential value. Specifically, an additional parameter describing the linear part of the height-dependent systematic errors was introduced into the data adjustment procedure according to the general equation

$$H_i^{\mathrm{helm}} = \frac{W_{\mathrm{o}}^{\mathrm{LVD}} - W_i}{\overline{g}_i} + \lambda\, H_i^{\mathrm{helm}}. \tag{10}$$

The estimated values of the fundamental parameter $W_{\mathrm{o}}^{\mathrm{LVD}}$ and the nuisance parameter λ from the LS adjustment of the above equation over the entire test network are provided in Table 4. Four different solutions were computed depending on the data weighting scheme that was adopted in the estimation algorithm. It should be noticed that two additional scenarios are now included in our experiments which correspond to the weight choices $p_i = (1/H_i^{\mathrm{helm}})^{1/2}$ and $p_i = (1/H_i^{\mathrm{helm}})^2$. The statistics of the adjusted height residuals that were obtained from these tests, i.e.,

$$e_i = H_i^{\mathrm{helm}} - \frac{\widehat{W}_{\mathrm{o}}^{\mathrm{LVD}} - W_i}{\overline{g}_i} - \widehat{\lambda} H_i^{\mathrm{helm}} \tag{11}$$

are summarized in Table 5.

From the results contained in Tables 4 and 5 it is noticed that the LS solution based on the weight choice $p_i = (1/H_i^{\mathrm{helm}})^2$ becomes unstable with respect to the nuisance parameter λ while the corresponding mean value of the adjusted height residuals in Table 5 is unacceptable. This is not a surprising result since the particular weight factor is rather harsh and significantly down-weights most of the available BMs, thus blocking them from the adjustment procedure. Therefore, this weight factor makes the separation of $\widehat{\lambda}$ and $\widehat{W}_{\mathrm{o}}^{\mathrm{LVD}}$ practically impossible.

On the other hand, the un-weighted solution and the weighted solutions with the weight choices $p_i = (1/H_i^{\mathrm{helm}})^{1/2}$ and $p_i = (1/H_i^{\mathrm{helm}})$ provide similar results that are statistically equivalent within their precision level. Any of the three corresponding estimates $\widehat{W}_{\mathrm{o}}^{\mathrm{LVD}}$ can be actually used as a representative estimate for the zero-height reference value of the HVD in continental Greece. In order to further evaluate these results, an alternative estimate was also computed using Eq. (1). For this purpose, the required "global" parameter W_{o} was set equal to the International Earth Rotation and Reference System Service's (IERS) conventional value 62,636,856.00 m^2 s^{-2} (Petit and Luzum 2010) while the surface gravity data and the geoid heights were extracted from EGM08. An estimated value $\widehat{W}_{\mathrm{o}}^{\mathrm{LVD}} = 62,636,859.66$ m^{2}s^{-2} was obtained in this case. This result has a small difference (0.29 m^2 s^{-2}) with the one given by the un-weighted LS solution of Table 1 while it is smaller by 0.64 m^2 s^{-2} compared to the LS estimates of the revised model of Eq. (10). These differences signify that the result provided by Eq. (1) is also affected by a height-correlated bias. The same conclusion may be also drawn from the comparison that was made with the value provided by Vatrt et al. (2009) for the HVD, i.e., $\widehat{W}_{\mathrm{o}}^{\mathrm{LVD}} = 62,636,859.44$ m^{2}s^{-2}. The difference found is 0.86 m^2 s^{-2} which corresponds approximately to 9 cm.

For a more realistic assessment of the accuracy level in our results given in Table 4, we have to consider the fact

Table 2 Estimates of the zero-height geopotential value for continental Greece by setting a height threshold to the initial data

	$\widehat{W}_{\mathrm{o}}^{\mathrm{LVD}}$ [m^2 s^{-2}]		
Height threshold for used BMs	Un-weighted LS	Weighted LS ($p_i = 1/H_i^{\mathrm{helm}}$)	Difference [cm]
<200 m (514 pts)	62,636,860.04	62,636,860.20	~1.6
<500 m (866 pts)	62,636,859.90	62,636,860.19	~3.0
<1,000 m (1,308 pts)	62,636,859.65	62,636,860.17	~5.3
<1,500 m (1,487 pts)	62,636,859.45	62,636,860.17	~7.3
<2,000 m (1,535 pts)	62,636,859.37	62,636,860.16	~8.1

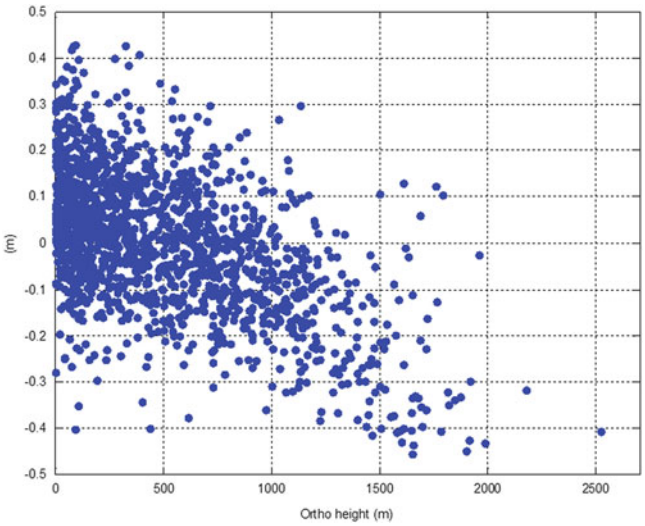

Fig. 3 Residual heights computed from the un-weighted LS adjustment of Eq. (2) over the Hellenic test network

Table 3 Statistics of the height residuals of the un-weighted LS adjustment solution. Unit: [m]

	Mean	Min	Max	Std
e_i	0.000	−0.456	0.429	0.150

Table 4 Estimates of the zero-height geopotential value for continental Greece from the revised model of Eq. (10)

LSA schemes	$\widehat{W}_{\mathrm{o}}^{\mathrm{LVD}}$ [m^2 s^{-2}]	$\widehat{\lambda}$ [$\times 10^{-4}$]
Un-weighted	62,636,860.30 ± 0.05	−1.882 ± 0.073
Weighted $p_i = (1/H_i^{\mathrm{helm}})^{1/2}$	62,636,860.28 ± 0.04	−1.832 ± 0.095
Weighted $p_i = (1/H_i^{\mathrm{helm}})$	62,636,860.23 ± 0.03	−1.725 ± 0.221
Weighted $p_i = (1/H_i^{\mathrm{helm}})^2$	62,636,860.12 ± 0.01	1.339 ± 3.660

Table 5 Statistics of the height residuals from the LS adjustment of Eq. (10). Unit: [m]

	Mean	Min	Max	Std
Un-weighted	0.000	−0.481	0.415	0.125
Weighted $p_i = (1/H_i^{\mathrm{helm}})^{1/2}$	0.000	−0.479	0.412	0.125
Weighted $p_i = (1/H_i^{\mathrm{helm}})$	0.000	−0.474	0.405	0.126
Weighted $p_i = (1/H_i^{\mathrm{helm}})^2$	−0.144	−0.821	0.340	0.188

that EGM08 contributes an apparent bias into the LS estimate $\widehat{W}_{\mathrm{o}}^{\mathrm{LVD}}$ due to its commission error over spatial wavelengths that overly exceed the extent of our test network. Obviously, this error component cannot be reduced through the (un-weighted or weighted) data averaging that takes place within the adjustment procedure and it is fully propagated into the final results. Its magnitude can be evaluated, in a statistical sense, from the following formula

$$\delta \widehat{W}_{\mathrm{o}}^{\mathrm{LVD}} = \sqrt{\sum_{n=2}^{n*} \sigma_e^2 (V_n)}, \tag{12}$$

where $n*$ depends on the extent ΔA of the test area ($n* << 180/\Delta A$) and $\sigma_e^2(V_n)$ are the gravitational potential error degree variances given by

$$\sigma_e^2 (V_n) = \left(\frac{GM}{\alpha}\right)^2 \sum_{m=0}^{n} \left(\sigma_{\overline{C}_{nm}}^2 + \sigma_{\overline{S}_{nm}}^2\right) \tag{13}$$

for

$$V = \frac{GM}{r} + \sum_{n=2}^{\infty} V_n. \tag{14}$$

In the above equations, V is the gravitational potential, $\sigma_{\overline{C}_{nm}}$ and $\sigma_{\overline{S}_{nm}}$ are the error standard deviations of the GGM spherical harmonic coefficients, GM is the Earth gravitational constant, α is the semi-major axis of the ellipsoid and r is the geocentric radius. For our study area that covers a region of 5.5° × 6°, the maximum degree $n*$ was selected equal to 15 (~1,300 km, full-wavelength) leading to an apparent bias into the various estimates $\widehat{W}_{\mathrm{o}}^{\mathrm{LVD}}$ which is about 3.5 cm or, equivalently, 0.35 m^2 s^{-2}. Therefore, the total accuracy of our results should be represented by the final error estimate

$$\widehat{\sigma} = \sqrt{\sigma_{\mathrm{LS}}^2 + \left(\delta \widehat{W}_{\mathrm{o}}^{\mathrm{LVD}}\right)^2} \simeq 0.35\ \mathrm{m^2 s^{-2}}. \tag{15}$$

where $\delta \widehat{W}_{\mathrm{o}}^{\mathrm{LVD}}$ is obtained from Eq. (12) and σ_{LS} corresponds to the statistical accuracy of the LS adjusted solutions given in Table 4. Note that the EGM08 *omission* error

for $n > 2{,}159$ should not be separately considered as its propagated effect on $\widehat{W}_{\mathrm{o}}^{\mathrm{LVD}}$ is well averaged out due to the large number of test points used in our study. It is evident that the EGM08 commission error over spatial wavelengths > 1,300 km dominates the estimation accuracy of the zero-height geopotential value for the HVD. Therefore, further accuracy improvements could be achieved with the use of an improved GGM, like for example a GOCE-based model (see, e.g., Gatti et al. 2013; Gerlach and Rummel 2013).

Conclusions and Future Work

In this study a method based on a weighted LS adjustment has been presented for the determination of the fundamental parameter $W_{\mathrm{o}}^{\mathrm{LVD}}$ of the HVD for the continental part of Greece utilizing Helmert orthometric heights, GPS data and EGM08 derived gravity and gravity potential values in a terrestrial network of 1,629 control stations. A series of LS adjustment tests using empirical height-dependent weighting and an augmented parametric model (see Eq. 10) were carried out in order to account for the systematic part of the data errors which has been attributed to a detected height-correlated bias. As discussed in the previous section, any of the first three geopotential estimates given in Table 4 can be selected as representative values for the zero-height reference level in the HVD, since the differences among them are statistically insignificant within their actual accuracy level.

In terms of future work, geoid heights from local high-resolution geoid solutions could be used along with GOCE-based GGMs for an improved determination of $W_{\mathrm{o}}^{\mathrm{LVD}}$ through the proposed or other combination methods. Moreover, further investigation regarding the weighting schemes of the LS adjustment procedure could be carried out.

Acknowledgement Dr. Grigoriadis, Dr. Vergos and Prof. Tziavos wish to acknowledge the funding provided for this work by the European Space Agency in the frame of the ESA-PRODEX GOCESeaComb project (C4000106380). The GPS data were kindly provided in the frame of a cooperation agreement between the Department of Geodesy and Surveying of the Aristotle University of Thessaloniki and KTIMATOLOGIO SA.

References

Ardalan A, Grafarend E, Kakkuri J (2002) National height datum, the Gauss-Listing geoid level value W(o) and its time variation (Baltic Sea Level Project : epochs 1990.8, 1993.8, 1997.4. J Geod 76:1–28

Ardalan A, Karimi R, Poutanen M (2010) A bias-free geodetic boundary value problem approach to height datum unification. J Geod 84:123–134

Burša M, Kouba J, Müller A, Raděj K, True SA, Vatrt V, Vojtísková M (2001) Determination of geopotential differences between local vertical datums and realization of a world height system. Stud Geophys Geod 45:127–132

Burša M, Kenyon S, Kouba J, Raděj K, Vatrt V, Vojtíšková M, Šimek J (2002) World height system specified by geopotential at tide gauge stations. IAG Symp 124:291–296

Burša M, Kenyon S, Kouba J, Sima Z, Vatrt V, Vojtísková M (2004) A global vertical reference frame based on four regional vertical datums. Stud Geophys Geod 48:493–502

Ekman M (1989) Impacts of geodynamic phenomena on systems for height and gravity. Bull Geod 63:281–296

Filmer MS, Featherstone WE, Kuhn M (2010) The effect of EGM2008-based normal, normal-orthometric and Helmert orthometric height systems on the Australian levelling network. J Geod 84(8):501–513

Gatti A, Reguzzoni M, Venuti G (2013) The height datum problem and the role of satellite gravity models. J Geod 87:15–22

Gerlach C, Rummel R (2013) Global height system unification with GOCE: a simulation study on the indirect bias term in the GBVP approach. J Geod 87:57–67

Gianniou M (2008) HEPOS: designing and implementing an RTK network. Geoinformatics 11(1):10–13

Heiskanen W, Moritz H (1967) Physical geodesy. WH Freeman, San Francisco, CA

Holmes SA, Pavlis NK (2006) A Fortran program for very-high-degree harmonic synthesis (version 05/01/2006). Program manual and software code available at http://earth-info.nima.mil/GandG/wgs84/gravitymod/egm2008/

Ihde J, Augath W, Sacher M (2002) The vertical reference system for Europe. IAG Symp 124:345–350

Jekeli C (2000) Heights, the geopotential and vertical datums. Department of Civil, Environmental Engineering and Geodetic Science, The Ohio State University, OSU Report No 459, Columbus, Ohio

Kotsakis C, Katsambalos K, Ampatzidis D (2012) Estimation of the zero-height geopotential level $W_{\mathrm{o}}^{\mathrm{LVD}}$ in a local vertical datum from inversion of co-located GPS, leveling and geoid heights: a case study in the Hellenic islands. J Geod 86(6):423–439

Pavlis NK, Holmes SA, Kenyon SC, Factor JK (2012) The development and evaluation of the Earth Gravitational Model 2008 (EGM2008). J Geophys Res 117(B4), B04406

Petit G, Luzum B (eds) (2010) IERS conventions 2010. International earth rotation and reference systems service, IERS Technical Note No 36, Verlag des Bundesamtes für Kartographie und Geodäsie, Frankfurt am Main

Rapp RH (1997) Use of potential coefficient models for geoid undulation determinations using a spherical harmonic representation of the height anomaly/geoid undulation difference. J Geod 71:282–289

Sánchez L (2007) Definition and realization of the SIRGAS vertical reference system within a globally unified height system. IAG Symp 130:638–645

Smith DA (1998) There is no such thing as 'the' EGM96 geoid: subtle points on the use of a global geopotential model. Int Geoid Serv Bull 8:17–27

Takos I (1989) New adjustment of the national geodetic networks in Greece (in Greek). Bulletin of the Hellenic Military Geographic Service 49(136):19–93

Tziavos IN, Vergos GS, Grigoriadis VN, Andritsanos VD (2012) Adjustment of collocated GPS, geoid and orthometric height observations in Greece. Geoid or orthometric height improvement? IAG Symp 136:481–488

Vatrt V, Sima Z, Vojtiskova M (2009) Vertical shifts of LVDs by EGM08 and Wo – preliminary result. Presented at the annual EUREF 2009 symposium, Florence, 27–30 May 2009

Tidal Systems and Reductions for Improvement of the Bulgarian National Vertical Reference System

Stanislava Valcheva, Iliya Yovev, and Rossen Grebenitcharsky

Abstract

Although discussed worldwide, the application of tidal systems in the Bulgarian National Vertical Reference System is still in its initial steps. The information available in the papers and technical reports concerning the current tidal system and/or tidal reductions applied to different quantities is either vague or missing.

The current paper shows the status of terrestrial gravity and levelling data in Bulgaria with respect to the tidal system. The differences between geopotential numbers and normal heights in mean and zero tidal system are examined. For data source, four levelling lines from the National First Order Levelling Network are used. In addition, a comparison between the calculated normal heights and the official data published in the "Catalogue of the National First Order Levelling Network Benchmarks in European Vertical Reference System 2007" is made. At the end of the paper, proposals for the proper choice of tidal system in the country are given, taking into account future international as well as local precise geodetic applications.

Keywords

Tidal system • Tidal reduction • Levelling data • Gravity data • Geopotential number • Normal height • Bulgarian vertical reference system

1 Introduction

The importance of the tidal systems is recognized in many geodetic activities: local and global geoid modelling; definition and improvements of local vertical datum; combination of terrestrial and satellite data, etc. The discussion on the subject worldwide in 1980s and 1990s helped understanding the nature of the tides, their impact on the various geodetic quantities as well as some complications due to the different tidal concepts. Similar discussion for Bulgaria could be very useful.

The application of tidal systems and reductions in Bulgaria is limited mainly in the frame of international projects like United European Levelling Network—UELN (Belyashki 2004), European Vertical Reference System (EVRS) (Pashova 2010; Sacher et al. 2008), Unification of gravity systems in Central and Eastern Europe—UNIGRACE (Milev et al. 2005, 2008), etc. Even though, the technical reports of these geodetic activities contain very little, if any information about the applied tidal reductions to measurements or the tidal system of the data itself. In local geodetic instructions this issues are not discussed at all. A recent literature review revealed few papers with main subject dedicated to tidal reductions and systems for geodetic measurements, and they are dated about 10–20 years ago (Zhekov et al. 1990; Stoyanov and Ivanov 2000; Darakchiev 2001). Despite the given recommendations for applying tidal

S. Valcheva (✉) • I. Yovev
University of Architecture, Civil Engineering and Geodesy, 1, Hristo Smirnenski Blvd., 1046 Sofia, Bulgaria
e-mail: valcheva.ss@gmail.com

R. Grebenitcharsky
School of Civil Engineering and Geoscience, Newcastle University, Newcastle upon Tyne, UK

U. Marti (ed.), *Gravity, Geoid and Height Systems*, International Association of Geodesy Symposia 141,
DOI 10.1007/978-3-319-10837-7_33,

reductions, until now there are no indications of taking into account that proposal and consequently such information in publications available is still sparse. As a result, most of the local geodetic quantities are in mixed tidal system and could introduce confusion and errors in local geoid determination or lead to inconsistencies with respect to global geopotential models applied on a local national level.

This paper aims to present the current status of the national terrestrial gravity and levelling data regarding the used tidal systems and to stress out the current practice for applying no tidal reductions at all to levelling and gravity data in Bulgaria. A comparison between the effect of different tidal systems (zero and mean) on geopotential numbers and normal heights at benchmarks of four levelling lines of Bulgarian National First Order Levelling Network (NFOLN) is presented. In conclusion, a suggestion for improvement of the National Vertical Reference System by a proper choice of tidal system is proposed, taking into account future geodetic applications related to gravity field and geoid modeling and utilizing data obtained from satellite based techniques like GOCE and GRACE gravity missions.

2 Problem Background

2.1 Worldwide Status of Levelling and Gravity Data in Relation to Their Tidal System

Historically, the presence or lack of tidal reductions applied to measured height differences has led to conventional tide-free or mean tidal system of the levelling data and the national height systems in different countries. With the introduction of the third tidal concept, mean crust over zero geoid, the implementation of zero tidal systems (both for Earth's crust and gravity field modeling) in national levellings according to IAG recommendations is realized (Ihde et al. 2008). Regarding regional or global activities, the common tidal system of the data is considered. Nevertheless, inconsistencies between the definition and the realization of reference systems could be found. An example of this is the first realization of EVRS, namely European Vertical Reference Frame 2000 (EVRF2000), based on UELN95/98 solution. By definition EVRS is zero tide with respect to the type of the system. However, many of the participating countries did not provide information about the tidal system of their data and as a result, EVRF2000 is in mixed tidal system (Mäkinen and Ihde 2009; Ihde et al. 2008; Sacher et al. 2008). An official inquiry revealed that most of these data are in mean tidal system and relevant correction was applied in order zero tide values for the next realization EVRF2007 to be obtained (Sacher et al. 2008).

In the case of gravity data, both the IAG recommendations and the current practice of gravity measurements are in the favour of zero-tide system (Ihde et al. 2008).

2.2 Status of Levelling and Gravity Data in Bulgaria

2.2.1 Status of Levelling Data

The establishment and first levelling of the NFOLN was done in mid 1930s and the obtained normal orthometric heights are based on local datum definition; Varna tide-gauge was the initial point for thus realized Black Sea Height System (BSHS). The second re-levelling of the NFOLN in the mid 1950s was used for introducing the Baltic Height System (BHS) in the country; its initial datum point is Kronstad tide-gauge and it uses normal heights. This height system is the official height system of Bulgaria. By definition, both BSHS and BHS are not tied to particular tidal system. Also, tidal systems and tidal reductions are subject neither to the related Bulgarian levelling instructions nor to the available Bulgarian technical reports following the levelling network observations and adjustments, including the third re-levelling of the NFOLN conducted from 1974 to 1984. To some extent, this fact explains the past and current practice in Bulgaria of applying no tidal reductions to measured height differences.

The fourth re-levelling of the NFOLN began in 1995 and is ongoing. According to the official information all available data at present are still under assessment.

The data from the third re-levelling of the NFOLN are also used for the participation of Bulgaria in the two realizations of EVRS, based on the Amsterdam tide-gauge. The official report (Belyashki 2004) detailing the EVRF2000 implementation on the territory of the country again does not consider tidal reductions applied to data or the tidal system of the calculated geopotential numbers and normal heights. The technical report, published by the Geodesy Department of the National Institute of Geodesy, Geophysics and Geography (NIGGG) in 2011 regarding computations to EVRF2007 in Bulgaria is more complete, despite that it also does not discuss any reductions applied to the measurements prior to their submission to the analysis center of Federal Agency for Cartography and Geodesy (Bundesamt für Kartographie und Geodäsie—BKG), as also stated in Pashova (2010). The report bears the information that the geopotential numbers and normal heights in the previous realization are in mean tidal system. It also gives the two formulae for computing tidal reductions in order to obtain zero tide values rather than mean tide values of geopotential differences and "*normal* height differences". This suggests that normal heights of BMs are not computed from the relative geopotential

numbers but via common line (or network) adjustment with initial data the normal heights of the starting/ending BMs and normal height differences (height differences with applied normal correction). Since the method of geopotential number or normal height computations is not explicitly stated in the report, the other possibility is the use of normal height differences in geopotential number computations. That should not be allowed; the geopotential numbers are path independent and an additional normal correction would lead to biased results. The geopotential number calculation should be done strictly with gravity data and measured height differences (without applied normal correction) and *prior to* applying line misclosure or line adjustment.

Local journal publications should be another source of discussion about tidal systems and reductions. However, there are only few papers emphasizing their importance and just one of them concerns levelling (Zhekov et al. 1990).[1] This publication presents the calculated tidal reductions to measured height differences in two NFOLN lines and gives the corresponding tidal reduction formula. At the end of the paper the authors give recommendation for tidal reduction application; however until now there is no indication of taking that suggestion into account.

At present, the current geodetic practice in Bulgaria is to apply no tidal reductions to measured height differences, i.e. to obtain their mean tide values.

2.2.2 Status of Gravity Data

Currently, most of the gravity data in Bulgaria are still in Potsdam Gravity System. In 1999 as part of the UNIGRACE project on the territory of the country there were conducted absolute gravity measurements and, consequently, used for the adjustment of the National Standard Gravity Network in IGSN71. There are no publicly available activity reports regarding the introduction of both Potsdam Gravity System (Borrass 1911) and IGSN71 (Morelli et al. 1974) in Bulgaria. There is no such report concerning the second international project in which our country took part in 2004—The Central Europe Regional Geodynamics Project 2 (CERGOP-2). In other related technical reports like Geodesy Department of NIGGG (2011) which use gravity values, the source of these data is often disregarded. In fact, there are no official documents regulating the gravity measurements processing scheme in Bulgaria and, consequently, there is no information about tidal systems and corresponding reductions.

[1]The second one (Darakchiev 2001) deals with tidal reductions to astronomic latitude. The third article (Stoyanov and Ivanov 2000) is examining the importance of a Geodetic Reference System (GRS) and a global geopotential model having the same permanent tidal system. It is a *proposal* for an improved GRS and as such the paper is focusing on conceptual rather than a specific implementation of the tidal system in Bulgarian geodetic practice.

Reviewing the local journal publications, one could see that the information about tidal systems and/or reductions on gravity data is very sparse. In Milev et al. (2005), which treats to some extent the activities regarding the two international projects, is mentioned the use of Wenzel's model for Earth tide influence on UNIGRACE (and only UNIGRACE) data, but there are no other details provided.

Another very recent paper (Tsenkov et al. 2011) states that tide reductions to measured gravity could be applied *prior* or *along with* the zero drift determination; however the important distinction between the permanent and time-dependant parts of the tides has not been made. Thus, reading this article one could assume that dealing with the tides and zero drift at the same time all tidal components (time-varying and permanent) are removed which would lead to non-tidal gravity values. Regrettably, that is not the case, because if the instrument's zero drift is eliminated according to Tsenkov et al. (2011), the remaining (nonlinear) time-varying parts of the tide will be distributed over the observed gravity values.

As a result of this limited information about the role of tides, the current practice in Bulgaria regarding observed gravity is to apply no tidal reductions of any kind. That leaves the gravity data in some sort of mixed tidal system.

3 Formulae Used

Keeping in mind the goal of the conducted experiment (the calculation of geopotential numbers and normal heights in mean and zero tidal system) and taking into account the status of the levelling and gravity data in Bulgaria, the following formulae were considered and applied. The units for the expressed formulae here are in [m s^{-2}] for gravity; [m^2 s^{-2}] for geopotential numbers and [m] for heights.

Reductions to observed gravity difference Δg_{ij}^{obs} are: Δg_{ij}^{L} (Longman 1959) and Δg_{ij}^{H} (Uotila 1980):

$$\begin{aligned}\Delta g_k^L = -\{&\tfrac{GM_L r}{d^3}\left(3\cos^2\theta_k - 1\right)\\ &+ \tfrac{3}{2}\tfrac{GM_L r^2}{d^4}\left(5\cos^2\theta_k - 3\cos\theta_k\right)\\ &+ \tfrac{GM_S r}{D^3}\left(3\cos^2\psi_k - 1\right)\}\times 10^{-8}, k = i, j\end{aligned} \tag{1}$$

where G is Newton's gravitational constant; M_L and M_S are masses of the Moon/Sun respectively; d and D are distances between centers of the Earth and the Moon/Sun; r is the distance from the point at Earth's surface to the center of the Earth; $\theta_k, k = i,j$ and $\psi_k, k = i,j$ are the zenith angles of the Moon/Sun at i and j BMs respectively.

$$\Delta g_k^H = -0.037\left(1 - 3\sin^2\varphi_k\right)\times 10^{-5} \tag{2}$$

where $\varphi_k, k = i,j$ represents the latitude of the corresponding BM.

Then the corrected gravity difference Δg_{ij} and the gravity value g_j at j-BM are as follows:

$$g_j = g_i + \Delta g_{ij} = g_i + \left(\Delta g_{ij}^{obs} + \Delta g_{ij}^{L} + \Delta g_{ij}^{H}\right) \quad (3)$$

with $\Delta g_{ij}^{R} = \Delta g_j^{R} - \Delta g_i^{R}, R = obs, L, H.$

The normal height H_j, the average value of the normal gravity along the normal plumb line $\overline{\gamma}_j$, the geopotential number C_j and the geopotential difference ΔC_{ij} (calculated as product of the levelled height difference Δh_{ij} and the average gravity value g_{ij}^{aver} between the two BMs), are obtained as given in Hofmann-Wellenhof and Moritz (2005):

$$C_j = C_i + \Delta C_{ij} = C_i + \Delta h_{ij} g_{ij}^{aver} \quad (4)$$

$$H_j = \frac{C_j}{\overline{\gamma}_j} \quad (5)$$

The formula used for the mean normal gravity $\overline{\gamma}_j$ is (Ihde et al. 2008):

$$\overline{\gamma}_j \approx (\gamma_0)_j \left[1 - \left(1 + f + \frac{\omega^2 a^2 b}{GM} - 2f\sin^2\varphi_j\right)\frac{H_j}{a} + \frac{H_j^2}{a^2}\right] \quad (6)$$

Here the symbols a, b, f, and ω denote respectively the semimajor axis, the semiminor axis, the flattening and the Earth's angular velocity, GM is the geocentric gravitational constant and γ_0 is the normal gravity on the ellipsoid. All values for these quantities as well as the formula for the calculation of γ_0 are taken from Moritz (1980).

The geopotential number of the initial BM (IBM) is converted in mean tidal system, according to Sacher et al. (2008):

$$C_{IBM}^{m} = C_{IBM}^{z} + 2.8841\sin^2\varphi_{IBM} + 0.0195\sin^4\varphi_{IBM} - 0.9722 \quad (7)$$

where φ^{IBM} represents the latitude of the initial BM. The subscripts here designate the tidal system of the quantity: 'm' for mean and 'z' for zero tide.

For converting the mean tide values of gravity g_j of each BM into the zero tide values, the formulae in Ekman (1989) are used:

$$g_j^{z} = g_j^{m} + \left(-30.4 + 91.2.\sin^2\varphi_j\right) \times 10^{-8} \quad (8)$$

For obtaining the zero tidal values of levelled height differences Δh_{ij} from mean tidal ones, the conversion is done by:

$$\begin{aligned}\Delta h_{ij}^{z} &= H_j - H_i \\ &= \Delta h_{ij}^{m} - 0.29541\left(\sin^2\varphi_j - \sin^2\varphi_i\right) \\ &\quad - 0.00042\left(\sin^4\varphi_j - \sin^4\varphi_i\right)\end{aligned} \quad (9)$$

Equation (8) is derived from analogous formula for correcting heights, presented in Ihde et al. (2008):

$$H_i^{z} = H_i^{m} + 0.09940 - 0.29541\sin^2\varphi_i - 0.00042\sin^4\varphi_i \quad (10)$$

On the other hand, Eq. (9) could be rewritten in the form:

$$H_i^{m} - H_i^{z} = -0.09940 + 0.29541\sin^2\varphi_i + 0.00042\sin^4\varphi_i \quad (11)$$

and to be used for direct computation of the differences in heights due to the tidal system at each BM without the use of any measurements.

4 Input Data, Performed Calculations and Results

In order to calculate geopotential numbers and normal heights in mean and zero tidal system, relevant data from the local geodetic data archive "Geokartfond" had been requested (see Table 1). The measured values refer to four lines situated in north-south direction across the territory of the whole country (see Fig. 1) and levelled in 2008–2009 as part of last re-levelling campaign of the NFOLN. The Century BM (CBM) of Varna is chosen for initial because it is the IBM for all NFOLN adjustments until now. Its geopotential number (zero tide value) is taken from the "Catalogue of the NFOLN BMs in EVRF2007" (Geodesy Department of NIGGG 2011).

In the beginning of our calculations we figured out that vital information necessary for our study concerning the obtained data from "Geokartfond" is missing. For all levelling data there was no date and time for observation records provided by the field teams; in one occasion there was no activity log sheet report. Although, the time of observation was present in the obtained gravity data, the date was not. There was also missing information about some of the gravity stations used—for example their coordinates; height and gravity values. Some of the missing information, particularly the date of gravity observation and all the necessary used information about the gravity points was retrieved from the field teams.

To obtain the mean tide values of the gravity, the observed gravity differences are corrected by Eq. (1) multiplied by factor 1.16 for the response of the real Earth (since the Longman's formulae refer to rigid Earth); after that Eq. (2) is applied. The gravity values at BMs in mean tidal system are computed by Eq. (3). With the mean tide geopotential number of the IBM obtained by Eq. (7), the geopotential numbers and normal heights of all BMs in mean tidal system are computed using Eq. (4) and Eq. (5). For zero

Table 1 Type of the obtained data from "Geokartfond" with their tidal system examined

Quantity	Symbol	Tidal system	Source of data/reference system
Height differences	Δh	Mean (uncorrected values)	Measurement
Gravity differences	Δg	Mixed (uncorrected values)	Measurement
Gravity values	g	Mean	IGSN71 value
Coordinates of BMs	φ,λ	Conventional nontidal	WGS84 value
Geopotential number of IBM	C_{IBM}	Zero	EVRF2007 value

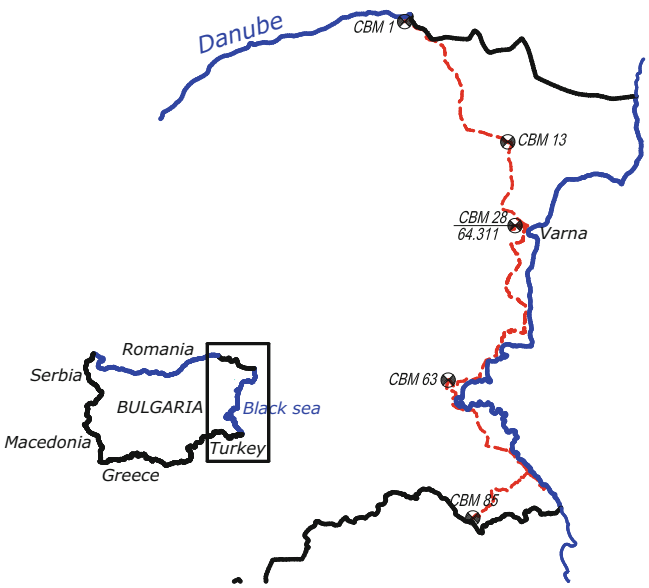

Fig. 1 Location of the levelling lines (*dashed red lines*) used in the conducted experiment along with their starting/ending century BMs (CBMs)

tide computations, the input value of the IBM is used; gravity values and measured height differences are corrected, according to Eqs. (8) and (9), and then the geopotential numbers and normal heights in zero tidal system by Eqs. (4) and (5) are obtained. Both times (in mean tide and zero tide calculations) for computing the average normal gravity along the normal plumb line Eq. (6) is used.

The results (plotted on Fig. 2) show differences between 32.8 and 43.7 mm in normal heights for mean and zero tidal systems, i.e. the normal heights in mean tidal system for the territory of Bulgaria are about 3.5 cm larger than normal heights in zero tidal system. To confirm the acquired results, they are checked against the differences obtained by Eq. (11) which allows direct computation of $H^m - H^z$ without any

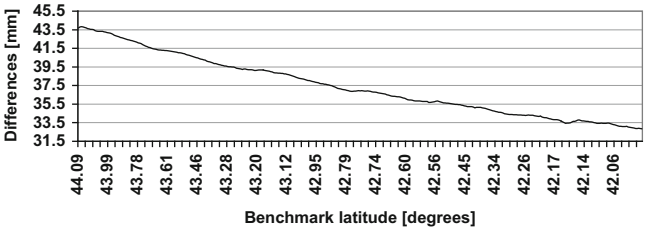

Fig. 2 Differences between normal heights in the two tidal systems (mean and zero)

Table 2 Comparison of the obtained differences between normal heights in mean and zero tidal system ($H^m - H^z$) with (Eqs. 1–9) and without measurements (Eq. 11)—a sample

BM No	Latitude [°]	$A = H^m - H^z$ [mm] (Eqs. 1–9)	$B = H^m - H^z$ [mm] (Eq. 11)	Agreement, A−B [μm]
CBM 1	44.09000	43.709	43.712	3
BM 1	44.10833	43.805	43.807	2
BM 2	44.11000	43.813	43.816	3
BM 3	44.10667	43.796	43.798	2
BM 4	44.09667	43.744	43.747	3

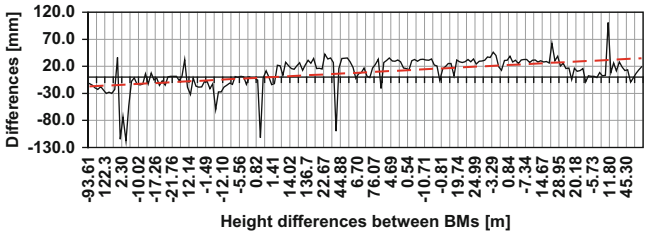

Fig. 3 Differences between normal heights in current calculations and the Catalogue (with the blunders omitted) and their trend (*dashed red line*)

measurements. A sample of that comparison is presented in Table 2 and the agreement of the data is within the accuracy of −5 μm to +3 μm, which is much better than observation errors.

Also a comparison between normal heights in zero tide system, obtained by current calculations, and the normal heights, given in the Catalogue (Geodesy Department of NIGGG 2011) is presented at Fig. 3. As it was already mentioned, the Catalogue is based on the previous re-levelling of the NFOLN, conducted in 1974–1984. In current re-levelling not all of the Catalogue BMs were used due to damages or destructions. Because of this reason only the common BMs between both re-levelling campaigns are used. Results show that most of the differences between the heights have magnitude of 2–4 cm; few are higher than 10 cm. Three cases of blunders have been detected, as well; for two of them the difference between the heights is about 8 m and for the third it is 14 m.

Conclusions and Recommendations

Taking into account the conducted research and considering the encountered obstacles, the following conclusions and recommendations are proposed:

First, it is necessary to implement and to maintain detailed data banks including all information required for the appropriate computation of gravity values and geopotential numbers. Providing all the data and complete meta-information is extremely important for precise local and international geodetic activities and must be considered as mandatory for all ongoing and future measurements.

Second, special care shall be given to the recording of the date and the time of measurements, the geographical (i.e. GPS) coordinates of the measured points, the heights and the gravity values for all the base points used, the field notes on events affecting the measurements, etc. Most of this information must be requested from and provided by the field teams following very strict quality assurance/quality control (QC/QA) procedures.

Third, when working with local terrestrial gravity data one should keep in mind that current practice in Bulgaria is *without application* of tidal reductions to observed gravity (including a proper reduction of time-dependent tidal components) but it has to be changed. Actually, gravity data might be a source of inconsistencies between the current calculations and the "Catalogue of the NFOLN BMs in EVRF2007", but in either case those discrepancies should be put under investigation, especially for the blunders found.

Finally, the obtained average difference of about 4 cm between the normal heights in mean and zero tidal system should be considered as significant in case of National Vertical Reference System improvement, local geoid modelling, terrestrial and satellite data combination, etc.

Based on these conclusions, the following recommendations are possible: For local geodetic purposes mean tidal system could be maintained for the time being. That will ensure fewer discrepancies in the obtained data due to the tidal system taking into account the current practice in the country. Nevertheless, the observed gravity still needs to be corrected for the effect of tides. For international activities data could be easily converted by Ekman's formulae to the necessary tidal system.

In the future, the implementation of the zero tidal system *only* should be considered. Thus, Bulgaria will have the opportunity to help increasing the accuracy of existing regional and global geoid models over it's or neighbouring territories or for computation of new gravity field and geoid products from combinations of terrestrial and satellite based techniques like GOCE and GRACE gravity missions, etc.

Acknowledgements The authors would like to thank local geodetic archive "Geokartfond" at Agency of Geodesy, Cartography and Cadastre for the provided data and financial support for presenting this paper at the International Symposium on Gravity, Geoid and Height Systems 2012 in Venice. The authors are also very grateful to Dr. Martina Sacher and the other two anonymous reviewers for their valuable comments, suggestions and recommendations taken into account in the final edition of this paper.

References

Belyashki T (2004) Incorporation of Bulgarian National Levelling Network into United European Levelling Network (UELN). Technical report, "Geokartfond" at Agency of Geodesy, Cartography and Cadastre, Sofia (in Bulgarian)

Borrass E (1911) Bericht über dierelativen Messungen der Schwerkraft mit Pendelapparaten in der Zeit von 1808 bis 1909 und über ihre Darstellung im Potsdamer Schweresystem. In: Verhandlungen der 16 allgemeinen Konferenz der internationalen Erdmessung, London 1909, Teil 3: Spezialbericht über die relativen Schweremessungen, Berlin (in German)

Darakchiev TS (2001) Tidal variations of the deflections of the vertical and their influence on the astronomical latitude observations. Geod Cartogr Land Manage 5:6–8 (in Bulgarian)

Ekman M (1989) Impacts of geodynamic phenomena on systems of height and gravity. Bull Geod 63:281–296

Geodesy Department of National Institute of Geodesy, Geophysics and Geography (NIGGG), Bulgarian Academy of Science (BAS) (2011) Catalogue of National First Order Levelling Network in EVRF2007. In: Calculation of the benchmark's heights of National First Order Levelling Network of Bulgaria in the European Vertical Reference System EVRS. Technical report, "Geokartfond" at Agency of Geodesy, Cartography and Cadastre, Sofia (in Bulgarian)

Hofmann-Wellenhof B, Moritz H (2005) Physical geodesy. Springer, Wien

Ihde J, Mäkinen J, Sacher M (2008) Conventions for the definition and realization of a European Vertical Reference System (EVRS) – EVRS Conventions 2007. Draft. Bundesamt für Kartographie und Geodäsie, Finnish Geodetic Institute. http://www.bkg.bund.de/geodIS/EVRS/SharedDocs/Downloads/Publications/EVRFConventions2007,templateId=raw,property=publicationFile.pdf/EVRFConventions2007.pdf . Accessed 22 Oct 2012

Longman IM (1959) Formulas for computing the tidal accelerations due to the Moon and the Sun. J Geophys Res 64:2351–2355

Mäkinen J, Ihde J (2009) The permanent tide in height systems. In: Sideris MG (ed) Observing our changing Earth. Proceedings of the 2007 IAG General Assembly, Perugia, Italy, 2–13 July 2007. IAG Symp 133:81–87

Milev G, Ruess D, Ullrich C, Vassileva K, Stoyanov L, Valev G, Mihailov E, Dimitrov N (2005) Absolute measurements and the gravity system of Bulgaria. Geod Cartogr Land Manage 5–6:10–17 (in Bulgarian)

Milev G, Valev G, Vassileva K, Mihailov E (2008) National gravity network of Bulgaria. Geod Cartogr Land Manage 5–6:4–7 (in Bulgarian)

Morelli C, Gantar C, Honkasalo T, McConnell K, Tanner J, Szabo B, Uotila U, Wahlen C (1974) The International Standardization Net 1971 (IGSN71). IUGG-IAG, Publ Spec No 4, Paris

Moritz H (1980) Geodetic reference system 1980. Bull Geod 54:395–405

Pashova L (2010) Height systems used in Bulgaria and prospects for joining the European Vertical Reference System (EVRS). Geomedia.

http://www.geomedia.bg/index.php/article:354?PHPSESSID=8ff09516ed2a7290d0b371fccbc6a069. Accessed 22 Oct 2012 (in Bulgarian)

Sacher M, Ihde J, Liebsch G, Mäkinen J (2008) EVRF2007 as realization of the European Vertical Reference System. EUREF Symposium, Brussels. http://www.bkg.bund.de/geodIS/EVRS/SharedDocs/Downloads/Publications/EVRF2007AsRealOfEVRS,templateId=raw,property=publicationFile.pdf/EVRF2007AsRealOfEVRS.pdf. Accessed 22 Oct 2012

Stoyanov V, Ivanov R (2000) Towards an improved geodetic reference system for Bulgaria. Geod Cartogr Land Manage 1:3–9 (in Bulgarian)

Tsenkov T, Belyashki T, Mihailov E (2011) Gravimetric measurements along the levelling lines of the National Levelling Network of Bulgaria. In: Proceedings of XIth international scientific conference VSU, vol 2, pp V1.13–V1.18. ISSN: 11314-071X, Sofia (in Bulgarian)

Uotila UA (1980) Note to the users of international gravity standardization net 1971. Bull Geod 54:407–408

Zhekov D, Zdravchev I, Gospodinov S (1990) Accounting for influence of luni-solar tides on the results of high precision levelling measurements in Bulgaria. Geod Cartogr Land Manage 5–6:10–17 (in Bulgarian)

Part VI

Gravity Field and Mass Transport Modeling

Consistent Combination of Gravity Field, Altimetry and Hydrographic Data

Silvia Müller, Jan Martin Brockmann, and Wolf-Dieter Schuh

Abstract

The ocean's mean dynamic topography as the difference between the mean sea surface and the geoid reflects many characteristics of the general ocean circulation. Consequently, it provides valuable information for evaluating or tuning ocean circulation models. However, the determination of the mean dynamic topography from satellite based gravity field and altimetric observations as well as in-situ data is not straightforward. We developed a rigorous combination method where both instrumental errors and omission errors are accounted for, including the determination of optimal relative weights between the observation groups. This method allows the direct determination of the normal equations of the mean dynamic topography on arbitrary grids. In this paper we focus on the steps for preprocessing the in-situ data. We show results for the North Atlantic Ocean based on a combined GRACE/GOCE gravity field, altimetric sea surface height observations from Jason-1 and Envisat and in-situ observations of salinity, temperature and pressure from Argo floats.

Keywords

Altimetry • Consistent combination • GOCE • GRACE • Mean dynamic topography

1 Introduction

The determination of the mean dynamic topography from satellite-based gravity field and altimetry data is not straightforward, as the data types differ in their representation and spatial resolution. While the accepted gravity field models are provided as a band-limited series of spherical harmonics, the altimetric observations are given as point values over the ocean. Usually, dedicated filter approaches are introduced to overcome this difficulty (see e.g. Becker et al. 2012; Becker 2012). In our recently developed approach the usage of a particular filter is avoided. The geoid and the mean dynamic topography are simultaneously assessed. Special attention is paid to the complete modeling and the consideration of the complete variance/covariance information of the observation groups within the model to provide the mean dynamic topography along with its consistent (inverse) covariance matrix or the normal equations on arbitrary grids respectively. Within inverse ocean modeling a cost function is minimized, which contains different contributions from quadratic model-data differences (e.g. temperature, salinity, mean dynamic topography) weighted by the particular inverse error covariance matrix. In case of the mean dynamic topography the derived normal equation matrix represents the appropriate weight matrix.

Complementary, hydrographic data can also be used to obtain information about the mean dynamic topography. The consistent integration of these data sets into the model requires a special data handling and the use of an additional bias parameter. The focus of this paper is on the preprocessing of hydrographic data sets—these are profile

S. Müller (✉) • J.M. Brockmann • W.-D. Schuh
Department of Theoretical Geodesy, Institute of Geodesy and Geoinformation, University of Bonn, Nussallee 17, 53115 Bonn, Germany
e-mail: silvia.mueller@geod.uni-bonn.de; brockmann@uni-bonn.de; schuh@uni-bonn.de

U. Marti (ed.), *Gravity, Geoid and Height Systems*, International Association of Geodesy Symposia 141,
DOI 10.1007/978-3-319-10837-7_34,

measurements of salinity, temperature and pressure of the Argo floats—and its rigorous combination with the satellite data. The different observation groups are combined in terms of normal equations. In order to provide an optimal estimation of the mean dynamic topography we implemented a rigorous variance component estimation to determine relative weights between the diverse observation groups. Additionally, we consider the impact of the different observation groups on the parameters of the mean dynamic topography. The focus of this study is on the North Atlantic Ocean.

The paper is organized as follows. The observations used in this study are briefly introduced in Sect. 2. The processing steps of the Argo float measurements are described in Sect. 3. In Sect. 4 we summarize the combination method of the different observation groups. Subsequently the obtained results are shown in Sect. 5. The paper closes with the discussion and an outlook in Sect. 6.

2 Data Types

2.1 Gravity Field Model

We use the static part of the GRACE gravity field model ITG-Grace2010 (Mayer-Gürr et al. 2010) which is expanded as a sum of spherical harmonics up to degree and order 180 and the GOCE gravity field model GOCE_EGM_TIMrelease3 (Pail et al. 2011) with a maximum spherical harmonic degree of 250. Both gravity field models are provided with the full covariance matrix of the potential coefficients so that the normal equations can be reconstructed.

2.2 Altimetry

To derive a profile of mean sea surface heights for the North Atlantic Ocean we consider corrected sea surface heights from Jason-1 and Envisat between October 2002 and February 2009. During the whole preprocessing steps a rigorous error propagation was implemented based on empirical covariance functions along the satellite tracks in order to determine the full covariance matrix of the resulting mean sea surface profile. We used monomission along track data sets provided by AVISO (http://www.aviso.oceanobs.com). Details of the processing steps of the altimetric data can be found in Becker (2012).

2.3 Argo Floats

The Argo project provides profile measurements of salinity, temperature and pressure. We used observations between October 2002 and February 2009 for the North Atlantic Ocean according to the considered altimetric observation period. The data used in this study were obtained from the French data centre Coriolis (http://www.coriolis.eu.org). Only delayed mode measurements which passed the quality controls (Wong et al. 2010) were used. The particular processing steps for the in-situ data are described below.

3 Processing of Argo Float Measurements

3.1 Dynamic Heights

Initially, density values ρ are derived from the salinity s, temperature t and pressure p measurements for different depths (see e.g. Fofonoff and Millard 1983). Based on these density profiles dynamic heights are calculated

$$\mathrm{DH} = \frac{1}{g} \int_{\zeta}^{P} \left(\frac{1}{\rho(s,t,p)} - \frac{1}{\rho(35,0,p)} \right) \mathrm{d}p \,, \qquad (1)$$

which reflect surface currents due to horizontal density variations relative to a presumed level of no motion P (see e.g. Gill 1982). According to this, the dynamic heights represent the baroclinic part of the ocean's dynamic topography from the level of no motion up to the surface ζ. We assume a level of no motion P corresponding to a depth of 1,500 m in this study. This choice turned out to be reasonable due to the amount of available data. Comparisons to dynamic heights relative to a depth of 1,950 m have shown an almost constant shift and no significant change in the horizontal gradients can be expected.

The derived dynamic heights **DH** are dependent on time and space. In order to model the stochastic behavior we computed a two-dimensional empirical autocovariance function (see e.g. Sansó and Schuh 1987) depending on the temporal distance Δt and spatial distance Δs. For this purpose we first subtract a space dependent deterministic trend from the dynamic heights **DH** and analyze the residual signal afterwards. The obtained covariances either dampen or amplify in space and can be modeled by the sum of two exponential functions with the coefficients c_1 and c_2. In the time domain the empirical covariances show an annual cycle which can be modeled by a cosine function with the coefficient a and the frequency b. The spatial and temporal dependencies are separated from each other and we use a product spatial-temporal covariance model

$$C(\Delta t, \Delta s) = a \cos(b \Delta t) \left[\frac{1}{2} e^{-c_1 \Delta s} + \frac{1}{2} e^{-c_2 \Delta s} \right] \qquad (2)$$

to approximate the empirically derived covariance function. Subsequently the covariance matrix $\boldsymbol{\Sigma}\,\{\mathbf{DH}\}$ of the dynamic heights **DH** can be assembled.

3.2 Time Variable Content

As we are only interested in the time averaged dynamic topography the time variable part contained in the dynamic heights **DH** must be removed. The time variable component of the dynamic topography is represented by the sea level anomalies—the differences between the actual sea surface and the mean sea surface. In the following, we assume that the sea level anomalies also represent the time variable component of the dynamic heights **DH**. The required quantities are derived by linear interpolation of the altimetric determined sea level anomalies along the satellite tracks in time and space onto the observation times and positions of the Argo float measurements. Within this interpolation procedure we implemented a rigorous error propagation yielding the covariance matrix $\boldsymbol{\Sigma}\{\mathbf{SLA}\}$ of the required sea level anomalies **SLA**. Finally we subtract the time variable part from the dynamic heights **DH** to compute mean dynamic heights **MDH**

$$\mathbf{MDH} = \mathbf{DH} - \mathbf{SLA} \tag{3}$$

with the covariance matrix

$$\boldsymbol{\Sigma}\{\mathbf{MDH}\} = \boldsymbol{\Sigma}\{\mathbf{DH}\} + \boldsymbol{\Sigma}\{\mathbf{SLA}\}\ . \tag{4}$$

3.3 Modeling of the Missing Part

As already mentioned the information obtained from the hydrographic data only represents the baroclinic part of the dynamic topography from the surface down to the assumed level of no motion of 1,500 m. To achieve a complete modeling and enable a consistent combination with the altimetric and gravity field data, the missing baroclinic part from the level of no motion down to the ocean bottom and the barotropic component must be considered. Denoting the missing component by $\Delta\mathbf{MDT}$ it can be written as

$$\Delta\mathbf{MDT} = \mathbf{MDT} - \mathbf{MDH}\ . \tag{5}$$

In the following the missing signal content is considered as random variable $\Delta\mathcal{MDT}$ which is characterized by its expectation $\boldsymbol{E}\{\Delta\mathcal{MDT}\}$ and the covariance $\boldsymbol{\Sigma}\{\Delta\mathcal{MDT}\}$. These quantities are now determined by comparisons with external estimates of the mean dynamic topography. Here we used the CLS09 (Rio et al. 2011), DTU10 (Andersen and Knudsen 2009) and Maximenko/Niiler (Maximenko et al. 2009) model and computed the particular differences between the three models and the derived mean dynamic heights **MDH**. Because we cannot prefer any of the models the mean values of the different deviations are analyzed to describe the expectation and covariance of the missing component. The mean value of these averaged differences is nearly zero so that the expectation $\boldsymbol{E}\{\Delta\mathcal{MDT}\}$ is assumed to be zero and

$$\Delta\mathbf{MDT} = \mathbf{0}\ . \tag{6}$$

In order to model the covariances of the missing signal we determined the empirical autocovariance function depending on the spherical distance d. This shows a fast decrease to negative values and damped oscillations. Accordingly, the empirical autocovariance function is approximated by the following combination of finite covariance and Bessel functions

$$\begin{aligned} C(d) = \Bigg[& \frac{1}{3}R_1^6\pi - \frac{1}{2}R_1^4 d^2\pi + \frac{1}{3}\left(R_1^4 d + \frac{4}{3}R_1^2 d^3 - \frac{1}{12}d^5\right) \\ & \sqrt{R_1^2 - \left(\frac{d}{2}\right)^2} + \left(R_1^4 d^2 - \frac{2}{3}R_1^6\right)\arcsin\frac{d}{2R_1}\Bigg] \\ & \left(2R_2^4\pi - 4R_2^4\arcsin\frac{d}{2R_2} - \left(6R_2^2 d - d^3\right)\sqrt{R_2^2 - \left(\frac{d}{2}\right)^2}\right. \\ & \left. + \sum_{i=1}^{4} a_i J_0(k_i d)\right)\ . \end{aligned} \tag{7}$$

The first term is a finite covariance function according to Sansó and Schuh (1987), where the parameter R_1 defines the half length of the support. The second term is composed of a finite covariance function according to Koch et al. (2010) with the half length of the support R_2 and a linear combination of four Bessel functions J_0 of first kind and order zero with the coefficients a_i and the frequencies k_i. This part models the fast decrease of the covariances to negative values by the finite covariance function according to Koch et al. (2010) and the oscillations by the Bessel functions. Additionally, the functions are multiplied with the finite covariance function according to Sansó and Schuh (1987) to describe the dampening of the oscillations.

The covariance matrix $\boldsymbol{\Sigma}\{\Delta\mathbf{MDT}\}$, describing the missing part, is assembled and we obtain quasi in-situ observations of the mean dynamic topography

$$\mathbf{MDT} = \mathbf{MDH} + \Delta\mathbf{MDT} = \mathbf{MDH} + \mathbf{0} \tag{8}$$

with the covariance matrix

$$\boldsymbol{\Sigma}\{\mathbf{MDT}\} = \boldsymbol{\Sigma}\{\mathbf{MDH}\} + \boldsymbol{\Sigma}\{\Delta\mathbf{MDT}\}\ . \tag{9}$$

Figure 1 shows the in-situ mean dynamic topography observations and its corresponding covariance matrix.

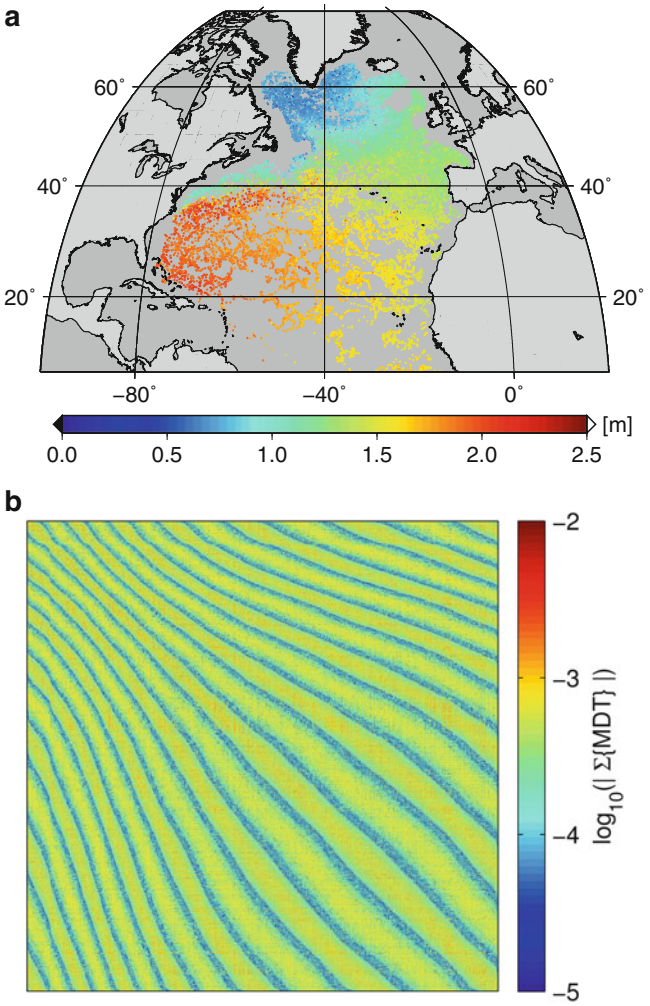

Fig. 1 (**a**) Quasi in-situ observed mean dynamic topography **MDT** and (**b**) its corresponding covariance matrix $\boldsymbol{\Sigma}$ **{MDT}**

4 Combination Method

The three different observation groups are combined in terms of normal equations. If only gravity field and altimetry observations are considered in our model, the unknowns of the model are the geoid represented by spherical harmonics and the mean dynamic topography parameterized by a linear combination of finite element base functions. The base functions can be for example linear or quadratic piecewise polynomials so that the unknowns of the mean dynamic topography parameterization are directly the mean dynamic topography and possibly its derivatives at the nodal points of the finite elements. According to this the altimetric mean sea surface is separated into the geoid and the mean dynamic topography. Within the model, different frequency domains of the observations are considered, so that the vector of the unknown gravity field parameters is separated into different subdomains. Special attention is paid to model the omission domain within the altimetric observation equations based on a priori information. In addition, we introduce smoothness conditions according to the Hilbert Space H_Γ^1 (Schuh and Becker 2010). We use Kaula's rule of thumb (Kaula 1966) as a first guess to fix the unknown coefficients. A detailed description of the developed method for combining gravity field and altimetry observations in a rigorous way can be found in Becker (2012).

In theory, the satellite data and the quasi in-situ mean dynamic topography data provide the same information about the mean dynamic topography or its horizontal gradients respectively. However, the signals have different reference levels or mean values. Here, we assume a constant shift between satellite and in-situ information. Thus, we introduce an auxiliary bias parameter accounting for different reference levels, if in-situ data is introduced in the model. Denoting the gravity field parameters with $\boldsymbol{x}_{cs}$, the parameters describing the finite element mesh of the mean dynamic topography with $\boldsymbol{x}_{FE}$ and the bias parameter with x_c, the combined normal equations can be written as

$$\begin{bmatrix} \boldsymbol{N}_{cs}^{\mathrm{G}} + \boldsymbol{N}_{cs}^{\mathrm{MSS}} + \boldsymbol{N}_{cs}^{\mathrm{s}} & \boldsymbol{N}_{cs,FE}^{\mathrm{MSS}} & \boldsymbol{0} \\ \boldsymbol{N}_{FE,cs}^{\mathrm{MSS}} & \boldsymbol{N}_{FE}^{\mathrm{MSS}} + \boldsymbol{N}_{FE}^{\mathrm{MDT}} & \boldsymbol{N}_{FE,c}^{\mathrm{MDT}} \\ \boldsymbol{0} & \boldsymbol{N}_{c,FE}^{\mathrm{MDT}} & N_{c}^{\mathrm{MDT}} \end{bmatrix} \begin{bmatrix} \boldsymbol{x}_{cs} \\ \boldsymbol{x}_{FE} \\ x_c \end{bmatrix} = \begin{bmatrix} \boldsymbol{n}_{cs}^{\mathrm{G}} + \boldsymbol{n}_{cs}^{\mathrm{MSS}} \\ \boldsymbol{n}_{FE}^{\mathrm{MSS}} + \boldsymbol{n}_{FE}^{\mathrm{MDT}} \\ n_{c}^{\mathrm{MDT}} \end{bmatrix} \tag{10}$$

or in short

$$\left(N^{\mathrm{G}} + N^{\mathrm{MSS}} + N^{\mathrm{s}} + N^{\mathrm{MDT}}\right) \boldsymbol{x} = \boldsymbol{n}^{\mathrm{G}} + \boldsymbol{n}^{\mathrm{MSS}} + \boldsymbol{n}^{\mathrm{MDT}} \tag{11}$$

with the components for the gravity field (G), the mean sea surface (MSS), the smoothness conditions (s) and the in-situ observations (MDT).

Note, that in principle the in-situ data and the altimetric mean sea surface are correlated groups of observations because the subtracted time variable part **SLA** of the dynamic topography depends on the mean sea surface. However, the correlations are negligibly small so that we consider both normal equations separably.

4.1 Relative Weighting: Variance Component Estimation

Relative weighting of the different observation groups plays an important role in order to provide an optimal estimation of the parameters. We determine the relative weights $1/\sigma_i^2$ via a rigorous variance component estimation (see e.g. Koch and Kusche 2002; Brockmann and Schuh 2010) so that the combined normal equations (11) are rewritten as

$$\left(\sum_i \frac{1}{\sigma_i^2} N_i\right) \boldsymbol{x} = \sum_i \frac{1}{\sigma_i^2} \boldsymbol{n}_i \,. \tag{12}$$

4.2 Contribution of Different Observation Groups to the Parameters

The overall solution $\tilde{\boldsymbol{x}}$ can be interpreted as weighted sum of the theoretical individual solutions $\boldsymbol{x}_i$ for the particular observation groups

$$\tilde{\boldsymbol{x}} = \boldsymbol{N}^{-1} \sum_i \frac{1}{\sigma_i^2} \boldsymbol{N}_i \boldsymbol{x}_i = \sum_i \boldsymbol{W}_i \boldsymbol{x}_i \,. \tag{13}$$

The weight matrices $\boldsymbol{W}_i$ sum up to the identity matrix $\boldsymbol{I}$, so that the main diagonal elements of the matrices $\boldsymbol{W}_i$ may be considered as the contribution of the individual observation group i to the overall estimation process of the parameters.

5 Results

The results shown here are obtained with the following model configuration. The nodal points of the finite elements were arranged on a regular triangulated $1° \times 1°$ grid. We used linear polynomials as base functions in order to represent the mean dynamic topography. Hence, the unknowns $\boldsymbol{x}_{FE}$ are the mean dynamic topography at the nodal points. The commission domain spans the spherical harmonics of degree 2–300 and the omission domain is described by a priori information provided by the EGM2008 (Pavlis et al. 2012) and Kaula's rule of thumb. See Becker et al. (2012) and Becker (2012) for details of the parameterization of the omission domain.

Figure 2 shows the progression of the relative weights of the different observation groups during the iterative variance component estimation process [see Sect. 4.1, (12)]. The weights of the GRACE and GOCE observations remain at approximately $1/\sigma_G^2 \approx 1$, while the impact of the smoothness conditions and the altimetric measurements decreases. The weight of the smoothness conditions reaches $1/\sigma_s^2 \approx 0.7$ and the altimetric data is downweighted by $1/\sigma_{MSS}^2 \approx 0.6$. In contrast, the relative weight of the Argo float measurements increases to $1/\sigma_{MDT}^2 \approx 4$. This indicates that the empirical error modeling of the altimetric and in-situ measurements must be reconsidered, which is subject to further studies but beyond the scope of this study. In case of the altimetric data the covariance matrix is composed of two terms—the covariance of the mean sea surface and the covariance describing the omission domain. The omission error model includes the error degree variances of the EGM2008. We assume, that the downweighting of the altimetric data probably indicates that the EGM2008 errors are underestimated. The covariance matrix of the quasi in-situ mean dynamic topography is the sum of the empirically determined covariance matrix of the dynamic heights $\boldsymbol{\Sigma}\{\mathbf{DH}\}$, the covariance matrix of the time variable part $\boldsymbol{\Sigma}\{\mathbf{SLA}\}$ and the covariance matrix of the missing part $\boldsymbol{\Sigma}\{\Delta\mathbf{MDT}\}$. The increasing impact of the Argo float measurements on the estimated parameters suggests that the empirically derived error model of the dynamic heights implies a priori unrealistic large variances and must be reconsidered.

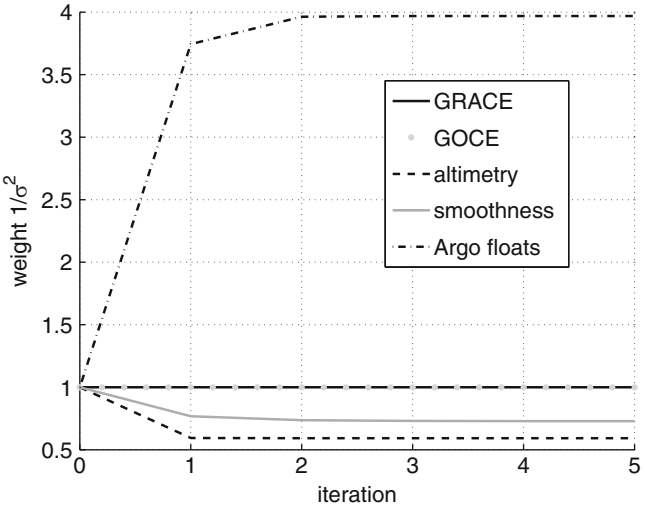

Fig. 2 Progression of relative weights between the observation groups resulting from variance component estimation

Figure 3 illustrates the resulting mean dynamic topography and its associated standard deviations. The mean dynamic topography shows some unrealistic short scale features especially at high latitudes. The standard deviation is 6.3 cm on average. It decreases to approximately 3.5 cm in regions where in-situ data is included in the computation and reaches its maximum at high latitudes greater than 66°N where only Envisat measurements are available and the oscillations of the mean dynamic topography are most pronounced. Closed-loop simulations have shown that these oscillations occur in case of insufficiently accurate information content of the integrated gravity field model at the defined spatial resolution of the finite elements. If the spatial resolution of the finite elements matches the frequency domain, in which the information content of the gravity field is highly accurate, the altimetry signal can be separated very well into geoid and mean dynamic topography and the combined model provides a smooth mean dynamic topography. In either case the characteristics of the mean dynamic topography are reflected by the associated error description and the method yields a consistent variance/covariance matrix. At high latitudes the spatial resolution of the finite elements increases so that the non-physical noise is amplified, while the standard deviations also increase.

The contributions of the altimetric mean sea surface and the Argo float measurements to the estimation of the mean dynamic topography parameters are shown in Fig. 4 [see Sect. 4.2, (13)]. The largest impact of the in-situ data can be

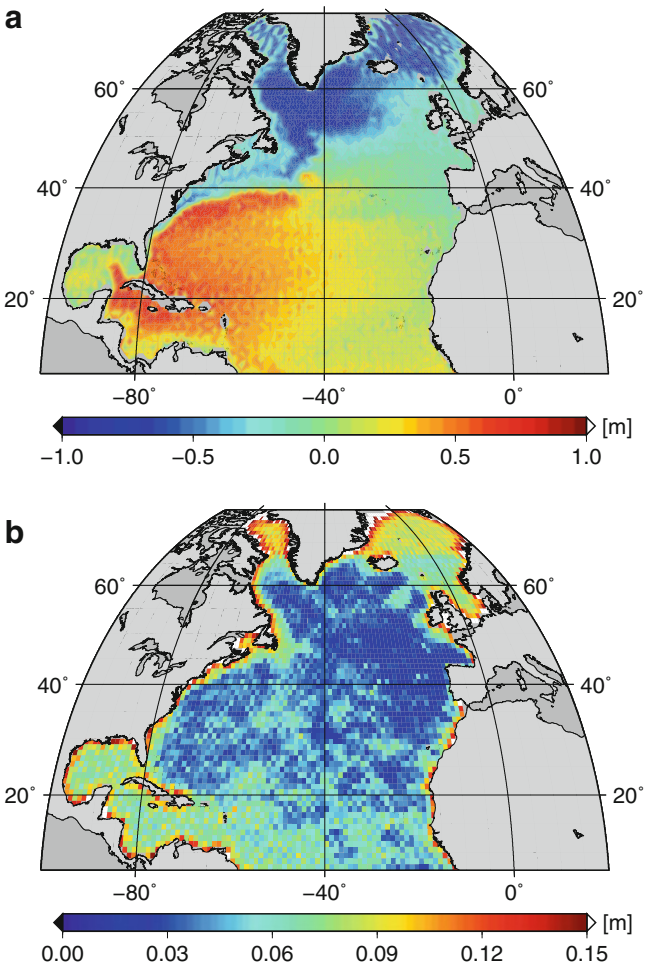

Fig. 3 (**a**) Mean dynamic topography estimated on a $1^\circ \times 1^\circ$ grid and (**b**) its associated standard deviations

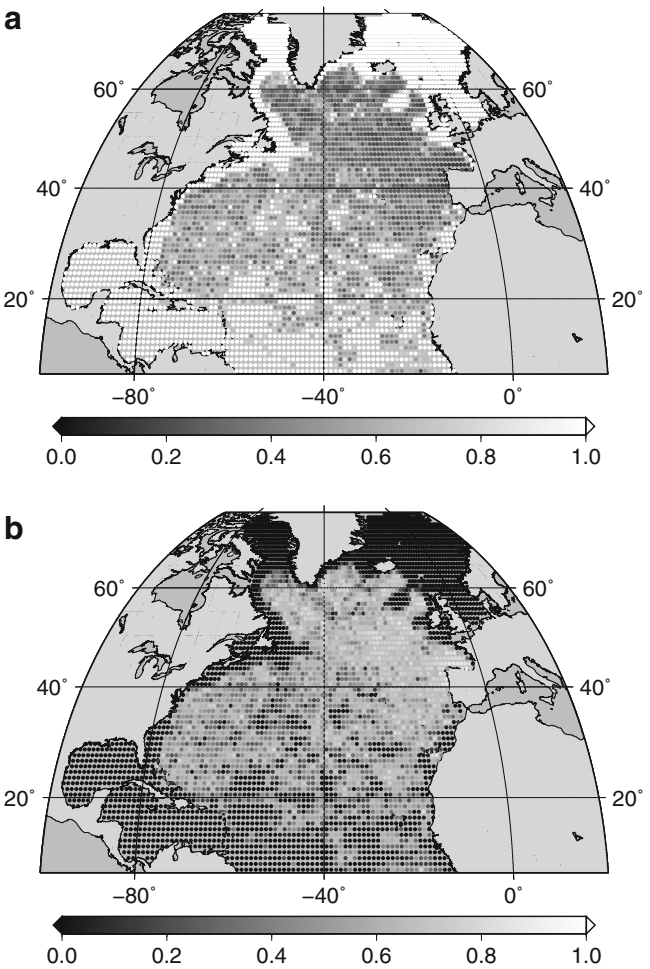

Fig. 4 Contribution of (**a**) the altimetric and (**b**) the Argo float measurements to the estimated mean dynamic topography

observed in regions where the observation density is high. In regions where both observation types are available for the computations the contribution of the altimetric measurements is 0.51 on average and the contribution of the in-situ data is accordingly 0.49.

6 Discussion and Outlook

We developed an integrated approach to combine gravity field, altimetry and in-situ data in a rigorous way. With the presented method we are able to provide the normal equations of the mean dynamic topography on arbitrary grids or the mean dynamic topography and its consistent covariance matrix respectively. Hence, we have direct access to the target quantities required by ocean circulation models. Special attention is paid to the complete modeling of all observations including the omission domain and the consistent error description as well as its rigorous propagation. In addition we implemented a rigorous variance component estimation to determine optimal relative weights between the different observation groups.

The focus of the study is on the determination of the mean dynamic topography and its associated covariance matrix in the North Atlantic Ocean, but the approach also opens up the opportunity to improve the gravity field and the mean dynamic topography in a joint estimation. However, this requires the integration of additional observations like (global) ocean-wide altimetric data and terrestrial gravity data for example. Up to now the estimation process is completely unrestricted. No explicit smoothness conditions are applied to the mean dynamic topography. In order to improve the global gravity field and the mean dynamic topography additional constraints like e.g. energy minimization strategies can be considered and applied. Another possible extension of the method is the parameterization of the time variability

of the ocean's dynamic topography within the estimation procedure. All these aspects are subject for further studies.

Acknowledgements This work was funded within the DFG priority programme SPP 1257 "Mass transport and mass distribution in the system Earth". The computations were performed on the JUROPA supercomputer at FZ Jülich. The computing time was granted by John von Neumann Institute for Computing (project HBN15).

References

Andersen OB, Knudsen P (2009) DNSC08 mean sea surface and mean dynamic topography models. J Geophys Res 114:C11001. doi:10.1029/2008JC005179

Becker S (2012) Konsistente Kombination von Schwerefeld, Altimetrie und hydrographischen Daten zur Modellierung der dynamischen Ozeantopographie. Ph.D. thesis, Universität Bonn. http://hss.ulb.uni-bonn.de/2012/2919/2919.htm

Becker S, Freiwald G, Losch M, Schuh W-D (2012) Rigorous fusion of gravity field, altimetry and stationary ocean models. J Geodyn. doi:10.1016/j.jog.2011.07.0069

Brockmann J-M, Schuh W-D (2010) Fast variance component estimation in GOCE data processing. In: Mertikas S (ed) Gravity, geoid and earth observation. IAG symposia. Springer, Berlin. doi:10.1007/978-3-642-10634-7_25

Fofonoff NP, Millard RC (1983) Algorithms for computation of fundamental properties of seawater. UNESCO Technical Papers in Marine Science, p 44

Gill AE (1982) Atmosphere-ocean dynamics. Academic, New York

Kaula WM (1966) Theory of satellite geodesy. Blaisdell Publishing Company, Massachusetts/Toronto/London

Koch KR, Kusche J (2002) Regularization of geopotential determination from satellite data by variance components. J Geod 76:259–268. doi:10.1007/s00190-002-0245-x

Koch KR, Kuhlmann H, Schuh W-D (2010) Approximating covariance matrices estimated in multivariate models by estimated auto- and cross-covariances. J Geod 84:383–397. doi:10.1007/s00190-010-0375-5

Maximenko N, Niiler P, Rio M-H, Melnichenko O, Centurioni L, Chambers D, Zlotnicki V, Galperin B (2009) Mean dynamic topography of the ocean derived from satellite and drifting buoy data using three different techniques. J Atmos Ocean Technol 26:1910–1918. doi:10.1175/2009JTECHO672.1

Mayer-Gürr T, Kurtenbach E, Eicker A (2010) ITG-Grace2010 gravity field model. http://www.igg.uni-bonn.de/apmg/index.php?id=itg-grace2010

Pail R, Bruinsma S, Migliaccio F, Förste C, Goiginger H, Schuh W-D, Höck E, Reguzzoni M, Brockmann J, Abrikosov O, Veicherts M, Fecher T, Mayrhofer R, Krasbutter I, Sansó F, Tscherning CC (2011) First GOCE gravity field models derived by three different approaches. J Geod 85(11):819–843. doi:10.1007/s00190-011-0467-x

Pavlis NK, Holmes SA, Kenyon S, Factor JK (2012) The development and evaluation of the Earth Gravitational Model 2008 (EGM2008). J Geophys Res 117:B04406. doi:10.1029/2011JB008916

Rio M-H, Guinehut S, Larnicol G (2011) New CNES-CLS09 global mean dynamic topography computed from the combination of GRACE data, altimetry, and in situ measurements. J Geophys Res 116:C07018. doi:10.1029/2010JC006505

Sansó F, Schuh W-D (1987) Finite covariance functions. Bull Géod 61:331–347

Schuh W-D, Becker S (2010) Potential field and smoothness conditions. In: Contadakis ME, Kaltsikis C, Spatalas S, Tokmakidis K, Tziavos IN (eds) The apple of knowledge-In honour of Prof. N. Arabelos. AUTH-Faculty of Rural and Surveying Engineering, University of Thessaloniki, Thessaloniki, pp 237–250

Wong A, Keeley R, Carval T, The Argo Data Management Team (2010) Argo quality control manual, Version 2.6. http://www.argodatamgt.org/content/download/341/2650/file/argo-quality-control-manual-V2.6.pdf, 2010

Local Hydrological Effects on Gravity at Metsähovi, Finland: Implications for Comparing Observations by the Superconducting Gravimeter with Global Hydrological Models and with GRACE

Jaakko Mäkinen, Tero Hokkanen, Heikki Virtanen, Arttu Raja-Halli, and Risto P. Mäkinen

Abstract

We construct a model for the influence of variation in local water storage on the observations of the superconducting gravimeter (SG) T020 in Metsähovi, Finland. The following hydrological components are accounted for: (1) soil moisture and groundwater in sediments, (2) groundwater in the fractures of the crystalline bedrock, (3) snow on the ground, and (4) snow on the laboratory roof. We show that due to the geometry of the local storage, its gravity influence at the SG is only a fraction of the influence of the corresponding Bouguer sheet, and discuss the implications for comparing the SG with variation in gravity observed with GRACE. We compare the SG residuals with the variation in gravity predicted from the local model and two models of continental water storage. The general patterns are similar but there are differences in amplitude and phase. Further research is outlined.

Keywords

Superconducting gravimeter • Hydrology • Soil moisture • Groundwater • Snow • Continental water storage • GRACE

1 Introduction

This paper treats local hydrology at Metsähovi, Finland, the site of the superconducting gravimeter (SG) GWR-T020. Modeling local hydrological effects in gravity at SG stations is important for many reasons. When the SG record is compared with gravity predicted using the storage of terrestrial water from regional-global hydrological models (RGHMs), or with regional variation in gravity observed with the GRACE satellite (Neumeyer et al. 2008; Weise et al. 2012; Crossley et al. 2012; Abe et al. 2012) the influence of the local hydrology enters the comparison as part of the SG record. Further, correction for all hydrological effects (local + regional + global) facilitates interpretation of the residual SG record for other phenomena.

We compare the SG with the RGHMs, not with GRACE. However, our results are relevant for SG/GRACE comparisons as well.

What are the issues in separating local and regional/global effects in a SG gravity record? The main signal in hydrology is seasonal and at this timescale regional and local water storage typically have similar patterns of variation (Virtanen et al. 2006). So have the corresponding gravity effects. When Neumeyer et al. (2008) regressed the SG record in Metsähovi on the local groundwater level to determine and remove the effects of local hydrology, they in fact removed an unknown but large part of the effects of the regional/global hydrology as well (Crossley et al. 2012). However, while the pattern may be similar, the amplitude of the local variation in terms of mass per surface unit depends on the local geology and may differ considerably from the regional average which is detected by GRACE and represented in RGHMs. Moreover,

J. Mäkinen • H. Virtanen (✉) • A. Raja-Halli
Finnish Geodetic Institute, Geodeetinrinne 2, 02431 Masala, Finland
e-mail: heikki.virtanen@fgi.fi

T. Hokkanen
Department of Civil and Environmental Engineering, Aalto University, School of Engineering, P.O. Box 16200, 00076 Aalto, Finland

R.P. Mäkinen
Finnish Environmental Institute, P.O. Box 140, 00251 Helsinki, Finland

U. Marti (ed.), *Gravity, Geoid and Height Systems*, International Association of Geodesy Symposia 141,
DOI 10.1007/978-3-319-10837-7_35,

since the local gravity effect is due to the direct attraction of the water masses it depends on the exact geometry of the water-carrying strata relative to the SG sensor, even if all of them are below the sensor. With relative gravity measurements, Mäkinen and Tattari (1991) observed a seasonal variation of 100 nm s^{-2} peak-to-peak in the gravity difference between two sites only 2 km apart, and used in-situ hydrological measurements to show that it is explained by the different local hydrological characteristics of the two sites.

Models for local hydrology at the SG sites may combine meteorological data, hydrological observation of storage parameters (e.g., soil moisture and groundwater level), and models of hydrological processes in various ways, see Van Camp et al. (2006), Longuevergne et al. (2009), Naujoks et al. (2010), Creutzfeldt et al. (2010).

The Metsähovi site (Figs. 1 and 2) was selected for the T020 expressly in order to minimize local hydrological effects. It is on an outcrop of crystalline bedrock in relatively flat terrain and the overburden in the immediate surroundings is thin. In our study area of 200×200 m^2 we have in-situ measurements of all storage components. We estimate the variation (1) in the attraction of local water storage in sediments; (2) in the attraction of local water storage in the fractures of the crystalline bedrock, (3) in the attraction of local snow on the ground and (4) on the laboratory roof. Our model is deterministic in the sense of Longuevergne et al. (2009): it is not adjusted to the gravity record but completely independent of it.

We then correct the record of the T020 for the local effects and compare it with variation in gravity predicted from the loading and attraction by regional and global water storage from two RGHMs: the GLDAS (Global Land Data Assimilation System; Rodell et al. 2004) and the ERA-Interim model (Dee et al. 2011).

The SG T020 began observations in 1994. Here we use the data since 2009 when the hydrological observations started in the present configuration. We decimate all time series to mean values of calendar month.

Previous hydrological studies at Metsähovi were performed by Virtanen (2000, 2001), Virtanen et al. (2006) and Hokkanen et al. (2006, 2007).

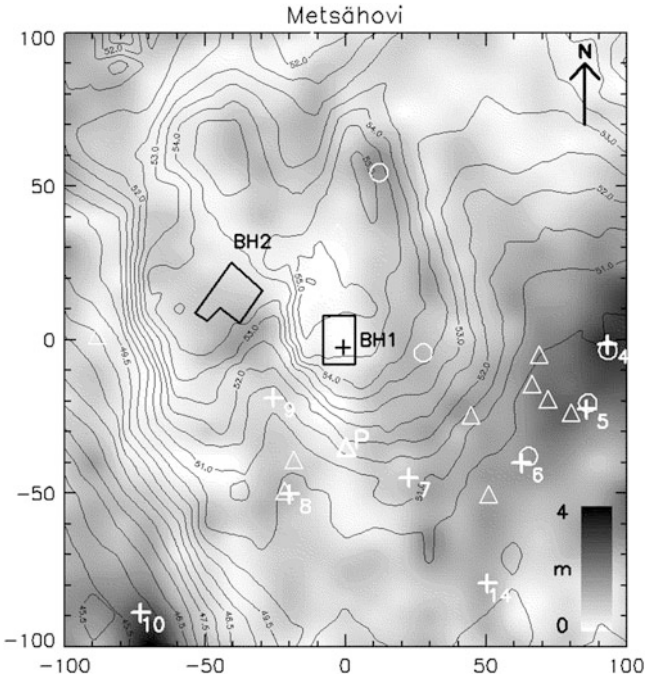

Fig. 1 Map of the Metsähovi area (200×200 m^2) of our local modeling. The isolines at 0.5 m interval show surface elevations and the *gray shades* show soil thickness in meter. The SG is in the center, marked by a *cross* inside the gravity laboratory. The SG sensor is at 55.6 m elevation. *Numbered crosses* mark the places of the groundwater tubes in soil. Three tubes are outside the plot area. The tube 6 used in Fig. 2 is at about (+60 m, −40 m) in the local coordinates. *Triangles* denote arrays of soil moisture sensors. The array "P" is about 30 m S of the gravity laboratory. BH1 (just W from the gravity laboratory) and BH2 are borehole wells in bedrock. A third borehole well for water use is inside the main building (NW from the gravity laboratory). *Small circles* denote dry access tubes. They are not used in this paper

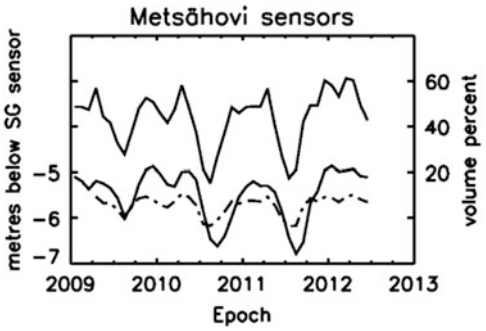

Fig. 2 Indicators of local water storage in Metsähovi. *Top*: volumetric soil moisture content between 0.1 and 0.5 m depth at array "P" (Fig. 1), in percent (*right-hand scale*). *Bottom solid curve*: groundwater level in borehole well BH1 (Fig. 1). *Bottom dash-dot curve*: groundwater level in groundwater tube T6 (Fig. 1). *Left-hand scale* shows height relative to the SG sensor

2 Metsähovi Station: Local Hydrogeology and Sensors

The Metsähovi station stands on a small hill on an outcrop of Precambrian granite (Fig. 1). Our detailed modeling is performed in the 200×200 m^2 area centered on the superconducting gravimeter. The surface heights (Fig. 1) come from leveling and real-time kinematic GPS. Soil thickness was estimated using a high-precision gravimetric survey in a 10×10 m^2 grid and control drillings. The uncertainty of the estimated soil thickness is 0.2 m (one-sigma). The slopes of the hill are covered by sandy moraine; deeper soil is silt and

clayish silt. There is a thin layer (0.2 m) of ground moraine on the bedrock below the other soil layers.

Groundwater in bedrock fractures is monitored using two borehole wells. Water level in both wells varies from 4 m to 7 m below ground surface. The well BH1 (Fig. 1) only a few meters from the SG is used here. It is 34 m deep and there is a strongly fractured zone at about 20 m depth. Results from a second well (BH2 in Fig. 1) are similar.

In 2009 we installed 11 groundwater observation tubes in the sediments. They extend down to bedrock, at 1–3 m depth below the surface (Fig. 1). They have only a short perforated section of 0.2 m, at the very bottom, designed for the thin layer of ground moraine on bedrock below silt and clay. The tubes 4, 5, 6, and 14 (Fig. 1) below the laboratory hill are connected to the same open aquifer as the borehole wells BH1 and BH2 in bedrock. The water table in this area is almost horizontal, i.e., it does not follow the topography. Tube 10 in the SW corner of the study area belongs to a different groundwater unit. The higher tubes (7, 8, 9) do not reach the water table. They observe water flowing down the slope of the laboratory hill in the ground moraine, and the associated pressure variations. In a dry season, many of the shallower tubes run dry.

Twelve arrays (Fig. 1) of soil moisture sensors were installed in 2006 and 2008. An array consists of maximally five sensors, installed within 1 m both horizontally and vertically. The array marked "P" in Fig. 1 has time domain reflectometry (TDR) sensors, the rest are capacitance sensors. We calibrated the capacitance sensors in laboratory using three different soil types from the area. For the TDR sensors, the calibration curve provided by the manufacturer was used.

More than 100 soil samples were collected from the study area between 2009 and 2012, from all depths down to the bedrock. All samples were sieved and many of them were analyzed with different geotechnical methods including odometer, pycnometer etc. From these analyses we determined the geological structure of the study area and the hydrogeological properties of the different soil types (Gerrits 2010).

Figure 2 shows the time series of three indicators of local water storage: soil moisture record from sensors in "P", groundwater in borehole well BH1, and groundwater in the sediments from well 6. There are minor differences in e.g., phase, but rather similar variation is seen.

3 Modelling the Local Gravity Effects

3.1 Local Water Storage in Sediments

The gravity effect is calculated from the 200×200 m^2 area (Fig. 1). Volumetric water content is interpolated from soil moisture sensors both laterally and vertically down to 1 m depth from surface. The pixel size for the soil moisture model is 20×20 m^2. Vertically 1–3 layers are used in each pixel, depending on soil thickness and geology. Note that the layering is relative to soil surface. From 1 m depth down to bedrock the groundwater level from the nearest groundwater tube is used, assuming a specific yield of 5 %.

As the gravity laboratory stands on exposed bedrock there is a large area around the SG where soil moisture does not contribute to gravity at all. The gravity effect is calculated using right rectangular prisms of $1 \times 1 \times 0.1$ m^3 and the formula by Nagy (1966). Soil thinner than 0.1 m is excluded from the calculation.

We have also tested a simpler approach, using only the array "P" (Fig. 1) that has sensors between the depths 0.1 and 0.5 m. In this alternative approach, we assumed that the variation in mean soil moisture observed with "P" (Fig. 2) between those depths can be generalized to the whole area of Fig. 1 and that the variation is zero deeper down.

The soil layers are inhomogeneous, i.e., the soil at "P" is not representative of the whole area and of all depths. Therefore it was somewhat unexpected that both the water content and the gravity effect computed in the two approaches differ in the scale only (Fig. 3). This is a useful result: "P" started operation in 2006 before the other arrays. The result means that the soil moisture time series can be extended to 2006 using it as a proxy. To some extent the scale difference may also depend on the calibration of the TDR sensors.

For further analysis we use the model of soil moisture based on all sensors and the detailed geology (the solid SM and SUM curves in Fig. 3).

3.2 Local Water Storage in the Fractures of the Crystalline Bedrock

The Metsähovi station stands on fractured Precambrian granite. Typical values for the specific yield of unconfined aquifers in such rocks are 1–2 % (Leveinen 2001). Despite earlier hydrogeological investigations (Weise 1992) and pumping experiments (Virtanen 2000) we must consider the specific yield unknown at the seasonal timescale relevant here. We assign to it the value 2 % from the upper range of the plausible values above; the reason for this is explained in Sect. 3.4.

We use the Bouguer sheet approximation. The calculated gravity effect is thus 8.4 nm s^{-2} for 1 m in groundwater level as observed in BH1. It can be shown that the gravity effect of a horizontal slab 4–7 m below the SG sensor within the 200×200 m^2 area (and in addition excluding the SW corner and the E margin in Fig. 1 where the groundwater is in sediments) is about 94 % of the full Bouguer sheet effect. Thus

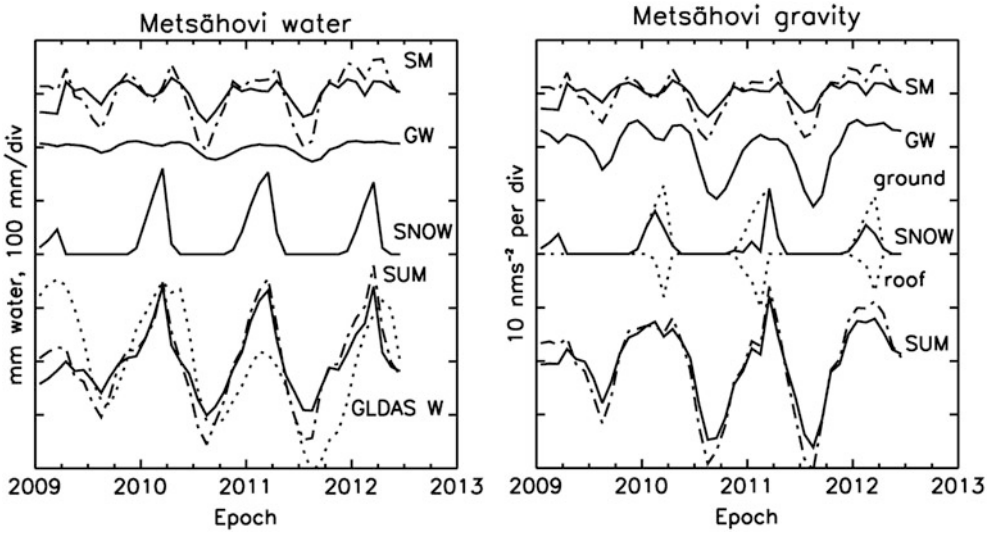

Fig. 3 *Left*: The estimated variation in local water content in the 200×200 m^2 area from various components of the hydrology, divided by the area to show mean value in millimeters. SM: water in the sediments from the detailed model (*solid curve*) and the simple model (*dash-dot curve*). GW: groundwater in bedrock. SNOW: snow on the ground. SUM: the total SM + GW + SNOW for both models of SM, detailed (*solid*) and simple (*dash-dot*). GLDAS W: water content in the $1° \times 1°$ cell of GLDAS. *Right*: The corresponding estimated gravity effect in nm s^{-2}. For SNOW we have three gravity effects: ground (*dotted curve*, positive), roof (*dotted curve*, negative), net (*solid curve*). There is no gravity graph for GLDAS W. Comments in text

our model for groundwater gravity approximately accounts for some groundwater outside the modeling area. We neglect the distinction.

The variation in the water level of BH1 is shown in Fig. 2. The estimated variation in water storage and in gravity are shown in Fig. 3.

3.3 Local Snow on the Ground and on the Laboratory Roof

A snow layer 0.5 m thick with a water equivalent (WE) of 100 mm on the surface in the 200×200 m^2 area of Fig. 1 gives a gravity effect of 8 nm s^{-2} at the location of the SG sensor. The effect is for a homogeneous layer; we take into account that the density increases slightly downwards. We measure the thickness and the WE with a snow sampler. Measurements are made at least once a month in a dense network around the station. The distribution of the snow is inhomogeneous and varies during a single season and between winter seasons; we calculate the attraction at each epoch using the average layer of that epoch.

The attraction of the snow layer on the ground is only 20 % of the attraction of the corresponding Bouguer sheet, because the area of the building does not enter the calculation and the topography is relatively flat. However, in the winter there is snow on the roof of the gravity laboratory as well and much of this snow is directly above the gravimeter. Virtanen (2000) reported on an experiment where the gravity effect of the snow on the roof (−20 nm s^{-2} at that time) was directly demonstrated in the SG record. We now monitor the roof snow through the winter with the snow sampler.

Figure 3 shows the WE of ground snow, and the estimated gravity effect of the ground snow, roof snow, and the sum of the two.

3.4 Combining the Components of the Local Model

It is instructive to compare the contribution of the components of the local hydrology to estimated variation in mass on the one hand (Fig. 3, left) and to estimated variation in gravity on the other (Fig. 3, right). We then gauge the latter as a percentage of the corresponding Bouguer sheet effect. The groundwater in bedrock makes only a small contribution to the total mass but a large contribution to gravity, as the response is nearly 100 % of the Bouguer response. For snow on the ground the Bouguer "coefficient" is about 20 %; for soil moisture (on the average) it is 20 % as well. Comparisons between the modeled response and the Bouguer response were recently also done by Deville et al. (2013).

What about the coefficient of the combined local effect? The share of different components varies during the year but we can look at the p-p (peak-to-peak) variation. The modeled local water storage is 220 mm p-p corresponding to 92 nm s^{-2} in Bouguer gravity; without the counter-effect of the roof snow (above the gravimeter), the p-p variation in modeled gravity is 31 nm s^{-2}. The Bouguer coefficient is thus 34 %. Thus, even if the local storage would be representative of the

regional mean storage, the SG would "see" only about one third of the Bouguer gravity rather than the 100 % "seen" by GRACE. Thus, if a SG/GRACE comparison is made at Metsähovi using the full signal of both sensors (Crossley et al. 2012) the results will necessarily be biased.

This conclusion is robust with respect to the details of our local model. First, for the groundwater (which is the only component where the Bouguer coefficient is close to unity) we used a specific yield that probably is an overestimate. Second, the small Bouguer coefficients of soil moisture and snow do not depend on the calibration of the soil moisture sensors or on the quality of our measurements of snow WE. Instead, they are simple consequences of the station geometry.

Regarding the estimated p-p variation in local storage, 220 mm appears quite large in view of the geological properties of the site, though a major part of the variation comes from snow. For comparison we have plotted (Fig. 3a, bottom) the variation in storage obtained from the GLDAS $1° \times 1°$ cell. The GLDAS gives a significantly larger p-p variation in storage than our local models. Similar comparisons are being pursued with the WSFS model (Vehviläinen 2007). They will be reported elsewhere.

4 The Loading and Attraction by Regional and Global Water Storage

As previously mentioned, we use the GLDAS/NOAH by Rodell et al. (2004) and include snow. The variation in water storage is convolved with a Green's function as described by Virtanen et al. (2006). The SPOTL program package by Agnew (2012) is used. To preserve global mass, the mass deficit/surplus of the GLDAS over the continents is distributed evenly over all oceans. The computations are performed in the Center of Mass (CM) reference frame (Agnew 2012). For calculating direct attraction, the load is put at the SG sensor level, i.e. the topography is neglected. The integration starts at 1 km distance from Metsähovi.

For comparison, we downloaded gravity predictions (Boy and Hinderer 2006) from the ERA-Interim hydrological model (Dee et al. 2011), available at the website of the Special Bureau of Loading of the IERS Global Geophysical Fluid Center (http://loading.u-strasbg.fr/GGP/). We use the non-local contribution only.

The gravity time series from GLDAS and ERA-Interim times series are shown in Fig. 4. Neither model includes groundwater, but their soil models probably cause the soil moisture component to account in part for variation in groundwater storage as well. Further discussion of the models is beyond the scope of this paper.

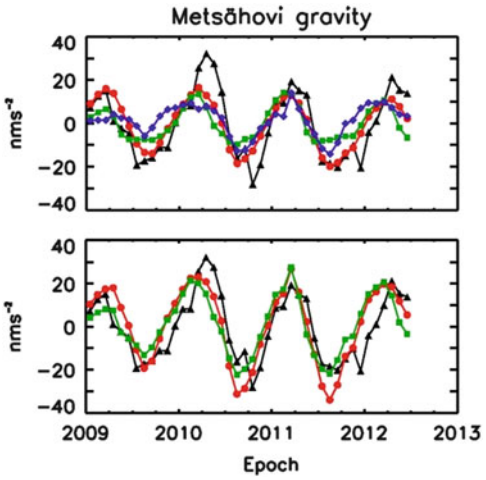

Fig. 4 *Top graph*: The record of the SG (*triangles*), the gravity effect from the GLDAS (*circles*), the gravity effect from the ERA-Interim (*squares*), the gravity effect from the local model (*diamonds*; the same as the dash-dot SUM in Fig. 3 right). *Bottom graph*: The record of the SG (*triangles*), local model plus GLDAS (*circles*), local model plus ERA-Interim (*squares*). Comments in text

5 The Gravity Record of the Superconducting Gravimeter

The gravity time series was de-tided with observed tidal parameters up to the period of 1 month; for longer periods the gravimetric factor 1.16 and zero phase lag were used. The effects of polar motion were corrected for using the IERS pole and the gravimetric factor 1.16. The influence of the atmosphere was corrected for using the local barometer and single admittance -3.1 nm s^{-2} (hPa)$^{-1}$ (Virtanen 2004). The effect of the Baltic Sea was corrected for using the tide gauge at Helsinki and the admittance $+28$ nm s^{-2} for 1 m of sea level (Virtanen 2004), appropriate for the seasonal timescale that is relevant here. Spikes and drift were eliminated and the data was decimated to 1-month averages (Fig. 4).

6 Combining the Local Model and the Regional Models

The SG signal, and the three gravity predictions: from the local hydrological model, from the GLDAS, and from the ERA-Interim are shown in Fig. 4 (top graph). All are primarily seasonal signals. The last-mentioned three are approximately in phase but their phase differs from the SG phase. When the local model is added to either GLDAS or to ERA-Interim (Fig. 4, bottom graph) rather good visual agreement with the SG is reached. However, the phase difference means that numerical differences are relatively large as we will presently see.

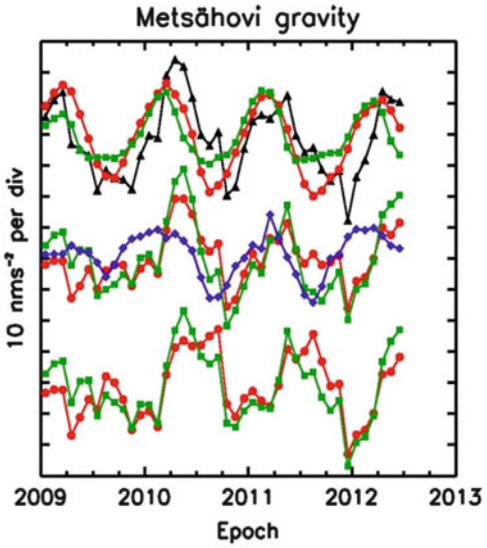

Fig. 5 *Top graph*: SG corrected with the local models (*triangles*), the gravity effect from the GLDAS (*circles*), the gravity effect from the ERA-Interim (*squares*). *Middle graph*: SG corrected with the GLDAS (*circles*), SG corrected with the ERA-Interim (*squares*), local model (*diamonds*). *Bottom graph*: SG corrected with both the GLDAS and the local model, SG corrected with both the ERA-Interim and the local model. Comments in text

In Fig. 5 we look at the SG residuals stepwise, after each hydrological correction. In the top graph we have corrected the SG for the local hydrology and compare the residual with GLDAS and ERA-Interim. The difference in phase causes here a a difference in scale as well. In the center graph we have first corrected the SG with GLDAS or ERA-Interim and compare the residuals with the local hydrology. It is obvious that scaling the contribution of the local hydrology differently would not improve the agreement. In the bottom graph we show the final SG residuals after all hydrological corrections. There is no essential difference between the GLDAS and ERA-Interim from this viewpoint.

Numerical values are given in Table 1. Looking at the model predictions, the relative size of the local/RGHM contributions to gravity is about 1:1 (local/ERA) or 2:3 (local/GLDAS). However, this result is without importance as long as the scale of the local contribution (primarily of the groundwater component) is not better known, and joint capacity of the models to explain observed gravity remains so poor. We note that the local model brings no further improvement to SG residuals after first correcting with GLDAS/ERA-Interim. In the case of the GLDAS, it actually makes the residuals larger. This is also true of the individual components of the local model (results not shown). The reasons for this are presently not understood.

Discussion and Conclusions

The signals we are analyzing are essentially seasonal and we have 3.5 cycles only. Conclusions here are thus only preliminary and more work is required.

We found that the combination of our local hydrological model and a RGHM (either GLDAS or ERA-Interim) provides a gravity prediction that closely resembles the seasonal SG residual. However, there is a difference in phase between the SG residual and the hydrological results. The reason for this is not understood at the moment. Because of the phase difference, the difference between them remains relatively large in the rms sense. Similar discrepancies between observations and models have been seen by the other authors cited in the Introduction.

Our local hydrological model for gravity is uncertain in amplitude but robust in phase. Its structure demonstrates that only a fraction of the variation in local water storage at Metsähovi is captured in gravity at the SG sensor, compared with the Bouguer sheet approximation. This result has important implications for methodology if the SG is compared with GRACE.

There are seasonal gravity signals of a few nm s^{-2} that are not corrected for in the SG processing: the 3-D density effects of atmospheric attraction (Klügel and Wziontek 2009), and ocean circulation (Kroner et al. 2009). Further, we calculated Baltic mass from surface elevations only and the steric correction is not included (see Virtanen et al. 2010). These corrections will be included but it is unlikely that they would change the conclusions.

The zone between the 200×200 m^2 square and 1 km circle is not yet included in the detailed calculation (see Chap. 4). For snow (essentially surface density), including the zone will increase the gravity effect from 8 nm s^{-2} to 12 nm s^{-2} per 100 mm water, or 50 %. That will be a scale-like effect. Further, it is plausible that soil moisture will be similar in this respect.

Table 1 Standard deviation of various observed and predicted gravity signals at Metsähovi

1	2	3	4	5	6
		GLDAS		SG–GLDAS	SG–local–GLDAS
SG	Local	ERA	SG–Local	SG–ERA	SG–local–ERA
15.5	7.0	11.3	12.3	8.4	10.4
		7.5		11.9	11.4

Unit is nm s^{-2}. Columns: (1) SG (2) local model, (3) GLDAS (top row) and ERA-Interim (bottom row), (4) SG corrected with the local model, (5) SG corrected with GLDAS (top row) or with ERA-Interim (bottom row), (6) SG corrected with both local model and with GLDAS (top row) or ERA-Interim (bottom row). Comments in text

In the future, modeling of local variation in storage will be improved. Recalibration of the soil moisture sensors, and groundwater pumping experiments will take place. Automatic measurement of snow cover WE and snow thickness will be installed. Comparisons with GRACE are currently underway.

Acknowledgments Part of the work was supported by the Academy of Finland (grant no. 117094). J. Mäkinen benefited from the co-operation in the COST Action ES0701, see http://www.cost-es0701.geoenvi.org/activities/conferencesworkshops. Comments by Tonie van Dam and an anonymous reviewer helped us to improve the paper.

References

Abe M et al (2012) A comparison of GRACE-derived temporal gravity variations with observations of six European superconducting gravimeters. Geophys J Int 191:545–556. doi:10.1111/j.1365-246X.2012.05641.x

Agnew DC (2012) SPOTL: some programs for ocean-tide loading. SIO Technical Report, Scripps Institution of Oceanography

Boy J-P, Hinderer J (2006) Study of the seasonal gravity signal in superconducting gravimeter data. J Geodyn 41:227–233

Creutzfeldt B, Güntner A, Thoss H, Merz B, Wziontek H (2010) Measuring the effect of local water storage changes on in-situ gravity observations: case study of the Geodetic Observatory-Wettzell, Germany. Water Resour Res 46, W08531. doi:10.1029/2009WR008359

Crossley D, de Linage C, Hinderer J, Boy J-P, Famiglietti J (2012) A comparison of the gravity field over Central Europe from superconducting gravimeters, GRACE and global hydrological models, using EOF analysis. Geophys J Int 189:877–897. doi:10.1111/j.1365-246X.2012.5404.x

Dee DP et al (2011) The ERA-Interim reanalysis: configuration and performance of the data assimilation system. QJR Meteorol Soc 137:553–597

Deville S, Jacob T, Chéry J, Champollion C (2013) On the impact of topography and building mask on time varying gravity due to local hydrology. Geophys J Int 192:82–93. doi:10.1093/gji/ggs007

Gerrits P (2010) 3D structural and hydrogeological modeling of Metsähovi research site, Master's thesis, Aalto University. http://repository.tudelft.nl/view/

Hokkanen T, Korhonen K, Virtanen H (2006) Hydrogeological effects on superconducting gravimeter measurements at Metsähovi, Finland. J Environ Eng Geophys 11:261–267

Hokkanen T, Korhonen K, Virtanen H, Laine E-L (2007) Effects of the fracture water of bedrock on superconducting gravimeter data. Near Surf Geophys 5:145–151

Klügel T, Wziontek H (2009) Correcting gravimeters and tiltmeters for atmospheric mass attraction using operational weather models. J Geodyn 48:204–210. doi:10.1016/j.jog.2009.09.010

Kroner C, Thomas M, Dobslaw H, Abe M, Weise A (2009) Seasonal effects of non-tidal oceanic mass shifts in observations with superconducting gravimeters. J Geodyn 48:354–359

Leveinen J (2001) Conceptual and analytical modeling of fracture zone aquifers in hard rock – implications of pumping tests in the Pohjukansalo test field, east-central Finland. Geological Survey of Finland, Report YST-105

Longuevergne L, Boy J-P, Florsch N, Viville D, Ferhat G, Ulrich P, Luck B, Hinderer J (2009) Local and global hydrological contributions to gravity variations observed in Strasbourg (France). J Geodyn 48:189–194. doi:10.1016/j.jog.2009.09.008

Mäkinen J, Tattari S (1991) Subsurface water and gravity. In: Poitevin C (ed) Proceedings of the workshop: non tidal gravity changes. Intercomparison between absolute and superconducting gravimeters, Walferdange, 5–7 September 1990 (Grand-Duchy of Luxembourg). Cahiers du Centre Européen de Géodynamique et de Séismologie, vol 3, pp 235–240

Nagy D (1966) The gravitational attraction of a right rectangular prism. Geophysics 31:361–371

Naujoks M, Kroner C, Weise A, Jahr T, Krause P, Eisner S (2010) Evaluating local hydrological modelling by temporal gravity observations and a gravimetric 3D model. Geophys J Int 182:233–249

Neumeyer J et al (2008) Analysis of gravity field variations derived from superconducting gravimeter recordings, the GRACE satellite and hydrological models at selected European sites. Earth Planets Space 60:505–518

Rodell M et al (2004) The global land data assimilation system. Bull Am Meteorol Soc 85:381–394

Van Camp M et al (2006) Hydrogeological investigations at the Membach station, Belgium, and applications to correct long periodic gravity variations. J Geophys Res 111, B10403. doi:10.1029/2006JB004405

Vehviläinen B (2007) Hydrological forecasting and real-time monitoring: the watershed simulation and forecasting system (WSFS). doi:10.1002/9780470511121.ch2

Virtanen H (2000) On the observed hydrological environmental effects on gravity at the Metsähovi station, Finland. Cahiers du Centre Européen de Géodynamique et de Séismologie 17:169–175

Virtanen H (2001) Hydrological studies at the gravity station Metsähovi in Finland. J Geodyn Soc Japan 47:328–333

Virtanen H (2004) Loading effects in Metsähovi from the atmosphere and the Baltic Sea. J Geodyn 38:407–422

Virtanen H et al (2006) Comparison of superconducting gravimeter observations with hydrological models of various spatial extents. Bull Inf Marées Terrestres 142:11361–11368

Virtanen J et al (2010) Baltic sea mass variations from GRACE: comparison with in situ and modelled sea level heights. In: Mertikas SP (ed) Gravity, geoid, and earth observation (GGEO2008), IAG symposium, Chania, Crête, Greece, 23–27 June 2008. Springer, IAG Symposia 135, pp 571–578

Weise A (1992) Neigungsmessungen in der Geodynamik – Ergebnisse von der 3-Komponenten-Station Metsähovi. Doctoral dissertation, Technical University of Clausthal

Weise A et al (2012) Tackling mass redistribution phenomena by time-dependent GRACE- and terrestrial gravity observations. J Geodyn 59–60:82–91. doi:10.1016/j.jog.2011.11.003

Global Groundwater Cycles and Extreme Events Responses Observed by Satellite Gravimetry

Shuanggen Jin and Guiping Feng

Abstract

The groundwater is one of key parameters in water resource management and hydrological cycle. However, the global groundwater and its changes are very difficultly monitored by traditional instruments. The recent Gravity Recovery and Climate Experiment (GRACE) mission launched in 2002 provided an opportunity to measure the global water storage and its changes. Some regional groundwater variations were well estimated and investigated from GRACE, however, global groundwater variations are not clear. In this paper, an approximate decade of the global groundwater is obtained after subtracting the soil moisture, snow, ice and canopy water from the hydrological model GLDAS (Global Land Data Assimilation System). Significant annual variations of global groundwater are found with the mean amplitude of 28.98 mm, while the semi-annual amplitude is almost half of annual amplitude in most parts of the world with the mean of 11.06 mm. The mean trend of global groundwater variations is 1.86 ± 0.36 mm/year. The trend mostly reflects the recent extreme events, e.g. groundwater depletion in Northwest India, California and North China, droughts in La Plata and Southeast USA, and flood in Amazon. In addition, the groundwater has an acceleration change in some areas with up to ± 4 mm/year^2.

Keywords

Groundwater • GRACE • GLDAS

1 Introduction

The groundwater is a basic resource for human life related to the agricultural and industrial production, which also plays a key role in water mass balance and hydrological cycle. The groundwater covers from the surface to depths of several hundred meters, which was monitored by traditional instruments, such as Ground Penetrating Radar (GPR) (Huisman et al. 2003), etc. However, these instruments are very difficult to monitor the global entire groundwater storage with high temporal-spatial resolution and its time-varying variability due to high cost and high labor intensity. Although semi-empirical hydrological models have been recently developed, e.g., GLDAS (Global Land Data Assimilation System) model, but the GLDAS did not provide the groundwater storage (e.g., Rodell et al. 2004; Jin et al. 2012).

Since the Gravity Recovery and Climate Experiment (GRACE) mission was launched in 2002, it has been widely used to monitor the Earth's time-varying gravity field and mass transport (Tapley et al. 2004), e.g., terrestrial water storage (TWS) variations (Wahr et al. 1998; Jin et al. 2010). Up to now, a number of progresses have been made in terrestrial water storage variations and confirming drought and floods events from GRACE (Schmidt et al. 2008; Steffen et al. 2009; Rodell et al. 2009; Famiglietti et al. 2011; Forootan and Kusche 2012). After excluding the land surface

S. Jin (✉) • G. Feng
Shanghai Astronomical Observatory, Chinese Academy of Sciences, Shanghai 200030, China
e-mail: sgjin@shao.ac.cn; sg.jin@yahoo.com

G. Feng
University of Chinese Academy of Sciences, Beijing 100049, China
e-mail: gpfeng@shao.ac.cn

U. Marti (ed.), *Gravity, Geoid and Height Systems*, International Association of Geodesy Symposia 141,
DOI 10.1007/978-3-319-10837-7_36,

total water from GRACE TWS, the groundwater variations is possibly monitored. Although scientists have explored the GRACE's potential to detect groundwater storage variations (e.g., Rodell et al. 2007; Yeh et al. 2006; Strassberg et al. 2007), but most of their investigations were focused on small regions. In this paper, about 10 years of global groundwater variations (August 2002–April 2012) are obtained by subtracting the GLDAS surface total water from GRACE-derived terrestrial water storages. The seasonal variations and trend of global groundwater are investigated from about 10 years of monthly groundwater time series as well as their responses to recent extreme events.

2 Observation Data and Models

2.1 Terrestrial Water Storage from GRACE

GRACE delivers monthly averages of the spherical harmonic coefficients describing the Earth's gravity field, whose changes are caused by fluctuations in continental water storage and the polar ice sheets, as well as by changes in atmospheric and oceanic mass distribution (Wahr et al. 2004; Swenson et al. 2003; Tapley et al. 2004). Atmospheric, barotropic oceanic mass and tidal effects have been removed during GRACE processing using climate and ocean circulation models (Bettadpur 2007). The terrestrial water storage anomalies over the land can be estimated by monthly gravitational coefficient anomalies (ΔC_{lm}, ΔS_{lm}) (Swenson and Wahr 2002):

$$\Delta\eta_{land}(\theta,\phi,t) = \frac{a\rho_{ave}}{3\rho_w}\sum_{l=0}^{\infty}\sum_{m=0}^{l}\tilde{P}_{lm}(\cos\theta)\frac{2l+1}{1+k_l} (\Delta C_{lm}\cos(m\phi) + \Delta S_{lm}\sin(m\phi)) \quad (1)$$

where θ is the colatitude, ϕ is the longitude, a is the equatorial radius of the Earth, ρ_{ave} is the average density of the solid Earth, ρ_w is the density of fresh water, $\tilde{P}_{lm}$ is the fully normalized associated Legendre polynomials of degree l and order m, and k_l is Love number of degree l (Han and Wahr 1995).

In order to estimate the precise terrestrial water storage with GRACE data, we have to make a number of corrections. Firstly, the degree 2 order 0 (C_{20}) coefficients were replaced by those derived from Satellite Laser Ranging (SLR) measurements due to large uncertainties in GRACE coefficient C_{20} (Cheng and Tapley 2004; Jin et al. 2011); secondly, the GRACE solutions do not provide degree 1 spherical harmonics coefficients (C_{11}, S_{11}, and C_{10}), so the monthly degree 1 coefficients calculated by Swenson et al. (2008) were used; thirdly, the effect of the postglacial rebound

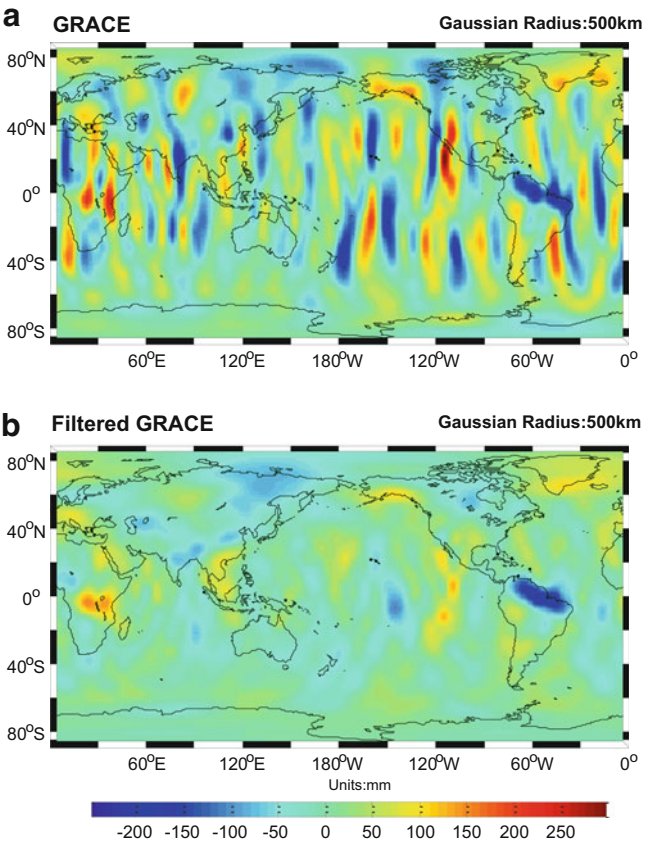

Fig. 1 Terrestrial water storage anomaly from GRACE in January 2003 with the 500 km width of Gaussian filter (**a**) and together with de-striping filter (**b**)

was removed using the model of Paulson et al. (2007); and finally, the errors of the Stokes coefficients are reduced using the 500 km width of Gaussian filter and de-striping filter (Wahr et al. 1998; Swenson and Wahr 2006). Finally, the total terrestrial water storage variations can be obtained well. Here we use the monthly GRACE Release 4 (RL04) solutions from August 2002 to April 2012 (excluding June 2003, January 2011, June 2011), which were provided by the Center for Space Research (CSR) at the University of Texas at Austin to calculate the terrestrial water storage anomalies (Bettadpur 2007). For example, Fig. 1 shows terrestrial water storage from GRACE in Jan. 2003 with the 500 km width of Gaussian filter and de-striping filter.

2.2 Groundwater from GRACE and Models

The terrestrial water storage from GRACE is the total water, including groundwater, snow, glaciers, soil moisture, surface water, and biological water. To get groundwater from GRACE, it needs the total land surface water, including the surface water, snow, glaciers, soil moisture and biological

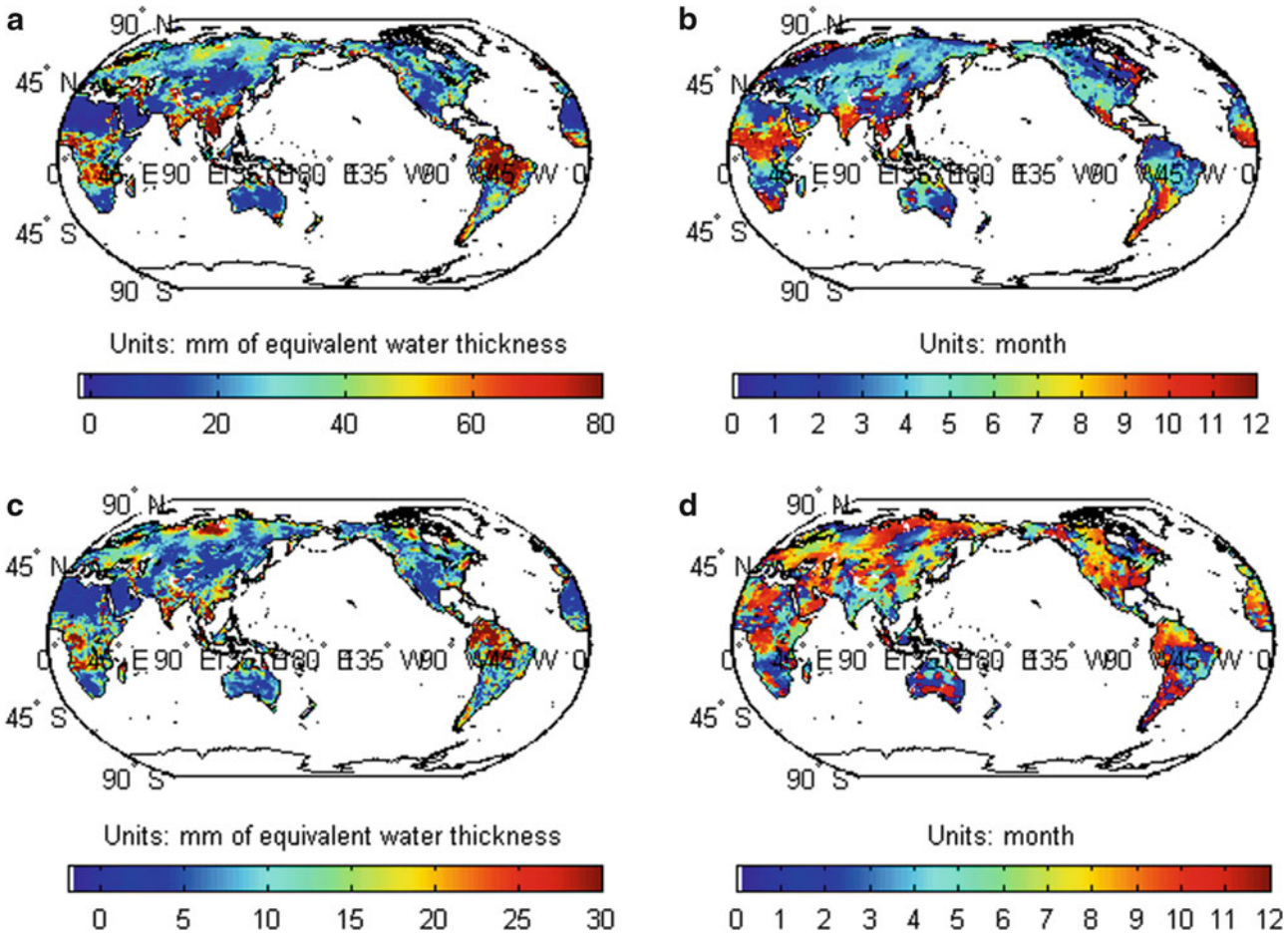

Fig. 2 Annual and semi-annual variations of global groundwater from GRACE minus GLDAS, (**a**) the annual amplitude; (**b**) the annual phase; (**c**) the semi-annual amplitude; and (**d**) the semi-annual phase

water. Nowadays, many hydrological models have been developed to describe the land water storage, such as GLDAS, CPC, NCEP, ECMWF and so on. By comparing and analysis, the hydrological models, GLDAS model is better to represent hydrological variations (Jin et al. 2012). The GLDAS model has been jointly developed by the National Aeronautics and Space Administration (NASA) Goddard Space Flight Center (GSFC) and the National Oceanic and Atmospheric Administration (NOAA) National Centers for Environmental Prediction (NCEP) (Rodell et al. 2004), including soil moisture, snow water equivalent, and canopy surface water. Since the GLDAS model does not cover the areas over latitude of 60°S, we do not discuss the Antarctic region. In order to get consistent results with GRACE, we use the same Gaussian smoothing filter and de-striping filter to process spherical harmonic coefficients that are inverted from the GLDAS model, to eliminate the error introduced by the data processing. After removing the GLDAS land surface total water from the total terrestrial water storage determined by GRACE, the monthly global groundwater storages are obtained from August 2002 to April 2012.

3 Results and Analysis

3.1 Seasonal Changes of Groundwater

The groundwater storage time series have significant seasonal variations, which are fitted with seasonal, secular and acceleration variations as:

$$GW(t) = A_a \cos(\omega_a t - \phi_a) + A_{sa} \cos(\omega_{sa} t - \phi_{sa}) + B + Ct + Dt^2 + \varepsilon \quad (2)$$

where t is the time, $GW(t)$ is the groundwater storage variations time series, A_a, ϕ_a, ω_a are annual amplitude, phase and frequency, respectively, $A_{sa}, \phi_{sa}, \omega_{sa}$ are semi-annual amplitude, phase and frequency, respectively, B is the constant, C is the trend, D is the acceleration, and $\varepsilon(t)$ is the unmodeled

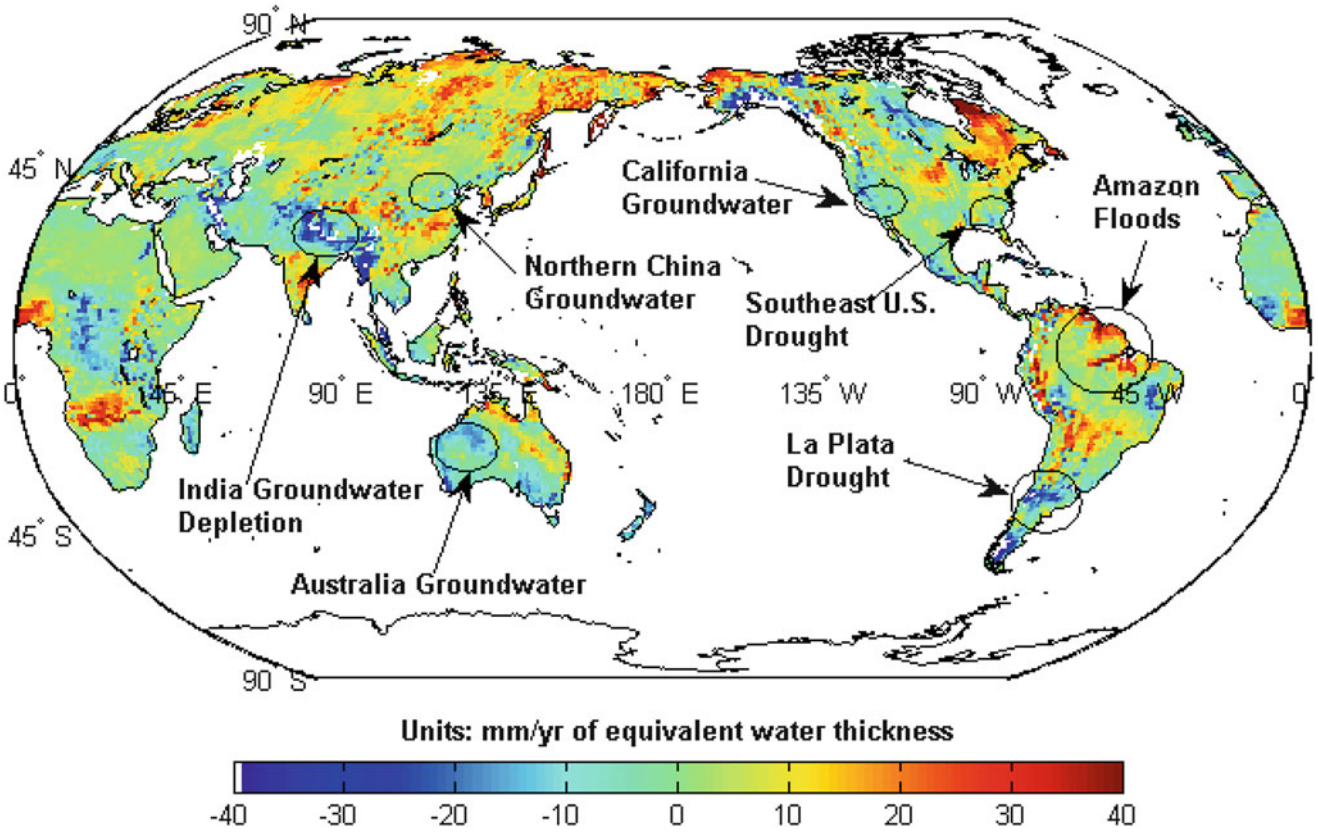

Fig. 3 The trend of global groundwater variations from GRACE-GLDAS

residual item. Using the least-squares method to fit the time series of groundwater storage variations at each grid point and the annual, semi-annual, trend and acceleration items of groundwater storage variations are estimated. Figure 2 shows the seasonal variations of global groundwater storage based on GRACE TWS minus GLDAS surface total water, (a) the annual amplitude; (b) the annual phase; (c) the semi-annual amplitude; and (d) the semi-annual phase. For the annual variations, the mean amplitude is 28.98 mm, while the semi-annual amplitude is almost half of annual amplitude in most parts of the world with the mean value of 11.06 mm.

In addition, some areas have larger annual amplitude of groundwater storage variations with up to 80 mm, e.g., Amazon River Basin in South America, Zambezi River Basin in Africa, the Ganges and the northwest India. While in northern Africa and southern Australia, due to drought and other reasons, the annual amplitude of groundwater storage is just about 10 mm.

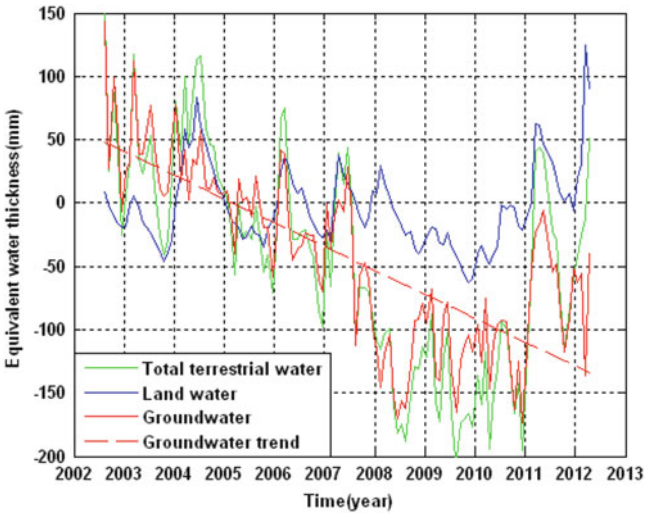

Fig. 4 Water variation time series from GRACE and GLDAS in West Australia

3.2 Secular Variations of Groundwater

Figure 3 shows the secular groundwater variations from GRACE minus GLDAS model. The mean trend of global groundwater variations is 1.86 ± 0.36 mm/year from GRACE-GLDAS. Most secular variations of groundwater reflect the recent extreme events, e.g., groundwater depletion in Northwest Indian (Rodell et al. 2009), California (Famiglietti et al. 2011) and North China, and droughts in La Plata and Southeast USA, Mid-Africa and West Australia as well as floods in Amazon.

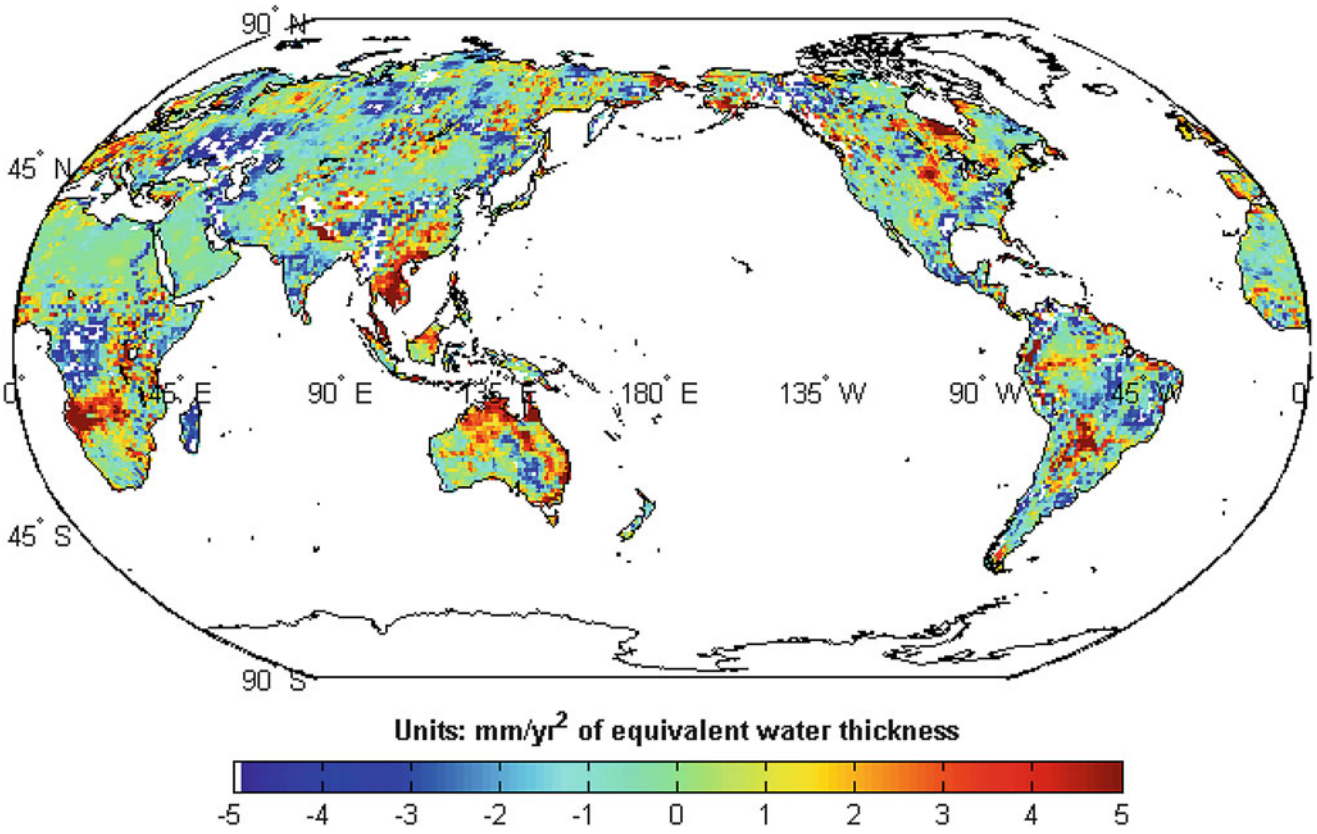

Fig. 5 Acceleration of global groundwater based on GRACE and GLDAS

For example, Fig. 4 show total water, land water and groundwater variation time series from GRACE and GRACE-GLDAS in West Australia, which shows clear groundwater loss due to recent droughts in West Australia. After 2011, the groundwater is increasing, possibly due to large floods. In addition, since the different glacier isostatic adjustment (GIA) models affect the trend of global groundwater storage variations. We further check the GIA models' effects from Paulson et al. (2007) and Peltier (2004) and find that the influence of different GIA models on the trend of groundwater storage variations is very small with about several millimeters per year, which can be ignored with respect to centimeters per year in secular groundwater storage variations.

3.3 Acceleration of Groundwater Variations

In order to further evaluate the groundwater variations, the acceleration term ($D \cdot t^2$) in Eq. (2) is estimated with fitting the groundwater variations time series. Figure 5 shows the acceleration of groundwater storage variations from GRACE minus GLDAS. It shows the acceleration with up to ± 4 mm/year^2 in some parts of the world, such as in Oceania, southern Africa and Amazon River Basin.

Conclusions

The groundwater storage variations in the world are investigated from GRACE-GLDAS. For the annual changes of groundwater storage, the mean amplitude and the mean annual phase are 28.98 mm and $-36.55°$ from GRACE-GLDAS, respectively. In South America Amazon River Basin, the Niger, Lake Chad and the Zambezi River Basin in the African continent, the Ganges and the northwest India in southeast Asia, the annual amplitude of groundwater storage variations is up to 80 mm, and in northern Africa and southern Australia, the annual amplitude of groundwater storage is less than about 10 mm due to drought and other reasons. For the semi-annual variations, the mean semi-annual amplitude and the mean semi-annual phase are 11.06 mm and 18.91° from GRACE-GLDAS, respectively. For the long-term variations, the mean trend of global groundwater variations is 1.86 ± 0.36 mm/year from GRACE-GLDAS. The trend of global groundwater variations mostly reflects the groundwater depletion and extreme climate events, e.g. groundwater depletion in Northwest India, California and North China, droughts in La Plata, Southeast USA and West Australia, and flood in Amazon. In addition, the groundwater has accelerating variations in some parts with up to ± 4 mm/year^2. Totally speaking, these results

indicate that the combined GLDAS and GRACE can well estimate the annual signals and the trend of groundwater storage changes. Since GRACE has a low spatial resolution and the hydrological model has larger uncertainties in surface total water, it needs to further investigate the precise groundwater variations in the future.

Acknowledgments We are grateful to thank the Center for Space Research for providing GRACE data. This research is supported by the Main Direction Project of Chinese Academy of Sciences (Grant No. KJCX2-EW-T03), Shanghai Science and Technology Commission Project (Grant No. 12DZ2273300), Shanghai Pujiang Talent Program Project (Grant No. 11PJ1411500) and National Natural Science Foundation of China (NSFC) Project (Grant No. 11173050).

References

Bettadpur S (2007) CSR level-2 processing standards document for product release 04, GRACE 327–742. The GRACE Project, Center for Space Research, University of Texas at Austin, Austin

Cheng M, Tapley BD (2004) Variations in the Earth's oblateness during the past 28 years. J Geophys Res 109, B09402. doi:10.1029/2004JB003028

Famiglietti J, Lo M, Ho SL et al (2011) Satellites measure recent rates of groundwater depletion in California's Central Valley. Geophys Res Lett 38, L03403. doi:10.1029/2010GL046442

Forootan E, Kusche J (2012) Separation of global time-variable gravity signals into maximally independent components. J Geod 86(7):477–497. doi:10.1007/s00190-011-0532-5

Han D, Wahr J (1995) The viscoelastic relaxation of a realistically stratified earth, and a further analysis of post-glacial rebound. Geophysical J Int 120:287–311

Huisman JA, Hubbard SS, Redman JD et al (2003) Measuring soil water content with ground penetrating radar: a review. Vadose Zone Journal 2:476–491

Jin SG, Chambers D, Tapley B (2010) Hydrological and oceanic effects on polar motion from GRACE and models. J Geophys Res 115, B02403. doi:10.1029/2009JB006635

Jin SG, Zhang L, Tapley B (2011) The understanding of length-of-day variations from satellite gravity and laser ranging measurements. Geophys J Int 184(2):651–660. doi:10.1111/j.1365-246X.2010.04869.x

Jin SG, Hassan A, Feng G (2012) Assessment of terrestrial water contributions to polar motion from GRACE and hydrological models. J Geodyn 62:40–48. doi:10.1016/j.jog.2012.01.009

Paulson A, Zhong S, Wahr J (2007) Inference of mantle viscosity from GRACE and relative sea level data. Geophys J Int 171:497–508. doi:10.1111/j.1365-246X.2007.03556.x

Peltier WR (2004) Global glacial isostasy and the surface of the ice-age Earth: the ICE-5G (VM2) model. Annu Rev Earth Planet Sci 32:111–149

Rodell M, Houser PR, Jambor U et al (2004) The global land data assimilation system. Bull Am Meteorol Soc 85(3):381–394. doi:10.1175/BAMS-85-3-381

Rodell M, Chen J, Kato H et al (2007) Estimating ground water storage changes in the Mississippi River basin (USA) using GRACE. J Hydrogeol 15(1):159–166. doi:10.1007/s10040-006-0103-7

Rodell M, Velicogna I, Famiglietti J (2009) Satellite-based estimates of groundwater depletion in India. Nature 460:999–1002. doi:10.1038/nature08238

Schmidt R, Petrovic S, Güntner A, Barthelmes F, Wünsch J, Kusche J (2008) Periodic components of water storage changes from GRACE and global hydrology models. J Geophys Res 113, B08419. doi:10.1029/2007JB005363

Steffen H, Petrovic S, Müller J, Schmidt R, Wünsch J, Barthelmes F, Kusche J (2009) Significance of secular trends of mass variations determined from GRACE solutions. J Geodyn 48:157–165

Strassberg G, Scanlon BR, Rodell M (2007) Comparison of seasonal terrestrial water storage variations from GRACE with groundwater-level measurements from the High Plains Aquifer (USA). Geophys Res Lett 34, L14402. doi:10.1029/2007GL030139

Swenson SC, Wahr J (2002) Methods for inferring regional surface-mass anomalies from Gravity Recovery and Climate Experiment (GRACE) measurements of time-variable gravity. J Geophys Res 107(B9):2193. doi:10.1029/2001JB000576

Swenson SC, Wahr J (2006) Post-processing removal of correlated errors in GRACE data. Geophys Res Lett 33, L08402. doi:10.1029/2005GL025285

Swenson S, Wahr J, Milly PCD (2003) Estimated accuracies of regional water storage variations inferred from the Gravity Recovery and Climate Experiment (GRACE). Water Resour Res 39(8):1223. doi:10.1029/2002WR001808

Swenson S, Chambers D, Wahr J (2008) Estimating geocenter variations from a combination of GRACE and ocean model output. J Geophys Res 113, B08410. doi:10.1029/2007JB005338

Tapley BD, Bettadpur S, Watkins M, Reigber C (2004) The gravity recovery and climate experiment: mission overview and early results. Geophys Res Lett 31(9), L09607

Wahr J, Molenaar M, Bryan F (1998) Time-variability of the Earth's gravity field: hydrological and oceanic effects and their possible detection using GRACE. J Geophys Res 103:30205–30229

Wahr J, Swenson S, Zlotnicki V, Velicogna I (2004) Time-variable gravity from GRACE: first results. Geophys Res Lett 31, L11501. doi:10.1029/2004GL019779

Yeh PJ-F, Swenson SC, Famiglietti JS et al (2006) Remote sensing of groundwater storage changes in Illinois using the Gravity Recovery and Climate Experiment (GRACE). Water Resour Res 42, W12203. doi:10.1029/2006WR005374

Part VII

Modeling and Inversion of Gravity-Solid Earth Coupling

Sensitivity of GOCE Gravity Gradients to Crustal Thickness and Density Variations: Case Study for the Northeast Atlantic Region

J. Ebbing, J. Bouman, M. Fuchs, S. Gradmann, and R. Haagmans

Abstract

We discuss the gravity gradient signal measured at the height of the GOCE satellite and compare it with the gravity gradients related to the density contrast between crust and mantle. The gravity gradients are reduced for the topographic masses to emphasize the lithospheric signal. Comparison with the Moho-related signal shows that with a density contrast of 400 kg/m^3, the amplitude of the calculated gradients is almost twice that of the observed field. The differences can only partly be explained by the uncertainty of the crustal thickness, but is clearly related to the applied density contrast. Calculation of the gravity gradients requires a reduced density contrast, which is an important consideration for establishing global models, which might otherwise overestimate crustal thickness.

Keywords

Gravity gradients • Moho depth • Density • Crust • Mantle

1 Introduction

Gravity data are often used to study crustal thickness variations and various approaches have been presented in recent years to use global gravity models for global Moho depth estimates (e.g. Sünkel 1985; Sjöberg and Bagherbandi 2011) or even based on the new GOCE gradient data (Sampietro 2011). Even though such estimates provide a valid picture on the global scale, locally the deviations between seismic and gravity-based Moho depths might be very large, and the effects of local variations are little studied. This is partly due to long-wavelength component in the gravity field that is caused by the sub-crustal density domains, e.g. the overall thickness of the lithospheric mantle and variations within (e.g. Ebbing 2007).

Data sets from the GOCE satellite mission (Bouman et al. 2011; Pail et al. 2011) have two main advantages compared with earlier global gravity models with respect to geophysical modeling. Firstly, the GOCE data have higher sensitivity in the transitional wavelength between earlier satellite and terrestrial gravity data. Only based on GOCE gravity data, it would be feasible to provide a gravity field with 80 km resolution (Bouman et al. 2011). The second and more revolutionary novelty is that GOCE measures gravity gradients. Gravity gradient data are generally sensitive to shallower structures than the gravity field itself and provide information about the variations in the gravity field in both the horizontal and vertical plane (see Fig. 1). Thus it might be feasible to apply gradient fields from satellite missions to study variations in crustal thickness, which in theory are less sensitive to the density structure of the upper mantle.

J. Ebbing (✉)
Department of Geosciences, Kiel University, Germany
e-mail: jebbing@geophysik.uni-kiel.de

S.Gradmann
Geological Survey of Norway, Trondheim, Norway

J. Bouman • M. Fuchs
Deutsches Geodätisches Forschungsinstitut (DGFI), Alfons-Goppel-Str. 11, 80539 Munich, Germany

R. Haagmans
ESA/ESTEC, Noordwijk, The Netherlands

U. Marti (ed.), *Gravity, Geoid and Height Systems*, International Association of Geodesy Symposia 141,
DOI 10.1007/978-3-319-10837-7_37,

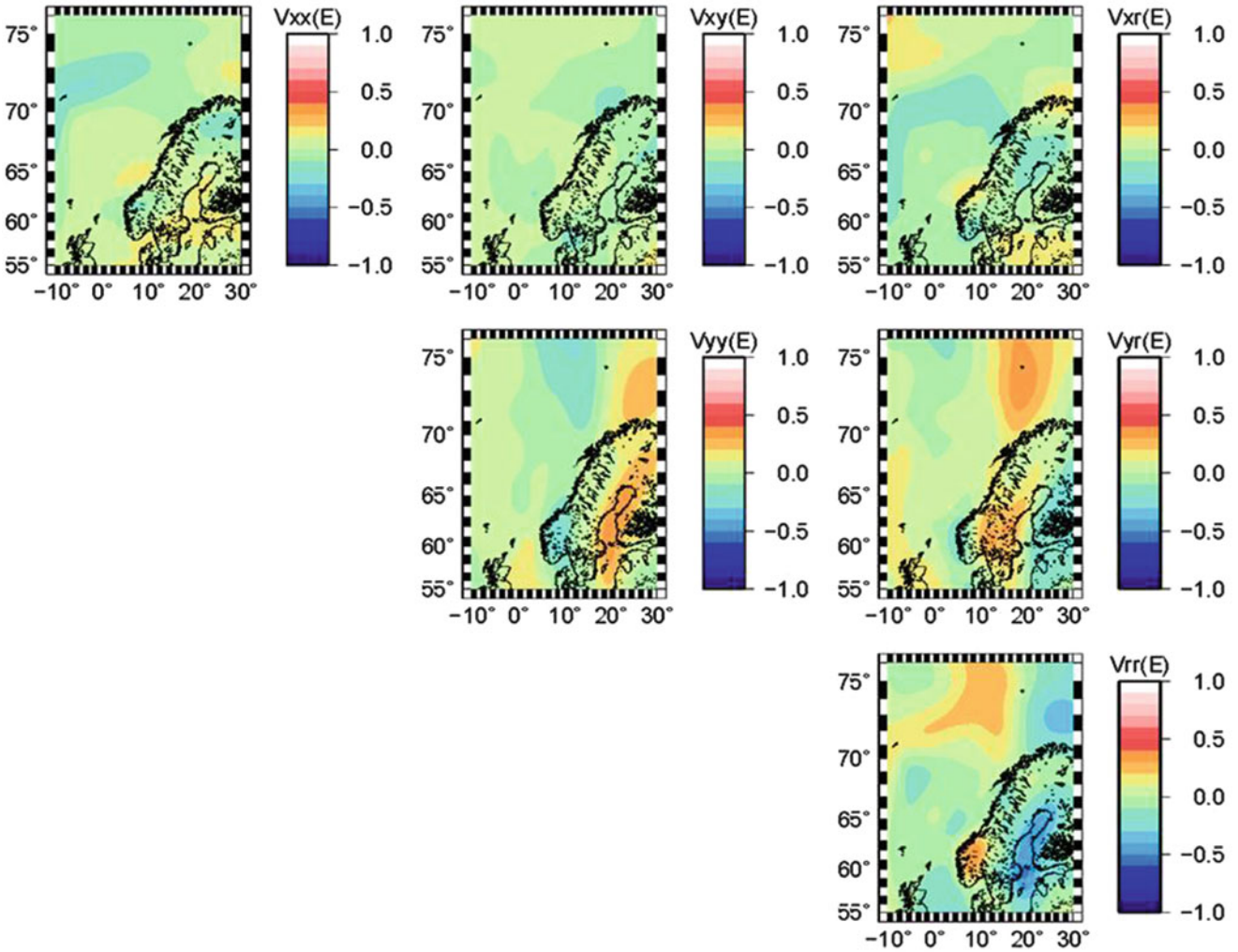

Fig. 1 Gravity gradients at orbital height from the model GOCO02S (Goiginger et al. 2011). Long wavelengths below spherical harmonic degree and order 10 have been subtracted. The coordinate system is END (earth-north-down), e.g. Vxx is the second derivative of the gravity potential in eastward direction

Here, we analyze the gravity gradients for the Northeast Atlantic region by forward modeling. Typically a density contrast of $+400\,\mathrm{kg/m^3}$ is used between the crust and mantle, both for isostatic studies and for gravity inversions (e.g. Ebbing and Olesen 2005). However, such a constant value does not reflect density changes associated with the Iceland plume and the changing thermal structure of the upper mantle, which results in a strong regional component in the geoid and gravity field (Ebbing and Olesen 2005). Even though gravity gradients should be less sensitive to regional trends, we analyze how modeling of the crustal structure on a regional scale is affected by uncertainties in the upper mantle structure. The gravity gradients at satellite height and the variation in the signal related to the uncertainty of the Moho depth interface and its associated density contrast are discussed.

2 Method and Data

2.1 Calculations with Tesseroids

The calculations of the gravity field and its derivatives at satellite height require taking into account the spherical geometry of the Earth (e.g. Bouman et al. 2013). In the following we calculate all gravity gradients using the tesseroid approximation for a spherical geometry with the tesseroid software (Uieda et al. 2011). The software performs direct calculation of the gravity gradient tensor components by discretizing the subsurface in spherical prisms (tesseroids). For the calculations we extended the study area by 5° in all directions to avoid edge effects. The noise level of the calculations has been evaluated using the Laplace equation, and

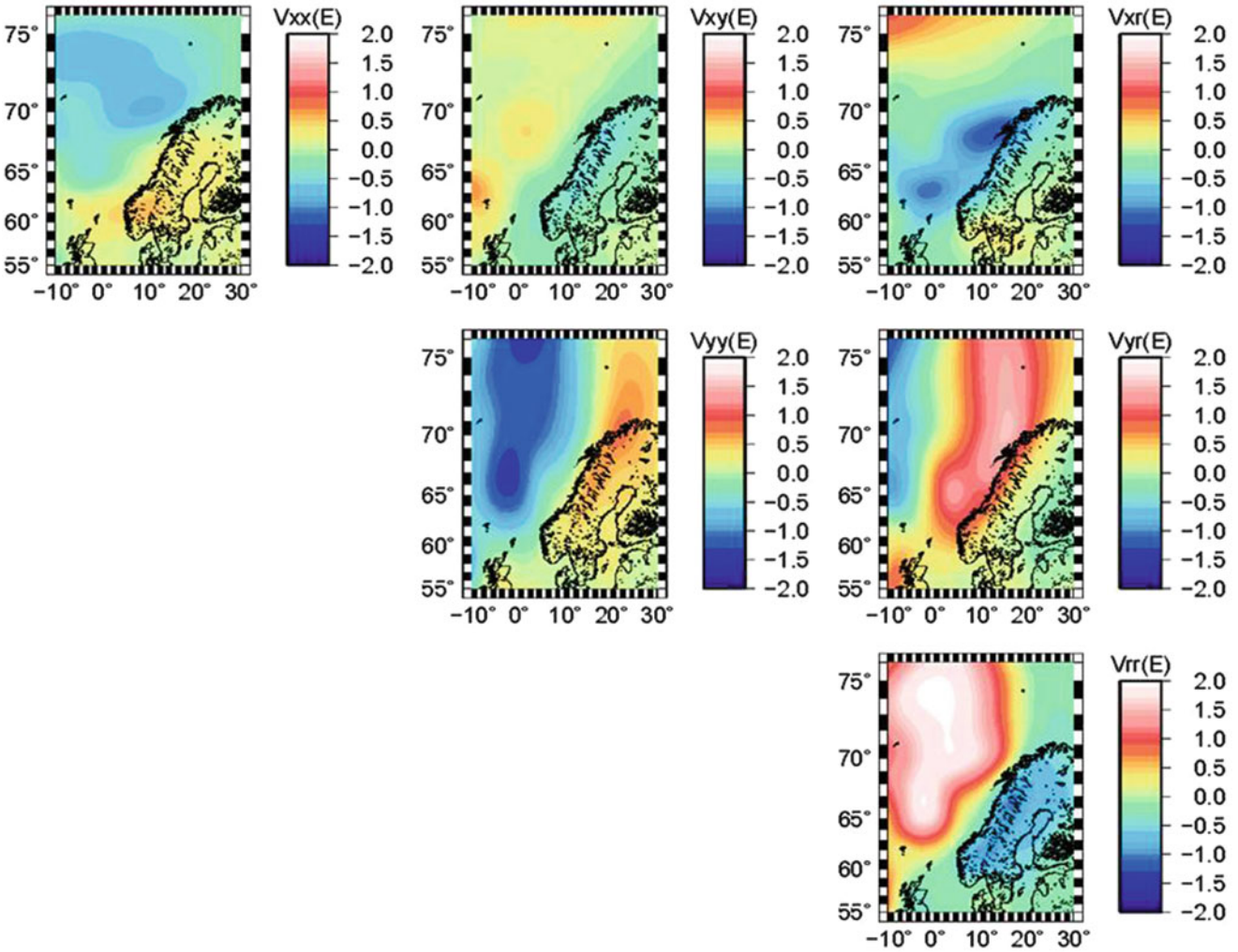

Fig. 2 Gravity gradients from GOCO2S (Fig. 1) after topographic mass reduction. For topographic masses a density of 2,670 kg/m^3 is used, while for areas below sea level a reduction density of −1,170 kg/m^3 is applied, which represents the density contrast between sea-water and the offshore reduction density of 2,200 kg/m^3

resulted in values several orders of magnitudes smaller than the error of GOCE measurements. While such calculation in tesseroids is computationally demanding, consideration of the spherical geometry is necessary to obtain reasonable results.

Álvarez et al. (2012) analyzed the error between the calculations with spherical prisms and rectangular ones for synthetic examples. For a block of 1° extension and 1 km elevation the differences between calculations with the two methods at satellite altitude were up to ∼0.16 E, which is significantly higher than the noise level of GOCE data, which is only in the order of mE. For the Northeast Atlantic region Bouman et al. (2013) demonstrated that the error by using a planar approximation instead of using a spherical geometry for the topographic mass reduction can reach 1 E comparable with 33 % of the topography-free signal at satellite level (Fig. 2).

2.2 GOCE Data and Topographic Mass Reduction

In this study we use data from the gravity model GOCO02S, which is a combined GOCE-GRACE gravity model (Goiginger et al. 2011). The difference to the more recent GOCO03S model (Mayer-Guerr et al. 2012) leads to differences of less than 1 mE at satellite altitude, which we can ignore for the current study.

To be able to compare the fields related to the crust-mantle interface, one has to reduce the observed gradients from the effect caused by topographic masses. Such a topographic mass reduction is equivalent to a complete Bouguer reduction for gravity data, and is here calculated using ETOPO1 (Amante and Eakins 2009) down sampled to 4 min resolution. The fields are calculated for a mean satellite height of 270 km. Even though the perigee height

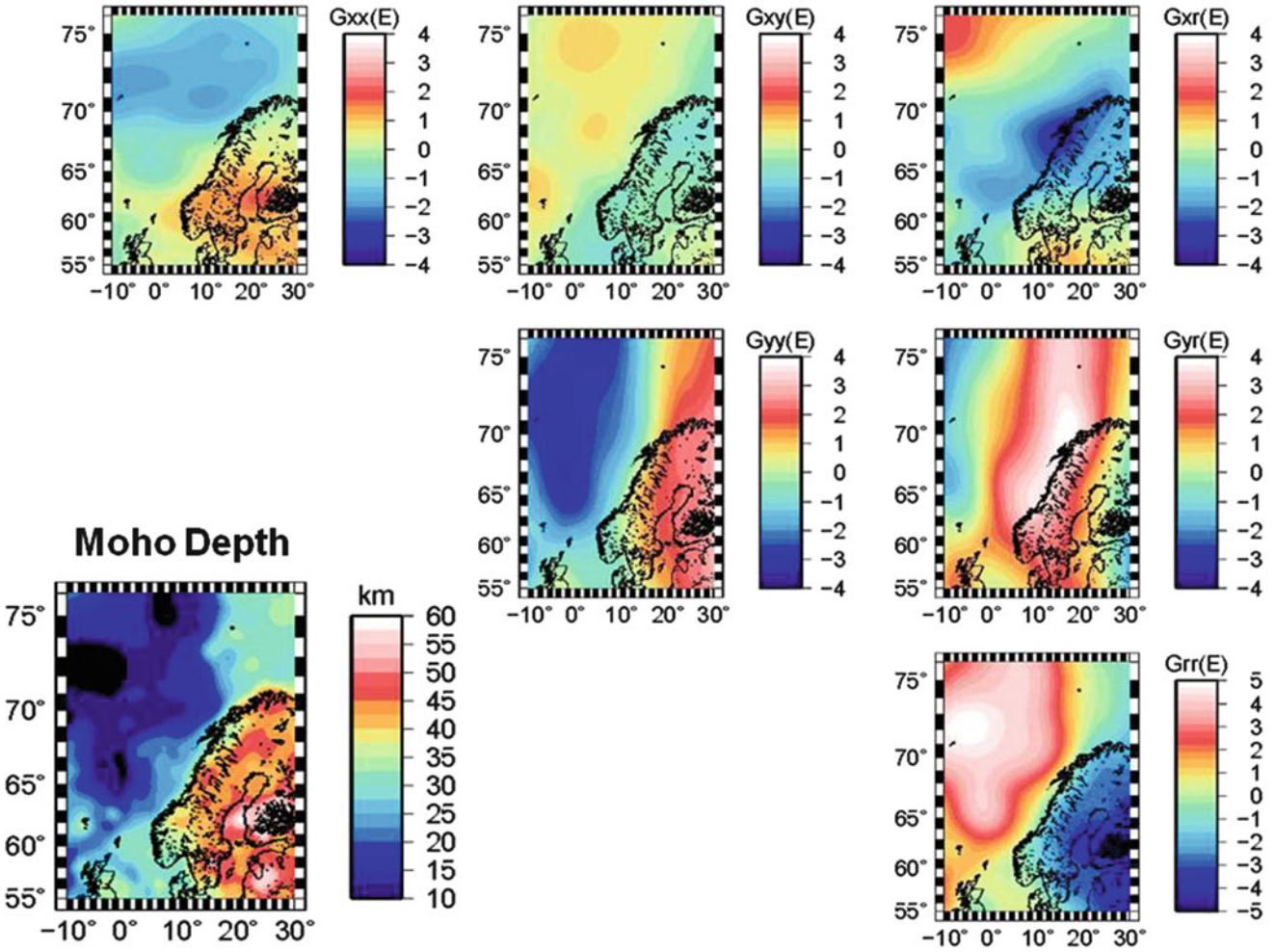

Fig. 3 Gravity gradients at satellite altitude calculated from the crustal thickness variation (*lower left*) from the compilation 'Moho depth of the European plate' by Grad et al. (2009) with a constant density contrast of +400 kg/m^3

of the GOCE satellite is ∼255 km, this translates into a mean height above the ellipsoid of 270 km for the Northeast Atlantic region.

In Figs. 1 and 2 the gravity data before and after topographic mass reduction are shown. Obviously, the topographic mass reduction leads to a significantly larger amplitude than in the original data, as is a normal observation for gravity data (e.g. Olesen et al. 2010). The small amplitude in the observed data indicates that near-isostatic equilibrium exists, and that the loading by topography and bathymetry is compensated in depth. Isostatic compensation occurs at the base of the lithosphere, but the main density contrast in the lithosphere exists at the Moho between the lower crust and upper mantle. This implies that it is reasonable to invert the residual field for the geometry of the Moho interface. However, for an area as large as the North Atlantic lateral density variations can be expected in the upper mantle which have to be considered as well.

3 Moho Depth and Uncertainties

Figure 3 shows the Moho depth of the study area after Grad et al. (2009). The compilation presents the Moho depth for the entire European plate, but we use here only the subset covering the Northeast Atlantic. All available regional seismic profiles and previous compilations have been used in compiling the data set. In the Northeast Atlantic region the Moho depth (Fig. 3) is changing considerable between the oceanic part of the study area (∼20 km) and the center of the Fennoscandian shield (∼60 km).

Based on the quality and characteristic of the input data, the authors assigned uncertainties to the depth estimates. The uncertainties differ for different seismic techniques, and even for similar techniques in similar areas but different station spacing. In general, the Moho depth estimates are expected to have an accuracy in the order of ±3–6 km (Fig. 4).

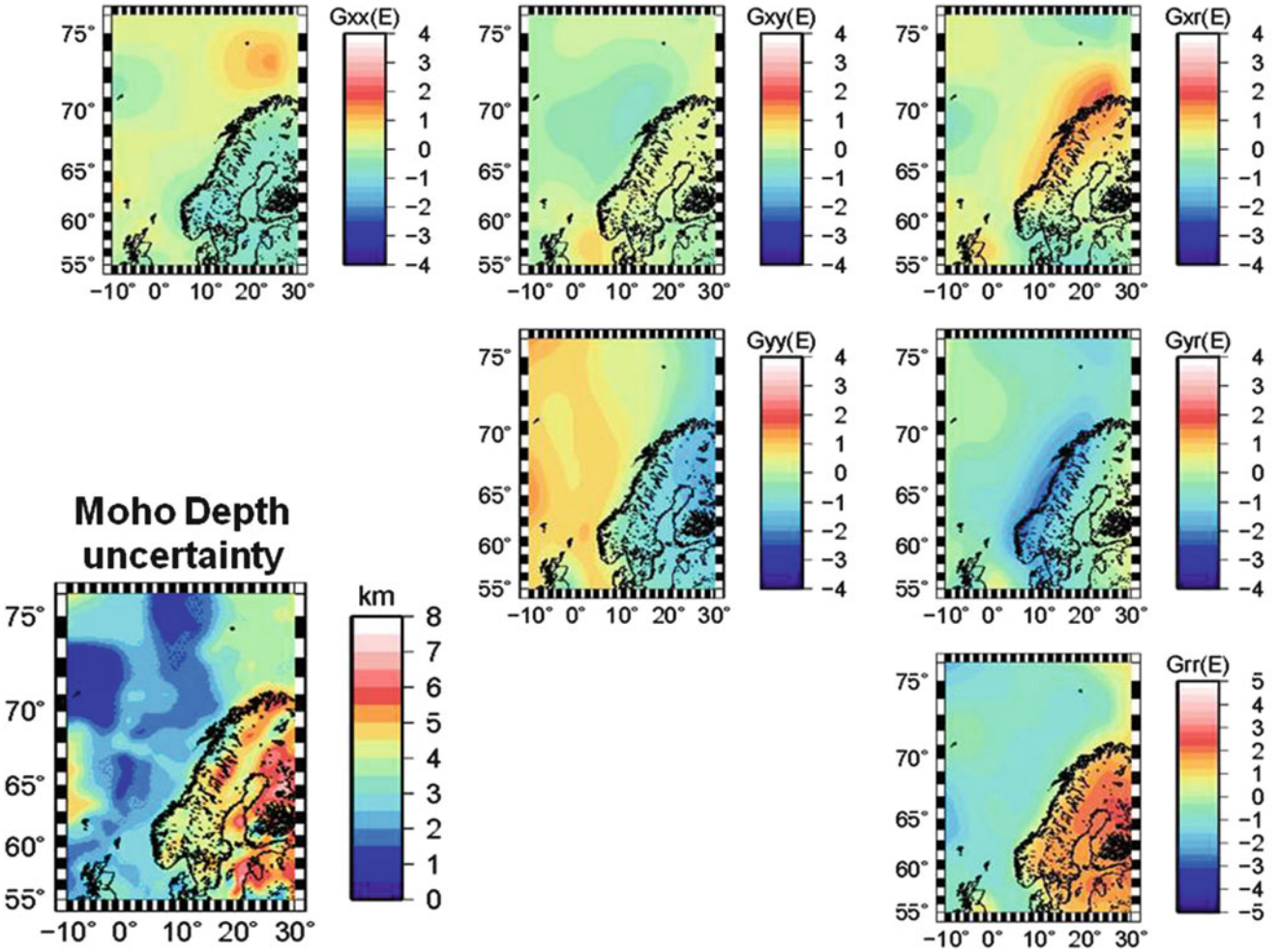

Fig. 4 Difference in the calculated gradient fields at satellite altitude related to the uncertainties (*lower left*) of the crustal thickness compilation. The uncertainties given by Grad et al. (2009) reflect the quality and spatial distribution of seismic data used in compiling the Moho depth (Fig. 1)

In comparison with other compilations and data sets for the study area, the data agree within the bounds given by the uncertainties. An example is the Southern Scandes, where different estimates have been published in recent years. E.g. the Grad et al. compilation uses almost none of the new refraction profiles from Stratford et al. (2009). This results in uncertainties in the compilation, which are in places up to ±4.5 km. Within these bounds the two compilations agree, but show a geologically quite different picture. For a more detailed discussion of the Moho depth map for the region see Ebbing et al. (2012).

4 Forward Calculations of Gravity Gradients

In the following we calculate the gradient fields, which can be expected from the Moho depth compilation. No attempt is made to optimize the geometry of the Moho interface by inverting for the differences between the forward calculation and the observed data. Instead we discuss the amplitudes, which can be expected to be related to the Moho geometry and its uncertainties; both in terms of density and geometry.

4.1 Gravity Gradients from Crustal Thickness Variations

The gravity gradients are calculated for a height of 270 km above the ellipsoid and for a station spacing of 0.1°. The station spacing is denser than necessary to represent the spatial resolution of GOCE, but is in agreement with the distance of observation points for the satellite.

The Moho depth is discretized in variations around a mean Moho depth of 32 km. This results in tesseroids with a relative density of $+400$ kg/m^3 for Moho depth <32 km and -400 kg/m^3 for Moho depths >32 km. The mean depth has been chosen in agreement with the average Moho depth

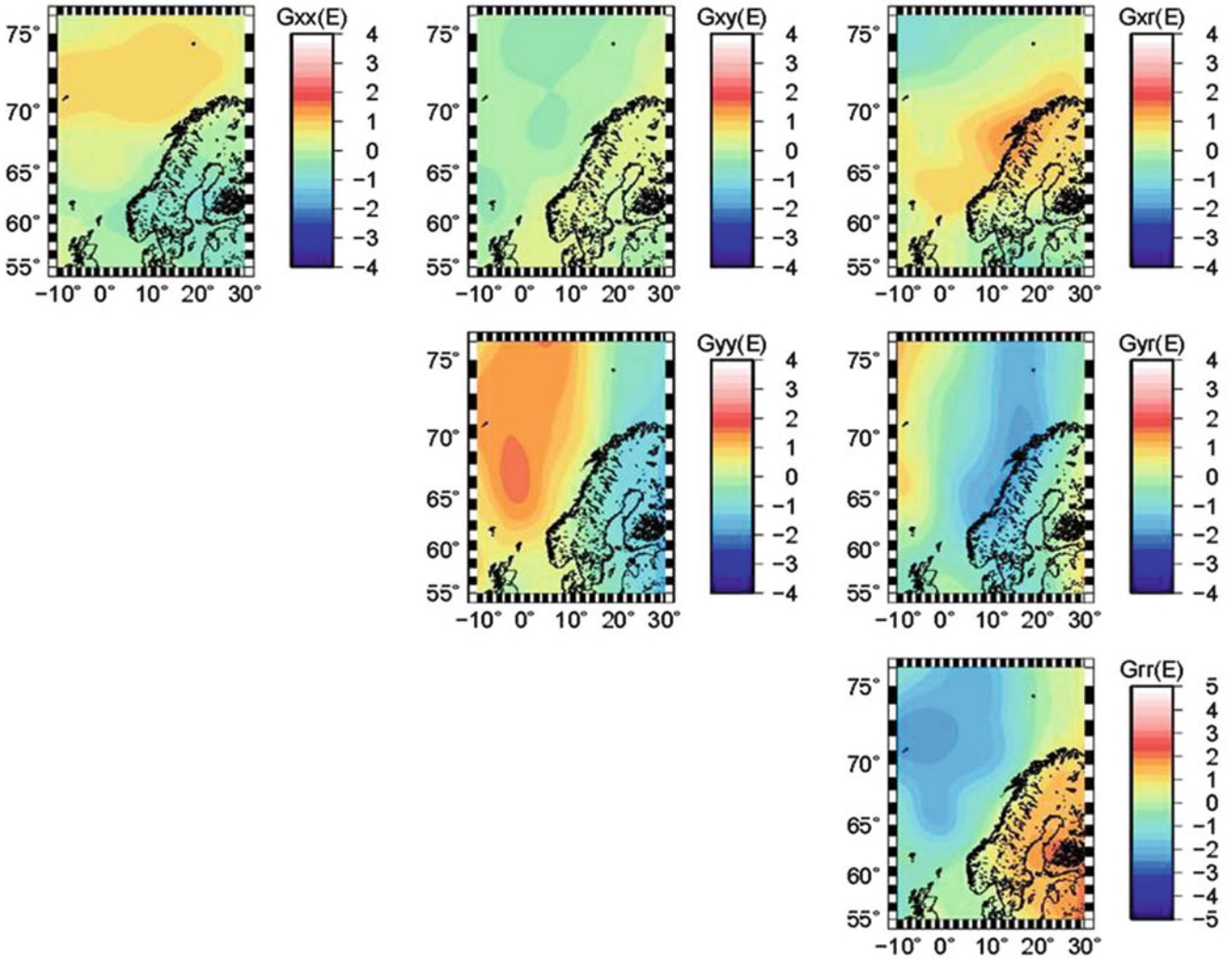

Fig. 5 Difference in the gravity gradient due to uncertainties of the density contrast at the Moho. The figure shows the difference between the calculations in Fig. 3 and the calculations with a density of −200 kg/m^3

at the Norwegian coastline, while the density contrast is a typical value often used in regional density models and isostatic studies (e.g. Ebbing and Olesen 2005). The lateral dimension of the tesseroids are $0.1 \times 0.1°$ as given for the Moho compilation.

4.2 Variations in Gravity Gradients from Uncertainties in Crustal Thickness

In the next step, we calculate the relative changes in the gradient fields from maximum variations in the Moho depth. This means that we first calculated a new Moho map with maximum deviation from the initial Moho depth compilation based on its uncertainties: Moho depths <32 km have been reduced by the stated uncertainty value, while Moho depths >32 km have been increased by the uncertainty value to be able to estimate the maximum effect. The gradient fields presented in Fig. 4 show the difference between the calculations shown in Fig. 3 and the calculations with a maximum undulation, and can be termed the uncertainties of gradient calculations due to the uncertainties of the Moho depth compilation.

4.3 Variations in Gravity Gradients from Variations of Density Contrast

Even more crucial than the variation in crustal thickness is the applied density contrast at the crust-mantle boundaries. The density of the upper mantle might vary significantly for the oceanic plate with distance to the spreading ridge (e.g. Chappel and Kusznir 2008), while the continental mantle might change in correlation with its tectonothermal age (e.g.

Afonso et al. 2008). At the same time the density of the lower crust varies from 2,900 to 3,000 kg/m^3 and can on the continental shelf increase due to processes like magmatic underplating (3,100 kg/m^3) or eclogitization (3,300 kg/m^3) to values similar to upper mantle rocks. Zoback and Mooney (2003) showed the increase of the average crustal density with increasing depth, which can lead to an almost indistinguishable density contrast for thick crust like in the center of the Fennoscandian shield. There, the need for the presence of a high-density lower crust to achieve both isostatic equilibrium and to explain the regional gravity field has been shown (e.g. Ebbing et al. 2012), and the density contrast between the lower crust and upper mantle is less than 200 kg/m^3.

The gradient fields presented in Fig. 5 show the difference between the calculations shown in Fig. 3 and the calculations with a density of −200 kg/m^3, and can be termed the uncertainties of gradient calculations due to the uncertainties of the density contrast.

4.4 Discussion of Results

The amplitude of the calculated gradients from the Moho interface is with ±5 E larger than the topographic mass reduced GOCE gradients, which is only in the order of ±3 E. However, the shape of the anomalies is quite similar between the calculated and measured field which indicates that the Moho interface, as expected, is a first order signal in the observed gravity gradients, even at satellite heights. An advantage is that the resolution and wavelength content of the gradients at satellite height is quite similar to the wavelength content normally used for an inversion for crustal thickness. The satellite data are less influenced by near-surface geological features with a subtle density contrast, but more affected by the main density contrasts. But such contrasts might also occur laterally between different crustal domains, e.g. between the oceanic crust and the continental shelf.

The tests on the uncertainties of the density contrast and geometry shows in general values with amplitude of ±2 E. The comparison with the observed fields and the residuals between the measured and observed fields shows that by varying geometry alone, it is difficult to minimize the misfit, and that the density contrast is the more crucial factor.

Using a density contrast of 200 kg/m^3 would probably lead to a better fit, and simple inversion within the limits given by a variation in density contrast could provide a first-order improvement over the entire study area. One might apply this to estimate the varying density contrast from the oceanic plate towards the Fennoscandian shield, but such an approach would neglect other intra-crustal density sources, and must be carefully interpreted in terms of its geological meaning.

Conclusions

Gravity gradients can be a useful tool to estimate crustal thickness in areas where few or no seismic constraints are available. The gradients at satellite height have a low spatial resolution, which makes them ideal to capture the wavelength normally associated with crustal thickness variations. The pitfalls in the use of gravity gradients instead of the gravity field are similar to the latter. The density contrast at the base of the crust influences largely the fields and any estimates of crustal thickness from gravity or gravity gradients data. The sensitivity tests show that for an inversion of crustal thickness a lower density contrast than conventionally used has to be applied.

In addition, any sensible crustal thickness estimate should as well consider isostasy, which however implies that on the regional or global scale variations in the lithospheric thickness have to be considered. While the gravity gradients do not overcome the ambiguity of potential fields, they certainly offer an additional useful tool to study lithospheric features, and to validate crustal or lithospheric models based on conventional gravity data sets.

Acknowledgment This work has been done in the framework of the ESA sponsored GOCE+ GeoExplore study as part of ESA's Support to Science Element (STSE). We thank the editors Pascal Willis and Carla Braitenberg and three anonymous reviewers for their comments which helped to improve the manuscript.

References

Afonso JC, Fernàndez M, Ranalli G, Griffin WL, Connolly JAD (2008) Integrated geophysical-petrological modeling of the lithosphere and sublithospheric upper mantle: methodology and applications. Geochem Geophys Geosyst 9(5). doi:10.1029/2007GC001834

Álvarez O, Gimenez M, Braitenberg C, Folguera A (2012) GOCE satellite derived gravity and gravity gradient corrected for topographic effect in the South Central Andes region. Geophysical J Int 190: 941–959. doi:10.1111/j.I365-246X.2012.05556.x

Amante C, Eakins BW (2009) ETOPO1 1 Arc-minute global relief model: procedures, data sources and analysis. NOAA Technical Memorandum NESDIS NGDC-24

Bouman J, Ebbing J, Fuchs M, Schmidt M, Bosch W, Schwatke C, Abdul Fattah R, Meekes S, Abbink O, Schavemaker Y (2011) Heterogeneous gravity data combination for Earth interior and geophysical exploration research. In: Proceedings GOCE User Workshop 2011, ESA SP-696

Bouman J, Ebbing J, Fuchs M (2013) Reference frame transformation of satellite gravity gradients and topographic mass reduction. JGR Solid Earth 118:1–17. doi:10.1029/2012JB009747

Chappel AR, Kusznir NJ (2008) Three-dimensional gravity inversion for Moho depth at rifted margins incorporating a lithosphere thermal gravity anomaly correction. Geophys J Int 174:1–13

Ebbing J (2007) Isostatic density modelling explains the missing root of the Scandes. Norw J Geol 87:13–20

Ebbing J, Olesen O (2005) The Northern and Southern Scandes – structural differences revealed by an analysis of gravity anomalies, the geoid and regional isostasy. Tectonophysics 411:73–87

Ebbing J, England RW, Korja T, Lauritsen T, Olesen O, Stratford W, Weidle C (2012) Structure of the Scandes lithosphere from surface to depth. Tectonophysics 536–537:1–24. doi:10.1016/j.bbr.2011.03.031

Goiginger H, Hoeck E, Rieser D, Mayer-Guerr T, Maier A, Krauss S, Pail R, Fecher T, Gruber T, Brockmann J, Krasbutter I, Schuh W, Jaeggi A, Prange L, Hausleitner W, Baur O, Kusche J (2011) The combined satellite-only global gravity field model GOCO02S. Presented at the 2011 general assembly of the European geosciences union, Vienna, Austria, 4–8 April

Grad M, Tiira T, ESC Working Group (2009) The Moho depth map of the European Plate. Geophys J Int 176:279–292

Mayer-Guerr T, Rieser D, Höck E, Brockmann JM, Schuh WD, Krasbutter I, Kusche J, Maier A, Krauss S, Hausleitner W, Baur O, Jäggi A, Meyer U, Prange L, Pail R, Fecher T, Gruber T (2012) The new combined satellite only model GOCO03s. Poster presented at the GGHS2012, Venice

Olesen O, Brönner M, Ebbing J, Gellein J, Gernigon L, Koziel J, LauritsenT MR, Sand M, Solheim D, Usov S (2010) New aeromagnetic and gravity compilations from Norway and adjacent areas – methods and applications. Petrol Geol Conf 7:559–586

Pail R, Bruinsma S, Migliaccio F, Förste C, Goiginger H, Schuh WD, Höck E, Reguzzoni M, Brockmann JM, Abrikosov O, Veicherts M, Fecher T, Mayrhofer R, Krasbutter I, Sansò F, Tscherning CC (2011) First GOCE gravity field models derived by three different approaches. J Geod 85:819–843. doi:10.1007/s00190-011-0467-x

Sampietro D (2011) GOCE exploitation for Moho modeling and applications. In: Proceedings of the 4th international GOCE user workshop, Munich, Germany, 31 Mar–1 Apr 2011

Sjöberg LE, Bagherbandi M (2011) A method of estimating the Moho density contrast with a tentative application by EGM08 and CRUST2.0. Acta Geophys 59(3):502–525

Stratford W, Thybo H, Faleide JI, Olesen O, Tryggvason A (2009) New Moho map for onshore southern Norway. Geophys J Int 178:1755–1765

Sünkel H (1985) An isostatic Earth model. Report No. 367, Department of Geodetic Science and Surveying, The Ohio State University, Columbus

Uieda L, Bomfim E, Braitenberg C, Molina E (2011) Optimal forward calculation method of the Marussi tensor due to a geologic structure at GOCE height. In: Proceedings GOCE user workshop 2011, ESA SP-696

Zoback ML, Mooney WD (2003) Lithospheric buoyancy and continental intraplate stresses. Int Geol Rev 45:95–118

Detecting the Elevated Crust to Mantle Section in the Kohistan-Ladakh Arc, Himalaya, from GOCE Observations

Daniele Tenze, Carla Braitenberg, Eva Sincich, and Patrizia Mariani

Abstract

The Kohistan Ladakh area in northeastern Pakistan is an exposed top to bottom crustal section, implying that high density rocks of the lower crust are at the surface. The new GOCE satellite observations improve the gravity field in this remote area, giving a new dataset for geophysical interpretation. We use the new data to determine the crustal thickness variations and to define the geometry of the overturned crustal columns constituting the base of the former island arc. For the first time the entire extension of the arc is traced with the help of the gravity field observed by GOCE. The entire arc generates a positive gravity signal up to 180 mGal, limited by two geological boundaries, the Main Karakorum Thrust at north, and the Main Mantle Thrust at south. The Main Karakorum thrust marks the transition from the Indian to the Eurasian plate. The crustal thickness varies here between 40 and 70 km. The three geologic units that define the Kohistan arc, the South Plutonic Complex, the Chilas and Gilgit Complexes, occupy the upper crust, with depths increasing northwards between 14 and 44 km. There are not enough constraints to model the eastern part of the arc, the Ladakh, but the similarity of the gravity signal suggests that the thickness of the upper dense crustal units is similar.

Keywords

Crustal thickness • Gravimetry • Satellite GOCE • Himalaya • Kohistan-Ladakh arc

1 Introduction

The aim of this work is to use the gravity observations of the GOCE satellite mission (Floberghagen et al. 2011) in a geologically unique part of the Himalayan orogen, which is the Kohistan-Ladakh arc. In the Kohistan the entire section of the crust from the mantle-crust transition, to the volcanic deposits in the upper crust is exposed (Fig. 1b, c) (Ahmad et al. 2008; Bard 1983; Dhuime et al. 2007, 2009; Garrido et al. 2007; Jagoutz and Schmidt 2012; Jagoutz et al. 2006, 2007, 2009, 2011; Mahéo et al. 2004; Petterson 2010; Rolland et al. 2002). The arc is located at the western syntaxis of the Himalayan belt. In analogy to the horizontal GPS velocities observed surrounding the eastern syntaxis (Jin and Zhu 2003; Jin et al. 2007) it can be expected that the horizontal velocities rotate anti-clockwise around the syntaxis. During geological evolution the Kohistan-Ladakh arc evolved from a volcanic island arc to an overturned piece of crustal section, where rocks formed at great crustal depth have been brought to the surface. The presence of these rocks is interesting for gravity studies, because they have relatively high density, and therefore generate a positive gravity signal. Only with the advent of the GOCE satellite gravity mission can the entire extent of the arc be studied. This gives a unique opportunity to study the arc and determine the density anomaly.

D. Tenze (✉) • C. Braitenberg • P. Mariani
Department of Mathematics and Geosciences, University of Trieste, Via Weiss 1, 34127 Trieste, Italy
e-mail: datenze@gmail.com; berg@units.it

E. Sincich
Laboratory for Multiphase Processes, University of Nova Gorica, Vipavska 11c SI-5270, Ajdovščina, Slovenia

U. Marti (ed.), *Gravity, Geoid and Height Systems*, International Association of Geodesy Symposia 141,
DOI 10.1007/978-3-319-10837-7_38, © Springer International Publishing Switzerland 2014

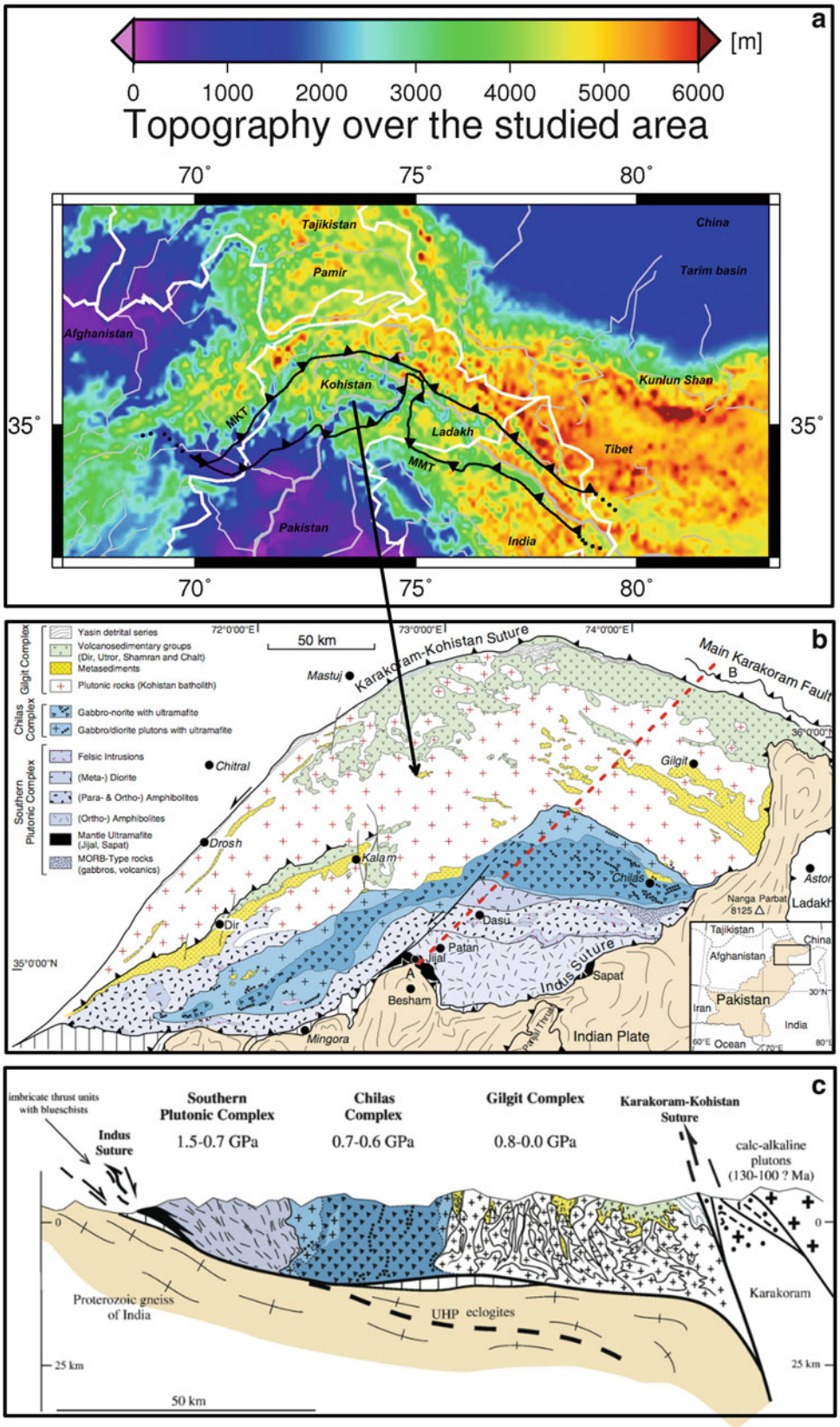

Fig. 1 (**a**) Topography of western Himalaya, centered on the Kohistan-Ladakh arc. *MKT* Main Karakorum Thrust, *MMT* Main Mantle Thrust. *White lines*: national borders, *grey lines*: rivers. (**b**) Geologic map of the Kohistan arc (Jagoutz and Schmidt 2012), the *red dashed line* represents the geologic section shown in (**c**) (Jagoutz et al. 2011)

The Kohistan-Ladakh arc is at the limit of resolution of the GOCE gravity field, due to its relatively small dimensions, as it is 180 km wide and 800 km long. The GOCE data give the first comprehensive gravity field over this complex, as terrestrial gravity data exist (Ebblin et al. 1983), but do not cover the entire regional extent. The questions that are to be solved are the entire extent of the arc, the thickness of the units formed by the high density rocks and the evolution of the arc in the framework of plate tectonics.

The GOCE satellite mission has measured the gravity gradient tensor at a height of 250 km between March 2009 and November 2013, producing a much higher resolution and precision of the gravity field with respect to previous satellites (Floberghagen et al. 2011; Rummel et al. 2011). The improvement of the gravity field is particularly evident in remote mountain areas of difficult access, where terrestrial gravity data are sparse. The time-wise geopotential gravity model (Pail et al. 2011) processes the GOCE satellite observations and reproduces them in spherical harmonic expansion up to degree and order 250, which corresponds to a resolution of 80 km. A first study using the GOCE field in the Himalayas is by Basuyau et al. (2013), where a joint inversion of teleseismic and GOCE gravity data is fulfilled. Shin et al. (2007) use the GRACE satellite to infer the Moho over the entire Tibetan plateau. To the north of Tibet and our study area, Steffen et al. (2011) undertook a study of the isostatic state and crustal thickness variations. In the present paper we have searched a relation between the GOCE satellite gravity signal and the geological information related to the high density units outcropping in the Kohistan region. The results confirm that the GOCE data resolve this structure and give a comprehensive field with which we improve the knowledge of the density units.

2 Regional Geology of the Kohistan-Ladakh Arc and Geodynamic Context

The Kohistan-Ladakh region is situated in north-east Pakistan, Himalaya, and its terrane is one of the best examples of a complete exposed section of an island arc type crust extending from the rocks relative to the uppermost crust to the crust-mantle transition (Petterson 2010). Moreover these formations are totally separated from the rocks deriving from a different geological history separated from the arc by two big fault systems (Fig. 1a): the Shyok Suture known also as Northern Suture or Main Karakorum Thrust (MKT) to the north, and the Indus-Tsangpo Suture known as the Main Mantle Thrust (MMT) to the south. The Kohistan Arc Complex represents the units relative to a fossil Cretaceous to Tertiary arc complex (Bard 1983) now entrapped between the Eurasian and the Indian plates within that collisional environment which created the Himalaya orogen.

The intra-oceanic subduction process which accreted the Kohistan island arc began around 117 Ma within the Tethyan oceanic plate (Dhuime et al. 2009) and then collided with the Indian and the Eurasian plate. Many papers have catalogued the different units outcropping in the Kohistan region (Dhuime et al. 2007, 2009; Garrido et al. 2007; Khan et al. 2009) and related these with the formations outcropping in the Ladakh region (Ahmad et al. 2008; Mahéo et al. 2004; Rolland et al. 2002). In the following we concentrate our detailed study on the Kohistan arc, the western part of the Kohistan-Ladakh arc. In accordance with Jagoutz and Schmidt (2012) the present work will consider three main formations: the Southern Plutonic Complex, the Chilas Complex and the Gilgit Complex (Fig. 1b). Burg et al. (2006) and Jagoutz et al. (2011) present a section of the crust crossing the Kohistan arc, red dashed line in Fig. 1b, in which the thickness of the different units is estimated along a generic profile (Fig. 1c). The geological model assumes the crust to have been segmented and trapped between the converging Indian and Eurasian plates, and tilted by 90°. The thickness of the units should be equal to the width of this piece of crust.

The Southern Plutonic Complex represents the lowermost ultramafic-mafic units outcropping in the area. It contains the Jijal Complex, a series of ultramafic-mafic metamorphosed igneous complexes representing the transition between the upper mantle and the lower crust (Dhuime et al. 2007, 2009; Garrido et al. 2006, 2007) and the Kamila Amphibolites, a unit characterized by metavolcanic and metapluntonic rocks (Dhuime et al. 2009; Petterson 2010).

The Chilas Complex is a large-volume, mafic-ultramafic plutonic body composed of gabbro norite, minor diorites and subordinate tonalites (Jagoutz et al. 2006, 2007).

The Gilgit Complex is dominated by the Kohistan batholith and its calc-alkaline domain. It represents the mid and upper arc crust of the island arc (Jagoutz and Schmidt 2012). Within this complex the rocks have predominantly quartz-, quartzmonzo- and granodiorites composition with intrusions of picro-basaltic dykes to leucogranites stocks and sheets (Petterson and Windley 1985).

3 Methodology

We use two methodological approaches for gravity inversion that are tuned to the scale of the investigation. In the first part, with the spectral inversion (Braitenberg and Zadro 1999; Braitenberg et al. 2000) and the flexural model (Braitenberg et al. 2002, 2003), the crustal thickness variation and the rigidity of the crust is determined. Then tightening the studied area to the Kohistan region, we use a prisms model (Nagy et al. 2000) to solve the forward and the inverse problem for estimating the thickness of the three main outcropping geological units of the Kohistan arc. The

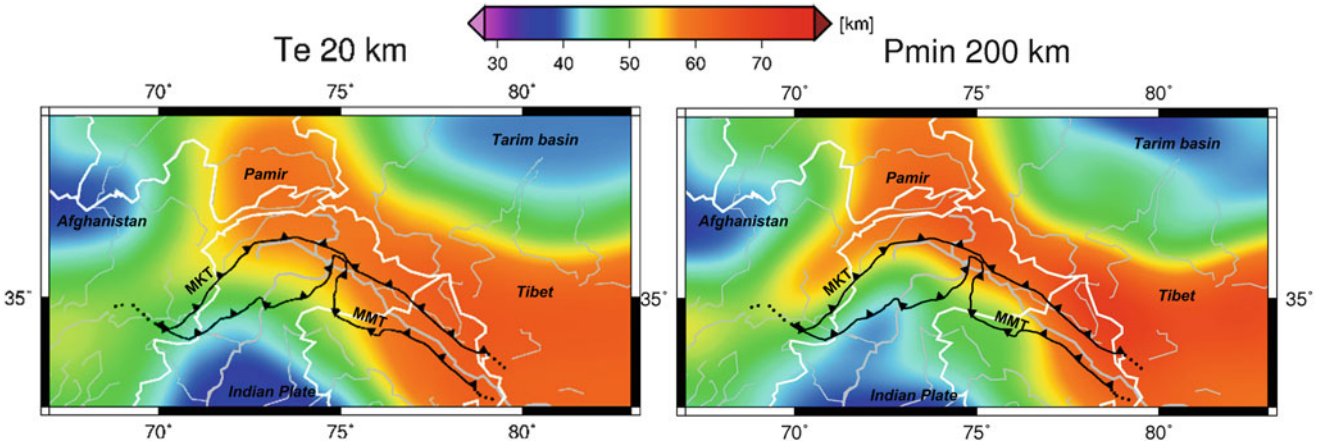

Fig. 2 The two Mohos obtained with the spectral inversion with low pass filter of 200 km and with the Flexural Model with an elastic thickness of 20 km. Even if the two methods are different the images looks similar

gravity field model is the GOCE geopotential *time-wise* model GO_CONS_GCF_2_TIM_R3 published in 2011 complete to degree and order 250 (Pail et al. 2011), (http://icgem.gfz-potsdam.de/ICGEM/). The gravity anomaly is calculated at a height of 8,900 m and successively reduced by the effect of topography using the algorithm proposed by (Forsberg 1985) obtaining the Bouguer gravity anomaly. The height of 8,900 m is chosen to be above the regional topography to allow a reduction of the observations for the topographic effect.

The main goal of the regional gravity spectral inversion and of the isostatic analysis is to remove the regional gravity signal and enhance the signal of the Kohistan-Ladakh arc.

The spectral inversion is an iterative method which is based on the Parker series expansion of the gravity field of a boundary separating layers of different density (Blakely 1996; Braitenberg and Zadro 1999; Braitenberg et al. 2000; Parker 1972), the results depend on the reference depth and the cut-off wavelength of the filter, that limits the frequencies entering the inversion (Braitenberg et al. 2008). Due to the properties of the earth filter (Blakely 1996) high wave number signals of the gravity field are not generated at Moho level, so the components of the Bouguer gravity anomalies with short wavelength are eliminated. We test different cutoff frequencies of the filter in the frame of this study, seeking the best agreement with the isostatic model. The cut-off frequencies range between 1/100 1/km and 1/400 1/km. The lower cut-off frequency produces a flatter Moho. Increasing the frequency too much results in unrealistic high amplitude oscillations in the Moho. We use the criterion of making the flexure Moho and the gravity Moho match to find the most adequate filter-frequency and elastic thickness.

The isostatic flexure model (Watts 2001) is an independent means to model the crustal thickness variations, starting with the topographic load (Braitenberg et al. 2002, 2003, 2007). Here the fundamental parameter is the elastic thickness: the greater the elastic thickness is, the more rigid the lithosphere and hence the smaller the oscillations of the crustal thickness generated by the load will be. The gravity field of the isostatic crustal thickness is calculated assuming a constant density contrast (300 kg/m^3) across the crust-mantle boundary (Mohorovičić discontinuity, Moho) using the spectral method (Parker 1972). We adopt the digital terrain model ETOPO1 of the *National Geophysical Data Center, National Oceanic and Atmospheric Administration* (NGDC, NOAA) (Amante and Eakins 2008) [http://www.ngdc.noaa.gov/ngdc.html]. The spectral and isostatic studies were principally made to obtain the regional gravity field and separate it from the local field generated by the crustal density inhomogeneities of the Kohistan Arc Complex. We make tests for the different filters, using the cut-off frequencies of 1/400, 1/300, 1/250, 1/200 and 1/100 1/km. We find a good agreement between the isostatic and the gravity Moho when eliminating wavelengths smaller than 200 km from the Bouguer gravity anomalies and for an equivalent elastic thickness of Te = 20 km. These values are also very similar to the ones that were found by Shin et al. (2007) and Braitenberg et al. (2000) for the Tibetan plateau. The agreement between the isostatic and the spectral Moho shows that there is full isostatic compensation in the area. This agrees to Steffen et al. (2011) who define isostatic compensation in terms of the ratio between Moho from gravity inversion and the isostatic Moho. Their analysis includes the Pamir Mountains where they find compensation between 90 and 110 %. The gravity and isostatic Moho depths are shown in Fig. 2. The Moho deepens sharply at the transition from the Indian plate across the Main Mantle Thrust reflecting the geometry of the thrust. The Moho is deep below the Tibet plateau, over 70 km, and shallow towards the Tarim Basin, between 35 and 47 km. The Pamir mountains have deep Moho values, around 60 km. These values agree well with the previous studies (Bassin et al. 2000; Shin et al. 2007; Steffen

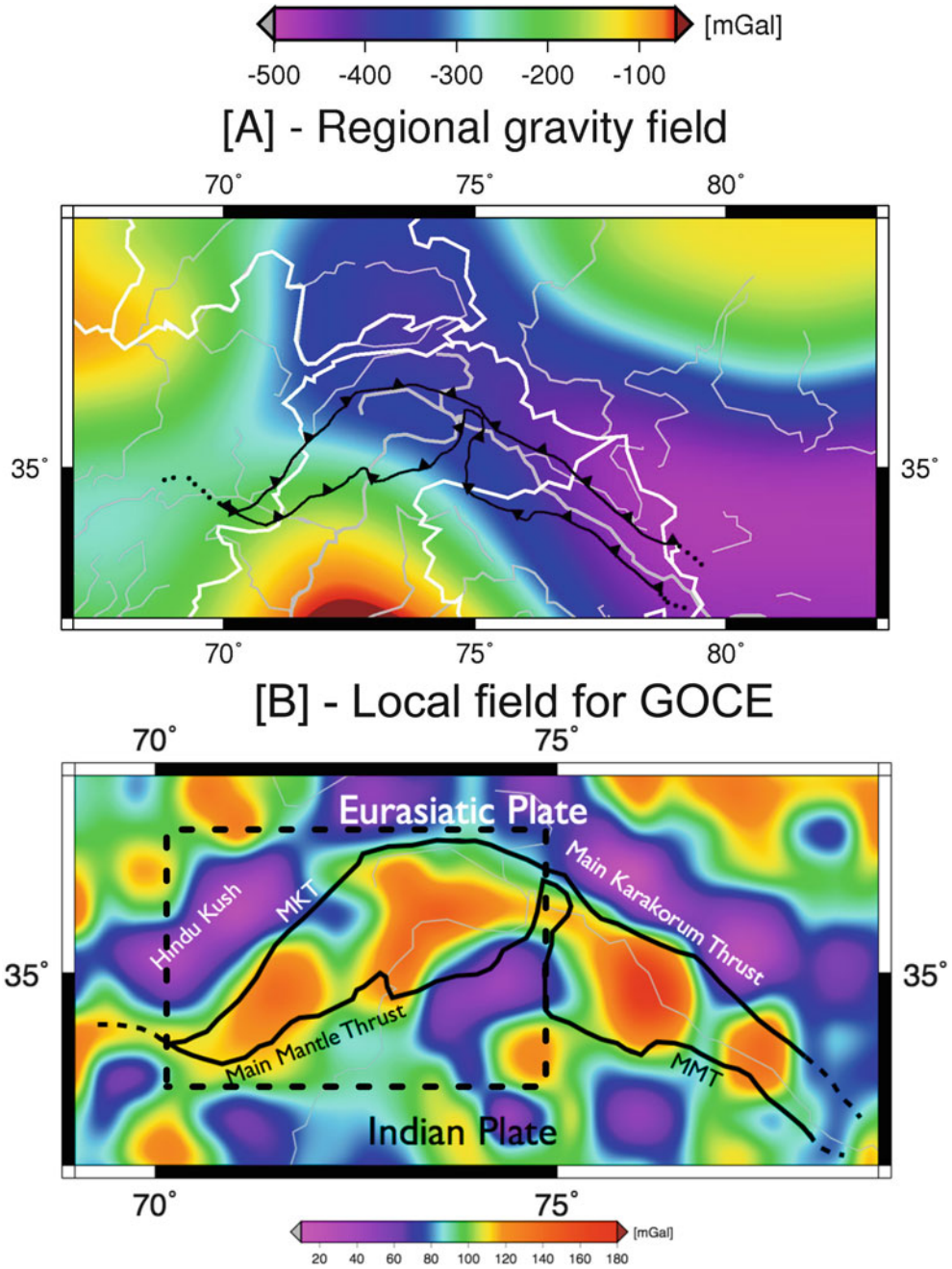

Fig. 3 (**a**) Regional gravity field calculated from the isostatic Moho with elastic thickness of 20 km, and density contrast of 300 kg/m^3. (**b**) The residual Bouguer gravity field, calculated at 8,900 m, which remains after subtracting the isostatic Moho. The signal is well correlated with the Main Karakoram Thrust, that delineates the Kohistan and Ladakh units to the North

et al. 2011). In the Kohistan area the value around 50 km agrees also with the CRUST2.0 model, although he latter has a smaller resolution of 2° (Bassin et al. 2000). The Moho depth follows the topography because the elastic thickness is relatively low.

The Bouguer gravity field which remains after subtracting the gravity field of the isostatic Moho (Fig. 3a) is given in Fig. 3b. The residual is well correlated with the Main Karakoram Thrust, that delineates the Kohistan and Ladakh units to the North. Both Kohistan and Ladakh generate a continuous relative increase in the gravity value, which we define a gravity high. The indentation separating the two arcs is associated to a decrease in the gravity value.

4 Gravity Model of the Kohistan Arc Complex

Once the Moho gravity effect has been estimated (Fig. 3a), we used the gravity residual (Fig. 3b) to analyze the Kohistan region. Our goal is to obtain a density model of the three main units based on the geological model that explains this residual gravity field. We adopt the geological map of Jagoutz and Schmidt (2012) and the cross section Jagoutz et al. (2011) and Burg et al. (2006) presented in Fig. 1, and create a forward prisms model of the three main formations: the Southern plutonic Complex, the Chilas Complex and the Gilgit Complex, each one with its own densities. The density values have been taken from the published ones (Miller and Christensen 1994) and are as follows. The Southern Plutonic Complex has a bulk density of 3,055 kg/m^3 and a thickness of 11 km, the Chilas Complex a bulk density of 2,965 kg/m^3 and a thickness of 11–17 km and the Gilgit Complex a bulk density of 2,789 kg/m^3 and a thickness of 11–21 km. The thickness of the units is based on the geologic section, extrapolating the depths from the section to the remainder of the arc. This model, which we term the forward model, is the starting point for the gravity inversion, that aims to optimize the thickness of the three geologic units and to obtain a best fit to the gravity observations. The gravity of the Kohistan Arc Complex is obtained from the sum of the gravity of the three units and is shown in Fig. 4a. The forward model has been used as first guess for the prisms inversion which refines the thickness of the prisms during the inversion process. The densities are not touched during the inversion, as it is not possible to invert for the geometry and the densities at the same time.

The inversion procedure is based on a Tikhonov regularization approach (Engl et al. 1996; Kügler and Sincich 2009). However, as is well known, because of the inherent ambiguity of the gravimetric data interpretation, any depth estimate relying exclusively on gravity data might be non unique and highly unstable. We overcome such a difficulty by integrating a priori information which acts as physical constraints within our inversion technique, which is in turn based on a minimization argument. In particular, we consider a total variation (TV) stabilizing function which favors solutions with controlled oscillation. The relevance of such a smoothness constraint is tuned by the choice of a weight parameter which is a multiplicative constant of the stabilizing function. Moreover such a parameter acts as a balance between accuracy and stability of the corresponding regularized solution. We shall outline in the following our interpretation model and discuss our parameter choices as well as the error propagation issue. In detail, the three main formations are approximated by a model with M vertical prisms. From a set of N gravity anomaly observations $g^0 = [g_1{}^0, \ldots, g_N{}^0]$ we compute a vector $Z = [z_1, \ldots, z_M]$ of prisms height of each prismatic cell of the given model. The prisms heights represent the thickness of the complex we are considering and are related with the observed gravity anomaly $g_j{}^0, j = 1, \ldots, N$ by a closed formula (Blakely 1996). In order to overcome the ill-posedness of the problem, we combine the gravimetric data misfit with TV regularization term which favors solutions with controlled oscillations. In such a way we reformulate our problems in the minimization of a Tikhonov type function, whose minimization was realized by the MATLAB routine fmincon which in turn is partly based on first order optimization procedure, as the quasi Newton method for nonlinear equations (Hanke 1995). This is a well known iteration method looking for the steepest descent of the function which requires the computation of first order partial derivatives. The implemented stopping rule is either an upper bound on the threshold on the gap between two consecutive iterations output or a fixed maximum number of iterations. As soon as one of these two criteria is satisfied the procedure stops. In most of the cases the iteration stops, because the maximum number of iterations has been exceeded. The typical number of iteration steps is about 10–15. Among many performed choices of the regularization parameter α, we select a close to optimal situation tuning $\alpha = 0.01$, which gives a satisfactory result in term of small gravity residuals. Such a choice for the regularization parameter α has been performed also by considering it as a rescaling factor between the gravimetric data misfits and the total variation term. Higher values of α tend to flatten the solution, lower values are also acceptable. Increasing the number of iterations does not appreciable alter the results, as already a good fit to the gravity values is achieved during the 15 iterations. The inversion starts from a first-guess prisms distribution that was built on the basis of the Kohistan geologic units. The inversion process refines this model to obtain a better fit to the gravity data. The algorithm is allowed to change only the lower extent of the prisms, the upper border being kept constant. The density of the prisms is constant and is that of the rocks of the geologic units. We have studied the influence of the data noise. For that purpose we perturbed a synthetic gravity anomaly by adding a pseudo-random Gaussian noise with zero mean and standard deviation 1 mGal. As a result, we obtain a standard deviation of the prism thickness residual of about 300–400 m.

The inversion process has given the three refined units shown in Fig. 4b with the respective gravity signal. The correction of the prisms through the inversion is up to 20 km, with the values increasing northwards, Fig. 4b. The inverse model assigns to the Southern Plutonic Complex a thickness which varies from 14 km to 17 km, to the Chilas Complex a thickness variable from 15 km to 22 km, to the Gilgit Complex a bulk density of 2,789 kg/m^3 and a thickness variable from 24 km to 44 km. These numbers reproduce the

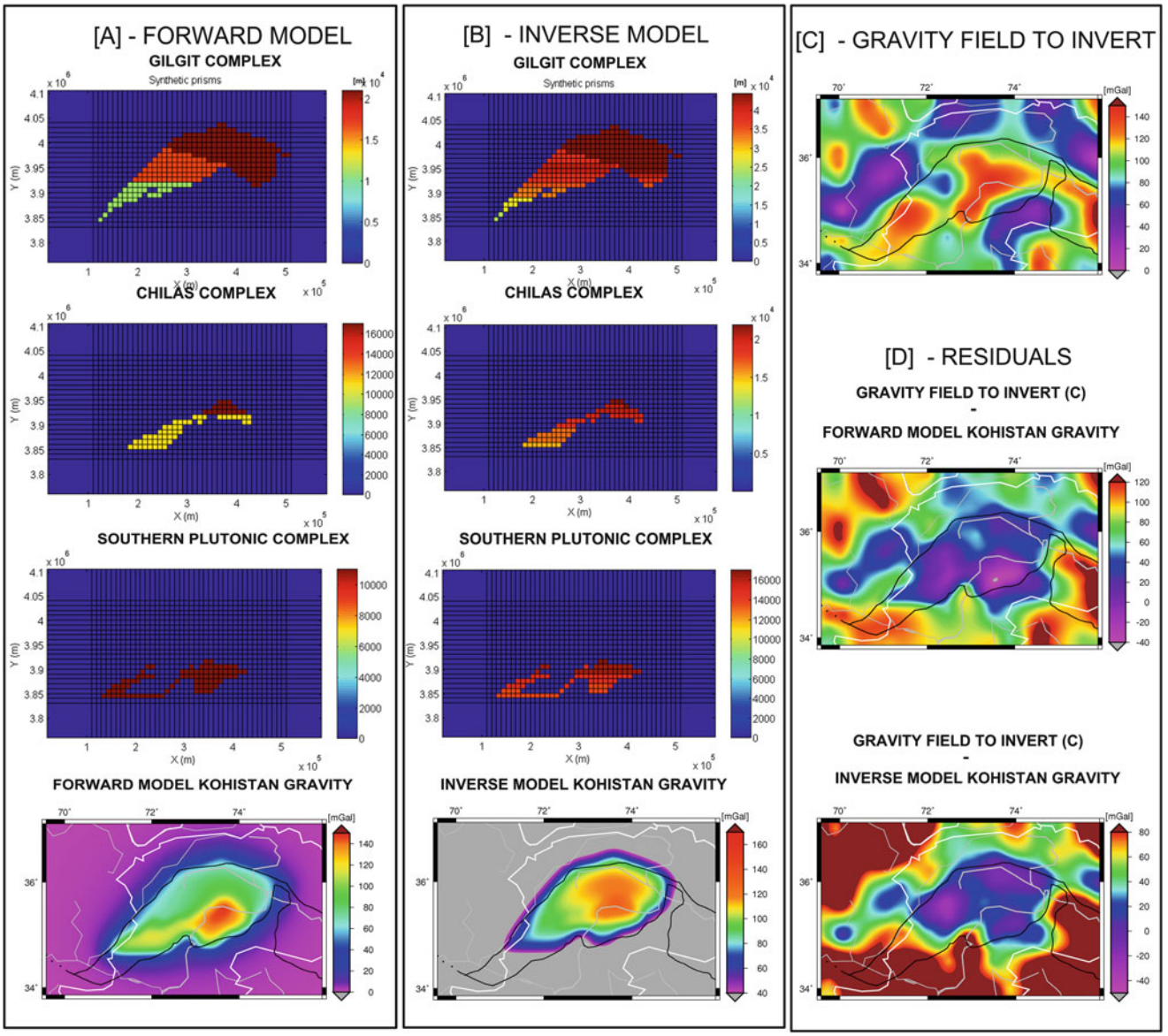

Fig. 4 The gravity model of the Kohistan Arc Complex: (**a**) The forward models - depth of the bottom of the prisms - of the three main geological units and the forward gravity signal calculated from them. (**b**) The inverse models - depth of the bottom of the prisms - of the three main geological units obtained with the inversion and the gravity signal calculated from them. (**c**) The field to invert, obtained from the spectral inversion with cutoff wavelength of 200 km. (**d**) The two final residuals obtained: one from the forward model and one from the inverse model

geologic-geophysical section of the Kohistan arc published by Jagoutz et al. (2011) shown in Fig. 1b and used for the forward model of the previous chapter. The correction in terms of the gravity effect reaches 170 mGal. The final gravity residual is shown in Fig. 4d and for the modeled region of the Kohistan varies between −30 and 10 mGal. The inversion process has definitely improved the initial forward models of the three units: The Southern Plutonic Complex is thinner in the south part with respect to the initial information, for the Chilas Complex there is a more gradual thickening toward north and finally, for the eastern part of the Gilgit Complex the inversion model gives a lower depth of the units, (compare Fig. 4a to b). The residuals show that the full modeling of the Kohistan arc requires further geologic units that are not considered in the present model. This will be part of the future study. For instance the presence of an eclogite layer (bulk density of 3,455 kg/m^3) has been proposed to reside beneath the Gilgit units, just above the subducting Indian plate. The effect of this unit would be to decrease the inverted prisms thickness in the northernmost part of our model. There are though too many uncertainties yet to include this unit in our modeling.

Conclusion

Our work shows that the GOCE gravity anomalies derived from the spherical harmonic expansion have sufficient resolution and precision to resolve the geologically important Kohistan-Ladakh arc, characterized by high density rocks from the lower crust reaching the surface. The correlation with the geology is enhanced, after separation of the regional gravity field. As crustal thickness variations from independent geophysical sources are not available, we use the isostatic model to make a first order Moho model and to estimate the regional gravity field. We find a good agreement between the flexural Moho with a Te value of 20 km and the gravity Moho obtained from inverting the long-wavelength part of the Bouguer gravity anomalies limited to a wavelength of 200 km. We find that the area is in isostatic equilibrium due to the fact that isostatic and gravity Moho are in good agreement.

Our findings are made possible only with the comprehensive field obtained from GOCE that allows us to homogeneously map the gravity field over the entire area and surrounding regions. Finally we use the gravity residual to test whether the existing geologic model of the Kohistan arc, which explains it being a crustal section extending from lower crust to the surface magmatic deposits, is compatible with the gravity field. The gravity residual is positive over the entire Kohistan-Ladakh arc, demonstrating its continuity and full east-west extension. The depth development of the units is only partially known from previous investigations, and only along one profile the depth extent of the units is known. We therefore could use the gravity inversion to estimate the thickness of the units over the whole arc, starting from the known information. Our final model explains the gravity signal better, as the residual is reduced from a starting value of 50 to 170 mGal to a final residual between −30 mGal and 10 mGal, when considering the modeled area of the Kohistan.

In future, a refinement of the inversion process is planned, with a greater variability of the prism densities and the extension of our study to the east, for a better understanding of the Ladakh province, which we expect to have high density superficial rocks as well judging from the gravity signal which is very similar to the one of the Kohistan.

References

Ahmad T, Tanaka T, Sachan HK, Asahara Y, Islam R, Khanna PP (2008) Geochemical and isotopic constrain on the age and origin of the Nidar Ophiolitic Complex, Ladakh, India: implications for the Neo-Tethyan subduction along the Indus suture zone. Tectonophysics 451:206–224. doi:10.1016/j.tecto.2007.11.049

Amante C, Eakins BW (2009) ETOPO1 1 arc-minute global relief model: procedures, data sources and analysis. National Geophysical Data Center, NOAA Technical Memorandum NESDIS NGDC-24, NOAA. doi:10.7289/V5C8276M

Bard JP (1983) Metamorphism of an obducted island arc: example of the Kohistan sequence (Pakistan) in the Himalayan collided range. Earth Planet Sci Lett 65:133–144

Bassin C, Laske G, Masters G (2000) The current limits of resolution for surface wave tomography in North America. Eos Trans AGU 81:F897

Basuyau C, Diament M, Tiberi C, Hetényi G, Vergne J, Peyrefitte A (2013) Joint inversion of teleseismic and GOCE gravity data: application to the Himalayas. Geophys J Int 193:149–160. doi:10.1093/gji/ggs110

Blakely JR (1996) Potential theory in gravity and magnetic applications. Cambridge University Press, Cambridge

Braitenberg C, Zadro M (1999) Iterative 3D gravity inversion with integration of seismologic data. Boll Geof Teor Appl 40(3/4): 469–476

Braitenberg C, Zadro M, Fang J, Wang Y, Hsu HT (2000) The gravity and isostatic Moho undulations in Qinghai. J Geodyn 30:489–505

Braitenberg C, Ebbing J, Götze H-J (2002) Inverse modeling of elastic thickness by convolution method – the Eastern Alps as a case example. Earth Planet Sci Lett 202:387–404

Braitenberg C, Wang Y, Fang J, Hsu HT (2003) Spatial variations of flexure parameters over the Tibet-Quinghai Plateau. Earth Planet Sci Lett 205:211–224, ISSN: 0012-821X

Braitenberg C, Wienecke S, Ebbing J, Born W, Redfield T (2007) Joint gravity and isostatic analysis for basement studies – a novel tool. Extended Abstracts, EGM 2007 International Workshop, Innovation in EM, Grav and Mag Methods: a new Perspective for Exploration, Villa Orlandi, Capri – Italy, 15–18 April 2007. http://apps.units.it/sitedirectory/PubblicazioniRicerca/DettagliProdotto.aspx?AuthorProductId=54848

Braitenberg C, Wienecke S, Ebbing J, Born W, Redfield T, Mariani P (2008) LithoFLEX Tutorial, user's manual. LithoFLEX Group, Trieste, Italy. http://www.lithoflex.org/lithoflex/home/basics/Lithoflex_tutorial.pdf

Burg JP, Jagoutz O, Hamid D, Hussain S (2006) Precollision tilt of crustal blocks in rifted island arcs: structural evidence from the Kohistan Arc. Tecton 25(5), 13 pp

Dhuime B, Bosch D, Bodinier JL, Garrido CJ, Bruguier O, Hussain SS, Dawood H (2007) Multistage evolution of the Jijal ultramafic complex (Kohistan, N Pakistan): implications for building the roots of island arcs. Earth Planet Sci Lett 261:179–200. doi:10.1016/j.epsl.2007.06.026

Dhuime B, Bosch D, Garrido CJ, Bodinier JL, Bruguier O, Hussain SS, Dawood H (2009) Geochemical architecture of the lower- to middle-crustal section of a paleo-island arc (Kohistan Complex, Jijal-Kamila area, northern Pakistan): implications for the evolution of an oceanic subduction zone. J Petrol 50:531–569. doi:10.1093/petrology/egp010

Ebblin C, Marussi A, Poretti G, Rahim SM, Richards P (1983) Gravity measurement in the Karakorum. Boll Geof Teor Appl 25:303–316

Engl HW, Hanke M, Neubauer A (1996) Regularization of inverse problems. Kluwer, Dordrecht, The Netherlands

Floberghagen R, Fehringer M, Lamarre D, Muzi D, Frommknecht B, Steiger C, Piñeiro J, da Costa A (2011) Mission design, operation and exploitation of the gravity field and steady-state ocean circulation explorer mission. J Geodesy 85:749–758. doi:10.1007/s00190-011-0498-3

Forsberg R (1985) Gravity field terrain effect computation by FFT. Bull Géod 59:342–360. doi:10.1007/BF02521068

Garrido CJ, Bodinier JL, Burg JP, Zeilinger G, Hussain S, Dawood H, Chaudhry MN, Gervilla F (2006) Petrogenesis of mafic garnet

granulite an the lower crust of the kohistan Paloe-arc Complex (Northern Pakistan): implications for intra-crustal differentiation of island arcs and generation of continental crust. J Petrol 47:1873–1914. doi:10.1093/petrology/egl030

Garrido CJ, Bodinier JL, Dhuime B, Bosch D, Chanefo I, Bruguier O, Hussain SS, Dawood H, Burg JP (2007) Origin of the island arc Moho transition zone via melt-rock reaction and its implications for intracrustal differentiation of island arcs: evidence from the Jijal complex (Kohistan complex, northern Pakistan). Geology 35:683–686. doi:10.1130/G23675A.1

Hanke M (1995) Conjugate gradient type methods for ill posed problems. Longman Scientific & Technical, Harlow. Pitman research notes in mathematics series

Jagoutz O, Schmidt MW (2012) The formation and bulk composition of modern juvenile continental crust: the Kohistan arc. Chem Geol 298–299:79–96. doi:10.1016/j.chemgeo.2011.10.022

Jagoutz O, Müntener O, Burg JP, Ulmer P, Jagoutz E (2006) Lower continental crust formation through focused flow in km-scale melt conduits: the zoned ultramafic bodies of the Chilas Complex in the Kohistan Island arc (NW Pakistan). Earth Planet Sci Lett 242(3–4):320–342

Jagoutz O, Müntener O, Ulmer P, Pettke T, Burg JP, Dawood H, Hussain S (2007) Petrology and mineral chemistry of lower crustal intrusions: the Chilas Complex, Kohistan (NW Pakistan). J Petrol 48(10):1895–1953. doi:10.1093/petrology/egm044

Jagoutz O, Burg JP, Hussain SS, Dawood H, Pettke T, Iizuka T, Maruyama S (2009) Construction of the granitoid crust of an island arc part I: geochronological and geochemical constraints from the plutonic Kohistan (NW Pakistan). Contrib Minaralog Petrol 158:739–755. doi:10.1007/s00410-009-0408-3

Jagoutz O, Müntener O, Schmidt MW, Burg JP (2011) The roles of flux- and decompression melting and their respective fractionation lines for continental crust formation: evidence from the Kohistan arc. Earth Planet Sci Lett 303:25–36. doi:10.1016/j.epsl.2010.12.017

Jin SG, Zhu W (2003) Active motion of tectonic blocks in Eastern Asia: evidence from GPS measurements. Acta Geol Sin 77:59–63. doi:10.1111/j.1755-6724.2003.tb00110.x

Jin SG, Park P, Zhu W (2007) Micro-plate tectonics and kinematics in Northeast Asia inferred from a dense set of GPS observations. Earth Planet Sci Lett 257(3–4):486–496. doi:10.1016/j.epsl.2007.03.011

Khan SD, Walker DJ, Hall SA, Burke KC, Sham MT, Stockli L (2009) Did the Kohistan-Ladakh island arc collide first with India? Bulletin of the Geological Society of America 121:366–384

Kügler P, Sincich E (2009) Logarithmic convergence rates for the identification of a nonlinear Robin coefficient. J Math Anal Appl 359:451–463. doi:10.1016/j.jmaa.2009.06.004

Mahéo G, Bertrand H, Guillot S, Villa IM, Keller F, Capiez P (2004) The South Ladakh ophiolites (NW Himalaya, India): an intra-oceanic tholeiitic arc origin with implication for the closure of the Neo-Tethys. Chem Geol 203:273–303. doi:10.1016/j.chemgeo.2003.10.007

Miller DJ, Christensen NI (1994) Seismic signature and geochemistry of an island arc: a multidisciplinary study of the Kohistan accreted terrane, northern Pakistan. J Geophys Res 99:11623–11642

Nagy D, Papp G, Benedek J (2000) The gravitational potential and its derivatives for the prisms. J Geodesy 74:552–560. doi:10.1007/s001900000116

Pail R, Bruinsma S, Migliaccio F, Förste C, Goiginger H, Schuh WD, Höck E, Reguzzoni M, Brockmann JM, Abrikosov O, Veicherts M, Fecher T, Mayrhofer R, Krasbutter I, Sansó F, Tscherning CC (2011) First GOCE gravity models derived by three different approaches. J Geodesy 85(11):819–843. doi:10.1007/s00190-011-0467-x

Parker RL (1972) The rapid calculation of potential anomalies. Geophys J Roy Astron Soc 31:447–455

Petterson MG (2010) A review of the geology and tectonics of the Kohistan island arc, north Pakistan. In: Kusky T et al (eds) The evolving continents. Special publication of the Geol Soc London 338:287–327. doi:10.1144/SP338.14

Petterson MG, Windley BF (1985) Rb-Sr dating of the Kohistan arc-batholith in the trans-Himalaya of north Pakistan, and tectonics implications. Earth Planet Sci Lett 74:45–57

Rolland Y, Picard C, Pecher A, Lapierre H, Bosch D, Keller F (2002) The cretaceous Ladakh arc of NW Himalaya – slab melting and melt – mantle interaction during fast northward drift of Indian Plate. Chem Geol 182:139–178. doi:10.1016/S0009-2541(01)00286-8

Rummel R, Yi W, Stummer C (2011) GOCE gravitational gradiometry. J Geodesy 85:777–790. doi:10.1007/s00190-011-0500-0

Shin Y, Xu H, Braitenberg C, Fang J, Wang Y (2007) Moho undulation beneath Tibet from GRACE-integrated gravity data. Geophys J Int 170(3):971–985. doi:10.1111/j.1365-246X.2007.03457.x

Steffen R, Steffen H, Jentzsch G (2011) A three-dimensional Moho depth model for the Tien Shan from EGM2008 gravity data. Tectonics 30, TC5091. doi:10.1029/2011TC002886

Watts AB (2001) Isostasy and flexure of the lithosphere. Cambridge University Press, Cambridge. ISBN 9780521006002

A Grip on Geological Units with GOCE

Carla Braitenberg

Abstract

The scope of this work is to show the observations of satellite GOCE in mapping geological units in a key area for mineral exploration, which is also a key location for understanding the formation of the America and Africa continents from the former western Gondwana. The observations of the satellite GOCE have allowed to achieve a qualitative leap ahead in today's global gravity. The new global field has an improved resolution of 80 km with precision of 5 mGal; this resolution is sufficient to study crustal thickness variations and the upper crustal structure. Geological macrostructures generating density variations are mapped for the first time by a global satellite derived field in continental areas, which opens a new series of applications in geophysical exploration. The study area is located in and around the Congo craton, which is a part of Africa poorly covered in ground gravity surveys, so that GOCE data are essential there. The GOCE gravity field is reduced by the effect of topography, of the isostatic crustal thickness and by sediments, obtaining the field representative of the geologic lineaments. The foldbelts surrounding the Congo craton are identified well through the field, generating signals near to 50 mGal. Compared to the existing geologic map, along the Kibalien belt, a narrow belt with increased density is distinguished, about 125 km wide, and 800 km long, that must be representative of a major compressive or magmatic geologic event that generated these rocks. The distinction of separate geologic units characterized by density variation is useful for identifying the areas where focused future geophysical and geologic mapping will be effective in the exploration of new mineral resources.

Keywords

GOCE • Congo craton • Gravity • Mineral exploration • New frontiers

1 Introduction

Density is an important parameter that allows to classify rock types, due to the characteristic densities in the transition from unconsolidated sediments, compact sedimentary rocks, volcanic, metamorphic and mantle rocks (e.g. Brocher 2005). Investigations using remote sensing with multispectral images are useful only for exposed rocks, and are less efficient in identifying different rock types in areas with thick vegetation, limiting applicability for terrestrial investigations as in the sub-Saharian range (e.g. van der Meer et al. 2012). For the first time with satellite GOCE (Floberghagen et al. 2011), resolution and precision have crossed the line that divided deep Earth investigations from the studies with direct impact in exploration of natural resources. The boost in resolution and precision of the gravity field was obtained with the space-borne observation of the full gradient tensor at low satellite height (250 km) (Rummel et al. 2011). After downward continuation of the observations to ground level

C. Braitenberg (✉)
Dipartimento di Matematica e Geoscienze, Universita' di Trieste, Via Weiss 1, 34100 Trieste, Italy
e-mail: berg@units.it

U. Marti (ed.), *Gravity, Geoid and Height Systems*, International Association of Geodesy Symposia 141,
DOI 10.1007/978-3-319-10837-7_39,

the precision at 80 km wavelength is comparable to that of an aero gravimetric campaign (measurements accuracy near to 4 mGal), with the great bonus of having a global access to the observations (Braitenberg et al. 2010). In fact the gravity anomaly error up to degrees 180, 200, and 250 derived from the cumulative error curves of the third generation GOCE only model TIM (Pail et al. 2011) spherical harmonic expansion is 0.8 mGal, 1.5 mGal and 5.1 mGal respectively (Bomfim et al. 2013). This does not imply that the aerogravimetric campaign cannot have greater spatial resolution, but it shows that at the long-wavelength end of the aero-gravimetric measurements the two observations are of similar precision. The precision of the GOCE observation is best represented in the degree-error curve of the spherical harmonic expansion, which we can translate into the resolution of the crustal body to be studied. Assuming that overlying density heterogeneities have been correctly reduced, and assuming that the density contrast at Moho level were known exactly, the Moho and basement theoretically can be recovered at a level of 0.1 km uncertainty, sufficient to successfully map the depth variations (Braitenberg et al. 2010; Reguzzoni and Sampietro 2012). These uncertainties consider only the error on the gravity data, and are valid under the assumption that the density contrasts at the boundary are known, and that the overlying density inhomogeneities have been stripped off the observations correctly prior inversion. For the Tibetan plateau and Himalayan range the GOCE data proved useful for defining the Moho seamlessly from the lowlands of India, through the Himalayas to the Tarim basin (Sampietro et al. 2014). New findings from GOCE data are most likely to occur where the GOCE gravity field improvement is the greatest, particularly over parts of Asia, Africa, South America and Antarctica (Hirt et al. 2011, 2012; Braitenberg et al. 2011a), as has been shown in detail for the Andes (Alvarez et al. 2012). In Europe the improvements are most likely to be restricted to high mountains (like Alps) and across the coastal areas, where the transition from terrestrial measurements to satellite altimetric observations occurs. The precision of the altimetric gravity data decreases towards the coast, approximately starting from a distance of 25 km from the coast, due to the footprint of the altimetric signal and due to the dynamic topography of ocean currents in shallow waters (Hwang et al. 2002).

Here an area is considered where terrestrial observations are scarce due to difficult terrain, making the new GOCE-derived field the best gravity-field today available. This area is located in and around the Congo craton, and straddles different countries as Cameroon, Central African Republic, South Sudan, Uganda, Tanzania, Democratic Republic of Congo, Republic of Congo, Gabon and Equatorial Guinea. The area is of general interest, being in a key position of the continent Gondwana, from which the South American and African continents were formed (De Wit et al. 2008a). The Congo craton is an old crustal nucleus with a deep lithospheric root, which constitutes an indeformable unit, against which the surrounding crustal units are deformed (e.g. Begg et al. 2009). We use the GOCE satellite to deliver some new data that help to unscramble these deformations, which cover 2 Ga years of Earth history, and have produced important mineral deposits as gold, platinum and iron. We demonstrate that the Bouguer field derived from the GOCE observations perfectly correlate to known geologic units. We then demonstrate that the GOCE observations differentiate the geologic structures, identifying the margins of the high density units formed by metamorphic addensations of rocks. The results have direct applicability in mineral exploration and show that the GOCE observations constitute an innovative tool for mineral exploration in remote areas.

2 The Area of Study and the GOCE Gravity Observations

2.1 The Geologic Macro-units and Expected Density Variations

North Central Africa (Fig. 1) has greatly benefited from the GOCE observations (see difference map between GOCE and EGM2008 (Pavlis et al. 2012) in Braitenberg et al. 2011b) and is geologically extremely important, due to great oil deposits onshore (Chad, Congo basins) and offshore (Niger delta, Congo craton oceanic margin), due to the high volcanic risk (Cameroon Volcanic Line) and due to its key position in understanding the evolution of West-Gondwana and the opening of the Atlantic (De Wit et al. 2008b). The map in Fig. 2 shows the main geologic units according to CGMW/UNESCO (1990), to which we refer for the detailed color coding of the units; as in Fig. 1 we have added country borders; the colored lines mark the outlines of selected geologic units that due to their rock constitution are generally expected to be accompanied by density variations and that we shall analyze in terms of the gravity field. The exact nomenclature of the numbered units according to the geologic map or according to Kadima et al. (2011) is given in Table 1. In general terms, the younger sediment units have lower density, the palaeozoic sediments have average density, as they have been mostly compacted, and therefore have a density that corresponds to the density of the rock grains, due to expected low porosity. Metamorphic units and magmatic units containing basalts have increased density, and granites have average density.

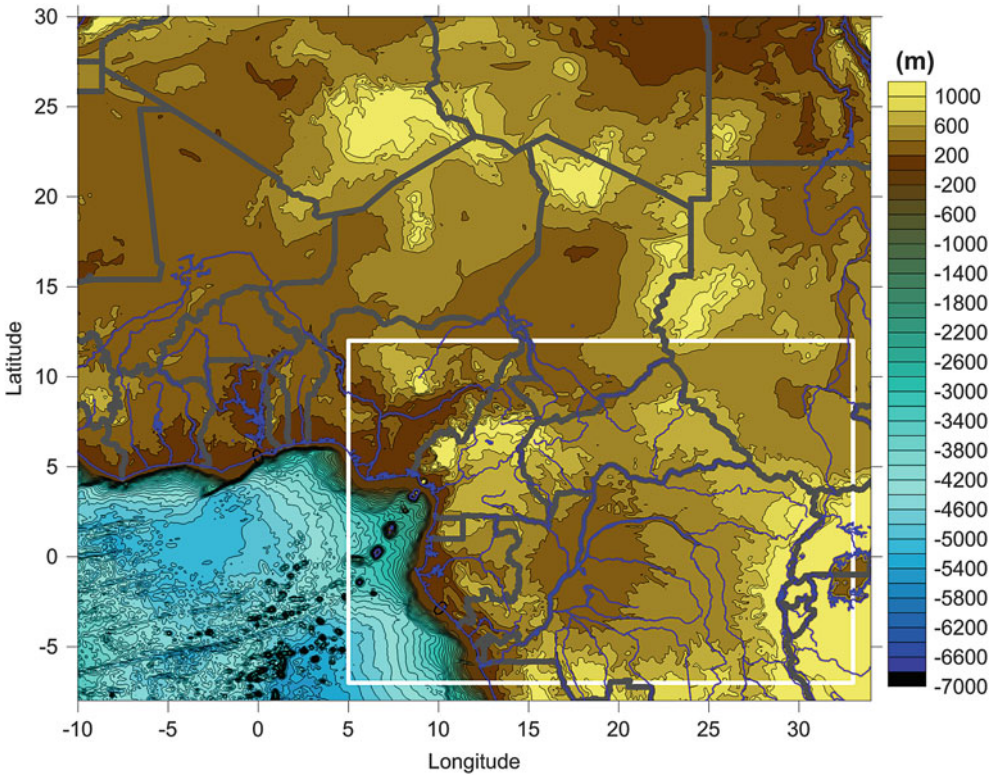

Fig. 1 Topography of Central North Africa. The *white square* shows the detailed study area centered on the Congo basin

2.2 The Reductions of the GOCE Gravity Field

We calculate the GOCE gravity values at 4,000 m height according to the Gravity Global model of Pail et al. (2011). The data are available through ESA (http://www.esa.int) and at the International Centre for Global Earth Models (ICGEM, http://icgem.gfz-potsdam.de/ICGEM/). We used the file go_cons_gcf_2_tim_r3.gfc and calculated the gravity anomaly with a grid spacing of 0.2° using the software of the EGM2008 synthesis and setting the parameter "isw" = 01, corresponding to "spherically approximated gravity anomaly". The choice of 4,000 m was taken in order to be above topography and be able to make the topographic reduction with the data points above the topographic masses. All reductions were made considering this 4,000 m height. As mentioned above, the formal error at the full resolution of the GOCE spherical harmonic expansion (N = 250) is estimated to be globally 5.1 mGal (Bomfim et al. 2013). The GOCE derived gravity field presents an improvement with respect to existing gravity data, as has been shown in studies aimed at the evaluation of the GOCE field (Hirt et al. 2011). We correct the observations for the effect of topography with standard Bouguer reduction density (2,670 kg/m^3 over land, 1,630 kg/m^3 over water) in spherical approximation. The digital terrain model refers to the ETOPO1 (Amante and Eakins 2009). It is further necessary to reduce the observations for the effect of crustal thickness variations in order to enhance the signal that is generated by the density variations that accompany the different geologic macro-units and are expected to be at upper crustal levels. A crustal thickness model from seismology is unavailable for the entire area, so we estimate the gravity effect of a flexural isostatic model by calculating the flexural isostatic thickening and a standard density contrast at the base of the crust. Different couples of effective elastic thickness and density contrast for the forward calculation of the gravity field are considered. In Table 2 the extreme values, the root mean square and the average values for the reduced fields are shown. The extreme values and root mean square values are greatly reduced after applying the isostatic reduction. It is seen that the reduction with a density of 500 kg/m^3 is more effective than the one with 300 kg/m^3, and that the reduction does not greatly depend on the choice of the effective elastic thickness. As expected the isostatic correction reduces the Bouguer variations, e.g. the greatest amplitudes due to topographic relief as continent-ocean transition and high elevation (Cameroon Volcanic Line, unit 12). The effect of sediments in the basins is another obvious negative gravity signal, due to the negative density contrast of sediments with respect to a reference standard crustal column. We reduce this contribution with the most up to date sediment thickness model having been

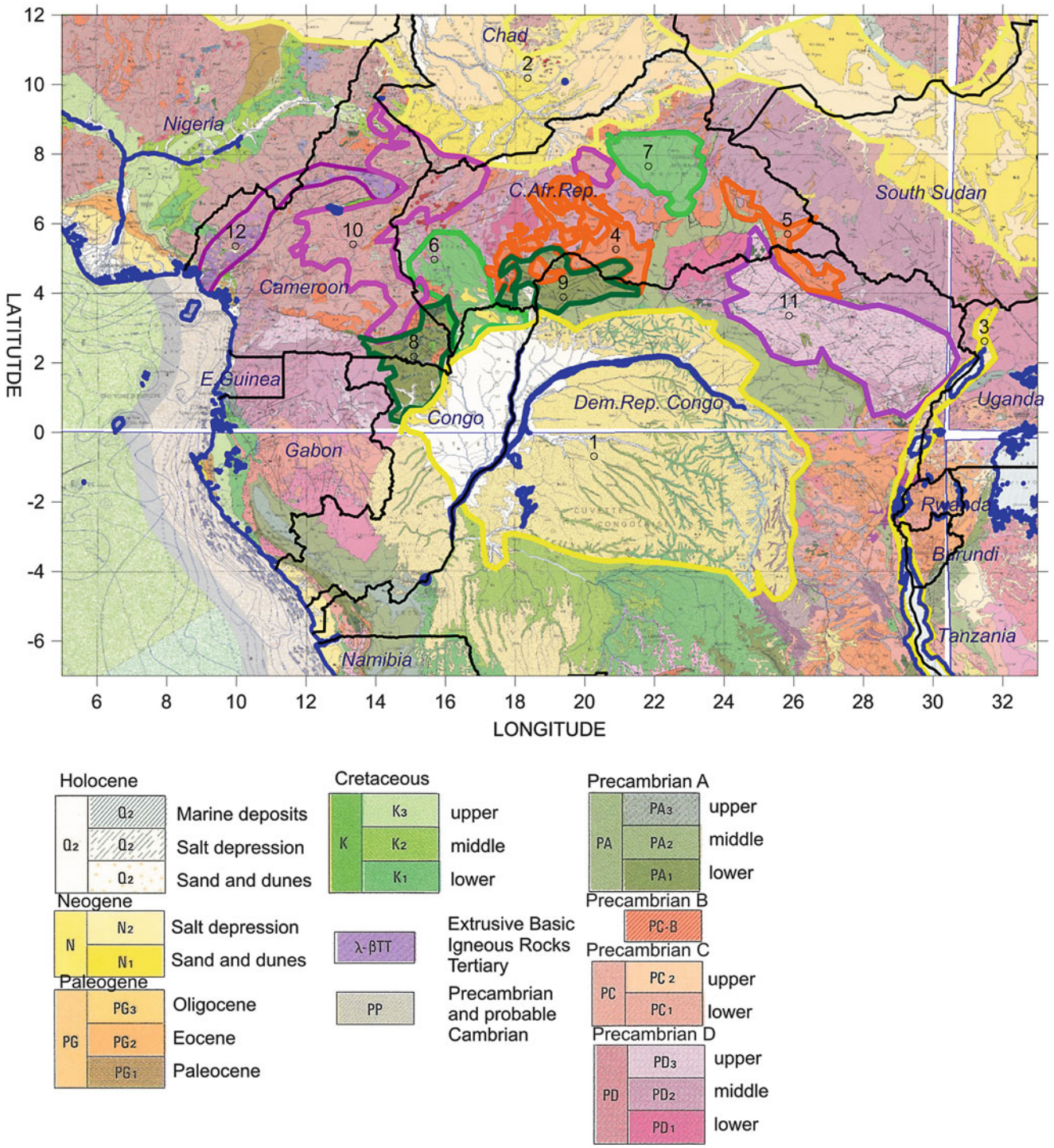

Fig. 2 Geologic map for the area centered on the Congo basin (CGMW/UNESCO 1990). The numbers refer to geologic units defined in Table 1. *Yellow lines* mark Tertiary sediments, *orange* mark Palaeozoic sediments, *green* mark Cretaceous rocks, *pink* to *purple* Precambrian units affected by metamorphism and magmatism, *dark violet* mark the Cameroon line, with Extrusive Tertiary Igneous rocks

compiled by TOTAL for the Commission for the Geologic Map of the World (Frizon de Lamotte and Raulin 2010), from which sediments are available in terms of sediment thickness isopachs. We adopt a linear first order variation of density with depth characterized by top density 2,250 kg/m^3 and bottom density 2,670 kg/m^3 at 8,000 km depth (e.g. Allen and Allen 2005). The top density corresponds to sand, the bottom density to granite, and the bottom depth is found to be a limit at which generally sediments are compacted so as to have closed liquid-filled pores and have acquired the grain density.

Table 1 Selected geological units expected to generate variations in the bulk density

Number of unit	Selected unit on geologic map in Fig. 2. Units and ages refer to UNESCO geologic map (CGMW/UNESCO 1990)
1	Congo basin sediments. Pliocene-Pleistocene coverage of sands and dunes
2	Chad sediments. Pleistocene coverage of sands and dunes
3	Sediments of east African rift
4	Oubangui-Bambari—Precambrian-B (1,300–1,600 Ma) alternates
5	Haut Mbomou—Precambrian-B (1,300–1,600 Ma)
6	Lower Cretaceous sediments Muabere'
7	Lower Cretaceous sediments Formation Moukka Ouadda
8	Sembe–Ouasso basin, West Precambrian A
9	Liki-Bembe basin, Bangui, Precambrian A
10	Ouham Pende Metamorphic rocks of undetermined age, syntectonic granites, Precambrian or Palaeozoic
11	Kibalian basement comprising greenstone belt, with Syntectonic granites, some amphibolite outcrops. North East Congo block. Upper Precambrian
12	Cameroon volcanic line, Tertiary extrusive igneous rocks

The numbers refer to Fig. 2

Table 2 Statistical parameters of the gravity anomaly, Bouguer values, gravity effect of sediments, and residual Bouguer after reduction for sediments and crustal thickness

	Min (mGal)	Max (mGal)	Mean (mGal)	Root mean square (mGal)
GOCE gravity anomaly	−62.3	89.2	−0.4	18.14
GOCE Bouguer anomaly (BG)	−179.6	320.3	−5.9	105.8
BG corrected isostasy; Te = 05 km, rho = 500 kg/m^3	−120.9	61.0	−26.2	25.0
BG corrected isostasy; Te = 15 km, rho = 500 kg/m^3	−137.5	59.8	−26.2	24.7
BG corrected isostasy; Te = 20 km, rho = 500 kg/m^3	−143.5	59.0	−26.2	24.6
BG corrected isostasy; Te = 05 km, rho = 300 kg/m^3	−111.4	128.3	−18.1	44.0
BG corrected isostasy; Te = 15 km, rho = 300 kg/m^3	−111.5	129.0	−18.1	44.1
BG corrected isostasy; Te = 20 km, rho = 300 kg/m^3	−111.3	128.6	−18.1	44.2
BG corrected sediments only	−145.4	348.8	20.7	105.1
BG corrected isostasy and sediments; Te = 05 km, rho = 500 kg/m^3	−67.3	82.1	0.33	16.1
BG corrected isostasy and sediments; Te = 15 km, rho = 500 kg/m^3	−88.1	79.1	0.33	16.3
BG corrected isostasy and sediments; Te = 20 km, rho = 500 kg/m^3	−94.0	76.9	0.34	16.5
BG corrected isostasy and sediments; Te = 05 km, rho = 300 kg/m^3	−78.3	140.6	8.5	40.8
BG corrected isostasy and sediments; Te = 15 km, rho = 300 kg/m^3	−82.3	143.3	8.5	41.0
BG corrected isostasy and sediments; Te = 20 km, rho = 300 kg/m^3	−83.0	146.1	8.5	41.2

Geographical window Longitude (−10°,32°), Latitude (−6°,30°). BG = Bouguer anomaly, Te = elastic thickness of the flexure model, rho = density contrast at isostatic Moho

The adequateness of this reduction is again evident when we consider the amplitude variation and the root mean square of the Bouguer values (Table 2). Here it is seen how the starting amplitude of the Bouguer values is reduced successfully after correcting for isostatic crustal thickness and then for sediments. The gravity anomaly, Bouguer field, the Bouguer field reduced for the gravity effect of the isostatic Moho (Te = 15 km and density contrast rho = 500 kg/m^3), and the final Bouguer residual reduced for the isostatic Moho and the sediments are mapped in Fig. 3a–d. We cannot exclude in principle that the residual Bouguer field is still affected by gravity signals generated at Moho level, but we find that the isostatic Moho is effective in reducing the long-wavelength and high-amplitude part of the Bouguer field, allowing the smaller scale features to be visible. The residual field may still contain some gravity from the Moho, but nonetheless the scope of enhancing the signal generated at shallower crustal levels is successfully accomplished.

2.3 Analysis of the Residual GOCE Gravity Field

The Bouguer gravity residual (Fig. 3d) represents the signal produced by the crustal density inhomogeneities of the basement underlying the sediments. The basement has undergone

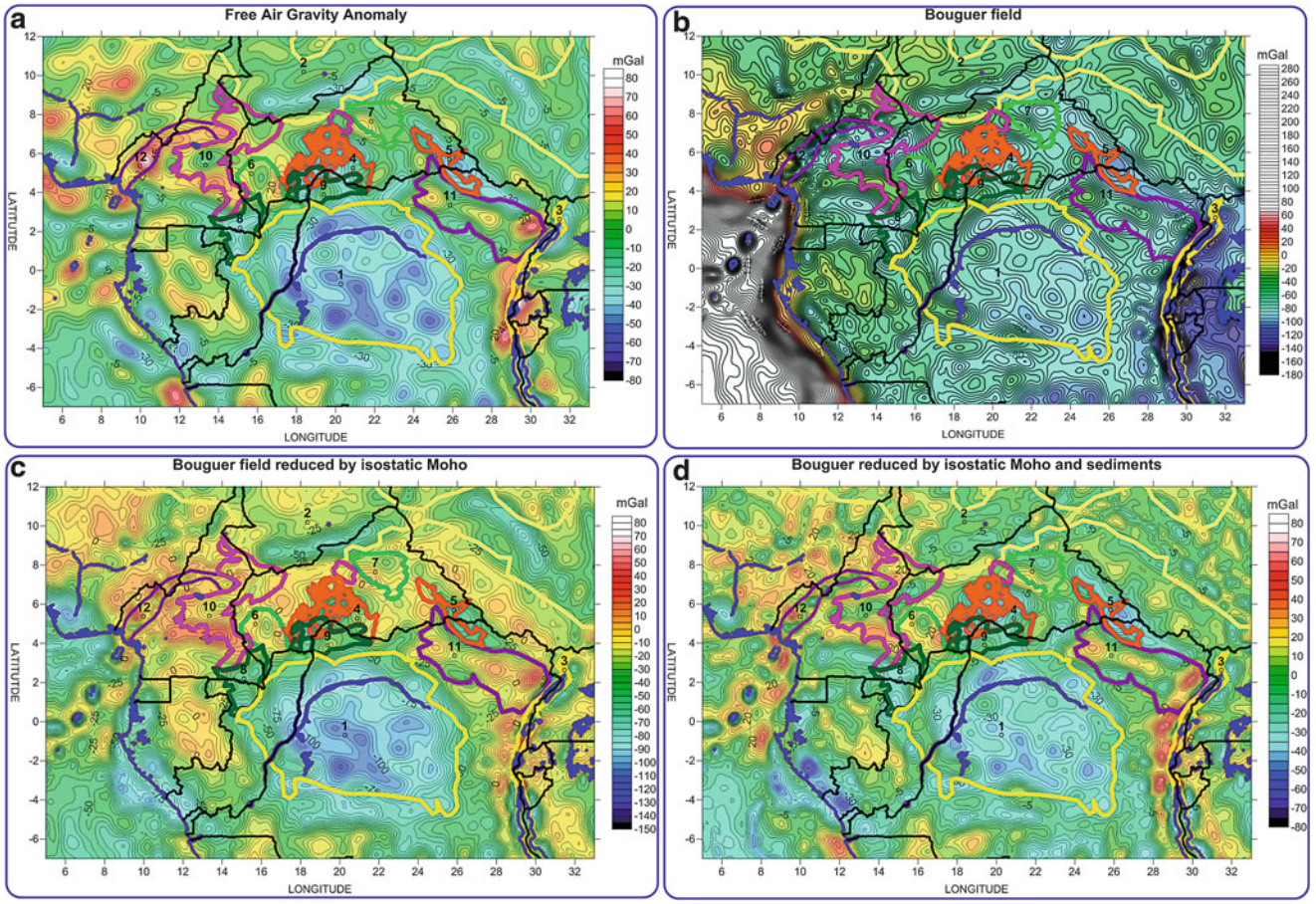

Fig. 3 The GOCE gravity fields: (**a**) gravity anomaly; (**b**) Bouguer field; (**c**) Bouguer field reduced for the gravity effect of the isostatic Moho (Te = 15 km and density contrast rho = 500 kg/m^3); (**d**) final Bouguer residual reduced for the isostatic Moho and the sediments

volcanic activity, orogenetic formations, and metamorphism, documenting events that presumably have affected also the crust, not only geologic units (for a general overview De Wit et al. 2008b). Exposed volcanic activity is the product of magmatic processes that reached the surface, but which are always accompanied by intrusions and underplating, increasing the density of the lower crust, and implying a thin lithosphere in order to allow the melting process to be initiated.

The residual GOCE values can be matched to several of the geologic units we marked in Fig. 2. We quantify this relation by calculating histograms of the gravity values pertaining to an identified geologic unit. The reduction of the Bouguer values for sediments and isostatic crustal thickness is well illustrated in the histograms over the Chad basin before reduction and after the first and second reduction stage (Fig. 4a). The Bouguer values are strongly negative, are a bit reduced by correction for the crustal thickness variations, and are scattered around zero after correcting for the sedimentary cover. This shows that the underlying basement has local anomalies, with varying positive and negative density contrast, the long range systematic signal having been reduced. The histogram for the free air gravity anomaly is also shown for comparison, and is slightly more negative than the Bouguer values reduced for crustal thickness and sediments effect. The histograms of the Bouguer residuals for the other selected geologic domains are shown in Fig. 4b. The negative values are found for the Pleistocene dunes and sediments that cover the Congo basin (unit 1), the nappes of the Oubanguides fold belt in the northern margin of the Congo craton (unit 4), and the Precambrian units Haut Mbomou of Precambrian age, presumably also nappes of a fold belt. Positive values are found for the 2.5 Ga metamorphic range bordering the craton, as the Kibalian range (11) and the Ouham Pende (10) domains, where the geologic map documents presence of dense rocks as amphibolites and magmatic products. The most positive residual values are found in the Kibalian range (11), along a lineament which does not have a counterpart on the geologic map, and therefore is of great interest. It is a major discontinuity that is missing on the geologic map and surely marks an important geologic metamorphic or magmatic event that produced increased rock density, generally related to a collisional boundary.

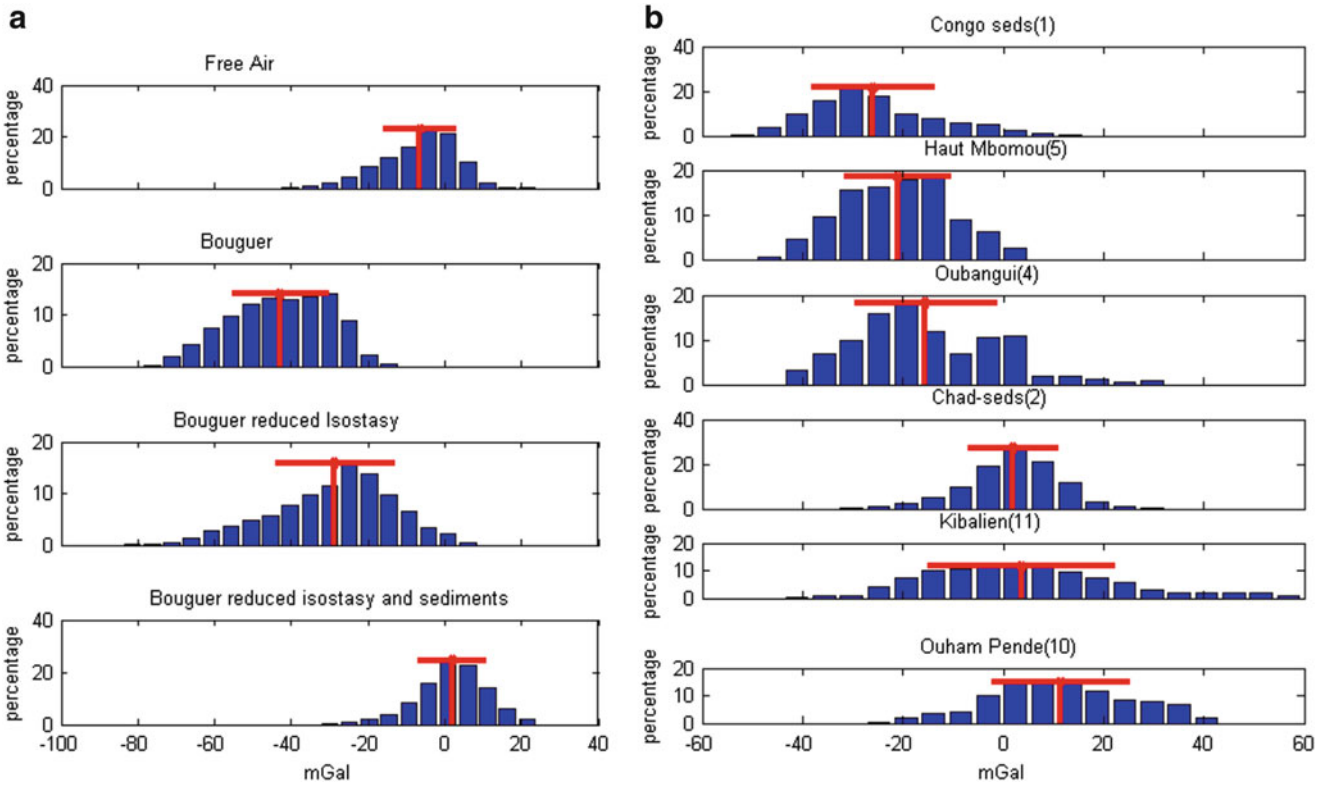

Fig. 4 The histogram of the observed and residual gravity values for a certain geologic domain. (**a**) Geological domain is the Chad basin. The histograms refer to the GOCE free air values, the GOCE Bouguer values, the GOCE Bouguer values reduced for crustal thickness variations, and then reduced also for sediments. (**b**) Histograms of the GOCE isostatic-sediment reduced Bouguer residuals for increasingly dense geologic domains. The numbers refer to the numbered domains of Fig. 2. *Red horizontal line*: average value of anomaly. *Vertical red line*: standard deviation of the values

Discussion and Conclusions

The Oubanguides and Kibalian units must be several km thick, considering that the anomalies reach up to 50 mGal. A rough estimate assuming the effects of an infinite plate layer of finite thickness, analogous to the Bouguer plate, gives us 3 mGal for a 1 km thick unit with 100 kg/m^3 density contrast. Referred to a standard upper crust of 2,670 kg/m^3, a basalt, gabbro, amphibolite reaches 200–300 kg/m^3 density contrast, a sediment nappe a negative density contrast of 170 kg/m^3. This translates to 9 km thick metamorphic unit of Kibalian and 5 km of nappes in the Oubanguides fold belt, demonstrating that the density inhomogeneities of the crust are severely affected by the geologic units reaching the surface. The lateral extent and considerable thickness implies these units to be representative of major geologic unit which must be considered when the evolution and accretion of the Congo craton is studied (e.g. Toteu et al. 2004). After having ascertained that the precision of the GOCE observations is enough to discriminate geologic units, we use the anomalies to follow the units where they are absent (or interpolated) on the geological map, either because they are covered by other units or because of lack of direct observations. The extent of the anomaly is a means to optimize the planning of integrative terrestrial geologic cartography. The linear positive anomaly in the Kibalian belt or North East Congo block (11) is much narrower than the geologic unit marked as uniform in the geologic map. This demonstrates that there is considerable difference in the rocks of this unit, with a marked narrow belt of rocks with increased density that must be due to a major geologic event that produced this increase in density. This belt could be of interest in the research of natural resources, as it merges at its southern extreme with the Kilo-Moto greenstone belt, where a large gold-deposit is productive, the Kilo-Moto gold mine (Agayo 1982).

The results show that for the first time a geodetic gravity satellite has the required precision and resolution to distinguish geologic units of different age and rock type. The data are available globally, so the procedure illustrated here has a direct applicability in other areas of Africa and east Asia, providing a remote geophysical tool for geologic mapping. The results for North Central Africa show that tectonic events since 2.5 Ga have left

an imprint on the densities of the crust, even greater than the more recent Central African Rift or Shear zone which has been thought to have an impact also at deeper levels (Ebinger and Sleep 1998). The Central Africa Rift (or Shear zone) develops in NE_SW orientation starting from the Cameroon Volcanic line and suddenly bends clockwise by about 90° to a NW-SE orientation. This rift takes up the direction of a succession of geologic elements all bearing the same orientation, and having an alternation of high and low densities, as evidenced by the GOCE data, that show aligned alternating gravity lineaments parallel to the eastern segment of the CAR rift and leading to the Eastern margin of the Congo craton, and being near to parallel to the main arm of the east African rift. Towards the western side of the Congo craton a similar alignment of gravity highs and lows is found, the most western one following the basins of the western African coastline. The rifting of America and Africa then was superimposed on this package of geologic subunits. It demonstrates a long lasting orientation of macro-tectonic forces that could be a further evidence to the longlasting mantle cell proposed by Collins et al. (2011) for the Phanerozoic orogenic systems dating back to 550 Ma. In the classification of Collins the sequence east of the Congo craton would be an internal orogenic system, extending the sequence to 2.5 Ga, and showing that the megacell not only leads to a sequence of orogens but involves backward rifting, in case the plate does not follow the movement of the cell as compact unit, but tears at a point of weakness, leading to rifting.

Acknowledgements The Italian Space Agency (ASI) is thanked for supporting the GOCE-Italy project. Partially the work was supported by PRIN contract 2008CR4455_003. I acknowledge the use of the EGM2008 gravity model software of Pavlis et al. (2012). I thank Lew Ashwal and Sharad Master, both Professors at School of Geosciences, University of the Witwatersrand, South Africa for inspiring discussions. I also wish to thank the Editor Pascal Willis and three anonymous reviewers of the manuscript for thoughtful comments and suggestions.

References

Agayo B (1982) The gold mines of Kilo-Moto in northeastern Zaire: 1905–1960, vol 4. PhD Thesis, University of Wisconsin, Madison, 943 pp

Allen PA, Allen JR (2005) Basin analysis, principles and applications, 2nd edn. Blackwell, Oxford. ISBN 0-632-05207-4

Alvarez O, Gimenez M, Braitenberg C, Folguera A (2012) GOCE Satellite derived Gravity and Gravity gradient corrected for topographic effect in the South Central Andes Region. Geophys J Int 190:941–959. doi:10.1111/j.1365-246X.2012.05556.x

Amante C, Eakins BW (2009) ETOPO1 1 arc-minute global relief model: procedures, data sources and analysis. NOAA Technical Memorandum NESDIS NGDC-24, March 2009, 19 pp

Begg GC, Griffin WL, Natapov LM, O'Reilly SY, Grand SP, O'Neill CJ, Hronsky JMA, Poudjom Djomani Y, Swain CJ, Deen T, Bowden P (2009) The lithospheric architecture of Africa: seismic tomography, mantle petrology, and tectonic evolution. Geosphere 5:23–50. doi:10.1130/GES00179.1

Bomfim E, Braitenberg C, Molina EC (2013) Mutual evaluation of global gravity models (EGM2008 and GOCE) and terrestrial data in Amazon Basin, Brazil. Geophys J Int 195(2):870–882. doi:10.1093/gji/ggt283

Braitenberg C, Mariani P, Reguzzoni M, Ussami N (2010) GOCE observationsfor detecting unknown tectonic features. In: Proceedings of the 'ESA Living Planet Symposium', Bergen, Norway, 28 June–2 July 2010 (ESA SP-686, December 2010), pp 1–6

Braitenberg C, Mariani P, Pivetta T (2011a) GOCE observations in exploration geophysics. In: Proceedings of the 4th international GOCE user workshop. Technische Universität München (TUM), Munich, Germany, 31 Mar–1 Apr 2011, pp 1–6. https://earth.esa.int/documents/10174/14195/GOCE_Observations_Exploration_Geophysics_C.Braitenberg.pdf/dedc92c7-cd3c-4076-9c15-f528bd25aef1?version=1.0

Braitenberg C, Mariani P, Ebbing J, Sprlak M (2011b) The enigmatic Chad lineament revisited with global gravity and gravity gradient fields. In: Van Hinsbergen DJJ, Buiter SJH, Torsvik TH, Gaina C, Webb S (eds) The formation and evolution of Africa: a synopsis of 3.8 Ga of Earth History. Geological Society, London, Special Publications, 357:329–341. doi:10.1144/SP357.18

Brocher TM (2005) Empirical relations between elastic wavespeeds and density in the earth's crust. Bull Seism Soc Am 95:2081–2092. doi:10.1785/0120050077

CGMW/UNESCO (1990) International geological map of Africa at 1:5000000. Third Edition 1985-1990, CGMW/UNESCO, Paris

Collins WJ, Belousova EA, Kemp AIS, Murphy JB (2011) Two contrasting Phanerozoic orogenic systems revealed by hafnium isotope data. Nat Geosci 4:333–337. doi:10.1038/NGEO1127

De Wit MJ, Brito Neves BB, Trouw RAJ, Pankhurst RJ (2008a) Pre-Cenozoic correlations across the South Atlantic region: 'the ties that bind'. In: Pankhurst RJ, Trouw RAJ, Brito Neves BB, De Wit MJ (eds) West Gondwana: Pre-Cenozoic correlations across the South Atlantic region. Geological Society, London, Special Publications, 294:1–8. doi:10.1144/SP294.1

De Wit MJ, Stankiewcz J, Reeves C (2008b) Restoring Pan-African–Brasiliano connections: more Gondwana control, less Trans-Atlantic corruption. In: Pankhurst RJ, Trouw RAJ, Brito Neves BB, De Wit MJ (eds) West Gondwana: Pre-Cenozoic correlations across the South Atlantic region. Geological Society, London, Special Publications, 294:399–412. doi:10.1144/SP294.20

Ebinger CJ, Sleep NH (1998) Cenozoic magmatism throughout east Africa resulting from impact of a single plume. Nature 395:788–791. doi:10.1038/27417

Floberghagen R, Fehringer M, Lamarre D, Muzi D, Frommknecht B, Steiger C, Piñeiro J, da Costa A (2011) Mission design, operation and exploitation of the gravity field and steady-state ocean circulation explorer (GOCE) mission. J Geod 85:749–758. doi:10.1007/s00190-011-0498-3

Frizon de Lamotte D, Raulin C (2010) Sediment isopachs of Africa. In: Milesi JP, Frizon de Lamotte D, de Kock G, Toteu F (eds) Tectonic map of Africa at 1:10,000,000 scale. CCGM/CGMW, Paris. ISBN 978-2-917310-06-9

Hirt C, Gruber T, Featherstone WE (2011) Evaluation of the first GOCE static gravity field models using terrestrial gravity, vertical deflections and EGM2008 quasigeoid heights. J Geod 85:723–740. doi:10.1007/s00190-011-0482-y

Hirt C, Kuhn M, Featherstone WE, Göttl F (2012) Topographic/isostatic evaluation of new-generation GOCE gravity field models. J Geophys Res 117, art. B05407. doi:10.1029/2011JB008878

Hwang C, Hsu HY, Jang RJ (2002) Global mean sea surface and marine gravity anomaly from multi-satellite altimetry: applications of deflection-geoid and inverse Vening Meinesz formulae. J Geod 76:407–418. doi:10.1007/s00190-002-0265-6

Kadima E, Delvaux D, Sebagenzi SN, Tackw L, Kabe SM (2011) Structure and geological history of the Congo Basin: an integrated interpretation of gravity, magnetic and reflection seismic data. Basin Res 23:499–527. doi:10.1111/j.1365-2117.2011.00500.x

Pail R, Bruinsma S, Migliaccio F, Förste C, Goiginger H, Schuh WD, Höck E, Reguzzoni M, Brockmann JM, Abrikosov O, Veicherts M, Fecher T, Mayrhofer R, Krasbutter I, Sansó F, Tscherning CC (2011) First GOCE gravity models derived by three different approaches. J Geod 85(11):819–843. doi:10.1007/s00190-011-0467-x

Pavlis NK, Holmes SA, Kenyon SC, Factor JK (2012) The development and evaluation of the Earth Gravitational Model 2008 (EGM2008). J Geophys Res 117, art. B04406. doi:10.1029/2011JB008916

Reguzzoni M, Sampietro D (2012) Moho estimation using GOCE data: a numerical simulation. In: Geodesy for Planet Earth, IAG Symposia, 136:205–214. doi:10.1007/978-3-642-20338-1_25

Rummel R, Yi W, Stummer C (2011) GOCE gravitational gradiometry. J Geod 85:777–790. doi:10.1007/s00190-011-0500-0

Sampietro D, Reguzzoni M, Braitenberg C (2014) The GOCE estimated Moho beneath the Tibetan Plateau and Himalayas. IAG Symp 139:391–397. doi:10.1007/978-3-642-37222-3__52

Toteu SF, Penaye J, Poudjom Djomani YP (2004) Geodynamic evolution of the Pan-African belt in central Africa with special reference to Cameroon. Can J Earth Sci 41:73–85. doi:10.1139/E03-079

Van der Meer FD, van der Werff HMA, van Ruitenbeek FJA, Hecker CA, Bakker WH, Noomen MF, van der Meijde M, Carranza EJM, Boudewijn de Smeth J, Woldai T (2012) Multi- and hyperspectral geologic remote sensing: a review. Int J Appl Earth Observ Geoinf 14:112–128. doi:10.1016/j.jag.2011.08.002, ISSN 0303-2434

Basement Structure of the Santos Basin from Gravity Data

Renata Constantino and Eder Cassola Molina

Abstract

The ocean basement represents the tectonic situation of a specific area and its knowledge is crucial in studies aimed at exploring the seabed. Due to the high sedimentation rate, especially in ocean basins, the topography of the basement is masked and its structures can be buried, inaccessible to direct observation. This paper aims to estimate the depth of the basement in the region of the Santos Basin in Brazil from a combined analysis of gravity data obtained from satellite altimetry and marine gravimetry, bathymetric data and sediment thickness. In the first step of the work the gravity effect of sediments in Santos Basin was calculated and the Crustal Mantle Interface (CMI) was modeled from constrained gravity inversion. Next, the reliability of the models so obtained was tested by flexural analysis. The flexural and gravity CMI proved to be in agreement. The gravity effect of the CMI and the gravity effect of the sediments were then calculated and subtracted from the original Bouguer anomaly. The residual field thus obtained, which is assumed to represent the topographical features of the basement, was inverted in the last step of the work, providing information that shows a basement with features of up to 700 m that appear to be in agreement with tectonic features previously discussed, such as the Avedis volcanic chain. The depth of the basement estimated during this study showed values ranging from 1,500 to 10,500 m, and the deepest region is consistent with the Cabo Frio Fault.

Keywords

Santos Basin basement • Gravimetry • Satellite altimetry

Abbreviation

CMI Crustal mantle interface

1 Introduction

The Santos Basin is a passive margin basin and its origin is related to the early tectonic pulses that caused the rupture of the Gondwana continent, in Neocomian, resulting in the opening of the South Atlantic Ocean and the opening of the African and American continents (Caldas and Zalán 2009). The basin is located in the southeastern region of the Brazilian continental margin (Fig. 1) spanning an area of 350,000 km^2.

According to Mio et al. (2006), the Santos Basin was formed from a rifting process during the afroamerican separation in the Mesozoic. The sediment accumulation occurred initially in fluvial-lacustrine conditions, subsequently passing through a stage of evaporite basin and evolving into a passive margin basin. These events may be reported as the major phases of the basin: covering the rift to passive margin transition. According to these authors, the rift phase is composed of a basal magmatism covered by a sequence deposited in fluvial-lacustrine environment, consisting of

R. Constantino (✉) • E.C. Molina
University of São Paulo, Rua do Matão, 1226, Cidade Universitária, CEP 05508-090 São Paulo, SP, Brazil
e-mail: renata@iag.usp.br; eder@iag.usp.br

U. Marti (ed.), *Gravity, Geoid and Height Systems*, International Association of Geodesy Symposia 141,
DOI 10.1007/978-3-319-10837-7_40,

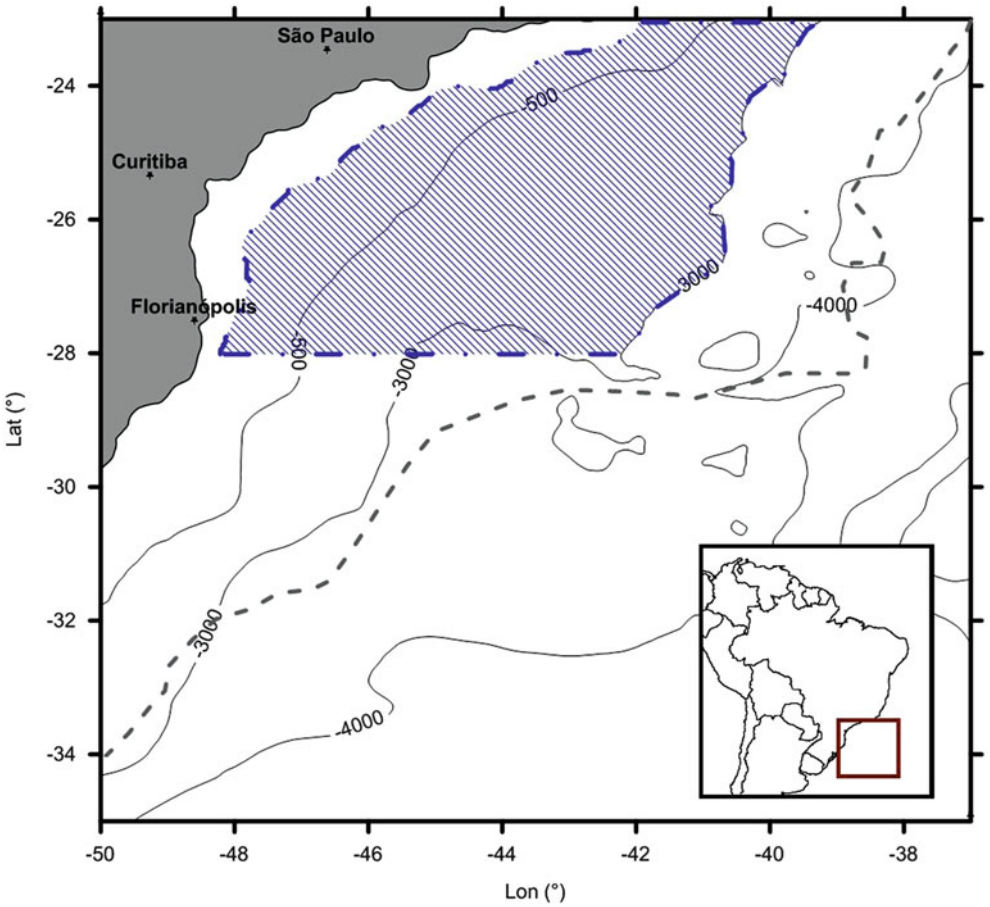

Fig. 1 Bathymetric map from GEBCO. The crosshatched region represents the Santos Basin area. The continent-ocean boundary, according to Cainelli and Moriak (1999), is represented by the *gray dashed line*. The bathymetric contours refer to the depths 500, 3,000 and 4,000 m

shales, carbonates and thick deposits associated with alluvial fans. The transition phase is composed of a thick section of evaporitic rocks deposited during Aptian restricted to a marine environment, with a contribution of deposits typical from *Sabkha* environment (characterized by evaporite-carbonate deposits with some siliciclastics). Above the evaporites of the transition phase, during the lower Albian, an extensive carbonate platform was installed, bordered by alluvial systems, initiating the phase of passive margin basin that continues today.

The structural evolution of the basin is influenced by heterogeneities that affect both the crust and the mantle, comprising suture zones between continental blocks, fold and thrust belts, shear zones and mafic dyke swarms. These discontinuities controlled the structural framework of the Santos Basin basement through the reactivation of structures during the stretch and opening process (Mio 2005).

The elements responsible for the structure of the basement as lateral density variations or the thickness of the elastic lithosphere can be recovered by isostasy and the observed gravity field. In this case it is necessary to estimate the overburden of the crust, which is determined from the depth of the basement, the ocean depth, the crustal thickness and their respective densities (Ebbing et al. 2006).

Use of the gravimetric data acquired by satellite altimetry can be a quick method to assess the structure of the seabed sediments due to their global distribution and quality (Woodward and Wood 2000). In oceanic areas the shorter wavelength components of the observed signal are generally correlated with the bathymetry. This fact has been used in previous studies such as Smith and Sandwell (1997) and Sandwell and Smith (2001) to create bathymetric models from the gravity data.

Many studies are found in literature where the seafloor is investigated through satellite altimetry data. Smith and Sandwell (1997) integrated ship data with satellite altimeter data to construct a map of the topography of the oceans. Ramillien and Cazenave (1997) used *in situ* data obtained from NGDC and ERS-1 Geodetic mission data to calculate the overall bathymetry of the oceans. Calmant and Baudry (1996) showed different techniques for obtaining bathymetric models from satellite altimetry data.

Recently, Reguzzoni and Sampietro (2010) have proved that it is possible to estimate the bathymetry also from GOCE observations.

During this work, the gravity data derived from satellite altimetry are used to map the topography of the basement, after removing the gravity effect of the sediments.

The interpretation of the gravity field is important to assist the interpretation of the seismic data or to provide information in areas where such data are scarce or unavailable. This is the case in the Santos Basin, where due to the high exploratory interest, most of the data were collected and processed by companies in the energy sector, and are unavailable for research purposes.

The present study aims to determine the configuration of the ocean basement in the Santos Basin through the combined analysis of gravity field data, bathymetry, sediment thickness and the thickness of the crust in the region.

2 Methodology

The starting point of this study is a database containing observations of gravity anomalies, calculated by Molina (2009) using satellite altimetry and marine geophysics; an estimate of the crustal thickness obtained from seismics (Leyden et al. 1971; Zalán et al. 2011); a model of the sediment thickness, obtained from the NGDC (Divins 2003), and a global bathymetric model available from GEBCO (BODC 2012). Additional density values for the study were taken from CRUST 2.0 (Bassin et al. 2000).

The methodology was developed based on Braitenberg et al. (2006), following the four steps described below and using the software LithoFLEX (Braitenberg et al. 2007).

2.1 Step 1: Modeling the Variation of the Moho from Inversion of the Gravity Field

The first part of the study consisted in modeling the variations of the Crustal Mantle Interface (CMI) from the inversion of the gravity field. The free-air data (Molina 2009) were transformed into Bouguer anomaly (Lowrie 1997) and then the effect of the sediment thickness was removed by using the Parker algorithm (Parker 1972), which expands the effect generated by the gravimetric discontinuity layer in a fifth order series. The calculation can be performed with a constant density contrast for any discontinuity. However, for more realistic results, the sediments compaction with depth should be considered. For this, we have used the model of sedimentary compaction described by Sclater and Christie (1980), based on an exponential reduction in porosity with depth. The gravity effect of sediments in the study area was calculated applying this methodology to a series of thin layers 10 m thick, with a laterally variable density. The values were calibrated using the Deep Sea Drilling Project (DSDP) data, Leg 39, site 356, corresponding to the latitude and longitude −28.2870 −41.0880 (Supko et al. 1997). After calculating the gravity effect of the sedimentary cover, the corrected field was inverted using the iterative gravity inversion model described by Braitenberg and Zadro (1999). For the inversion procedure, some starting parameters are required: the reference depth of the density interface, the density contrast across the interface and a cutoff wavelength. The first two values were found by innumerous tests performed to achieve the best agreement with punctual seismic values. The last one was found by calculating the decay of the amplitude spectrum of the gravity field (Russo and Speed 1994).

2.2 Step 2: Flexural Analysis

This step involves the flexural analysis in the region, providing an independent way to determine the undulations of the CMI, allowing the reliability of the results obtained in step 1 to be checked.

The flexural analysis is based on the methodology introduced by Braitenberg et al. (2002, 2003).

Considering the flexure model of a thin plate (Watts 2001), it is generally admitted that the flexure $w(\vec{r})$ is approximately equal to the deviations from a flat CMI. In this work, the CMI is calculated by the convolution of the crustal load $h(\vec{r})$ with the response function $s(\vec{r})$

$$w(\vec{r}) = s(\vec{r}) * h(\vec{r})$$

For each node of the topographic load grid, a flexural response curve is calculated with the analytic solution described by Wienecke (2006), named analytical solution for an elastic plate (ASEP). Using a number of response functions, each corresponding to a value of elastic thickness (Te), the corresponding flexural CMI is obtained. In this work, a set of flexural response curves was prepared, using the values of Te between 0 and 25 km at 1 km interval. In this step spatial variations of Te were also calculated. For this, the root mean square (RMS) error considering the observed CMI and the flexural CMI was determined in windows of length of 100 km by 100 km. The inverted Te for a particular window is the one that minimizes the RMS error, and therefore achieves the best fit approximation with the observed CMI.

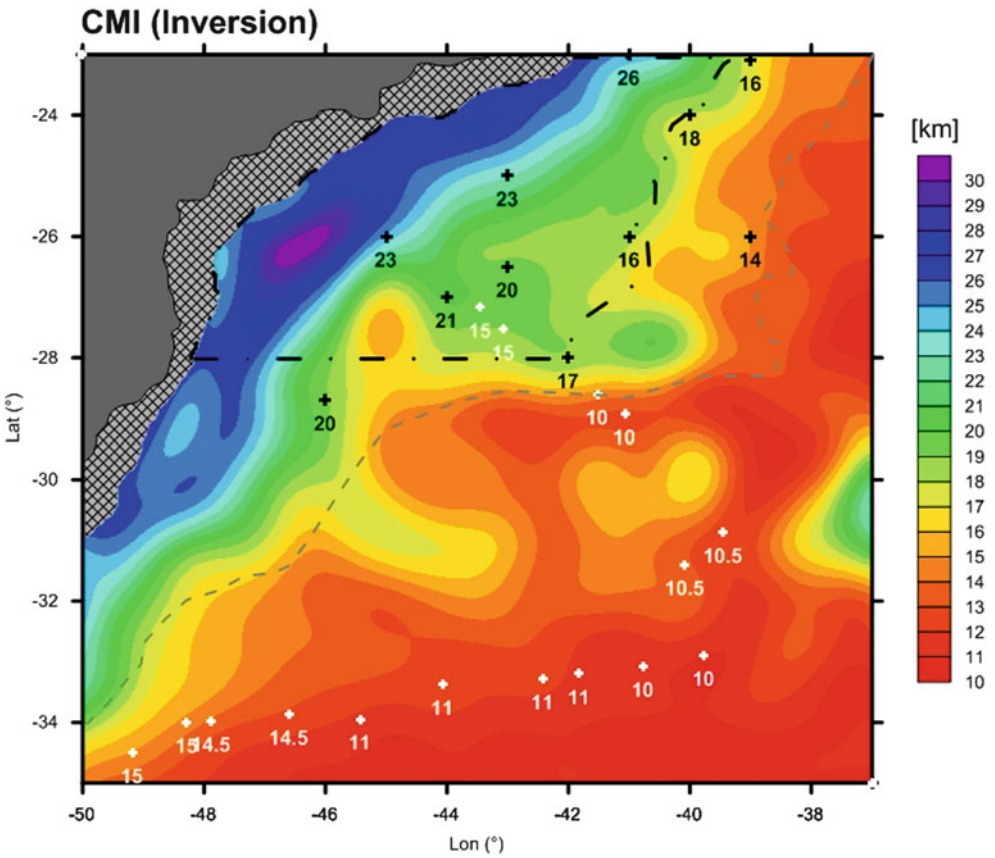

Fig. 2 Crust Mantle Interface map (CMI) obtained from inversion of the gravity field. The area of the Santos Basin is represented by the *black dashed polygon*, after Moreira et al. (2007). Values marked in *black* are constraining data from Zalán et al. (2011) and white from Leyden et al. (1971). The *crosshatched* region represents the area where gravity data are not suitable for the analysis. The continent-ocean boundary, according to Cainelli and Moriak (1999), is represented by the *gray dashed line*

2.3 Step 3: Gravity Effect of the CMI

In this step, the gravity effect of the CMI is calculated with a constant density contrast along the discontinuity, applying the Parker algorithm, (Parker 1972). The objective of this procedure is to remove the gravity effect of the sediments and the CMI from the Free air anomaly:

$$g_{res} = g_{FA} - g_{sed} - g_{CMI}$$

The residual field thus obtained (g_{res}) is inverted in the next step of the methodology, providing the desired basement topography. The residual obtained by subtracting the gravity effect of CMI and sediments from the Bouguer anomaly is used to highlight tectonic structures.

2.4 Step 4: Inversion of the Residual Gravity Field

The basement structure of Santos Basin is calculated at this last step. This is done by the inversion of the residual gravity field (g_{res}) found in step 3, using the Iterative Gravity Inversion model (Braitenberg and Zadro 1999).

3 Results

The basement topography is calculated by following the four steps described before. The calculations in step 1 showed that the sediment layer contributed with approximately 10–30 mGal to the gravimetric signal.

For the inversion procedure, the decay of the amplitude spectrum of the gravity field (Russo and Speed 1994) provided the cutoff wavelength of 115 km. The gravity field was inverted assuming a laterally variable density contrast between the lower crust and the upper mantle. These values were taken from the CRUST 2.0 model. To evaluate the impact of possible differences related to data accuracy, tests were done changing density values in steps of 100 kg/m^3. The resulting values presented the maximum differences in the order of hundreds of meters, thus not affecting the final results.

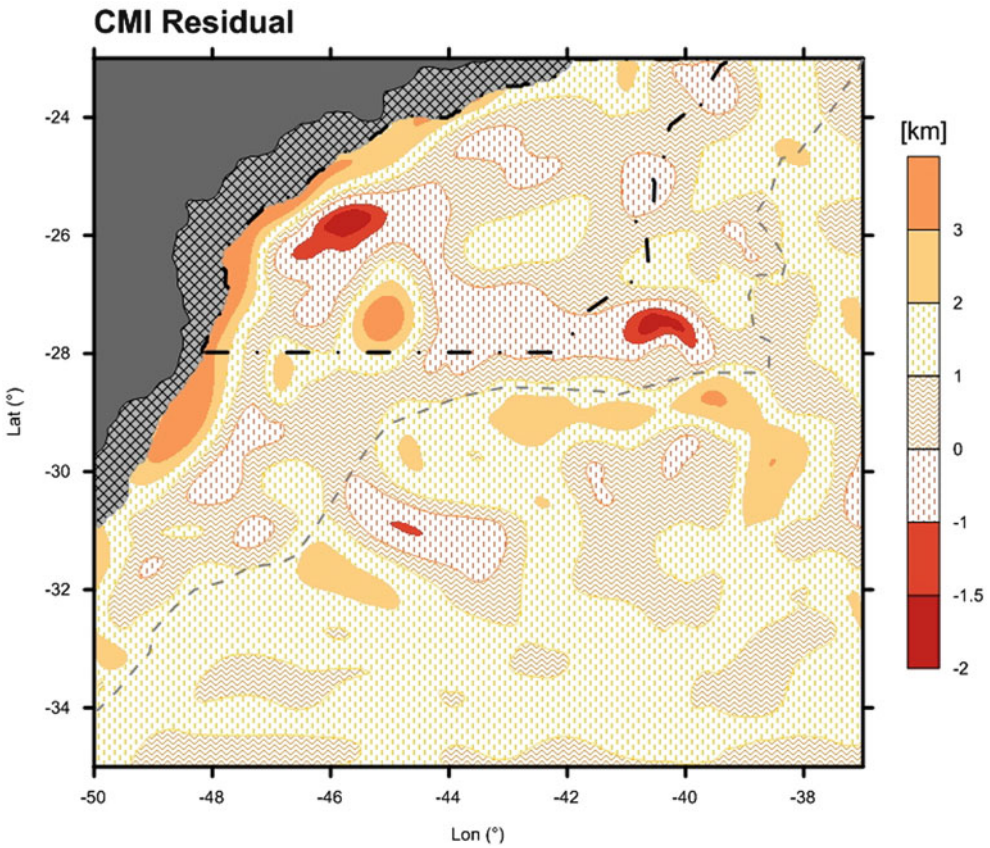

Fig. 3 Difference between values obtained by inversion of the gravity data and by flexural analysis. Positive values represent a flexural CMI shallower than gravity CMI. The area of the Santos Basin is represented by the *black dashed polygon*, after Moreira et al. (2007). The *crosshatched* region represents the area where gravity data are not suitable for the analysis. The continent-ocean boundary, according to Cainelli and Moriak (1999), is represented by the *gray dashed line*

The inversion process was performed for a series of depth-reference values ranging from 20 km to 30 km. The RMS error was calculated between the results and the values obtained by seismic inversion with constraining data obtained from Leyden et al. (1971) and Zalán et al. (2011). After the analysis of the results, the best RMS error value of approximately 1.9 km was found for the reference depth of 28.7 km (Fig. 2).

The second step involves calculating the flexure $w(\vec{r})$ along the plate. First, the equivalent topography was calculated based on Kumar et al. (2011), and then the flexure was calculated based on the flexure model of a thin plate.

The flexural rigidity is calculated using a moving window of 100 km width and 100 km length with a 20 km offset along the data. Standard values for the Young modulus ($E = 100$ GPa), the Poisson radius ($\upsilon = 0.25$) and the mean gravity acceleration (9.81 m/s^2) were used. The density values of the mantle (3,370 kg/m^3) and the crust (2,880 kg/m^3) are average values provided by the CRUST 2.0 model. The elastic thickness (Te) varied from 1 km to 25 km. Such values should be in agreement with the local rheology and are based on Tassara et al. (2007).

The values obtained by the flexural analysis are in agreement with the gravity CMI, as shown in Fig. 3. Overall, the difference is small, ranging from −3 km to 2.5 km. The highest values are close to the area where the input gravity data are unreliable due the proximity of the shoreline (shaded in gray in the Fig. 3) and may represent, at least in part, the influence of these data.

In the next step the gravity effect of the CMI obtained in step 2 is computed. This effect added to the gravity effect of sediments is subtracted from the Bouguer field resulting in the residual shown in Fig. 4. Subtracting the field from the free air gravity anomaly, results in the residual field of the basement, which will be inverted in the last step of this work.

For the inversion of this residual field, a constant density contrast of 1,570 kg/m^3, based on values from CRUST 2.0 model, related to the density contrast between the upper crust (2,600 kg/m^3) and the water (1,030 kg/m^3) were used. All wavelengths are taken into account and the reference depth was defined as the zero level (Hwang 1999).

By basement in this study we refer to the physical surface that lies below the sediment layer. The sediment thickness

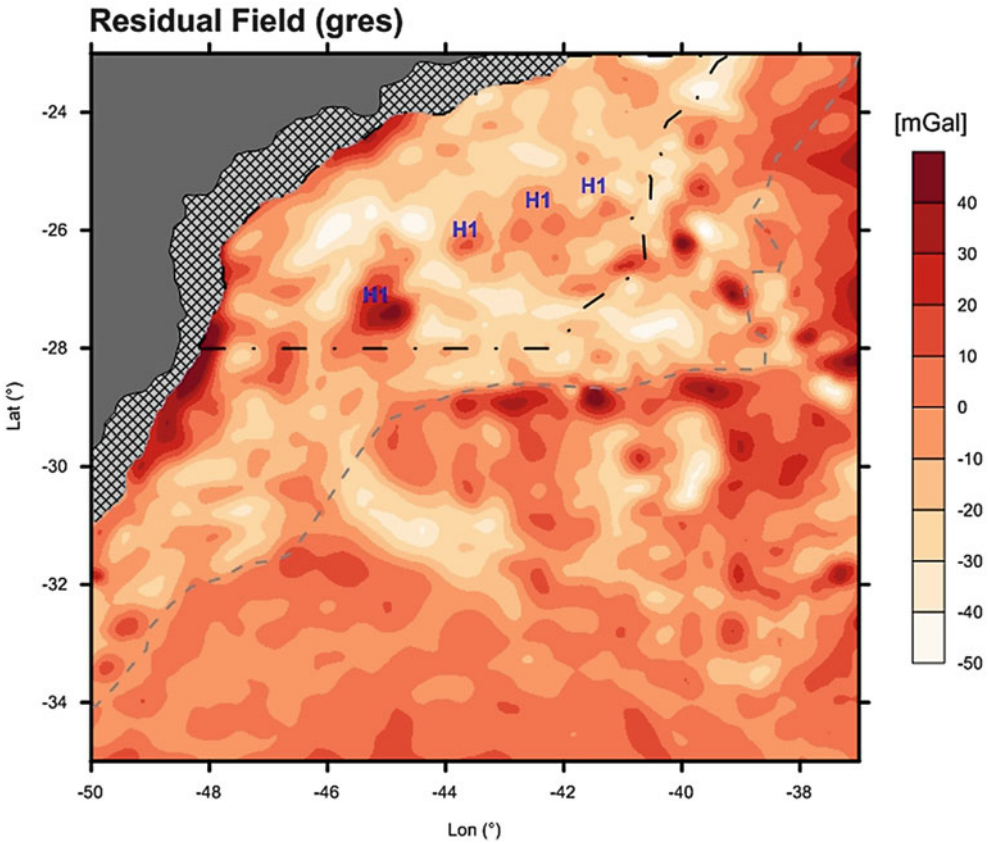

Fig. 4 Gravimetric field residuals. The area of the Santos Basin is represented by the *black dashed polygon*, after Moreira et al. (2007). H1 represents gravity anomalies discussed in the text. The *crosshatched* region represents the area where gravity data are not suitable for the analysis. The continent-ocean boundary, according to Cainelli and Moriak (1999) is represented by the *gray dashed line*

data used in this study represents the depth of the acoustic basement, defined as the deepest reflector observable in the seismic reflection profiles, and may not necessarily represent the base of the sediments. The result of this work provides the base of the sediments and will be called the gravimetric basement (Fig. 5a). The depth of the basement ranges from 0 m to 7.000 m. Comparing to bathymetric data (Fig. 5b), this depth is greater and it is possible to see salient features that are not present in the bathymetric model. This can be due to the sedimentary cover that conceals tectonic features of the basement. The basement topography is shown in Fig. 6 in a 3D perspective.

Discussion and Conclusions

The results of this study show that some basement features, that could be determined from the available data following the methodology proposed by Braitenberg et al. (2006), are hidden by the sedimentary layer in the region of the Santos Basin.

The implementation of the first stage of this methodology allowed the determination of the depth of the CMI from the inversion of the corrected gravity field, using seismic constrained data obtained by Leyden et al. (1971) and Zalán et al. (2011). The results showed an RMS error of approximately 1.9 km between the values of the obtained model and constraining data.

To check the consistency of the results, the depth of the CMI was determined by an independent method involving the flexural analysis, showing small differences from the previous estimate. The analysis showed that the largest differences may be associated with salt intrusions present in the sediment layers of the Santos Basin, which are described in the literature (Meisling et al. 2001; Izeli 2008; Caldas and Zalán 2009; Souza et al. 2009).

Subtracting the gravimetric signal of the CMI and of the sediment layer from the observed gravity field, the residual gravity field for the basement was obtained. The gravimetric signal of the sediments was calculated based on the model of Sclater and Christie (1980), taking into account the compaction with depth and the gravity field of CMI was later calculated by Parker algorithm (Parker 1972).

Analyzing the residual gravity field after removing sediments and CMI from the Bouguer field (Fig. 4),

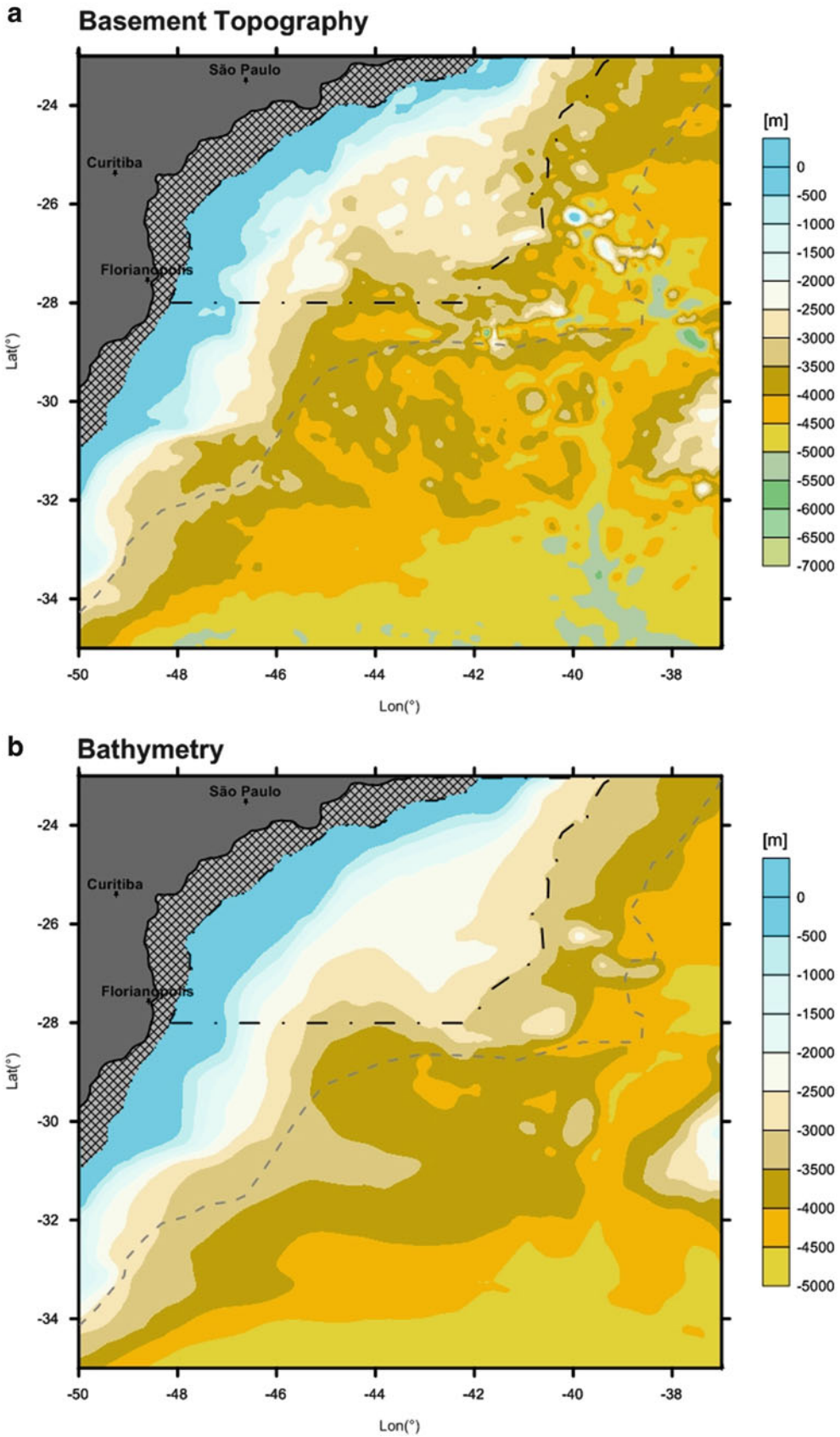

Fig. 5 (**a**) Basement topography modeled in this study; (**b**) bathymetry. The area of the Santos Basin is represented by the *black dashed polygon*, after Moreira et al. (2007). The *crosshatched* region represents the area where the input gravity data are not suitable for the analysis

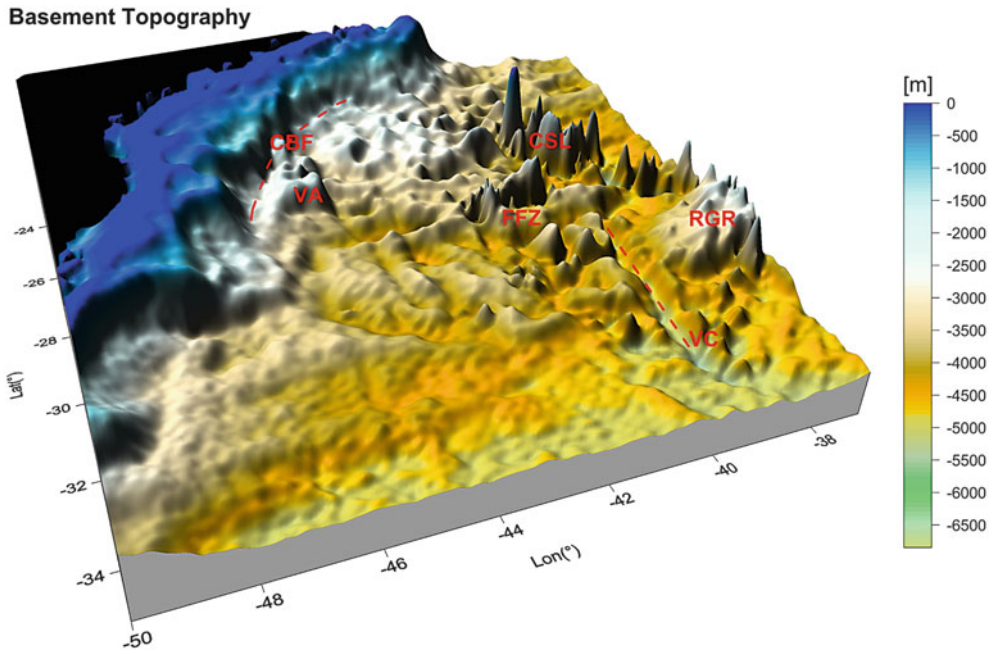

Fig. 6 3D basement topography. Features discussed in the text are marked in *red*. *CBF* Cabo Frio fault, *VA* Volcanic Avedis chain, *FFZ* Florianopolis Fracture zone, *RGR* Rio Grande Rise, *CSL* Cruzeiro do Sul lineament, *VC* Vema channel

inside the area marked as Santos Basin, it is possible to see a strip of positive gravity anomalies trending northeast-southwest. These anomalies were discussed in previous works such as Demercian (1996) and Meisling et al. (2001). According to Meisling et al. (2001), these gravity anomalies, when analyzed with regional seismic profiles, can be interpreted as volcanic rocks, that in some instances, are unconformably overlain, or progressively onlapped, by thin Aptian evaporites, whose seismic facies are well layered and interpreted to be anhydrite. According to these authors, these anticlines were ridges of high ground during evaporite deposition. Along some of the ridges, volcanic activity continued during and after the Aptian, mobilizing the evaporites and covering them with volcanoclastic deposits. An example is the Avedis volcanic chain in the southern Santos Basin, which has been mapped as a presalt high by Demercian (1996).

The northern portion of the Santos Basin is characterized by large-scale tectonic features and intense diapirism. The processes that generate these features were originated mainly by basement uplift during the Late Cretaceous in the adjacent portion of the basin. According to Macedo et al. (2004), a thickstack of coastal sediments generated by this event, created a large-scale displacement of marine sediments of the basin toward the Plateau of São Paulo, on top of the evaporitic layer (Aptian). This displacement is accommodated along the Cabo Frio fault.

The basement depth is shown in Figs. 5a and 6. Analyzing the basement structure, it is possible to see a set of volcanic chains, related to the Rio Grande Rise (RGR), Florianopolis Fracture Zone (FFZ) (Mohriak et al. 2002) and Cruzeiro do Sul lineament (CSL) (Mohriak et al. 2010). A valley at approximately −40° longitude, between latitude −29° and −31°, trending northwards, can be associated to the Vema channel (VC) (Mohriak et al. 2002). Inside Santos Basin area, one can see some features as the Volcanic Avedis chain (VA), already discussed above, and the long and narrow feature, coinciding with the Cabo Frio fault (CBF) (Macedo et al. 2004; Assine et al. 2008; Caldas and Zalán 2009).

The methodology used during this study showed that it is possible to obtain a three-dimensional model of the basement in oceanic areas from gravimetric data obtained by ship and by satellite altimetry, bathymetric data and information about the thickness of the sediments and the crustal structure of the region. This kind of analysis can provide important insights for hydrocarbon exploration in such regions.

Acknowledgments We thank CNPq, for the master's scholarship related to this project; Carla Braitenberg for permission to use the software Lithoflex; Andres Tassara for the elastic thickness data; Iata Anderson de Souza for fruitful discussion during this work; Naomi Ussami for helping with the interpretation and all reviewers and editors that helped us improving the publication of this paper.

References

Assine ML, Correa FS, Chang HQ (2008) Migração de depocentros na Bacia de Santos: importância na exploração de hidrocarbonetos. Revista Brasileira de Geociências 38(2):111–127

Bassin C, Laske G, Masters G (2000) The current limits of resolution for surface wave tomography in North America. Eos Trans AGU 81:F897

Braitenberg C, Zadro M (1999) Iterative 3D gravity inversion with integration of seismologic data. Bollettino Di GeofisicaTeoricaedApplicata 40(3–4):469–475

Braitenberg C, Ebbing J, Götze HJ (2002) Inverse modelling of elastic thickness by convolution method: the Eastern Alps as a case example, Earth Planet. Sci Lett 202:387–404

Braitenberg C, Wang Y, Fang J, Hsu HT (2003) Spatial variations of flexure parameters over the Tibet-Quinghai plateau. Earth Planet Sci Lett 205:211–224

Braitenberg C, Wienecke S, Wang Y (2006) Basement structures from satellite-derived gravity field: South China Sea ridge. J Geophys Res 111, B05407. doi:10.1029/2005JB003938

Braitenberg C, Wienecke S, Ebbing J, Born W, Redfield T (2007) Joint gravity and isostatic analysis for basement studies – a novel tool, extended abstracts. EGM 2007 international workshop, innovation in EM, Grav and Mag methods: a new perspective for exploration, Villa Orlandi, Capri – Italy, 15–18 April 2007

British Oceanographic Data Centre, Intergovernmental Oceanographic Commission and International Hydrographic Organization (BODC, IOC, IHO) (2012) Centenary edition of the GEBCO digital atlas on behalf of the intergovernmental oceanographic commission and the international hydrographic organization as part of the general bathymetricchart of the oceans, [CD-ROM], Liverpool, UK

Cainelli C, Moriak WU (1999) Some remarks on the evolution of sedimentary basins along the Eastern Brazilian continental margin. Episodes 22(3):206–216

Caldas MF, Zalán PV (2009) Reconstituição cinemática e tectono-sedimentação associada a domos salinos nas águas profundas da Bacia de Santos, Brasil. Boletim de Geociências da Petrobrás 15(2):531–549, 17(2):227–248

Calmant S, Baudry N (1996) Modelling bathymetry by inverting satellite altimetry data: a review. Mar Geophys Res 18:123–134

Demercian LS (1996) A halocinese na evolução do Sul da Bacia de Santos do Aptiano ao Cretáceo Superior. Master's thesis, Universidade Federal do Rio Grande do Sul, Porto Alegre, Brazil, 201 p

Divins DL (2003) NGDC total sediment thickness of the world's oceans and marginal seas. http://www.ngdc.noaa.gov/mgg/sedthick/sedthick.html

Ebbing J, Braitenberg C, Götze HJ (2006) The lithospheric density structure of the Eastern Alps. Tectonophysics 414:145–155

Hwang C (1999) A bathymetric model for the Souch China Sea from Satellite altimetry and depth data. Mar Geod 22:37–51

Izeli MGB (2008) Controle estrutural do embasamento emerso na porção central da Bacia de Santos, utilizando sensoriamento remoto e interpretação sísmica. Trabalho de conclusão de curso de Geologia do Instituto de Geociências e Ciências Exatas – UNESP, Rio Claro, Brasil, 65 p

Kumar RTR, Maji TK, Kandpal SC, Sengupta D, Nair RR (2011) Elastic thickness estimates at northeast passive margin of North America and its implications. J Earth Syst 120(3):447–458

Leyden R, v Ludwig WJ, Ewing J (1971) Structure of the continental margin of Punta del Este, Uruguay, and Rio de Janeiro, Brazil. AAPG Bull 55:2161–2173

Lowrie W (1997) Fundamentals of geophysics. Cambridge University Press, Cambridge, 354 pp

Macedo JM, Drehmer LH, Andrade DE, Mello MR, Martinéz MA (2004) Falha de Cabo Frio: um importante fator condicionante do sistema petrolífero na Bacia de Santos. In: XLII Brazilian National Congress of Geology, 2004, Araxá. Proceedings OF XLII Congresso Brasileiro de Geologia, 2004. v. CD. p. 806

Meisling KE, Cobbold PR, Mount VS (2001) Segmentation of an obliquely rifted margin, Campos and Santos basins, southeastern Brazil. AAPG Bull 85(11):1903–1924

Mio E (2005) Modelagem crustal da Bacia de Santos pela integração de métodos geofísicos. Rio Claro. 94 p

Mio E, Chang HK, Correa FS (2006) Integração de métodos geofísicos na modelagem crustal da bacia de santos. Revista Brasileira de Geofísica 23(3):275–284

Mohriak WU, Rosendahl BR, Turner JP and Valente SC (2002) Crustal architecture of South Atlantic volcanic margins. In: Menzies MA, Klemperer SL, Ebinger CJ, Baker J (eds) Volcanic rifted margins, vol 362. Geological Society of America Special Paper, Boulder, CO, pp 159–202

Mohriak WU, Nóbrega M, Odeagard ME, Gomes BS, Dickson WG (2010) Geological and geophysical interpretation of the Rio Grande Rise, south-eastern Brazilian margin: extensional tectonics and rifting of continental and oceanic crusts. Petrol Geosci 16:231–245

Molina EC (2009) O uso de dados de missões geodésicas de altimetria por satélite e gravimetria marinha para a representação dos elementos do campo de gravidade terrestre. Tese de livre docência, Departamento de Geofísica do IAG-USP, Universidade de São Paulo, 100 pp

Moreira JLP, Madeira CV, Gil JÁ, Machado MAP (2007) Bacia de Santos. Boletim de Geociências da Petrobrás 15(2):531–549

Parker RL (1972) The rapid calculation of potential anomalies. Geophys J Roy Astron Soc 31:447–455

Ramillien G, Cazenave A (1997) Global bathymetry derived from altimeter data of the ERS-1 geodetic mission. J Geodyn 23:129–149

Reguzzoni M, Sampietro D (2010) An inverse gravimetric problem with GOCE data. In: Mertikas SP (ed) International Association of Geodesy Symposia, "Gravity, Geoid and Earth Observation", IAG Commission 2: Gravity Field, Chania, Crete, Greece, 23–27 June 2008, vol 135. Springer, Berlin, pp 451–456

Russo RM, Speed RC (1994) Spectral analysis of gravity anomalies and the architecture of tectonic wedging, NE Venezuela and Trinidad. Tectonics 13(2):613–622

Sandwell DT, Smith WHF (2001) Bathymetric estimation. In: Fu L-L, Cazenave A (eds) Satellite altimetry and earth sciences. Elsevier, New York, NY, pp 441–457

Sclater JG, Christie PAF (1980) Continental stretching: an explanation of the post mid-Cretaceous subsidence of the central North Sea basin. J Geophys Res 85:3711–3739

Smith WHF, Sandwell DT (1997) Global sea floor topography from satellite altimetry and ship depth soundings. Science 277: 1956–1962

Souza IA, Ebert HD, Castro JC, Soares AS, Silva GHT, Benvenutti CF (2009) Caracterização das falhas de transferência na porção norte da Bacia de Santos a partir da integração de dados geológicos e geofísicos. Boletim de Geociências da Petrobras 17(1):109–132

Supko PR, Perch-Nielsen K, Carlson RL (1997) General synthesis of central and south Atlantic drilling results, LEG 39, Deep Sea Drilling Project. doi:10.2973/dsdp.proc.39.101

Tassara A, Swain C, Hackney R, Kirby J (2007) Elastic thickness structure of South America estimated using wavelets and satellite-derived gravity data. Earth Planet Sci Lett 253:17–36

Watts AB (2001) Isostasy and flexure of the lithosphere. Cambridge University Press, Cambridge, 458 pp

Wienecke S (2006) A new analytical solution for the calculation of flexural rigidity: significance and applications. PhD thesis, Free University of Berlin, Berlin. http://www.diss.fu-berlin.de/2006/42

Woodward D, Wood R (2000) Bathymetry sediment thickness and crustal structure from satellite gravity data. Explor Geophys 31(2):89–93. doi:10.1071/EG00089

Zalán PV, Severino MCG, Rigoti CA, Magnaviva LP, Oliveira JAB, Vianna AR (2011) An entirely new 3D-view of the crustal and mantle structure of a South Atlantic passive margin – Santos, Campos and Espírito Santo Basins, Brazil. Search and Discovery, Article #30177

Part VIII

Gravity Field of Planetary Bodies

Observing the Gravity Field of Different Planets and Moons by Space-Borne Techniques: Predictions by Fast Error Propagation Tools

P.N.A.M. Visser

Abstract

In the first decade of the twenty first century, great strides have been made in observing the Earth's gravity field by space-borne techniques such as high-low Satellite-to-Satellite tracking by the Global Positioning System (hl-SST, providing 3D information about orbit perturbations), low-low Satellite-to-Satellite tracking (ll-SST) and Satellite Gravity Gradiometry (SGG). In addition, great advances have been made in (preparations for) gravity field recovery for other bodies in the solar system as well, including Mars and the Moon, using tracking from the Deep Space Network (DSN), but also techniques such as hl-SST, ll-SST, Satellite Laser Ranging (SLR) and Delta VLBI.

The purpose of the work described in this paper is to gain insight in the possibilities of observing the gravity field of various planetary bodies by space-borne observation techniques. For low-earth orbiting (LEO) satellites, efficient error propagation tools are available that allow an assessment of the gravity field performance as a function of orbital geometry and instrument or observation technique. These tools have been extended for use to other bodies in our solar system, including the Earth's Moon, Jupiter, Mars, Titan, Enceladus, Europa and Phobos, which are in the scientific spotlight for various reasons. The gravity field performance has been assessed for satellites orbiting these bodies assuming these satellites can make use of DSN tracking or can acquire ll-SST or SGG observations.

Keywords

Error propagation tools • Moons • Planets • Space-borne gravimetry

1 Introduction

In the past decade, significant advances have been made in the observation, modeling and interpretation of not only the gravity field of the Earth, but also of other celestial bodies in the solar system. For the Earth, continuous three-dimensional (3D) tracking in combination with a high-precision accelerometer allowed for the first time the derivation of homogeneous gravity field models for medium to long wavelengths (CHAMP, Reigber et al. 1999). The addition of low-low Satellite-to-Satellite tracking, or ll-SST, enabled the observation of temporal gravity variations (GRACE, Tapley and Reigber 1999). Finally, using a space-borne gradiometer further enhanced the observation of Earth's gravity field down to spatial scales of 100 km and below (GOCE, Drinkwater et al. 2007).

Also for other celestial bodies such as the Earth's Moon and Mars already significant gravity field information has been extracted by analyzing DSN—and for the Moon also hl-SST, Satellite Laser Ranging (SLR) and VLBI—tracking to—or by—missions such as Clementine, Lunar Prospector, LRO, SELENE and Mars Global Surveyor (Smith et al. 2009; Matsumoto et al. 2010). Major improvements can be expected from the GRAIL mission, which—like GRACE—makes use of the ll-SST technique. Due to the absence

P.N.A.M. Visser (✉)
Faculty of Aerospace Engineering, Delft University of Technology, Kluyverweg 1, 2629 HS Delft, The Netherlands
e-mail: P.N.A.M.Visser@tudelft.nl

U. Marti (ed.), *Gravity, Geoid and Height Systems*, International Association of Geodesy Symposia 141,
DOI 10.1007/978-3-319-10837-7_41, © Springer International Publishing Switzerland 2014

of a (significant) atmosphere, the GRAIL satellites will fly very low at the end of their mission possibly allowing the construction of a gravity field model with a spatial resolution of 10 km (NASA 2012a).

In addition, DSN tracking of *e.g.* the Galileo and Cassini/Huygens missions during their encounters with the icy moons Europa and Titan allowed for the retrieval of gravity field information, be it rather coarse, which helps to reveal secrets about their internal structure (Iess et al. 2010; Rappaport et al. 2008). It is interesting to note that especially SLR techniques are progressing fast allowing tracking of very remote satellites (*cf.* the MESSENGER mission to Mercury, Smith et al. 2006).

It is fair to conclude that precise and detailed knowledge of the gravity field of celestial bodies is essential for revealing and understanding their internal structure and composition, and also for applications such as mission operations. A number of spaceborne techniques, including hl-SST, ll-SST and gradiometry are at our disposal for determining the gravity field of not only Earth, but also for example the Moon. Recent technological developments, such as Micro-ElectroMechanical systems (MEMS) based accelerometers and possibly gradiometers, might lead to miniaturized instruments that are feasible for future missions to other celestial bodies in our solar system (Flokstra et al. 2009). Therefore, it is interesting to consider and study future mission scenarios for determining the gravity field of these bodies. Detailed concept studies and full-scale simulations of for example high degree and order gravity field recovery using spaceborne gravimetry are time consuming and require significant computing resources. Fortunately, efficient error propagation tools exist and have been used as a first step for designing gravity field satellite missions for the Earth (Colombo 1984; Rosborough 1987; Visser 2005), thereby reducing the search space and limiting the number of satellite missions that are interesting for detailed and comprehensive further study. It is interesting to note that the match between error predictions by these tools and actual performance is quite close for a mission like the European Space Agency GOCE satellite, for which detailed observation error models were available (ESA 1999; Pail et al. 2011). The tools can be used in the early design phases of gravity field satellite missions to other celestial bodies as well. This paper contains results for a selection of observation techniques, a selection of celestial bodies and a selection of orbital geometries to show the potential of these tools. It has to be stressed that these results should be seen as a first step in the design process of possible gravity field missions.

This paper is organized as follows: after briefly introducing the selected planets and moons (Sect. 2), a few words will be spent on the methodology of the error propagation tools (Sect. 3). This will be followed by an overview of results (Sect. 4). The paper will be concluded with a short discussion (see section "Discussion and Conclusions").

Table 1 Selected planets and moons (*cf.* NASA 2012b)

Body	Mass (kg)	Mean equat. radius (km)	Rotation per. (Earth days)
Earth	5.9722×10^{24}	6,378.1	0.99727
Mars	6.4185×10^{23}	3,396.2	1.02595
Jupiter	1.8986×10^{27}	71,492.0	0.414
Moon	7.349×10^{22}	1,736.0	27.3217
Europa	4.80×10^{22}	1,569.0	3.551
Titan	1.3455×10^{23}	2,575.0	15.9454
Enceladus	1.08×10^{20}	250.0	1.3702
Phobos	10.6×10^{15}	13.4	0.31891

2 Planets and Moons

A limited selection of celestial bodies in the solar system has been made. The rationale between this selection is the possibility to assess the impact of different dimensions of such bodies (mass, size, but also rotation rate). For example, Jupiter is selected as an example of a giant planet and Phobos as an example of a very small moon. The other selected bodies more or less fill the range between these two extremes (Table 1).

For all the selected bodies, the retrieval of (more detailed) gravity information is valuable to address interesting scientific issues. The Earth speaks for itself. For Mars, gravity field information is crucial for *e.g.* analyzing the nature of the Tharsis region (Boyce 2008). For Jupiter, more information about its gravity field will help to learn more about its internal structure (Guillot et al. 2004). The Moon is interesting as non-hydrostatic (or isostatically uncompensated) components of its gravity field are relatively large (Bills and Lemoine 1995). More detailed gravity field information is required for drawing final conclusions about the existence of *e.g.* (subsurface) oceans on the icy moons Europa and Titan (Anderson et al. 1998; Rappaport et al. 2008; Iess et al. 2010), and also Enceladus (Porco et al. 2006). Finally, precise measurements of the gravity field of Phobos will help to put new constraints on the origin of this small moon of Mars (Rosenblatt et al. 2011). Please note many more questions and also many applications can be mentioned. This paragraph is however not intended to be complete and just serves to exemplify the importance of gravity field information.

3 Methodology

The error propagation tools provide estimates of the precision of spherical harmonic (SH) coefficients representing the gravity field potential of the celestial body of interest. It might be argued that SH coefficients are not the most efficient representation form for all celestial bodies, especially those with a very irregular shape (*e.g.* Phobos). However, because of the computational efficiency of the error propagation tools, it is feasible to use even very high degree and order SH expansions and thus predict the performance for small spatial structures or features if so required. The SH coefficient error estimates are based on the inverse of the normal equations that result from a least-squares estimation process that takes into account the choice of observation technique, orbital geometry and measurement error spectrum, possibly frequency dependent (see *e.g.* Schrama 1991). In case of a circular repeat orbit (most planetary orbiters fly in near-circular orbits, especially gravity field satellites) and constant measurement time interval, it can be proved that the normal matrix becomes block-diagonal when organized per SH order. In addition, it can be proved that even and odd parities of SH coefficients are uncorrelated (Colombo 1984). The maximum size of the matrix blocks that have to be inverted is therefore equal to about half the maximum SH degree (Colombo 1984). It has to be mentioned that for this specific block-diagonal structure of the normal matrix, one more condition has to be met: the number of orbital revolutions in the repeat period has to be larger than twice the maximum SH degree. On a typical standard PC (cost around €1,000 in October 2012), about 10 s CPU time is required per mission scenario for an error estimate up to degree and order 150.

Furthermore, the method of error propagation requires the establishment of transfer functions that establish the relationship between SH coefficients and the observations in the frequency domain. For this paper, the considered observation techniques are hl-SST, ll-SST and SGG. For the first two techniques use is made of a linearized orbit perturbation theory. For SGG, which can be considered an in-situ observation technique, a direct linear relationship exists with the SH coefficients. The transfer functions for orbit perturbations, ll-SST and SGG have been derived, and their validity shown, by several authors (see *e.g.* Colombo 1984; Rosborough 1987; Schrama 1991; Visser 2005). The last two techniques are capable of providing continuous observations with a constant time interval. For hl-SST tracking, it can be argued that for Earth orbiting satellites perturbations in 3 directions can be derived continuously with a constant time interval as well using for example tracking by the Global Positioning System (GPS). However, when relying on for example DSN tracking, this will not be the case. As a (very) rough approximation, it is therefore assumed that DSN tracking provides continuous information about the radial velocity of the satellite (in a next step the error propagation tools might be compared and possibly calibrated by selected rigorous full-scale simulations). In case the mission duration is long enough and in case the satellite is not in phase lock with the Earth a full coverage can be obtained. For the Moon, which is in phase lock, this means that the performance assessment should be interpreted with care. In fact, it can be argued that this performance assessment then would hold for the near side only.

It has to be noted that other observation techniques might have been considered as well and the error propagation tools can easily be adapted to include those. For example, there have been a number of planetary orbiters that carried an altimeter. Associated observations also provide information about radial orbit perturbations. However, it is not straightforward to use altimeter observations directly for gravity field determination, because assumptions have to be made about how the topography of the celestial body of interest was formed (*e.g.* degree of isostatic compensation). Using altimeter crossovers is also not straightforward, since it requires a very precise positioning of the spacecraft for determining the exact crossover location and also provides a sparse global coverage (Mazarico et al. 2012).

As a baseline, for all missions to be assessed a mission duration of four Earth months has been assumed (which is a hypothetical mission duration in case of DSN tracking, for which a longer period will be required to have full global coverage). Polar orbits are taken to guarantee global coverage. The observation time interval is taken equal to 1 min. For Doppler tracking by DSN or the derived radial velocities, an integration interval of 1 min is applied as well. The assumed precision for radial velocities, ll-SST range-rates and SGG observations is taken equal to 1 cm/s, 100 μm/s and 1 E (Eötvös Unit), respectively. The separation angle for the ll-SST observations is 1° orbital angle. Observation errors are assumed to have a Gaussian distribution. When using gravity gradiometry, it is assumed that the three diagonal components are available. Nominally, errors are estimated for a SH expansion complete to degree and order 150.

4 Results

As a first example, the lunar gravity field performance for the selected observations techniques is compared for a satellite in a polar orbit at an altitude of 73 km. Please note that this example is not to be interpreted as the possible performance by the GRAIL mission. In fact, the performance for GRAIL is expected to be much better due to the lower instrument noise ($\ll$100 μm/s) and its much lower altitude (50 km and below), *cf.* MIT (2012)). The repeat period is one Lunar day or about 28 Earth days. The normal equations are scaled by

Table 2 Satellite altitudes for the investigated satellite gravity mission to the selected celestial bodies

Body	Height (km)	Repeat period		Number of repeats
		n_{rev}	$n_{body_{day}}$	
Earth	265	671	42	3.0
Mars	139	568	41	3.0
Jupiter	2,965	324	103	3.0
Moon	73	341	1	4.5
Europa	69	499	12	3.0
Titan	106	1,045	7	1.0
Enceladus	11	371	31	3.0
Phobos	0.6	293	132	3.0

Please note that the repeat period is specified in terms of orbital revolutions n_{rev} and the number of planet/moon days $n_{body_{day}}$, i.e. the period such a planet/moon needs to complete one revolution around its axis

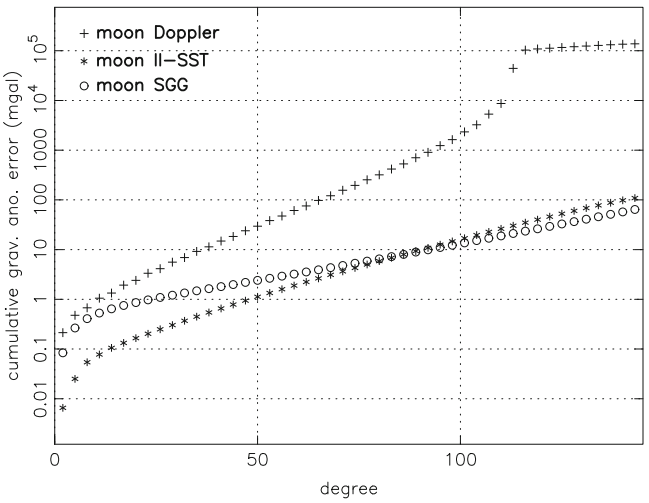

Fig. 1 Lunar gravity field performance in terms of cumulative gravity anomaly error based on Doppler, ll-SST range-rate and SGG observations for a satellite altitude of 73 km

a factor of 4.5 to have a mission duration of about four Earth months (Table 2). The estimated performance is displayed in Fig. 1 in terms of cumulative gravity anomaly error. Please note that if required, the errors can also be represented in terms of other gravity field functionals, such as equipotential surface (geoid, selenoid, ...), deflections of the vertical, etc. The shape of these curves is as anticipated: the slope is the steepest for Doppler and the least steep for SGG observations. Doppler observations represent orbit perturbations that are obtained by integration in time of the (gravitational) accelerations that the satellite experiences, whereas SGG observations are obtained by taking the difference between very adjacent, typically at a distance of 0.5 m or less, accelerations thereby enhancing shorter wavelengths. The ll-SST observations represent orbit perturbation differences between two relatively nearby satellites resulting in a slope in between those of Doppler and SGG observations. Based on the curves in Fig. 1, it might be concluded that the ll-SST technique is the superior one for lunar gravity field retrieval up to degree and order 90, or a smallest spatial scale of about 60 km. For smaller spatial scales, the SGG technique displays a better performance. The Doppler technique leads to a relatively poor performance and as stated above, it can be argued that this performance is achievable only for the near side due to the phase lock of the Moon with the Earth. As also stated before, these results should be considered as an example of the capabilities of the error propagation tools as a preliminary step in the design process. The relative performance of the different techniques depends of course on the underlying assumptions that were made. For example, the error curves scale proportionally with the assumed observation noise level and signature. The chosen noise levels for all the techniques were taken at rather conservative levels. If the noise level for the ll-SST is a factor 10 better, i.e. 10 μm/s, the associated error curve will shift by one order of magnitude and the SH degree at which the ll-SST curve intersects with the SGG one will shift to a significantly higher degree. Of course, a similar "vice-versa" reasoning can be used when reducing the noise level of SGG observations. As another example, a bandwidth limitation (i.e. high noise at low frequencies), which is typical for a gradiometer, will significantly degrade the performance for low SH degrees. Hence, the error analysis can be refined and lead to more realistic gravity field retrieval performance assessments if more information becomes available about the noise characteristics of the observation technique(s) and/or selected instruments.

The error curve for the Doppler observations displays a distinct increase around degree 115. This can be explained by considering the Doppler integration interval of 1 min. For the Lunar mission, the satellite travels a distance equal to about 3.12° in terms of orbital angle, which is around 1/115th of an orbital revolution, or the inverse of the SH degree where the jump kicks in.

As a second example, polar orbits were selected for other celestial bodies with altitudes that are scaled by the radius of the associated body of interest, i.e.:

$$\frac{a_b}{r_b} = \frac{a_e}{r_e} \tag{1}$$

where a_i and r_i represent respectively the semi-major axis of the satellite orbit and radius of the selected celestial body ($i = b$), where the Earth ($i = e$) serves as reference using an altitude of about 300 km. Please note that also other scaling rules can be applied and of course other altitudes can be selected. The scaling is applied to take into account the consideration that for smaller bodies gravity signals will dampen out faster with increasing altitude.

The scaling rule of Eq. (1) leads to different repeat orbits and associated number of orbital revolutions (Table 2), which

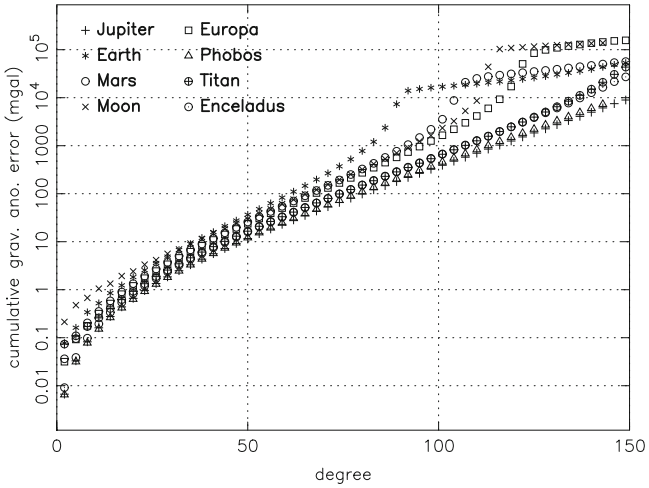

Fig. 2 Gravity field performance in terms of cumulative gravity anomaly error based on Doppler observations for scaled satellite altitudes (using a reference altitude of $\approx$ 300 km for the Earth)

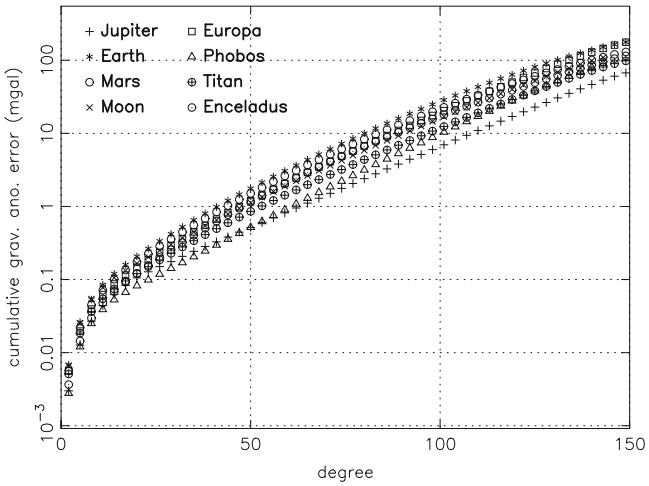

Fig. 3 Gravity field performance in terms of cumulative gravity anomaly error based on ll-SST range rate observations for scaled satellite altitudes (see Fig. 2)

for all bodies, except Phobos, is above 300, i.e. formal error estimates can be obtained for SH coefficients up to degree and order 150 (140 is taken for Phobos). Different repeat periods are obtained, which is the reason for scaling the normal equations with the specified number of repeats to end up with a four Earth month observation period for all selected mission scenarios.

The gravity field performance for the several celestial bodies is displayed in Figs. 2, 3 and 4 for radial Doppler, ll-SST range-rate and SGG observations, respectively, in terms of cumulative gravity anomaly error. It can be observed that curves look quite similar for the Doppler and ll-SST observation techniques for SH degrees up to at least 50, for all selected celestial bodies (both the very small and big ones). For the Doppler technique (Fig. 2), jumps occur at

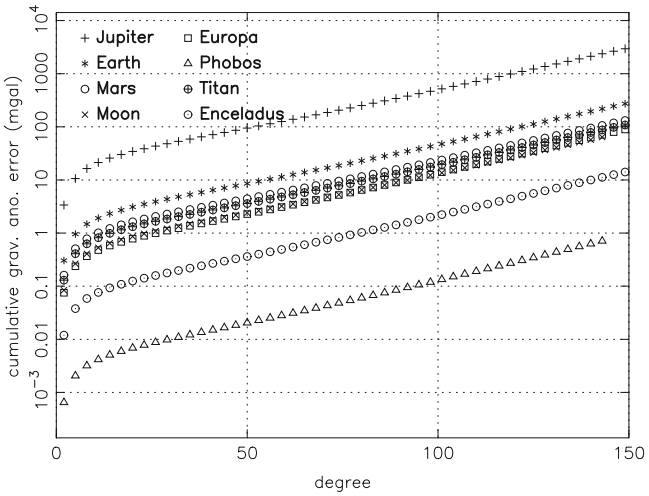

Fig. 4 Gravity field performance in terms of cumulative gravity anomaly error based on SGG observations for scaled satellite altitudes (see Fig. 2)

different SH degree which can be explained by the different rotation rates for the selected satellite orbits combined with Doppler integration interval of 1 min (see also the explanation above for the Lunar mission scenarios, Fig. 1). For the SGG observation technique, the error curves are also very similar, except for the absolute magnitude. In terms of cumulative gravity anomaly error, the errors for the largest selected planet (Jupiter) are between 3 and 4 orders of magnitude larger than for the smallest selected moon (Phobos). A preliminary conclusion might be that the SGG technique is relatively promising for small bodies. As stated before, the Doppler and ll-SST observation techniques provide information about (relative) orbit perturbations, which are obtained by integration of the equations of motion or integration of the gravitational acceleration. SGG observations however are obtained by differentiation of the gravitational acceleration. By using scaled altitudes Eq. (1), the SGG technique has a natural advantage for small bodies as compared to the other techniques.

Discussion and Conclusions

Efficient error propagation tools originally used for Earth gravity field satellite missions have been adjusted to enable first assessments of gravity field retrieval performance for satellite missions to other celestial bodies. A number of space-borne gravimetry techniques have been selected to serve as example, including (hypothetical) Doppler observations of the radial velocity of the satellite, ll-SST range rate observations, and SGG observations.

The gravity field retrieval performance was assessed for nominal mission scenarios, where the mission duration is equal to four Earth months and the satellites fly in polar repeat orbits. Concerning the different techniques,

results are in agreement with intuition and experience for the Earth. For Doppler tracking, the error curves have the steepest slope, i.e. gravity field retrieval errors grow relatively fast with increased spatial resolution. On the other hand for SGG observations, the slope is the smallest, i.e. the SGG technique performs relatively well at short spatial scales.

The conducted error propagation assessments described in the previous sections can be considered as a nice exercise to show the capability of the used tools for designing possible future gravity field mission to different celestial bodies in our solar system. When mission and instrument design evolve, more realistic observation error spectra can be used to improve the gravity field performance estimates. It can be stated that the error propagation tools are very flexible and can easily accommodate many observation techniques, orbital geometries and different celestial bodies. These tools provide a first quick insight into gravity field mission concepts that are feasible and can be selected for more comprehensive study.

References

Anderson JD, Schubert G, Jacobson RA et al (1998) Europa's differentiated internal structure: inferences from four galileo encounters. Science 281:2019–2022

Bills BG, Lemoine FG (1995) Gravitational and topographic isotropy of the earth, moon, mars, and venus. J Geophys Res 100(E12):26275. doi:10.1029/95JE02982

Boyce JM (2008) The smithsonian book of mars Konecky & Konecky, Old Saybrook, CT, p 107. ISBN 1-56852-714-4

Colombo OL (1984) The global mapping of gravity with two satellites. vol 7, no. 3. Netherlands Geodetic Commission, Publications on Geodesy, New Series

Drinkwater M, Haagmans R, Muzzi D et al (2007) The GOCE gravity mission: ESA's first core explorer. In: 3^{rd} GOCE user workshop, 6–8 November 2006, Frascati, pp 1–7. ESA SP-627

ESA (1999) Gravity field and steady-state ocean circulation mission Reports for mission selection, The four candidate earth explorer core missions, SP-1233(1). European Space Agency (July 1999)

Flokstra J, Cupurus R, Wiegerink RJ, van Essen MC (2009) A MEMS-based gravity gradiometer for future planetary missions. Cryogenics 49(11):665–668. ISSN 0011-2275

Guillot T, Stevenson DJ, Hubbard WB, Saumon D (2004) Chapter 3: The interior of jupiter. In: Bagenal F, Dowling TE, McKinnon WB (eds) Jupiter: the planet, satellites and magnetosphere. Cambridge University Press, Cambridge. ISBN 0-521-81808-7

Iess L, Rappaport NJ, Jacobson RA et al (2010) Gravity field, shape, and moment of inertia of titan. Science 327:1367–1369

Matsumoto K, Goossens S, Ishihara Y et al (2010) An improved lunar gravity field model from SELENE and historical tracking data: Revealing the farside gravity features. J Geophys Res 115(E06007):1–20. doi:10.1029/2009JE003499

Mazarico E, Rowlands DD, Neumann GA et al (2012) Orbit determination of the lunar reconnaissance orbiter. J Geod 86:193–207. doi:10.1007/s00190-011-0509-4

MIT (2012) GRAIL Gravity recovery and interior laboratory. http://moon.mit.edu/overview.html. Last accessed 23 Nov 2012

NASA (2012a) GRAIL gravity recovery and interior laboratory. http://www.nasa.gov/mission_pages/grail/main/. Last accessed 8 Oct 2012

NASA (2012b) Lunar and planetary science. http://nssdc.gsfc.nasa.gov/planetary. Last accessed 25 Oct 2012

Pail R, Bruinsma S, Migliaccio F et al (2011) First GOCE gravity field models derived by three different approaches. J Geod 85:819–843. doi: 10.1007/s00190–011–0467–x)

Porco CC, Helfenstein P, Thomas PC et al (2006) Cassini observes the active south pole of enceladus. Science 311:1393–1401. doi:10.1126/science.1123013

Rappaport NJ, Iess L, Wahr J et al (2008) Can cassini detect a subsurface ocean in titan from gravity measurements? Icarus 194:711–720

Reigber Ch, Schwintzer P, Lühr H (1999) The CHAMP geopotential mission. In: Marson I, Sünkel H (ed) Bollettino di Geofisica Teorica e Applicata, vol 40, no. 3–4. pp. 285–289. Istituto Nazionale di Oceanografia e di Geofisica Sperimentale - OHS, Trieste, Italy. ISSN 0006-6729

Rosborough GW (1987) Radial, transverse, and normal satellite position perturbations due to the geopotential. Celest Mech 40:409–421

Rosenblatt P, Rivoldini A, Rambaux N, Dehant V (2011) Mass distribution inside Phobos: a key observational constraint for the origin of Phobos. In: EPSC Abstracts, vol 6, EPSC-DPS2011-761, EPSC-DPS Joint Meeting 2011

Schrama EJO (1991) Gravity field error analysis: Applications of global positioning system receivers and gradiometers on low orbiting platforms. J Geophys Res 96(B12):20041–20051

Smith DE, Zuber MT, Sun X et al (2006) Two-way laser link over interplanetary distance. Science 311(53). doi: 10.1126/science.1120091

Smith DE, Zuber MT, Torrence MH et al (2009) Time variations of Mars' gravitational field and seasonal changes in the masses of the polar ice caps. J Geophys Res 114(E05002):1–15 doi:10.1029/2008JE003267

Tapley BD, Reigber Ch (1999) GRACE: A satellite-to-satellite tracking geopotential mapping mission. In: Marson I, Sünkel H (eds) Bollettino di Geofisica Teorica e Applicata, vol 40, no 3–4, p 291. Istituto Nazionale di Oceanografia e di Geofisica Sperimentale - OHS, Trieste, Italy. ISSN 0006-6729

Visser PNAM (2005) Low-low satellite-to-satellite tracking: Applicability of analytical linear orbit perturbation theory. J Geod 79(1–3):160–166

Sensitivity of Simulated LRO Tracking Data to the Lunar Gravity Field

Andrea Maier and Oliver Baur

Abstract

The Lunar Reconnaissance Orbiter (LRO) is the first spacecraft in interplanetary space routinely tracked with 1-way optical laser ranges. Therefore, the mission is a suitable testbed to investigate the potential of laser ranging for precise orbit determination and lunar gravity field recovery compared to radiometric observations. As a first step, we simulated laser ranges and range-rates from various ground stations to LRO. The synthetic data were used to retrieve the satellite orbit. Further, we estimated three sets of spherical harmonic coefficients representing the lunar gravity field: one set based on laser ranges, one set based on range-rates, and one set based on laser ranges and range-rates. We found laser ranging to be capable of recovering the coefficients up to degree and order $\approx$ 12 without applying regularization. From a joint inversion we conclude that laser ranges only slightly improve the findings obtained from range-rates. Preliminary real data results based on twelve days of laser ranging observations show a range residual root mean square (RMS) value of 2.3 m. The RMS value in total position between our solution and a published LRO orbit derived from radiometric data and altimetric crossovers is about 550 m.

Keywords

Laser ranging • LRO • Lunar gravity field • Orbit determination

1 Introduction

The first efforts to gain a better understanding of the Moon's gravity field from satellite data started in 1966 with the launch of the lunar orbiter mission Luna-10. It was followed by further satellites of the Luna program, the Lunar Orbiters, the subsatellites of Apollo, and the more recent missions Clementine and Lunar Prospector (LP). A detailed gravity field model was obtained from tracking data to LP due to its low average altitude of 100 and 30 km during the nominal and the extended mission phase, respectively (Konopliv et al. 2001).

The 1:1 spin-orbit resonance of the Earth-Moon system does not allow direct tracking over the Moon's farside. This severely hampers gravity field determination as the coefficients of higher degree and order (d/o) have unrealistically high amplitudes if no a priori information is used; on the other hand, regularization induces biases to the solution (Floberghagen 2002).

The Japanese SELENE mission provided the first global data set of the Moon by incorporating three satellites: a main orbiter in a circular orbit and two sub-satellites in elliptical orbits. In addition to classical radiometric tracking data, 4-way Doppler tracking between a ground station, the main orbiter, and a sub-satellite was employed as well as Very Long Baseline Interferometry between the sub-satellites and two ground stations (Goossens et al. 2011; Kikuchi et al. 2009).

A. Maier (✉)
Astronomical Institute, University of Bern, Sidlerstrasse 5, 3012 Bern, Switzerland

Space Research Institute, Austrian Academy of Sciences, Schmiedlstraße 6, 8042 Graz, Austria
e-mail: andrea.maier@aiub.unibe.ch

O. Baur
Space Research Institute, Austrian Academy of Sciences, Schmiedlstraße 6, 8042 Graz, Austria

U. Marti (ed.), *Gravity, Geoid and Height Systems*, International Association of Geodesy Symposia 141,
DOI 10.1007/978-3-319-10837-7_42,

Table 1 LRO mission phases

Launch	2009-06-18
Cruise	2009-06-18 to 2009-06-23
Lunar orbit acquisition	2009-06-23
Commissioning	2009-06-23 to 2009-09-14
Nominal mission	2009-09-15 to 2010-09-15
Science mission	2010-09-16 to 2012-09-15
First extended science mission	2012-09-16 to 2014-09-15
Second extended science mission phase	since 2014-09-16

A further unique satellite mission, the Lunar Reconnaissance Orbiter (LRO), was launched in 2009 to prepare for future in-situ lunar exploration. This includes the development of high-resolution global topography maps of the lunar surface, the characterization of the radiation environment, and the assessment of potential resources (Chin et al. 2007). The mission phases are summarized in Table 1. LRO is the first satellite at the distance of the Moon routinely tracked with optical 1-way laser ranges in addition to radiometric techniques (Zuber et al. 2010). In 2005 first successful optical laser ranging experiments to MESSENGER and Mars GlobalSurveyor were accomplished (Neumann et al. 2006).

The orbit of LRO was designed as polar and near-circular with a mean altitude of 50 km during the polar mapping phase (late 2009 to late 2011). The eccentricity is bounded by station keeping maneuvers performed every four weeks. The orbital period is 113 min.

LRO has a Lunar Orbiter Laser Altimeter (LOLA) aboard with a nominal ranging accuracy of 10 cm (Zuber et al. 2010). Due to this high accuracy, the orbit determination must be as accurate as possible.

This contribution focuses on LRO orbit determination and gravity field recovery from optical laser ranges. The work is motivated by the use of this technique for interplanetary spacecraft tracking. We assess the potential of laser observations against orbit and gravity field determination from Doppler range-rates. For this purpose, we simulated idealized observations to LRO. As the simulations are supposed to reflect the basic characteristics of the real orbit, they lack the details of the pre-launch simulations by Rowlands et al. (2009).

The NASA software package GEODYN/SOLVE was used for data simulation, orbit determination, and gravity field parameter estimation (Pavlis et al. 2006).

2 Tracking Data

LRO tracking is mainly accomplished with a radio frequency link at S-band which results in ranges and range-rates with a nominal precision of 10 m ($1\,\sigma$) and 1 mm s^{-1} ($1\,\sigma$), respectively (Currier et al. 2007). S-band tracking is performed by

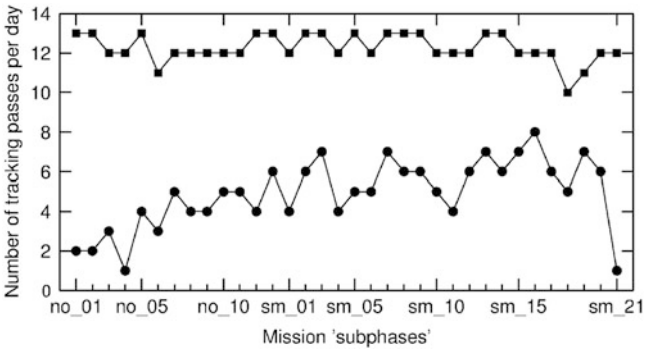

Fig. 1 Average number of Doppler passes (*squares*) and laser ranging passes (*circles*) per day for the nominal mission phase ('subphases' no_01 to no_13) and the science mission phase ('subphases' sm_01 to sm_21)

five stations, namely White Sands (New Mexico), Dongara (Australia), Weilheim (Germany), Kiruna (Sweden), and South Point (Hawaii). At least 30 min of each orbit is tracked via S-band. Orbits determined only from Doppler tracking are supposed to have an accuracy of about 10 m radially and 300 m in along-track and across-track directions (Zuber et al. 2010). However, since there is a high-accuracy altimeter aboard, the radial component needs to be reconstructed to the sub-meter-level.

LOLA can be used to accumulate crossovers, i.e. points on the lunar surface where spacecraft trajectories intersect. The difference in altitude at groundtrack intersection is minimized and acts like a constraint for the orbit solution (Rowlands et al. 2009; Mazarico et al. 2010). When altimetric crossovers are used in addition to radiometric observations, the average overlap RMS differences in total position decrease by approximately 20 % (cf. Table 3 in Mazarico et al. 2012).

To meet the accuracy requirement for the radial component, LRO is tracked with optical laser in addition to S-band. The 1-way time-of-flight measurements provide 1-way laser ranges with a precision of 10 cm (Smith et al. 2008). The primary ground station is located in Greenbelt, Maryland. Several stations from the International Laser Ranging Service (Pearlman et al. 2002) support laser tracking to LRO, such as Yarragadee (Australia), McDonald (Texas), Grasse (France), and Herstmonceux (UK).

Figure 1 compares the number of Doppler passes against the number of laser ranging passes.[1] Although Doppler tracking is the primary data source, the orbital accuracy requirements can only be met by combining S-band tracking, laser ranging, and altimetric crossovers (Zuber et al. 2010). The spatial coverage of laser ranges is shown in Fig. 2.

[1] ftp://pds-geosciences.wustl.edu; last access February 6, 2013.

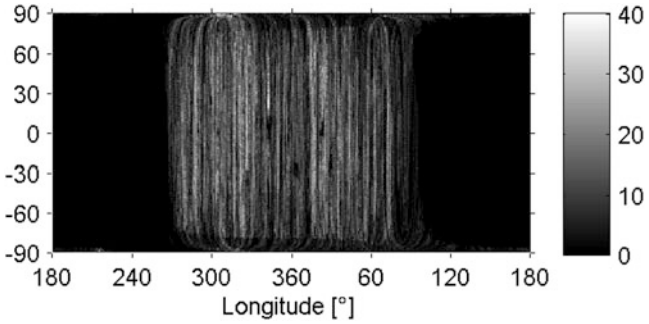

Fig. 2 Total number of laser ranges to LRO during the nominal mission phase, averaged over a 1° × 1° grid. The western limb of the Moon as seen from the Earth is located at 270°

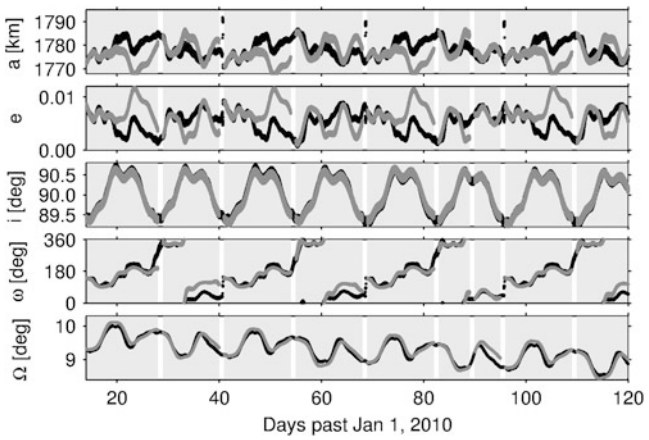

Fig. 3 Kepler elements of simulated LRO orbit considering gravity field coefficients up to d/o 12 (*gray*) compared to Kepler elements derived from SPICE (*black*). Semimajor axis (a), eccentricity (e), inclination (i), and argument of perigee (ω) are expressed in the body-fixed reference frame. Right ascension (Ω) is expressed in the J2000 reference frame. *Light gray sections* indicate individual arcs

3 Simulation Studies

A series of simulation studies has been conducted to investigate to which extent the gravity field recovery from LRO tracking data is influenced by

- the tracking data type,
- the noise level,
- the distribution of the tracking data on the lunar surface, and
- the number of estimated gravity field coefficients.

An LRO trajectory was simulated that should reflect the basic characteristics of the 'true' trajectory. The initial state vector was obtained using the SPICE toolkit (Acton 1996) within the MATLAB environment.[2] The only perturbation taken into account for the LRO orbit simulation was the lunar gravity field. Measurement biases, the time drift rate and the frequency aging rate of the LRO clock, and the instability of the ground station clocks, which complicate the processing of real tracking data (Mazarico et al. 2012), were not considered in our simulations. JGL165P1[1] (Konopliv et al. 2001) served as the 'true' gravity field model. The maximum d/o considered for simulating the observations was 5, 12, and 16. A higher resolution was not taken into account because beyond d/o 16 the normal equation system turned to become ill-conditioned and we wanted to avoid regularization. The typical arc length was about two weeks as this is the time span not interrupted by maneuvers. About 100 days of LRO orbit was simulated. The simulated trajectory is in good agreement with the 'true' trajectory from SPICE (Fig. 3). The differences between simulated and 'true' trajectory decrease with increasing maximum resolution for orbit simulation.

Laser ranges and Doppler data have been simulated from three stations each (Table 2) that observed 82 % of all laser ranges and 90 % of all Doppler range-rates during the nominal mission phase. The number of simulated observations is listed in Table 3. Observations have been simulated using two types of spatial coverage modes. The first mode (referred to as 'even coverage') generates observations on the nearside as well as on the farside of the Moon. The even coverage mode

Table 2 Simulation of tracking data

	Laser ranges	Doppler range-rates
Station name	Greenbelt, Maryland (GO1L)	White Sands, New Mexico (WS1S)
	Yaragadee, Australia (YARL)	Dongara, Australia (USPS)
	McDonald, Texas (MDOL)	Kiruna, Sweden (KU1S)
Elevation cut-off angle	20°	0°
Interval between	5 s (even coverage)	5 s (even coverage)
Observations	varying (uneven coverage)	varying (uneven coverage)
Coverage mode	even/uneven	even/uneven
Noise level	0 cm/10 cm	0 mm s^{-1}/1 mm s^{-1}

Table 3 Approximate number of simulated observations during a time span of about 100 days

Coverage mode	Number (Laser ranges)	Number (Doppler)
Even	568,000 (GO1L)	867,000 (USPS)
	629,000 (YARL)	854,000 (WS1S)
	609,000 (MDOL)	815,000 (KU1S)
	$\sum = 1,806,000$	$\sum = 2,536,000$
Uneven	64,000 (GO1L)	135,000 (USPS)
	46,000 (YARL)	377,000 (WS1S)
	23,000 (MDOL)	58,000 (KU1S)
	$\sum = 133,000$	$\sum = 570,000$

[2] http://naif.jpl.nasa.gov/naif/toolkit_MATLAB.html.

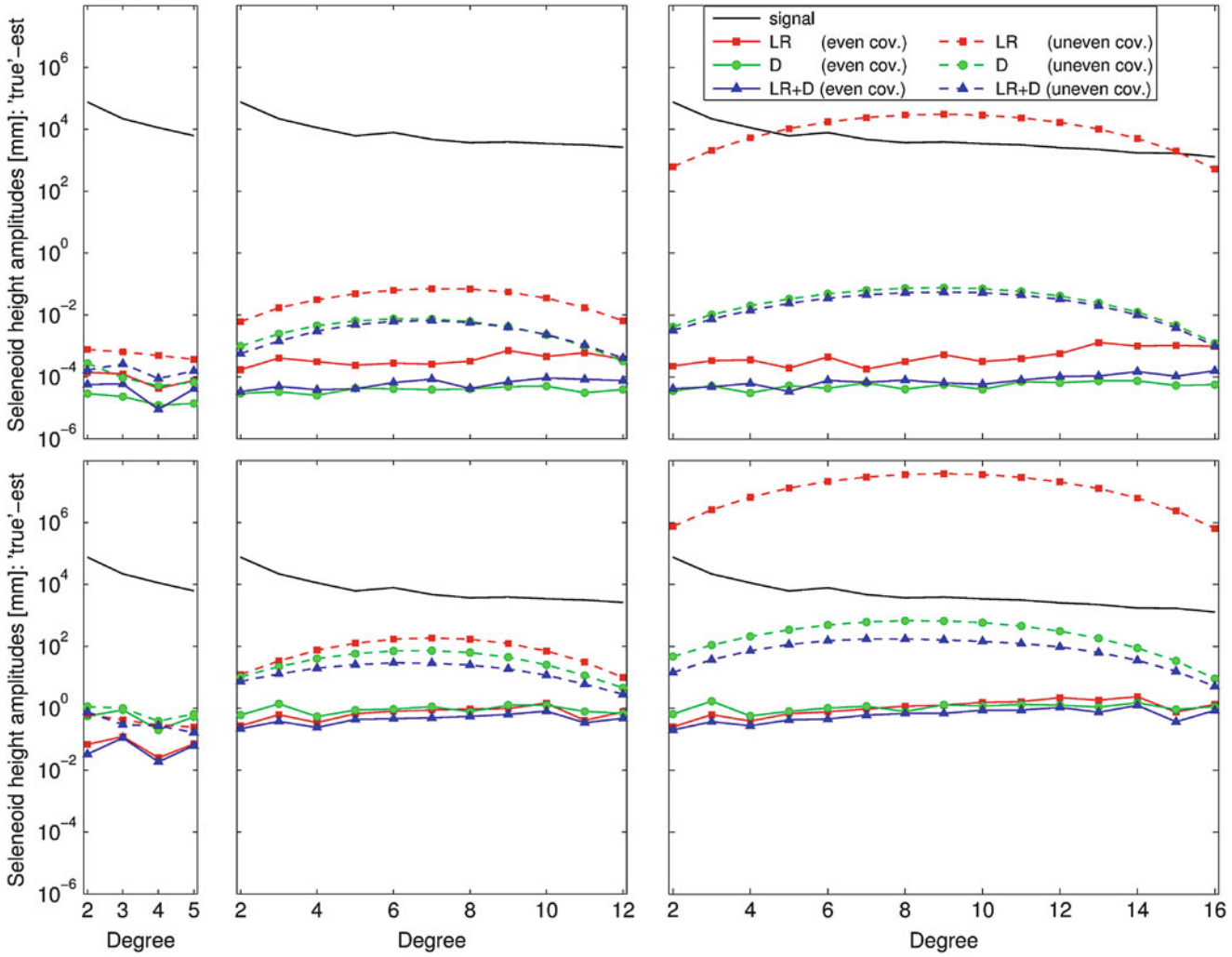

Fig. 4 Differences between 'true' and reconstructed coefficients based on simulated laser ranges only (*red*), Doppler data only (*green*), and laser ranges and Doppler data (*blue*) expressed in selenoid height amplitudes. Results are based on even (*solid lines*) and uneven coverage mode (*dashed lines*). Top and bottom panels represent the results using zero noise level and nonzero noise level, respectively. The left, middle, right panels show the results for coefficients estimated to d/o 5, 12, and 16, respectively (Color figure online)

is only of theoretical interest; it assumes globally available direct tracking data. The second mode (referred to as 'uneven coverage') represents the real case: laser ranges and Doppler data were only simulated on the nearside of the Moon. In contrast to the pre-launch simulations performed by Rowlands et al. (2009), we were able to simulate observations during the periods when the stations actually tracked the spacecraft. See Table 2 for more details about the simulation settings.

The presented simulation studies are closed-loop scenarios aiming at the recovery of the 'true' gravity field coefficients. A perfect orbit was generated by using one and the same gravity field model (JGL165P1) for both orbit simulation and a priori model for the parameter estimation process. Omission errors were not taken into account. Ideally, the differences between 'true' and reconstructed gravity field coefficients are zero. Figure 4 depicts these differences in terms of selenoid height amplitudes. Significantly better results could be achieved with global tracking data than with data solely distributed over the nearside. In case of uneven coverage, the level of precision degrades rapidly with increasing number of estimated coefficients. If the observations are superposed with white noise, the amplitudes are generally well above the noise-free solutions. Figure 4 suggests that it might be possible to estimate coefficients up to d/o 16 by combining laser ranges and Doppler data without applying any regularization. However, the lack of farside data notably hampers the parameter estimation even for coefficients of low d/o. In summary, one can deduce from Fig. 4 that the level of precision degrades with (i) increasing number of estimated coefficients, (ii) decreasing number of simulated observations, and (iii) increasing noise level.

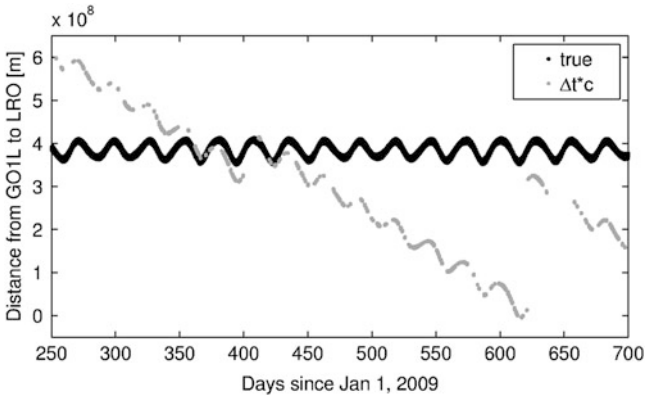

Fig. 5 Distances from GO1L to LRO computed from the normal point files (*gray*) and from the 'true' satellite orbit retrieved from SPICE (*black*)

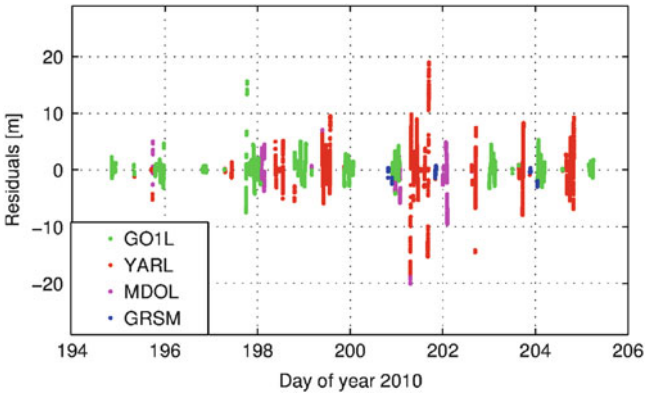

Fig. 6 Residuals between observed and computed ranges (Color figure online)

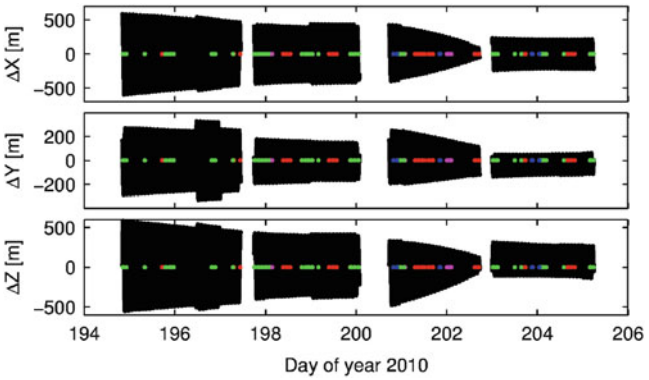

Fig. 7 Difference between the 'true' SPICE orbit and the estimated orbit (*black*). The observation periods for each station are according to the color coding in Fig. 6 (Color figure online)

4 Real Data Analysis

Laser ranges to LRO are available in terms of 5-seconds normal points. The data files[1] we processed contain the time of laser emittance at the ground station and the time of arrival at the spacecraft, among other useful information. By multiplying the elapsed time (Δt) with the velocity of light (c), the runtime of the pulse can be converted to a 1-way distance. Figure 5 shows an example for the distances derived from the observation files compared to the distances from the station to the 'true' satellite positions.[3] The non-synchronous clocks at the station and aboard the spacecraft impose a huge bias, a drift, and a drift rate on the observations.

As a first try of real data analysis, we processed laser ranges from July 13 to July 24, 2010. Normal points are available from GO1L, YARL, MDOL, and GRSM (Grasse, France). The arc length varies between two and three days. On average, 4,000 normal points are available per arc. An elevation cut-off angle of 20° was used. LP150Q served as a priori gravity field model and the third-body gravitational potential was modeled as point masses for all planets of the solar system and the Sun. For each arc, a state vector, pass per pass measurement biases for each station, drift rate and aging rate of the LRO clock, and a solar radiation pressure coefficient (cannonball model) have been estimated.

The estimated drift rate varies between −21.2 and −21.07 m and is similar to published values (Mao et al. 2011). The range residuals, i.e. the differences between observed and computed ranges, are depicted in Fig. 6. They show systematic effects because drift rate and aging rate are estimated only once per arc. The root mean square (RMS) value averaged over all arcs and all stations is 2.3 m. Our results agree with Mao et al. (2011) stating that the range residuals are nominally less than 10 m. In addition, we compared the 'true' LRO positions from SPICE with our preliminary results (Fig. 7). The RMS differences in total position is about 550 m.

Conclusions and Outlook

In order to assess the potential of laser ranging for interplanetary satellite missions, we investigated orbit determination and gravity field recovery from LRO tracking data. Concerning our simulation studies, future work will have to deal with omission error handling and the use of different gravity field models for orbit simulation and a priori information within the parameter estimation process. Despite of idealized assumptions, the simulation results (Sect. 3) clearly point to the relative contribution of each tracking type to gravity field determination. As expected, the best results are achieved by combining Doppler range-rates and laser ranges.

[3]The LRO positions retrieved from SPICE are based on radiometric tracking data and altimetric crossovers from July 13, 2009 to January 31, 2011 (Mazarico et al. 2012). Laser ranges are not yet integrated in this solution.

The processing of real tracking data has to be refined. We expect the range residuals and the orbit differences to decrease once rigorous data editing is performed, albedo is modeled, the cannonball model is exchanged for a satellite macro-model (Smith et al. 2008), and empirical accelerations are estimated. It has to be kept in mind though that laser ranges are considerably sparser compared to range-rates; as such, a straightforward comparison of orbits determined from laser ranges opposed to orbits determined from range-rates is hardly possible. Our preliminary results suggest a laser-based orbit accuracy of some few hundreds of meters.

It should be noted that the Gravity Recovery and Interior Laboratory mission provides a lunar gravity field model (Zuber et al. 2013) with much higher resolution compared to the potential of LRO. Nevertheless, laser ranging might be valuable to determine the very low-degree lunar gravity field coefficients and the lunar k_2 Love number. Most importantly, LRO is an interesting testbed to investigate and assess the benefit of laser ranging for deep-space applications.

Acknowledgements The software package GEODYN/SOLVE was kindly provided by the NASA Goddard Space Flight Center. We acknowledge helpful support by David D. Rowlands.

References

Acton CH (1996) Ancillary data services of NASA's navigation and ancillary information facility. Planet Space Sci 44(1):65–70

Chin G, Brylow S, Foote M, Garvin J, Kasper J, Keller J, Litvak M, Mitrofanov I, Paige D, Raney K, Robinson M, Sanin A, Smith D, Spence H, Spudis P, Stern SA, Zuber M (2007) Lunar reconnaissance orbiter overview: The instrument suite and mission. Space Sci Rev 129(4):391–419. doi:10.1007/s11214-007-9153-y

Currier SF, Clason RN, Midon MM, Schupler BR, Anderson ML (2007) NASA ground network support of the lunar reconnaissance orbiter. In: Ground system architectures workshop, Manhattan Beach, California, 26–30 March 2007. http://sunset.usc.edu/gsaw/gsaw2007/s6/schupler.pdf

Floberghagen R (2002) Lunar gravimetry: Revealing the far-side. In: Astrophysics and space science library, vol 273. Kluwer Academic, Netherlands

Goossens S, Matsumoto K, Rowlands DD, Lemoine FG, Noda H, Araki H (2011) Orbit determination of the SELENE satellites using multi-satellite data types and evaluation of SELENE gravity field models. J Geod 85(8):487–504. doi:10.1007/s00190-011-0446-2

Kikuchi F, Liu Q, Hanada H, Kawano N, Matsumoto K, Iwata T, Goossens S, Asari K, Ishihara Y, Tsuruta S, Ishikawa T, Noda H, Namiki N, Petrova N, Harada Y, Ping J, Sasaki S (2009) Picosecond accuracy VLBI of the two subsatellites of SELENE (KAGUYA) using multifrequency and same beam methods. Radio Sci 44(2). doi:10.1029/2008RS003997

Konopliv A, Asmar SW, Carranza E, Sjogren WL, Yuan DN (2001) Recent gravity models as a result of the lunar prospector mission. Icarus 150(1):1–18. doi:10.1006/icar.2000.6573

Mao D, McGarry J, Torrence M, Neumann G, Mazarico E, Barker M, Sun X, Rowlands D, Golder J, Zagwodzki T, Cavanaugh J, Zuber M, Smith D (2011) Laser ranging experiment on lunar reconnaissance orbiter: Timing determination and orbit constraints. In: 17th International Workshop on Laser Ranging, Bad Kötzting, Germany, 16–20 May 2011. http://cddis.gsfc.nasa.gov/lw17/docs/papers/session13/02-Mao_LRO-LR_Kotzting2011_paper_final.pdf

Mazarico E, Neumann GA, Rowlands DD, Smith DE (2010) Geodetic constraints from multi-beam laser altimeter crossovers. J Geod 84(6):343–354. doi:10.1007/s00190-010-0379-1

Mazarico E, Rowlands DD, Neumann GA, Smith DE, Torrence MH, Lemoine FG, Zuber MT (2012) Orbit determination of the lunar reconnaissance orbiter. J Geod 86(3):193–207. doi:10.1007/s00190-011-0509-4

Neumann GA, Cavanaugh JF, Coyle DB, McGarry J, Smith DE, Sun X (2006) Laser ranging at interplanetary distances. In: 15th International Workshop on Laser Ranging, Canberra, 15–20 October 2006. http://cddis.gsfc.nasa.gov/lw15/docs/papers/LaserRangingatInterplanetaryDistances.pdf

Pavlis DE, Poulose SG, McCarthy JJ (2006) GEODYN operations manuals. Contractor Report, SGT Inc., Greenbelt

Pearlman MR, Degnan JJ, Bosworth JM (2002) The international laser ranging service. Adv Space Res 30(2):135–143. doi:10.1016/S0273-1177(02)00277-6

Rowlands DD, Lemoine FG, Chinn DS, Luthcke SB (2009) A simulation study of multi-beam altimetry for lunar reconnaissance orbiter and other planetary missions. J Geod 83(8):709–721. doi:10.1007/s00190-008-0285-y

Smith D, Zuber M, Lemoine F, Torrence M, Mazarico E (2008) Orbit determination of LRO at the moon. In: 16th International Workshop on Laser Ranging, Poznán, 13–17 October 2008. http://cddis.gsfc.nasa.gov/lw16/docs/presentations/sci_2_Smith.pdf

Zuber MT, Smith DE, Zellar RS, Neumann GA, Sun X, Katz RB, Kleyner I, Matuszeski A, McGarry JF, Ott MN, Ramos-Izquierdo LA, Rowlands DD, Torrence MH, Zagwodzki TW (2010) The lunar reconnaissance orbiter laser ranging investigation. Space Sci Rev 150:63–80. doi:10.1007/s11214-009-9511-z

Zuber MT, Smith DE, Watkins MM, Asmar SW, Konopliv AS, Lemoine FG, Melosh HJ, Neumann GA, Phillips RJ, Solomon SC, Wieczorek MA, Williams JG, Goossens SJ, Kruizinga G, Mazarico E, Park RS, Yuan DN (2013) Gravity field of the moon from the gravity recovery and interior laboratory (GRAIL) mission. Science 339(6120):668–671. doi:10.1126/science.1231507

List of Reviewers

Jonas Ågren
Matthew James Amos
Ole Baltazar Andersen
Dimitrios N. Arabelos
Alireza A. Ardalan
Joseph Awange
Franz Barthelmes
Tomislav Bašić
Ludovico Biagi
Mirjam Bilker-Koivula
Heike Bock
Sylvain Bonvalot
Alessandra Borghi
Johannes Bouman
Sean L. Bruinsma
Daniela Carrion
Vicki Childers
Sten Claessens
Róbert Čunderlík
Nadim Dayoub
Silvio De Freitas
Franck Pereira Dos Santos
Hermann Drewes
Artu Ellmann
Georgia Fotopoulos
Reinhard Falk
William Edward Featherstone
Rune Floberghagen
Christoph Foerste
Rene Forsberg
Oliver Francis
Yoichi Fukuda
Christian Gerlach
Alessandro Germak
Erik W. Grafarend
Vassilios Grigoriadis
Thomas Gruber
Matija Herceg
Christian Hirt
Petr Holota
Jianliang Huang
Urs Hugentobler
Adrian Jäggi
Thomas Jahr
Zhiheng Jiang
Shuanggen Jin
William Kearsley
Steve C. Kenyon
Ali Kilicoglu
K.-R. Koch
Christopher Kotsakis
Jan Kouba
Jan Krynski
Norbert Kühtreiber
Martin Lederer
Frank Lemoine
Verena Lieb
Urs Marti
Gwendoline Metivier
Bruno Meurers
Ulrich Meyer
Vadim Nagornyi
Pavel Novak
Maria Cristina Pacino
Spiros Pagiatakis
Roland Pail
Vojtech Pálinkáš
Isabelle Panet
Nikolaos Konstantinos Pavlis
Bjørn Ragnvald Pettersen
Markku Poutanen
Elena Rangelova
Mirko Reguzzoni
Tilo Reubelt
John C. Ries
Daniel R. Roman
Axel Rülke
Martina Sacher
Daniele Sampietro
Laura Sánchez
Marcelo Santos
Uwe Schäfer

U. Marti (ed.), *Gravity, Geoid and Height Systems*, International Association of Geodesy Symposia 141,
DOI 10.1007/978-3-319-10837-7, © Springer International Publishing Switzerland 2014

Ulrich Schreiber
Wolf-Dieter Schuh
Josef Sebera
C.K. Shum
Michael G. Sideris
Lars E. Sjöberg
Nico Sneeuw
Dag Solheim
Holger Steffen
Rebekka Steffen
Gabriel Strykowski
Alex Sun
Robert Tenzer
Ludger Timmen
Claudia Tocho
Carl Christian Tscherning
Dimitrios Tsoulis
Ilias Tziavos
Michel Van Camp
Tonie van Dam
Georgios S. Vergos
Martin Vermeer
Isabelle Vigo
Pieter N.A.M. Visser
Leonid F. Vitushkin
Christian Voigt
X.W. Wang
Yan Ming Wang
Hartmut Wziontek
Philip Woodworth
Jianguo Yan
Hasan Yildiz
Norbert Zehentner
M. Zhong

Index

U. Marti (ed.), *Gravity, Geoid and Height Systems*, International Association of Geodesy Symposia 141,
DOI 10.1007/978-3-319-10837-7, © Springer International Publishing Switzerland 2014